



Journal of Engineering for Gas Turbines and Power

Published Quarterly by ASME

VOLUME 126 • NUMBER 2 • APRIL 2004

TECHNICAL PAPERS

Gas Turbines: IGTI Scholar Lecture

- 205 Millimeter-Scale, Micro-Electro-Mechanical Systems Gas Turbine Engines (2003-GT-38866)
Alan H. Epstein

Fuels and Combustion Technology

- 227 Reducing Grid Dependency in Droplet Collision Modeling
David P. Schmidt and Christopher J. Rutland
- 234 The Selective Non-Catalytic Removal (SNCR) of Nitric Oxides From Engine Exhaust Streams: Comparison of Three Processes
Jerald A. Caton and Zhiyong Xia
- 241 A Mathematical Model for Schlieren and Shadowgraph Images of Transient Expanding Spherical Thin Flames
Farzan Parsinejad, Matyas Matio, and Mohamad Metghalchi
- 248 Development of the Radially Stratified Flame Core Low NO_x Burner: From Fundamentals to Industrial Applications
J. M. Beér, M. A. Toqan, J. M. Haynes, and R. W. Borio
- 254 Combustion Structures in Lifted Ethanol Spray Flames
Stephen K. Marley, Eric J. Welle, and Kevin M. Lyons

Gas Turbines: Aircraft Engine

- 258 Preliminary Gas Turbine Design Using the Multidisciplinary Design System MOPEDS (2002-GT-30496)
P. Jeschke, J. Kurzke, R. Schaber, and C. Riegler
- 265 A Computer Code for Gas Turbine Engine Weight and Disk Life Estimation (2002-GT-30500)
Michael T. Tong, Ian Halliwell, and Louis J. Ghosn

Gas Turbines: Combustion and Fuels

- 271 On the Use of Helmholtz Resonators for Damping Acoustic Pulsations in Industrial Gas Turbines (2001-GT-039)
V. Bellucci, C. Paschereit, P. Flohr, and F. Magni
- 276 Flashback in a Swirl Burner With Cylindrical Premixing Zone (2001-GT-054)
J. Fritz, M. Kröner, and T. Sattelmayer
- 284 Fuel-Cooled Thermal Management for Advanced Aeroengines (2002-GT-30070)
He Huang, Louis J. Spadaccini, and David R. Sobel

Gas Turbines: Cycle Innovations

- 294 Introduction and Performance Prediction of a Nutating-Disk Engine (1999-GT-279)
T. Korakianitis, L. Meyer, M. Boruta, and H. E. McCormick
- 300 Pre-integrated Nonequilibrium Combustion-Response Mapping for Gas Turbine Emissions (2001-GT-386)
T. Korakianitis, R. Dyer, and N. Subramanian

(Contents continued on inside back cover)

This journal is printed on acid-free paper, which exceeds the ANSI Z39.48-1992 specification for permanence of paper and library materials. ™
 85% recycled content, including 10% post-consumer fibers.

Editor

LEE S. LANGSTON (2006)

Assistant to the Editor

LIZ LANGSTON

Associate Editors

Fuels and Combustion Technologies

S. GOLLAHALLI (2004)

Internal Combustion Engines

D. ASSANIS (2005)

Nuclear

R. DUFFY (2004)

International Gas Turbine Institute

IGTI Review Chair

E. BENVENUTI (2002)

H. R. SIMMONS (2003)

A. J. STRAZISAR (2004)

Combustion and Fuels

P. MALTE (2006)

Structures and Dynamics

N. ARAKERE (2004)

M. MIGNOLET (2005)

BOARD ON COMMUNICATIONS

Chair and Vice-President

OZDEN OCHOA

OFFICERS OF THE ASME

President, REGINALD VACHON

Executive Director, V. R. CARTER

Treasurer, R. E. NICKELL

PUBLISHING STAFF

Managing Director, Engineering

THOMAS G. LOUGHLIN

Director, Technical Publishing

PHILIP DI VIETRO

Production Coordinator

JUDITH SIERANT

Production Assistant

MARISOL ANDINO

Transactions of the ASME, Journal of Engineering for Gas Turbines and Power (ISSN 0742-4795) is published quarterly (Jan., April, July, Oct.) by The American Society of Mechanical Engineers, Three Park Avenue, New York, NY 10016. Periodicals postage paid at New York, NY and additional mailing offices. POSTMASTER: Send address changes to Transactions of the ASME, Journal of Engineering for Gas Turbines and Power, c/o THE AMERICAN SOCIETY OF MECHANICAL ENGINEERS, 22 Law Drive, Box 2300, Fairfield, NJ 07007-2300.

CHANGES OF ADDRESS must be received at Society headquarters seven weeks before they are to be effective. Please send old label and new address.

STATEMENT from By-Laws. The Society shall not be responsible for statements or opinions advanced in papers or ... printed in its publications (B7.1, par. 3).

COPYRIGHT © 2004 by the American Society of Mechanical Engineers. For authorization to photocopy material for internal or personal use under circumstances not falling within the fair use provisions of the Copyright Act, contact the Copyright Clearance Center (CCC), 222 Rosewood Drive, Danvers, MA 01923, Tel: 978-750-8400, www.copyright.com.

INDEXED by Applied Mechanics Reviews and Engineering Information, Inc. Canadian Goods & Services Tax Registration #126148048

- 306 Degradation Effects on Combined Cycle Power Plant Performance—Part III: Gas and Steam Turbine Component Degradation Effects (2002-GT-30513)
A. I. Zwebek and P. Pilidis
- 316 Inherent CO₂ Capture Using Chemical Looping Combustion in a Natural Gas Fired Power Cycle (2002-GT-30129)
Ø. Brandvoll and O. Bolland
- 322 Carbon Dioxide Emission Analysis With Energy Payback Effect (2002-GT-30448)
Motoaki Utamura
- Gas Turbines: Cycle Innovations, and Electric Power*
- 329 Small-Scale Well-Proven Inherently Safe Nuclear Power Conversion (2002-GT-30509)
G. A. K. Crommelin
- Gas Turbines: Electric Power*
- 334 Gas Turbine Test Parameters Corrections Including Operation With Water Injection (2002-GT-30466)
K. Mathioudakis
- Gas Turbines: Heat Transfer and Turbomachinery*
- 342 The Development of High-Performance Leaf Seals (2002-GT-30243)
H. Nakane, A. Maekawa, E. Akita, K. Akagi, T. Nakano, S. Nishimoto, S. Hashimoto, T. Shinohara, and H. Uehara
- Gas Turbines: Industrial and Cogeneration*
- 351 Effect of Inlet Air Cooling by Ice Storage on Unit Sizing of a Gas Turbine Cogeneration Plant (2002-GT-30484)
Ryohei Yakoyama and Koichi Ito
- Gas Turbines: Microturbines and Small Turbomachinery*
- 358 Microscale Radial-Flow Compressor Impeller Made of Silicon Nitride: Manufacturing and Performance (2003-GT-38933)
Sangkyun Kang, James P. Johnston, Toshiyuki Arima, Minoru Matsunaga, Hideaki Tsuru, and Friedrich B. Prinz
- Gas Turbines: Structures and Dynamics*
- 366 On the Control of Synchronous Vibration in Rotor/Magnetic Bearing Systems Involving Auxiliary Bearing Contact (2002-GT-30292)
P. S. Keogh, M. O. T. Cole, M. N. Sahinkaya, and C. R. Burrows
- 373 Neural Network Emulation of a Magnetically Suspended Rotor (2002-GT-30294)
A. Escalante, V. Guzmán, M. Parada, L. Medina, and S. E. Diaz
- 385 Load History Effects on Fretting Contacts of Isotropic Materials (2002-GT-30297)
P. T. Rajeev, H. Murthy, and T. N. Farris
- 391 Critical Plane Fatigue Modeling and Characterization of Single Crystal Nickel Superalloys (2002-GT-30300)
Rajiv A. Naik, Daniel P. DeLuca, and Dilip M. Shah
- 401 Dynamic Response of a Hydrodynamic Thrust Bearing-Mounted Rotor (2002-GT-30314)
T. N. Shiau, K. S. Hsu, and J. R. Chang
- 408 Dynamic Response of Squeeze Film Dampers Operating With Bubbly Mixtures (2002-GT-30317)
Luis San Andres and Oscar C. De Santiago
- 416 The Identification of the Unbalance of a Flexible Rotating Machine From a Single Rundown (2002-GT-30420)
A. W. Lees, J. K. Sinha, and M. I. Friswell
- Internal Combustion Engines*
- 422 A Model for Droplet Vaporization for Use in Gasoline and HCCI Engine Applications
Youngchul Ra and Rolf D. Feitz
- 429 Cycle-Resolved NO Measurements in a Two-Stroke Large-Bore Natural Gas Engine
Paulius V. Puzinauskas, Daniel B. Olsen, and Bryan D. Willson

ANNOUNCEMENTS

- 442 Arthur H. Lefebvre—In Memoriam
- 443 Information for Authors

(Contents continued)

Journal of Engineering for Gas Turbines and Power

APRIL 2004

Volume 126, Number 2

The ASME Journal of Engineering for Gas Turbines and Power is abstracted and indexed in the following:

AESIS (Australia's Geoscience, Minerals, & Petroleum Database), Applied Science & Technology Index, AMR Abstracts Database, Aquatic Sciences and Fisheries Abstracts, Civil Engineering Abstracts, Compendex (The electronic equivalent of Engineering Index), Computer & Information Systems Abstracts, Corrosion Abstracts, Current Contents, Engineered Materials Abstracts, Engineering Index, Enviroline (The electronic equivalent of Environment Abstracts), Environment Abstracts, Environmental Science and Pollution Management, Fluidex, INSPEC, Mechanical & Transportation Engineering Abstracts, Mechanical Engineering Abstracts, METADEX (The electronic equivalent of Metals Abstracts and Alloys Index), Pollution Abstracts, Referativnyi Zhurnal, Science Citation Index, SciSearch (The electronic equivalent of Science Citation Index), Shock and Vibration Digest

Millimeter-Scale, Micro-Electro-Mechanical Systems Gas Turbine Engines

Alan H. Epstein
Gas Turbine Laboratory
Massachusetts Institute of Technology
Cambridge, MA 01239
e-mail: Epstein@mit.edu

The confluence of market demand for greatly improved compact power sources for portable electronics with the rapidly expanding capability of micromachining technology has made feasible the development of gas turbines in the millimeter-size range. With airfoil spans measured in 100's of microns rather than meters, these "microengines" have about 1 millionth the air flow of large gas turbines and thus should produce about one millionth the power, 10–100 W. Based on semiconductor industry-derived processing of materials such as silicon and silicon carbide to submicron accuracy, such devices are known as micro-electro-mechanical systems (MEMS). Current millimeter-scale designs use centrifugal turbomachinery with pressure ratios in the range of 2:1 to 4:1 and turbine inlet temperatures of 1200–1600 K. The projected performance of these engines are on a par with gas turbines of the 1940s. The thermodynamics of MEMS gas turbines are the same as those for large engines but the mechanics differ due to scaling considerations and manufacturing constraints. The principal challenge is to arrive at a design which meets the thermodynamic and component functional requirements while staying within the realm of realizable micromachining technology. This paper reviews the state of the art of millimeter-size gas turbine engines, including system design and integration, manufacturing, materials, component design, accessories, applications, and economics. It discusses the underlying technical issues, reviews current design approaches, and discusses future development and applications. [DOI: 10.1115/1.1739245]

Introduction

For most of the 60-year-plus history of the gas turbine, economic forces have directed the industry toward ever larger engines, currently exceeding 100,000 lbs of thrust for aircraft propulsion and 400 MW for electric power production applications. In the 1990s, interest in smaller-size engines increased, in the few hundred pound thrust range for small aircraft and missiles and in the 20–250 kW size for distributed power production (popularly known as "microturbines"). More recently, interest has developed in even smaller size machines, 1–10 kW, several of which are marketed commercially, [1,2]. Gas turbines below a few hundred kilowatts in size generally use centrifugal turbomachinery (often derivative of automotive turbocharger technology in the smaller sizes), but are otherwise very similar to their larger brethren in that they are fabricated in much the same way (cast, forged, machined, and assembled) from the same materials (steel, titanium, nickel superalloys). Recently, manufacturing technologies developed by the semiconductor industry have opened a new and very different design space for gas turbine engines—one that enables gas turbines with diameters of millimeters rather than meters, with airfoil dimensions in microns rather than millimeters. These shirt-button-sized gas turbine engines are the focus of this review.

Interest in millimeter-scale gas turbines is fueled by both a technology push and a user pull. The technology push is the development of micromachining capability based on semiconductor manufacturing techniques. This enables the fabrication of complex small parts and assemblies—devices with dimensions in the 1–10,000 μm size range with submicron precision. Such parts are produced with photolithographically defined features and many can be made simultaneously, offering the promise of low produc-

tion cost in large-scale production. Such assemblies are known in the U.S. as micro-electrical-mechanical systems (MEMS) and have been the subject of thousands of publications over the last two decades, [3]. In Japan and Europe, devices of this type are known as "microsystems," a term which may encompass a wider variety of fabrication approaches. Early work in MEMS focused on sensors and simple actuators, and many devices based on this technology are in large-scale production, such as pressure transducers and airbag accelerometers for automobiles. More recently, fluid handling is receiving attention. For example, MEMS valves are commercially available, and there are many emerging biomedical diagnostic applications. Also, chemical engineers are pursuing MEMS chemical reactors (chemical plants) on a chip, [4].

User pull is predominantly one of electric power. The proliferation of small, portable electronics—computers, digital assistants, cell phones, GPS receivers, etc.—requires compact energy supplies. Increasingly, these electronics demand energy supplies whose energy and power density exceed that of the best batteries available today. Also, the continuing advance in microelectronics permits the shrinking of electronic subsystems of mobile devices such as ground robots and air vehicles. These small, and in some cases very small, mobile systems require increasingly compact power and propulsion. Hydrocarbon fuels burned in air have 20–30 times the energy density of the best current lithium chemistry-based batteries, so that fuelled systems need only be modestly efficient to compete well with batteries.

Given the need for high power density energy conversion in very small packages, a millimeter-scale gas turbine is an obvious candidate. The air flow through gas turbines of this size is about six orders of magnitude smaller than that of the largest engines and thus they should produce about a million times less power, 10–100 watts with equivalent cycles. Work first started on MEMS approaches in the mid 1990s, [5–7]. Researchers rapidly discovered that gas turbines at these small sizes have no fewer engineering challenges than do conventional machines and that many of the solutions evolved over six decades of technology development do not apply in the new design space. This paper reviews work on

Contributed by the International Gas Turbine Institute (IGTI) of THE AMERICAN SOCIETY OF MECHANICAL ENGINEERS for publication in the ASME JOURNAL OF ENGINEERING FOR GAS TURBINES AND POWER. Paper presented at the International Gas Turbine and Aeroengine Congress and Exhibition, Atlanta, GA, June 16–19, 2003, Paper No. 2003-GT-38866. Manuscript received by IGTI, October 2002, final revision, March 2003. Associate Editor: H. R. Simmons.

MEMS gas turbine engines for propulsion and power production. It begins with a short discussion of scaling and preliminary design considerations, and then presents a concise overview of relevant MEMS manufacturing techniques. In more depth, it examines the microscale implications for cycle analysis, aerodynamic and structural design, materials, bearings and rotor dynamics, combustion, and controls and accessories. The gas turbine engine as a system is then considered. This review then discusses propulsion and power applications and briefly looks at derivative technologies such as combined cycles, cogeneration, turbopumps, and rocket engines. The paper concludes with thoughts on future developments.

Thermodynamic and Scaling Considerations

Thermal power systems encompass a multitude of technical disciplines. The architecture of the overall system is determined by thermodynamics while the design of the system's components is influenced by fluid and structural mechanics and by material, electrical and fabrication concerns. The physical constraints on the design of the mechanical and electrical components are often different at microscale than at more familiar sizes so that the optimal component and system designs are different as well. Conceptually, any of the thermodynamic systems in use today could be realized at microscale. Brayton (air) cycle and the Rankine (vapor) cycle machines are steady flow devices while the Otto, [8], Diesel, and Stirling cycles are unsteady engines. The Brayton power cycle (gas turbine) is superior based on considerations of power density, simplicity of fabrication, ease of initial demonstration, ultimate efficiency, and thermal anisotropy.

A conventional, macroscopic gas turbine generator consists of a compressor, a combustion chamber, and a turbine driven by the combustion exhaust that powers the compressor. The residual enthalpy in the exhaust stream provides thrust or can power an electric generator. A macroscale gas turbine with a meter-diameter air intake area generates power on the order of 100 MW. Thus, tens of watts would be produced when such a device is scaled to millimeter size if the power per unit of air flow is maintained. When based on rotating machinery, such power density requires combustor exit temperatures of 1200–1600 K; rotor peripheral speeds of 300–600 m/s and thus rotating structures centrifugally stressed to several hundred MPa since the power density of both turbomachinery and electrical machines scale with the square of the speed, as does the rotor material centrifugal stress; low friction bearings; tight geometric tolerances and clearances between rotating and static parts to inhibit fluid leakage (the clearances in large engines are maintained at about one part in 2000 of the diameter); and thermal isolation of the hot and cold sections.

These thermodynamic considerations are no different at micro than at macroscale. But the physics and mechanics influencing the design of the components do change with scale, so that the optimal detailed designs can be quite different. Examples of these differences include the viscous forces in the fluid (larger at microscale), usable strength of materials (larger at microscale), surface area-to-volume ratios (larger at microscale), chemical reaction times (invariant), realizable electric field strength (higher at microscale), and manufacturing constraints (limited mainly to two-dimensional, planar geometries given current microfabrication technology).

There are many thermodynamic and architectural design choices in a device as complex as a gas turbine engine. These involve tradeoffs among fabrication difficulty, structural design, heat transfer, and fluid mechanics. Given a primary goal of demonstrating that a high power density MEMS heat engine is physically realizable, MIT's research effort adopted the design philosophy that the first engine should be as simple as possible, with performance traded for simplicity. For example, a recuperated cycle, which requires the addition of a heat exchanger transferring heat from the turbine exhaust to the compressor discharge fluid, offers many benefits including reduced fuel consumption and re-

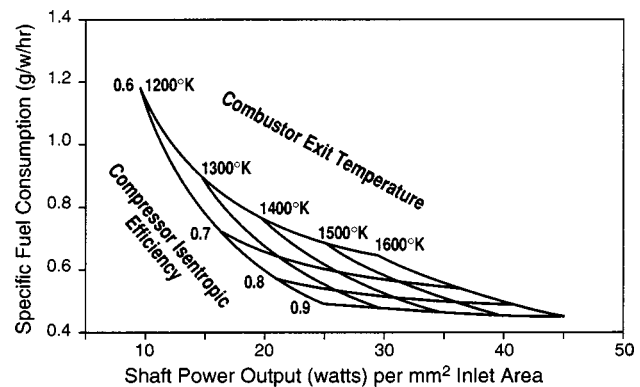


Fig. 1 Simple cycle gas turbine performance with H₂ fuel

laxed turbomachinery performance requirements, but it introduces additional design and fabrication complexity. Thus, the first designs are simple cycle gas turbines.

How big should a “micro” engine be? A micron, a millimeter, a centimeter? Determination of the optimal size for such a device involves considerations of application requirements, fluid mechanics and combustion, manufacturing constraints, and economics. The requirements for many power production applications favor a larger engine size, 50–100 W. Viscous effects in the fluid and combustor residence time requirements also favor larger engine size. Current semiconductor manufacturing technology places both upper and lower limits on engine size. The upper size limit is set mainly by etching depth capability, a few hundred microns at this time. The lower limit is set by feature resolution and aspect ratio. Economic concerns include manufacturing yield and cost. A wafer of fixed size (say, 200 mm diameter) would yield many more low power engines than high power engines at essentially the same manufacturing cost per wafer. (Note that the sum of the power produced by all of the engines on the wafer would remain constant at 1–10 kW.) When commercialized, applications and market forces may establish a strong preference here. For the first demonstrations of a concept, a minimum technical risk approach is attractive. Analysis suggested that fluid mechanics would be difficult at smaller scales, so the largest size near the edge of current microfabrication technology, about a centimeter in diameter, was chosen as a focus of MIT's efforts.

Performance calculations indicate that the power per unit air flow from the configuration discussed below is 50–150 W/(g/sec) of air flow (Fig. 1). For a given rotor radius, the air flow rate is limited primarily by airfoil span as set by stress in the turbine blade roots. Calculations suggest that it might be possible to improve the specific work, fuel consumption, and air flow rate in later designs with recuperators to realize microengines with power outputs of as much as 50–100 W, power specific fuel consumption of 0.3–0.4 g/w-hr, and thrust-to-weight ratios of 100:1. This level of specific fuel consumption approaches that of current small gas turbine engines but the thrust-to-weight ratio is 5–10 times better than that of the best aircraft engine. The extremely high thrust-to-weight ratio is simply a result of the so-called “cube-square law.” All else being the same as the engine is scaled down linearly, the air flow and thus the power decreases with the intake area (the square of the linear size) while the weight decreases with the volume of the engine (the cube of the linear size), so that the power-to-weight ratio increases linearly as the engine size is reduced. Detailed calculations show that the actual scaling is not quite this dramatic since the specific power is lower at the very small sizes, [5]. A principal point is that a micro-heat engine is a different device than more familiar full-sized engines, with different weaknesses and different strengths.

Mechanics Scaling. While the thermodynamics are invariant down to this scale, the mechanics are not. The fluid mechanics, for

example, are scale-dependent, [9]. One aspect is that viscous forces are more important at small scale. Pressure ratios of 2:1 to 4:1 per stage imply turbomachinery tip Mach numbers that are in the high subsonic or supersonic range. Airfoil chords on the order of a millimeter imply that a device with room temperature inflow, such as a compressor, will operate at Reynolds numbers in the tens of thousands. With higher gas temperatures, turbines of similar size will operate at a Reynolds number of a few thousand. These are small values compared to the 10^5 – 10^6 range of large-scale turbomachinery and viscous losses will be concomitantly larger. But viscous losses make up only about a third of the total fluid loss in a high speed turbomachine (three-dimensional, tip leakage, and shock wave losses account for most of the rest) so that the decrease in machine efficiency with size is not so dramatic. The increased viscous forces also mean that fluid drag in small gaps and on rotating disks will be relatively higher. Unless gas flow passages are smaller than one micron, the fluid behavior can be represented as continuum flow so that molecular kinetics, Knudsen number considerations, are not important.

Heat transfer is another aspect of fluid mechanics in which microdevices operate in a different design space than large-scale machines. The fluid temperatures and velocities are the same but the viscous forces are larger, so the fluid film heat transfer coefficients are higher by a factor of about three. Not only is there more heat transfer to or from the structure but thermal conductance within the structure is higher due to the short length scale. Thus, temperature gradients within the structure are reduced. This is helpful in reducing thermal stress but makes thermal isolation challenging.

For structural mechanics, it is the change in material properties with length scale that is most important. Very small length scale influences both material properties and material selection. In engines a few millimeters in diameter, design features such as blade tips, fillets, orifices, seals, etc. may be only a few microns in size. Here, differences between mechanical design and material properties begin to blur. The scale is not so small (atomic lattice or dislocation core size) that continuum mechanics no longer applies. Thus, elastic, plastic, heat conduction, creep, and oxidation behaviors do not change, but fracture strength can differ. Material selection is influenced both by mechanical requirements and by fabrication constraints. For example, structure ceramics such as silicon carbide (SiC) and silicon nitride (Si_3N_4) have long been recognized as attractive candidates for gas turbine components due to their high strength, low density, and good oxidation resistance. Their use has been limited, however, by the lack of technology to manufacture flaw-free material in sizes large enough for conventional engines. Shrinking engine size by three orders of magnitude virtually eliminates this problem. Indeed, mass-produced, single-crystal semiconductor materials are essentially perfect down to the atomic level so that their usable strength is an order of magnitude better than conventional metals. This higher strength can be used to realize lighter structures, higher rotation speeds (and thus higher power densities) at constant geometry, or simplified geometry (and thus manufacturing) at constant peripheral speed. An additional material consideration is that thermal shock susceptibility decreases as part size shrinks. Thus, materials such as alumina (Al_2O_3) which have very high temperature capabilities but are not considered high temperature structural ceramics due to their susceptibility to thermal shock are viable at millimeter length scales (Fig. 2). Since these have not been considered as MEMS materials in the past, there is currently little suitable manufacturing technology available, [10].

Overview of a MEMS Gas Turbine Engine Design

Efforts at MIT were initially directed at showing that a MEMS-based gas turbine is indeed possible, by demonstrating benchtop operation of such a device. This implies that, for a first demonstration, it would be expedient to trade engine performance for simplicity, especially fabrication simplicity. Most current, high

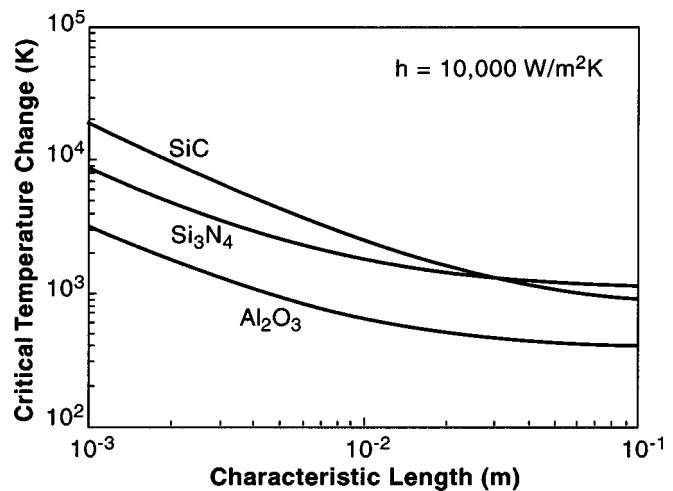


Fig. 2 Critical temperature change to cause fracture via thermal shock

precision, microfabrication technology applies mainly to silicon. Since Si rapidly loses strength above 950 K, this becomes an upper limit to the turbine rotor temperature. But 950 K is too low a combustor exit temperature to close the engine cycle (i.e., produce net power) with the component efficiencies available, so cooling is required for Si turbines. The simplest way to cool the turbine in a millimeter-sized machine is to eliminate the shaft, and thus conduct the turbine heat to the compressor, rejecting the heat to the compressor fluid. This has the great advantage of simplicity and the great disadvantage of lowering the pressure ratio of the now non-adiabatic compressor from about 4:1 to 2:1 with a concomitant decrease in cycle power output and efficiency. Hydrogen was chosen as the first fuel to simplify the combustor development. This expedient arrangement was referred to as the H_2 demo engine. It is a gas generator/turbojet designed with the objective of demonstrating the concept of a MEMS gas turbine. It does not contain electrical machinery or controls, all of which are external.

The MIT H_2 demo engine design is shown in Fig. 3. The centrifugal compressor and radial turbine rotor diameters are 8 mm and 6 mm, respectively. The compressor discharge air wraps around the outside of the combustor to cool the combustor walls, capturing the waste heat and so increasing the combustor efficiency while reducing the external package temperature. The rotor radial loads are supported on a journal bearing on the periphery of the compressor. Thrust bearings on the centerline and a thrust balance piston behind the compressor disk support the axial loads. The balance piston is the air source for the hydrostatic journal bearing pressurization. The thrust bearings and balance piston are supplied from external air sources. The design peripheral speed of the compressor is 500 m/s so that the rotation rate is 1.2 Mrpm. External air is used to start the machine. With 400 μm span airfoils, the unit is sized to pump about 0.36 grams/sec of air, pro-

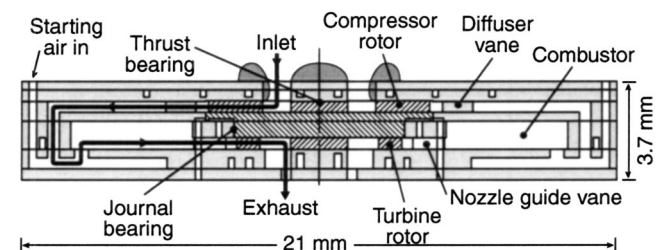


Fig. 3 H_2 demo engine with conduction-cooled turbine constructed from six silicon wafers

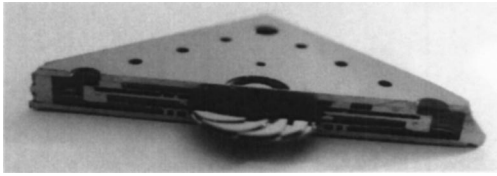


Fig. 4 Cutaway H₂ demo gas turbine chip

ducing 0.1 Newtons of thrust or 17 watts of shaft power. A cutaway engine chip is shown in Fig. 4. In this particular engine build, the airfoil span is 225 μm and the disks are 300 μm thick.

The following sections elaborate on the component technologies of this engine design. It starts with a primer on microfabrication and then goes on to turbomachinery aerodynamic design, structures and materials, combustion, bearings and rotor dynamics, and controls and accessories. A system integration discussion then expands on the high-level tradeoffs which define the design space of a MEMS gas turbine engine.

A Primer on Micromachining

Gas turbine engine design has always been constrained by the practicality of manufacturing parts in the desired shape and size and with the material properties needed. As with conventional metal fabrication, the mechanical and electrical properties of MEMS materials can be strongly influenced by the fabrication process.

While an old-school designer may have admonished his team “Don’t let the manufacturing people tell you what you can’t do!”, design for manufacturing is now an important concern in industry. Major decisions in engine architecture are often set by manufacturing constraints. Of course this was true in the design of Whittle’s first jet engine, in which the prominent external, reverse flow combustors reflected the need to keep the turbine very close to the compressor to control rotor dynamics given that the forging technology of the day could only produce short, small diameter shafts integral with a disk, [11].

Compared to manufacturing technologies familiar at large scale, current microfabrication technology is quite constrained in the geometries that can be produced and this severely limits engine design options. Indeed, the principal challenge is to arrive at a design which meets the thermodynamic and component functional requirements while staying within the realm of realizable micromachining technology. The following paragraphs present a simple overview of current micromachining technology important to this application and then discuss how it influences the design of very small rotating machinery. These technologies were derived from the semiconductor industry 15–20 years ago, but the business of micromachining has now progressed to the level that considerable process equipment (known as “tools”) is developed specifically for these purposes, [12].

The primary fabrication processes important in this application are etching of photolithographically defined planar geometries and bonding of multiple wafers. The usual starting point is a flat wafer of the base material, most often single-crystal silicon. These wafers are typically 0.5 to 1.0 mm thick and 100 to 300 mm in diameter, the larger size representing the most modern technology. Since a single device of interest here is typically a centimeter or two square, dozens to hundreds fit on a single wafer (Fig. 5). Ideally, the processing of all the devices on a wafer is carried out in parallel, leading to one of the great advantages of this micromachining approach, low unit cost. To greatly simplify a complex process with very many options, the devices of interest will serve as illustrative examples.

First, the wafers are coated with a light-sensitive photoresist. A high contrast black-and-white pattern defining the geometry is then optically transferred to the resist either by means of a contact exposure with a glass plate containing the pattern (a “mask”), or

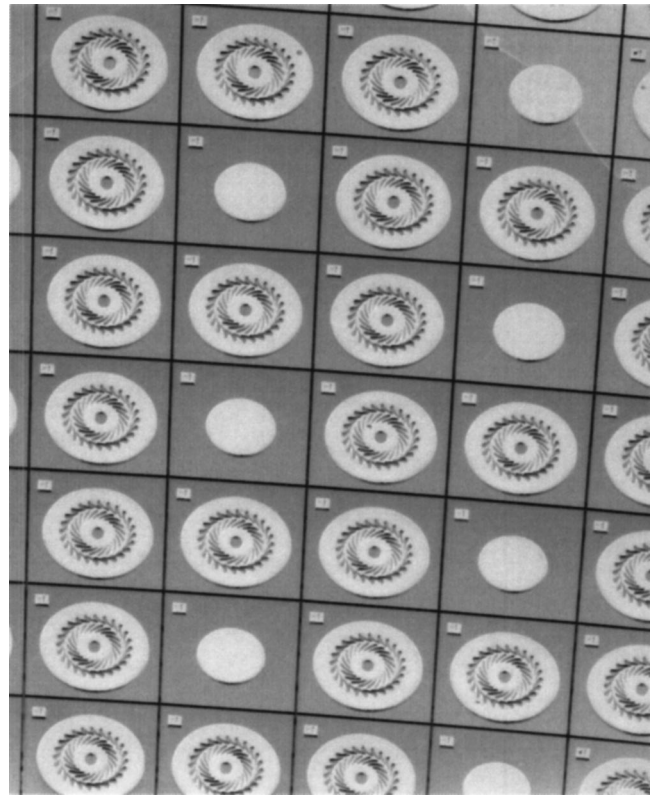


Fig. 5 Si wafer of radial inflow turbine stages

by direct optical or e-beam writing. The photoresist is then chemically developed as though it were photographic film, baked, and then the exposed areas are removed with a solvent. This leaves bare silicon in the areas to be etched and photoresist-protected silicon elsewhere. The etching process is based on the principle that the bare silicon is etched at a much higher rate, typically 50–100 \times , than the mask material. Many different options for making masks have been developed, including a wide variety of photoresists and various oxide or metal films. By using several layers of masking material, each sensitive to different solvents, multi-depth structures can be defined. Photoresist on top of SiO₂ is one example.

The exposed areas of the wafer can now be etched, either chemically or with a plasma. The devices we are concerned with here require structures which are 100’s of microns high with very steep walls, thus a current technology of great interest is deep reactive ion etching (DRIE). In the DRIE machine, the wafer is etched by plasma-assisted fluorine chemistry for several tens of seconds, then the gas composition is changed and a micron or so of a teflon-like polymer is deposited which preferentially protects the vertical surfaces, and then the etch cycle is repeated, [13]. The average depth of a feature is a function of the etch time and the local geometry. The etch anisotropy (steepness of the walls) can be changed by adjusting the plasma properties, gas composition, and pressure. In addition, these adjustments may alter the uniformity of the etch rate across the wafer by a few percent since no machine is perfect. One feature of current tools is that the etch rate is a function of local geometry such as the lateral extent of a feature. This means that, for example, different width trenches etch at different rates, presenting a challenge to the designer of a complex planar structure. A DRIE tool typically etches silicon at an average rate of 1–3 μm per minute, the precise rate being feature and depth-dependent. Thus, structures that are many hundreds of microns deep require many hours of etching. Such a tool currently costs \$0.5–1.0 M and etches one wafer at a time, so the

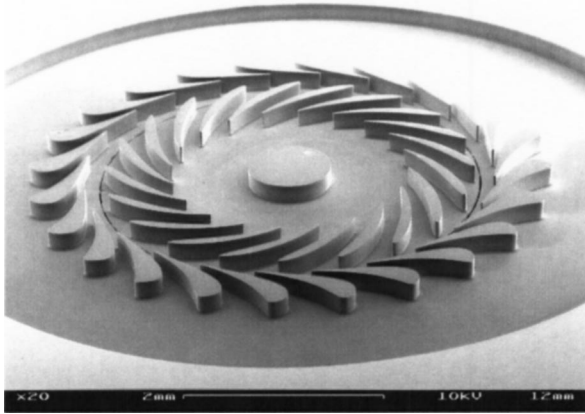


Fig. 6 A 4:1 pressure ratio, 4 mm rotor dia radial inflow turbine stage

etching operation is a dominant factor in the cost of producing such deep mechanical structures. Both sides of a wafer may be etched sequentially.

Figure 6 is an image of a 4 mm rotor diameter, radial inflow air turbine designed to produce 60 watts of mechanical power at a tip speed of 500 m/s, [14,15]. The airfoil span is 200 μm . The cylindrical structure in the center is a thrust pad for an axial thrust air bearing. The circumferential gap between the rotor and stator blades is a 15 μm wide air journal bearing required to support the radial loads. The trailing edge of the rotor blades is 25 μm thick (uniform to within 0.5 μm) and the blade roots have 10 μm radius fillets for stress relief. While the airfoils appear planar in the fig-

ure, they are actually slightly tapered from hub to tip. Current technology can yield a taper uniformity of about 30:1 to 50:1 with either a positive or negative slope. At the current state of the art, the airfoil length can be controlled to better than 1 μm across the disk, which is sufficient to achieve high-speed operation without the need for dynamic balancing. Turbomachines of similar geometry have been produced with blade spans of over 400 μm .

The processing of a 4 mm diameter turbine stage is illustrated in Fig. 7 as a somewhat simplified example. Note that the vertical scaling in the figure is vastly exaggerated for clarity since the thickness of the layers varies so much (about 1 μm of silicon dioxide and 10 μm of photoresist on 450 μm of silicon). It is a 16-step process for wafer 1, requiring two photo masks. It includes multiple steps of oxide growth (to protect the surface for wafer bonding), patterning, wet etching (with a buffered hydrofluoric acid solution known as BOE), deep reactive ion etching (DRIE), and wafer bonding (of the rotor wafer, #1, to an adjoining wafer, #2, to prevent the rotor from falling out during processing). Note that wafer 2 in the figure was previously processed since it contains additional thrust bearing and plumbing features which are not shown here for clarity. In fact, it is more complex to fabricate than the rotor wafer illustrated.

The second basic fabrication technology of interest here is the bonding together of processed wafers in precision alignment so as to form multilayer structures. There are several classes of wafer bonding technologies. One uses an intermediate bonding layer such as a gold eutectic or SiO_2 . These approaches, however, result in structures which have limited temperature capabilities, a few hundred $^\circ\text{C}$. It is also possible to directly bond silicon to silicon and realize the material's intrinsic strength through the entire usable temperature range of the material, [16,17]. Direct bonding requires very smooth (better than 10 nanometers) and very clean surfaces (a single 1 μm diameter particle can keep

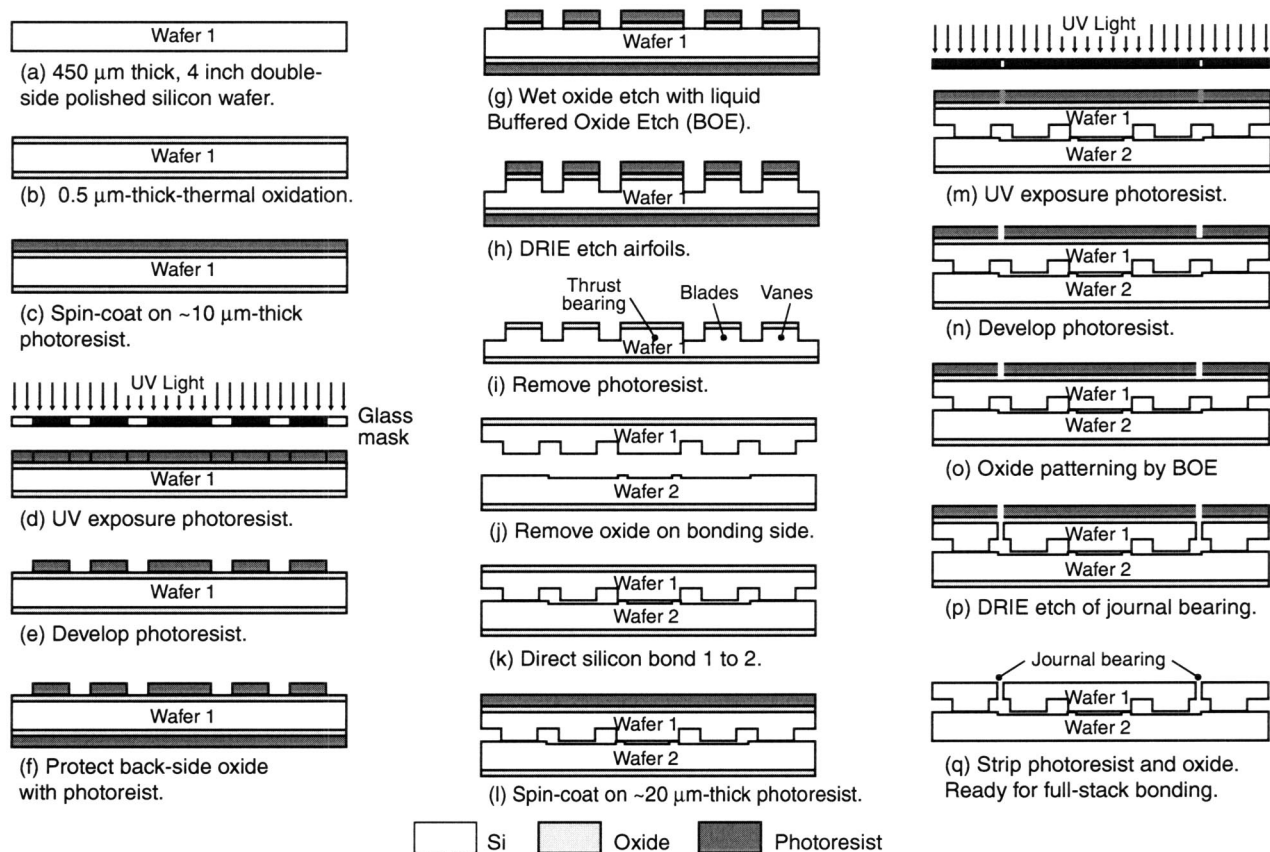


Fig. 7 Simplified processing steps to produce the turbine in Fig. 6 in a wafer stack. (Figure courtesy of N. Miki.)

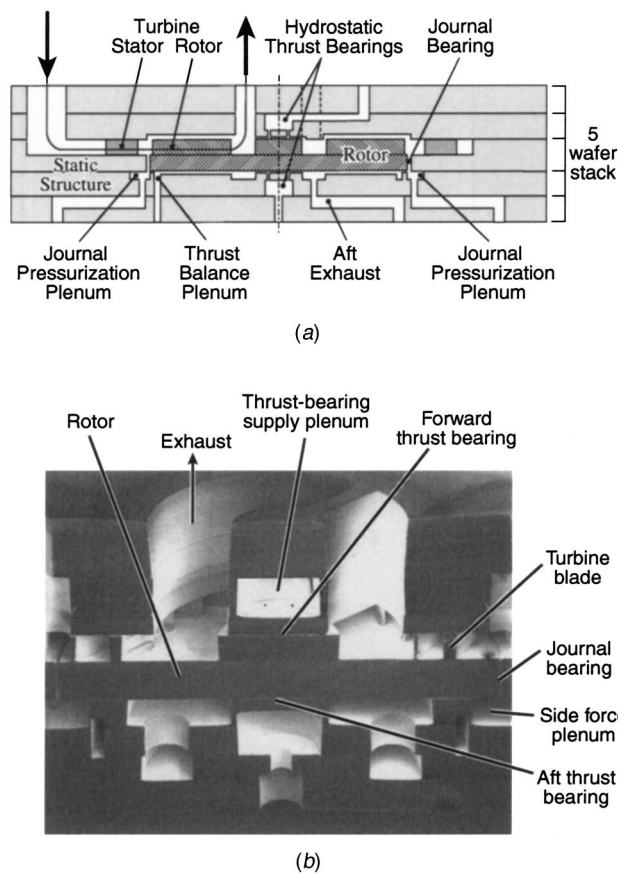


Fig. 8 Complete, five-layer turbine "stack" including bearings and fluid plumbing; (a) conceptual cross-section, (b) electron microscope image of cross-section

several square centimeters of surface from bonding). Thus, a very high standard of cleanliness and wafer handling must be maintained throughout the fabrication process. The wafers to be bonded are hydrated and then aligned using reference marks previously etched in the surface. The aligned wafers are brought into contact and held there by Van der Waals forces. The stack of wafers is then pressed and heated to a few hundred degrees for tens of minutes. Finally, the stack is annealed for about one hour at 1100°C in an inert gas furnace. (If a lower temperature is used, a much longer time will be needed for annealing.) Such a stack, well processed from clean wafers, will not have any discernable bond lines, even under high magnification. Tests show the bonds to be as strong as the base material. The current state of the art is stacks of 5–6 wafers aligned across a wafer to 0.5–1.0 μm . More wafers can be bonded if alignment precision is less important. Note that the annealing temperature is generally higher than devices encounter in operation. This process step thus represents the limiting temperature for the selection of materials to be included within the device, [18]. Figure 8 shows the turbine layer of Fig. 6 bonded as the center of a stack of five wafers, the others contain the thrust bearings and fluid plumbing.

A third fabrication technology of interest for microrotating machinery is that which realizes a freely spinning rotor within a wafer-bonded structure. We require completed micromachines which include freely rotating assemblies with clearances measured in microns. While it is possible to separately fabricate rotors, insert them into a stationary structure, and then bond an overlying static structure, this implies pick-and-place hand operations (rather than parallel processing of complete wafers) and increases the difficulty in maintaining surfaces sufficiently clean

for bonding. A fundamentally different approach is to arrange a sequence of fabrication steps with all processing done at the wafer level so that a freely rotating captured rotor is the end product. The process must be such that the rotor is not free at any time during which it can fall out, i.e., it must be mechanically constrained at all times. There are several ways that this can be accomplished. For example, the layer containing the rotor can be "glued" to adjoining wafers with an oxide during fabrication. This glue can then be dissolved away to free the rotor after the device is completely fabricated. In one version of the 4 mm turbine of Fig. 6, an SiO_2 film bonds the rotor layer at the thrust bearing pad to the adjoining wafer, before the journal bearing is etched. Another approach employs "break-off tabs" or mechanical fuses, flimsy structures which retain the rotor in place during fabrication and are mechanically failed after fabrication is complete to release the rotor, [19]. Both approaches have been proven successful.

The last MEMS technology we will mention is that for electronic circuitry, mainly for embedded sensors and electric machinery such as actuators, motors, and generators. The circuitry is generally constructed by laying down alternating insulating and conducting layers, typically by using vapor deposition or sputtering approaches, and patterning them as they are applied using the photoresist technology outlined above. While the microelectronics industry has developed an extremely wide set of such technologies, only a small subset are compatible with the relatively harsh environment of the processing needed to realize wafer-bonded mechanical structures hundreds of microns deep. Specifically, the high wafer annealing temperatures limit the conductor choices to polysilicon or high temperature metals such as platinum or tungsten. The energetic etching processes require relatively thick masking material which limits the smallest electrical feature size to the order of a micron, rather than the tens of nanometers used in state-of-the-art microelectronic devices.

Using the above technologies, shapes are restricted to mainly prismatic or "extruded" geometries of constant height. Ongoing research with greyscale lithography suggests that smoothly variable etch depths (and thus airfoils of variable span) may be feasible in the near term, [20]. Conceptually, more complex three-dimensional shapes can be constructed of multiple precision-aligned two-dimensional layers. But layering is expensive with current technology and 5–6 is considered a large number of precision-aligned layers for a microdevice. Since three-dimensional rotating machine geometries are difficult to realize, planar geometries are preferred. While three-dimensional shapes are difficult, in-plane two-dimensional geometric complexity is essentially free in manufacture since photolithography and etching process an entire wafer at one time. These are much different manufacturing constraints than are common in the large-scale world so it is not surprising the optimal machine design may also be different.

Turbomachinery Fluid Mechanics

The turbomachine designs considered to date for MEMS engine applications have all been centrifugal since this geometry is readily compatible with manufacturing techniques involving planar lithography. (It is also possible to manufacture single axial flow stages by using intrinsic stresses generated in the manufacturing process to warp what otherwise would be planar paddles into twisted blades, but such techniques have not been pursued for high-speed turbomachinery.) In most ways, the fluid mechanics of microturbomachinery are similar to that of large-scale machines. For example, high tip speeds are needed to achieve high pressure ratios per stage. Micromachines are different in two significant ways: small Reynolds numbers (increased viscous forces in the

fluid) and, currently, two-dimensional, prismatic geometry limitations. The low Reynolds numbers, 10^3 – 10^5 , are simply a reflection of the small size, and place the designs in the laminar or transitional range. These values are low enough that it is difficult to diffuse the flow, either in a rotor or a stator, without separation. This implies that either most of the stage work must come from the centrifugal pressure change or that some separation must be tolerated. The design challenges introduced by the low Reynolds numbers are exacerbated by geometric restrictions imposed by current microfabrication technology. In particular, the fabrication constraint of constant passage height is a problem in these high-speed designs. High work on the fluid means large fluid density changes. In conventional centrifugal turbomachinery, density change is accommodated in compressors by contracting or in turbines by expanding the height of the flow path. However, conventional microfabrication technology is not amenable to tapering passage heights, so all devices built to date have a constant span. How these design challenges manifest themselves are somewhat different in compressors and turbines.

A common fluid design challenge is turning the flow to angles orthogonal to the lithographically defined etch plane, such as at the impeller eye or the outer periphery of the compressor diffuser. At conventional scale, these geometries would be carefully contoured and perhaps turning vanes would be added. Such geometry is currently difficult to produce with microfabrication, which most naturally produces sharp right angles that are deleterious to the fluid flow. For example, at the 2 mm diameter inlet to a compressor impeller, three-dimensional computational fluid dynamics (CFD) simulations show that a right-angle turn costs 5% in compressor efficiency and 15% in mass flow compared to a smooth turn, [21]. Engineering approaches to this problem include lowering the Mach number at the turns (by increasing the flow area), smoothing the turns with steps or angles (which adds fabrication complexity), and adding externally produced contoured parts when the turns are at the inlet or outlet to the chip.

Compressor Aerodynamic Design. The engine cycle demands pressure ratios of 2–4, the higher the better. This implies that transonic tip Mach numbers and therefore rotor tip peripheral speeds in the 400–500 m/s range are needed. This yields Reynolds numbers (Re) in the range of 10^4 for millimeter-chord blades. The sensitivity of two-dimensional blade performance to Re in this regime is illustrated in Fig. 9, which presents the variations of efficiency with size for a radial flow compressor and turbine. While this analysis suggests that for low loss it is desirable to maximize chord, note that the span of the airfoils is less than the chord, implying that aero designs should include endwall considerations at this scale.

In conventional size machines the flow path contracts to control diffusion. Since this was not possible with established micromachining technology, the first approach taken was to control diffusion in blade and vane passages by tailoring the airfoil thickness rather than the passage height, [21,22]. This approach results in very thick blades, as can be seen in the 4:1 pressure ratio compressor shown in Fig. 10. Compared to conventional blading, the trailing edges are relatively thick and the exit angle is quite high. The design trade is between thick trailing edges (which add loss to the rotor) or high rotor exit angles (which result in reduced work at constant wheel speed, increased diffuser loss, and reduced operating range).

Although the geometry is two-dimensional the fluid flow is not. The relatively short blade spans, thick airfoil tips, and low Reynolds numbers result in large hub-to-tip flow variations, especially at the impeller exit. This imposes a spanwise variation on stator inlet angle of 15–20 deg for the geometries examined. This cannot be accommodated by twisting the airfoils, which is not permitted in current microfabrication. The limited ability to diffuse the flow without separation at these Reynolds numbers also precludes the use of vaneless diffusers if high efficiency is required, since the flow rapidly separates off parallel endwalls.

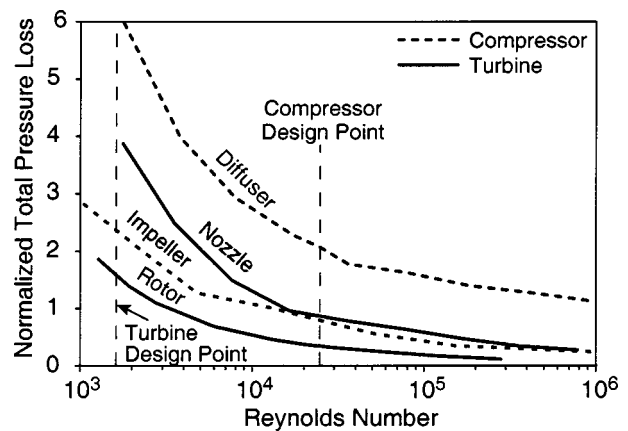


Fig. 9 Calculated sensitivity of two-dimensional airfoil loss with Reynolds number, [9]

While extensive two-dimensional and three-dimensional numerical simulations have been used to help in the design and analysis of the micromachines, as in all high-speed turbomachinery development, test data are needed. Instrumentation suitable for fluid flow measurements in turbomachinery with blade spans of a few hundred microns and turning at over a million rpm is not readily available. While it is theoretically possible to microfabricate the required instrumentation into the turbomachine, this approach to instrumentation is at least as difficult as fabricating the microturbomachine in the first place. Instead, the standard technique of using a scaled turbomachine test rig was adopted, [23]. In this case the test rig was a $75\times$ linear scaleup of a 4 mm diameter compressor (sufficiently large with a 300 mm rotor diameter for conventional instrumentation) rather than the 2 – $4\times$ scaledown common in industry. The geometry tested was a model of a 2:1 pressure ratio, 4 mm diameter compressor with a design tip speed of 400 m/sec for use in a micromotor-driven air compressor, [24]. This design used the thick-blade-to-control-diffusion philosophy discussed above. The rig was operated at reduced inlet pressure to match the full-scale design Reynolds number of about 20,000. A comparison of a steady three-dimensional viscous CFD (FLUENT) simulation to data is shown in Fig. 11. The simulation domain included the blade tip gaps and right-angle turn at the inlet. It predicts the pressure rise and mass flow rate to 5% and 10%, respectively.

Tight clearances are considered highly desirable for compressor aerodynamics in general but are a two-edged sword for the thick-bladed designs discussed above. Small tip clearance reduces leak-

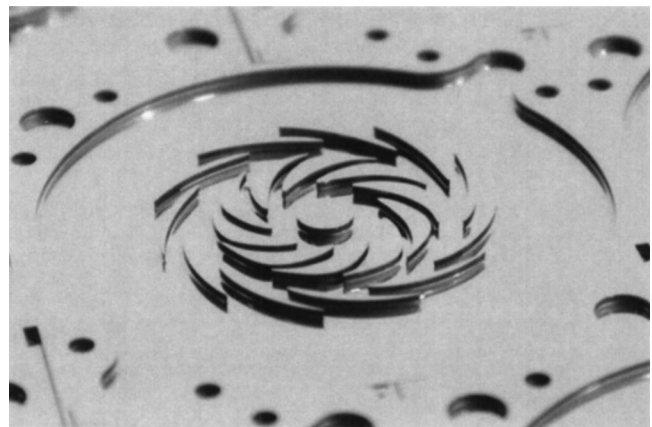


Fig. 10 A 500 m/s tip speed, 8 mm dia. centrifugal engine compressor

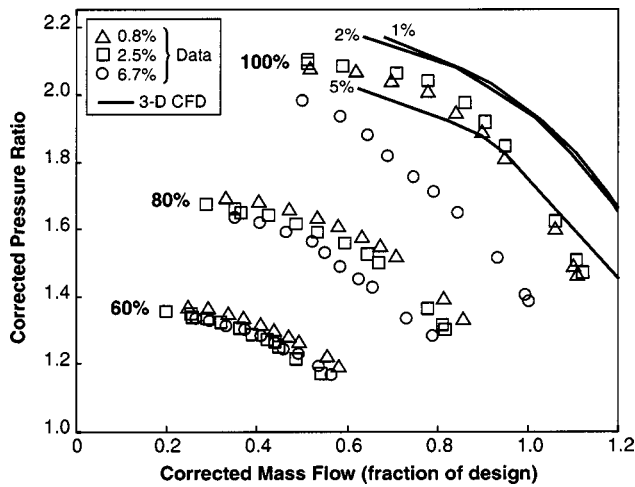


Fig. 11 Sensitivity of compressor pressure rise to tip clearance (% span)

age flow and its associated losses, but increases drag for designs in which the blade tip is at least as wide as the passage. The full-scale blading dimensions of the microcompressor tested scaled up was a blade chord of about $1000 \mu\text{m}$ and a span of $225 \mu\text{m}$. Thus the design minimum tip clearance of $2 \mu\text{m}$ (set to avoid blade tip rubs) represents 0.2% of chord and 1% of span. Figure 11 includes measurements of the sensitivity of this design to tip clearance.

Recent microfabrication advances using greyscale lithography approaches suggest that variable span turbomachinery may indeed be feasible, [20]. This would facilitate designs with attached flow on thin blades. Compared to the thick blade approach, three-dimensional CFD simulations of thin blade compressors with a tip shroud show about twice the mass flow for the same maximum span and wheel speed, an increase in pressure ratio from 2.5 to 3.5, and an increase in adiabatic efficiency from 50% to 70%, [25].

Isomura et al. have taken a different approach to centimeter-scale centrifugal compressors, [26,27]. They have chosen to scale a conventional three-dimensional aerodynamic machine with an inducer down to a 12 mm diameter for a design 2 g/s mass flow rate and 3:1 pressure ratio. The test article is machined from aluminum on a high-precision five-axis miller. No test results have been reported to date.

Kang et al. [28] have built a 12 mm diameter conventional geometry centrifugal compressor from silicon nitride using a rapid prototype technology known as mold shape deposition manufacture. It was designed to produce a pressure ratio of 3:1 at 500 m/s tip speed with a mass flow of 2.5 g/s and an efficiency of 65–70%. To date, they report testing up to 250 m/s and performance consistent with CFD analysis.

A major aerodynamic design issue peculiar to these very small machines is their sensitivity to heat addition. It is difficult to design a centimeter-scale gas turbine engine to be completely adiabatic, thus there will be some degree of heat addition through conduction. An isothermal compressor at fixed temperature exhibits behavior close to that of an adiabatic machine with the same amount of heat added at the inlet, [29]. Thus, the influence of the heat addition shows up as reductions in mass flow, pressure rise, and adiabatic efficiency. The effect of heat addition on compressor efficiency and pressure ratio are shown in Fig. 12. These effects can be quite dramatic at high levels of heat flow. The influence of this nonadiabatic behavior on the overall cycle performance will be discussed later.

The ultimate efficiency potential for compressors in this size range has yet to be determined. Figure 13 plots the polytropic efficiency of a number of aeroengines and ground-based gas tur-

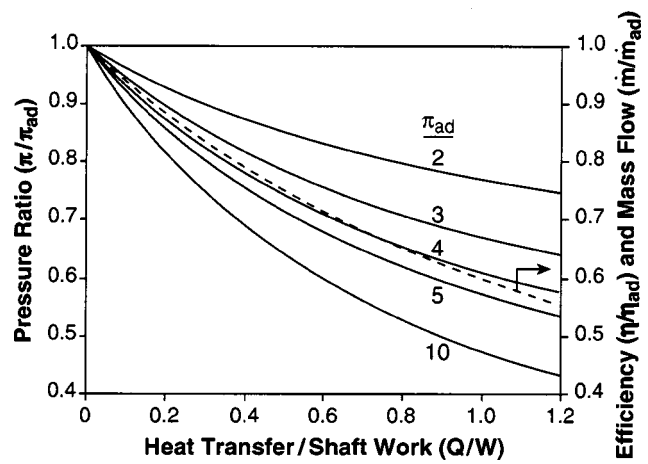


Fig. 12 The influence of heat addition on compressor performance (pressure ratio is π , the subscript “ad” refers to the adiabatic condition)

bine compressors using inlet-corrected mass flow as an indicator of size. The efficiency decreases with size but how much of this is intrinsic to the fluid physics and how much is due to the discrepancy in development effort (little engines have little budgets) is not clear. (Note that there is an inconsistency of about a percent in this data due to different definitions of efficiency, i.e., whether losses in the inlet guide vanes and the exit vanes or struts are included.)

Turbine Aerodynamic and Heat Transfer Design. While the aerodynamic design of a microfabricated, centimeter-diameter radial inflow turbine shares many of the design challenges of a similar scale compressor, such as a constant airfoil span manufacturing constraint, the emphasis is different. Diffusion within the blade passages is not the dominant issue it is with the compressor, so the thick blade shapes are not attractive. The Reynolds numbers are lower, however, given increased viscosity of the high temperature combustor exit fluid. The nozzle guide vanes (NGVs) operate at a Re of 1000–2000 for millimeter-chord airfoils.

One 6 mm diameter constant-span engine turbine is shown in Fig. 14. With a $400 \mu\text{m}$ span it is designed to produce 53 W of shaft power at a pressure ratio (T-S) of 2.1, tip speed of 370 m/s, and mass flow of 0.28 g/s. The reaction is 0.2 which means that the flow is accelerating through the turbine. Three-dimensional CFD simulations were used to explore the performance of this design using FLUENT. The calculational domain included the blade tip gap regions, the discharge of bearing air into the turbine,

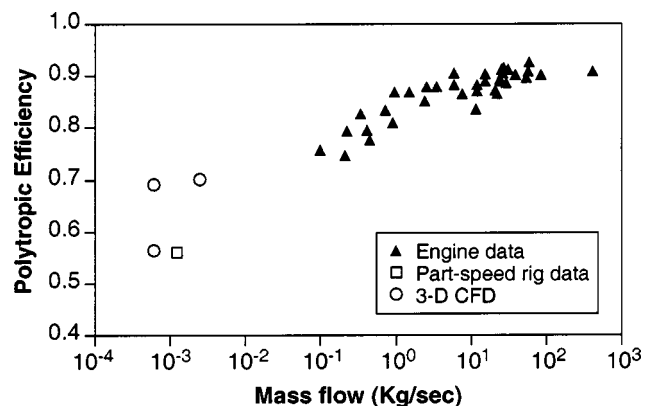


Fig. 13 Variation of engine compressor polytropic efficiency with size

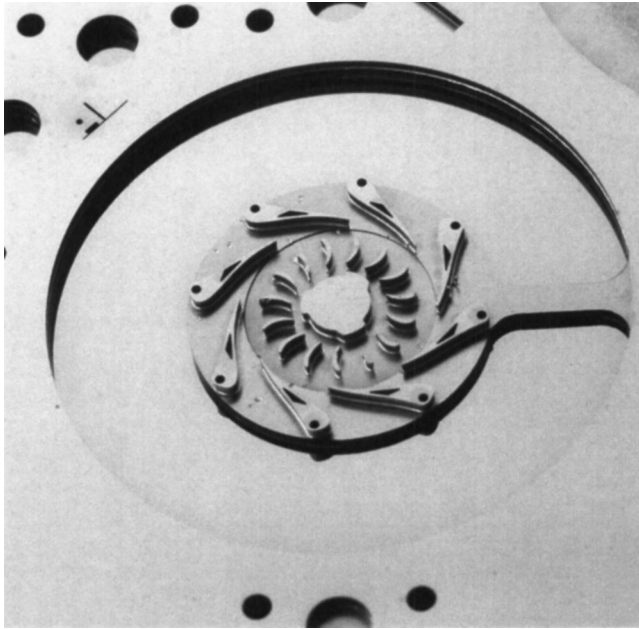


Fig. 14 Silicon engine radial inflow turbine inside annular combustor; the flow passages in the NGV's are for bearing and balance air

and the right-angle turn and duct downstream of the rotor. These calculations predict that this design has an adiabatic efficiency of about 60%. The remainder of the power goes to NGV losses (9%), rotor losses (11%), and exit losses (20%), [30]. These are very low aspect ratio airfoils (~ 0.25) and this is reflected in the shear on the endwalls being about twice that on the airfoil surfaces. The exit losses, the largest source of inefficiency, consist of residual swirl, losses in the right-angle turn, and lack of pressure recovery in the downstream duct. This implies that (a) the rotor exit Mach number should be reduced if possible, and (b) that the turbine would benefit from an exit diffuser.

High engine-specific powers require turbine inlet temperatures (TIT) above the 950 K capability of uncooled single-crystal Si. The MIT demo engine was designed with a TIT of 1600 K and so requires turbine cooling. In the demo design the turbine is conductively cooled through the structure. The heat flow is on the same order as the shaft power, and the resultant entropy reduction is equivalent to 1–2% improvement in turbine efficiency. Advanced engine designs may use film cooling. A major issue in this case is the stability of a cold boundary layer on a rotating disk with radial inflow. While this is, in general, an unstable flow, Philippon has shown through analysis and CFD simulation that the region of interest for these millimeter-scale turbines lies in a

stable regime (e.g., the boundary layers should stay attached), [30]. He then designed film-cooled turbines and analyzed these designs with CFD simulation.

Based upon the work to date, it should be possible to realize microfabricated single-stage compressors with adiabatic pressure ratios above 4:1 at 500 m/s tip speed with total-to-static efficiencies of 50–60%. Achievable turbine efficiencies may be 5–10% higher.

Combustion

The primary design requirements for gas turbine combustors include large temperature rise, high efficiency, low pressure drop, structural integrity, ignition, stability, and low emissions. These requirements are no different for a microcombustor which may flow less than 1 g/s of air than for a 100 kg/sec large machine, but the implementation required to achieve them can be. A comparison between a modern aircraft engine combustor and a microengine is shown in Table 1, [31]. Scaling considerations result in the power density of a microcombustor exceeding that of a large engine. However, the combustor volume relative to the rest of the microengine is much larger, by a factor of 40, than that of a large engine. The reasons for this scaling can be understood in reference to the basics of combustion science, [32].

Combustion requires the mixing of fuel and air followed by chemical reaction. The time required to complete these processes is generally referred to as the required combustion residence time and effectively sets the minimum volume of the combustor for a given mass flow. The mixing time can scale with device size but the chemical reaction times do not. In a large engine, mixing may account for more than 90% of combustor residence time. A useful metric is the homogeneous Damkohler number, which is the ratio of the actual fluid residence time in the combustor to the reaction time. Obviously a Damkohler of one or greater is needed for complete combustion and therefore high combustion efficiency. One difference between large and microscale machines is the increased surface area-to-volume ratio at small sizes. This offers more area for catalysts; it also implies that microcombustors have proportionately larger heat losses. While combustor heat loss is negligible for large-scale engines, it is a dominant design factor at microscale since it can reduce the combustor efficiency and lower the reaction temperature. This narrows the flammability limits and decreases the kinetic rates, which drops the effective Damkohler number. As an example, Fig. 15, [31], illustrates the viable design space for an H_2 -fuelled, 0.07 cc microcombustor as a function of the heat lost to the walls and as constrained by flame stability, structure limits, and cycle requirement considerations. The design space shown permits a trade between heat loss and stoichiometry, which is especially important when burning hydrocarbons with narrow stoichiometry bounds.

The design details are dependent on the fuel chosen. The design approach first taken was to separate the fuel-air mixing from the chemical reaction. This is accomplished by premixing the fuel

Table 1 A comparison of a microengine combustor with a large aeroengine combustor

| | Conventional Combustor | Micro-Combustor |
|-------------------------|------------------------|---------------------------------------|
| Length | 0.2 m | 0.001 m |
| Volume | 0.073 m ³ | 6.6 × 10 ⁻⁸ m ³ |
| Cross-sectional area | 0.36 m ² | 6 × 10 ⁻⁵ m ² |
| Inlet total pressure | 37.5 atm | 4 atm |
| Inlet total temperature | 870 K | 500 K |
| Mass flow rate | 140 kg/s | 1.8 × 10 ⁻⁴ kg/s |
| Residence time | ~7 ms | ~0.5 ms |
| Efficiency | >99% | >90% |
| Pressure ratio | >0.95 | >0.95 |
| Exit temperature | 1800 K | 1600 K |
| Power Density | 1960 MW/m ³ | 3000 MW/m ³ |

(Note: residence times are calculated using inlet pressure and an average flow temperature of 1000 K)

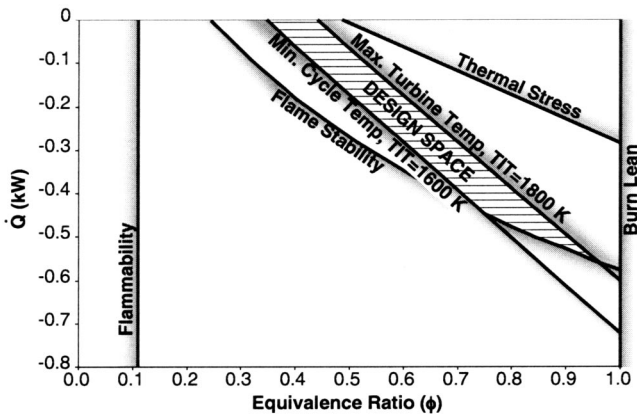


Fig. 15 Design space for Si H₂ microcombustor

with the compressor discharge air upstream of the combustor flame holders. This permits a reduction of the combustor residence time required by a factor of about 10 from the usual 5–10 msec. The disadvantage of this approach is a susceptibility to flashback from the combustor into the premix zone, which must be avoided. To expedite the demonstration of a micro-gas turbine engine, hydrogen was chosen as the initial fuel because of its wide flammability limits and fast reaction time. This is the same approach taken by von Ohain when developing the first jet engine in Germany in the 1930s. Hydrogen is particularly attractive because it will burn at equivalence ratios, ϕ , as low as 0.3 which yields adiabatic combustion temperatures below 1500 K, facilitating the realization of simple premixed designs.

Microcombustor technology has been developed in several full-sized (i.e., micro) test rigs which duplicate the geometry of an engine but with the rotating parts replaced with stationary swirl vanes, [33]. In the Si micromachined geometry of Figs. 3 and 4, to reduce heat losses through the walls and therefore to increase combustor efficiency, the inlet air wraps around the outside of the 0.2 cc combustor before entering through flame holders in a reversed flow configuration. This configuration is similar to the traditional reverse-flow engine combustor but scaled down to 0.1–0.3 g/sec air flow rate. The Si liner in this case is conduction rather than film-cooled. In this premixed approach, fuel is injected near the inlet of the upstream duct to allow time for fuel-air mixing without requiring additional combustor volume. This design takes advantage of microfabrication's ability to produce similar geometric features simultaneously, using 90 fuel injection ports, each 120 μm in diameter, to promote uniform fuel-air mixing. A simple hot wire loop provides ignition, [34].

The combustor was tested in several configurations including variations of flame holder and dilution hole geometry. Combustion efficiencies approaching 100% have been reported with pressure ratios of about 0.95–0.98. The H₂ data in Fig. 16 show the variation of combustor efficiency versus mass flow rate for two configurations, one purely premixed (no dilution holes) and one in which dilution holes have been added to the liner creating a dual-zone combustor, [31]. The missing data is due to instrumentation burnout. The dual-zone configuration, in which the dilution jets set up recirculation zones within the combustor, extends the operating range by about a factor of two at a cost of 10–20% in combustor efficiency. These combustors have been operated at exit temperatures above 1800 K.

Hydrocarbon fuels such as methane and propane have reaction rates only about 20% of those of H₂, requiring larger combustor volumes for the same heat release. They also must react closer to stoichiometric and therefore at higher temperatures, above 2000 K. For gas phase (homogeneous) combustion designs this requires a multizone burner (stoichiometric zone followed by a dilution region) as used on most large gas turbines. Alternatively, hetero-

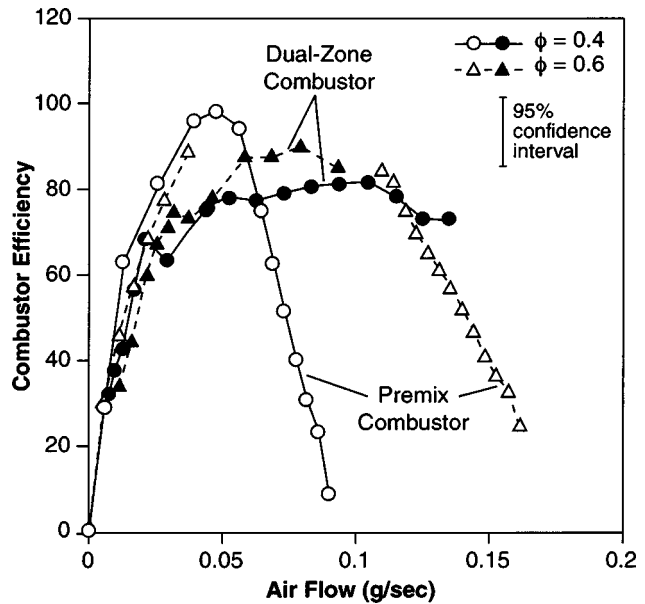


Fig. 16 Measured performance of 0.2 cc, Si microcombustors using H₂ fuel

geneous reactions on the surface of a catalyst can widen the flammability limits and so reduce the combustion temperature. Both approaches have been demonstrated at microscale. Ethylene (which has a high reaction rate) and propane have been burned in the H₂ combustors described above. The combustion efficiency with ethylene approached 90% while that for propane was closer to 60%. These fuels need larger combustor volumes compared to hydrogen for the same heat release. Data for a variety of geometries and fuels is reduced in terms of Damkohler number in Fig. 17, which shows that values of greater than 2 are needed for high chemical efficiency, [31].

Catalytic microcombustors have been produced by filling the combustor volume of the above geometries with a platinum-coated nickel foam. For propane, the catalyst increased the heat release in the same volume by a factor of 4–5 compared to the propane-air results discussed above. Pressure drops through the foam are only 1–2%, [35]. Presumably catalytic combustor per-

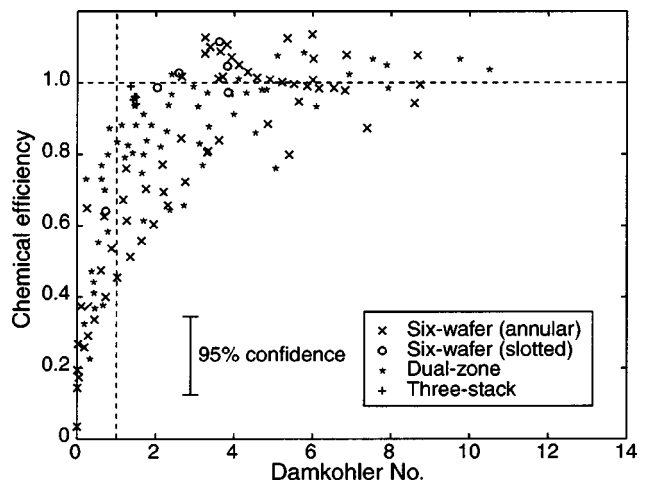


Fig. 17 Measured microcombustor performance as a function of Damkohler number

formance can be improved by a better choice of catalyst (platinum was selected for H_2) and a geometry optimized for catalytic rather than gas-phase combustion.

Takahashi et al. [36] are developing combustors designed for somewhat larger gas turbines, with flow rates of about 2 g/s. Designed for methane, these are a miniature version of can-type industrial combustion chambers with a convection-cooled liner and dilution holes. These are conventionally machined with volumes of 2–4 cc. The combustion efficiencies of these units have been demonstrated as above 99% at equivalence ratios of about 0.37 with a design combustor exit temperature of 1323 K. The design residence time is about 6.5 ms. Matsuo et al. [37] constructed a still larger (20 cc volume, 16 g/s flow rate) conventionally machined combustor burning liquefied natural gas. They report a combustor exit temperature of about 1200 K.

Overall, experiments and calculations to date indicate that high-efficiency combustion systems can be engineered at microscale and achieve the heat release rate and efficiency needed for very small gas turbine engines.

Bearings and Rotor Dynamics

The mechanical design of gas turbine engines is dominated by the bearings and rotor dynamics considerations of high-speed rotating machinery. Micromachines are no different in this regard. As in all high-speed rotating machinery, the basic mechanical architecture of the device must be laid out so as to avoid rotor dynamic problems. The high peripheral speeds required by the fluid and electromechanics lead to designs which are supercritical (operate above the natural resonant frequency of the rotor system), just as they often are in large gas turbines.

Key design requirements imposed by the rotor dynamics are that mechanical critical (resonant) frequencies lie outside the steady-state operating envelope, and that any critical frequencies that must be traversed during acceleration are of sufficiently low amplitude to avoid rubs or unacceptable vibrations. The bearings play an important role in the rotor dynamics since their location and dynamical properties (stiffness and damping) are a major determinant of the rotor dynamics. The bearings in turn must support the rotor against all radial and axial loads seen in service. In addition to the rotor dynamic forces, the bearing loads under normal operation include all the net pressure and electrical forces acting on the rotor as well as the weight of the rotor times the external accelerations imposed on the device. For aircraft engines this is usually chosen as 9 g's, but a small device dropped on a hard floor from two meters experiences considerably larger peak accelerations. An additional requirement for portable equipment is that the rotor support be independent of device orientation. The bearing technology chosen must be compatible with the high temperatures in a gas turbine engine (or be protected within cooled compartments) and be compatible with the fabrication processes.

Early MEMS rotating machines have been mainly microelectronic motors or gear trains turning at significantly lower speeds and for shorter times than are of interest here, so these made do with dry friction bearings operating for limited periods. The higher speeds and longer lives desired for micro-heat engines require low friction bearings. The very small size of these devices precludes the incorporation of commercially available rolling contact bearings. A microfabricated bearing solution is needed. Both electromagnetic and air bearings have been considered for this application.

Electromagnetic bearings can be implemented with either magnetic or electric fields providing the rotor support force. Although extensive work has been done on the application of magnetic bearings to large rotating machinery, work is just beginning on magnetic bearings for micromachines. In addition to their complexity, magnetic bearings have two major challenges in this application. First, magnetic materials are not compatible with most microfabrication technologies, limiting device fabrication options. Second, Curie point considerations limit the temperatures at which magnetic designs can operate to below those encountered

in the micro-gas turbine, so considerable cooling may be needed. For these reasons, the first efforts concentrated on designs employing electric fields. The designs examined did not appear promising in that the forces produced were marginal compared to the bearing loads expected, [38]. Also, since electromagnetic bearings are unstable, feedback stabilization is needed, adding to system complexity.

Gas bearings support their load on thin layers of pressurized gas. For micromachines such as turbines they have intrinsic advantages over electromagnetic approaches, including no temperature limits, high load-bearing capability, and relative manufacturing simplicity. At large scale, gas bearings are used in many high-speed turbomachinery applications, including aircraft environmental control units, auxiliary power units, 30–70 kW “microturbines,” and turbochargers, [39]. At smaller scale, gas bearings have been used in gyroscopic instruments for many years. All else being the same, the relative load-bearing capability of a gas bearing improves as size decreases since the volume-to-surface area ratio (and thus the inertial load) scales inversely with size. Rotor and bearing dynamics scaling is more complex, [40]. However, rotor dynamics in this application are somewhat simplified compared to large engines since the structure is very stiff, so only rigid-body modes need be considered. In the following paragraphs we will first discuss journal bearings which support radial loads and then consider thrust bearings needed for axial loads.

The simplest journal bearing is a cylindrical rotor within a close-fitting circular journal. Other more complex variations used in large-size machines include foil bearings and wave bearings. These can offer several advantages but are more difficult to manufacture at very small size. Thus, the plane cylindrical geometry was the first approach adopted since it seemed the easiest to microfabricate. Gas bearings of this type can be categorized into two general classes which have differing load capacities and dynamical characteristics. When the gas pressure is supplied from an external source and the bearing support forces are not a first order function of speed, the bearing is termed *hydrostatic*. When the bearing support forces are derived from the motion of the rotor, then the design is *hydrodynamic*. Hybrid implementations combining aspects of both are also possible. Since the MEMS gas turbines include air compressors, both approaches are applicable. Both can readily support the loads of machines in this size range and can be used at very high temperatures. The two types of bearings have differing load and dynamic characteristics. In hydrodynamic bearings, the load capacity increases with the speed since the film pressure supporting the rotor is generated by the rotor motion. This can be true for a hydrostatic bearing as well if the film pressure is increased with increasing rotor speed, for example if the pressure is derived from an engine compressor. However, when the supporting film pressure in a hydrostatic bearing is kept constant, the load capacity decreases slightly with increasing speed. The calculated unit load capacity (support force per unit area of bearing) of plane journal microbearings is compared with the measured capacity of conventional air foil bearings in Fig. 18. The hydrostatic bearing is at a constant pressure. For hydrodynamic bearings the load capacity is a function both of rotational speed and of bearing length (L) to diameter (D) ratio. Microbearings currently have low L/D 's due to manufacturing constraints, so their load capacity is less.

The relevant physical parameters determining the bearing behavior are the length-to-diameter ratio (L/D); the journal gap-to-length ratio (g/L); and nondimensional forms of the peripheral Mach number of the rotor (a measure of compressibility), the Reynolds number, and the mass of the rotor. For a bearing supported on a hydrodynamic film, the load bearing capability scales inversely with $(g/D)^5$ which tends to dominate the design considerations, [41].

The design space available for the micro-journal bearing is greatly constrained by manufacturing capability, especially if the rotor and journal structure are fabricated at the same time (which

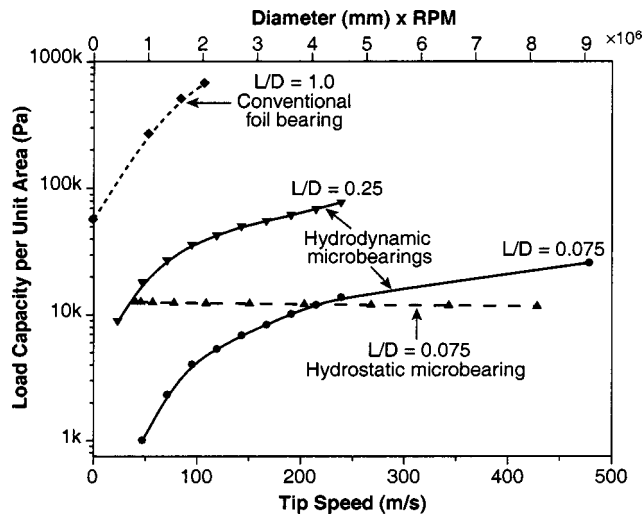


Fig. 18 Gas bearing radial unit load capacity variation with speed. (Figure courtesy of L. Liu.)

avoids the need for assembly and so facilitates low-cost wafer-level manufacturing). The most important constraint is the etching of vertical side walls. Recent advances of etching technology yield taper ratios of about 30:1 to 50:1 on narrow (10–20 μm) etched vertical channels 300–500 μm deep, [15]. This capability defines the bearing length while the taper ratio delimits the bearing gap, g . For hydrodynamic bearings we wish to maximize the footprint and minimize gap/diameter to maximize load capacity, so the bearing should be on the largest diameter available, the periphery of the rotor. The penalty for the high diameter is relatively high area and surface speed, thus high bearing drag, and low L/D and therefore reduced stability. In the radial 4000 μm diameter turbine shown in Fig. 6, the journal bearing is 300 μm long and about 15 μm wide, so it has an L/D of 0.075, g/D of 0.038, and peripheral Mach number of 1. This relatively short, wide-gapped, high-speed bearing is well outside the range of analytical and experimental results reported in the gas bearing literature. It is much closer to an air seal in aspect ratio.

The dynamical behavior of the rotor is of first-order concern because the high rotational speeds needed for high power density by the turbo and electrical machinery require the rotor to operate at rotational frequencies several times the lowest radial resonant frequency of the bearing/rotor system. The dynamics of gas bearings on a stiff rotor can be simply represented by the rotor mounted on a set of springs and dampers, as illustrated in Fig. 19. The fluid in the bearing acts as both the springs and the principal source of damping. It also generates the destabilizing cross-stiffness forces which cause instability at high speeds. As in many conventional engines, the rotor must traverse the critical frequency and avoid instabilities at higher speeds. For example, Fig. 20 illustrates the whirl radius versus speed for a 4 mm diameter turbine with a 12 μm wide bearing. Plotted on the figure are experimental data and a fit of an analytical fluid mechanic spring-mass-damper model of the system to that data. The resonant peak amplitude is reached as the rotor crosses a “rotor critical” (resonant) frequency. If the peak excursion exceeds the bearing clearance, then the rotor hits the wall, i.e., “crashes.” A well-known characteristic of a spring-mounted rotor system (a so-called “Jeffcott rotor”) is that at speeds below the critical frequency the rotor revolves around its geometric center, while well above the critical frequency the rotor revolves around its center of mass. Thus the dotted line in the figure, the asymptote of the curve fit, is a measurement of the rotor imbalance expressed in terms of radial displacement of the rotor center of mass from the geometric center.

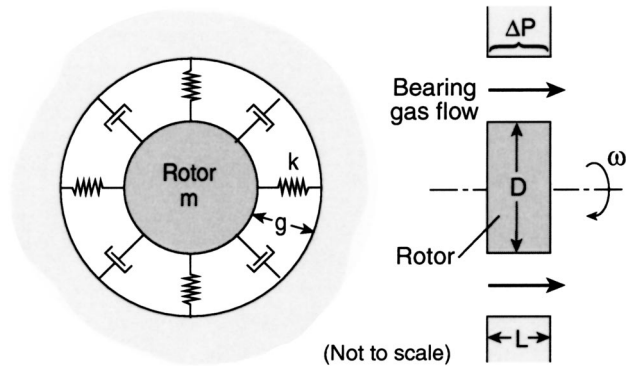


Fig. 19 Gas journal bearing model

The measured imbalance shown in the figure is $\sim 2 \mu\text{m}$, compared to the 12 μm bearing clearance (i.e., at 12 μm imbalance the rotor would strike the wall on every revolution).

We thus have two rotor dynamic design considerations, traversing the critical frequency and ensuring that the frequency for the onset of instability is above the operating range. For a hydrostatic bearing the critical frequency simply scales with the pressure in the bearing. The damping ratio (mainly viscous damping) decreases with increasing speed. Thus, the maximum amplitude the rotor experiences while crossing the critical frequency increases with bearing pressure, i.e., the peak in Fig. 20 moves up and to the right with increasing pressure, [42]. This suggests the strategy of crossing the critical frequency at low pressure and low speed and then increasing the pressure to stiffen the bearing as the rotor accelerates to increase the speed at onset of instability, [43].

The rotor imbalance is another factor which influences both the peak amplitude crossing the critical frequency and the onset of instability. Large rotating machines are usually dynamically balanced by measuring the imbalance and then adding or subtracting mass to reduce it. In many micromachines it is possible to avoid the need for dynamic balancing because the base material used to date (single-crystal silicon) is extremely uniform and, with sufficient care, the etching uniformity is sufficient to produce adequately balanced rotors. Typically, the center of mass is within 1–5 μm of the geometric center. For the turbine in Fig. 6, the blades must be etched to about $\pm 1 \mu\text{m}$ span uniformity across the 4000 μm diameter disk. For rotors made up of several wafers, the alignment between wafers must also be considered (also about 1 μm is needed), [44]. Using the balance measurement capability evident in Fig. 20 and laser etching, it is also possible to dynami-

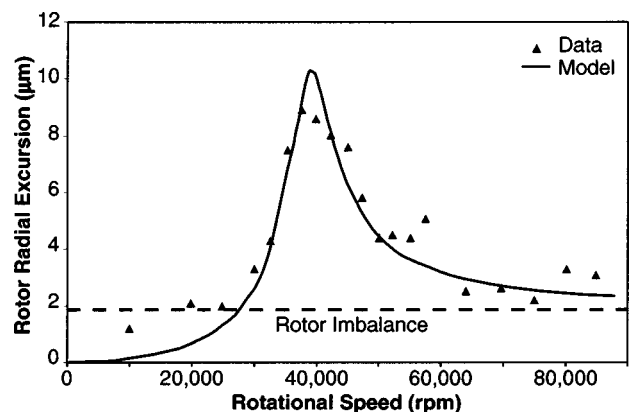


Fig. 20 Transcritical response of the micro-journal gas bearing in Fig. 6. (Figure courtesy of C. J. Teo.)

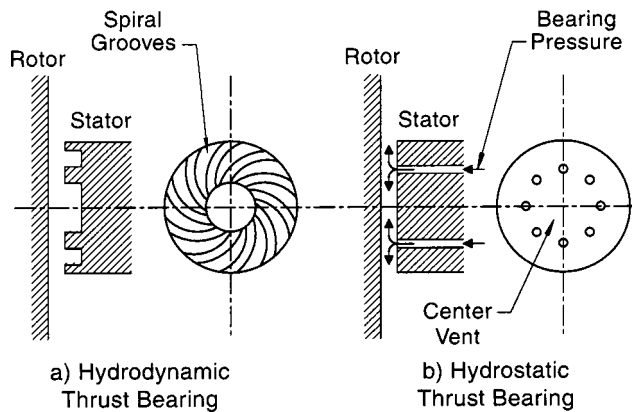


Fig. 21 Geometry of (a) hydrodynamic and (b) hydrostatic thrust bearings (not to scale)

cally balance a microrotor. It is unclear at this time whether dynamic balancing or manufacturing uniformity is a superior approach.

Hydrostatic bearings are stable from zero speed up to the stability boundary. However, centered hydrodynamic bearings are unstable at low rotational speed but stable at high speeds. Commonly, such bearings are stabilized by the application of a unidirectional force which pushes the rotor toward the journal wall, as measured by the eccentricity, the minimum approach distance of the rotor to the wall as a fraction of the average gap (0=centered, 1=wall strike). At conventional scale, the rotor weight is often the source of this side force. At microscale, (1) the rotor weight is negligible, and (2) insensitivity to orientation is desirable, so a scheme has been adopted which uses differential gas pressure to force the rotor eccentric. Extensive numerical modeling of these microbearing flows has shown that such a rotor will be stable at eccentricities above 0.8–0.9, [45]. For the geometry of the turbine in Fig. 6, the rotor must thus operate between 1–2 μm from the journal wall. This implies that deviations from circularity of the journal and rotor must be small compared to 1 μm , an additional manufacturing requirement.

A rotor must be supported against axial as well as radial loads and so requires thrust bearings in addition to the radial bearings discussed above. Both hydrostatic and hydrodynamic approaches have been demonstrated. In either approach, the bearing must support the axial loads and remain stable. The devices built to date have been designed for subcritical thrust-bearing operation so that bearing behavior traversing the critical frequency is not an issue.

Hydrostatic thrust bearings meter external air through supply orifices onto the bearing surface. The 400 μm diameter thrust pad at the rotor center of the 4 mm diameter turbine in Fig. 6 rotates relative to a stationary thrust bearing surface of similar diameter. The stationary bearing surface is perforated with a circular array of 12 μm diameter nozzle orifices fed from a plenum which supplies the gas lubricating film between the bearing surfaces. A cross section is shown in Fig. 21. At a rotor-stator gap of 1.2 μm , a flow of 10 sccm at 2–5 atm is needed to provide sufficient load capacity (0.5 N) and axial stiffness (2×10^5 N/m). Stiffness is maximized when the pressure drop through the supply orifices equals that of the radial outflow from the orifice discharge to the bearing edge.

Hydrodynamic thrust bearings use viscous drag, often enhanced with shallow spiral grooves, to generate a pressure gradient in the bearing which increases toward the rotor center. The pressurized gas film provides the bearing load capacity and stiffness. This self-pumping eliminates the need for an external air supply and simplifies the manufacture since bearing air supply plumbing is not required, reducing the number of wafers needed. It also adds an additional design consideration—rotor liftoff, i.e., the mini-

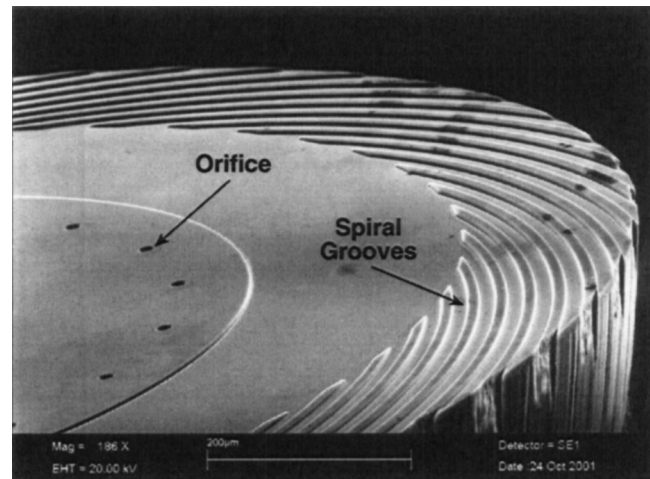


Fig. 22 Hybrid hydrodynamic (spiral grooves) and hydrostatic (orifices) 0.7 mm dia. thrust bearing

um rotational speed needed to develop sufficient pressure to eliminate rubbing between the stationary and rotating parts. Figure 22 is a 700 μm diameter hydrodynamic thrust bearing with 1.5 μm deep spiral grooves that was tested on the microturbine of Fig. 6. It lifts off at about 80,000 rpm. Such a bearing at 10^6 rpm will dissipate about 0.2 watts, about the same as that of a hydrostatic bearing of equal load capacity, [46].

Structures and Materials

Structural considerations for the design of a MEMS gas turbine are in many ways similar to those of conventional engines. The design space is defined by the requirements of the thermodynamics (which require high stress and high temperatures), the properties of the materials, and the manufacturing capabilities. The material properties, in turn, are very much dependent on their processing. This section reviews materials selection, structural design features, high-temperature structures, analysis of such microstructures, and packaging (installation) technology.

Materials. Materials for gas turbine engines must exhibit high specific strength (strength/density) at high temperatures. High-temperature operation also requires creep and oxidation resistance. Other properties of interest include fracture toughness, modulus, and resistance to thermal shock (Table 2). MEMS processing technologies are much more mature for silicon than for other materials so it is the first material a MEMS engineer considers (not so for a gas turbine designer). In terms of strength at temperature, single-crystal Si is the equal of common nickel alloys and, because it has only 1/3 the density, its specific strength is much higher, as illustrated in Fig. 23. It is quite oxidation-resistant and has thermal conductivity approaching that of copper, so it is resistant to thermal shock. On these grounds, it is not a bad material for gas turbine engines. However, at temperatures below about 900 K, Si is brittle, so usable strength is very much a function of the details of the processing. Structural life must be assessed with statistical methods.

Chen et al. [47] have reported room temperature strengths up to 4 GPa for micromachined Si specimens. Moon et al. [48] have measured the strength and creep rate of Si at temperatures up to 1000 K. From these measurements and a detailed model of the creep behavior of the material, it appears that long-lived structures can be designed for stress levels up to about 500 MPa at 850 K. Oxidation is another concern for high temperature structures. Conductively cooled Si combustor tests were run at exit temperatures up to 1800 K, [33]. The thickness of the oxide layers grown were in agreement with standard models of Si oxidation. These imply that uncoated Si airfoils can have a life of a few hundred

Table 2 Design considerations and material properties of interest for gas turbines

| | Ni-Based Super Alloys | Titanium Alloys | Micro SiC | Micro Silicon |
|---|-----------------------|----------------------|----------------------|----------------------|
| Centrifugal stress $[\sqrt{\sigma_f/\rho}]$ (m/s) | 330 | 420 | 670 | 1000 |
| Thermal stress $[\alpha E/\sigma_{f/y}]$ | 2.7×10^{-3} | 1.2×10^{-3} | 1.1×10^{-3} | 0.9×10^{-3} |
| Stiffness $[E/\rho]$ (MPa/Kgm ⁻³) | ~26 | ~25 | ~95 | ~70 |
| Max temp.(°C) (life limit) | ~1000 (creep) | ~300 (strength) | ~1500 (oxidation) | ~600 (creep) |

hours. Longer lives may require coatings. Si nozzle guide vanes run for 5 hrs at 1600 K in a microcombustor exhaust show little degradation, Fig. 24.

Silicon carbide has about 600 K more temperature capability than Si, but the SiC microfabrication technology is much less mature. SiC is available in single-crystal wafers and can be precision etched but SiC wafers cost 100× more than Si at the moment and etch rates are about 10× slower. An alternative to direct SiC etching is to etch a female mold in Si and then fill the mold (for example, by chemical vapor deposition, CVD), and dissolve away the Si, leaving an SiC precision structure. The challenges here are realizing SiC with the needed mechanical properties and dealing with the intrinsic stresses induced by the combination of the high temperatures of the CVD process and the difference in coefficient of thermal expansion between the two materials. A variation on this approach is to use CVD to fill cavities in Si wafers with SiC, bond another Si wafer over the filled cavity, and then process the pair as though it were a standard Si wafer. This yields SiC-reinforced silicon structures which have more temperature capability than Si but are easier to manufacture than SiC,

[49]. The increased temperature capability of a turbine like that in Fig. 6 increases with the thickness of the SiC insert, Fig. 25. Another approach being pursued is reaction sintering of powdered SiC to form parts such as turbine rotors, [50].

Additional structural materials of interest for MEMS gas turbines include glasses for thermal and electrical isolation, and very high temperature materials such as sapphire. There is considerable microfabrication experience with glass but very little with the refractory ceramics because these have not been considered as MEMS materials in the past.

Structural Design Considerations. Structural design of a MEMS gas turbine has many of the same considerations as the design of large machines: basic engine layout is set by rotor dynamic considerations, centrifugal stress is the primary rotor load, stress concentrations must be avoided, and hot section life is creep and oxidation-limited. Some large engine concerns do not exist at micron scale. For example, the microrotors are very stiff so that backbone bending is not a concern; thermal stress from temperature gradients is not important at these sizes; maintenance is not a

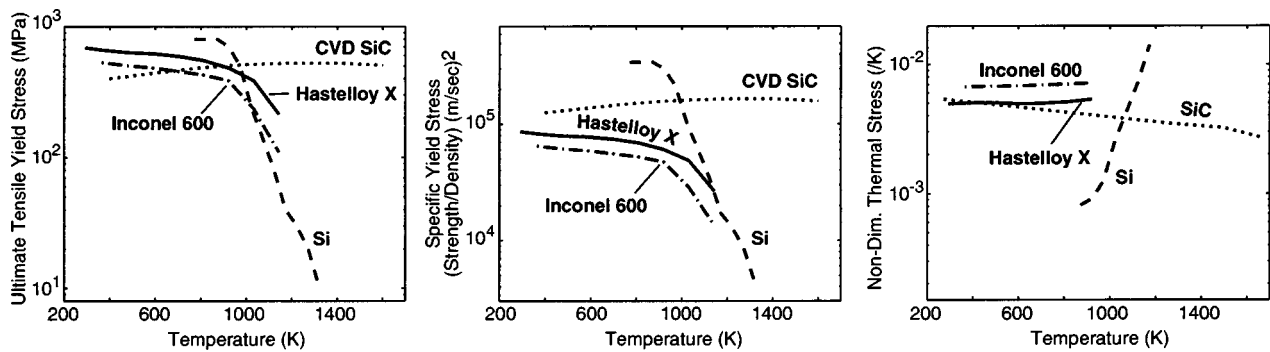


Fig. 23 Material properties relevant to high speed, high temperature rotating machinery

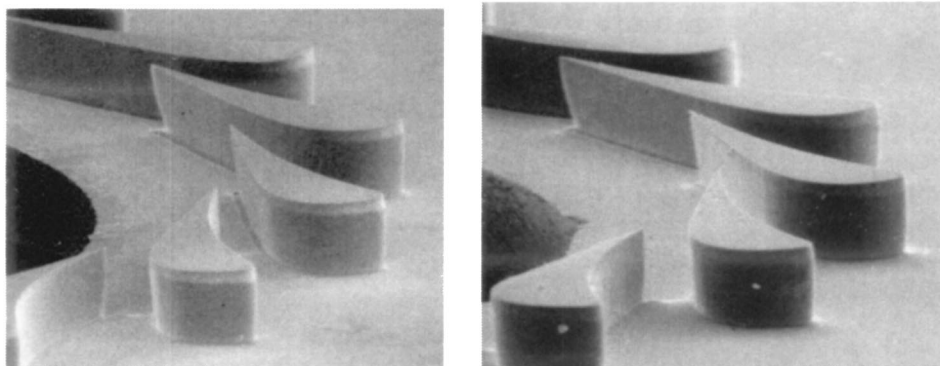


Fig. 24 200 μm high, Si turbine blades new and after 5 hrs at 1600 K gas temperature in a microcombustor exhaust

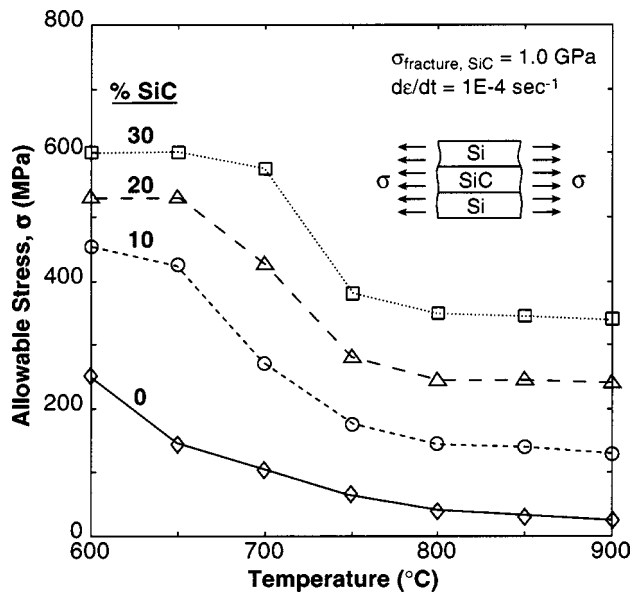


Fig. 25 Usable strength of Si/SiC/Si hybrid structure in tension. (Figure courtesy of H.-S. Moon.)

design issue; and fasteners do not exist here so the engineering details involved with bolting, static sealing, etc., do not exist, [51].

Although many of the design considerations are independent of size, the engineering values are not, of course. Airfoils need fillets at the roots to avoid stress concentrations with radii of 10–30 μm . Surface finish is important with roughness measured in nanometers. Forced response excitation of blade rows must be avoided with blade-bending frequencies on the order of megahertz rather than kilohertz, the rotor once-per-rev frequency is 20 KHz rather than 200 Hz. For the turbine of Fig. 6, the lowest blade mode is 2.5 MHz while the blade-passing frequency is 0.9 MHz.

Below 850–900 K, silicon is a brittle material so that probabilistic analysis is a preferred method for failure analysis. Such techniques applied to the turbine rotor geometry of Fig. 6 at peripheral speeds of 500 m/s predict failure probabilities of 10^{-10} to 10^{-8} , depending upon the flaw population assumed, [52]. In a rotor constructed from single-crystal Si, all of the flaws are likely to be surface flaws. In a rotor of CVD SiC, volumetric flaws may also exist. In either case, the flaw population and thus the usable strength of the material is a strong function of the manufacture, as it is at any scale. A variation of a factor of four in strength has been reported for deep-etched Si depending upon post-etch surface treatment, [53].

Large engines use standard tubing fittings and electrical connectors to pass fluids and electrical signals to the outside world. These do not exist at microscale. Most computer chips and MEMS devices do not require fluid connections and those that do operate not much above room temperature. For these applications, there are a variety of adhesives and polymer systems. A micro-gas turbine can have a surface temperature above 700 K and require fluid connection at pressures of 10 atm or more, so that high-strength high-temperature packaging approaches are needed. One approach which has proven successful is an adaptation of the hermetic package technology used for military electronics. This joins Kovar (a nickel alloy) tubing to silicon using glass as the bonding agent. The joining is done in a furnace above 1100 K to melt the glass. Such joints can withstand pressures above 200 atm, [54].

Engine Controls and Accessories

All gas turbine engines require control systems to insure safe operation. Typically, the control system adjusts the fuel flow to deliver the requested power, and monitors engine operation to

avoid unsafe conditions such as over-speed, over-temperature, or surge. Such a control system consists of sensors (speed, pressure, temperature, etc.), a feedback controller with a suitable set of control laws (now implemented in a digital computer), actuators such as a fuel control valve (often called a fuel management unit or FMU), and compressor stability devices as needed (bleed valves, fences, variable stators). Engine accessories include an ignition system, fuel pump, lubrication system, and starter. All of this functionality is needed for a millimeter-scale MEMS gas turbine and all must fit within a micro chip if the accessories are not to dwarf the engine. Following in the tradition of large engine development, the controls and accessories have received less attention to date than the major engine subsystems such as the compressor, turbine, and combustor but they are no less important to the ultimate success of the concept.

Engine Controls. The simplest engine control would consist of a single sensor feeding a digital controller which commands the fuel flow rate valves. The functional requirements for the valving and the sensors stem from the engine dynamics as represented in the control laws and from the engine environment. There is a very rich literature on MEMS sensors and valves, literally thousands of papers, and some units are commercially available. As for large engines, however, the combination of harsh environment, high-frequency response, high accuracy, and high reliability means that sensors and actuators for MEMS-scale gas turbines must be specifically engineered for that environment.

Engine control laws are generally based on reduced order models of the engine dynamics. The dynamics of millimeter-scale engines are, of course, much faster than larger engines and can also include phenomena not seen in large engines. The additional dynamics arise if there is significant heat transfer from the hot section into the compressor, [55]. In this case the heat transfer degrades the compressor performance so that the pressure ratio and mass flow are a function of hot section temperature as well as shaft speed. Since the heat transfer has a time constant not much faster than the rotor acceleration, it alters the dynamics of the gas turbine from that of a first-order system (as large engines are) to a second-order system, requiring additional sophistication in the control law design. The best way of avoiding this complexity is to thermally isolate the hot and cold sections of the engine, which is, of course, desirable for improved thermodynamic performance.

Sensors. Large-scale gas turbines use compressor pressure ratio and/or rpm as the primary input to the fuel control system. Sensor selection for a MEMS engine is a trade among observability of the state (dynamical information represented by the sensed quantity), response time, difficulty of fabrication, and environmental compatibility. Liu [55] used a dynamic model of a MEMS engine to evaluate the suitability of various sensor options including rpm and compressor discharge pressure or temperature. Of these, rpm is the most sensitive and temperature the least. Sensing is complicated by the high rotational frequencies (1,000,000 rpm) and high temperatures (600 K at the compressor discharge) in a very small engine. In principle, sensors can be fabricated integrally with an engine or located remotely, with each approach presenting challenges. A sensor remote from the gas path suffers reduced frequency response, which is already a challenge at the MEMS scale. In addition, it is difficult to be very remote from the gas path in an 0.5 mm long engine. Integral sensors must withstand the high temperature of the gas path. Even for sensors fabricated in the cold sections, they must be capable of withstanding a wafer-processing environment that exceeds 1000–1400 K. This effectively precludes the use of low temperature materials such as polymers and most metals in the device design. Integral sensors have several advantages, however. They can be very small and thus have high-frequency response, and many can be fabricated in parallel for low-cost redundancy.

One integral solution was developed by Tang [56] who adapted a hot-film-type sensor to this application (Fig. 26). Designed for

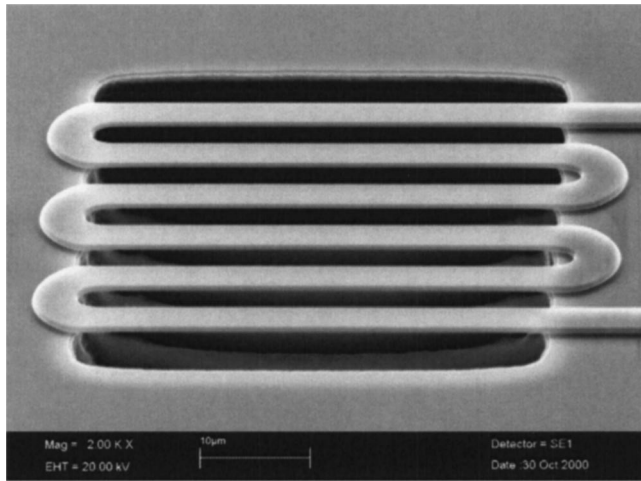


Fig. 26 A 50 μm sq hot film RPM and temperature sensor

placement on the wall above a rotor blade tip, this 50 μm square sensor is a heated, serpentine, polysilicon resistor positioned over a trench for thermal isolation. The sensor and its leadouts are all polysilicon which is selectively doped to adjust its resistivity (high for the sensor, low for the leads). Polysilicon has the advantage that it is compatible with most semiconductor fabrication techniques and can withstand high temperatures. Simulations confirmed by shock tube testing showed this approach to have sufficient sensitivity and frequency response to respond to the flow perturbations above a compressor blade tip as predicted by a three-dimensional CFD simulation. With a total thickness of less than 1 μm , such sensors could be fabricated on the casing above the compressor blade tips. This type of resistor has also been shown to be usable as an igniter.

Fuel Control Valves. Very small engines are the topic of this discussion so the fuel control valves should be equivalently small. If integrated within the engine, the valve design must then be fully compatible with the fabrication and operating conditions of the gas turbine. This choice strongly constrains the valve design space. For example, the high processing and operating temperatures prohibit the use of polymers, so a hard valve seat must be used. The principal design requirements are flow rate, pressure, frequency response, very low power consumption and leakage, and high temperature capability.

Yang et al. [57] developed MEMS fuel-metering valves for gaseous hydrocarbon fuels such as propane. The design is a simple silicon spring-mounted plunger opened by electrostatic forces and closed by a combination of the spring and fluid pressure forces. The electrostatic approach has the advantages that very little power is needed to open a valve (40 nW) and the electrical materials (polysilicon) are compatible with high temperature semiconductor fabrication technology. Such a valve is shown in Fig. 27. The 2 mm square valve has a 1000 μm diameter plunger which rises 3 μm off the seat when actuated. An 8-inch wafer of valves would contain about 5000 individual units. The valve opens against 10 atm pressure and, when open, flows 35 sccm of N_2 at a pressure drop of 0.5 atm. Frequency response is several hundred hertz. Cyclic testing of the valve has demonstrated a 50,000+ cycle life for the units tested. This design is on-off. The actuation-pressure scaling laws favor small valves so the intent is to use a parallel array of 20 on-off valves, each with a capacity of 5% of the maximum fuel flow, to meter the fuel. All 20 valves would consume less than 1 mW total power and operate at temperatures approaching 1000 K so they can be embedded in an engine chip. Many other arrangements are possible, such as logarithmic spacing of the valve orifice sizes to give finer fuel flow control.

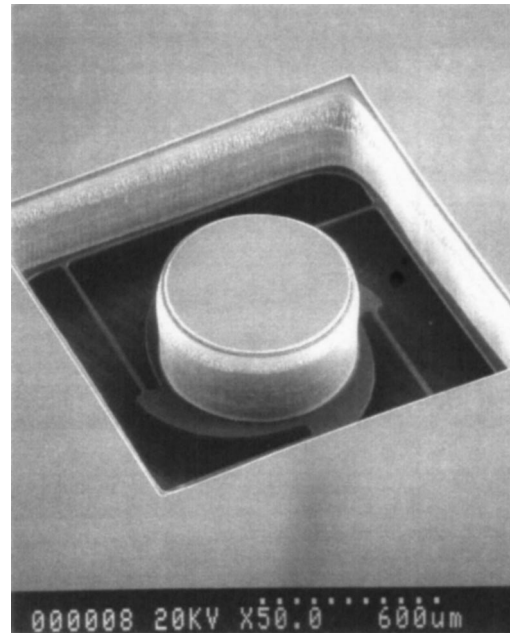


Fig. 27 A 1 mm dia. fuel control valve on Si beam springs

Starter-Generator. Microelectrical machinery is required for power generation and electric starting, if desired. There is an extensive literature on microelectric motors, which is not reviewed here, but little work on generators. The requirements for the devices of interest here differ from previous work in that the power densities needed are at least two orders of magnitude greater than that of conventional size and previous micromachines. Also, the thermal environment is much harsher. Integrating the electric machine within the engine offers the advantage of mechanical simplicity in that no additional bearings or structures are required over that needed for the fluid machinery. There is also a supply of cooling air available.

Both electric and magnetic machine designs can be considered and, to first order, both approaches can yield about equivalent power densities. Since the magnetic machines are material property-limited at high temperature and because of the challenges of microfabricating magnetic materials (which are not compatible with standard semiconductor manufacturing techniques), electric designs were first explored. Power density scales with electric field strength squared, frequency, and rotational speed. The micromachinery of interest here operates at peripheral velocities 1–2 orders of magnitude higher than previously reported micromotors, and so yields concomitantly more power. Electric machines may be configured in many ways. Here an induction design was chosen since it requires neither electrical contact with the rotor nor knowledge of the rotor position.

The operation of an electric induction machine can be understood with reference to Fig. 28, [58]. The machine consists of two components, a rotor and a stator. The rotor is comprised of a 5–20 μm thick good insulator covered with a few microns of a poor conductor (200 $\text{M}\Omega$ sheet resistivity). The stator consists of a set of conductive radial electrodes supported by an insulator. A traveling electric potential is imposed on the stator electrodes with the aid of external electronics. The resulting rotating electric field then induces an image charge on the rotor. Depending on the relative phase between the motion of rotor charges (set by the rotor mechanical speed) and that of the stator field (set by the external electronics), the machine will operate as a motor, generator, or brake. Torque increases with the square of the electric field strength and frequency. The maximum electric field strength that an air gap can maintain without breakdown is a function of the gap dimension. In air, the breakdown field is a maximum at a gap

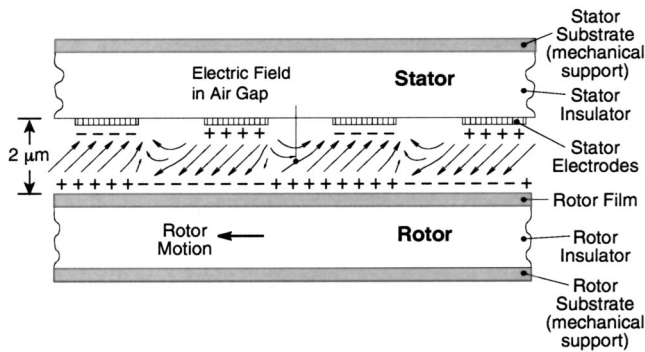


Fig. 28 Fields and charges in a microscale electric induction motor-generator

of a few microns so that micromachines can potentially realize higher power density than large machines of the same design. Frequency is constrained by external electronics design and by fabrication constraints on the stator electrode geometry. Current technology is limited to about 300 volts and 1–2 MHz. This is consistent with a 6 mm diameter machine producing about 10 watts at a 3 μm air gap. A 4 mm diameter, six-phase, 131-pole (786 electrodes, each 4 μm wide) stator for such a machine is shown in Fig. 29, [59]. Note that such an electric motor generator occupies less than 20 μm thickness at the surface of the rotor and stator (mainly the insulator thickness). Thus the power density of this machine (excluding the external electronics) is many times that of a conventional magnetic motor generator, on the order of 100 MW/m³. Fréchet et al. [60] have reported a similar design run as an electric motor. The torque produced by these devices has agreed with theoretical predictions but high power operation has yet to be reported.

To maximize power output, induction machines such as these require the spacing between the rotor and stator to be on the order of the stator pitch. The electrical torque produced scales with the square of the rotor-stator spacing, a few microns in this case. However, in these high-speed machines, the rotor periphery is at sonic velocity so the viscous drag in a gap of only 2–3 microns is extremely large. Indeed, this drag is the major loss mechanism for such an electrical machine. Thus, there is a basic design tradeoff for the electric motor generator between power density and efficiency. While it may be possible to alter the local geometry to reduce the drag somewhat, [24], the drag still makes up about half the total loss and limits the efficiency (shaft to net electrical) of these designs to 40–50%.

A magnetic induction machine has many fewer poles so that the optimum rotor-stator spacing is much larger (30–50 μm) and the drag concomitantly lower. Koser and Lang [61] designed such a machine based on the microplating technology developed by Park

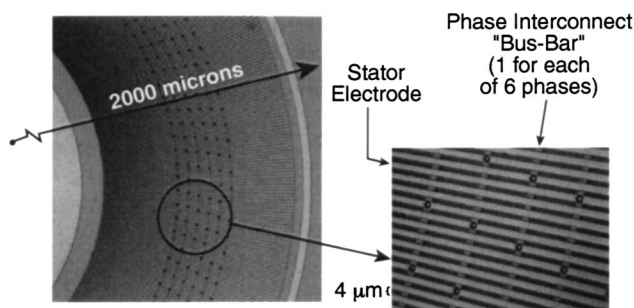


Fig. 29 A 131-pole, 6-phase, 4 mm dia. electric induction stator

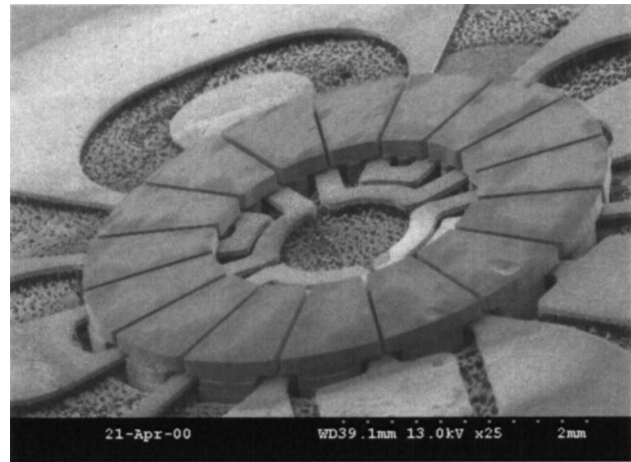


Fig. 30 A 4-pole stator for a 4 mm dia. magnetic motor-generator. (Figure courtesy of M. Allen.)

et al. [62]. A four-pole stator for a 4 mm diameter, induction motor generator, designed to be functionally equivalent to the electric machine in Fig. 29, is shown in Fig. 30. More recent versions of this stator include a laminated magnetic return path to reduce eddy current losses. The efficiency of this magnetic generator is calculated to approach 60%. It has the additional advantage that its external low-frequency low-voltage electronics are easier to engineer and more compact than the high-frequency high-voltage electronics of electric machines. Current stator materials are limited to only 500 K, however. Advanced materials may increase the operating temperature to 800 K. The rotor requires several hundred microns of iron for the magnetic path, which presents structural design challenges at 1,000,000 rpm. Magnetic machines will require careful thermal management when embedded within a MEMS gas turbine engine.

Engine Design Trades, Component Integration, and Design Evolution

Gas turbine engines are more than a set of components bolted together. Rather, a successful gas turbine is a highly integrated system engineered to meet specific requirements, often with artful compromises between conflicting demands of the fluid, thermo, structural, and manufacturing engineering. A MEMS gas turbine is no different in this respect. The two dominant design considerations are the fabrication complexity and the thermodynamic cycle requirements. The principal challenge is to arrive at a design which meets the thermodynamic and component functional requirements while staying within the realm of realizable micromachining technology.

For any gas turbine, maximizing net engine output power includes maximizing both power per unit mass flow (specific power) and mass flow. Specific power is sensitive to component efficiency and pressure ratio, especially at the low-pressure ratios under consideration here, 2:1 to 4:1. High-pressure ratio in a single-stage centrifugal machine implies high wheel speeds; 500 m/s peripheral speed was chosen as the maximum compatible with geometrically simple Si construction. This also requires bearings and rotor dynamics capable of such high-speed operation. High efficiency implies optimal airfoil design and tight clearances. Tight clearances, in turn, imply high manufacturing precision, careful design for centrifugal and thermal growth, and robustness to the occasional high-speed rub. The other key to high specific power is high turbine inlet temperature (TIT). This requires high temperature materials for the turbine or cooling or both. High mass flows require high through-flow Mach numbers and large flow areas. With these requirements in mind, let's examine how these trades influence the design of a MEMS gas tur-

bine. Specifically, the next section discusses why the demo engine design in Figs. 3 and 4 is so configured. The principal geometric constraint on the design is that imposed by the current state of the art in precision (micron-level accuracy) etch-depth capability of 300–500 μm . We will start with the turbomachinery.

The engine design of Fig. 3 requires six wafers: two form the rotor (and the annular combustor volume), and two are needed on each side of the rotor for the hydrostatic thrust bearings and their associated plumbing. Replacing the hydrostatic bearings with hydrodynamic ones would eliminate one wafer. Adding a generator mounted on a rotating compressor tip shroud would add one wafer. Adding control valves would add an additional wafer above the compressor. Such a complete, self-contained (other than electronics) gas turbine generator could thus be built with seven or eight wafers, not including external electronics.

In a centrifugal compressor and turbine of geometry similar to those in Figs. 10 and 14, turning at 400–500 m/s tip speed, turbomachine design is constrained to a blade span of 400–500 μm by fabrication technology and bending stress at the blade roots. Given the blade height, air flow increases with rotor diameter. Rotor diameter is constrained by the number of engines required per wafer and by etching uniformity (if a design goal is to avoid the necessity of dynamically balancing the rotor). Etch uniformity scales inversely with rotor area and blade height (i.e., mass flow is constrained by etch uniformity technology). Another factor influencing uniformity is rotor/stator airfoil count. Etch rate is a function of the local geometry, so for best circumferential uniformity there should be an even multiple of rotor and stator airfoils. This, of course, is deleterious to long-term vibrational life for the airfoils. If the rotor is fabricated from more than one wafer and etched with multiple masks, then mask and wafer alignment is an issue which favors the fewest possible wafers and masks. Rotor diameters up to 10 mm with 400–500 μm blade spans, fabricated from 1–3 wafers, are consistent with current capabilities.

Bearing placement is another first-order concern. The bearings must support the load and remain in their stable operating regime. The load capability of air bearings scales with the bearing area. The bearing length is constrained by current etching technology to 300–500 μm (and widths of 10–25 μm), so load capacity scales with bearing diameter. For hydrostatic journal bearings of constant length, the optimum width of the bearing for maximum stable operating speed scales inversely with diameter. So as the bearing diameter is reduced, the air required to operate the bearing goes up (since the flow per unit area grows faster than the area shrinks) and the load capacity goes down. This implies that bearing diameter should be maximized, i.e., on the rotor diameter. Placing the bearing here also eliminates the need for a seal on the rotor, since in this case the leakage air is the air bearing fluid, but this approach increases bearing drag.

The cycle needs turbine inlet temperatures of at least 1400–1600 K to meet the application goals. These relatively high temperatures are needed due to the relatively high losses in the components and the secondary systems such as bearings. For example, the shaft mechanical losses are 4–8% of the shaft work for the design in Figs. 3 and 4, ten times that of engines in the 5,000–30,000 lb thrust range. These temperatures are above the 900–950 K maximum operating temperature of a single-crystal Si rotor. In the engine design of Fig. 3, the turbine rotor is conductively cooled through the compressor disk to the compressor air, which has a quite deleterious effect on the cycle performance and thus on the net engine output. Improving performance requires thermally isolating the turbine from the compressor which can be accomplished by hollowing the shaft between them (100–200 μm of the turbine disk in Fig. 14). When this is done, the temperature capability of the turbine rotor must be increased. As for large engines, some combination of increased material capability and improved cooling is needed. Improved material capability can be provided by reinforcing the Si turbine disk with SiC, with the temperature capability increasing with fraction of SiC. So-called “film cool-

ing” (it is really a film insulation) is the most effective cooling technique here since, in this case, the heat is prevented from entering the solid.

As with large engines, improving performance at the MEMS scale will require some combination of more complex designs, better materials, and improved manufacturing technology. For example, cycle pressure ratios much over 4:1–5:1 will require multiple spools (probably not concentric). Higher turbine inlet temperatures will require improved cooling and fabrication technology for such materials as silicon carbide, silicon nitride, and sapphire. Improved propulsive efficiency can be realized with bypass engine designs. Better compression system performance will require more attention to thermal isolation. These are all physically possible but will require considerable investment in both the disciplinary and microfabrication technologies.

Ongoing Technical Developments

As of this writing, no one has yet reported an operating gas turbine engine at this scale. Many of the turbomachinery efforts appear to be currently wrestling with rotor dynamics issues. At MIT, the requisite component technologies for the H₂ demo engine of Figs. 3 and 4 have been demonstrated at the component level—turbine, bearings, combustor, etc.—but a complete device fabricated to the design specification has yet to be tested. The challenge appears to be one mainly of stringent process control in a long, complex fabrication sequence, which is different in detail but in many ways as challenging as that for a microprocessor. Meanwhile, work is ongoing on improving component aerodynamic performance, hydrocarbon combustors, thermal isolation, high temperature materials (SiC), bearing system robustness, and electric and magnetic generators.

MEMS gas turbines differ not only in design and manufacture from conventional engines, they differ in development process as well. Specifically, since the engines are monolithic blocks of silicon, they cannot be disassembled, reworked, and then reassembled during development. Instead, a new engine must be built from scratch. This is a process which takes about three months since even a seemingly minor change, for example increasing bearing clearance, may require some process development. Conceptually, the parallelism inherent in the MEMS manufacture could be an advantage in development. For example, if the optimum clearance was unknown, a wafer could be built with engines of various clearances. To date, this approach has not proven productive at MIT since the majority of the problems encountered have largely been unanticipated or attributable to inadequate process control.

Future developments can be considered in three broad categories: evolution of MEMS gas turbines in both technology and application, other approaches to gas turbine engines in the centimeter-size range, and additional applications for millimeter-to-centimeter-sized devices based on the technologies discussed above.

The current MEMS engine design has a projected performance level comparable with gas turbines of the 1940s (Fig. 31). At these low-cycle pressure ratios, small improvements in pressure ratio and component efficiency have disproportionate returns of efficiency and output power (Fig. 32). So it is likely that the performance of these devices can be increased, perhaps up to that of the 1950s. Some of the improvements will come from component evolution, others from new configurations or more complex cycles. The approaches of recuperated engines and combined cycles have been explored.

Combined Cycles. Cycles with heat exchangers are attractive at microscale because heat exchangers scale favorably as size is reduced. MEMS heat exchangers have the advantage of high effectiveness and their repetitive structure is readily producible by microfabrication techniques. A micrograph of a high-temperature

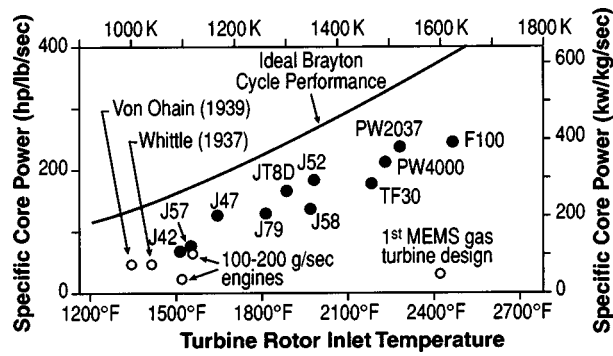


Fig. 31 Specific core power versus turbine rotor inlet temperature (after Koff)

heat exchanger is shown in Fig. 33, [63]. There is now a large literature on MEMS heat exchangers, including both single and multiple-phase devices, and their behavior, [64].

Given the high temperatures and poor efficiencies of these very small gas turbines, their exhaust contains relatively large amounts of high quality heat. Thus, performance is greatly improved when this waste heat is productively utilized. Calculations suggest that both MEMS-combined cycles and cogeneration cycles are feasible. One such steam-combined cycle system increases the net system output by about 50% over that of the gas turbine alone, [65]. Cogen systems providing cooling or condensing water are obvious applications when the gas turbine is used for portable power generation.

Alternate Approaches. Several teams are working to build gas turbines in the few grams/sec mass flow range using a wider set of manufacturing technologies than MEMS, including conventional metal-forming techniques, [37,66,67] and mold shape deposition manufacture, [28]. Such an approach has its own set of advantages and disadvantages. One major advantage is the lack of an upper size constraint imposed by microfabrication technology, so that engines in the hundreds of watts may be feasible. Its principal challenge compared to the MEMS approach may be one of

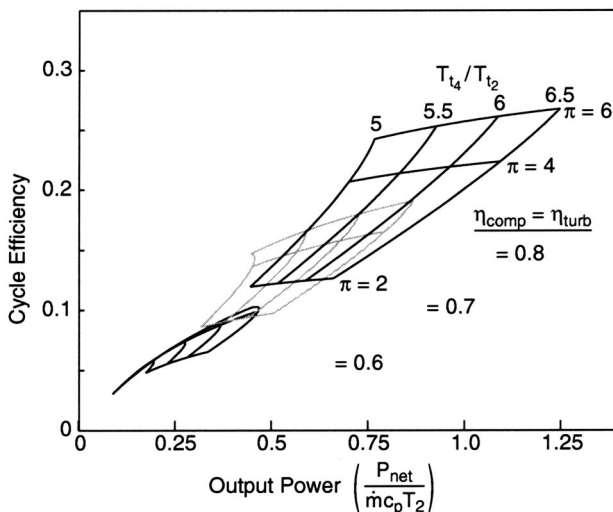


Fig. 32 Simple cycle performance variation for low pressure ratios, π (γ =adiabatic efficiency, T_{t4} =turbine inlet temperature, T_{t2} =compressor inlet temperature). (Figure courtesy of M. Monroe.)

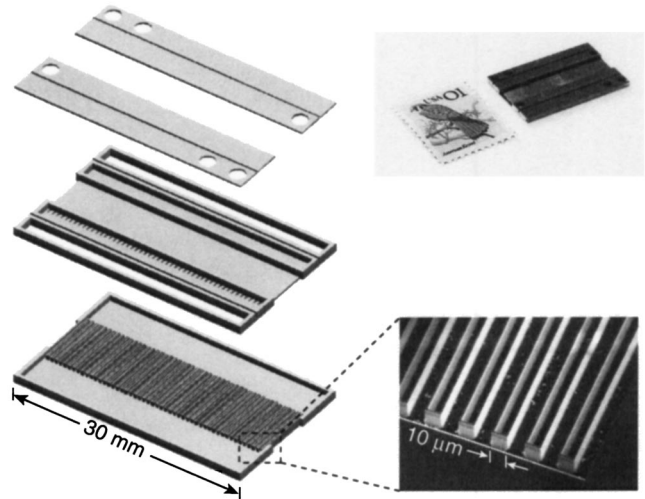


Fig. 33 Micron-scale counterflow heat exchanger. (Figure courtesy of J. Brisson.)

manufacturing cost. However, there are many low-cost precision manufacturing technologies for small parts and a need such as this may foster new ones.

Additional Devices. The technology needed for a MEMS gas turbine is based on microscale high-speed rotating machinery including disciplinary foundations in aerodynamics, combustion, materials, electromechanics, controls, and bearings. The same technologies can be applied to other microscale systems. One example is a motor-driven air blower or compressor, [60]. Another example is a micro-bipropellant liquid rocket motor which is under development, [68]. This propulsion system includes a regeneratively cooled silicon thrust chamber and nozzle (Fig. 34), turbopumps (Fig. 35), and liquid control valves, [69,70]. The propellant flow rate is about 5 g/s. The silicon thrust chamber is designed to operate at chamber pressures of 125 atm and temperatures of 3000 K. The pressure in the liquid cooling jacket around the combustion chamber is above 200 atm. These devices operate at much higher power densities than those of the current gas turbine components and demonstrate that very high pressure, high power density silicon structures and devices are feasible. Preliminary tests of the cooled thrust chamber and turbopump are promising. In support of the engineering design of these devices, fundamental studies have been conducted on cavitation in micropumps, [71], and the cooling behavior of a variety of rocket propellants in microgeometries, [72].

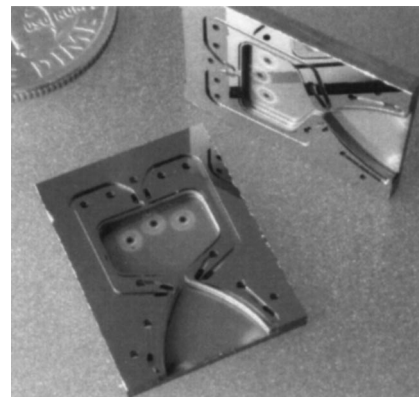


Fig. 34 A 15 N (3.3 lb) thrust bipropellant liquid rocket engine

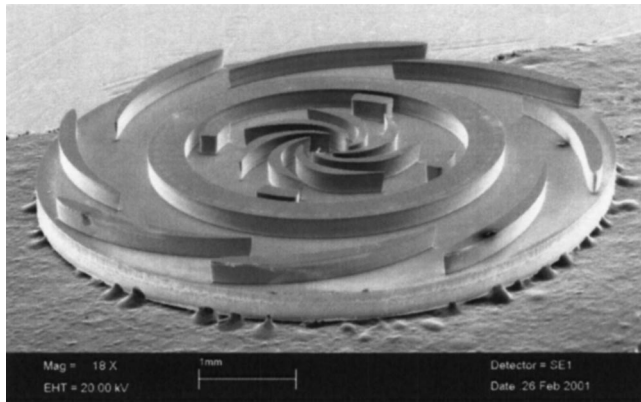


Fig. 35 A 2.5 g/sec turbopump rotor (the pump is the inner blade row, the turbine the outer)

Pacing Technology. Microfabrication is the pacing technology in the development of MEMS gas turbine engines. Fortunately, the rate of progress and innovation in MEMS fabrication dwarfs those of the more mature technologies familiar to gas turbine developers. Much of this progress stems from the wide promise that MEMS offers for a variety of applications, justifying large research investments across a broad set of approaches, [73]. Indeed, several fabrication limitations that existed at the start of this effort in the mid 1990s have since disappeared. Thus, many of the engineering design constraints now attributable to the microfabrication process limitations are likely to be relaxed as new technology is developed.

Economics and the Future of Millimeter-Scale Gas Turbines

Whittle and Von Ohain were successful in their early jet engine developments because they set engineering goals based on the requirement of going fast, significantly faster than the piston-powered aircraft of the day, [74]. In contrast, the gas turbine developers who based their requirements on competing on range with piston-powered propeller aircraft were unsuccessful at that time because their goal required much higher levels of performance, performance that was many years away. In this sense, we can ask what is required to make millimeter-scale gas turbines real—real in that machines are in production and making a discernable impact on society. There are two answers, one technical, the other economic. Many of the detailed technical issues were discussed above, but some must be considered in concert with the economics of power production. In the broadest sense, to be more than a curiosity, these very small gas turbine engines must fulfill societal needs. What are the possible applications and what levels of performance are needed for each? The answers must consider the alternative engineering solutions to each potential application.

The two major applications of these very small gas turbines mirror those of large engines, power production and aeronautical propulsion. Power production in the short term is aimed at portable applications where the very much larger energy density of a hydrocarbon fuel compared to a lithium battery chemistry means that even a very inefficient gas turbine can be attractive (Table 3). In the short term, a 5–10% overall system efficiency (chemical to net electric power output) is sufficient to make a gas turbine engine solution an attractive alternative to a battery. Figure 36 is a concept of an engine packaged in the form factor of a high performance 50 W military battery (which costs about \$100). Most of the volume is fuel which implies that, in this application, specific fuel consumption is more important than specific power (since multiple engines could be packaged together).

A somewhat different compact power application is auxiliary power for flight vehicles, especially ones with high temperature

Table 3 Harnessing available energy

| Energy Source | Potential* Whr/kg | Practical Whr/kg** Based on Conversion Device Efficiency |
|-----------------|-------------------|--|
| Lithium battery | 1400 | 175 (LiSO ₂) 300 (LiSOCl ₂) |
| TNT | 1400 | NA |
| Methanol | 6200 | 1500–3100 |
| Diesel fuel | 13,200 | 1320–5000 |
| Hydrogen | 33,000 | 1150–23,000 |

*Based on enthalpy

** $(\text{System conversion efficiency}) \times (\text{Energy available in fuel})$

environments. Highly redundant, distributed power for actuation, sensors, etc., may be attractive in many applications.

Competing with a 50–60% efficient central power plant requires much higher performance. Even including cogen use of the waste heat, a local gas turbine must have an efficiency of 20–30%, a level which looks many years away at this time. Should these levels be approached, then the redundancy and extreme quietness and compactness may make an array of millimeter-scale machines an attractive solution. Emergency power applications would not require as high performance as base power and can be an attractive application for these small machines if the capital costs are sufficiently low.

In addition to compactness and redundancy, one advantage that millimeter-scale gas turbines do offer for many applications is that they are very, very quiet, even in large arrays. This stems from their high frequencies (blade passing is several hundred kilohertz, beyond the audible range) and short length scales (millimeter-diameter exhaust jets, which mix rapidly). The high frequency sound that is produced is relatively easy to muffle and quick to attenuate naturally.

Propulsion is an obvious application for very small engines since cubed-square scaling means that they can have very high thrust-to-weight ratios and be extremely compact. The U.S. Defense Department is investing in reconnaissance airplanes with gross takeoff weights as low as 50–100 g. These aircraft have lift-to-drag ratios on the order of 5 so that an 0.1 N class thrust MEMS gas turbine such as that in Fig. 3 is an attractive power plant. It is much better than a battery-powered electric solution,

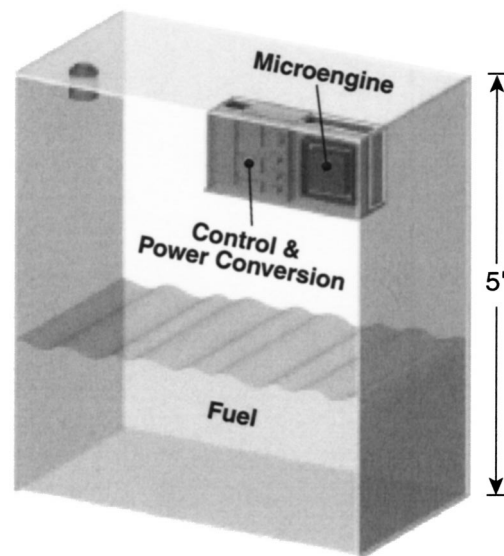


Fig. 36 Concept of a MEMS gas turbine engine packaged as a standard military battery

and IC engines in production are ten times too large, very noisy, and have poor fuel consumption. For subsonic flight applications, thrust and propulsive efficiency can be increased by adopting bypass engine configurations. High-speed flight may be another attractive application. Here the intrinsic high temperature capability (900 K) of even a silicon engine cold section means that the propulsion system can operate at high ambient temperatures. Configurations other than a gas turbine may also be realized, such as a ramjet or pulse detonation engine. Independent of the speed regime, clearly several engines can be used to realize increased thrust levels for larger vehicles. How large a thrust level is a function of how many engines can be practically assembled together (large phased array radars may use 10^5 modules) and the performance of the millimeter-scale engines relative to that of large engines. Since it is unlikely that engines of this size will approach the fuel economy of large engines, their use may be restricted to short duration applications use such as lift engines, where very high thrust-to-weight ratio, compactness, and redundancy may command a premium.

Both gas turbine engines and complex semiconductor devices are very expensive to develop and there is no reason to believe that a marriage of the two will prove substantially less so. Development costs can be amortized over many units. Manufacturing cost, however, is always a major issue for mass-produced devices. There is vast experience on the production cost of semiconductor wafers in large-scale production, much less on MEMS. For example, a standard 200 mm diameter silicon CMOS wafer from a foundry may cost \$600–1000 in large-scale production quantities (the industry is currently moving to 300 mm diameter wafers to reduce costs). A specialized wafer produced in small lots (such as GaAs used for radar and RF) may be ten times more expensive. The cost per chip is also a function of the number of chips per wafer (i.e., the size of the chip). Thus, a geometrically large, state-of-the-art microprocessor chip may cost \$200 to manufacture, while a small watch chip is only tens of cents. From this we infer that a wafer of MEMS gas turbines might produce several kilowatts of power and cost several thousand dollar to manufacture, putting the specific cost in the \$0.5–5 per watt range. On the low end this cost approaches that of large power plants.

If the more optimistic projections of their price and performance are achieved, then it is possible that these millimeter-scale machines and the technologies on which they are based may begin to transform the mechanical infrastructure of society in a manner similar to the changes in information handling wrought by the microprocessor. They will augment and even displace large central facilities. Distributed power, water treatment, and chemical processing may be realized, providing a more robust society. Many of the more significant changes this technology will engender are likely unrecognized at this time.

Concluding Remarks

Over the past eight years, research has started on very small gas turbine engines and related technologies. It is quite clear from the work to date that millimeter-scale gas turbine engines and similar high-speed rotating machinery, combustion, and energy conversion systems are technically feasible. One approach to realizing devices at these scales utilizes the semiconductor industry-derived micromachining technology known as MEMS. The economic impact of these devices will be dependent on the performance levels and the manufacturing costs, both of which have yet to be proven. It is certainly possible, however, that MEMS gas turbines may one day be competitive with conventional machines in a cost per installed kilowatt. Even at much higher costs, they will be very useful as compact power sources for portable electronics, equipment, and small vehicles.

Acknowledgments

Much of the work summarized herein is the intellectual accomplishment of a team at MIT including current and former research engineers and faculty—A. Ayon, K. Breuer, J. Brisson, F. Ehrich, R. Ghodssi, Y. Gong, S. Jacobson, R. Khanna, J. Lang, H. Li, C. Livermore, Y. Peles, M. Schmidt, S. Senturia, Z. Spakovszky, M. Spearing, C. Tan, S. Umans, I. Waitz, X. Zhang—and a large number of extraordinarily talented and hardworking graduate students, post-docs, and technicians. D. Park prepared the manuscript (and many, many others). It has been a great pleasure working with them all.

Special thanks goes to Drs. R. Paur and T. Doligalski of the US Army Research Office who were among the first to recognize the potential value of this technology and have nurtured it over the years.

The author would also like to thank Dr. J. L. Kerrebrock for 35 years as a mentor, colleague, and friend.

The research at MIT cited herein has been supported by the U.S. Army and DARPA.

References

- [1] Gerendas, M., and Pfister, R., 2000, "Development of a Very Small Aero-Engine," ASME Paper 2000-GT-0536.
- [2] Nakajima, T., Fukikawa, Y., Goto, T., and Iio, M., 1995, "The Development of the Micro Gas Turbine Generator," 1995 Yokohama International Gas Turbine Congress, Yokohama, Japan.
- [3] Senturia, S., 2001, *Microsystem Design*, Kluwer Academic Publishers, Boston, MA.
- [4] Jensen, K. F., 2001, "Microreaction Engineering—Is Small Better?" *Chem. Eng. Sci.*, **56**, pp. 293–303.
- [5] Epstein, A. H., and Senturia, S. D., 1997, "Macro Power From Micro Machinery," *Science*, **276**, p. 1211.
- [6] Epstein, A. H., Senturia, S. D., Al-Midani, O., Anathasuresh, G., Ayón, A., Breuer, K., Chen, K.-S., Ehrich, F. E., Esteve, E., Fréchette, L., Gauba, G., Ghodssi, R., Groshenry, C., Jacobson, S., Kerrebrock, J. L., Lang, J. H., Lin, C.-C., London, A., Lopata, J., Mehra, A., Mur Miranda, J. O., Nagle, S., Orr, D. J., Piekos, E., Schmidt, M. A., Shirley, G., Spearing, S. M., Tan, C. S., Tzeng, Y.-S., and Waitz, I. A., 1997, "Micro-Heat Engines, Gas Turbines, and Rocket Engines," Paper No. AIAA 97-1773.
- [7] Groshenry, C., 1995, "Preliminary Design Study of a Micro-Gas Turbine Engine," M.S. thesis, MIT Department of Aeronautics and Astronautics, MIT, Cambridge, MA.
- [8] Park, D.-E., Lee, D.-H., Yoon, J.-B., Kwon, S., and Yoon, E., 2002, "Design and Fabrication of Micromachined Internal Combustion Engine as a Power Source for Microsystems," *Technical Digest of MEMS 2002*, 15th IEEE International Conference on Micro Electro Mechanical Systems, Las Vegas, NV, IEEE, Piscataway, NJ, pp. 272–275.
- [9] Jacobson, S. A., 1998, "Aerothermal Challenges in the Design of a Microfabricated Gas Turbine Engine," AIAA 98-2545, 29th AIAA Fluid Dynamics Conference, Albuquerque, NM.
- [10] Spearing, M. S., 2000, "Materials Issues in Microelectro-Mechanical Systems (MEMS)," *Acta Mater.*, **48**, pp. 179–196.
- [11] Hawthorne, W. R., 1994, "Reflections on United Kingdom Aircraft Gas Turbine History," *ASME J. Eng. Gas Turbines Power*, **116**, pp. 495–510.
- [12] Madou, M., 1997, *Fundamentals of Microfabrication*, CRC Press, Boca Raton, FL.
- [13] Ayón, A. A., Lin, C. C., Braff, R., Bayt, R., Sawin, H. H., and Schmidt, M., 1998, "Etching Characteristics and Profile Control in a Time Multiplexed Inductively Coupled Plasma Etcher," 1998 Solid State Sensors and Actuator Workshop, Hilton Head, SC.
- [14] Lin, C. C., 1999, "Development of a Microfabricated Turbine-Driven Air Bearing Rig," Ph.D. thesis, MIT Department of Mechanical Engineering, MIT, Cambridge, MA.
- [15] Lin, C. C., Ghodssi, R., Ayón, A. A., Chen, D. Z., Jacobson, S., Breuer, K. S., Epstein, A. H., and Schmidt, M. A., 1999, "Fabrication and Characterization of a Micro Turbine/Bearing Rig," Presented at MEMS '99, Orlando, FL.
- [16] Mirza, A. R., and Ayón, A. A., 1999, "Silicon Wafer Bonding for MEMS Manufacturing," *Solid State Technol.*, **42**, pp. 73–78.
- [17] Miki, N., Zhang, X., Khanna, R., Ayón, A. A., Ward, D., and Spearing, S. M., 2002, "A Study of Multi-Stack Silicon-Direct Wafer Bonding for MEMS Manufacturing," *Fifteenth IEEE International Conference on Micro Electro Mechanical Systems (MEMS2002)*, Las Vegas, NV, IEEE, Piscataway, NJ, pp. 407–410.
- [18] Mehra, A., Ayón, A. A., Waitz, I. A., and Schmidt, M. A., 1999, "Microfabrication of High Temperature Silicon Devices Using Wafer Bonding and Deep Reactive Ion Etching," *J. Microelectromech. Syst.*, **8**, pp. 152–160.
- [19] Fréchette, L. G., Jacobson, S. A., Breuer, K. S., Ehrich, F. F., Ghodssi, R., Khanna, R., Wong, C. W., Zhang, X., Schmidt, M. A., and Epstein, A. H., 2000, "Demonstration of a Microfabricated High-Speed Turbine Supported on

- Gas Bearings," Hilton Head Solid-State Sensor & Actuator Workshop, Hilton Head Island, SC, pp. 43–47.
- [20] Ghodssi, R., 2003, private communication.
- [21] Mehra, A., Jacobson, S. A., Tan, C. S., and Epstein, A. H., 1998, "Aerodynamic Design Considerations for the Turbomachinery of a Micro Gas Turbine Engine," Presented at the 25th National and 1st International Conference on Fluid Mechanics and Power, New Delhi, India.
- [22] Mehra, A., 1997, "Computational Investigation and Design of Low Reynolds Number Micro-Turbomachinery," M.S. thesis, MIT Department of Aeronautics and Astronautics, MIT, Cambridge, MA.
- [23] Shirley, G., 1998, "An Experimental Investigation of a Low Reynolds Number, High Mach Number Centrifugal Compressor," M.S. thesis, MIT Department of Aeronautics and Astronautics, MIT, Cambridge, MA.
- [24] Fréchet, L. G., 2000, "Development of a Microfabricated Silicon Motor-Driven Compression System," Ph.D. thesis, MIT Department of Aeronautics and Astronautics, MIT, Cambridge, MA.
- [25] Sirakov, B., 2003, private communication.
- [26] Isomura, K., Murayama, M., Yamaguchi, H., Ijichi, N., Asakura, H., Saji, N., Shiga, O., Takahashi, K., Kawakubo, T., Watanabe, T., Yamagata, A., Tange, H., Tanaka, S., Genda, T., and Esashi, M., 2002, "Design Study of a Micro-machined Gas Turbine With Three-Dimensional Impeller," Presented at the 9th International Symposium on Transport Phenomena and Dynamics of Rotating Machinery, Honolulu, HI.
- [27] Isomura, K., Murayama, M., Yamaguchi, H., Ijichi, N., Asakura, H., Saji, N., Shiga, O., Takahashi, K., Tanaka, S., Genda, T., and Esashi, M., 2002, "Development of Microturbocharger and Microcombustor for a Three-Dimensional Gas Turbine at Microscale," ASME Paper GT-2002-30580.
- [28] Kang, S., Johnston, J. P., Arima, T., Matsunaga, M., Tsuru, H., and Prinz, F. B., 2003, "Micro-Scale Radial-Flow Compressor Impeller Made of Silicon Nitride, Manufacturing and Performance," ASME Paper GT-2003-38933.
- [29] Gong, Y., 2002, private communication.
- [30] Philippon, B., 2001, "Design of a Film Cooled MEMS Micro Turbine," M.S. thesis, MIT Department of Aeronautics and Astronautics, MIT, Cambridge, MA.
- [31] Spadaccini, C. M., Mehra, A., Lee, J., Lukachko, S., Zhang, X., and Waitz, I. A., 2002, "High Power Density Silicon Combustion Systems for Micro Gas Turbine Engines," ASME Paper GT-2002-30082.
- [32] Waitz, I. A., Gautam, G., and Tzeng, Y.-S., 1998, "Combustors for Micro-Gas Turbine Engines," ASME J. Fluids Eng., **120**, 109–117.
- [33] Mehra, A., Zhang, X., Ayón, A. A., Waitz, I. A., Schmidt, M. A., and Spadaccini, C. M., 2000, "A 6-Wafer Combustion System for a Silicon Micro Gas Turbine Engine," J. Microelectromech. Syst., **9**, pp. 517–527.
- [34] Zhang, X., Mehra, A., Ayón, A. A., and Waitz, I. A., 2002, "Development of Polysilicon Igniters and Temperature Sensors for a Micro Gas Turbine Engine," *Technical Digest of MEMS 2002*, 15th IEEE International Conference on Micro Electro Mechanical Systems, Las Vegas, NV, IEEE, Piscataway, NJ, pp. 280–283.
- [35] Spadaccini, C. M., Zhang, X., Cadou, C. P., Miki, N., and Waitz, I. A., 2002, "Development of a Catalytic Silicon Micro-Combustor for Hydrocarbon-Fueled Power MEMS," *Technical Digest of MEMS 2002*, 15th IEEE International Conference on Micro Electro Mechanical Systems, Las Vegas, NV, IEEE, Piscataway, NJ, pp. 228–231.
- [36] Takahashi, K., Murayama, M., Isomura, K., and Tanaka, S., 2002, "Development of a Methane Fueled Combustor for Micro-Scaled Gas Turbine," *Technical Digest of Power MEMS 2002*, Tsukuba, Japan, IEEE, Piscataway, NJ, pp. 44–46.
- [37] Matsuo, E., Yoshiki, H., Nagashima, T., and Kato, C., 2002, "Development of Ultra Micro Gas Turbines," *Technical Digest of Power MEMS 2002*, Tsukuba, Japan, IEEE, Piscataway, NJ, pp. 36–39.
- [38] Mur Miranda, J. O., 1997, "Feasibility of Electrostatic Bearings for Micro Turbo Machinery," M. Eng. thesis, MIT Department of Electrical Engineering and Computer Science, MIT, Cambridge, MA.
- [39] Walton, J. F., and Hesmat, H., 2002, "Application of Foil Bearings to Turbomachinery Including Vertical Operation," ASME J. Eng. Gas Turbine Power, **124**, pp. 1032–1039.
- [40] Spakovszky, Z. S., 2003, "Scaling Laws for Ultra-Short Hydrostatic Gas Journal Bearings," 19th Biennial Conference on Mechanical Vibration and Noise, ASME Paper No. DETC2003/VIB-48468.
- [41] Breuer, K., Ehrich, F., Fréchet, L., Jacobson, S., Lin, C.-C., Orr, D. J., Piekos, E., Savoulides, N., and Wong, C.-W., 2003, "Challenges for Lubrication in High Speed MEMS," *Nanotribology*, Hsu and Ying, eds., Kluwer Academic Press, Dordrecht, The Netherlands.
- [42] Liu, L., Teo, C. J., Miki, N., Epstein, A. H., and Spakovszky, Z. S., 2003, "Hydrostatic Gas Journal Bearings for Micro-Turbomachinery," to be presented at the 19th Biennial Conference on Mechanical Vibration and Noise.
- [43] Ehrich, F. F., and Jacobson, S. A., 2003, "Development of High Speed Gas Bearings for High-Power-Density Micro-Devices," ASME J. Eng. Gas Turbines Power, **125**, pp. 141–148.
- [44] Miki, N., Teo, C. J., Ho, L., and Zhang, X., 2002, "Precision Fabrication of High-Speed Micro-Rotors Using Deep Reactive Ion Etching (DRIE)," Solid-State Sensor, Actuator and Microsystems Workshop, Hilton Head Island, SC.
- [45] Piekos, E. S., and Breuer, K. S., 1998, "Pseudospectral Orbit Simulation of Non-Ideal Gas-Lubricated Journal Bearings for Microfabricated Turbomachines," ASME Paper No. 98-Trib-48, presented at the Joint ASME/STLE Tribology Conference, Toronto, Canada; also to appear in ASME J. Tribol. .
- [46] Wong, C. W., Zhang, X., Jacobson, S. A., and Epstein, A. H., 2002, "A Self-Acting Thrust Bearing for High Speed Micro-Rotors," *Technical Digest of MEMS 2002*, 15th IEEE International Conference on Micro Electro Mechanical Systems, Las Vegas, NV, IEEE, Piscataway, NJ, pp. 276–279.
- [47] Chen, K.-S., Ayón, A., and Spearing, S. M., 1999, "Controlling and Testing the Fracture Strength of Silicon at the Mesoscale," to be published in the J. Am. Ceram. Soc. .
- [48] Moon, H.-S., Anand, L., and Spearing, S. M., 2002, "A Constitutive Model for the Mechanical Behavior of Single Crystal Silicon at Elevated Temperature," *Mater. Res. Soc. Symp. Proc.*, Materials Research Society, Warrendale, PA, **687**, Paper No. B9.6.
- [49] Choi, D., Shinavski, R. J., Steffier, W. S., Hoyt, S., and Spearing, S. M., 2001, "Process Development of Silicon-Silicon Carbide Hybrid Micro-Engine Structures," *Materials Research Society Symposium Proceedings*, Materials Research Society, Warrendale, PA, **687**, Paper No. B5.44.
- [50] Sugimoto, S., Tanaka, S., Li, J.-F., Watanabe, R., and Esashi, M., 2000, "Silicon Carbide Micro-Reaction-Sintering Using a Multilayer Silicon Mold," IEEE Transducers, pp. 775–780.
- [51] Spearing, S. M., and Chen, K. S., 1997, "Micro-Gas Turbine Engine Materials and Structures," Presented at 21st Annual Cocoa Beach Conference and Exposition on Composite, Advanced Ceramics, Materials and Structures.
- [52] Chen, K.-S., Spearing, S. M., and Nemeth, N. N., 2001, "Structural Design of a Silicon Micro-Turbo-Generator," AIAA J., **39**, pp. 720–728.
- [53] Chen, K.-S., Ayón, A. A., Lohner, K. A., Kepets, M. A., Melconian, T. K., and Spearing, S. M., 1998, "Dependence of Silicon Fracture Strength and Surface Morphology on Deep Reactive Ion Etching Parameters," Presented at the MRS fall Meeting, Boston, MA.
- [54] Harrison, T. S., London, A. P., and Spearing, S. M., 2001, "High Temperature, High Pressure Fluid Connections for Power Micro-Systems," *Mat. Res. Soc. Symp. Proc.*, Materials Research Society, Warrendale, PA, **657**, p. 654.
- [55] Liu, C., 2000, "Dynamical System Modeling of a Micro Gas Turbine Engine," M.S. thesis, MIT Department of Aeronautics and Astronautics, MIT, Cambridge, MA.
- [56] Tang, D., 2001, "Rotor Speed Microsensor for the MIT Microengine," M.S. thesis, MIT Department of Mechanical Engineering, MIT, Cambridge, MA.
- [57] Yang, X., Holke, A., and Schmidt, M. A., 2002, "An Electrostatic, On/Off MEMS Valve for Gas Fuel Delivery of a Microengine," Solid-State Sensor, Actuator and Microsystems Workshop, Hilton Head Island, SC.
- [58] Nagle, S. F., and Lang, J. H., 1999, "A Micro-Scale Electric-Induction Machine for a Micro Gas Turbine Generator," 27th Annual Meeting of the Electrostatics Society of America.
- [59] Ghodssi, R., Fréchet, L. G., Nagle, S. F., Zhang, X., Ayón, A. A., Senturia, S. D., and Schmidt, M. A., 1999, "Thick Buried Oxide in Silicon (TBOS): An Integrated Fabrication Technology for Multi-Stack Wafer-Bonded MEMS Processes," *Transducers 99*, IEEE, Piscataway, NJ, pp. 1456–1459.
- [60] Fréchet, L. G., Nagle, S. F., Ghodssi, R., Umans, S. D., Schmidt, M. A., and Lang, J. H., 2001, "An Electrostatic Induction Micromotor Supported on Gas-Lubricated Bearings," IEEE 14th International Micro Electro Mechanical Systems Conference, MEMS 2001, Interlaken, Switzerland.
- [61] Koser, H., and Lang, J. H., 2000, "Modeling a High Power Density MEMS Magnetic Induction Machine," *Proc. Fourth International Conference On Modeling and Simulation of Microsystems*, Hilton Head, SC, Transducer Research Foundation, Cleveland, OH, pp. 286–289.
- [62] Park, J. W., Cros, F., and Allen, M. G., 2002, "A Sacrificial Layer Approach to Highly Laminated Magnetic Cores," *MEMS 2002 IEEE International Conference*, Las Vegas, NV, IEEE, Piscataway, NJ, pp. 380–383.
- [63] Sullivan, S., Zhang, X., Ayón, A. A., and Brisson, J. G., 2001, "Demonstration of a Microscale Heat Exchanger for a Silicon Micro Gas Turbine Engine," *Transducers 01*, IEEE Piscataway, NJ, pp. 1606–1609.
- [64] Harris, C., Kelly, K., Wang, T., McCandless, A., and Motakef, S., 2002, "Fabrication, Modeling, and Testing of Micro-Cross-Flow Heat Exchangers," J. Microelectromech. Syst., **11**, pp. 726–735.
- [65] Cui, L., 2003, "Design and System Analysis of Micro-Scale Rankine Cycle Power Systems," M.S. thesis, MIT Department of Aeronautics and Astronautics, MIT, Cambridge, MA.
- [66] Isomura, K., Murayama, M., and Kawakubo, T., 2001, "Feasibility Study of a Gas Turbine at Micro Scale," ASME Paper 2001-GT-101.
- [67] Isomura, K., Murayama, M., Yamaguchi, H., Ijichi, N., Saji, N., Shiga, O., Tanaka, S., Genda, T., Hara, M., and Esashi, M., 2002, "Component Development of Micromachined Gas Turbine Generators," *Technical Digest of Power MEMS 2002*, Tsukuba, Japan, IEEE, Piscataway, NJ, pp. 32–35.
- [68] London, A. P., Epstein, A. H., and Kerrebrock, J. L., 2001, "A High Pressure Bipropellant Microrocket Engine," J. Propul. Power, **17**, pp. 780–787.
- [69] Deux, A., 2001, "Design of a Silicon Microfabricated Rocket Engine Turbopump," M.S. thesis, MIT Department of Aeronautics and Astronautics, MIT, Cambridge, MA.
- [70] Jamonet, L., 2002, "Testing of a Microrocket Engine Turbopump," M.S. thesis, MIT Department of Aeronautics and Astronautics, MIT, Cambridge, MA.
- [71] Pennathur, S., Peles, Y., and Epstein, A. H., 2002, "Cavitation at Micro-Scale in MEMS Fluid Machinery," ASME Paper IMECE 2002-33328.
- [72] Joppin, C., 2002, "Cooling Performance of Storable Propellants for a Micro Rocket Engine," M.S. thesis, MIT Department of Aeronautics and Astronautics, MIT, Cambridge, MA.
- [73] National Research Council, 2002, *Implications of Emerging Micro- and Nanotechnologies*, The National Academies Press, Washington, DC.
- [74] Golley, J., *Genesis of the Jet*, 1996, Gunston, B., tech. ed., Airlife Publishing, Shrewsbury, England.

Reducing Grid Dependency in Droplet Collision Modeling

David P. Schmidt¹

Department of Mechanical and
Industrial Engineering,
University of Massachusetts,
Box 32210
Amherst, MA 01003-2210

Christopher J. Rutland

University of Wisconsin Madison,
1500 Engineering Drive,
Madison, WI 53706

Droplet collision models have been criticized for creating large mesh dependency in spray calculations. These numerical errors are very troublesome; they behave erratically and interfere with the predictive ability of physical models. The collision method used in KIVA can cause mesh dependent changes in average drop size of over 40 microns. In order to reduce mesh dependency, a new method has been developed for calculating the incidence of collision. The solution is to create a special collision mesh that is optimized for accuracy. The mesh is created automatically during the spray calculation. Additionally, a different stochastic collision sampling technique is also used. The new method, called the NTC algorithm, was incorporated into KIVA and found to be much faster than older algorithms. Calculations with 60,000 parcels required only a few CPU minutes. With the new NTC method and collision mesh, the mesh dependence of the drop size is only nine microns. This remaining mesh dependency is found to be due to the drag calculations and is not the fault of the collision algorithm. [DOI: 10.1115/1.1564066]

Introduction

Droplet collisions are an important, fundamental physical process in diesel fuel injection. In the core of the diesel spray, the droplet number density is very high. The effect of interphase drag and a broad size distribution creates a wide spectrum of droplet velocities. These large relative velocities between the drops then cause numerous collisions. Turbulent dispersion further promotes relative velocity between individual drops and subsequent collisions. Thus, any complete spray model must consider droplet collisions.

Collisions lead to several outcomes: bouncing, coalescence, and shattering. All collisions are inelastic and result in an exchange of momentum, which alters the distribution of droplet velocities in the spray. Drop size is affected through coalescence, which opposes breakup by agglomerating smaller drops into larger ones. According to early modeling work by O'Rourke, coalescence can cause a sevenfold increase in average drop size, [1]. Gavaises et al. reaffirmed the importance of collision, though they observed a less dramatic size dependence [2]. Shattering is also possible at the high collision Weber numbers that can occur in sprays, [3]. Current uncertainties in predicting the outcomes of collisions do not change the fact that collision must alter the velocity, if not the size, of the two participating droplets. Collision will thus affect both the velocity and size distribution of the spray. However, the first critical step in understanding droplet collisions is calculating the incidence of collision.

Droplet collision rates have proven very difficult to calculate. In addition to the complex physics, droplet collision has presented several numerical difficulties. These difficulties include high computational cost and large numerical errors. The problems arise out of three main causes. The first is that a real spray has millions of droplets. In spray calculations only a sample of these drops are tracked as computational "parcels." Hence, the location of droplets are not known exactly. One must use some statistical technique to infer the droplet collisions from the tracks of the parcels. The second difficulty is the tendency of collision calculations to consume large amounts of CPU time. The cost of collision calculations usually increases with the number of parcels squared, discouraging the use of a large number of parcels. The third issue is

that sprays often evolve on length scales that are too small for the gas phase mesh to capture. Since the cell location of droplets is used to judge proximity, sprays are usually underresolved. In light of the large role that droplet collisions can have in determining drop size and velocity, this situation is unfortunate.

The most widely used approach currently is O'Rourke's Monte Carlo algorithm, as implemented in KIVA, [4]. O'Rourke's algorithm has had remarkable success and is based on sound reasoning. O'Rourke's algorithm is consistent with the stochastic nature of spray simulations, where only a sample of droplets is tracked. The tracked parcels represent varying numbers of drops. The size, number of drops, and velocities of parcels determine the probability of colliding with other parcels. Only parcels within the same gas phase cell are permitted to collide. This approach is second-order accurate in space, but Schmidt and Rutland showed that it can fail dramatically with typical mesh resolution, [5]. The problems of mesh dependency are particularly severe when using a Cartesian mesh, as shown in Fig. 1. The grid dependency can clearly be seen in the "clover leaf" pattern that forms from what should be an axisymmetric calculation. The grid dependency also causes large quantitative fluctuations in the predicted drop size.

There can be no doubt that collision is responsible for this artifact. Turning collision off removes the artifact, as seen in Fig. 2. Other researchers have observed that collision is highly mesh-dependent, which greatly alters predicted drop size. Aneja and Abraham [6], Hieber [7], and Post and Abraham [8], Nordin [9], among others, have reported that Sauter mean diameter and penetration of diesel sprays can be severely mesh-dependent. All of these sources confirm that droplet collision calculations are largely to blame for mesh dependency.

The artifact shown in Fig. 1 is not always present. Its occurrence depends on the mesh resolution, the number of parcels used, ambient gas density, and whether the mesh is polar or Cartesian. The distinctive shape of Fig. 1 is only observed when the injector is coincident with a Cartesian mesh node and the axis of injection runs parallel to the mesh lines. Figure 3 helps illustrate why this artifact occurs. Standard collision algorithms based on kinetic theory allow parcels to collide only if the parcels are in the same cell. The probability of a pair of parcels colliding is proportional to their velocity relative to each other. The parcels most likely to collide have trajectories nearly 90 degrees apart. These pairs of parcels have the greatest velocity difference. Since the collisions result in either coalescence or an inelastic bouncing, the trajectories near cell boundaries are preferentially eliminated.

Moving the injection off of the vertex does not improve the situation. Though the easily recognizable clover leaf artifact disap-

¹Corresponding author

Contributed by the Internal Combustion Engine Division of THE AMERICAN SOCIETY OF MECHANICAL ENGINEERS for publication in the ASME JOURNAL OF ENGINEERING FOR GAS TURBINES AND POWER. Manuscript received by ICE Division November 2001; final revision received by ASME Headquarters August 2002. Associate Editor: D. Assanis.

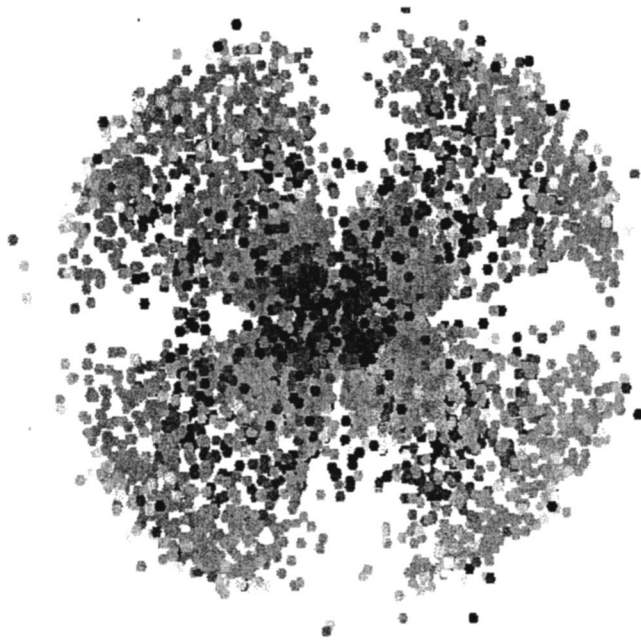


Fig. 1 Simulation of a hollow-cone spray using the standard KIVA3V Release 2 code with collision (O'Rourke's) turned on and breakup and turbulence turned off. The simulation is done with the injector on a vertex of a Cartesian mesh. The injection is directed towards the viewer, and the drops are shaded by diameter.

pears, the calculation is still grossly underresolved. Now, pairs of parcels that are on the far opposite sides of the injection may collide, so long as they have not crossed a cell boundary. Figure 4 illustrates how the most likely collision partners are actually the furthest apart in the cell. These pairs are not appropriate, and can cause the spray cone to artificially narrow. This narrowing is not as easily recognizable as the clover leaf, but is still very undesirable.

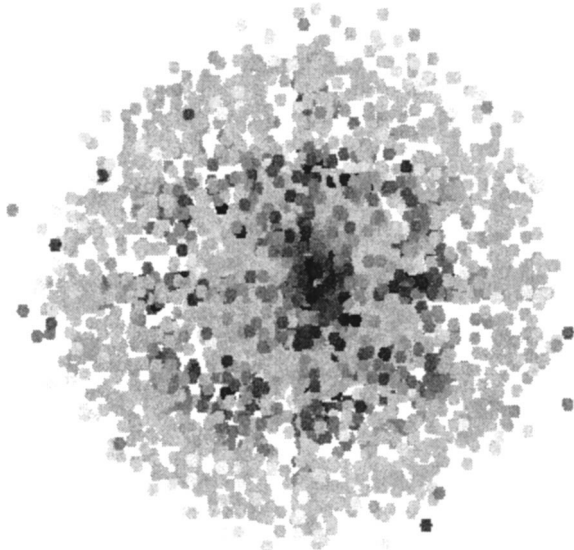


Fig. 2 Simulation of a hollow-cone spray using the standard KIVA3V Release 2 code with collision, breakup and turbulence turned off. The simulation is done with the injector on a vertex of a Cartesian mesh. The injection is directed towards the viewer, and the drops are shaded by diameter.

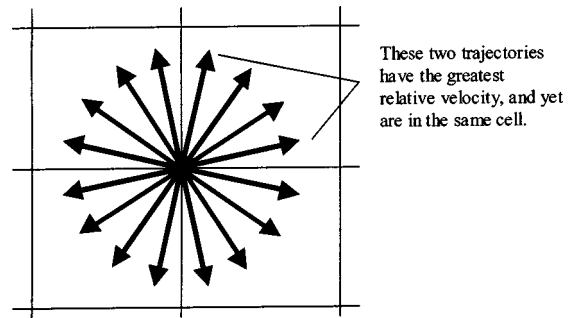


Fig. 3 A sketch of the parcel trajectories around an injection located at a vertex. The trajectories that are nearly 90 deg apart are the most likely collision partners.

The mesh dependency demonstrated in Figs. 1 through 4 is not entirely the fault of the collision algorithm. O'Rourke's collision method is soundly based on kinetic theory. The problem is that the point of injection is essentially a singularity. The sampling used for collision calculations should ideally take place on length scales that are shorter than the length scales of the spray. Adding to the difficulties, the natural polar symmetry of the singularity is not consistent with the 90-deg resolution (at best) of the Cartesian cells. The correlation between parcel location and velocity is not resolvable on a Cartesian mesh.

A new algorithm, first reported in Schmidt and Rutland [5], was developed to help resolve the mesh dependency problems. The method was based on the no time counter (NTC) method used in gas dynamics for direct simulation Monte Carlo (DSMC) calculations. However, Schmidt and Rutland reconstructed the algorithm from basic probability assumptions so that it could be applied to sprays, where the number of droplets per parcel is variable. Like O'Rourke's algorithm, the NTC algorithm is first-order accurate in time and second-order accurate in space. The algorithm was tested against analytical solutions and found to converge to the exact answer.

There are two significant improvements with the NTC algorithm. The first improvement is speed. The NTC algorithm achieves its results without consuming significant amounts of CPU time. For example, the calculation of collision between 60,000 thousand parcels requires less than three minutes of CPU time for 20 milliseconds of simulated injection duration. The second improvement is the use of a fully automatically generated collision mesh. It is possible to generate a collision mesh that is optimized for accuracy without any user intervention. The collision mesh achieves very high spatial resolution without incurring significant CPU cost. The mesh is cylindrical, oriented around the injection axis, and sized just large enough to contain all of the parcels. The mesh resolution is then set as fine as possible while

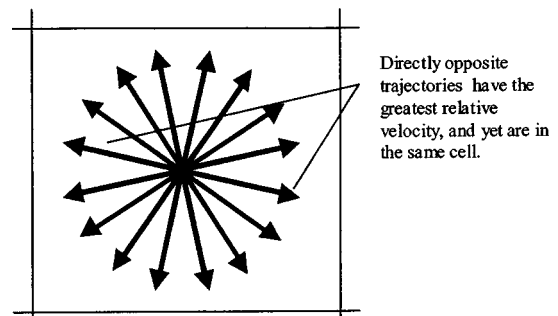


Fig. 4 A sketch of the parcel trajectories around an injection located at a cell center. The trajectories that are 180 deg apart are the most likely collision partners.

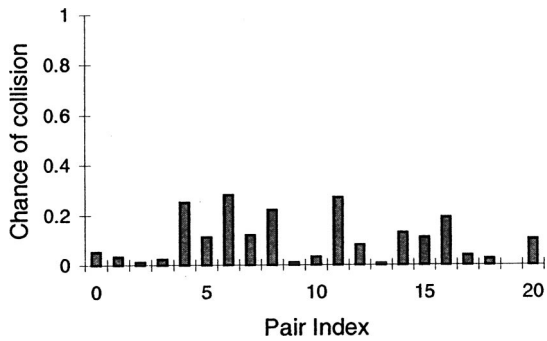


Fig. 5 A plot of the chance of collision for all possible collision pairs in a given cell

maintaining a significant sample size of drops in each collision cell. This approach allows the code to achieve millimeter-level resolution of the spray while only costing the user a few CPU minutes. Because the NTC algorithm is numerically consistent, the user can be assured of getting very accurate results.

The NTC method is very new. It is not clear how much grid dependency is present in the old collision algorithm and what reduction in grid dependency will occur with the NTC method. The following text summarizes the function of the NTC algorithm and then evaluates the grid dependency of the collision calculation. The physics of collision are not the central focus of this investigation and are not changed from O'Rourke's original collision outcomes. For modeling the physical outcomes, the reader should consult Post and Abraham [10].

Methodology

The NTC method involves stochastic subsampling of the parcels within each drop. This results in much faster collision calculations. Unlike O'Rourke's method, which incurs a cost that increases with the square of the number of parcels, the NTC method has a linear cost. Also, O'Rourke's method assumes that multiple collisions can occur between parcels and that this process is governed by a Poisson distribution. The Poisson distribution is not correct unless collision has no consequences for the parcels. Since collision changes parcels' velocities, drop size, and drop number, the method of repeated sampling used by the NTC method generates more accurate answers.

The NTC method is derived from the basic probability model for stochastic collision. The basic probability model requires that the cell size is sufficiently small that spatial variations in spray quantities can be neglected. These assumptions are a subset of those required for deriving the O'Rourke collision model. For a detailed derivation, see Schmidt and Rutland [5].

Given N parcels, there are N^2 possible collision partners. O'Rourke's scheme scans through all the possibilities and eliminates parcels that are not in the same cell. For parcels in the same cell, there is a probability of collision based on size, relative velocity, and the number of drops in the parcel. An example of 21 probabilities is shown in Fig. 5. The cost of this method is proportional to N^2 . To run with 10,000 parcels, for example, requires an effort proportional to one hundred million possible collision partners.

The NTC method first sorts the parcels into groups that reside in the same cell. This grouping only requires order N operations. Next, the NTC method picks a stochastic subsample from all the possible pairs in a cell. The number of picked pairs does not affect the final average answer, so long as the number meets constraints derived in Schmidt and Rutland [5]. The number of pairs in the subsample would be a fraction of the 21 pairs shown in Fig. 5. The probabilities for the subsample pairs are multiplied by the reciprocal of this fraction, increasing the probability of collision. An example of subsampled pairs is shown in Fig. 6. Sampling is

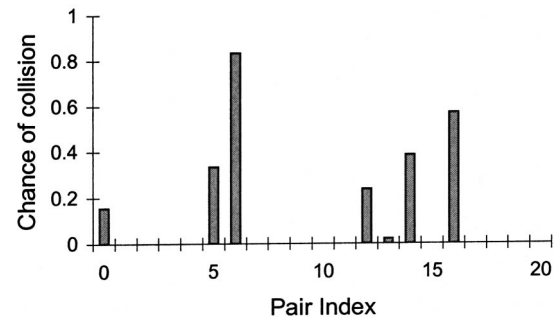


Fig. 6 A subsample of possible collision partners drawn from the example in Fig. 5. The probabilities have been multiplied by the number of possible pairs divided by the subsample size.

done with replacement so that multiple collisions for a pair can be correctly calculated. The resulting method incurs a cost that is linearly proportional to the number of parcels, as opposed to the N -squared cost of many existing methods. The accuracy of the NTC method has been validated with analytical solutions. Surprisingly, the NTC method has less random fluctuation around the exact answer than O'Rourke's method.

The other critical part of the NTC collision algorithm is the use of a collision mesh. O'Rourke's collision model is grid-dependent because of a lack of spatial resolution. O'Rourke calculated the incidence of collision using the gas-phase mesh, which is not sufficiently refined for collision calculations. However, there is no requirement to use the gas-phase mesh for collision calculations. The NTC implementation automatically creates a cylindrical mesh around the axis of injection. This mesh is independent of the gas phase and is used only for collision. The mesh resolution is set as fine as possible, while keeping a sufficient sample size in the cells near the spray center. The more parcels that are used in the calculation, the finer the collision mesh. Thus the collision mesh is optimized for accuracy by controlling both spatial and statistical resolution.

The special mesh is essential, because it provides flexible yet high resolution of the spray with little CPU cost. The mesh is automatically recreated every time step. The mesh is randomly rotated around the axis of the spray, so that the cell boundaries are stochastic. Since the parcels move, the extent of the mesh will always change. This stochastic mesh generation helps to suppress artifacts. Parcels get more of a chance to collide based on proximity, because two parcels that are near each other are likely to end up in the same cell. With a fixed collision mesh, two nearby parcels could be perpetually in different cells if their trajectories are aligned with cell boundaries.

A cylindrical collision mesh is ideal for sprays. The natural grouping avoids the problems shown in Figs. 3 and 4. Only parcels with a similar angular trajectory will be in the same cell. An example of a collision mesh is shown in Fig. 7. In practice, the resolution is usually on the order of a few millimeters. The extent of the meshed domain is always just sufficient to include the entire spray. The collision mesh implementation has been generalized, so that it will automatically wrap around an injection with any orientation in any sort of engine mesh. The only limitation is that the current implementation is for a single spray.

The basic steps in assembling the collision mesh are as follows:

1. Establish a local coordinate system, with an axial unit vector that is aligned with the direction of injection. Establish the direction of the radial unit vector so that it is orthogonal to the axial vector. The orientation of the radial vector around the axial vector is chosen stochastically. The third unit vector is then determined with a cross product of the other two.
2. Using the local polar coordinates, determine the maximum

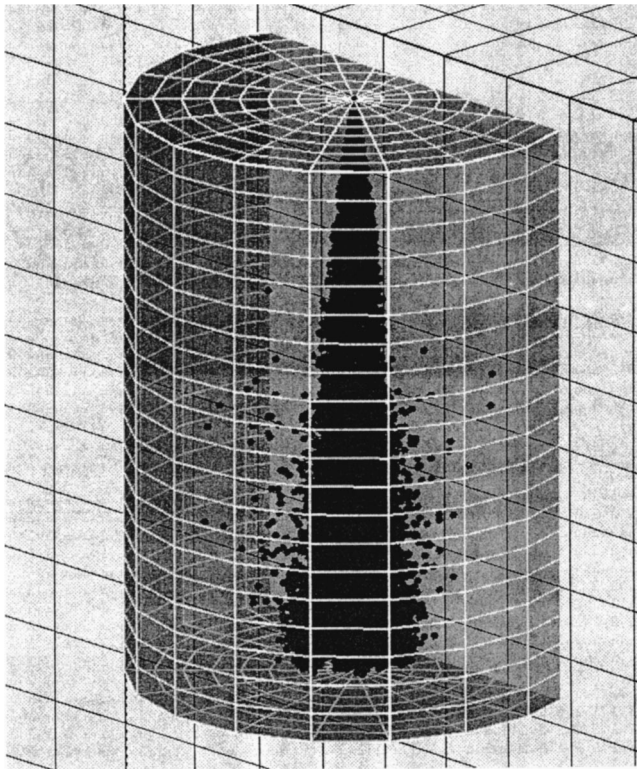


Fig. 7 A collision mesh enveloping a diesel spray. The gas phase mesh is in the background.

radial and axial extent of the spray. The angular extent of the spray is usually 360 deg, unless one is performing a sector or two-dimensional calculation.

3. Estimate a reasonable resolution in the axial and radial directions so that a predetermined average number of parcels per cell will be maintained. This average number can be as low as five parcels per cell, since nonuniformity of the sprays tends to provide large numbers of parcels per cell where collision rates are significant. In the current implementation, the ratio of the axial extent of the spray to the radial extent is used to establish cell aspect ratio. For the azimuthal direction, 20 cells are adequate to resolve a full 360 deg. For sector calculations, fewer azimuthal cells are needed.

4. Calculate the location of all parcels in the collision mesh. This step requires a transformation from the absolute coordinate system to the local polar coordinate system. Because the collision mesh is regular, the cell location is easily determined from the parcel location in the local coordinate system.

Though this implementation requires significant programming effort, the execution time is minimal. The cost of collision, including the generation of the collision mesh, is typically less than 1% of the simulation.

Results

The NTC method has been tested against several analytical solutions for particle collision. The scheme was shown to be first-order accurate in time and second-order accurate in space. For example, the code was tested using the spatially varying problem of a planar spray oriented along the x -axis. The particles were distributed using an exponential probability density function for y -position. The parcels were scattered with a uniform probability in the x and z direction, and given random velocity, number, and diameter with a uniform probability distribution. A view of this test case is shown in Fig. 8. The spatial accuracy of the algorithm was measured by forcing the collision mesh to be increasingly

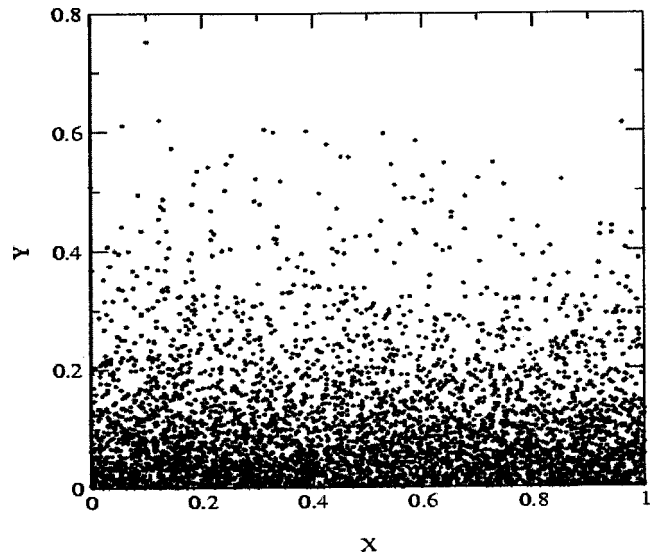


Fig. 8 A test case used to determine the accuracy of the NTC method. Parcels are distributed according to prescribed probabilities so that an analytical solution for the incidence of collision is possible. Note the strong spatial variation in the parcel density.

fine. The error was defined as the difference between the analytical solution and the prediction of the NTC algorithm. Figure 9 shows that with a very fine mesh, the error is less than 1%. With too coarse of a mesh, the error approaches 100%. This is also true of O'Rourke's method. These huge errors reinforce the importance of having adequate mesh resolution. Fortunately, with the NTC method and the collision mesh, the fine resolution required for good accuracy is easy to attain with no significant CPU penalty.

Next, the NTC algorithm was installed in KIVA. First, a diesel-type spray was simulated in KIVA with three different meshes. The domain was a cylinder with a diameter of 5 cm and a height of 20 cm and the injection duration was 3 ms. The cylinder was divided into three Cartesian meshes, with the resolutions shown in Table 1. A test calculation was performed to show the typical behavior of the collision mesh. This calculation used 40,000 par-

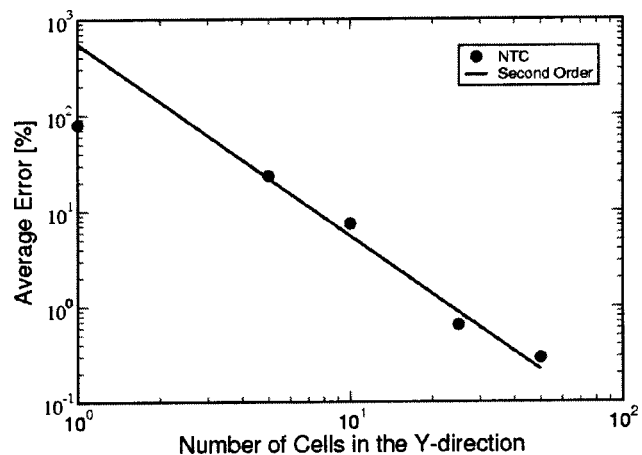


Fig. 9 The spatial accuracy of the NTC method is second order. With 25 cells in the collision mesh in the y -direction, the error is less than 1%.

Table 1 A description of the meshes used in the tests shown below

| | Cells in X Direction | Cells in Y Direction | Cells in Z direction | Total Cells |
|--------|----------------------|----------------------|----------------------|-------------|
| Coarse | 15 | 15 | 20 | 4500 |
| Medium | 30 | 30 | 100 | 90,000 |
| Fine | 45 | 45 | 150 | 303,750 |

cells and the medium gas phase mesh. The NTC collision algorithm was used with the TAB breakup model. Turbulence and turbulent drop dispersion were simulated with the standard *k*-epsilon model, as normally implemented in KIVA. This test was intended to show the resolution of the collision mesh in practical use. A plot of the axial and radial resolution is shown in Fig. 10. For the azimuthal direction twenty collision cells were used, which provides an angular resolution of 18 deg. The figure shows that the mesh starts out very fine because the spray occupies a very small volume. As the spray elongates axially during the early part of injection, the collision mesh elongates in the axial direction. Later, the radial spreading of the spray requires a wider collision mesh. The resolution in both directions becomes approximately 3 mm.

For the remaining calculations, all spray models were turned off, with the exception of drag and collision. The gas phase was solved without a turbulence model. The test case was not intended to generate physically reasonable results, but to show clearly the numerical behavior of the collision model. Because of the high computational cost of O'Rourke's algorithm, only 8,000 parcels could be used. For testing purposes, the same number of parcels were used for all subsequent comparisons between O'Rourke's algorithm and NTC. As a baseline, Fig. 11 shows the results with the original KIVA3V Release 2 code, including the original collision algorithm. The average drop size is very sensitive to the mesh resolution. The predicted drop size increased by 60% from the coarsest mesh to the finest. This difference of 40 microns is unacceptable for a modern CFD code. Even more troubling, the variation in drop size is not predictable. As the mesh is refined, the drop size decreases and then increases. The effect of the numerical error is thus unpredictable.

The nonmonotonic behavior of the drop size dependence on grid size is a consequence of two competing errors. When the mesh is very coarse, the number density of the spray is underpredicted. The fundamental assumption that the droplets are uniformly distributed within a cell leads to the minimum possible density of droplets. Because collision rate depends nonlinearly on

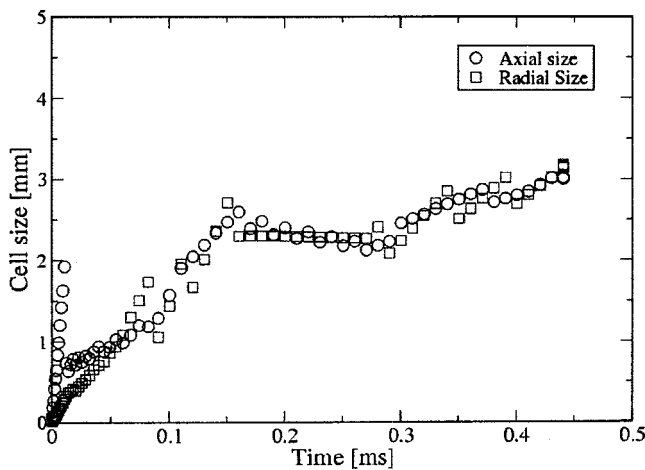


Fig. 10 Collision mesh resolution in the axial and radial directions as a function of time

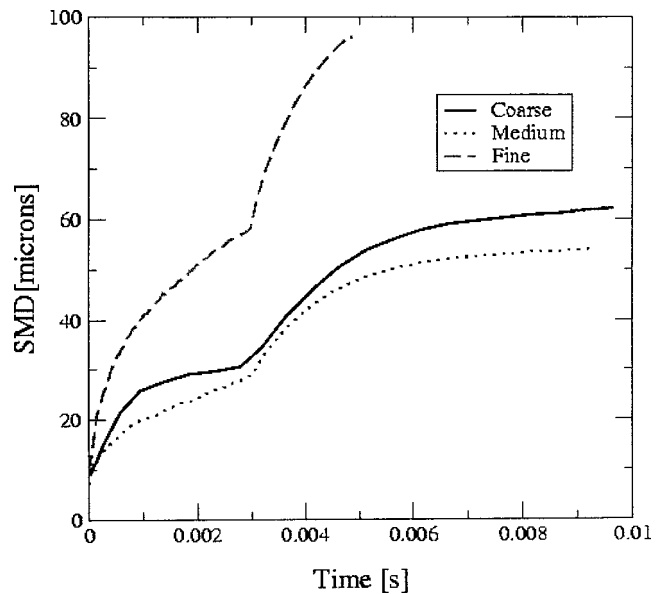


Fig. 11 Calculated average drop size for a diesel-type spray using KIVA3V Release 2 with three different Cartesian meshes. This figure shows the grid dependency of O'Rourke's collision model. The evaporation, breakup, and turbulence models were turned off, and collision was turned on.

number density, this uniform distribution leads to the minimum possible collision prediction. Refining the mesh helps to capture the nonuniformity in number density. However, as the mesh becomes very fine, the number of parcels per cell diminishes. This causes a statistical loss of resolution. When there are too few drops per cell, O'Rourke's algorithm relies heavily on the Poisson distribution to calculate multiple collisions between parcels. Since the Poisson distribution considers multiple collisions to be independent events, it always overpredicts collision incidence. If the mesh were made finer yet, it is possible that the predicted drop size could drop, since the probability of having only a single parcel in a cell would go up, leading to a suppression of collision. Post and Abraham also noticed this problem, [8].

Next, the NTC collision model was used, and the results are shown in Fig. 12. The predicted drop size is much less mesh-dependent. The NTC algorithm does not suffer from the under-resolution problem as much as O'Rourke's because the mesh is automatically set as fine as possible. There also is no problem with loss of statistical resolution, because the automatic mesh resolution considers the number of parcels per cell. The results shown in Fig. 12 are a significant improvement over the original KIVA collision algorithm. However, the results are not perfect. There is still some grid dependency in the NTC results. This grid dependence is not directly a fault of the NTC method, since the NTC algorithm does not rely on the gas phase mesh in any way. The mesh dependence is, instead, an indirect consequence of the mesh sensitivity of the coupling between the spray and gas phase momentum equation.

The corrupting influence of the momentum and drag coupling is clearly demonstrated by imposing a velocity of zero on the gas-phase. The velocity updates in KIVA were temporarily turned off, so that the code would run with a zero gas phase velocity. This trivial gas phase flow field was chosen because it is grid independent. Another important feature is that there will be no interpolation error of the local gas velocity to the particle position, because the zero velocity flow field is perfectly uniform. As the results in Fig. 13 show, the NTC method becomes perfectly grid independent. This result is expected, since the gas phase mesh is now completely unconnected from the calculation. However, when the same test is applied using O'Rourke's collision model, the final

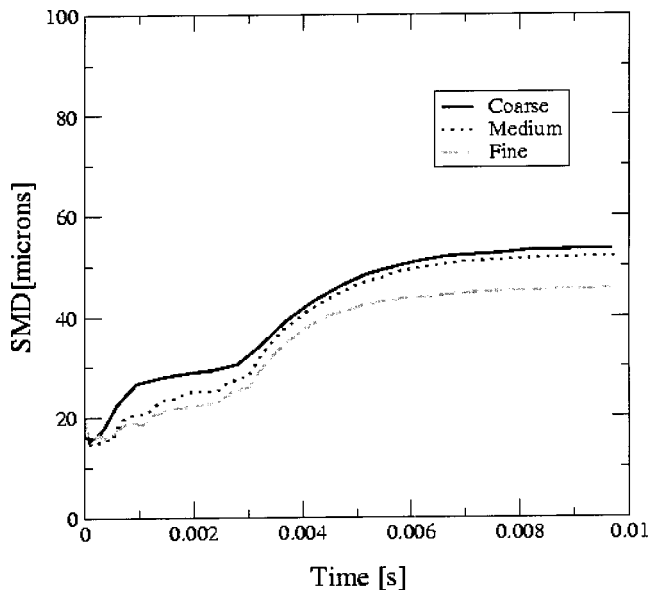


Fig. 12 The same test as shown in Fig. 7, but with the NTC collision algorithm. Note the reduced mesh dependency.

drop size varies from 32 to 39 microns, showing moderate grid dependency. As a final test of the NTC algorithm, a calculation was performed with varying numbers of parcels. Because the mesh automatically sets its refinement based on the number of parcels, this test simultaneously shows the affect of number of parcels and collision mesh resolution. As can be seen in Fig. 14, the predicted drop size is not significantly mesh dependent or sensitive to the number of parcels. The result of this test is important. It shows that the new algorithm is not mesh dependent. The small amount of mesh dependency seen in Fig. 12 cannot be due to droplet collision. Since all other models were turned off, the only remaining source of mesh dependency is the basic momentum coupling between the gas phase and the droplets.

In order to see the qualitative impact of the NTC algorithm on the structure of hollow cone spray computations, the simulation in Fig. 1 was repeated using the NTC method. The results with the

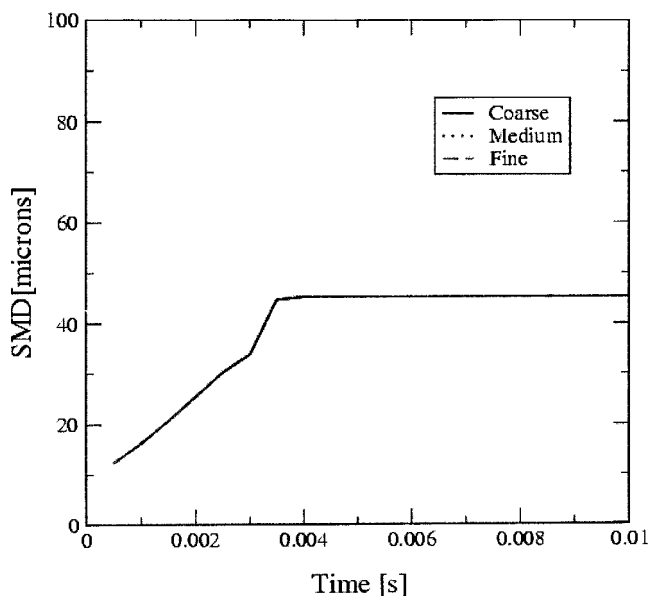


Fig. 13 The prediction of the NTC collision algorithm when the gas velocity is constrained to zero. The results are perfectly grid independent.

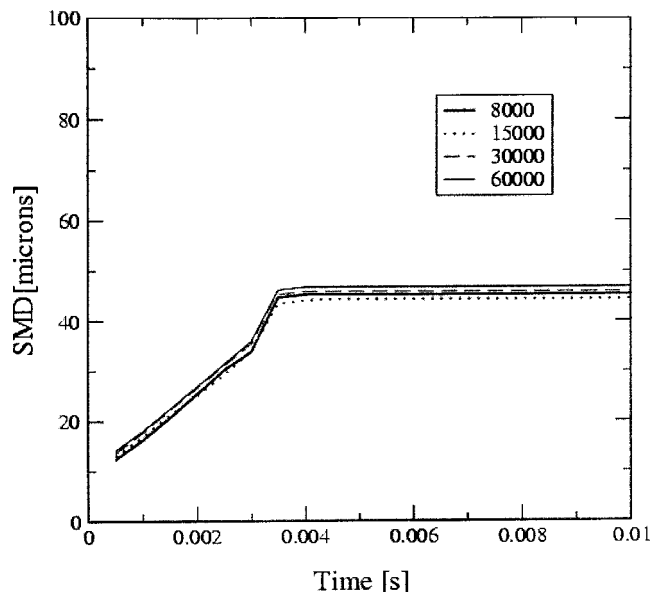


Fig. 14 The prediction of the NTC collision algorithm when the gas velocity is constrained to zero. The results show the effect of simultaneously changing the number of parcels used and the collision mesh resolution.

NTC method are shown in Fig. 15. The NTC method has significantly improved the simulation of the hollow-cone spray. The view shows that the spray is basically axisymmetric, unlike the clover leaf pattern that formed in Fig 1.

Conclusions

The NTC collision model has been demonstrated as a faster, more accurate, successor to current collision algorithms. The method is very fast: the collision calculation shown in Fig. 14 performed with 60,000 parcels took only about two minutes on a desktop computer. As another benefit, the NTC method shows only minimal mesh sensitivity. The use of a special collision mesh is mostly responsible for the reduced mesh dependency. The

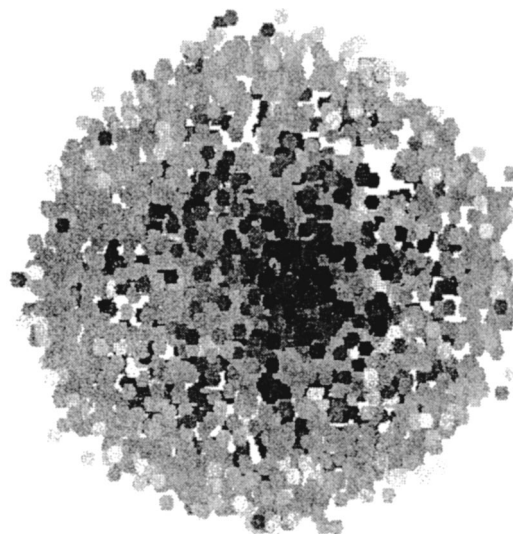


Fig. 15 Simulation of a hollow-cone spray using the standard KIVA3V Release 2 code with the NTC collision algorithm turned on and breakup and turbulence turned off. Simulation is done with the injector on a vertex of a Cartesian mesh. Injection is directed towards the viewer, and the drops are shaded by diameter.

small, remaining, grid dependence is actually not a limitation of the collision algorithm, but is due to the errors of the gas phase solution. If the gas phase solution were grid-independent, then the collision results would also be grid-independent. The NTC collision algorithm would be a good match with advanced interpolation schemes and momentum coupling techniques, such as Béard et al. [11]. The combination of accurate collision calculations and accurate coupling between the phases will produce spray simulations with much less grid dependence.

Acknowledgments

We thank Renault SA, which recognized the problems with calculating collision and sponsored the original development of the NTC algorithm. We also thank the Convergent Thinking LLC consulting firm, who lent advice and computer resources for the KIVA calculations.

References

- [1] O'Rourke, P. J., 1981, "Collective Drop Effects on Vaporizing Liquid Sprays," Ph.D. thesis, Department of Mechanical and Aerospace Engineering, Princeton University, Princeton, NJ.

- [2] Gavaises, M., Theodorakakos, A., Bergeles, G., and Brenn, G., 1996, "Evaluation of the Effect of Droplet Collisions on Spray Mixing," *Proc. Inst. Mech. Eng.*, **210**, pp. 465-475.
- [3] Georjon, Thierry L., and Reitz, Rolf D., 1999, "A Drop Shattering Collision Model for Multidimensional Spray Computations," *Atomization Sprays*, **9**(3), pp. 231-254.
- [4] Amsden, A. A., 1989, "KIVA-II: A Computer Program for Chemically Reactive Flows With Sprays," Los Alamos Report LA-11560-MS, May.
- [5] Schmidt, David P., and Rutland, C. J., 2000, "A New Droplet Collision Algorithm," *J. Comput. Phys.*, **164**, pp. 62-80.
- [6] Aneja, R., and Abraham, J., 1998, "How Far does the Liquid Penetrate in a Diesel Engine: Computed Results vs. Measurements?" *Combust. Sci. Technol.*, **138**, pp. 233-255.
- [7] Hieber, Simone, "An Investigation of the Mesh Dependence of the Stochastic Droplet Model Applied to Dense Liquid Sprays," Masters thesis, Mathematics Department, Michigan Technical University.
- [8] Post, S. L., and Abraham, J., 2002, "Modeling Collisions Among Drops With a Non-Uniform Spatial Distribution," 15th ILASS Americas, Madison, WI.
- [9] Nordin, Niklas, 2000, "Complex Chemistry Modeling of Diesel Spray Combustion," Ph.D. thesis, Chalmers University of Technology.
- [10] Post, S., and Abraham, J., 2002, "Modeling the Outcome of Drop-Drop Collisions in Diesel Sprays," *Int. J. Multiphase Flow*, **28**(6), pp. 997-1019.
- [11] Béard, P., Duclos, J-M, Habchi, C., Bruneaux, G., Mokaddem, K., and Baritaud, T., 2000, "Extension of Lagrangian-Eulerian Spray Modeling: Application to High Pressure Evaporating Diesel Sprays," SAE Paper No. 2000-01-1893.

The Selective Non-Catalytic Removal (SNCR) of Nitric Oxides From Engine Exhaust Streams: Comparison of Three Processes

Jerald A. Caton

Zhiyong Xia

Department of Mechanical Engineering,
Texas A&M University,
College Station, TX 77943-3123

Three processes for the selective non-catalytic removal (SNCR) of nitric oxides from engine exhaust gases are compared. The three processes are similar but each uses a different chemical agent: ammonia, urea, or cyanuric acid. A number of operating conditions have been studied. In particular, results for the removal of nitric oxide are significantly different for the three processes as the oxygen concentration varies. Ammonia, urea, and cyanuric acid were found to be most effective at low, intermediate, and high oxygen concentrations, respectively. The implications of these results for a range of engines and engine applications are discussed. [DOI: 10.1115/1.1688366]

Introduction

Combustion processes are known to result in a number of nitrogen species. Of these, the nitrogen species which are regulated are nitric oxide (NO), and nitrogen dioxide (NO₂) which together are known as NO_x. These nitrogen compounds are responsible for urban smog (including ozone) and some forms of acid precipitation, [1,2]. Another nitrogen species of interest is nitrous oxide (N₂O). Although currently not regulated, nitrous oxide has been classified as a greenhouse gas. Typically, nitrogen dioxide and nitrous oxide constitute less than 1% of the primary nitrogen compounds from combustion sources.

There are at least three major categories of methods of reducing nitric oxides: (1) treating the fuel, (2) minimizing the formation of nitric oxides at the source, and (3) removing nitric oxides by some means before expelling them into the atmosphere. For fuel treatment, the concept is to minimize any fuel-bound nitrogen. For the second category, the guiding philosophy for combustion modifications to reduce nitric oxides formation is to lower the combustion temperatures and reduce the amount of oxygen, [3]. Some examples of combustion modification methods are: staged air addition, steam and water injection, reburning, burner design modifications, furnace design modifications, boiler design modifications, and exhaust gas recirculation.

The other method for nitric oxides reduction is termed post-combustion gas treatment. Some examples of this category are: selective non-catalytic reduction (SNCR), selective catalytic reduction (SCR), non-selective catalytic reduction (NSCR), scrubbing methods, and techniques using electric fields. Other possibilities include combining SNCR and SCR techniques (e.g., [4]). Also, the use of plasmas combined with a version of SNCR using ammonia has been documented, [5]. A comprehensive review of nitric oxides reduction methods can be found in Bowman [3].

In general, the SNCR techniques involve injecting one or more chemical agents downstream of the primary combustion zone. The reduction of nitric oxide by these processes is a complex set of chemical reactions between the radicals produced by the injected chemicals and the products of combustion. A necessary prerequisite for an effective chemical agent is the presence of at least one nitrogen atom in its molecular structure.

For most cases, SNCR is effective over a narrow temperature

range, [3]. Reduction at higher temperatures is poor because the reducing agent itself oxidizes to NO. Below the optimum temperature, the selective reduction reactions are too slow and unreacted agent can be emitted (e.g., ammonia slip). In existing combustion systems, the spatial location of the optimum temperatures (referred to as the temperature "window") may vary with operating conditions or occur in regions of large thermal gradients. This places severe design constraints on the agent injection system which must disperse the chemical compound throughout the entire combustion product stream and mix with the nitric oxides while the gases are within the appropriate temperature window.

In general, a number of factors affect the overall performance of SNCR processes. These factors include the detail chemistry, the mixing of the agent with the exhaust gases, the nonuniformity of the gas temperatures, and the possibility of catalytic reactions. The chemistry is affected by the specific agent, temperature, pressure, concentrations of species, and residence time. Specific features of the chemistry that are important include the ratio of the agent to nitric oxide concentration, and the oxygen, carbon monoxide, and water concentrations.

The chemistry for these processes is complicated and the reactions that are most important for the removal of nitric oxide vary with operating conditions, [6]. In general, for these processes to be successful radical production is necessary. The radicals are responsible for generating the active species which reduce NO to N₂. The chemistry of these processes has been extensively studied, and related references are cited below relative to each process.

There are three main SNCR processes currently being implemented: (1) the thermal DeNO_x process which uses ammonia (NH₃), (2) the RAPRENO_x process which uses cyanuric acid ((HNCO)₃), and (3) the NO_xOUT process which uses urea (NH₂·CO·NH₂). For the cyanuric acid process, for most cases, the cyanuric acid sublimates to gaseous isocyanic acid (HNCO). Each of these processes is briefly described next.

The Ammonia Process. This was the original SNCR process and has been named Thermal DeNO_x. In this process, ammonia is injected into the hot exhaust gas. The form of the ammonia may be as aqueous (with water) solution or as anhydrous (no water) ammonia. This process was discovered in 1972, [7,8], for use in exhaust streams such as from furnaces and boilers. Since the original work, many groups have explored the ammonia process both experimentally and numerically, (e.g., [8–12]).

Specific concerns with the ammonia process include the storage, handling, and delivery of the ammonia. Also, any ammonia

Contributed by the Internal Combustion Engine Division of THE AMERICAN SOCIETY OF MECHANICAL ENGINEERS for publication in the ASME JOURNAL OF ENGINEERING FOR GAS TURBINES AND POWER. Manuscript received by the ICE Division, May 2001; final revision received June 2002. Associate Editor: D. Assanis.

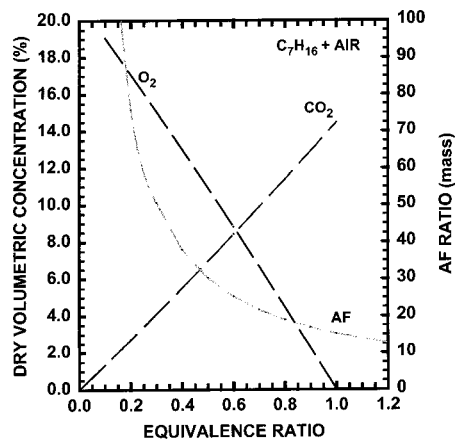
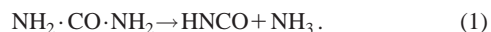


Fig. 1 Dry volumetric concentrations of oxygen and carbon dioxide and the mass air fuel ratio as a function of equivalence ratio for C₇H₁₆ and air combustion

not consumed in the process may be emitted (“ammonia slip”) as a result of this process. For these and other reasons, alternative agents have been proposed over the years. Two of these that have received significant interest include cyanuric acid and urea. Although it was the last of the three processes to be discovered, the cyanuric acid process will be discussed next, since the urea process can be described as a combination of the ammonia and cyanuric acid processes.

The Cyanuric Acid Process. In this process, known as the RAPRENOx process, solid cyanuric acid is injected into the hot exhaust gases. The solid cyanuric acid sublimates at about 650 K to gaseous isocyanic acid (HNCO). The isocyanic acid initiates a series of reactions for appropriate conditions which result in the removal of nitric oxide. This process was first proposed by Perry and Siebers [13], and has been studied by a number of investigators (e.g., [14–20]). One characteristic of this process is the possible emission of nitrous oxide (N₂O). Although all three of the processes may produce N₂O, the cyanuric acid process appears to have the potential to produce the most.

The Urea Process. NOxOUT is the name of the process which uses urea, [21]. In this process, typically either solid urea or a urea solution (with water) is injected into the hot exhaust gases. Urea may decompose into HNCO and NH₃ under certain conditions, [15]:



For these reasons, the urea process has been described as a combination of the ammonia process and the cyanuric acid process. As discussed by Jørdal et al. [22], however, the thermal breakdown of urea at temperatures above 600 K may lead to the formation of NH₂ and NCO radicals, and H₂ molecules in equal proportions. Numerical studies of the urea process for these other urea decomposition paths have been reported by Alzueta et al. [23]. Alternatively, urea has been found to decompose into biuret (NH₂CO(NH)CONH₂) under different conditions, [24].

The urea process has been studied numerically by several groups (e.g., [22,25,26]). A key feature of the modeling has been the treatment of the urea decomposition (as previously mentioned). Also, Brouwer et al. [27] have reported on a model which includes all three processes.

Importance of Oxygen Level. Applications involving combustion include a wide range of devices such as boilers, furnaces, gas turbines, diesel engines, and spark-ignition engines. For a number of reasons, these devices are operated with combustion at different stoichiometries. Figure 1 shows the dry volumetric concentrations of oxygen and carbon dioxide (product species), and

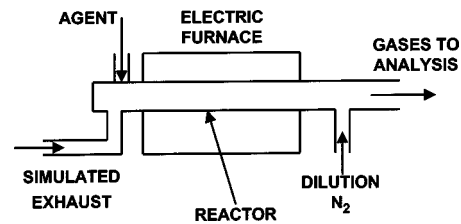


Fig. 2 Schematic of typical experimental system

the mass air-fuel ratio as functions of equivalence ratio for the complete combustion of heptane (C₇H₁₆) and air. Although these numbers are specific for heptane, results are similar for other hydrocarbon fuels. As shown, the oxygen level in the exhaust gases may range from less than 1% to over 15% (by volume) depending on the overall equivalence ratio (or air-fuel ratio).

In general, combustion devices are designed to operate effectively within a number of constraints. These constraints often impose that the overall equivalence ratio must be within a particular range. For example, a successful design for medium-speed diesel engines typically uses a quiescent mixture (as opposed to a swirling mixture) and relies on fuel atomization and penetration for good combustion. To insure the success of the combustion event, the overall reactant mixture must possess excess air. For this application, mixtures with an equivalence ratio of about 0.5 have proven successful.

On the other hand, a smaller automotive engine may be designed to operate closer to stoichiometric mixtures. This is a decision often dictated by the requirements of the exhaust catalyst system. As a further example, gas turbines are often operated with high excess air levels to insure adequate cooling of the turbine blades. For this reason, gas turbines may be operated with an overall equivalence ratio of about 0.3 (oxygen concentrations of about 15%).

The original studies of SNCR processes focussed on cases with oxygen concentrations of about 1 or 2% which would be typical of furnaces and boilers (e.g., [8]). Since then, a number of studies have examined cases for higher oxygen concentrations. For example, Caton et al. [10,11] have reported on cases for the use of ammonia with oxygen concentrations up to 15%. Also, Kasuya et al. [28] have reported on results for ammonia for oxygen concentrations up to 50%. For the use of urea for oxygen concentrations up to 15%, Srivatsa [29] and Caton and Srivatsa [30] have completed these studies. For the cyanuric acid process, Caton and Siebers [15] have reported results for three oxygen levels. The objective of this paper is to compare the three processes and to examine the importance of the oxygen (or overall equivalence ratio) on the combustion process.

Experiments

The data discussed below have been obtained from similar experimental systems. Figure 2 is a schematic of a typical experimental system. The overall experimental facility consists of four distinct systems: (1) the input gas mixture metering and delivery system, (2) the chemical agent metering and delivery system, (3) the furnace and reactor assembly (reaction zone) and (4) the output gas mixture analysis system.

As shown in Fig. 2, the chemical agent is injected into the input gas mixture stream prior to entering the heated section. The mixture then flows into the reactor which is inside the furnace. Additional nitrogen gas is added to the gases leaving the furnace section to dilute the stream, and thus minimize any reactions after leaving the furnace. The additional nitrogen also minimizes the concentration of water which may cause interference in the subsequent gas analysis. Each of the systems are described below.

Input Gas Mixture. In these experiments, the exhaust gas was simulated by using bottle gases. Comparisons with the use of actual exhaust have demonstrated that the use of simulated exhaust gas is an effective technique, [14]. The advantages of simulated exhaust include that the input gas stream is well characterized, is not subject to transient variations, and is not limited to a relatively narrow range of compositions.

Mass flow controllers are used to insure accurate metering of the individual gases. The individual gas streams are combined and the mixture enters the furnace. The total mass flow of the gas mixture is constant for a set of experiments which results in varying volume flow rate (and varying residence time) in the reactor for different reactor temperatures.

Metering and Delivery of the Chemical Agent. The mode of delivery of the chemical agent to the simulated exhaust stream is mainly dependent on the phase of the agent. For ammonia as a gas, the delivery is straightforward and is the same as the delivery of the other gases (e.g., [10,11]).

For urea as a solution with water, the solution is fed into the exhaust stream by the use of a syringe which is advanced at a controlled rate using a precision stepper motor, [30]. The stepper motor drives the plunger of the syringe at required feed rates. The output from the syringe is fed into a heated region close to the point of inlet to the reactor. The urea solution vaporizes before it enters the reactor.

The minimum amount of water needed to keep the urea in solution depended on the solubility of urea, [31]. For the conditions of this work, the amount of water introduced into the gas mixture with the solution was estimated to be about 320 ppm. Since each urea molecule could theoretically reduce two nitric oxide molecules, the urea feed rate for ideal conditions would be one-half the nitric flow rate (on a mole basis). Not all of the urea was utilized in the experiment, however, due to resolidification of some of the urea. To compensate, the selected urea solution feed rate was approximately twice the ideal rate. This high feed rate was necessary to insure the maximum possible nitric oxide removal for comparison purposes. Such a high urea feed rate, however, would not be practical or desirable in an actual application.

Since cyanuric acid is not soluble in water to any appreciable degree, it must be utilized as a solid powder, [14]. A dry powder feed system was used. This feed system was similar to the urea solution feed system described above. The cyanuric acid is carefully packed into a syringe which is advanced at a controlled rate using a precision stepper motor. The stepper motor drives the plunger of the syringe at required feed rates. The output from the syringe is fed into a heated region upstream of the reactor which serves as a vaporizer. In this vaporizer, the cyanuric acid powder sublimates to vapor before it enters the reactor. A small amount of metered nitrogen gas is used to carry the vapor into the reactor.

The amount of cyanuric acid for these experiments was selected so as to insure the maximum possible reduction of nitric oxide, [15]. Although this high amount would not be practical for actual applications, for purposes of this study, this amount provided less ambiguous comparisons. The amount selected was a molar ratio of cyanuric acid to nitric oxide of 1.42, or a isocyanic acid (HNCO) to nitric oxide ratio of 4.27.

Furnace and Reactor Assembly. To simulate the hot exhaust gases, the gas mixture was heated to the required temperature levels. An electric furnace was used for this purpose. An important characteristic of this heating process is that the gas temperature be uniform throughout the reactor. This was accomplished by a multiple-zone furnace with individual control of each zone.

The reactor is constructed of quartz tube to minimize any catalytic reactions that might occur with steel or other metal reactors, [32]. For the experiments reported here, the geometry (internal diameter and heated length) of each of the reactors is included in Table 1.

Table 1 Experimental conditions

| | Ammonia Process | Urea Process | Cyanuric Acid Process |
|---|-------------------------------|------------------------------|----------------------------|
| Agent | Ammonia | Urea | Cyanuric Acid |
| Name | Thermal DeNO _x Gas | NO _x OUT Solution | RAPRENO _x Solid |
| Phase of agent | Gas | Solution | Solid |
| Experimental temp range (K) | 800–1200 | 800–1200 | 670–1340 |
| Temp (K) for best performance | 1150 | 1150 | 1200 |
| Inlet NO (ppm) | 330 | 330 | 330 |
| Inlet CO (ppm) | 0 | 600 | 1260 |
| Inlet H ₂ O | 0 | ~320 ppm | 4.5% |
| Inlet O ₂ (%) | 0–15 | 0–15 | 0, 1.9, 12.3 |
| O ₂ (%) for best performance | 1.0 | 5.0 | 12 |
| Beta, β* | 1.5 | ~2.0 | 4.27 |
| Residence time at 1025 K (sec) | 2.1 | 2.1 | 0.85 |
| Reactor length (cm) | 61 | 61 | 37 |
| Reactor ID (mm) | 18 | 18 | 16.5 |
| Reference | Caton et al. [11] | Srivatsa and Caton [30] | Caton and Siebers [15] |

*β is the ratio of agent to nitric oxide (see text).

Outlet Gas Analysis Systems. To complete an analysis of the output gases, additional (dilution) nitrogen is added to the exit flow stream before the analysis. The dilution nitrogen is often a large factor of the exhaust stream—perhaps a factor of five. The dilution nitrogen helps to prevent water condensation in the unheated portions of the exhaust system, and helps to minimize interference of species such as CO₂ and H₂O with the measurements of the other species.

For these experiments, the output gases from the reactor are analyzed by a Fourier transform infrared (FTIR) spectrometer and by a chemiluminescent NO_x analyzer. In cases where both analysis techniques were used, the agreement was good. The use of an FTIR spectrometer is necessary in these experiments to obtain quantitative knowledge of species such as NH₃, HNCO, N₂O which are not generally obtained from conventional gas analyzers. Details of the apparatus and experimental procedure can be found elsewhere, [10,11,15,30].

Experimental Conditions

Table 1 lists the typical experimental conditions for these experiments. The table lists each of the three processes, typical operating conditions, and the relevant references. As shown, the typical temperature range examined in these experiments is between 650 and 1350 K, the inlet nitric oxide concentration is 330 ppm, and the typical inlet oxygen concentration is between 0 and 15%. Also listed is the temperature for the highest nitric oxide removal rate (best performance).

Since the mass flow rate was constant for each set of experiments, the residence time varied with temperature. Table 1 shows the computed residence times evaluated for 1025 K which were either 0.85 or 2.1 seconds. The mass flow rate is related to the residence time as follows:

$$\dot{m} = \frac{\text{Vol} \rho_{\text{act}}}{\tau_{\text{res}}} \quad (2)$$

where Vol is the reactor volume, ρ_{act} is the actual gas density, and τ_{res} is the residence time.

Another item listed in Table 1 is the ratio of the concentration of the agent (on a one nitrogen atom basis) to the concentration of the nitric oxide. The literature has defined this ratio as

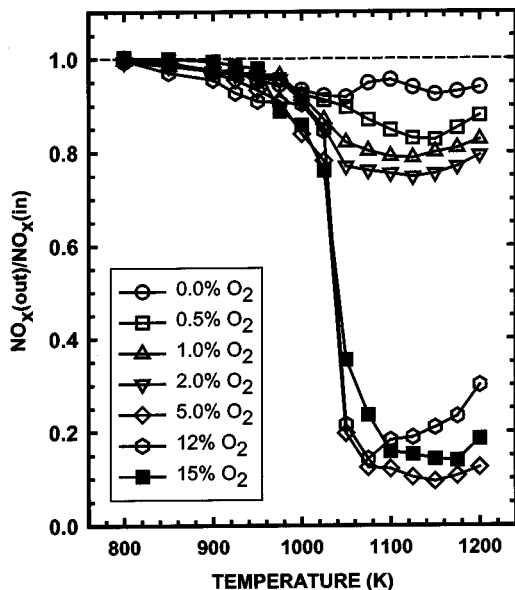
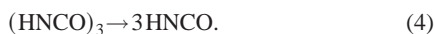


Fig. 3 The ratio of outlet NO_x and inlet NO_x as a functions of reactor temperature for seven levels of oxygen for 600 ppm carbon monoxide and a residence time of 2.1 secs using urea

$$\beta = \frac{[\text{NH}_i]}{[\text{NO}]} \quad (3)$$

where $[\text{NH}_i]$ is the concentration of the nitrogen containing agent normalized to a one nitrogen atom basis, and $[\text{NO}]$ is the concentration of the nitric oxide. This ratio is also known as the normalized stoichiometric ratio (NSR) and can be determined based on the number of nitrogen atoms per molecule. Since ammonia (NH_3) has one nitrogen atom per molecule, the ratio of the concentrations is the same as the β ratio. For urea, since there are two nitrogen atoms per urea molecule, the concentration of urea is one-half of the nitric oxide concentration for a β ratio of one. Finally, for cyanuric acid, the β ratio is three times the concentration ratio.

Table 1 lists the actual β values used in the three experiments. As mentioned above, for each experiment the values selected were more than the ideal value to insure the maximum possible removal. For ammonia, the β ratio was 1.5, and for urea the β ratio was about 2. For cyanuric acid, however, the cyanuric acid decomposes to isocyanic acid (HNCO) which is the active agent:



So, the ratio of cyanuric acid to the nitric oxide was 1.42, but the ratio of the isocyanic acid to the nitric oxide was 4.27.

These experiments were conducted at different times in two laboratories, but the major items were essentially the same. The CO and H_2O concentrations listed for each process were selected such that the individual processes were close to optimum. For example, for the ammonia process no CO or H_2O were used, but for the urea and cyanuric acid processes the CO and H_2O concentrations were nonzero. The reason that CO and H_2O concentrations affect these processes differently is explained elsewhere, [15].

Experimental Results and Discussion

Figure 3 is an example of the results of a typical experiment which used urea as the agent. This figure shows the ratio of the reactor outlet and inlet nitric oxides (NO_x) as a function of reactor (or gas) temperature for a number of oxygen concentrations, [30]. Since the amount of NO_2 was less than 3% for these experiments,

the following discussion is simplified by considering only nitric oxide. The nitric oxide removal is often defined as

$$\text{NO Removal} = 1 - \frac{\text{NO}_{\text{out}}}{\text{NO}_{\text{in}}} \quad (5)$$

Therefore, as the ratio plotted in Fig. 3 decreases, the nitric oxide removal increases. For these experiments, the carbon monoxide concentration was 600 ppm, the water concentration was about 320 ppm, and the residence time was 2.1 seconds. The concentration of oxygen was 0, 0.5, 1, 2, 5, 12, and 15%.

As shown, the removal of nitric oxide is not significant for temperatures below about 950 K. For sufficient oxygen concentrations (between 5 and 15% for these conditions), the nitric oxide removal becomes significant for temperatures above about 1050 K. Overall maximum nitric oxide removal for these conditions occurs for a temperature of 1150 K for 5% oxygen. As the gas temperatures increase above about 1150 K, the nitric oxide removal decreases.

With respect to the effects of oxygen concentration, Fig. 3 shows significant differences. For no oxygen (0%), the nitric oxide removal was less than 10% for all temperatures. For temperatures greater than 1050 K, as the oxygen concentration increases to 2%, the removal of nitric oxide increases. Then as the oxygen concentrations increase above this value, the removal is different at different temperatures. The following considers a temperature of 1150 K where the maximum removal was attained.

For 1150 K, the removal was about 17% for 0.5% oxygen, and about 25% for 2% oxygen. For further increases in the oxygen concentration, the nitric oxide removal increased significantly. As shown, for 5% oxygen, the removal is 90% at 1150 K (the maximum overall removal). For further increases in the oxygen concentration, the removal decreases somewhat, but is still typically above about 75%. Clearly, the effect of oxygen concentrations is important.

Similar experiments have been completed for the ammonia process, [10,11], and for the cyanuric acid process, [15]. Related work with respect to the ammonia process has also been reported by Smith and Caton [33], and for the cyanuric acid process by Smith and Caton [34].

Figure 4 illustrates the effect of oxygen concentration on the nitric oxide removal for the three processes. For the urea process, the removal level decreases from 0% to about 90% as the oxygen concentration increases from 0 to 5%. As the oxygen concentration continues to increase, the nitric oxide removal level decreases from 90% to about 80% at the highest oxygen concentrations.

For the ammonia process, the removal level decreases from near 0% to over 95% as the oxygen concentration increases from 0% to 1%. As the oxygen concentration continues to increase from 1% to 15%, the nitric oxide removal level decreases in a near linear fashion from 95% to about 70%.

Finally, for the cyanuric acid process, the nitric oxide removal increases rapidly as the oxygen concentration increases from 0 to 2%, and then increases more gradually as the oxygen concentration continues to increase from 2% to 12%. For these conditions (see Table 1), the maximum overall nitric oxide removal using cyanuric acid is obtained for 12% oxygen.

Discussion of the Key Reactions

In this section, the key chemical reactions of these processes will be discussed. The majority of this information is available from a number of references (e.g., [6,12,18,35]). A common characteristic of these SNCR processes is the production of radicals which is necessary so that the overall reaction mechanism is self-sustaining. Reaction steps responsible for generation of radicals are



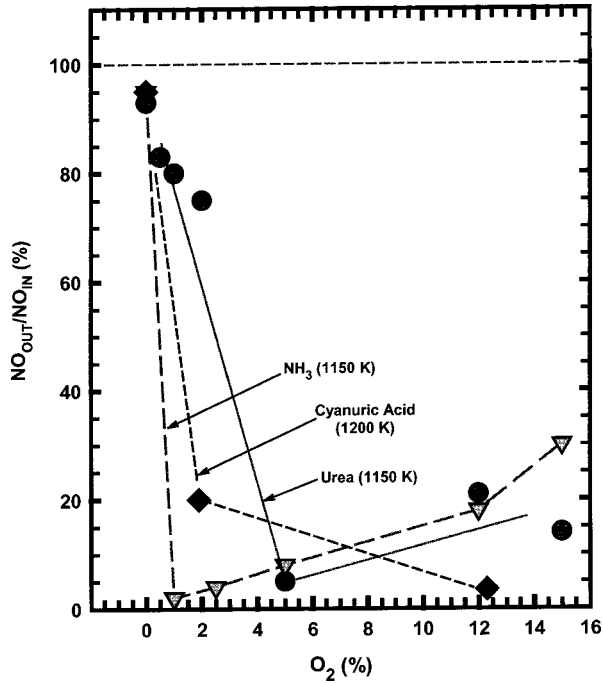
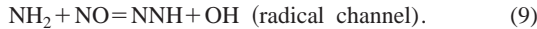
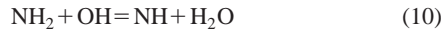


Fig. 4 Nitric oxide reduction as functions of oxygen concentration for the three SNCR processes. Conditions for these results are listed in Table 1.

Ammonia Process. The ammonia process begins with the break down of ammonia to NH_2 by O and OH radicals. The process continues with the following reactions to remove nitric oxide



The following reactions are important competing reactions in these processes that result in NO formation:



The above reactions now may be considered with respect to variations in the oxygen concentrations. If no oxygen is present, no OH radicals will be produced and the overall mechanism will not proceed. For high levels of oxygen, the OH radical concentration will be high, and the competing reactions (Eqs. (10)–(14)) will become increasingly important. As a result, the NH_2 concentrations will be increasingly lower, and the key reactions (Eqs. (8) and (9)) will be less effective. For lower levels of oxygen (and hence OH radicals), the competing reactions will be less important, and the key reactions will dominate. In other words, higher oxygen concentrations promote the competing reactions (Eqs. (10)–(14)) and tend to decrease the effectiveness of ammonia in reducing NO.

Cyanuric Acid Process. For the cyanuric acid process, the HNCO (which is formed from the decomposition of cyanuric acid) converts to NCO and NH_2 (which are the effective NO reducing species for this process) by the following reactions:

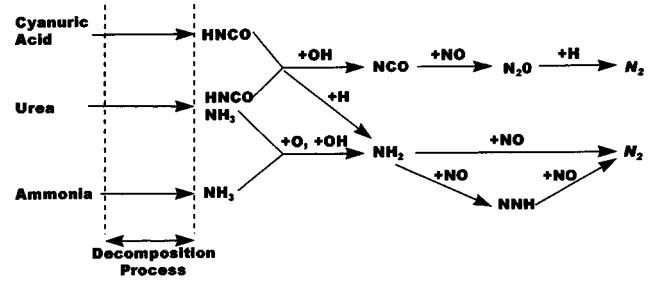
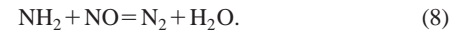


Fig. 5 Schematic figure of the possible chemical pathways for the reduction of nitric oxide (NO) to molecular nitrogen (N_2) using cyanuric acid, urea, or ammonia



Reactions (15) and (17) are the more important, [3], of these four. The formation of NCO and NH_2 then results in the following:



These three reactions, then, are the key nitric oxide removal steps. The supporting reactions which supply the necessary radicals (H, OH, and O), are



For high oxygen levels, the H radical decreases (Eq. (6)), and therefore, NH_2 from reaction (15) decreases. Further, for high oxygen levels, OH radicals increase (Eq. (5)) and NCO from the reaction of Eq. (17) increases. The increases in NCO increase the conversion of NO to N_2O . Finally, the “O” radical concentration increases, but sensitivity calculations (e.g., [12]) show that reactions involving “O” are not too significant. Therefore, the higher oxygen levels enhance the cyanuric acid process.

Urea Process. Depending on the products of urea decomposition, the urea process may be divided into the above cases in proportion to the specific concentrations of the products of decomposition. For example, for the cases of urea decomposition that result in equal amounts of ammonia and isocyanic acid, the net effect of oxygen may be a combination of the above reactions (Eqs. (6)–(20)). The results of Fig. 4 tend to support this assumption. The details of this combination are beyond the scope of the current paper. For other decomposition products, the results can be obtained from similar arguments (see e.g., [23]).

Overall Processes. Figure 5 is a summary of the possible major chemical pathways for the removal of nitric oxide using the three agents: ammonia, urea, and cyanuric acid. As shown, from left to right, the first step is the decomposition of the chemical agent. Cyanuric acid sublimates to HNCO molecules, and urea may decompose into some combination of HNCO and NH_3 . Continuing from left to right, the next major step is the reactions with the radicals OH, O, and H. The major species resulting from these reactions are NCO and NH_2 . NCO may react with NO to produce N_2O which in turn reacts with H to produce N_2 . NH_2 may react with NO to produce N_2 . Although this is a simplified diagram, it does show the most common major pathways.

As mentioned above, for the ammonia process, increasing the oxygen concentration will promote the reactions that convert NH_2 radicals to NO which will tend to decrease the effectiveness of the ammonia process. On the other hand, for the cyanuric acid process, increasing the oxygen concentration will tend to favor the

production of NCO, and hence, increase the effectiveness of the cyanuric acid process. Finally, the urea process may be a combination of the two other processes as indicated in Fig. 5.

Implications to Engine Exhaust

As discussed above, the composition of engine exhaust will be different for different applications. For engine designs based on low equivalence ratio operation such that the exhaust has more than 10% oxygen, the use of cyanuric acid may be more effective. The system, however, would need to be carefully designed to avoid the production and emission of nitrous oxide.

For other engines at or near stoichiometric operation, the use of ammonia may be more effective. For engine operation with equivalence ratios between these two cases, the urea process may be the most effective of the three possible candidates.

In addition to the appropriate match of the agent to the specific oxygen concentrations, the process must fulfill other considerations to be successful. For all three processes, of course, the selected agent (ammonia, cyanuric acid, or urea) must be injected into the exhaust gases at the appropriate temperature (~1200 K). This is a high temperature for the exhaust of most internal combustion engines. To obtain this high exhaust temperature, either off-design operating conditions could be selected, or the exhaust gas could be heated. This exhaust gas heating could be completed by the combustion of a small amount of fuel in a special exhaust reactor.

The success of the overall process is a function of the completeness of the mixing, and the sufficiency of a long enough residence time at the appropriate temperature. Finally, combinations of these processes with plasmas and catalysts is a consideration.

Summary and Conclusions

This paper has compared the three major SNCR processes for the removal of nitric oxides using ammonia, urea, or cyanuric acid. The three processes share a few common characteristics such as: (1) the processes require some minimum amount of oxygen, (2) the processes are optimal for a narrow temperature range (for the reported experiments, about 1150–1200 K), (3) the processes are affected by the presence of carbon monoxide and water to varying degrees, and (4) the processes do not require additional fuel or other substances to proceed.

Although these processes share some common characteristics, each of these processes has unique features and each of these processes is most effective for specific conditions. In particular, the processes are most effective for different oxygen concentrations. The ammonia process is most effective for low oxygen concentrations, and the cyanuric acid process is most effective for high oxygen concentrations. The urea process is most effective for intermediate values of oxygen concentrations. Because each of these processes is more effective for certain oxygen concentrations, these processes may be more effective for certain engine applications. For example, the cyanuric acid process would be expected to be more effective for applications with higher air-fuel ratio operation such as diesel engines. The ammonia process is expected to be more effective for near stoichiometric operated engines.

Acknowledgments

This work is supported in part by a grant from the Texas Advanced Research Program of the State of Texas under Grant No. 000512-0191-1999. The contents of this paper, however, do not necessarily reflect the opinions or views of the sponsors.

References

- [1] Sawyer, R. F., 1981, "The Formation and Destruction of Pollutants in Combustion Processes: Clearing the Air on the Role of Combustion Research," *Eighteenth Symposium (International) on Combustion*, The Combustion Institute, Pittsburgh, pp. 1–22.
- [2] Prather, M. J., and Logan, J. A., 1994, "Combustion's Impact on the Global

- Atmosphere," *The Twenty-Fifth Symposium (International) on Combustion*, The Combustion Institute, Pittsburgh, pp. 1513–1527.
- [3] Bowman, C. T., 1992, "Control of Combustion-Generated Nitrogen Oxide Emissions: Technology Driven by Regulation," *The Twenty-Fourth Symposium (International) on Combustion*, The Combustion Institute, Pittsburgh, pp. 859–878.
- [4] Groff, P. W., and Gullett, B. K., 1997, "Industrial Boiler Retrofit for NO_x Control: Combined Selective Noncatalytic Reduction and Selective Catalytic Reduction," *Environ. Prog.*, **16**(2), pp. 116–120.
- [5] Chang, M. B., and Cheng, C. F., 1997, "Plasma-Assisted Removal of NO From Gas Streams via Ammonia Injection," *Environmental Engineering Science*, **14**(4), pp. 193–200.
- [6] Miller, J. A., 1996, "Theory and Modeling in Combustion Chemistry," *The Twenty-Sixth Symposium (International) on Combustion*, The Combustion Institute, Pittsburgh, pp. 461–480.
- [7] Lyon, R. K., 1975, "Method for the Reduction of the Concentration of NO in Combustion Effluents Using Ammonia," U.S. Patent No. 3,900,554.
- [8] Lyon, R. K., 1987, "Thermal DeNO_x: Controlling Nitrogen Oxides Emissions by a Noncatalytic Process," *Environ. Sci. Technol.*, **21**(3), pp. 231–236.
- [9] Miller, J. A., Branch, M. C., and Kee, R. J., 1981, "A Chemical Kinetic Model for the Selective Reduction of Nitric Oxide by Ammonia," *Combust. Flame*, **43**, pp. 81–98.
- [10] Caton, J. A., Narney, J. K. III, and Laster, W. R., 1994, "Nitric Oxide Reductions and Nitrous Oxide Emissions Using Ammonia in a Selective Non-Catalytic Process for Exhaust Streams With Up to 15% Oxygen," *Proceedings of the 1994 Central States Section/Combustion Institute Spring Technical Meeting*, Madison, WI, June, Paper No. 15, pp. 90–95.
- [11] Caton, J. A., Narney, II, J. K., Cariappa, C., and Laster, W. R., 1995, "The Selective Non-Catalytic Reduction of Nitric Oxide Using Ammonia at up to 15% Oxygen," *Can. J. Chem. Eng.*, **73**(3), pp. 345–350.
- [12] Bowman, C. T., 1997, "Mechanisms and Modeling of Gas-Phase Aftertreatment Methods for NO Removal From Combustion Products," *Physical and Chemical Aspects of Combustion*, eds., F. L. Dryer and R. F. Sawyer, eds., Gordon and Breach, London, pp. 29–68.
- [13] Perry, R. A., and Siebers, D. L., 1986, "Rapid Reduction of Nitrogen Oxides in Exhaust Gas Streams," *Nature (London)*, **324**, pp. 657–658.
- [14] Caton, J. A., and Siebers, D. L., 1989, "Reduction of Nitrogen Oxides in Engine Exhaust Gases by the Addition of Cyanuric Acid," *ASME J. Eng. Gas Turbines Power*, **111**, pp. 387–393.
- [15] Caton, J. A., and Siebers, D. L., 1989, "Comparison of Nitric Oxide Removal by Cyanuric Acid and by Ammonia," *Combust. Sci. Technol.*, **65**, pp. 277–293.
- [16] Caton, J. A., and Siebers, D. L., 1991, "Effects of Hydrogen Addition on the Removal of Nitric Oxide in Exhaust Gases by Cyanuric Acid," *The Twenty-Third (International) Symposium on Combustion*, The Combustion Institute, Pittsburgh, PA, pp. 225–230.
- [17] Siebers, D. L., and Caton, J. A., 1990, "Removal of Nitric Oxide From Exhaust Gas With Cyanuric Acid," *Combust. Flame*, **79**, pp. 31–46.
- [18] Miller, J. A., and Bowman, C. T., 1991, "Kinetic Modeling of the Reduction of Nitric Oxide in Combustion Products by Isocyanic Acid," *Int. J. Chem. Kinet.*, **23**, pp. 89–313.
- [19] Cariappa, C., Caton, J. A., and Laster, W. R., 1994, "Modeling the Physical Effects of Selective Non-Catalytic Removal of Nitric Oxide With Cyanuric Acid," *Proceedings of the 1994 Central States Section/Combustion Institute Spring Technical Meeting*, Madison, WI, June, Paper No. 16, pp. 96–101.
- [20] Cariappa, C., Caton, J. A., and Smith, T. S., 1995, "Modeling the Selective Non-Catalytic Reduction of Nitric Oxide Using Isocyanic Acid," *Proceedings of the 1995 Central States Section/Combustion Institute Spring Technical Meeting*, San Antonio, TX, Apr. 24–25, Paper No. 95S-58, pp. 299–304.
- [21] Arand, J. K., Muzio, L. J., and Sotter, J. G., 1980, "Urea Reduction of Nitric Oxides in Combustion Effluents," U.S. Patent No. 4,208,386, June 17.
- [22] Jødal, M., Nielsen, C., Hulgaard, T., and Dam-Johansen, K., 1990, "Pilot-Scale Experiments With Ammonia and Urea as Reductants in Selective Non-Catalytic Reduction of Nitric Oxide," *The Twenty-Third Symposium (International) on Combustion*, The Combustion Institute, Pittsburgh, pp. 237–243.
- [23] Alzueta, M. U., Bilbao, R., Millera, A., Oliva, M., and Ibanez, J. C., 2000, "Impact of New Findings Concerning Urea Thermal Decomposition on the Modeling of the Urea-SNCR Process," *Energy Fuels*, **14**(2), pp. 509–510.
- [24] Muzio, L. J., Martz, T. D., Montgomery, T. A., Quartucy, G. C., Cole, J. A., and Kramlich, J. C., 1990, "N₂O Formation in Selective Non-Catalytic Nitric Oxides Reduction Process," *Fall International Symposium of the American Flame Research Committee*, San Francisco, Nov., Paper No. 39.
- [25] Glarborg, P., Kristensen, P. G., Jensen, S. H., and Dam-Johansen, K., 1994, "A Flow Reactor Study of HNCO Oxidation Chemistry," *Combust. Flame*, **98**, pp. 241–258.
- [26] Alzueta, M. U., Bilbao, R., Millera, A., Oliva, M., and Ibanez, J. C., 1998, "Interactions Between Nitric Oxide and Urea Under Flow Reactor Conditions," *Energy Fuels*, **12**, pp. 1001–1007.
- [27] Brouwer, J., Heap, M. P., Pershing, D. W., and Smith, P. J., 1996, "A Model for Prediction of Selective Non-Catalytic Reduction of Nitrogen Oxides by Ammonia, Urea, and Cyanuric Acid With Mixing Limitations in the Presence of CO," *The Twenty-Sixth Symposium (International) on Combustion*, The Combustion Institute, Pittsburgh, pp. 2117–2124.
- [28] Kasuya, F., Glarborg, P., Johnsson, J. E., and Dam-Johansen, K., 1995, "The Thermal DeNO_x Process: Influence of Partial Pressures and Temperature," *Chem. Eng. Sci.*, **50**(9), pp. 1455–1466.
- [29] Srivatsa, S., 1997, "The Selective Non-Catalytic Reduction of Nitric Oxides

Using Urea as the Chemical Agent: An Experimental Approach," M.S. thesis, Department of Mechanical Engineering, Texas A&M University, Dec.

- [30] Srivatsa, S., and Caton, J. A., 1998, "Selective Non-Catalytic Reduction of Nitric Oxides by Urea: Effects of Oxygen and Carbon Monoxide," *Proceedings of the 1998 Central States Section/Combustion Institute Spring Technical Meeting*, Paper No. 98-53, pp. 273–278, Lexington, KY, May 31–June 2, Paper No. 98-53; pp. 273–278.
- [31] Chao, G. T., 1977, "Urea: Its Properties and Manufacture," Chao's Institute, West Covina, CA.
- [32] Heap, M. P., Chen, S. L., Kramlich, J. C., McCarthy, J. M., and Pershing, D. W., 1988, "An Advanced Selective Reduction Process for NO_x Control," *Nature* (London), **335**, pp. 620–622.
- [33] Smith, T. S., and Caton, J. A., 1995, "Reductions and Conversions of Nitrogen Compounds Using Ammonia in a Selective Non-Catalytic Process for Exhaust Streams at Pressures up to 515 kPa," *Proceedings of the 1995 Central States Section/Combustion Institute Spring Technical Meeting*, San Antonio, TX, Apr. Paper No. 95S-015, pp. 69–74; 24–25.
- [34] Smith, T. S., and Caton, J. A., 1995, "Nitric Oxide Reductions and Nitrous Oxide Emissions Using Isocyanic Acid in a Selective Non-Catalytic Process for Exhaust Streams at Pressures up to 515 kPa," *Proceedings of the 1995 Central States Section/Combustion Institute Spring Technical Meeting*, San Antonio, TX, Apr. 24–25, Paper No. 95S-016, pp. 75–80.
- [35] Miller, J. A., and Glarborg, P., 1996, "Modeling the Formation of N₂O and NO₂ in the Thermal De-Nox Process," *Gas Phase Chemical Reaction Systems: Experiments and Models 100 Years After Max Bodenstein*, J. Wlfrum, H.-R. Volpp, R. Rannacher, and J. Warnatz, eds., special issue of Springer Series in Chemical Physics, **61**, Springer-Verlag, Berlin, pp. 318–333.

Farzan Parsinejad
Matyas Matlo
Mohamad Metghalchi
e-mail: metghal@coe.neu.edu

Mechanical, Industrial and Manufacturing
Engineering Department,
Northeastern University,
334 Snell Engineering Center,
Boston, MA 02115

A Mathematical Model for Schlieren and Shadowgraph Images of Transient Expanding Spherical Thin Flames

Optical behavior of spherical flames is investigated using both Schlieren and shadowgraph methods. A mathematical model has been developed to predict the intensity of refracted light beams interacting with a transient expanding thin flame. Experimental facilities have been built to visualize transient expanding spherical flames. The facilities include a cylindrical chamber with two end glasses for optical observation. Shadowgraph and Schlieren pictures of flame propagation have been taken using a high-speed charged coupled device camera. Experimental results are in very good agreement with those predicted by the theoretical model. Schlieren and shadowgraph techniques have also been used to view smooth, cracked and cellular flames; these techniques will be useful in future in studies to determine the stability of propagating flame. [DOI: 10.1115/1.1688368]

Introduction

The study of flame and combustion using optical techniques dates back to the mid 1940's, [1–5]. Large changes of temperature and composition occurring in flames give rise to rapid variation in the refractive index. These variations in index of refraction of the media will in turn introduce distortions, which can be viewed using optical techniques. Optical techniques that enable us to track the ray direction changes include Schlieren and shadowgraph, which both fall into the category of geometrical optics. It is clear that these methods cannot be applied to combustion phenomena to best advantage without an understanding of the refractive index field and the way that geometrical optics is able to theoretically predict distortion in ray directions due to changes of index of refraction.

Shadowgraph and Schlieren photography are relatively old ideas in the field of physical optics. Schlieren optics was first used in the 17th century to address refractive errors in using telescopes to view objects close to the horizon, [1]. It was later discovered that Schlieren and shadowgraph photography could be used to visualize the changes in density in a system, [1].

Although optics of inhomogeneous media was first introduced by Robert Hooke [3], it was in 1859 that Toepler re-invented the Schlieren technique and named it after optical inhomogeneities in glass, which were known in German as “Schlieren,” [3].

Today, shadowgraph technique is most often used to photograph changes in density within high-speed compressible fluid flow systems, because the sensitivity of the technique is proportional to the second derivative of density within the system. Sensitivity of Schlieren photography, on the other hand, is proportional to the first derivative, [1]. These methods are also commonly used in the study of combustion. Several studies of laminar burning speed [6–10] have used either Schlieren or shadowgraph techniques to observe flame propagation and to study the formation of cellular flames from a smooth laminar flame.

The investigation of the burning speed of transient expanding spherical flames carried out by Metghalchi and co-workers [10–15] requires use of both Schlieren and shadowgraph photography to observe the propagation of spherical flames using various fuels

and diluents. Therefore, it is important to learn more about interaction of light beams with expanding flames. A few researchers [6,16] have performed similar studies to learn more about light interaction in these techniques with different types of flames. However, the authors did not come across any studies in the literature on the same analysis of premixed expanding spherical flames using shadowgraph or Schlieren photography. Specially, among the various studies [8–10,17] there is not a consensus over the best location of flame edge or flame radius that will result in differences in flame speed measurements. The objective of this study is to predict the light intensity pattern on the Schlieren and shadowgraph images of a flame using theoretical laws of optics, and to figure out the location of the reaction zone and the edge of the flame.

In this paper the optical behavior of spherical flames has been investigated using both Schlieren and shadowgraph techniques. A mathematical model has been developed to study interaction of light beams with an expanding flame of negligible thickness. The results of this research will be helpful in better understanding the Schlieren and shadowgraph images and implementing them in the flame speed measurement analysis. Schlieren and shadowgraph techniques also enable us to view smooth, cracked and cellular flames; these techniques along with a comprehensive stability theory, will be useful in studying the stability of flame propagation in the future.

Experimental Facilities

An experimental facility has been built to observe flame propagation. It includes a cylindrical chamber with windows capable of withstanding pressures up to 50 bars. The cylindrical vessel is made of SAE4140 steel with an inner diameter of 133.35 mm, [15]. The windows are 34.93 mm thick Pyrex with a high durability against pressure and temperature shocks and very good optical properties. There are several ports in the walls for instrumentation and for the gas handling system. The vessel is filled with fuel and oxidizer using a manifold system including a vacuum pump and different pressure gages with varying range.

The light source for the optical system is a 10-Watt Halogen lamp with a condensing lens and a very small pinhole of 0.3 mm, which provides a sharp and intense illumination throughout the whole system. Two aluminized spherical mirrors with 1/8 wavelength surface accuracy, over-coated with silicon monoxide and

Contributed by the Fuels and Combustion Technologies Division of THE AMERICAN SOCIETY OF MECHANICAL ENGINEERS for publication in the ASME JOURNAL OF ENGINEERING FOR GAS TURBINES AND POWER. Manuscript received by the FCT Division Nov. 2001; final revision received by the ASME Headquarters July 2002. Associate Editor: S. Gollahalli.

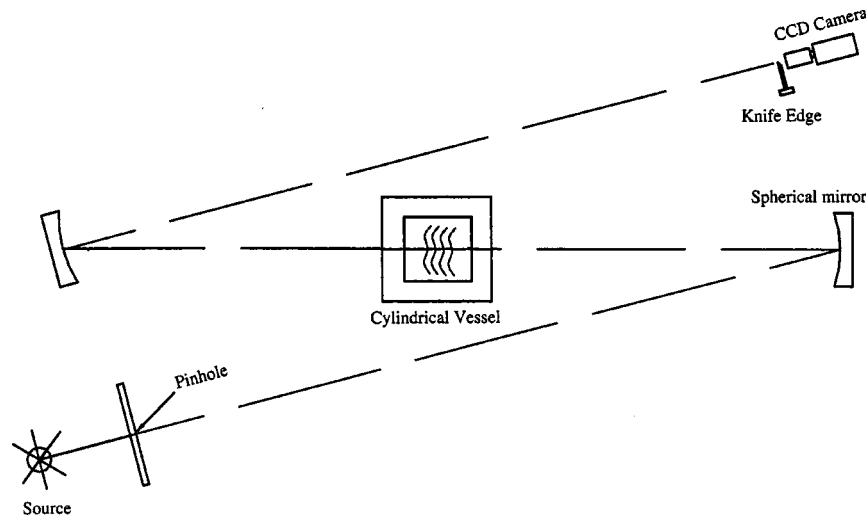


Fig. 1 Schematic diagram of optical system, [1]

mounted in metal stands with a diameter of 152.4 mm and focal length of 1524 mm long, are placed on two sides of the chamber.

A Z-type, [1], Schlieren/shadowgraph ensemble has been set up to visualize the flame propagation of different fuel/oxidizer mixtures. A high-speed charged coupled device camera (1108-0014, Redlake Inc.) with a capture rate of up to 8000 frames per second is placed very close to the focal point of the second mirror. The capture rate and shutter speed of the camera were changed depending on the burning speed of the mixture and the brightness of the flame. The schematic diagram of the optical system is shown in Fig. 1.

Mathematical Modeling

Refractive Behavior of a Spherical Flame. Assuming that the spherical flames studied in the investigation behave approximately as a transparent sphere of much lower density (about 1/7 to 1/6 of the unburned gas density) than its surroundings, the flame can be analyzed as an optical device that causes a certain refraction of light passing through it. This has to do with the fact that the burned gas temperature is almost 6–7 times the unburned gas temperature. There is a temperature variation from the flame center up to its edge, but even at the maximum temperature difference, i.e., on the order of 100 K, the variation of density and index of refraction are very small and can be neglected.

When a beam of light passes through an interface between regions of different indices of refraction, the beam will either speed up or slow down depending on whether it passes into a rarer or denser substance. The inside of the sphere, representing burned gas, is less dense than the unburned gas, and the light beam will move faster through the burned gas. Figure 2 shows incident and

refracting rays interacting with a spherical flame. Light enters the flame with an incident angle of θ_i and bends due to refraction with an angle θ_r . It finally leaves the flame with a scattering angle χ . These angles are related by Snell's law, [5]:

$$\frac{\sin \theta_r}{\sin \theta_i} = \frac{\eta_u}{\eta_b} \quad (1)$$

η is the index of refraction. Subscripts b and u represent the burned and unburned gases in the system respectively. Equation (1) can be modified using angles complementary to θ_r and θ_i (as shown in Fig. 2):

$$\frac{\cos \alpha_r}{\cos \alpha_i} = \frac{\eta_u}{\eta_b} \quad (2)$$

where α_r and α_i are the complementary angles to θ_r and θ_i .

The deflected beam continues across the flame, and as it leaves the flame it deflects once again. This time the beam enters a region of higher density, and therefore the beam will deflect towards the normal line. Again, the light bends away from the horizontal diameter of the sphere. The final path of the light beam upon leaving the flame is at some angle χ from the incoming ray where χ is the total deflection of the light beam after passing through the flame. This angle is a function of the relative distance between the incident beam and the horizontal diameter (b/R), called impact parameter, where R is the radius of the flame.

The angle χ can be determined using geometry:

$$\chi = 2(\alpha_i - \alpha_r) \quad (3)$$

The relationship between the densities and index of refraction of the burned and unburned gases is, [4–5]:

$$(\eta_b - 1) = (\eta_u - 1) \frac{\rho_b}{\rho_u} \quad (4)$$

As ρ_b/ρ_u becomes smaller, η_b approaches 1 and Eq. (2) becomes $\cos(\alpha_r) = \eta_u \cos(\alpha_i)$. Using the first two terms of the Taylor series expansion of the cosine function will result in

$$1 - \frac{1}{2} \alpha_r^2 = \eta_u \cos(\alpha_i) \quad (5)$$

Given Eq. (5) and $\eta_u = 1.00029$ (index of refraction for air at 300 K), [5], the minimum possible value for α_i defined as critical angle $\alpha_{i,cr}$, is 1.379 deg (0.02408 radians) yielding the maximum scattering angle to be 2.759 deg (0.0482 radians). The incoming beam, having an incident angle less than critical incident angle

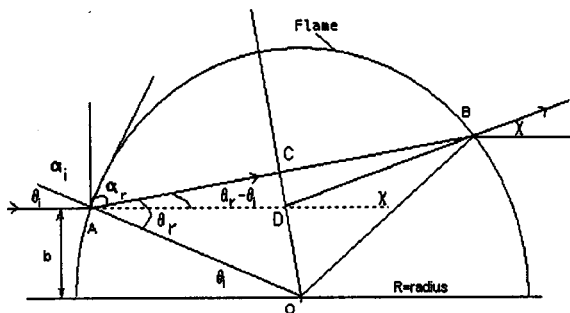


Fig. 2 Ray tracing of refraction through a spherical flame

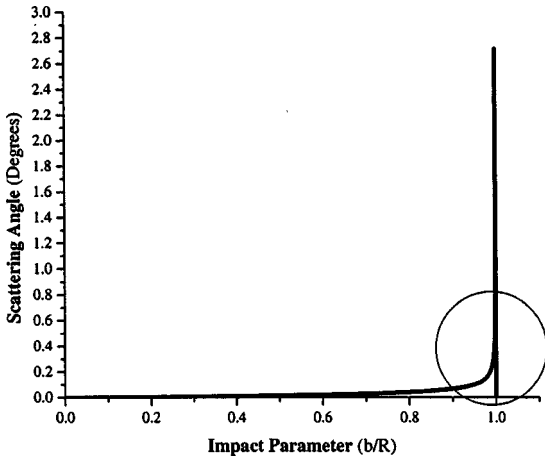


Fig. 3 The scattering angle χ as a function of impact parameter (b/R)

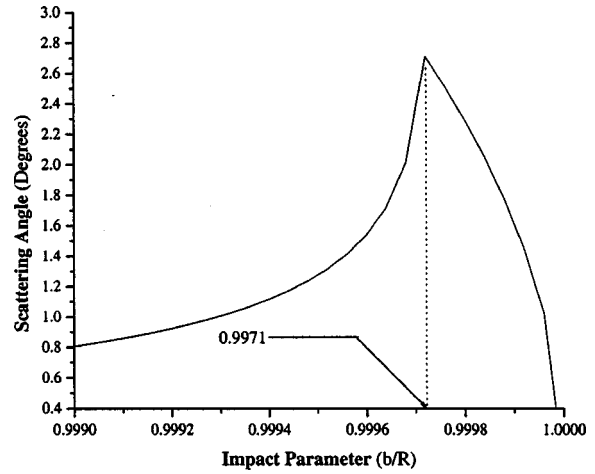


Fig. 4 The scattering angle χ as a function of impact parameter (b/R) close to the critical point

($\theta_{i,cr} = \pi/2 - \alpha_{i,cr}$), will be refracted through the flame and for incident angles higher than critical incident angle, the light beam will be reflected.

Scattering Angle. The scattering angle χ defined in Eq. (3) can be related to the index of refraction of the unburned gas and impact parameter defined as b/R . The angle α_i in Eq. (3) is equal to the inverse cosine of b/R . Using the Taylor series expansion of the cosine of α_i and the first two terms yield

$$\alpha_i = \left(2 \left(1 - \frac{b}{R} \right) \right)^{1/2}. \quad (6)$$

Combining Eqs. (3), (5), and (6) provides the basic form for the scattering angle as a function of the incident ray's impact parameter and unburned gas index of refraction:

$$\chi = 2 \left(\left(2 \left(1 - \frac{b}{R} \right) \right)^{1/2} - \left(2 \left(1 - \eta_u \frac{b}{R} \right) \right)^{1/2} \right). \quad (7)$$

For angles of incidence below the critical angle, the scattering angle is very small. Above the critical value, the scattering angle is based on only the first term of the function because the second term no longer exists. Depending upon the value of b/R , Eq. (7) can be written for two different ranges of impact parameter:

$$\chi = \begin{cases} 2\sqrt{2} \left(\left(1 - \frac{b}{R} \right)^{1/2} - \left(1 - \eta_u \frac{b}{R} \right)^{1/2} \right) & 0 \leq \frac{b}{R} \leq \frac{1}{\eta_u} \quad (8a) \\ 2\sqrt{2} \left(1 - \frac{b}{R} \right)^{1/2} & \frac{1}{\eta_u} \leq \frac{b}{R} \leq 1. \quad (8b) \end{cases}$$

Figures 3 and 4 show scattering angle as a function of impact parameter. Figure 3 shows the scattering angle over a wide range of impact parameter from 0 to 1. Figure 4 shows the scattering angle for impact parameters from 0.999 to 1. It can be seen that scattering angle is maximum at critical incident angle where $b/R = 1/\eta_u$ and drops off when incident angle deviates from critical value.

Shadowgraph Intensity. The purpose of shadowgraphy is to observe the changes in density within a system that is transparent. These changes are shown by the ray displacement resulting from deflection. To make the differences in density visible, the light passing through the system must be of uniform intensity. The deviated light beam falls on a perpendicular surface or is directed into a camera. The intensity of the light on the screen will change as it travels through the media of varying density. Figure 5 shows the behavior of the light beam passing through a spherical flame. In this figure, y is the displacement of a light ray on the viewing field as caused by refraction through the flame. The distance from the center of the flame to the viewing field is L , and for small angles of χ :

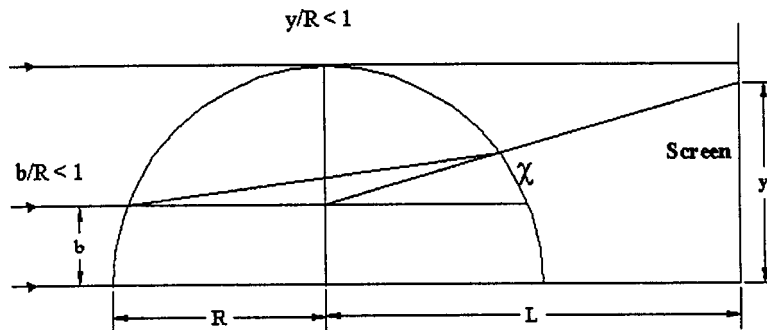


Fig. 5 The deflection of light ray passing through a spherical flame with total displacement y , [1]

$$y = b + L\chi. \quad (9)$$

The relationship for the intensity in this system is given to be, [1]:

$$I(y) = I_0 \left(\frac{b}{y} \right) \left| \frac{db}{dy} \right| \quad y < R \quad (10)$$

$$I(y) = I_0 + I \left(\frac{b}{y} \right) \left| \frac{db}{dy} \right| \quad y > R \quad (11)$$

I_0 is the uniform incident beam intensity.

Figure 5 represents the case where $y < R$ and Fig. 6 shows the deflected ray through the flame where $y > R$.

Equation (9) can be used to derive a relation for intensity as a function of η_u and impact parameter (b/R):

$$\frac{dy}{db} = \left| 1 + L \left(\frac{d\chi}{db} \right) \right|. \quad (12)$$

Combining Eqs. (8)–(12) yields

$$I = \begin{cases} I_0 \left(\frac{b}{y} \right) \left(1 + L \frac{\sqrt{2}}{R} \left(\frac{\eta_u}{\sqrt{1-\eta_u \frac{b}{R}}} - \frac{1}{\sqrt{1-\frac{b}{R}}} \right) \right)^{-1} & 0 < \frac{b}{R} \leq 0.954 \end{cases} \quad (13a)$$

$$I = \begin{cases} I_0 + I_0 \left(\frac{b}{y} \right) \left(1 + L \frac{\sqrt{2}}{R} \left(\frac{\eta_u}{\sqrt{1-\eta_u \frac{b}{R}}} - \frac{1}{\sqrt{1-\frac{b}{R}}} \right) \right)^{-1} & 0.954 < \frac{b}{R} \leq \frac{1}{\eta_u} \end{cases} \quad (13b)$$

$$I = \begin{cases} I_0 + I_0 \left(\frac{b}{y} \right) \left(1 + L \frac{\sqrt{2}}{R} \left(-\frac{1}{\sqrt{1-\frac{b}{R}}} \right) \right)^{-1} & \frac{1}{\eta_u} < \frac{b}{R} \leq 1 \end{cases} \quad (13c)$$

The first region of intensity in Eq. (13a) is where the light passes through the flame with an incident angle less than its critical value, having a small scattering angle such that the ray displacement (y) on the screen would be less than R . Based on the dimensions of our experimental set up, $L/R = 25$, hence by Eq. (9) the maximum value for b/R in which $y \leq R$ would be 0.954. The second Eq. (13b) is valid where the light incident angle is still less than the critical value but the scattering angle is high enough to make the ray displacement (y) on the screen larger than R . In this case, as is shown in Fig. 6, the extra additive I_0 causes the intensity to increase suddenly, making a bright ring around the edge of the flame in the image. The third region accounts for the rays whose angles are larger than the critical angle where the light rays would not refract into the flame but instead reflect off the outer surface of the flame. This region is represented by Eq. (13c). However, since the area between the incident ray, where the angle is larger than the critical angle and the outer surface of the flame is small, the behavior of the intensity in this region is difficult to show graphically. Figure 7 shows relative intensity (I/I_0) versus normalized light displacement with respect to flame radius in which L/R is assumed to be 25. As is shown in the figure, the

relative intensity decreases when normalized displacement (y/R) increases from zero to 1. Then intensity jumps up to a peak at normalized displacement equal to 1 and gradually drops off afterward until it reaches the value of 1. Based on this, we expect to see a similar pattern of light intensity in a shadowgraph picture, knowing that the intensity rise happens at flame edge since $y = R$.

Schlieren Intensity. The intensity of the Schlieren image is an “edited” version of the shadowgraph. In this system, the light propagates from the source through an aperture located at the focal point of a spherical mirror. The light leaving a mirror becomes a completely parallel beam that passes through the test section. The light refracts at the flame, and continues to a second spherical mirror identical to the first. The beam from the second mirror focuses the light into a point, which is approximately the same size and shape as the aperture where the light entered the system. After the focal point, the beam inverts and is captured by a high-speed camera. The light refracted by the flame will not pass through the focal point at the end of the system. Shadowgraph images show all of the light from the source, the refracted and the

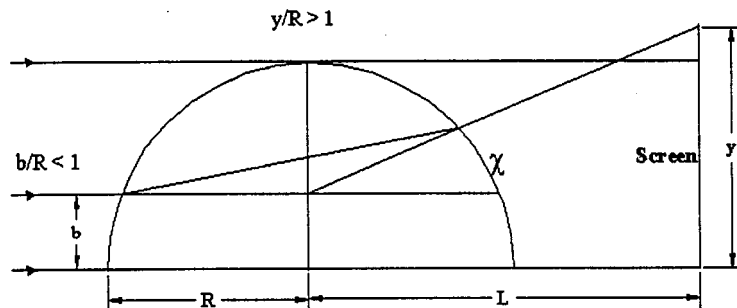


Fig. 6 The deflection of light ray passing through a spherical flame when $y > R$, [1]

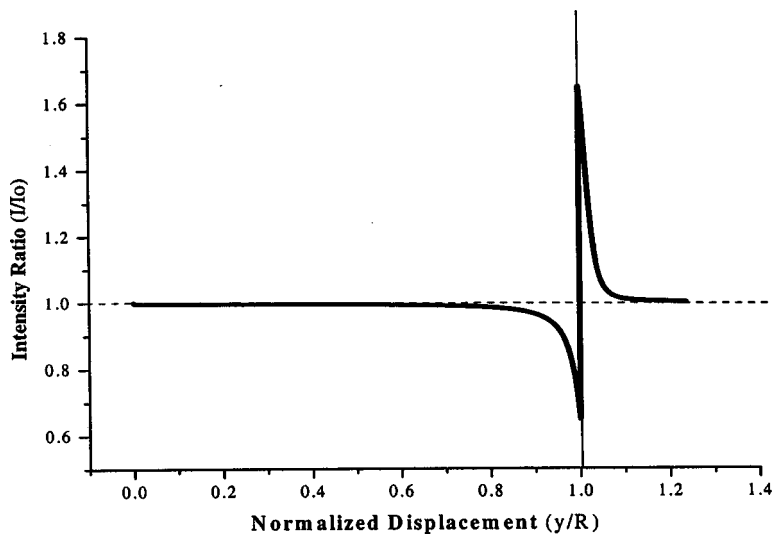


Fig. 7 Shadowgraph relative intensity versus normalized y/R

undisturbed beams. In a Schlieren system, the undisturbed light is removed from the image using a knife edge. As a result, only light that deflects a certain amount when passing through the system reaches the camera. The size of the knife edge in relation to the focal length of the mirrors determines the amount of light falling on the camera lens. The knife edge may be circular, vertical or horizontal, and must be placed as close as possible to the corresponding focal point in the path of the light. Figure 8 shows a ray tracing of the Schlieren system.

The displacement of the refracted beam at the focal point of the mirror (R_b) is related to the scattering angle, the distance from the flame to the mirror (L), and the focal length of the mirror, (FL). The knife edge blocks out all of the light within a certain distance of the focal point, thereby darkening the entire image with little or no refraction.

The focal length of the mirrors used in this system is 1524 mm. Circular knife edges with radii of 2 and 3 mm were used in the system. For these, the ratio R_b/FL is 0.00131 and 0.00197. The ratio of R_b/FL plays a major role in the Schlieren set up. Deviated rays having a scattering angle larger than this ratio would pass the knife edge thus making a bright rim on the image. Using the above values for R_b/FL and Eq. (8), one finds that the corresponding impact parameters (b/R) above which the deflected light passes the knife edge are 0.92 for the 2 mm block and 0.96 for the 3 mm block.

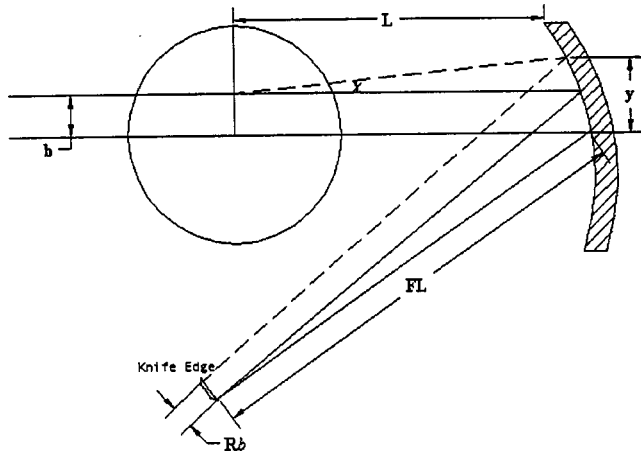


Fig. 8 Ray tracing of Schlieren system, [1]

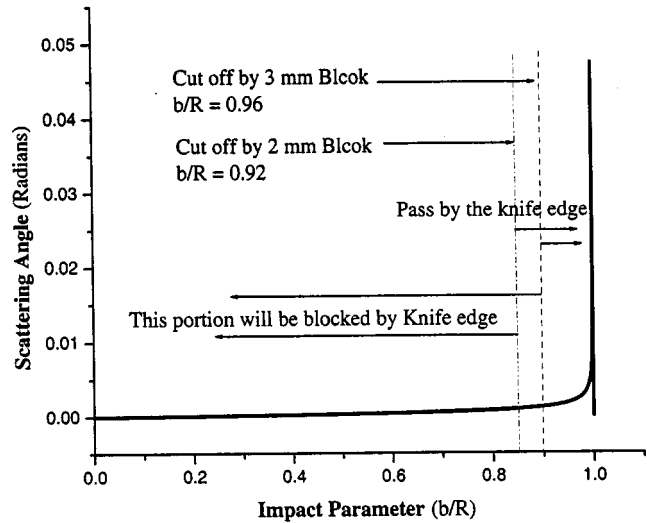


Fig. 9 Scattering angle and the portion of rays, which by passes the knife edge for Schlieren system

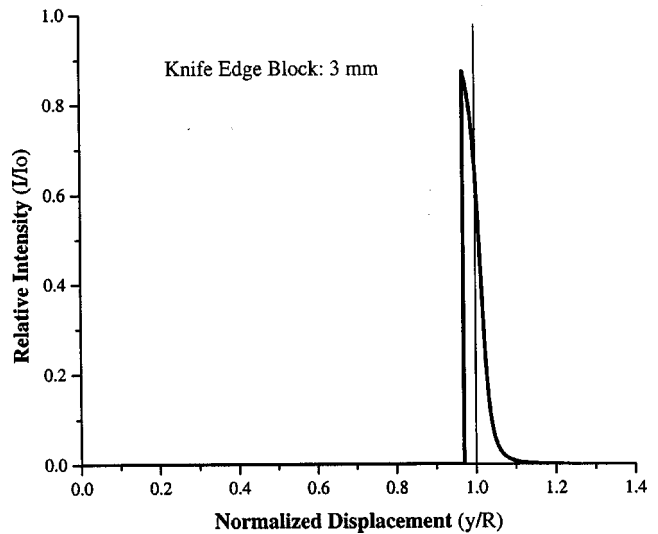


Fig. 10 Intensity of Schlieren image versus normalized displacement y/R

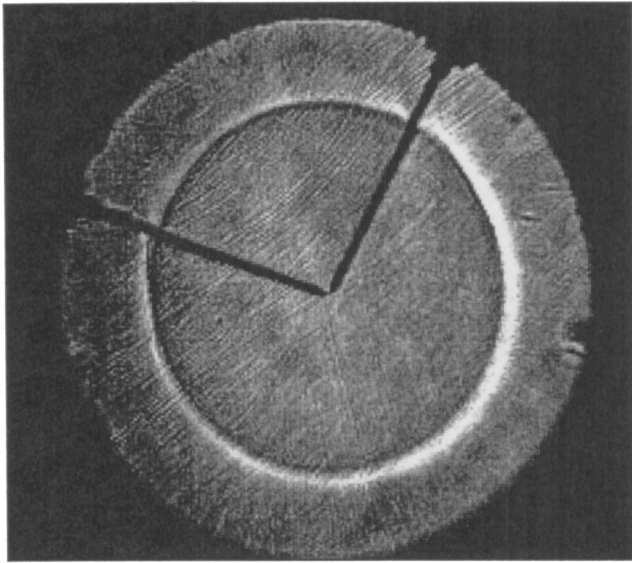


Fig. 11 Shadowgraph image of methane/air flame 10 ms after ignition

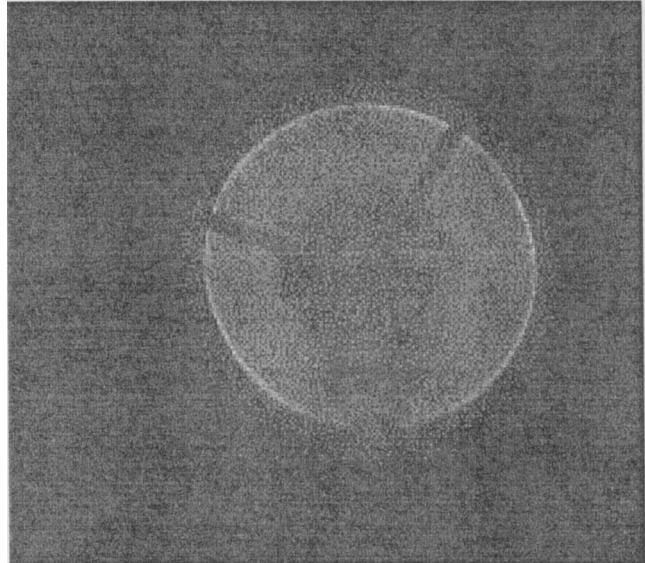


Fig. 12 Schlieren image of methane/air flame 30 ms. after ignition

Figure 9 shows the scattering angle and two different ratios corresponding to two different circular knife edges, versus the impact parameter on the spherical flame.

Using Eqs. (8)–(11) and considering that the relative intensity is zero, except within a certain range of impact parameter, the

intensity of Schlieren is similar to shadowgraph and is shown in Fig. 10 for a circular knife edge of 3 mm radius. For this knife edge size (3 mm), relative intensity is zero for impact parameters (b/R) of less than 0.96 and larger than 0.989. Consequently, intensity is zero for all values of normalized displacement (y/R)

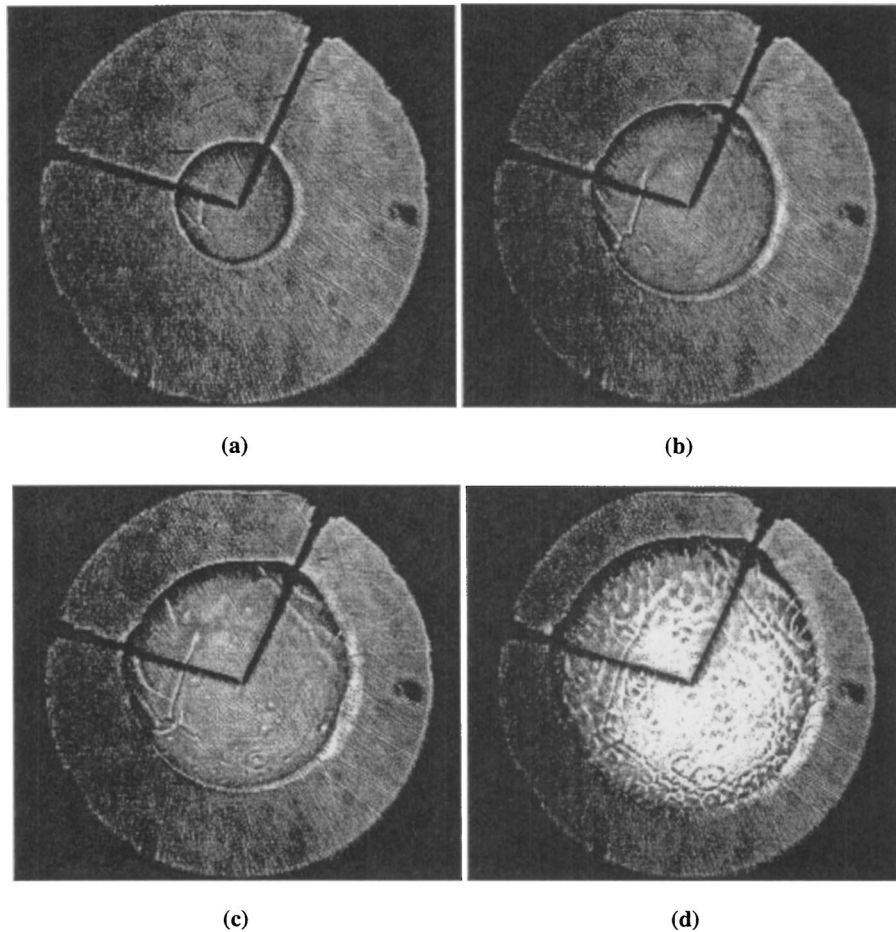


Fig. 13 Shadowgraph chronology of methane/air flame turning into cellular flame

less than 0.96968. Relative intensity will then jump up at normalized displacement equal to 0.96968 to a value of 0.874 and drop off to zero when y/R becomes larger than 1.2, as shown in Fig. 10. Note that the relative intensity at the edge of the flame where $y=R$, is 0.647 which implies that the jump in intensity in a Schlieren picture doesn't correspond to the flame edge. This is in contrast with shadowgraph pictures.

Experimental Results

Figure 11 is a shadowgraph image of a spherical stoichiometric methane-air flame with initial pressure 1 atmosphere and initial temperature 298 K. This image has been taken 15 ms after ignition. The intensity of the light decreases gradually along the radius as impact parameter approaches 1 (scattering angle increases and reaches its maximum value). The light intensity increases suddenly when impact parameter becomes 1, and this is consistent with the theoretical results of Fig. 7. Other experimental results show the same trend [10,14,15].

Figure 12 shows the Schlieren picture of the same flame. As can be seen, the image up to the point where the impact parameter is less than 0.96 or the normalized displacement is 0.96968, is dark since the knife edge has blocked all the scattered rays. At the point where the impact parameter is 0.96, there is a jump in light intensity. The light intensity then decreases as the impact parameter approaches 0.989 or normalized displacement approaches 1.2. This can be seen as a bright rim, which gradually becomes dark. One should be careful in locating the flame edge, since the rise in intensity of light in the picture doesn't exactly correspond to the edge of the flame as was mentioned before. These findings are consistent with the theoretical results shown in Fig. 10.

Figure 13 shows a chronology of flame propagation for stoichiometric methane-air mixture with initial pressure and temperature of 5 atm and 298 K, respectively. This figure is presented to show the capabilities of the shadowgraph and Schlieren techniques in viewing the instabilities of the flame. The study of this phenomenon will be further work in our laboratory. The first image was taken 10 ms after ignition and the next ones were each taken 10 ms after the previous images. The importance of the 10 ms increment was to give enough time for this flame to develop changes that are easily clarified in the captured images. When pressure and temperature exceeds a certain amount the instability in the flame can be viewed in the form of cracks on the surface of the flame, and then, as the pressure and temperature increase, cells appear on the flame and make it unstable. These pictures can be used to model instabilities in expanding spherical flames.

Conclusions

A mathematical model covering the interaction of light beams and thin flame has been developed. Experimental facilities have been built to take shadowgraph and Schlieren pictures of expanding spherical flames. As was predicted by theory, experimental results show the same behavior of the intensity variation on the images. The theoretical model also predicts the location of flame

edge, which will be useful in making accurate measurements of flame speed. Shadowgraph and Schlieren systems help us to observe cracks and cell development on the propagating flame experimentally. In the future, with better understanding of these methods we will be able to study the stability of flames more accurately.

Acknowledgment

This work was supported by US Army Research Office, Grant number DAAD19-01-1-0587 under technical monitoring of Dr. David Mann. The authors are grateful to Prof. James C. Keck of Massachusetts Institute of Technology for great discussions.

References

- [1] Meyer-Arendt, ed., 1992, *Selected Papers on Schlieren Optics*, Optical Engineering Press.
- [2] Marton, L. C., 1981, *Methods of Experimental Physics*, Part A, Academic Press, San Diego, **18**, pp. 355–360.
- [3] Settles, G. S., 2001, *Schlieren and Shadowgraph Techniques: Visualizing Phenomena in Transparent Media*, Springer-Verlag, New York.
- [4] Weinberg, F. J., 1963, *Optics of Flames*, Butterworths, Washington, DC.
- [5] Wood, Robert, 1936, *Physical Optics*, Macmillan, New York, pp. 80–87.
- [6] Durox, D., and Ducruix, S., 2000, "Concerning the Location of the Schlieren Limit in Premixed Flame," *Combust. Flame*, **120**, pp. 595–598.
- [7] Tse, S. D., Zhu, D. L., and Law, C. K., 2000, "Morphology and Burning Rates of Expanding Spherical Flames in H_2/O_2 /Inert Mixtures up to 60 Atmospheres," *Proceedings of the Combustion Institute*, **28**, pp. 1793–1800.
- [8] Rozenchan, G., Tse, S. D., Zhu, D. L., and Law, C. K., 2001, "Laminar Burning Rates and Markstein Lengths of CH_4/O_2 /Inert Mixtures at High Pressures," American Institute of Aeronautics and Astronautics 39th Aerospace Science Meeting and Exhibit, Reno, NV.
- [9] Aung, K. T., Hassan, M. L., and Faeth, G. M., 1997, "Flame Stretch Parameters of Laminar Premixed Hydrogen/Air Flames at Normal Temperature and Pressure," *Combust. Flame*, **109**, pp. 1–24.
- [10] Rahim, F., and Metghalchi, M., 2001, "Burning Velocity for Spherical Flames in Cylindrical and Spherical Chambers," *Eastern States Combustion Institute*, Hilton Head, Dec. 2–5, pp. 412–415.
- [11] Metghalchi, M., and Keck, J. C., 1982, "Burning Velocities of Mixtures of Air With Methanol, Isooctane and Indolence at High Pressure and Temperature," *Combust. Flame*, **48**, pp. 191–210.
- [12] Metghalchi, M., and Keck, J. C., 1980, "Laminar Burning Velocity of Propane-Air Mixtures at High Temperature and Pressure," *Combust. Flame*, **38**, pp. 143–154.
- [13] Elia, M., Ulinski, M., and Metghalchi, M., 2001, "Laminar Burning Velocity of Methane-Air-Diluent Mixtures," *ASME J. Eng. Gas Turbines Power*, **123**, pp. 190–196.
- [14] Rahim, F., and Metghalchi, M., 2002, "Development of Reaction Mechanism and Measurement of Burning Speeds of Methane/Oxidizer/Diluent Mixtures at Low Temperatures and High Pressures," *Combustion Institute*, Western States Section, San Diego, CA.
- [15] Rahim, F., Elia, M., Ulinski, M., and Metghalchi, M., 2002, "Burning Velocity Measurements of Methane-Oxygen-Argon Mixtures and an Application to Extend Methane-Air Burning Velocity Measurements," *Int. J. Engine Res.*, **3**(2), pp. 81–92.
- [16] Weinberg, F. J., 1955, "Location of the Schlieren Image in a Flame," *Fuel*, **34**, pp. S84–S88.
- [17] Bradley, D., Hicks, R. A., Lawes, M., Sheppard, C. G. W., and Woolley, R., 1998, "The Measurement of Laminar Burning Velocities and Markstein Numbers for Iso-Octane-Air and n-Heptane-Air Mixtures at Elevated Temperatures and Pressures in an Explosion Bomb," *Combust. Flame*, **115**, pp. 126–144.

Development of the Radially Stratified Flame Core Low NO_x Burner: From Fundamentals to Industrial Applications

J. M. Beér

M. A. Toqan

J. M. Haynes

Department of Chemical Engineering,
Massachusetts Institute of Technology,
Room 66-548,
Cambridge, MA 02139-4307

R. W. Borio

49 Deerfield Drive,
Somers, CT 06071

Research and development of the low NO_x radially stratified flame core (RSFC) burner is followed from its fundamental concept through prototype burner design, pilot scale experiments at M.I.T. and scale-up and commercial design by ABB-CE (now ALSTOM Power) to applications in industrial and utility plant boilers. The principle that turbulence can be significantly damped in a rotating flow field with a strong positive radial density gradient was used to increase the fuel rich zone residence time in internally staged low NO_x burners. The continuous interaction of ideas from laboratory experimental and computational studies with those from the commercial design and industrial scale tests played a pivotal role in the development of the final product, the commercial RSFC burner. Examples of application in gas, oil, and coal fired industrial and utility boilers are discussed. [DOI: 10.1115/1.1688767]

Introduction

Nitrogen oxides, NO_x, formed in combustion processes are notable for their contribution to atmospheric pollution causing smog and tropospheric ozone to form by their photochemical reaction with hydrocarbons, and also, because, of all the pollutants, NO_x is the one most amenable to control by primary measures of combustion modifications. Combustion process modification is the most cost effective method of NO_x emissions control, and even if post combustion clean up, e.g., SCR, is required to comply with very tight emission targets, maximum reduction of NO_x by primary measures makes good technical and economic sense.

The thermodynamics and kinetics of formation and destruction of nitrogen oxides, NO_x, are discussed in several reviews, e.g., Miller and Bowman [1] and Bowman [2]. The principal sources of NO formation in combustion processes are:

- attack of atomic oxygen upon atmospheric, molecular nitrogen, N₂ ("thermal" or Zeldovich NO),
- attack of hydrocarbon fragments such as CH or CH₂, upon molecular nitrogen ("prompt" or Fenimore NO), and
- oxidation of heterocyclic nitrogen compounds in oils and coals (fuel-NO).

Figure 1 illustrates the chemical pathways of nitrogen compound interconversions, [3]. Of special practical interest are the fuel-rich pyrolysis processes (middle column) which can lead to the conversion of NO_x to the innocuous N₂.

It follows from the chemical pathways in Fig. 1 that NO_x emissions can be controlled by a combination of fuel-air mixing, residence times and heat extraction from the flame. The goals of combustion chemistry are hence achieved by tools of combustion physics: fluid dynamics and heat transfer. The general conditions for reduced NO_x emissions include:

- reduced peak flame temperatures in fuel-lean flame regions
- sequencing fuel-rich and fuel-lean combustion zones by staging the air and/or the fuel flow.

The engineering response has been the distributed air burner (Fig. 2) which provides for high-temperature fuel-rich pyrolysis near the burner followed by a fuel lean flame zone in which combustion is completed. One problem with the distributed air burner is that it is difficult to ensure sufficient residence time in the fuel-rich flame for the NO_x reducing reactions to run their course because of premature fuel-air mixing.

In the mid 1980s, a novel burner design was developed at MIT based on the principle of radial density stratification. In flames with a strong positive radial density gradient and a rotating burner air flow around the fuel injection, air-fuel mixing near the burner is suppressed and more time is provided for the pyrolysis reactions in the fuel-rich zone.

The concept of radial stratification was studied by Emmons et al. [4], Chigier et al. [5], and Beér et al. [6]. These early studies were not related to NO_x control; they were aimed at the better understanding of the mechanism of laminarization of turbulent diffusion flames in a rotating flow environment. Schlieren photographs of a free initially turbulent methane jet burning in air in the center of a cylindrical screen showed that the rotation of the screen can laminarize the jet, decrease entrainment and increase residence time in the fuel rich flame zone (Fig. 3), [5].

In a centrifugal force field with radially increasing density, heavier layers of fluid can be moved radially inwards and lighter layers outwards by the process of turbulent mixing. Turbulence, however, is damped by the action of the centrifugal force, which leads to the laminarization of the flow. A dimensionless criterion, the "modified Richardson number," Ri*, was recommended by Beér et al. [6] for the quantitative characterization of turbulence damping by radial stratification. Ri* represents the ratio of the rate of work required for mixing in rotating flow with positive density gradient, and of the rate of work of turbulence generation. For a swirling flow in cylindrical coordinates (*r, z*), with local mean axial and tangential velocity components *U* and *W*, and density, *ρ*, the modified Richardson number can be given as

$$Ri^* = 1/\rho dp/dr W^2/r / (dU/dr)^2.$$

Ri* = 1 corresponds to complete damping of turbulence, but laminarization of the flow begins at values as low as Ri* = 0.04.

Control of fuel-air mixing by radial stratification was adopted

Contributed by the Fuels and Combustion Division of THE AMERICAN SOCIETY OF MECHANICAL ENGINEERS for publication in the ASME JOURNAL OF ENGINEERING FOR GAS TURBINES AND POWER. Manuscript received by the F&C Division August 2002; final revision received August 2003. Associate Editor: S. Gollahalli.

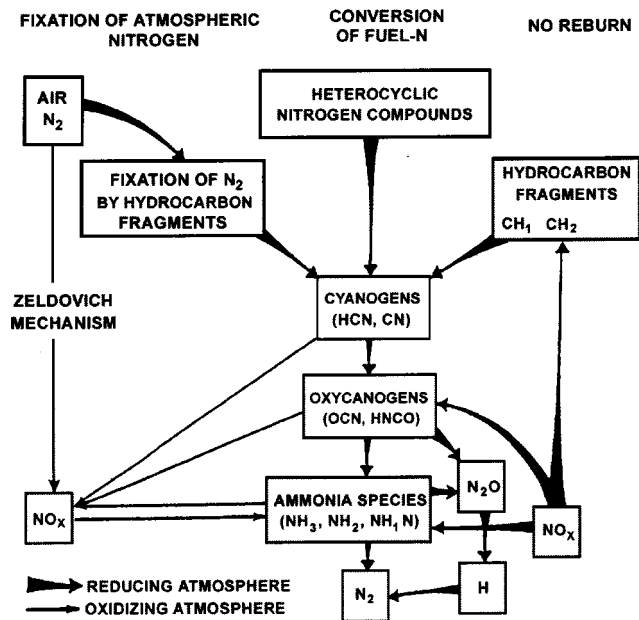


Fig. 1 Formation and reduction of nitrogen oxides in combustion, [3]

as a means of suppressing premature air admixing in the pyrolysis zone of the flame and hence to allow increased residence time for the fuel rich reactions to run their course.

Based on the above principle, a 1.5 MW prototype radially stratified flame core (RSFC) burner was designed, constructed and tested at M.I.T. in 1986. Computational fluid dynamics (CFD) modeling and experimental studies using the Flame Tunnel of the M.I.T. Combustion Research Facility were carried out with burning natural gas, heavy fuel oil, and pulverized coal during the period of 1986–1994. The RSFC burner technology was patented by M.I.T. and was licensed by ABB-CE Services for commercialization.

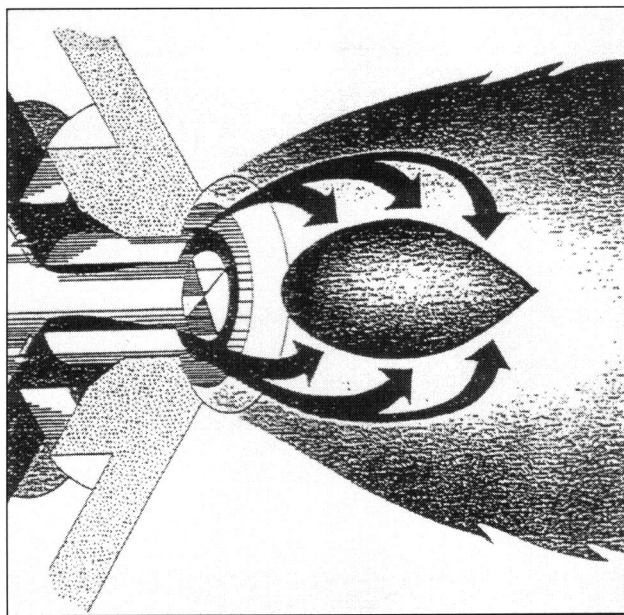


Fig. 2 Low NO_x burner schematic

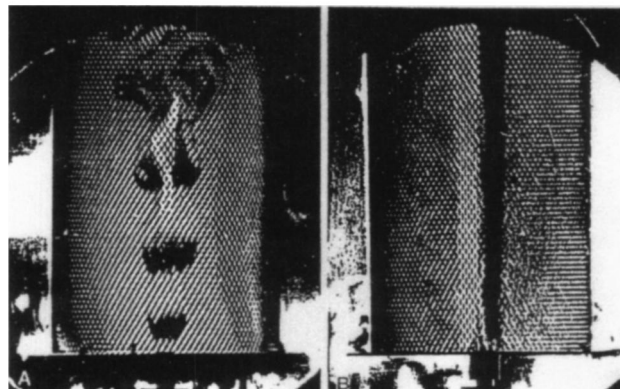


Fig. 3 Schlieren photographs of a turbulent methane jet flame in a cylindrical screen, [5]. Left: stationary screen; right: rotating screen.

The commercialization and scale-up studies were supported by additional computer modeling at both M.I.T. and ABB-CE, and experimental testing using the ABB-PPL industrial scale burner facility (ISBF). In the experiments, a 21 MW burner was tested with natural gas, HFO, and Coal.

RSFC Experiments at M.I.T.

The schematic of the prototype RSFC burner is shown in Fig. 4, [7]. The burner air is introduced around the fuel gun through three coaxial annular nozzles. The mass flow and the degree of swirl in the individual annuli can be controlled independently. Any one of the nozzles can be used for the injection of externally recirculated flue gas.

The experiments have been carried out in the $1.2 \times 1.2 \times 4.5 \text{ m}^3$ flame tunnel of the M.I.T. Combustion Research Facility. The flame tunnel is of sectional design with water cooled or partially cooled 0.3 m wide sections to permit the simulation of heat extraction in industrial furnaces and boilers by the suitable variation of heat extraction along the flame.

The natural gas fired burner performance is illustrated by Fig. 5 (Toqan et al. [8]). Radial stratification reduced NO_x emissions from an uncontrolled level of 240 ppm (3% O_2) to 70 ppm. A small amount of steam injection into the fuel gas (0.12 kg steam/kg fuel) reduced it further to 60 ppm, and external flue gas recirculation produced linearly decreasing emissions down to 14

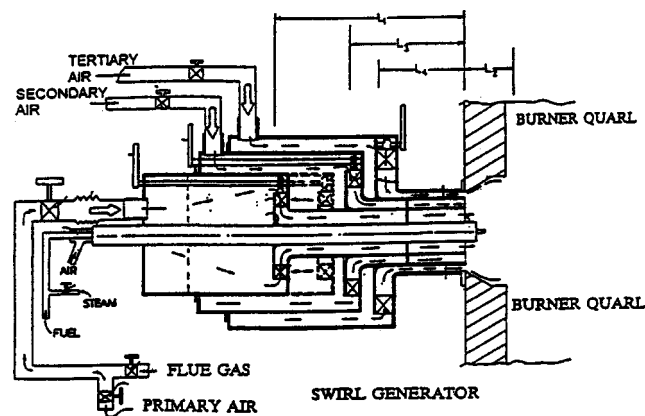


Fig. 4 Schematic of laboratory prototype low NO_x RSFC burner, [7]

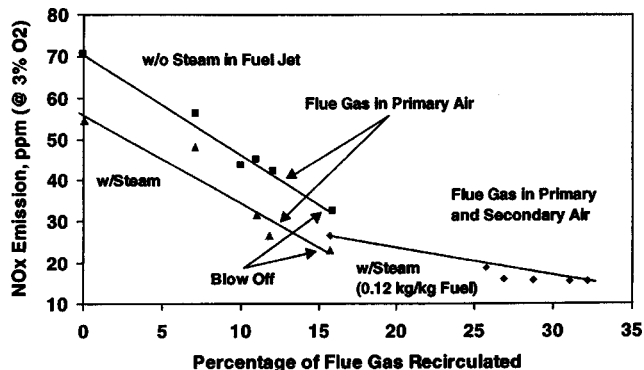


Fig. 5 NO_x emission form a density stratified natural gas/air turbulent diffusion flame. The effects of steam injection and flue gas recirculation (steam/fuel ratio=0.12 kg/kg. O_2 at exit =3%, [8]).

ppm at 32% recirculated flue gas. The air preheat was 555 K. The results of stratification can be seen also on the methane concentration contour lines in Fig. 6, [8].

Experiments with HFO (0.5% N) at 1 MW thermal input and 533 K air preheat (Shihadeh [9]) showed a reduction in NO_x from an uncontrolled 300 ppm (3% O_2) to 91 ppm. Narrow oil spray angle favored radial density stratification and moderately high atomizing air pressure of 4.0 to 4.8 bar (60–70 psi) resulted in sufficiently fine drop size distribution without excessive entrainment of burner air into the pyrolyzing fuel stream.

The effect of oil spray characteristics upon NO_x emission are shown in Fig. 7, [9].

For a high volatile pulverized bituminous coal, experimental data (Rodgers et al. [10]) are given in Table 1 for three cases: two cases with overfire air and one for burner operation without overfire air. NO_x emission of 217 ppm with burnout of >99.5% at SR=1.08 was achieved with a stratified flame, without overfire air.

The variation of NO_x emission with the stoichiometric ratio of the burner, air is shown in Fig. 8. The cases with SR<1.08 involve overfire air.

CFD Modeling

A commercial code (Fluent 3.03) capable of treating two phase chemically reacting turbulent flows and having the capacity to model an axisymmetric domain of at least 25,000 spatial nodes was selected for the computations. In the code, the dynamics of the continuous phase fluid flow are characterized in an Eulerian frame of reference by a system of partial differential equations (PDEs) for the conservation of mass, momentum and energy, turbulence quantities, and chemical species. Pressure, velocity, en-

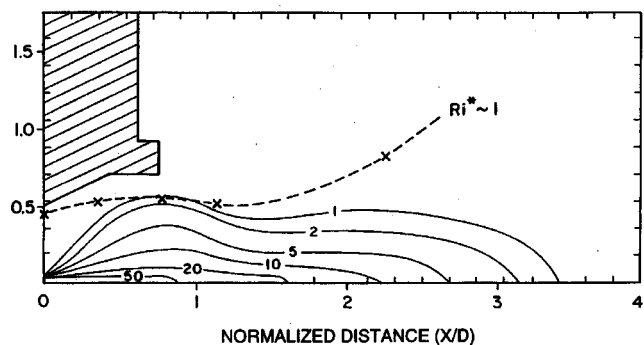


Fig. 6 Methane isoconcentration lines in stratified natural gas flame. Dotted line: regions of damped turbulence, $Ri^* \sim 1$, [8].

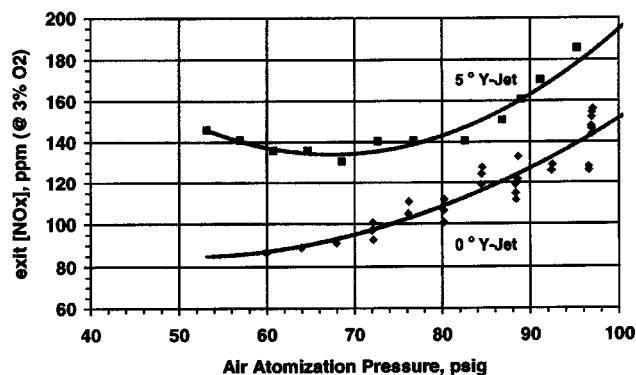


Fig. 7 NO_x emission as a function of air atomization pressure for 0 and 5 deg Y-jet atomizers, [9]

thalpy, turbulence quantities, and chemical species concentrations are computed directly from the governing PDEs. The trajectories of the liquid phase are evaluated in the Lagrangian frame of reference. NO_x and soot concentrations are computed through post processor operation. Thermal, prompt, and fuel-NO formations are computed and the effect of turbulent fluctuations upon the NO formation rates has been considered. Additional details of the CFD calculations are discussed elsewhere (Sun [11] and Haynes [12]).

For the RSFC computations, a burner with a narrow-angle oil spray surrounded by three concentric nozzles for the injection of the combustion air with variable swirl was chosen. There is a

Table 1 Pulverized coal experimental data, [10]

| | w OFA I | w OFA II | w/o OFA |
|---|-----------|-----------|-----------|
| Heat input (MW) | 1.5 | 1.5 | 1.5 |
| Overall SR | 1.21 | 1.13 | 1.08 |
| First stage SR | 0.82 | 0.92 | 1.08 |
| Total air (Nm ³ /h) | 1628 | 1460 | 1446 |
| Transport/coal ratio | 1.5 | 1.5 | 1.5 |
| Transport % | 13.5 | 14.7 | 15.1 |
| Primary %/swirl no. | 37.2/2.35 | 44.8/2.35 | 12.7/1.21 |
| Second. %/swirl no. | 5.3/2.52 | 6.9/2.52 | 27.2/1.63 |
| Tertiary %/swirl no. | 11.6/1.66 | 18.5/1.66 | 45/1.66 |
| OFA % | 32.4 | 15.6 | 0 |
| CO (ppm) | 45 | 33 | 30 |
| CO ₂ (%) | 15.5 | 15.9 | 16.7 |
| O ₂ (%) | 3.7 | 2.0 | 1.5 |
| NO_x (ppm @3% O ₂) | 70 | 107 | 217 |
| Carbon conv. (%) | 99.3 | 99.52 | 99.54 |

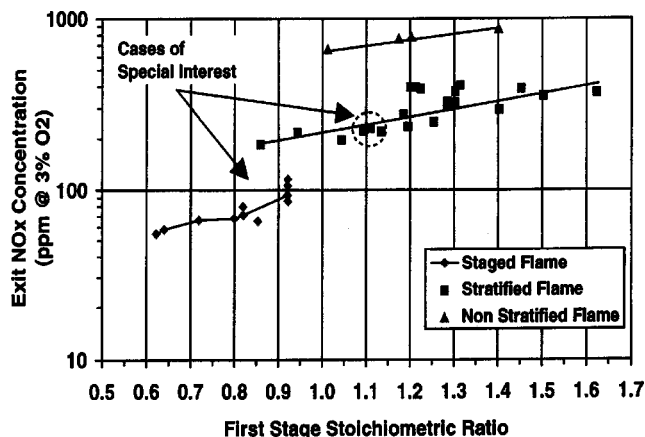


Fig. 8 NO_x emissions burning HV bituminous pulverized coal, [10]

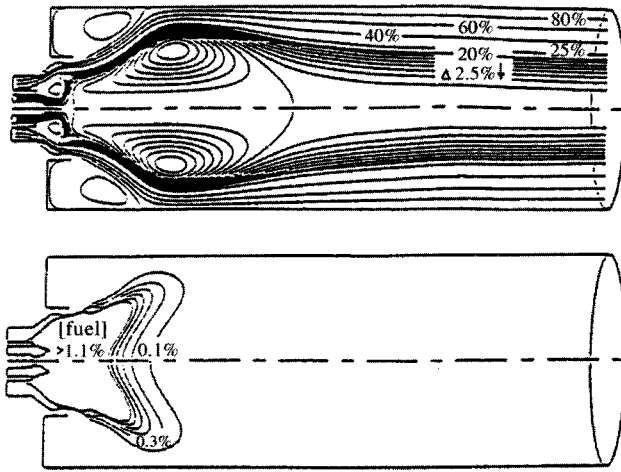


Fig. 9 Flame type A, [12,13]

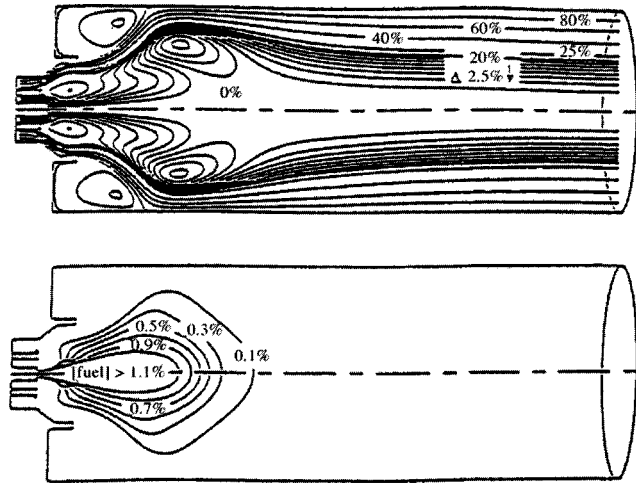


Fig. 11 Flame type B, [12,13]

short divergent quarl at the burner exit. In all the cases, the bulk of the combustion air, more than 70%, is injected through the outer, tertiary annulus, about 20% introduced as an annular jet immediately surrounding the oil spray, and the rest of the air through the second annular nozzle.

Results of computations are shown in Figs. 9, 10, and 11. The upper graphs in these figures represent stream function distributions, i.e. the percentage of the burner air flow within stream tubes, and the lower graphs show the distribution of unburned fuel in the flame.

Three characteristic flame types were identified, [12,13]:

- Short well-stirred flame, Type A (Fig. 9) with high volumetric heat release and 99.9% fuel burnout at a combustion length of $X/D=2.3$. It is a high NO_x flame. This flame type was produced with high burner air velocities (>200 ft/s) and high swirl numbers ($S>0.9$) in both the primary and tertiary air flows.
- Long flame, Type C (Fig. 10). There are two internal recirculation zones (IRZs) in the flow field. One of these is on the flame axis and is driven by the primary air flow; the other, more downstream and radially displaced, is driven by the tertiary air jet. Type C is a long ($X/D=6.6$), low NO_x flame. This flame was produced with reduced primary air swirl.
- A flame of medium length, Type B (Fig. 11). Two IRZs as in Type C, but the fuel-rich primary and secondary air flows, after penetrating partially the IRZ on the axis, are diverted

radially to flow along the outer boundary of the large IRZ set up by the tertiary air flow. This is a medium long flame ($X/D=4.6$) with low NO_x emission. This flame was produced with reduced primary air velocity and reduced tertiary air swirl.

Figures 12, 13, and 14 show oil droplet trajectories for the above flame types. In every case, the spray angle is 5 deg and the mean droplet size 35 μm . The effects of the flow field upon the spray are clearly seen. For flame Type A, the droplets are diverted at the upstream stagnation point of the IRZ and enter a fuel-lean

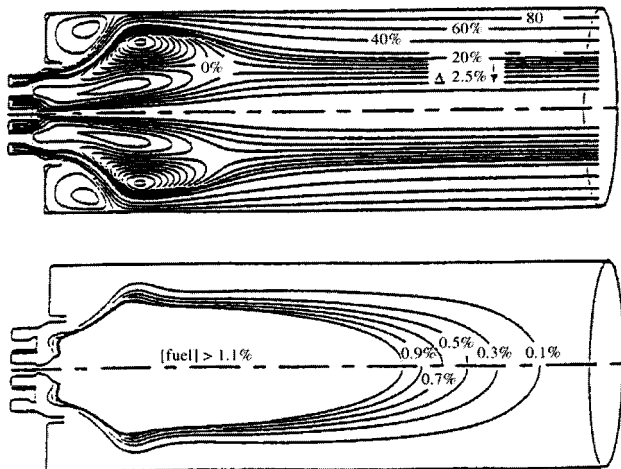


Fig. 10 Flame type C, [12,13]

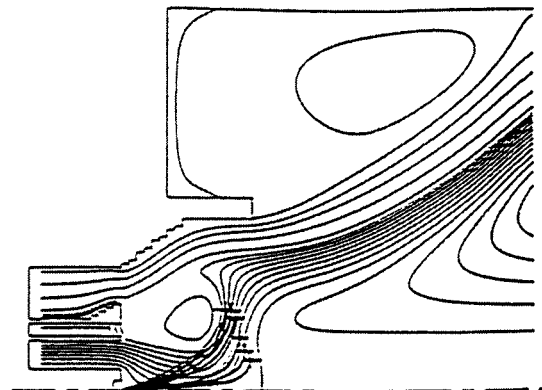


Fig. 12 Oil droplet trajectories in flame type A, [12,13]

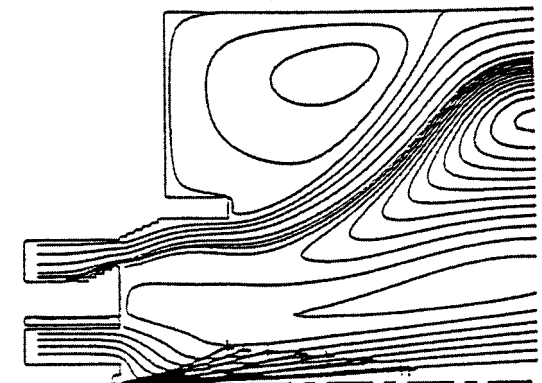


Fig. 13 Oil droplet trajectories in flame type C, [12,13]

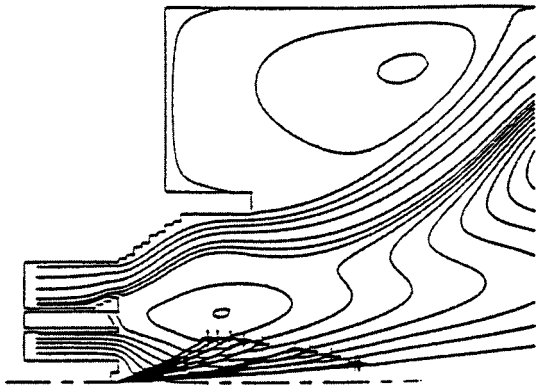


Fig. 14 Oil droplet trajectories in flame type B, [12,13]

highly turbulent shear region. Their fast burning leads to high NO formation. In the case of flame Type C, the spray penetrates along the axis that results in a long flame. Type B is the optimal, stratified flame in which the path of the droplets is lengthened without their early exposure to the high O₂ tertiary air stream.

Industrial Scale Test at ABB Power Plant Laboratories

Experimental data obtained in the front fired 2.4×2.7×7.3 m³ 21 MW_{th} industrial scale boiler facility (ISBF) have shown trends similar to those of the CFD calculations, [13]. Nominal test conditions were 12 to 21 MW firing rate, 2.5–3.0 % O₂ in the flue gas, and 533–563 K air preheat. The three characteristic flame types were obtained experimentally. Figure 15 shows NO_x and opacity levels as a function of CO concentrations for the three flame types. The combustion lengths of the Type A, Type B, and Type C flames were X/D=2 to 2.3; 7 to 8; and 10, respectively.

First Commercial Application (HFO or NG), [14]

The first commercial application of ABB's RSFC burner was a retrofit, four burner, wall-fired, 1950 VU 50 type boiler operating at 50 t/h 40 atm/670 K superheated steam flow. There are four burners, 11 MW_{th} each, operating either with No. 6 fuel oil (steam atomized) or natural gas. The burners were designed for "plug-in" installation in the existing windboxes. No OFA or FGR supplies were installed with the RSFC burners. The air preheat is 500 K.

State regulations require 195 ppm (3% O₂) or .25 lb/MM Btu when firing No. 6 oil and 161 ppm or .2 lb/MMBtu for natural gas. Post retrofit CO and opacity levels are not permitted to exceed baseline, normal operating levels.

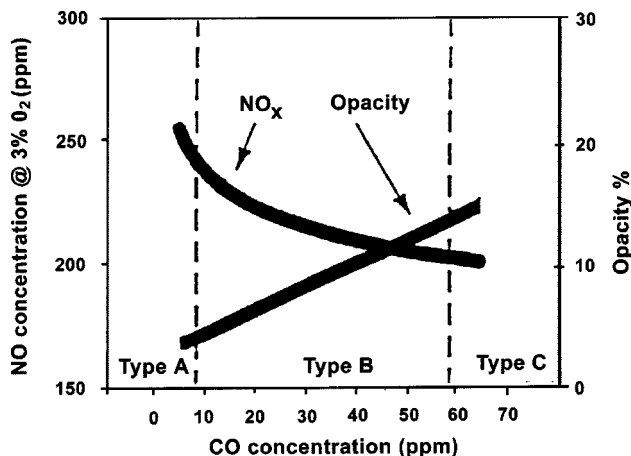


Fig. 15 Experimental CO emissions versus NO_x and opacity (ISBF), [13]

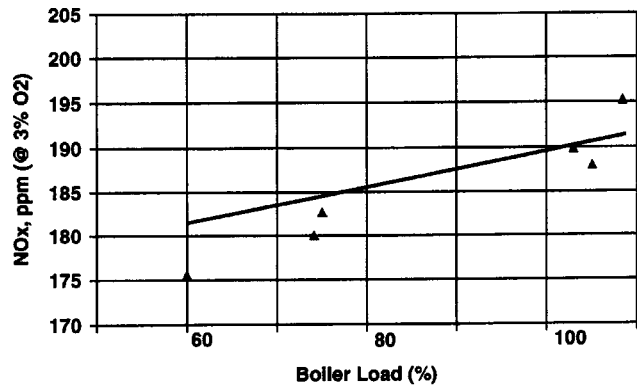


Fig. 16 Residual oil RSFC results, NO_x emissions with boiler load variation, [14]

Figure 16 illustrates the relationship between NO_x and boiler steam flow over the normal operating range of the boiler. NO_x was less than 195 ppm over the entire load range when firing No. 6 oils with 0.4% N. Baseline pre-retrofit NO_x was approximately 274 ppm when firing a 0.27% fuel. CO emissions through the entire operating steam flow range of the boiler varied in the range of up to 26 ppm; it is less than 5 ppm (3% O₂) at an operating O₂ level of 1.7%. Opacity is typically less than 10% and does not exceed 20%.

NO_x emissions with natural gas were less than one half of the regulatory limit of 161 ppm (corrected to 3% O₂) over the normal boiler range. Figure 17 shows the NO_x emissions as a function of boiler load. Combustion air is supplied to the burner at 500 K. The burners have been in normal dispatch service since May 1996 and have proven to be both operationally reliable, as well as continuing to achieve emissions performance levels at or below accepted limits.

Following the successful demonstration at the industrial site on natural gas and residual oil, ABB continued the development of the burner for pulverized coal firing. The modification of the oil-and-gas-fired design to burn coal focused on the coal nozzle assembly and minor variation in the burner annuli air splits.

Utility Application (Pulverized Coal), [14,15]

The first coal-fired application of the RSFC burner was a retrofit, six front-wall burners, 1955 Riley utility boiler operating at 136,000 kg/hr (33 MW) steam flow. The unit fires pulverized bituminous coal (15% moisture, 10% ash, 31% volatiles) from three Riley Atrita pulverizers. Nominal grind of 60% though 200 mesh is typical of current operation. Each pulverizer feeds two burners. ABB supplied six, 21 MW burners using 590 K preheated

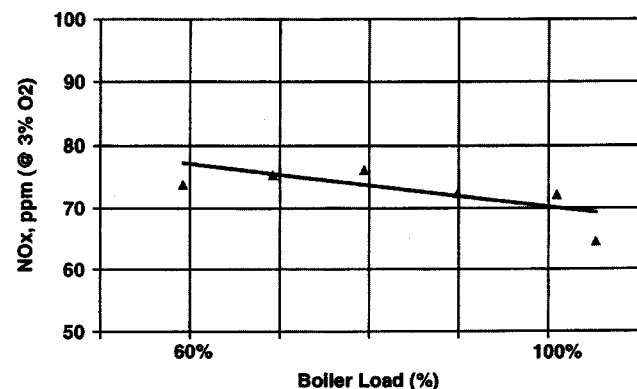


Fig. 17 Natural gas: RSFC NO_x emissions with boiler load variation, [14]

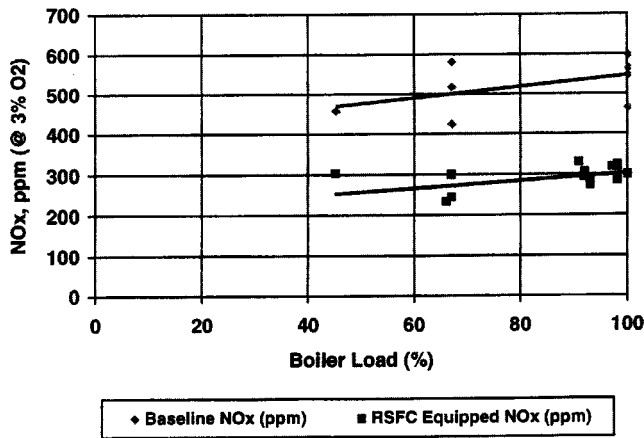


Fig. 18 Coal: baseline and RSFC burner NO_x with boiler load variation, [14]

air without modification of the existing windbox. The burners are arranged in two rows of three burners each. The burners are ignited with No. 2 oil ignitors with HEA spark.

The utility site had baseline NO_x value of 600 ppm (@ 3% O₂), and had to meet regulatory limits of 330 ppm (@ 3% O₂), which corresponds to .45 lb/MBtu (397 ppm corrected to 6% O₂). After the RSFC installation, NO_x emissions were less than 50% of the baseline values across the load range (Fig. 18), and the RSFC's flame shaping capability resulted in emissions which were insensitive to excess air variation (Fig. 19). Once the flame shape is optimized for the particular boiler/burner arrangement, no further adjustments are necessary over the load range. Boiler superheater and reheater steam temperature control adjustment has been greatly simplified due to the RSFCs optimized aerodynamics. Previous slagging within the burner throat has been eliminated, resulting in improved availability.

Coal/Oil Fired Boiler (RSFC+OFA), [15]

A 120,000 kg/h steam, Kawasaki Heavy Industries design boiler was retrofitted by ABB C-E Services with six RSFC burners capable of firing pulverized coal or heavy fuel oil. The boiler was also equipped with a system of multiple compartment overfire

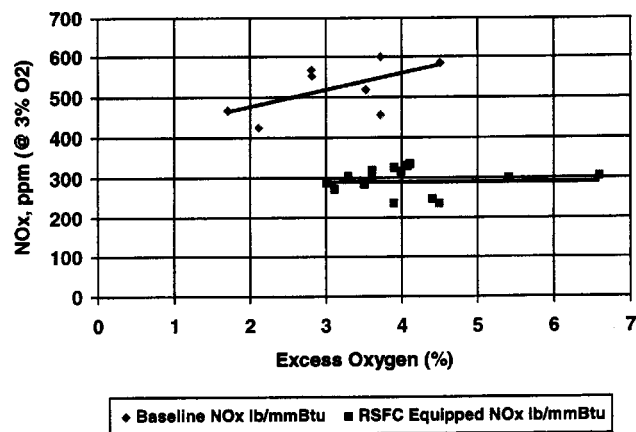


Fig. 19 Coal: baseline and post RSFC NO_x variation with excess oxygen, [14]

air registers especially suitable to optimize mixing of OFA with the bulk furnace gases. While burning a 31.8% vol bituminous coal, NO_x emissions of 0.21 lb/MBtu (162 ppm at 3% O₂) were achieved representing a 65% reduction over the pre retrofit NO_x emissions.

Conclusions

The RSFC concept is based on a novel application of fundamental principles for achieving low NO_x emission from staged combustion of gas, oil, and pulverized coal. Pilot scale experiments, physical and computational modeling, and scale-up studies have each contributed to a thorough understanding of how the air-fuel mixing required for low NO_x emission is achieved in RSFC burner flame. The simple, highly flexible and reliable commercial design of RSFC burners has led to their successful industrial and utility boiler applications.

The development has been remarkable also for its rare combination of fundamental ideas, computational and laboratory research, R&D, design of a commercial product and field applications; it has given intellectual satisfaction to many who participated at M.I.T. and in ABB CE.

Acknowledgments

Richard LaFlesh made important contributions over the years of development to the commercialization of the RSFC by Alstom Services Co. The authors thank Mr. Donald McGaffigan for his assistance in the preparation of the manuscript and the computer graphic design of the figures.

References

- [1] Miller, J. A., and Bowman, S. T., 1989, "Mechanism and Modeling of Nitrogen Chemistry in Combustion," *Prog. Energy Combust. Sci.*, **15**, p. 287.
- [2] Bowman, S. T., 1992, *Twenty-Fourth Symposium International on Combustion*, (Invited Lecture), The Combustion Institute, Pittsburgh, PA, pp. 859–878.
- [3] Beér, J. M., 1988, "Stationary Combustion; The Environmental Leitmotiv," The H.C. Hottel Plenary Lecture, *Proc. Comb. Inst.* The Combustion Institute, Pittsburgh, PA, pp. 1–16.
- [4] Emmons, H. W., and Shu Jing Ying, 1967, *Proc. Comb. Inst.* The Combustion Institute, Pittsburgh, PA, pp. 475–488.
- [5] Chigier, N. A., Beér, J. M., Grecov, D., and Bassindale, K., 1970, "Jet Flames in Rotating Flow Fields," *Combust. Flame*, **14**, p. 171.
- [6] Beér, J. M., Chigier, N., Davies, T. W., and Bassindale, K., 1971, "Laminarization of Turbulent Flames in Rotating Environments," *Combust. Flame*, **16**, p. 39.
- [7] Beér, J. M., Marotta, A., Toqan, M. A., 1955, "Combustion System for Reduction of Nitrogen Oxides," U.S. Patent. Assignee: M.I.T.
- [8] Toqan, M. A., Beér, J. M., Jansohn, P., Sun, N., Shihadeh, A., and Teare, J. D., 1992, "Low NO_x Emission From Radially Stratified Natural Gas-Air Turbulent Diffusion Flames," *Twenty-Fourth Symposium (International) on Combustion*, The Combustion Institute, Pittsburgh, PA, pp. 1391–1397.
- [9] Shihadeh, A. L., Toqan, M. A., Beér, J. M., Lewis, P. F., Teare, J. D., Jimenez, J. L., and Barta, L., 1994, "Low NO_x Emission from Aerodynamically Staged Oil-Air Turbulent Diffusion Flames," *FACT*, **18**, ASME, New York, pp. 195–200.
- [10] Rodgers, L. W., Sivy, J. L., J. L. Koslosky, J., Gorell, Beér, J. M., Lewis, P., and Barta, L., 1994, "NO_x Control update for Low Emission Boiler System," Eleventh Annual International Pittsburgh Coal Conference, U.S. D.O.E. Sept.
- [11] Sun, Norman, 1994, "Numerical Modeling and Experimental Investigation of Radially Stratified Low NO_x Natural Gas Flames," MS thesis, Department of Mechanical Engineering, M.I.T., Cambridge, MA.
- [12] Haynes, J. M., 1996, "Aerodynamic Design of Low NO_x Diffusion Flames Using the Radially Stratified Flame Core Burner," Ph.D. thesis, M.I.T. Feb.
- [13] Haynes, J. M., et al., 1996, "Aerodynamic Modeling and Scale-Up of a Low NO_x Oil Burner," *Int. Joint Power Gen Conference*, **4**, FACT-Vol. 12, ASME, New York, pp. 313–323.
- [14] Toqan, M. A., Nicholson, O. G., Briggs, O., Borio, R.-W., and Beér, J. M., 1997, "Low NO_x Burners for Boilers and Furnaces: Design and Application," *Power-Gen*, Madrid.
- [15] LaFlesh, R., Briggs, O., Barlow, D., and Wessel, G., 1999, "Update on ABB C-E's RSFC Low NO_x Wall Burner Technology," *Int. Joint Power Generation Conf.*, San Francisco, FACT-Vol. 23, ASME, New York, **1**, pp. 63–70.

Stephen K. Marley

Eric J. Welle

Kevin M. Lyons¹

e-mail: lyons@eos.ncsu.edu

Department of Mechanical and Aerospace
Engineering,
North Carolina State University,
Box 7910,
Raleigh, NC 27695-7910

Combustion Structures in Lifted Ethanol Spray Flames

The development of a double flame structure in lifted ethanol spray flames is visualized using OH planar laser-induced fluorescence (PLIF). While the OH images indicate a single reaction zone exists without co-flow, the addition of low-speed co-flow facilitates the formation of a double flame structure that consists of two diverging flame fronts originating at the leading edge of the reaction zone. The outer reaction zone burns steadily in a diffusion mode, and the strained inner flame structure is characterized by both diffusion and partially premixed combustion exhibiting local extinction and re-ignition events. [DOI: 10.1115/1.1688768]

Introduction

Reaction zones in spray flames are of fundamental and industrial interest. Since many practical devices, including gas turbines, introduce fuel as a spray, an understanding of spray combustion structures may facilitate the design of combustors with increased stability, efficiency, and reduced emissions. While lifted gaseous flames have been studied extensively, [1], experimental research on reaction zones in lifted spray flames is sparse. Early studies of sprays suggested a structure similar to that of a corresponding gas diffusion flame, since most of the droplets evaporate close to the fuel nozzle and only a single reaction zone is present, [2,3]. More recent investigations have reported that the flame can exhibit a double structure, originating at the leading edge, that diverges with increasing downstream location, [4–6]. This multibranch reaction zone structure is of general interest regarding the nature of the leading edge of double and triple flames. Triple flames are the subject of intense experimental and numerical investigations related to their fundamental role in flame stabilization and propagation, [7]. Related spray studies utilized either air-blast injection of the fuel spray with no other external oxidizer flow, [5,6], or a pressure-swirl nozzle surrounded by a large bluff body with co-flow supplied by a thin annular ring, [4], and have not addressed the role of air entrainment to any degree. The double flame structure, specifically from pressure-swirl nozzles in co-flow, is a focus of this paper. Visualizing reaction zones, diffusion or partially premixed, and assessing the effect of air entrainment on the leading edge of these zones is a novel aspect of this technical brief. In addition, the OH-PLIF results from this work provide a basis for comparison between lifted spray flames and the characteristics of lifted gaseous jet diffusion flames with similar co-flow.

Experimental Setup

The burner used in this study is illustrated in Fig. 1 and is composed of a central spray nozzle surrounded by an annular air co-flow. A 45 deg solid cone pressure-swirl nozzle supplies the desired ethanol fuel spray with a manufacturer specified overall Sauter mean diameter of 75 microns at 482 kPa injection pressure differential across the nozzle orifice and a flow rate of 0.864 liters per hour. The Reynolds number of the spray, based on the initial sheet thickness of the spray cone, [8], is calculated to be 1600 at the injector exit. Rizk and Lefebvre [9] give an expression for the determination of the film thickness inside the nozzle orifice. This method of computing a characteristic Reynolds number, which is usually applicable for hollow cone pressure-swirl nozzles, is vali-

dated by the results of Drallmeier and Peters [10]. The solid cone pressure-swirl nozzle used in their investigation, of the same design utilized in this study, possesses characteristics similar to those seen in hollow cone nozzles, with the effect of the initial sheet on droplet size and liquid volume flux clearly evident. Thus, the spray presented here can also be characterized as a thin conical sheet at the nozzle orifice. Compressed air delivers the co-flow at variable flow rates (0 to 0.29 m/s) via six ports located at the base of the burner (one ten-mesh and three 20-mesh stainless steel screens produce a uniform velocity profile across the co-flow).

OH-PLIF was employed to obtain instantaneous planar images of the reaction zones in the spray flame. OH is a good marker of the fuel-lean side of reaction zones in diffusion flames, but signals are generally broader in premixed flames because of the long-lived presence of OH molecules in the hot combustion products, [5,11]. OH fluorescence in diffusion flames appears as a thin band, since the reactions are occurring along the stoichiometric contour between the fuel and oxidizer flows. Partially premixed combustion zones exhibit “broad” regions of OH, thicker than seen in pure diffusion flames, and have been observed previously in both initially non-premixed and partially premixed flames, [12,13]. The output of a frequency doubled Nd:YAG pumped dye laser is used to excite the hydroxyl (OH) radical. The dye laser output of 562.50 nm is doubled to 281.25 nm which excites the $R_1(8)$ transition of the $A^2\Sigma - X^2\Pi(1,0)$ band. Fluorescence is then collected from the (0,0) and (1,1) bands ($\lambda \approx 306-312$ nm), [14]. A Pellin-Broca prism provides UV beam separation, and a series of focusing lenses produce a 38-mm high laser sheet. Positioned at 90 deg to the laser sheet is an ICCD camera with a detection gate width of 200 nanoseconds (576×384 array with a 105 mm UV-Nikkor lens; WG-305 and UG-11 filters capture fluorescence and reduce elastic scattering signal from droplets).

Results and Discussion

With respect to the results of past work without air co-flow, [4], terminology is introduced to simplify the discussion of the two-dimensional planar images. The double reaction zone consists of two diverging flame fronts on each side of the spray centerline that join together at the flame base, or leading edge. These two flame structures may be labeled the inner and outer reaction zones, depending on their radial positions relative to the axis of symmetry. Due to viscous effects, a shear (or mixing) layer is created at the interface between the spray cone and the surrounding gas flow. Shear layers contribute to transport and mixing in turbulent flows, and aid in the formation of a flammable mixture to support the inner reaction zone. Description of the spray flame structure is facilitated by the representative OH images shown in Fig. 2 along with a photograph of the flame. Figures 2(a) and 2(b) (zero co-flow) show the leading edge of the reaction zone stabilized near the fuel nozzle (7.8 mm downstream). These images

¹To whom correspondence should be addressed.

Contributed by the Fuels and Combustion Division of THE AMERICAN SOCIETY OF MECHANICAL ENGINEERS for publication in the ASME JOURNAL OF ENGINEERING FOR GAS TURBINES AND POWER. Manuscript received by the F&C Division October 2002; final revision received February 2003. Associate Editor: S. Gollahalli.

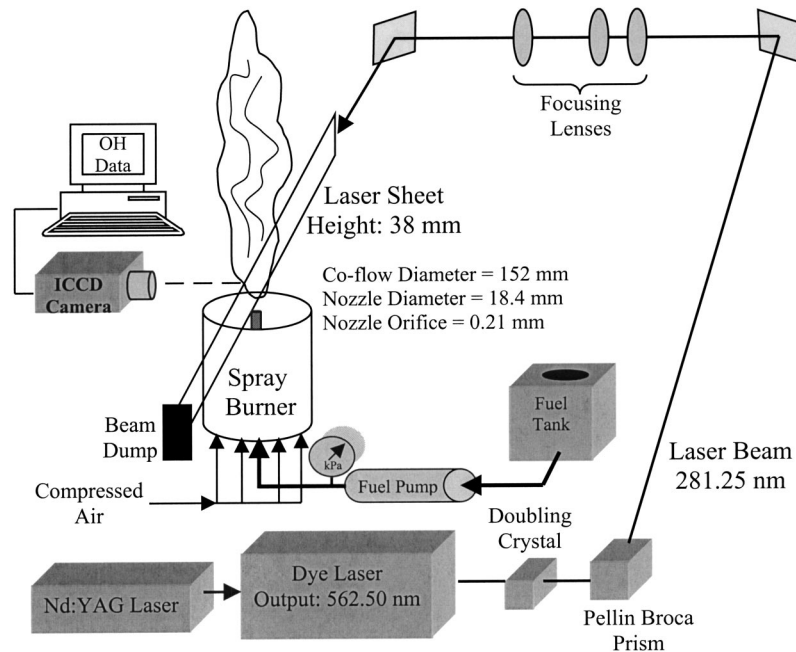


Fig. 1 Layout of the burner and optical setup for acquisition of OH-PLIF images

portray a single branch structure similar to that witnessed in lifted gaseous jet diffusion flames, [15]. Since the leading edge of the flame is located close to the tip of the fuel nozzle both axially and radially, there is insufficient entrainment of ambient air to support an inner reaction zone. MacGregor [16] showed that spray jets are not as efficient as gaseous jets at entraining ambient air, and in this case there is not enough time for significant momentum transfer, thus entrainment, to occur before the reaction zone develops. This result is in contrast to the images obtained by Friedman and Rensizbulut [4], where a well-developed double reaction zone structure was observed without co-flow. The hollow cone pressure-swirl nozzle used in their study has a 50% higher nominal fuel flow rate (at 861 kPa pressure differential) and a wider 60 deg cone angle, resulting in increased momentum and jet spread providing conditions favorable to air entrainment and the formation of an inner reaction zone even without co-flow. Figure 2(b), without co-flow, shows a small cusp at the leading edge as the reaction zone wraps around the stabilization point. This cusp is thought to exist as a result of transient large scale mixing structures, interacting intermittently with the flame base, that can stretch the reaction zone around the leading edge as they rotate (see Fig. 9 in [15], [17]). This observation explains why no cusp is observed in Fig. 2(a). Kelman et al. [18] also observed roll up of the flame base around large-scale fuel eddies of lifted methane jet flames, resulting in air entrainment around the leading edge. These recirculation zones in burning sprays contain small droplets that follow the gas flow near the spray edge and vaporize easily for subsequent burning near the flame leading edge, which is critical in lifted spray flame stabilization, [6].

The addition of low-speed (0.29 m/s) air co-flow induces a transition from a single to a dual reaction zone as seen from the images in Fig. 2(c)–2(f). It is important to note that the data presented for these co-flow cases represent the same experimental conditions. The interaction of local flow turbulence with the flame base results in an oscillating liftoff height. As this process occurs, the double reaction zone undergoes a series of progressive changes that give insight into the characteristics of turbulent spray flames. The annular co-flow convects the flame downstream allowing sufficient air entrainment to support a secondary reaction

zone along the mixing layer. Initially, the OH at the stabilization point becomes more pronounced and an inner reaction zone is only present near the leading edge (Fig. 2(c) and 2(d)). Small pockets of OH are also noticeable at locations downstream of the inner reaction zone in some images. These isolated regions of combustion are likely pinched off of the lower inner reaction zone due to excessive strain rates that quench local combustion. The OH profile of the inner zone is noticeably thinner than the outer zone as a result of increased local strain at the flame front, [18]. Figure 2(e) shows a detached inner reaction zone structure illustrating flame and product fragments as “patches” of OH radicals. Extinction and re-ignition processes allow adequate time for local partial premixing to occur. The level of induced strain (at the inner zone interface) prevents the existence of segregated diffusion and premixed components of the partially premixed structure, thus a single merged reacting layer exists, [13,19]. Finally, in Fig. 2(f), the flame has lifted to its most downstream location (15.7 mm liftoff height). In this case, the flame has a fully developed inner reaction zone with areas of local extinction. The inner OH structure is again significantly thinner than the outer reaction zone due to strain. Also, the inner zone is wrinkled but does not have the large OH blotches, indicative of local premixing, that were observed in the previous case (Fig. 2(e)). Therefore, the inner reaction zone burns in a predominately diffusion mode.

Entrainment has been shown to have a significant impact on both the structure and stabilization of spray flames. Axisymmetric co-flows used in sprays are able to lift the flame base into downstream regimes of the spray (droplets, fuel vapor, and air) and permit significant air entrainment near the shear layer. This entrainment, along with the atomization characteristics of the poly-disperse spray, allows an inner reaction zone to form. This fact explains the widening of the leading edge as the liftoff height increases. The spray spreads out as it propagates, further atomizing the droplets and providing a wider region favorable to reaction zone stabilization. One common theme is the role of turbulent mixing in leading edge behavior and inner flame structure. The flame is stabilized at the edge of the spray where the smallest droplets are rapidly vaporized and mixed, independent of the larger ballistic droplets which cross the inner reaction zone and

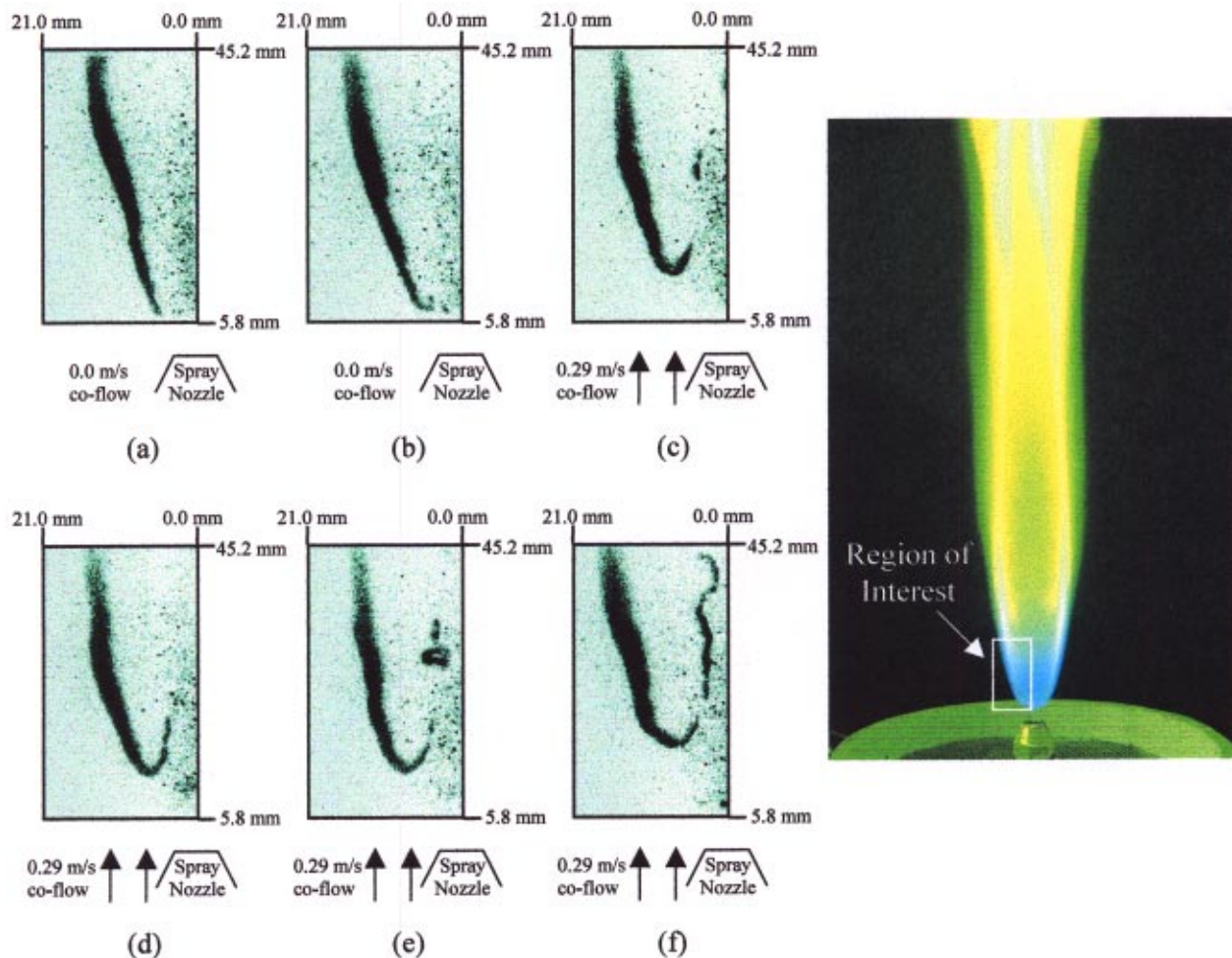


Fig. 2 Instantaneous OH-PLIF images and photograph of spray flame at increasing liftoff heights

feed the outer diffusion flame and bulk combustion downstream. As seen from the OH images (Fig. 2(f)), lifting the base of the flame far enough downstream allows the oxidizer to penetrate the fuel spray and form a wrinkled inner diffusion flame with the exception of cases exhibiting isolated blotches of OH which involve partial premixing. The thin, wrinkled nature of the inner zone, when compared to the smooth boundary of the outer structure, indicates that inner zone combustion exists along the shear layer created between the momentum dominated region of the spray and entrained gases. The shear layer provides a region of enhanced mixing and aids in the entrainment of air due to large scale vortices, [20]. It is important to note that, when a fully developed inner zone exists, the hot region between the two reaction zones, laden with droplets, is primarily responsible for diffusion of fuel vapor to feed both flame structures, [19]. The oxidizer for the inner zone diffuses into the flame from the spray side of the flame front.

Conclusions

The structure of a lifted ethanol spray flame has been investigated using OH-PLIF. Overall, the morphology of the flame is primarily controlled by both the air co-flow velocity and the droplet distribution. Without co-flow, the flame exhibits a single flame structure similar to that observed in lifted gaseous jet diffusion flames. The addition of low-speed co-flow lifts the flame and permits increased entrainment of air. The presence of oxidizer within the fuel spray creates a unique scenario that is not seen in non-premixed gas flames. A double flame structure develops that origi-

nates at the leading edge and diverges with increased downstream location. The inner reaction zone burns in both a diffusion and a partially premixed mode. Future work is aimed at obtaining quantitative data, especially drop size and velocity distributions, to validate models of evaporation and combustion. Also of interest is the investigation of spray flames under pressure and with co-flow swirl (to enhance the flame stability), conditions typically found in gas turbines.

Acknowledgments

This research has been supported by ARO Contract AMSRL-RO-RI 40131-EG (Dr. David Mann, Technical Monitor) and NSF Grant CTS 99-09125 (Dr. Farley Fisher, Technical Monitor). The spray nozzle used in this experiment was supplied by Delavan Spray Technologies (Part Number 0.50-45 deg B).

References

- [1] Pitts, W. M., 1988, "Assessment of Theories for the Behavior and Blowout of Lifted Turbulent Jet Diffusion Flames," *Twenty-Second International Symposium on Combustion*, The Combustion Institute, Pittsburgh, PA, **22**, pp. 809–816.
- [2] Onuma, Y., Tsuji, T., and Ogasawara, M., 1974, "Studies on the Flame Structure of a Spray Burner," *Bull. JSME*, **17**(112), pp. 1296–1304.
- [3] Onuma, Y., and Ogasawara, M., 1975, "Studies on the Structure of a Spray Combustion Flame," *Fifteenth International Symposium on Combustion*, The Combustion Institute, Pittsburgh, PA, **15**, pp. 453–465.
- [4] Friedman, J. A., and Renssizbulut, M., 1999, "Investigating a Methanol Spray Flame Interacting With an Annular Air Jet Using Phase-Doppler Interferom-

- etry and Planar Laser-Induced Fluorescence,” *Combust. Flame*, **117**, pp. 661–684.
- [5] Cessou, A., and Stepowski, D., 1996, “Planar Laser Induced Fluorescence Measurement of [OH] in the Stabilization Stage of a Spray Jet Flame,” *Combust. Sci. Technol.*, **118**, pp. 361–381.
- [6] Cessou, A., Goix, P., and Stepowski, D., 1999, “Simple Description of the Combustion Structures in the Stabilization Stage of a Spray Jet Flame,” *Atomization Sprays*, **9**, pp. 1–27.
- [7] Plessing, T., Terhoeven, P., Peters, N., and Mansour, M. S., 1998, “An Experimental and Numerical Study of Laminar Triple Flames,” *Combust. Flame*, **115**, pp. 335–353.
- [8] Lefebvre, A. H., 1989, *Atomization and Sprays*, Hemisphere, New York, Chaps. 5–6.
- [9] Rizk, N. K., and Lefebvre, A. H., 1985, “Internal Flow Characteristics of Simplex Swirl Atomizers,” *J. Propul. Power*, **1**, pp. 193–199.
- [10] Drallmeier, J. A., and Peters, J. E., 1994, “Liquid- and Vapor-Phase Dynamics of a Solid-Cone Pressure Swirl Atomizer,” *Atomization Sprays*, **4**, pp. 135–158.
- [11] Donbar, J. M., Driscoll, J. F., and Carter, C. D., 2000, “Reaction Zone Structure in Turbulent Nonpremixed Jet Flames—From CH-OH PLIF Images,” *Combust. Flame*, **122**, pp. 1–19.
- [12] Kelman, J. B., and Masri, A. R., 1997, “Simultaneous Imaging of Temperature and OH Number Density in Turbulent Diffusion Flames,” *Combust. Sci. Technol.*, **122**, pp. 1–32.
- [13] Tanoff, M. A., Smooke, M. D., Osborne, R. J., Brown, T. M., and Pitz, R. W., 1996, “The Sensitive Structure of Partially Premixed Methane-Air vs. Air Counterflow Flames,” *Twenty-Sixth International Symposium on Combustion*, The Combustion Institute, Pittsburgh, PA, **26**, pp. 1121–1128.
- [14] Dieke, G. H., and Crosswhite, H. M., 1962, “The Ultraviolet Bands of OH,” *J. Quant. Spectrosc. Radiat. Transf.*, **2**, pp. 97–199.
- [15] Watson, K. A., Lyons, K. M., Donbar, J. M., and Carter, C. D., 1999, “Scalar and Velocity Field Measurements in a Lifted CH₄-Air Diffusion Flame,” *Combust. Flame*, **117**, pp. 257–271.
- [16] MacGregor, S. A., 1991, “Air Entrainment in Spray Jets,” *Int. J. Heat Fluid Flow*, **12**, pp. 279–283.
- [17] Kaminski, C. F., Bai, X. S., Hult, J., Dreizler, A., Lindenmaier, S., and Fuchs, L., 2000, “Flame Growth and Wrinkling in a Turbulent Flow,” *Appl. Phys. B: Photophys. Laser Chem.*, **71**, pp. 711–716.
- [18] Kelman, J. B., Eltobaji, A. J., and Masri, A. R., 1998, “Laser Imaging in the Stabilization Region of Turbulent Lifted Flames,” *Combust. Sci. Technol.*, **135**, pp. 117–134.
- [19] Continillo, G., and Sirignano, W. A., 1990, “Counterflow Spray Combustion Modeling,” *Combust. Flame*, **81**, pp. 325–340.
- [20] Lazaro, B. J., and Lasheras, J. C., 1988, “Droplet Dispersion and Transport Mechanisms in a Turbulent, Free Shear-Layer,” *Twenty-Second International Symposium on Combustion*, The Combustion Institute, Pittsburgh, PA, **22**, pp. 1991–1998.

Preliminary Gas Turbine Design Using the Multidisciplinary Design System MOPEDS

P. Jeschke¹

J. Kurzke

R. Schaber

C. Riegler

MTU Aero Engines GmbH,
Dachauer Str. 665,
80995 Munich, Germany

A prototype preliminary design task for gas turbines is set up to outline the four major requirements a preliminary design program must typically meet: assessment of all major engine components and their interrelations; inclusion of all relevant disciplines; designing over several operating points; and model fidelity zooming at least for individual components. It is described how the "MODular Performance and Engine Design System" (MOPEDS)—MTU Aero Engines' software package for the preliminary design of airborne and stationary gas turbines—fulfills these requirements. The program structure, the graphical user interface, and the physical models are briefly presented. A typical design example is carried out emphasizing the necessity for a numerical procedure to find a solution to the many variables and constraints that the design problem comprises. Finally, some dominating multidisciplinary effects are discussed. [DOI: 10.1115/1.1639009]

Introduction

During the preliminary design phase of gas turbines the main parameters are fixed. These, in return, fix most of the risks and financial resources associated with the development, manufacture, and operation of the engine under concern. The preliminary design process must in contrast to that be carried out very quickly so that engine suppliers are able to evaluate numerous concepts with respect to the market requirements at a given short time. This brings up the need for an adequate software tool that accurately and quickly guides the designer through the preliminary design process. MTU Aero Engines uses such a software package. It is called "MODular Performance and Engine Design System" (MOPEDS).

The preliminary design of a new engine usually starts with the thermodynamic cycle. It is fixed so that all aircraft requirements are met at all relevant operating points of the flight mission. From the cycle the engine configuration is then derived. Subsequently all engine components are designed aerodynamically and mechanically with respect to a good matching of the components, well-behaved off-design characteristics over the whole mission, low cost, ease of manufacture, reliability, noise legislation, emission regulation, etc. Such a preliminary design process is characterized by three major features upon which MOPEDS is built: all major engine components and their interrelations are assessed; several relevant disciplines are considered; designing is done on several operating points and the off-design characteristics are adequately checked.

Once the preliminary design phase is completed its results must be smoothly fed into the detailed design process. For this reason more sophisticated methods are included in MOPEDS. These higher fidelity methods are typically applied for singular components that are included in the company's work share. These methods are the ones used in the specialist departments, so that they provide the "interface" through which the pre-design results are passed to the detailed design and vice versa. The designer in the specialist department is then able to add one higher order of detail to the design and, simultaneously by running MOPEDS, is able to see how his changes affect the performance of other components

and the overall engine. Throughout the long lasting detailed design phase the overall engine behavior is monitored thereby. "Model fidelity zooming" i.e., the application of models of different degrees of detail, is the fourth major feature of MOPEDS.

Representative for several known multidisciplinary engine simulation systems, the popular Numerical Propulsion System Simulation NPSS [1], shall be mentioned. NPSS is made to model all engine components with several disciplines and the full range of model fidelities as is shown in Fig. 1. One of the strengths of NPSS is the ability to include highest fidelity methods such as multidimensional CFD modeling for several components simultaneously if not for all. Somewhat to the contrary, the preliminary engine design tasks are clearly the focus of MOPEDS, so that mainly lower model fidelity methods, such as one-dimensional and two-dimensional methods, are included so far. It is intended to thoroughly exploit the first-order effects using this ability before any second-order effects are tracked in the design process with higher fidelity methods. No attempt is made to model all-engine effects with high fidelity methods within MOPEDS.

Halliwel [2] gives an excellent overview of the preliminary design task. Following his ideas, a prototype preliminary engine design task is described in Section 1. The thus created prototype problem is used to emphasize the necessity for an integrated multidisciplinary tool and it is the measure for MOPEDS which is described in Section 2. In the spirit of the prototype problem some exemplary pre-design results are then shown in Section 3.

1 A Prototype Preliminary Design Task

The prototype preliminary design task to be set up in the following can by no means be generic. The design variables, constraints, figures of merit, and operating points considered are generally completely different in number and type for each individual engine project. We still try to give some idea of the preliminary engine design task.

The engine design ideally starts with the aircraft and engine demands such as flight mission, number of engines, thrust and SFC requirements, maximum size and weight, installation requirements, etc., fixed. These determine the engine's thermodynamic cycle which in return fixes the engine configuration. Say, for the prototype problem, a typical medium-sized commercial aircraft is considered whose engine cycle requirements can be met by an air-breathing high-bypass ratio two-spool mixed turbofan engine. The major cycle design variables are then

overall pressure ratio,
HP/LP pressure ratio split,

¹To whom correspondence should be addressed.

Contributed by the International Gas Turbine Institute (IGTI) of THE AMERICAN SOCIETY OF MECHANICAL ENGINEERS for publication in the ASME JOURNAL OF ENGINEERING FOR GAS TURBINES AND POWER. Paper presented at the International Gas Turbine and Aeroengine Congress and Exhibition, Amsterdam, The Netherlands, June 3–6, 2002; Paper No. 2002-GT-30496. Manuscript received by IGTI, December 2001, final revision, March 2002. Associate Editor: E. Benvenuti.

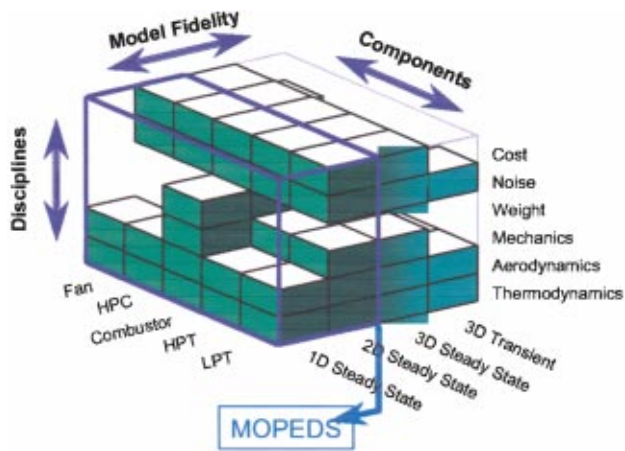


Fig. 1 Cube adopted from [1]

fan outer pressure ratio,
bypass ratio,
inlet flow, and
turbine inlet temperature.

Cycle constraints are derived from the flight envelope requirements or typically arise from temperature limits imposed to assure sufficient mechanical strength or to limit the cooling flow demand:

net thrust required,
maximum HPC exit and HPT, LPT inlet temperatures, and
maximum fan diameter.

A possible figure of merit is
minimum specific fuel consumption.

The preliminary aerodynamic design variables for turbo components are typically
rotational speed,
stagewise distribution of reaction, loading, flow rate,
flowpath radius ratios and flowpath slopes, and
blading parameters, such as: pitch-to-chord ratio, aspect ratio, taper ratio, axial and tip clearance, profile thickness ratio, relative trailing edge thickness, etc.

Typical aerodynamic constraints, especially for compressors, are
maximum rotor tip Mach numbers,
minimum de Haller numbers,
minimum surge margin, and
several geometrical constraints like limits on radius ratios.

And possible figures of merit could be
maximum component efficiency,
minimum number of stages,
minimum number of blades, and
minimum component length.

Preliminary mechanical design variables for turbo components are typically
materials,
blade profile area and moment of resistance,
blade root geometry, and
disk geometry.

Typical constraints are
maximum metal temperatures,
frequency bounds, and
maximum low and high cycle fatigue stresses.

Figures of merit could be
minimum weight,
minimum number of parts, and
minimum cost.

Variables, constraints, and figures of merit for burner, ducts, nozzles, nacelle, shafts, bearings, etc., are to be considered also. Further constraints arise from noise legislations and emission regulations as well as maintenance costs, life cycle costs, etc. This

easily amounts to an order of 100 variables and constraints and an overall figure of merit combined from several weighted individual ones.

An adequate preliminary design furthermore assesses all important operating points of the required flight mission. Each engine component is given a nominal design point where the independent design variables are specified. All other points in the envelope are formally treated as off-design points and the dependent variables can be taken to define constraints there. The design variables are then to be chosen to give balanced component characteristics over the whole flight mission.

The nominal design point is most conveniently chosen to be the point with the severest conditions or the strongest influence on the figure of merit. This usually amounts to a high speed and max through-flow point for the nominal aerodynamic design of compressors, nozzles and ducts, say max climb, and possibly a cruise point for the design of turbines. The severest mechanical integrity constraints generally arise at hot day takeoff so that the mechanical designing is done there. Further operating points have to be considered that are relevant for external constraints such as noise legislation, for instance. An example of the important operating points is then

hot day takeoff,
standard day max climb,
standard day cruise,
sideline, cutback, approach,

and others must be considered for burner design, assessment of emission limits, etc.

What makes the design task so challenging are the many design variables and constraints to be considered at several operating points of the flight mission. The strong coupling of the effects of all disciplines as well as the strong interrelation of all engine components puts up the need to consider all of the variables and constraints simultaneously. For instance, the limited takeoff metal temperatures of the turbines are a direct function of the cycle variables set in the max climb cycle design point and the turbo component efficiencies. These component efficiencies, however, are a direct function of the aero design variables set at the aero design point max climb or cruise. This gives for these temperature constraints a direct dependence on several design variables of different disciplines set at different operating points. This problem can only be adequately tracked by an integral computer program that simulates these interrelations.

2 The Simulation Tool

The traditional way of solving the preliminary design task described in the previous section is to run several stand-alone programs, one for each subtask. A loop over a series of such individual programs is done until convergence is achieved. However, due to the time-consuming process the mentioned strong interrelation of the engine components, the coupling of the disciplines, and the engine characteristics on all of the important operating points are not adequately captured. Often this shortcoming is very costly compensated for, when the loops must be closed in the subsequent detailed design phase.

MOPEDS was built to overcome this shortcoming. It focuses on the multidisciplinary, all-engine, multi-operating point modeling ability and extensively supports the designer so that he usually can arrive at a "converged" design. The following section describes the underlying program structure before subsequently a brief sketch of the graphical user interface and the implemented physical models is given.

2.1 Program Structure. MOPEDS is an extension of the in-house performance program "MODular Performance Synthesis" (MOPS), [3], and shares its program structure. Performance programs deal with all-engine effects so that their program structure generally is well suited for such a task and the thermodynamic performance is always the backbone for any preliminary design. It was therefore obvious to base MOPEDS on MOPS.

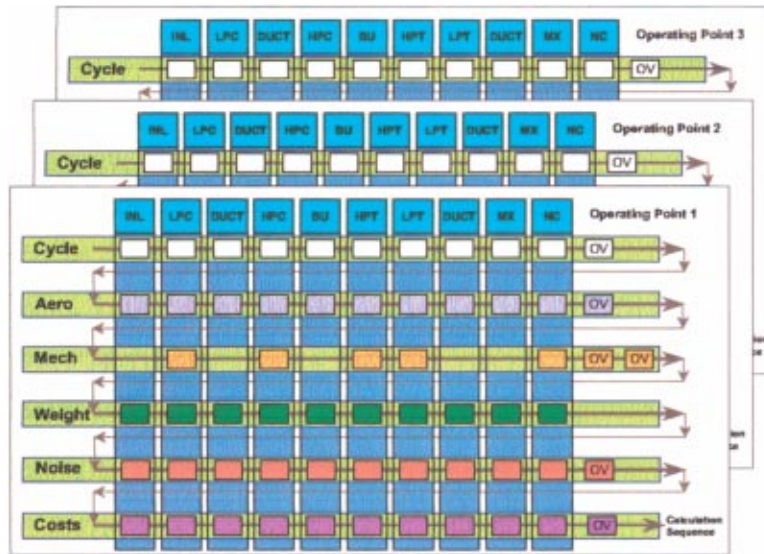


Fig. 2 Modularity

The program is divided up into the four levels:

- Level 1: graphical user interface (GUI)
- Level 2: program control
- Level 3: modules
- Level 4: “physical” modelling

Each level contains a self-sufficient package of programs and data is passed exclusively through standardized interfaces between the levels. Level 1 contains the programs for the GUI which is described in Section 2.2 in more detail. Level 2 routines control all input and output operations as well as the run time data transfer between the modules residing in level 3. Any purely mathematical operations like those necessary for a Newton-Raphson iteration are done in level 2 and all external programs are called from there. One of these is the commercial package iSight (Engineous [4]). On command of the user a predefined MOPEDS slave process is passed to iSight at any point of the design process. iSight’s full range of numerical procedures ranging from simple parameter studies to optimizations is thereby available at run time. On termination of the iSight subprocess the command is given back to MOPEDS and the necessary data is passed over by the control program.

Level 3 contains all the modules. As depicted in Fig. 2 the level 3 program structure forms a matrix whose columns represent the engine components, whose rows represent the disciplines, and whose elements are defined to be *modules*. Effectively, each module is a standardized subroutine that stand-alone contains all physical information associated with its position in the matrix. It has standardized interfaces for data transfer in vertical and horizontal direction and to the level 2 control program. Depending on whether its physical content is needed or not it is included in the configuration set up for a specific preliminary design task or not. Somewhat outside the matrix the so-called overall-modules reside which are responsible for data that cannot be related to a single discipline or engine component, e.g., thrust and SFC evaluation or assessment of rotor dynamics. At run time a loop over the modules, which are successively called as is sketched in Fig. 2, is repeated until any iteration is brought to convergence at each operating point. An outer loop over all the operating points specified by the user then completes the process which in total is controlled by the level 2 control program. Each module’s variables are uniquely defined at each operating point and are treated by the control program as independent or dependent variables, constraints, or figures of merit depending on the problem under con-

cern. There is no limit on the number of operating points and variables to be considered by the user apart from his own choice to limit the complexity of the problem.

According to the module’s self-sufficient character, all of the extensive descriptions of the module’s underlying physics and its variables are directly implemented in the module’s source code. From there it is automatically translated to html format to make it accessible for the user via the GUI (see Section 2.2).

From within the modules the level 4 subroutines containing the “physical” models (see Section 2.3) are called through standardized interfaces. The level 4 programs are the “specialist’s” programs held and maintained by the corresponding departments. Any “translation” of variables from MOPEDS definition to the level 4 definition is automatically done within the modules freeing the user from this task. The user may choose to be confronted exclusively with the MOPEDS nomenclature, which assures a unique definition throughout all of MOPEDS, or may use the level 4 nomenclature for the limited number of input data needed to configure the level 4 calculation. The first practice is possibly the preliminary designer’s choice who sets up the whole MOPEDS process. The specialist who is concentrated on and is used to the level 4 program may choose the latter.

Any “model fidelity zooming” is realized by selecting the corresponding level 4 routines included in the module. All necessary translation of data from one level 4 routine to the other is again automatically done by the module.

The modules are surely the physical heart of the tool and assure the full modularity of the tool. Practically any engine configuration can be set up ranging from simple single shaft engines to multispool, recuperated, intercooled, stationary, or air-borne engines. All disciplines can be covered ranging from thermodynamics and aerodynamics down to noise and cost assessment.

2.2 Graphical User Interface. The mentioned almost limitless flexibility has its price when it comes to setting up the design process, monitor its progress during run time and interpret the results. The provision of well organized input and output data sets as well as extensive help features eases this situation.

The control program of MOPEDS reads input data exclusively from ASCII files. With help of these lengthy but all flexible and well organized files the user may set up his design task. This includes the specification of the engine configuration, the input of all physical data, and the setup of the mathematical problem to be

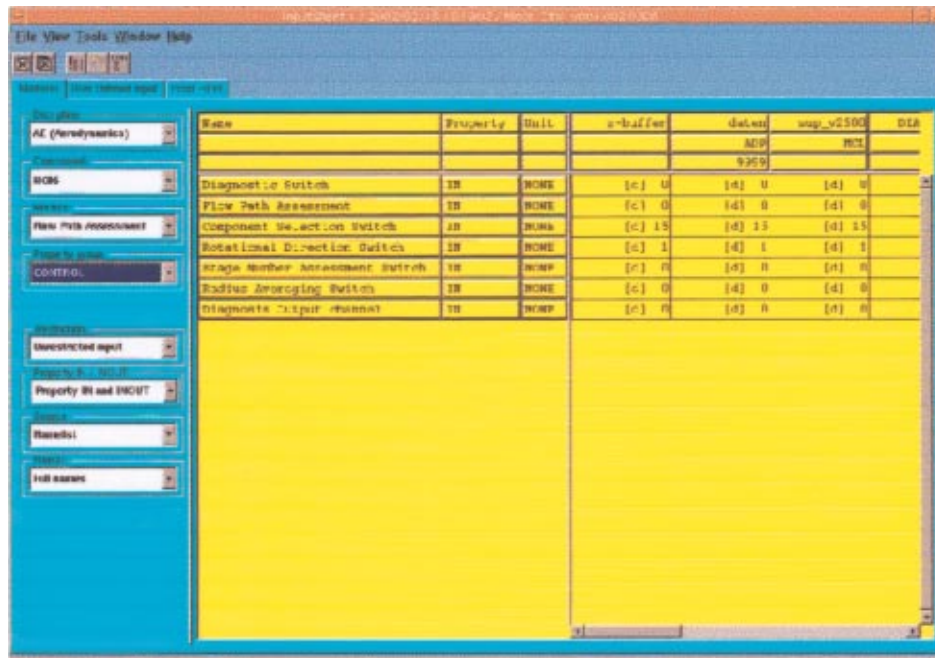


Fig. 3 Input sheet window for modules

solved, i.e., the input of the iteration/optimization scheme, the number of operating points considered, the models to be used, etc. Input data sets for standard design tasks are provided so that the data generally must not be created from scratch. A strict file administration assures the reproducibility of any MOPEDES run.

The ASCII file system is manipulated through the graphical user interface (GUI). The GUI consists of several elements. Two of them are the so-called *input sheet* and *output sheet* windows for modules. No matter which module is considered the user is confronted with the one input sheet shown in Fig. 3 and an analogous output sheet window. He is thereby freed from the numerous individual interfaces of the stand-alone programs that are included in MOPEDES. Furthermore, a description of all the modules' variables and physical models can be invoked from within these windows. The user is thereby well guided when specifying each module's input data and interpreting its results. Constraining himself to the proposed input values and judging the results as advised, he may even apply the modules' methods if he is not an expert.

A rather large collection of graphical outputs is provided. They are initiated from within the output sheet and they display the module's results. Examples of these outputs are turbine loading diagrams, velocity vectors, flow path geometries, stress and temperature distributions, noise levels, ICAO parameter distributions, etc. The commercial package TECPLOT (AMTEC [5]) is directly linked to the output sheet to automatically produce the displays during run time. TECPLOT also provides the basis for subsequent postprocessing individually carried out by the user.

2.3 Physical Models. All in MOPEDES included programs are the in-house developed and over the years validated programs of the specialists' departments. The currently available "physical" models are subdivided into the disciplines

- thermodynamics,
- aerodynamics,
- mechanics,
- weight assessment,
- noise assessment, and
- cost assessment.

To give some idea of the models included so far they shall be very shortly listed as follows: Steady and unsteady "zero-dimensional" performance models for all relevant engine components. Meanline

(one-dimensional) and through flow (two-dimensional) aerodynamic codes for the turbo components and ducts. Burner design and assessment of emissions in terms of ICAO parameters. Blade and blade root steady and unsteady mechanics assessed by one-dimensional beam theory methods. Containment formulas constraining the mechanical casing design. One-dimensional finite difference and two-dimensional finite element codes solving the elasticity and heat conduction equations for disks. Shaft design and rotor dynamics based on beam theory methods and a parametric bearing design concept. Several weight assessment methods, some calculating masses from the laid out geometry and some based on simple correlations. Engine noise determined for single engine components and the overall system. Finally, several correlations for the costs of development, manufacture, maintenance and the life cycle of the engine.

Model fidelity zooming is readily applied for the one-dimensional and two-dimensional aerodynamic and mechanic models. The data transfer as well as the conversion of data from one level of accuracy to the other is fully automated.

The huge amount of design variables, some of which mentioned in Section 1, that need to be specified as input to the many physical models, make it impossible to consider all of them simultaneously even with a tool like MOPEDES. For this reason a database of generic component models has been set up. These generic component models contain all input data for a physical model in, as far as practical, dimensionless form to allow scaling of components correctly taking into account the corresponding similarity rules. It is then generally possible to consider only a very small number of design variables while fixing all others by the generic model. Most of the data base models set up for MOPEDES are geometric component models like those for turbo components whose geometry is nondimensionally provided as radius ratios, area ratios, aspect ratios, pitch-to-chord ratios, etc. Since the generic models are usually set up with reference to already designed engine components, they can easily be read into MOPEDES when it comes to analyze a given engine. Figure 4 shows the general arrangement of an engine whose geometry is completely provided by generic models.

However, MOPEDES provides one other way to free the user from explicitly specifying the many design variables. So-called

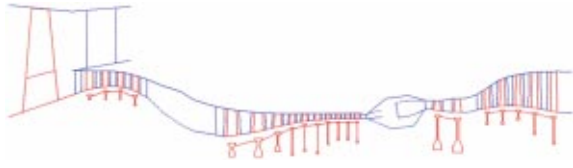


Fig. 4 General arrangement of an engine to be analyzed

knowledge bases have been programmed for all input variables. These contain rules to set the input values depending on the situation. Examples of which are rules for typical stage-wise distributions of reaction, loading, and flow rate for turbo components. The user may invoke these knowledge bases for singular design values, several, or even all. A fully automatic engine design is done by invoking all of them. The example provided in Section 3 makes use of such full automatic designs. Applying the full automatic scheme the designer is able to arrive at a first solution from where he can start to fine tune his design.

3 Application Example

MOPEDES is used to solve a simple artificial preliminary design problem. Say, the problem is to design a high pressure compressor upgrade for a given engine. Apart from rather small necessary adaptations, all engine components other than the HP compressor may not be changed and the underlying thermodynamic cycle is kept constant in terms of pressure ratios, mass flows, and thrust requirements.

The high-bypass ratio, two-spool, mixed turbofan engine considered in Section 1 is taken as a basis and the problem is solved in the spirit of the design task sketched in Section 1. However, several simplifications are made to keep the design problem easy: Aerodynamic design is done only for turbo components based on meanline codes. Mechanical design is only carried out for blade roots and disks. It is also based on one-dimensional methods. Besides thermodynamics, aerodynamics, and mechanics no further disciplines are looked at. The three mission points *hot day takeoff*, *standard day max climb*, and *standard day cruise* are considered. The thermodynamic cycle is specified at max climb and the aerodynamic design of all engine components is made there. All components can then simultaneously be run in off-design mode thermo/aerodynamically at all other operating points. Furthermore, aerodynamic meanline calculations are only done at the design point, where appropriate component maps are scaled accordingly. These maps are used at all off-design points, thereby avoiding any aerodynamic off-design calculations at run time.

The max climb design point is taken to be defined thermodynamically by

Ma=0.8, alt=10,668 m, $\Delta T_{ISA}=0$, $F_N=25,000$ N,
 $w_2=150$ kg/s, BPR=5, $p_{25}/p_2=3.0$, $p_{14}/p_2=1.7$,
 $p_3/p_{26}=13$, fixed secondary air system,
 and all of these values are kept constant.

The many aerodynamic design variables mentioned in Section 1 are reduced to only the three

$$\text{radius ratio HPC exit} \quad (1)$$

$$\text{High Spool Speed}_{MCL} \quad (2)$$

$$\text{number of HPC stages} \quad (3)$$

by taking all others from the MOPEDES knowledge base. The only explicitly defined aerodynamic constraint is

$$\text{minimum Surge Margin}_{MCL} \quad (4)$$

The mechanical design is chosen to be done at hot day takeoff rotation:

Ma=0.2, alt=0, $\Delta T_{ISA}=15$ K, $F_N=11,5000$ N.

In order to keep our example simple, the blading design variables like blade profile area and blade moment of resistance are taken from the same knowledge base that is used for the aerodynamic

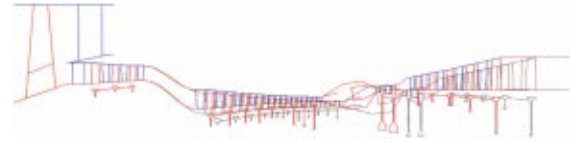


Fig. 5 General arrangement before (longer engine length) and after optimization (shorter engine length)

blade design. The blades and vanes are then simply mechanically analyzed at takeoff. A close coupling between aero and mechanical blading design is avoided thereby. Merely the blade roots and the disks are designed: materials and geometry are found during run time exactly fulfilling stress and temperature constraints at takeoff and providing minimum weights. No independent mechanical design variables then appear. However, the constraint

$$\text{maximum Stresses}_{MCL} \quad (5)$$

formally stands which especially puts limits on the values of *radius ratio HPC exit* and *High Spool Speed*_{MCL} beyond which the mechanical design is not feasible anymore.

The cruise point

Ma=0.8, alt=10,668 m, $\Delta T_{ISA}=0$, $F_N=20,000$ N

is used in the example to evaluate SFC there.

The design task's figure of merit is defined to be a weighted function of

$$\text{minimum SFC}_{BCR} \quad (6)$$

$$\text{minimum } \sum \text{HPC Vanes} + \text{Blades} \quad (7)$$

$$\text{minimum } \sum \text{Mass Disks HPC} + \text{HPT}. \quad (8)$$

The number of blades and vanes is hereby interpreted as some measure of costs in our simple example. The disk masses are taken as some measure of component weights.

The thus defined design task forms the basis for the following optimization and parameter studies. To set up a problem like this from scratch takes an experienced preliminary designer a few hours and run time on a typical workstation for each of the following studies is in the order of a few minutes.

It must be clearly said that the following results are meant to show exemplary results, that by no means are to be taken for granted in absolute terms. Preliminary design in general first of all provides trends and not absolute results and this is even more valid for the artificial prototype problem presented here.

3.1 Optimization. A numerical optimization scheme based on a coupled genetic and gradient based algorithm is used to solve the prototype problem. It is defined by the design variables (1)–(3), the constraints (4), (5), and the figures of merit (6)–(8). The optimization is started from some arbitrary initial solution that could represent the given gas turbine whose HP compressor is to be improved.

In Fig. 5 the initial engine configuration and the optimized one are shown and Table 1 compares starting values with optimal values. The improvements shown in Table 1 are of course strongly dependent on the initial solution and the choice of figure of merit. However, the example serves to illustrate the value of a tool as presented herein. Even though the investigated problem is somehow “academic,” it comprises a truly multidisciplinary, multi-operating-point investigation of the overall gas turbine engine. A preliminary designer could by no means produce results like this—not to speak of a more realistic problem with more variables—in such a short time without an integral tool like MOPEDES.

However, there obviously can be several pitfalls when numerically investigating a problem of high complexity. Especially the

Table 1 Optimization

| | Optimal Value/Start Value |
|---------------------------------------|---------------------------|
| Radius ratio HPC exit | 0.91/0.89 |
| High spool speed _{MCL} [RPM] | 13506/12000 |
| Number of HPC stages | 9/11 |
| SFC _{BCR} | 0.96 |
| $\eta_{HPC,MCL}$ | 1.03 |
| $\eta_{HPT,MCL}$ | 1.02 |
| Σ HPC vanes+blades | 0.93 |
| Σ mass disks HPC+HPT | 1.4 |

physical accuracy of the used models must always be carefully checked. This is even more true if a numerical optimization is used that could exploit some model's strange trends outside the model's typical range of application. One means of checking the validity of a numerically obtained solution is to vary the design variables in its vicinity. Not only the optimum can be checked thereby but also the models by investigating their trends carefully. This shall be done in the following parameter studies. The parameters are deliberately varied over a wider range than is reasonable for a normal design to show how the models behave. Still, these parameter studies are another typical preliminary design result that can be achieved with MOPEDS—even though one might typically not vary the design variables (1)–(3) directly.

3.2 HPC Radius Ratio Variation. Varying the design variable (1) effectively means that the radial position of the HPC is changed. The HPC and HPT flow path annuli and the bladings in terms of blade inlet and exit angles, pitch-to-chord ratios, etc., are then individually and fully automatically designed at each run by use of the knowledge bases. The engine's LP components are left almost unchanged except for some adaptations necessary for the extreme HPC radius ratios. Minor LPT design changes automatically result from different LPT entry conditions during the parameter study.

Some of the most dominant effects of this parameter study are shown in Fig. 6. First, an optimum of the HPC efficiency $\eta_{HPC,MCL}$ can be identified around radius ratio 0.9. For lower radius ratios the higher stage loadings ψ and the associated large profile losses become dominant so that $\eta_{HPC,MCL}$ falls there. At very high radius ratios the lower loading can no longer compensate for the increasing secondary flow losses and radial clearance losses caused by the "short" blades especially in the rear of the HPC. $\eta_{HPC,MCL}$ falls there again. The highly loaded HPT stages benefit from higher blade speeds over the full range of radius ratios. The SFC_{BCR} distribution directly reflect the $\eta_{HPC,MCL}$ and $\eta_{HPC,MCL}$ trends, since all other component efficiencies are merely unchanged. The exchange rates between SFC and the component

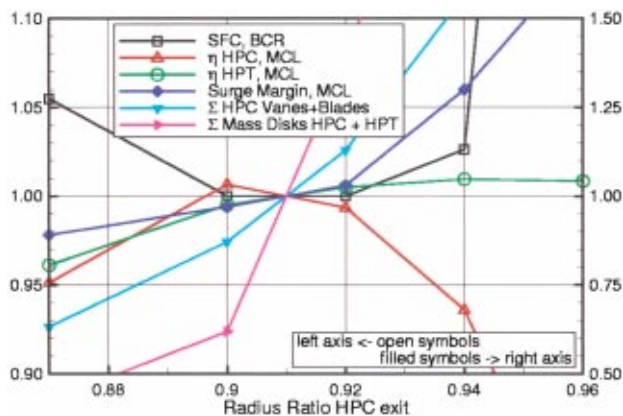


Fig. 6 HPC radius ratio variation. Dependent variables are divided by the optimal values of Section 3.1.

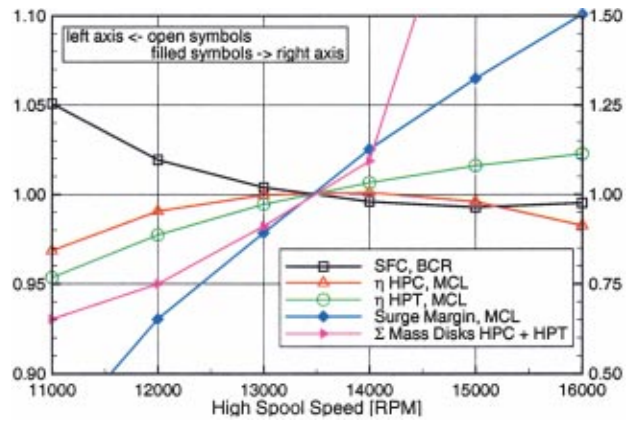


Fig. 7 High spool speed variation at MCL. Dependent variables are divided by the optimal values of Section 3.1.

efficiencies directly follow from the underlying thermodynamic cycle and the aerodynamic off-design characteristics.

The number of blades and vanes given in Fig. 6 is almost a linear function of the flow path radius since pitch-to-chord ratios and aspect ratios are almost constant for each run. The number of blades and vanes can be closely linked to the costs of manufacture.

The disks are strongly influenced by the increasing centrifugal forces at higher radius ratios which leads to larger and heavier disks as can be seen in Fig. 6. The disk temperature distribution has a minor additional effect: The mainstream gas temperatures and the secondary air system temperatures are affected by the HPC efficiency. This leads to higher disk hub and rim temperatures for the rear HPC disks and the HPT disks at lower HPC efficiencies. More stringent temperatures then generally lead to heavier disks.

3.3 High Spool Speed Variation. Exactly in the same spirit as before the design variable (2), the high spool speed, is varied leaving everything else constant. Merely the HPC and HPT bladings and disks are individually designed for each speed and some minor LPT design adjustments follow automatically.

The HPC, HPT efficiencies and the HPC surge margin are strongly affected by the spool speed as is seen in Fig. 7. High losses result from the high loadings at low speeds and the surge margin vanishes at some point. At higher speeds the loading is reduced but the Mach number losses become increasingly dominant so that an HPC efficiency optimum is again found. This, again is not the case for the highly loaded HPT. The disk design is equally strongly affected by the centrifugal forces changing with speed and at some speed no solution for the HPT disks can be found anymore.

3.4 HPC Stage Number Variation. Finally the design variable (3), the number of HPC stages, is varied leaving everything else constant. Merely the HPC flow path annulus design, the HPC blading design, and the HPC disk design are significantly affected by the varying number of HPC stages.

The typical strong dependence of HPC efficiency and surge margin on the different stage loadings, as a result of the variation of the number of stages, is observed in Fig. 8. Higher loads lead to drastically falling efficiencies and surge margins whereas only for very high number of stages the increased wetted area finally outweighs the benefit of lower loadings and reduces the HPC efficiency.

4 Conclusions

The overall engine performance is to first order dominated by the parameters set by the preliminary design. These main param-

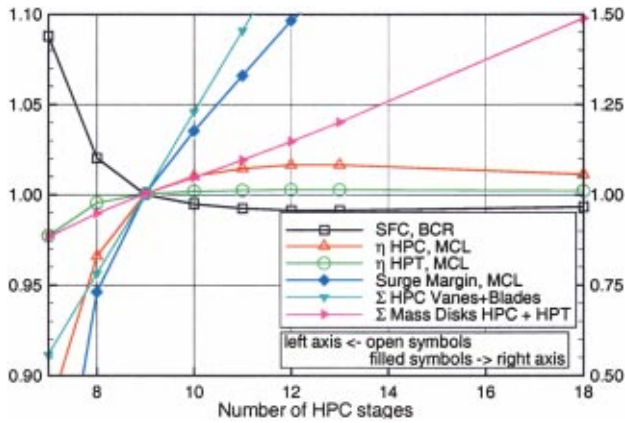


Fig. 8 HPC stage number variation. Dependent variables are divided by the optimal values of Section 3.1.

eters must therefore be selected with highest care before any second or higher order effects can be exploited such as those caught with three-dimensional blade design, for instance. It has been shown that a solution to these main parameters can only be found with help of an integrated multidisciplinary tool such as MOPEDS due to the complexity of the problem. The complexity arises from the need to consider many design variables and constraints at several operating points of the flight mission. The strong coupling of the effects of all disciplines as well as the strong interrelation of all engine components furthermore puts up the need to consider all of the variables and constraints simultaneously. Any shortcoming in the preliminary design is generally very costly compensated for in the subsequent detailed design phase.

Acknowledgments

Representative for the many MTU colleagues joining the MOPEDS team over the last years, the authors want to especially acknowledge the contribution of Martin Ulmke, Arno Schlöder, and Markus Hartmuth who programmed the system structure and the GUI. Specially acknowledged are also the very fruitful discussions with Arthur Schäffler.

MOPEDS has been developed under the four year financial grant "Bay08" of the "Bayerische Staatsministerium für Wirtschaft Forschung und Technologie."

Nomenclature

- alt = flight altitude
 - BCR = cruise
 - BPR = bypass ratio
 - F_N = net thrust
 - MCL = max climb
 - Ma = Mach number
 - p_{25}/p_2 = LPC core pressure ratio
 - p_{14}/p_2 = fan outer pressure ratio
 - p_3/p_{26} = HPC pressure ratio
 - SFC_{BCR} = thrust specific fuel consumption at cruise
 - TO = takeoff
 - w_2 = fan entry mass flow
 - ΔT_{ISA} = delta to ISA temperature
 - $\eta_{HPC, MCL}$ = isentropic efficiency HPC at max climb
 - $\eta_{HPT, MCL}$ = isentropic efficiency HPT at max climb
 - ψ = stage enthalpy diff. divided by blade speed squared
- High Spool
 $Speed_{MCL}$ = HP speed at max climb
- Surge
 $Margin_{MCL}$ = surge margin at max climb
- Σ HPC Vanes
 + Blades = sum of HPC blades and vanes
- Σ Mass
 Disks HPC
 + HPT = sum of HPC and HPT disk masses

References

- [1] Claus, R.W., et al., "Numerical Propulsion System Simulation," Comput. Syst. Eng., 2 (4).
- [2] Halliwell, I., "Preliminary Design of Gas Turbine Engines," ASME Turbo Expo 2001, June 4-7, New Orleans, LA.
- [3] Kurzke, J., 1992 "Calculation of Installation Effects Within Performance Computer Programs," AGARD-LS-183.
- [4] Engineous Software Inc., NC.
- [5] AMTEC Engineering Inc.

A Computer Code for Gas Turbine Engine Weight and Disk Life Estimation

Michael T. Tong
NASA Glenn Research Center,
21000 Brookpark Road,
Mail Stop 60-7,
Cleveland, OH 44135-3191

Ian Halliwell
Modern Technologies Corporation,
Cleveland, OH

Louis J. Ghosn
Ohio Aerospace Institute,
Brook Park, OH

Reliable engine-weight estimation at the conceptual design stage is critical to the development of new aircraft engines. It helps to identify the best engine concept amongst several candidates. In this paper, the major enhancements to NASA's engine-weight estimate computer code (WATE) are described. These enhancements include the incorporation of improved weight-calculation routines for the compressor and turbine disks using the finite difference technique. Furthermore, the stress distribution for various disk geometries was also incorporated, for a life-prediction module to calculate disk life. A material database, consisting of the material data of most of the commonly used aerospace materials, has also been incorporated into WATE. Collectively, these enhancements provide a more realistic and systematic way to calculate the engine weight. They also provide additional insight into the design tradeoff between engine life and engine weight. To demonstrate the new capabilities, the enhanced WATE code is used to perform an engine weight/life tradeoff assessment on a production aircraft engine.

[DOI: 10.1115/1.1691980]

Introduction

Engine weight is a key design parameter for any new aircraft engine. It affects aircraft range and is a key element in fuel burn. Weight is also considered an indicator of engine cost. Reliable engine-weight estimation at the conceptual design stage is critical to the development of new aircraft engines. It helps to identify the best engine concept amongst several candidates.

Equally important, aircraft engines must meet safety demands. Fatigue loading of turbine components associated with continuous aircraft takeoff/cruise/landing cycles is a principal source of degradation in turbomachinery. A disk burst is potentially the most catastrophic failure possible in an engine and thus disks are designed with overspeed capability and low cycle fatigue life as primary objectives. The requirement for higher turbine stage work without additional stages has resulted in increased turbine blade tip speeds and higher turbine inlet temperatures in advanced commercial aircraft engines. This trend has resulted in significant increases in turbine stage disk rim loading and a more severe thermal environment, thereby making it more difficult to design turbine disks for a specific life requirement meeting current goals. Current trend indicates that both turbine blade tip speeds and turbine inlet temperatures will continue to increase in advanced commercial engines as higher turbine work levels are achieved. Advanced turbine disk concepts are required to insure long life disks in commercial engines, without resulting in severe weight, performance, or cost penalties.

At NASA Glenn Research Center (GRC), the Weight Analysis of Turbine Engines (WATE) computer code [1], originally developed by Boeing Aircraft, is currently used to estimate the engine weight of various conceptual engine designs. The code was originally developed for NASA in 1979, but since then, substantial improvements have been made to the code to improve the weight calculations for most of the engine components. Recently a series of efforts were performed at GRC to enhance the capability of the WATE code. In this paper, these WATE code enhancements are

described. The major enhancements include the incorporation of improved weight-calculation routines for the compressor and turbine disks using the finite difference technique. Furthermore, the stress distribution for various disk geometries was also incorporated, for a life-prediction module to calculate disk life. A material database, consisting of the material data of most of the commonly used aerospace materials, has also been incorporated into WATE. Collectively, these enhancements provide a more realistic and systematic way to calculate the engine weight. They also provide additional insight into the design tradeoff between engine life, weight, and cost. The current effort paves the way for an automated engine design tool, which would easily allow engine developers to perform design tradeoffs between engine performance, durability, and cost. To demonstrate the new capabilities, the improved WATE code is used to perform an engine weight/life tradeoff assessment on a production aircraft engine.

Objective

The objective of the current work is to enhance the current engine flow-path design tool so that it will allow engine developers to easily perform design tradeoffs between engine weight, durability, and eventually, cost.

Turbomachinery Disk Design Methodology

A typical disk design is based on the blading geometry, weight, and rotational speed that will already have been specified in the design of the turbomachinery flowpath. Figure 1 shows how blades are typically attached to a disk, and introduces some of the nomenclature. The typical three disk models (ring, web, and hyperbolic) are shown in Figs. 2–4. The flowpath height or blade span is defined via the blade tip and hub radii, which are primary inputs to the WATE code. The disk rim thickness is assumed to be equal to the axial chord at the hub of the blade. The height of the blade root is also specified within the program, as a percentage of the airfoil height, and it defines the outer limit of the live disk. Note that some allowance must be made for the cavity, since this is not modeled specifically. Moving inwards towards the centerline, additional rim height is then required to support the stresses generated by the dead weight, and this is specified as a function of the rim thickness. Regardless of the disk type, the distribution of thickness for the remainder of the disk is specified initially by

Contributed by the International Gas Turbine Institute (IGTI) of THE AMERICAN SOCIETY OF MECHANICAL ENGINEERS for publication in the ASME JOURNAL OF ENGINEERING FOR GAS TURBINES AND POWER. Paper presented at the International Gas Turbine and Aeroengine Congress and Exhibition, Amsterdam, The Netherlands, June 3–6, 2002; Paper No. 2002-GT-30500. Manuscript received by IGTI, Dec. 2001, final revision, Mar. 2002. Associate Editor: E. Benvenuti.

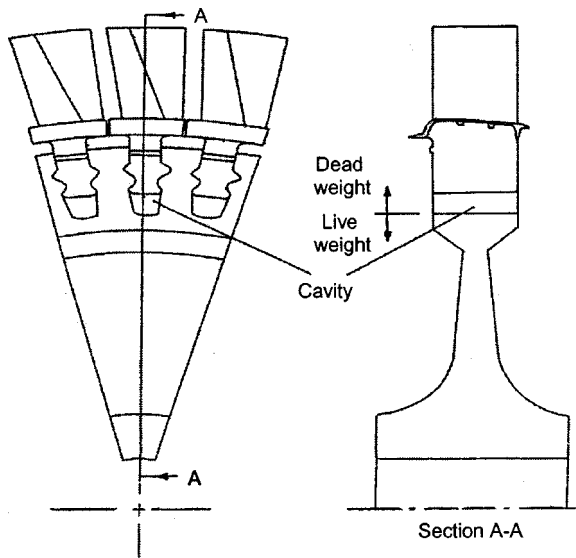
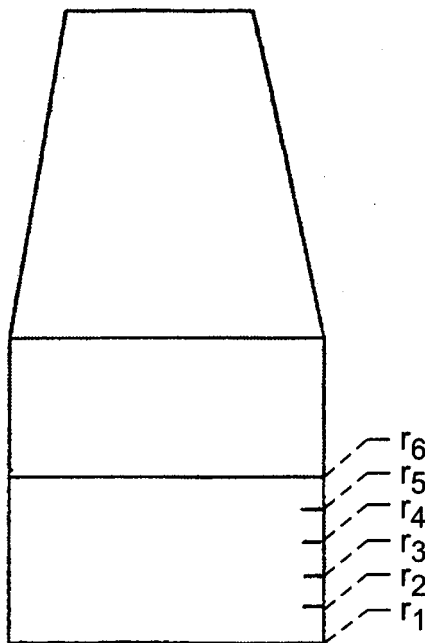


Fig. 1 Disk/blade assembly

minimum default values at key radial locations. Stresses are calculated at these and other radii using a finite difference method, and compared against a design stress that includes a safety margin for a specific material. If the calculated stress is above the design criteria, some disk thickness is increased sequentially in an iterative manner until the stress design criteria are satisfied at all radial stations.

A disk must be designed to withstand the centrifugal stresses generated by the rotating blades at the maximum rotational speed of the spool and to transmit the torque generated by the turbine blading to the appropriate compressor rotor. Only that portion of the disk inboard of the blade root is considered to carry the stresses, and this is referred to as the live disk. The parts of the



$$t_1 = t_2 = t_3 = t_4 = t_5 = t_6$$

Fig. 2 Radial stations and locations of design control calculations in a ring disk

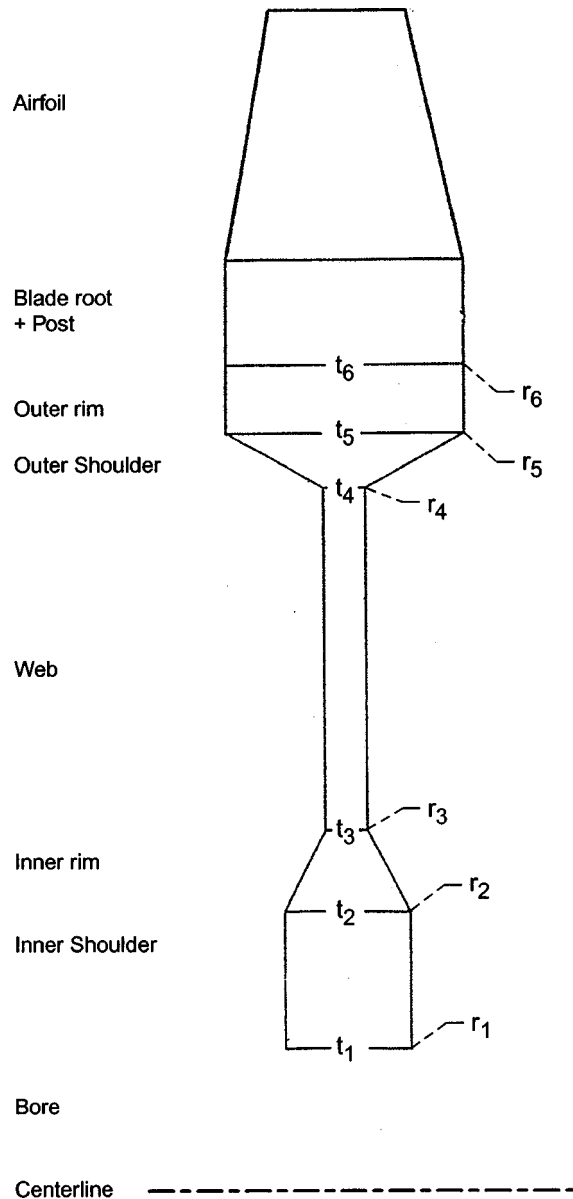


Fig. 3 Radial stations and locations of design control calculations in a web disk

disk between the blade roots (posts), as well as the blade roots themselves and the airfoils, constitute dead weight. Although it is the design of the live disk which is being addressed here, the posts must not be neglected when the total disk weight is quoted. The dead weight produces the pull stresses on the rim of the live disk, but as one moves inwards through the disk towards the bore, the disk must also support an increasing proportion of the centrifugal stress generated by its own weight.

The average stress at the outer radius of the live disk is estimated by smearing the total centrifugal force of the dead weight around the circumference. The weight of the blades, including platforms and roots, and the axial chord at the root should already be known from the flowpath design. The radial location of the center of gravity of the combined dead weight must be known, however, in order to calculate the radial pull stress at the live rim, and consequently certain assumptions are made regarding the height and weight of the blade root, and the weight of the posts. The assumptions are as follows, where the term "total blade" refers to the "airfoil+platform+root."

For the ring disk:

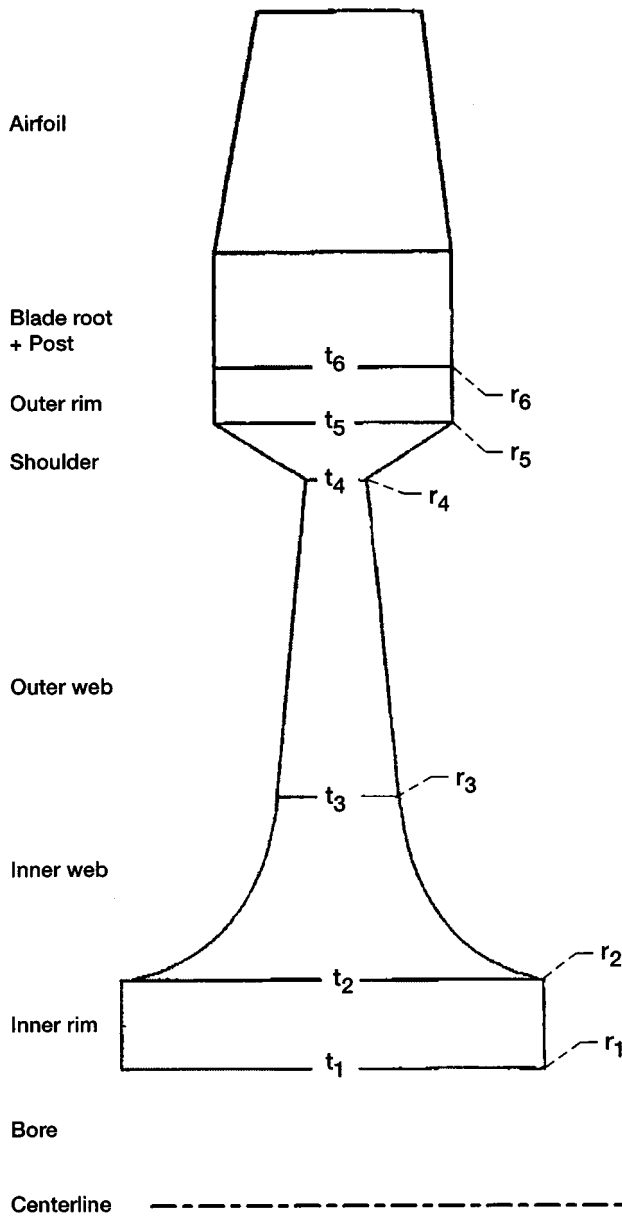


Fig. 4 Radial stations and locations of design control calculations in a hyperbolic disk

height of the blade root=17.65% airfoil height
 weight of the blade root=20% total blade weight
 weight of the post=10% total blade weight

For the web disk:

height of the blade root=25.00% airfoil height
 weight of the blade root=20% total blade weight
 weight of the post=20% total blade weight

For the hyperbolic disk:

height of the blade root=53.85% airfoil height
 weight of the blade root=50% total blade weight
 weight of the post=20% total blade weight

Disk Stress Analysis

The differential equation of equilibrium, [2], takes the form

$$\frac{d}{dr}(tr\sigma_r) - t\sigma_\theta + t\rho\omega^2 r^2 = 0 \quad (1)$$

where

$$\sigma_r = \frac{E}{1-\nu^2} \left[\frac{du}{dr} + \nu \frac{u}{r} - (1+\nu)\alpha T \right] \quad (2)$$

$$\sigma_\theta = \frac{E}{1-\nu^2} \left[\frac{u}{r} + \nu \frac{du}{dr} - (1+\nu)\alpha T \right] \quad (3)$$

The radial steady-state temperature distribution for a disk is given by Fourier's law of conduction from, [3],

$$T = T_{\text{bore}} + \frac{\Delta T}{\ln\left(\frac{r_o}{r_i}\right)} \ln\left(\frac{r}{r_i}\right) - T_0 \quad (4)$$

For a thin slice of disk material, the disk thickness, t , can be approximated by

$$t = mr + n$$

$$m = \text{slope} = \frac{\Delta t}{\Delta r}$$

$$n = t - m \frac{\Delta t}{\Delta r}$$

Substitute Eqs. (2) to (4) and the disk thickness t into Eq. (1) results in a single differential equation with one variable, displacement:

$$\frac{d^2 u}{dr^2} + \left(\frac{2mr+n}{mr^2+nr} - \frac{\nu}{r} \right) \frac{du}{dr} + \left[-\frac{\nu}{r^2} - \frac{1}{r^2} + \frac{\nu}{r} \left(\frac{2mr+n}{mr^2+nr} \right) \right] u$$

$$= \alpha(1+\nu) \left[\frac{dT}{dr} + \left(\frac{2mr+n}{mr^2+nr} - 1 \right) T \right] - \frac{\rho\omega^2(1-\nu^2)}{E} r \quad (5)$$

Equation (5) is solved numerically using finite difference method with boundary conditions:

$$\sigma_r = 0 \quad \text{at } r = r_i; \quad \text{thus, } \frac{du}{dr} + \nu \frac{u}{r} - (1+\nu)\alpha T = 0$$

$$\sigma_r = \text{rimstress} \quad \text{at } r = r_o;$$

$$\text{thus, } \frac{du}{dr} + \nu \frac{u}{r} - \frac{\text{rimstress} \cdot (1-\nu^2)}{E} - (1+\nu)\alpha T = 0$$

rimstress = average centrifugal stress at the live rim

$$= \frac{n_b m_b r_{eg}}{2\pi r_c} \omega^2$$

The design criteria for the disk are

$$\frac{\sigma_y}{sf \cdot \sigma_e} - 1.0 > 0 \quad (\text{design margin}) \quad (6)$$

and

$$\frac{0.47\sigma_{\text{uts}}}{\sigma_{\text{avg}}} - 1.0 > 0 \quad (\text{disk burst criteria}). \quad (7)$$

Disk Design Process

Ring Disk. The ring disk model is shown in Fig. 2. The design process for a ring disk consists of the following steps:

1. The thickness of the disk is set to the blade hub axial chord.
2. The lower limit for the bore radius, r_1 , is calculated, based on the disk radius ratio provided in the input file and the airfoil hub radius. It should be noted that this will probably not be reached.
3. All the six thickness values are set to the value of the disk width in Step 1.

4. The radial extent of the disk from the outer live disk radius inwards is set initially to 0.1 inch.
5. The initial live disk height is divided into five equal sections to obtain radii r_1 through r_6 .
6. The stress calculations are carried out and the design is checked for compliance with the design stress criteria (Eqs. (6) and (7)).
7. If the design criteria are not satisfied at every radial location, the disk inner radius is reduced and Steps 5 and 6 are repeated.
8. If the design criteria are satisfied, disk weight is calculated and the disk design process is completed.
9. If the lower limit on bore radius (established in Step 2) is reached and the design criteria have still not been met, the program prints an appropriate message and stops.

Web Disk. The web disk model is shown in Fig. 3. The design process for a web disk consists of the following steps:

1. The thickness of the disk outer rim is set to the blade hub axial chord.
2. The heights of the inner and outer rims and the inner and outer shoulders are specified by internal default values.
3. Minimum and maximum web and inner rim thickness are set by internal defaults.
4. Definition of the live disk geometry is initiated. The bore radius is fixed via the airfoil hub radius and the input value of disk radius ratio.
5. The six reference radii and thickness are set from the initial disk geometry.
6. The stress calculations are carried out and the design is checked for compliance with the design stress criteria (Eqs. (6) and (7)).
7. If the design criteria are not satisfied at every radial location, the web thickness is held constant and the bore thickness is increased sequentially and Steps 5 and 6 are repeated. If the design criteria remain unsatisfied when the maximum limit on bore thickness is reached, the design process reverts to the minimum bore thickness, but the web thickness is increased, and Steps 4 to 6 are repeated.
8. If the design criteria are satisfied with neither the maximum bore thickness nor the maximum web thickness (established in Step 3) being exceeded, an acceptable web disk design is achieved and its weight is calculated. If the design criteria cannot be met within those limits, the program prints an appropriate message and stops.

Hyperbolic Disk. The hyperbolic disk model is shown in Fig. 4. The design process for a hyperbolic disk consists of the following steps:

1. The width of the disk outer rim is set to the hub axial chord.
2. The initial disk geometry is set up, which consists of the outer rim height, the shoulder height, the minimum outer web thickness, and the inner rim height. The maximum bore width and height are also established.
3. The six reference radii and thickness are set from the initial disk geometry.
4. Using a value of 1.0 for the disk shape factor, dsf , the inner portion of the initial disk geometry is defined, with the inner web thickness distribution being given by

$$\frac{t_4}{(r_4 - r_3)} (r_3 - r)^{dsf}.$$
5. The stress analysis routine is called and comparisons are made with the design stress criteria (Eqs. (6) and (7)) at all the radial locations.
6. If the design criteria are not satisfied, the disk shape factor is increased and Steps 2 to 5 are repeated.
7. If the maximum limit on bore width is encountered before a

satisfactory design is obtained, the value of the outer web thickness is increased, the disk shape factor is reset to 1.0, and Steps 2 to 5 are repeated.

8. If the design criteria are satisfied, disk weight is calculated and the disk design process is completed.
9. A maximum limit for the outer web thickness is defined to be the outer rim thickness. A maximum limit for the disk shape factor is defined such that the inner web thickness does not exceed the bore thickness, which in turn is equal to one third of the live rim radius. If the maximum limits on outer web thickness and disk shape factor are both reached without a satisfactory disk design being achieved, the program prints an appropriate message and stops.

Optimum Disk Design. The code has an option to optimize the disk design. If this option is activated, the code will step through the design of ring, web, and hyperbolic disks sequentially. Provided that disks of each type are possible for the input conditions and geometry, the total weights will be accumulated. If it is not possible to design a disk of a particular type, the program will skip to the next configuration. The disk of minimum weight will finally be selected from the designs that are possible, and the corresponding output files will be generated.

To facilitate the optimization process, a self-adaptive numerical iteration scheme is used to solve Eq. (5). At every iteration, the step size is self-adjusted (increases or decreases) based on the differences in the design margin between the current and previous iterations. The self-adaptive numerical scheme greatly improves the computing efficiency of stress calculations, and enhances the process of disk-design optimization.

Turbine Disk Life Estimation

Using the disk-design methodology described in the previous section, the disks are designed at the sizing point of a flight cycle. The sizing point can be the on-design or an off-design cycle condition. For a new engine design, the flight cycle is based on engineering judgment and input from the airframe manufacturer on its anticipated usage.

The basic mission life of a turbine disk is assumed to be governed by low cycle fatigue crack initiation due to major start-stop cycles. Life is assessed using the maximum strain range or stress range depending upon availability of information. Since any cracking in a disk is not acceptable, fatigue crack initiation is a sufficient criterion for the lifing calculations required herein. The equivalent Von Mises strain or stress ranges at various critical radial locations are calculated and compared with existing experimental fatigue life curves tabulated for the various disk materials. When experimental fatigue results are unavailable, approximations of the fatigue resistance can be obtained with the aid of empirical correlations previously established between fatigue properties and corresponding tensile test properties. One such correlation that has seen widespread use for several decades is the Method of Universal Slopes (MUS) equation proposed by Manson [4] shown below.

$$\Delta \varepsilon_t = \Delta \varepsilon_{el} + \Delta \varepsilon_{in} = \frac{3.5 \sigma_{uts}}{E} (N_f)^{-0.12} + D^{0.6} (N_f)^{-0.60} \quad (8)$$

The MUS equation has been used extensively, for example, in the design of the Space Shuttle main engines, by using a reduction factor of 3 on computed MUS life, [5], i.e., $N_f/3$.

It is recognized that actual disk lives depend upon countless details of a highly localized nature. Since such details cannot be known until a finalized design has been achieved and therefore cannot be accounted for during the earliest stages of design that is of concern herein.

Material Database

A material database, consisting of the material data of most of the commonly-used aerospace materials, has been incorporated

Table 1 Material Database

| | | |
|-------------|-------------|--------------|
| Alloy 713C | Inconel-625 | N-155 |
| Alloy 713LC | Inconel-690 | V-57 |
| B-1900 | Inconel-706 | 4130 steel |
| MAR-M247 | Inconel-718 | 4340 steel |
| IN-100 | Rene 41 | 410 steel |
| MAR-M302 | TD Nickel | 17-4PH steel |
| MAR-M509 | Ti-6Al-4V | Udimet-500 |
| WI-52 | Ti-17 | Udimet-700 |
| Hastelloy-X | Ti-6-2-4-2 | Udimet-710 |
| Hastelloy-S | Haynes-1 88 | Waspaloy |
| Inconel-600 | L-605 | Rene-80 |
| Inconel-601 | Alloy-901 | Rene-95 |
| Inconel-617 | A-286 | |

into WATE. These material data include density, modulus, yield and ultimate strengths, Poison's ratio, as well as some fatigue data. These data were mostly obtained from [6–8]. The list of materials is shown in Table 1.

Other Enhancements of Wate Code

In addition to the disk stress/life methodology and material database, the following capabilities are added to the WATE code:

1. Variation of disk type (ring, web, or hyperbolic) and material with compressor/turbine stages
2. Option to let user specify correlation for tip-speed versus 1st stage pressure ratio for the compressor
3. Option to let user specify component length.

A controlling capability, developed by Boeing Aircrafts, has also been added to the WATE code. This provides an ability to control the position or dimensions of certain components using the inputs provided in WATE. By adding this capability, the time

Table 2 Materials for Turbomachinery Components

| | |
|----------------|------------------------------|
| Fan: | |
| blades | Ti 6-4 |
| disk | Ti 17 |
| disk type | ring |
| LP compressor: | |
| blades | Ti 6-4 |
| disk | Ti 17 |
| disk type | ring |
| HP compressor: | |
| blades | Ti 6-4 (stages 1 to 6) |
| | Inconel-718 (stages 7 to 10) |
| disk | Ti 17 (stages 1 to 6) |
| | Inconel-718 (stages 7 to 10) |
| disk type | ring (stage 1) |
| | web (stages 2 to 10) |
| HP turbine: | |
| blades | Rene-80 |
| disk type | hyperbolic |
| LP turbine: | |
| blades | Rene-80 |
| disk type | web |

to generate a viable flowpath can be greatly reduced, since the need to iterate manually is no longer necessary. A control can be created for all the inputs that would be used to match one component to another.

Application of the Computer Code

An engine sizing and weight estimation was performed on a 300-passenger aircraft engine (similar to a GE-90 engine), based on the thermodynamic parameters generated by an engine cycle analysis. The turbomachinery components and their materials are listed in Table 2.

For the turbine disk materials, three different alloys were assessed and their fatigue lives compared:

| | Engine A | Engine B | Engine C |
|--|-------------|----------|----------|
| HP and LP turbine disks: | Inconel-718 | Rene-95 | Rene-88* |
| The results: | | | |
| Total engine dry wt. (kg): | 7537 | 7461 | 7580 |
| Total engine weight (kg): | 10,182 | 10,105 | 10,226 |
| Total HP and LP disk wt. (kg): | 989 | 900 | 1034 |
| Minimum turbine (HPT) disk life (flight cycles): | 3292 | 6000 | >30,000 |

*Note: based on the limited data published by Huron and Roth [9].

The results show that although Engine C is the heaviest among the three engines, it has the longest turbine disk life. In comparison, the dry weight of a GE-90 engine is 7559 kg, [10]. Typical commercial production engines require 15,000 to 20,000 flight cycles in the hot section components to satisfy customer and manufacturer requirements. The enhanced WATE code provides

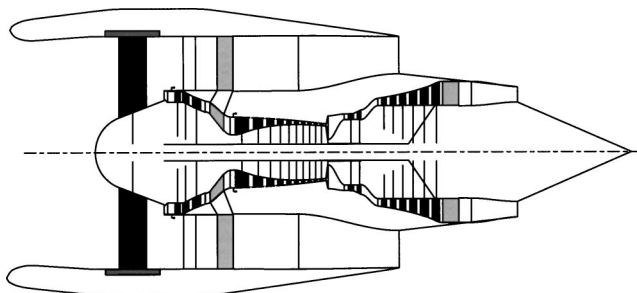


Fig. 5 Flowpath of a 300-passenger aircraft engine

additional insight into the design tradeoff between engine life and engine weight. Flowpath of Engine C is shown in Fig. 5.

Conclusions

The current enhancements, based on material database and structural analysis, is a major improvement over most existing preliminary design codes, which usually either do not consider structural integrity per se, or merely rely on general empirical guidelines. Collectively, these enhancements provide a more realistic and systematic way to estimate the engine size and weight at the preliminary design stage. They also provide additional insight into the design tradeoff between engine life and engine weight. Since materials and weight can affect engine cost, the current effort paves the way for an automated engine design tool, which would allow engine developers to easily perform design tradeoffs between engine performance, durability, and cost.

Acknowledgments

The authors wish to acknowledge the efforts of Dr. Gary R. Halford of NASA Glenn Research Center in providing an insight in the fatigue lifing used in this study.

Nomenclature

D = true tensile ductility= $\ln[(\%RA)/(100-\%RA)]$
 E = modulus of elasticity
 N_f = cycles to fatigue crack initiation failure
 RA = reduction in area at failure
 T_0 = reference temperature=room temperature
 $T_{\text{bore}} = T_{\text{max}} - \Delta T$
 T_{max} = maximum disk metal temperature, assumed to be at the rim; user input
 ΔT = temperature difference between disk rim and bore; user input
 c = axial chord at the blade hub
 n_b = number of blades
 m_b = mass of one blade
 r_{cg} = radius of the c.g. of the dead weight
 r = radial distance
 r_1, r_2, \dots, r_6 = various radial location along the disk
 r_l = outer radius of the live disk
 r_i = inner radius (disk bore)
 r_o = outer radius (disk rim)
 Δr = change in radius
 sf = 1.1, safety factor
 t = local disk thickness at r
 Δt = change in disk thickness
 u = radial displacement
 ρ = disk material density
 ω = rotational speed, (rad/sec)
 α = coefficient of thermal expansion
 ν = Poisson's ratio

σ_y = yield strength of the disk material at the local temperature
 σ_e = equivalent or Von Mises stress
 $\sigma_{\theta\text{avg}}$ = average tangential stress of the disk
 σ_{uts} = ultimate tensile strength
 σ_r = radial stress
 σ_θ = tangential stress
 $\Delta \epsilon_r$ = total strain range
 $\Delta \epsilon_{el}$ = elastic strain range
 $\Delta \epsilon_{in}$ = inelastic strain range

References

- [1] Onat, E., and Klees, G. W., 1979, "A Method to Estimate Weight and Dimensions of Large and Small Gas Turbine Engines," NASA CR-159481.
- [2] Ugural, A. C., and Fenster, S. K., 1987, *Advanced Strength and Applied Elasticity*, Second Ed., Elsevier, New York.
- [3] Holman, J. P., 1990, *Heat Transfer*, Seventh Ed., McGraw-Hill, New York.
- [4] Manson, S. S., 1965, "Fatigue: A Complex Subject—Some Simple Approximations, Experimental Mechanics," *Exp. Mech.*, **5**(7), pp. 193–226.
- [5] Newell, J. F., 1994, "A Note of Appreciation for the MUS," *Material Durability/Life Prediction Modeling: Materials for the 21st Century*, PVP-290, ASME, New York, pp. 57–58.
- [6] Gibson, C., ed., 1998, *Aerospace Structural Metals Handbook*, Vols 4 and 5, CINDAS/USAF/CRDA Handbooks Operation, Purdue University, West Lafayette, IN.
- [7] Boyer, R., et al., 1994, *Materials Properties Handbook—Titanium Alloys*, ASM International, Materials Park, OH, Sections III and IV.
- [8] ASM Handbook Committee, 1990, *Metals Handbook*, 10th Ed., Vols. 1 and 2, ASM International, Materials Park, OH.
- [9] Huron, E. S., and Roth, P. G., 1996, "The Influence of Inclusions of Low Cycle Fatigue Life in a P/M Nickel-Base Disk Superalloy," *Superalloys 1996*, R. D. Kissinger et al., eds., TMS, Warrendale, PA, pp. 359–368.
- [10] Gunston, B., ed., 2000, "General Electric GE90," *Jane's Aero-Engines*, Jane's Information Group Ltd., Surrey, UK, Issue 8, p. 430.

V. Bellucci

e-mail: valter.bellucci@power.alstom.com

P. Flohr

e-mail: peter.flohr@power.alstom.com

ALSTOM (Switzerland) Ltd.,
Im Segelhof 1,
CH-5405 Baden-Dättwil, Switzerland

C. O. Paschereit

Technical University of Berlin, D-10623 Berlin,
Germany
e-mail: oliver.paschereit@tu-berlin.de

F. Magni

ALSTOM (Switzerland) Ltd.,
Haselstrasse 16,
CH-5401 Baden, Switzerland
e-mail: fulvio.magni@power.alstom.com

On the Use of Helmholtz Resonators for Damping Acoustic Pulsations in Industrial Gas Turbines

In this work, the application of Helmholtz resonators for damping low-frequency pulsations in gas turbine combustion chambers is discussed. We present a nonlinear model for predicting the acoustic response of resonators including the effect of purging air. Atmospheric experiments are used to validate the model, which is employed to design a resonator arrangement for damping low-frequency pulsations in an ALSTOM GT11N2 gas turbine. The predicted damper impedances are used as the boundary condition in the three-dimensional analysis of the combustion chamber. The suggested arrangement leads to a significant extension of the low-pulsation operating regime of the engine.

[DOI: 10.1115/1.1473152]

Introduction

In modern gas turbines operating with premixed combustion flames, the suppression of pressure pulsations is an important task related to the quality of the combustion process and to the structural integrity of engines. High pressure pulsations may occur when the resonance frequencies of the system are excited by heat release fluctuations independent of the acoustic field (“loud-speaker” behavior of the flame). Heat release fluctuations are also generated by acoustic fluctuations in the premixed stream. The feedback mechanism inherent in such processes (“amplifier” behavior of the flame) may lead to combustion instabilities, the amplitude of pulsations being limited only by nonlinearities. Thus, the suppression of pressure pulsations is an important task which may be addressed by means of passive control methods like the use of Helmholtz resonators.

A one-throat Helmholtz resonator consists of a cavity with a neck through which the fluid inside the resonator communicates with an external medium (Fig. 1). When a Helmholtz resonator is applied to an enclosure, in correspondence of the neck mouth a frequency-dependent boundary is realized. Helmholtz [1] developed a theory to predict the neck mouth impedance $Z(\omega)$, i.e., the ratio in the frequency domain between acoustic pressure and acoustic velocity normal to the neck mouth. When the neck is short and narrow with respect to the wavelength (low-frequency range), all the fluid particles in the neck are assumed to fluctuate with the same acoustic speed (“harmonic oscillator” model). The inertia of the fluid fluctuating under the effect of the acoustic field and the compressibility of the fluid inside the resonator cavity are both represented by the reactance X . The resistance R is related to dissipative processes occurring inside the neck, i.e., the viscous acoustic damping and the conversion of acoustic energy into shedding of vortices generated at the rims of the neck ends (the vortices being convected downstream and dissipated into heat by turbulence).

Helmholtz resonators are coupled to enclosures in order to reduce pressure pulsations. The mechanism responsible for the

damping is mathematically analyzed by replacing the boundary A_n of the enclosure with a wall of impedance Z . To study the characteristics of the wall uncoupled from the enclosure, one can consider a plane wave of frequency ω incident on the wall under anechoic conditions for the reflected wave ([2]). This analysis shows that for a given frequency and pressure amplitude in front of the resonator, the maximum acoustic power absorption is achieved for $X=0$ (the condition $X=0$ is satisfied at the resonator resonance frequency ω_r).

When the resonator is coupled to the enclosure, sound reflection from the enclosure boundary must be considered. The effect of the damper on the resonance frequency ω_N of the enclosure without resonator has been studied by several authors ([3,4]). The analysis has been performed under the following assumptions: acoustically compact (point-impedance) resonator; harmonic oscillator model for the damper; ω_N in the low frequency range where the average separation between eigenfrequencies is much larger than the average modal bandwidth; sound generation by means of point sources located inside the enclosure. The pressure amplitude field of the coupled system has been compared to that of the enclosure without the resonator. At the frequency ω_N , amplitude reduction occurs when $\omega_r = \omega_N$ due to the sound cancelation performed by the neck mouth (seen as a “pseudo-source”) on the acoustic field produced by the sound source inside the enclosure. In particular, when $|Z| \ll 1$ the pressure on the neck mouth is small and the “pseudo-source” velocity is tuned to cancel the pressure produced by the sound source inside the enclosure. The analysis also shows that if the excitation is not confined to ω_N , amplitude maxima may occur for frequencies close to ω_N . In the frequency range including the new maxima and for a given damping coefficient of the enclosure, the sound reduction may be maximized by appropriately tuning the resonator damping. Note that the resonator

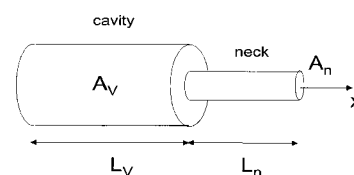


Fig. 1 Helmholtz resonator

Contributed by the International Gas Turbine Institute (IGTI) of THE AMERICAN SOCIETY OF MECHANICAL ENGINEERS for publication in the ASME JOURNAL OF ENGINEERING FOR GAS TURBINES AND POWER. Paper presented at the International Gas Turbine and Aeroengine Congress and Exhibition, New Orleans, LA, June 4–7, 2001; Paper 01-GT-039. Manuscript received by IGTI, December 2000, final revision, March 2001. Associate Editor: R. Natole.

damping which gives the maximum reduction in pressure amplitude does not coincide with the damping of the maximum power absorption (in fact the acoustic power injected by the source into the enclosure is a function of the resonator impedance).

For combustion applications, dampers modeled as harmonic oscillators have been coupled to the oscillator represented by the mass of fluid in the fuel/air mixing nozzle ([5]). The air in the combustor provided the compliance (equivalent spring in the mechanical analogy) for the oscillators. A negative combustor damping accounted for the amplification behavior of the flame. The optimum damping of eigenmodes was again obtained with a resonance frequency of resonators aligned with the natural frequency of the uncoupled combustor and nozzle system.

According to the above considerations, when a Helmholtz resonator is applied to a combustion chamber, ω_r must be tuned to the frequency to be damped in the combustor. Furthermore, an accurate prediction of viscous and pressure loss effects is fundamental for the correct evaluation of absorbed power and impedance. Such modeling must include the effect of the mean flow permanently purging the resonator in order to avoid overheating. Once the damper has been designed, its impedance applied to the enclosure permits to simulate the pressure field in the system for a given excitation.

In this work, a nonlinear resonator model including mean flow effects is presented. The model is calibrated using experiments under atmospheric conditions and is used to design a resonator arrangement for suppressing a low-frequency peak occurring in an ALSTOM GT11N2 gas turbine. A three-dimensional acoustic analysis of the combustor is performed in order to establish the location of resonators according to the shape of the mode to be suppressed and to compute the pressure spectrum by using the predicted resonator impedances as a boundary condition for the combustor. The pressure spectrum so predicted indicates a good acoustic attenuation and suggests the implementation of the resonator arrangement to the engine. Finally, the spectrum is measured in the gas turbine combustor and compared with the predicted one.

Helmholtz Resonator Model

A schematic of a purged resonator for gas turbine combustion chambers is shown in Fig. 2. The purging air is supplied from the gas turbine plenum and enters the resonator through the inlet tube (two-throat resonator). The neck mouth communicates directly with the combustion chamber. In the Helmholtz model ([1]), the resonator impedance is expressed as

$$Z = -\hat{p}_f / \hat{u}_n = R + iX, \quad (1)$$

where R accounts for internal losses and

$$X = \omega \rho L_n - \frac{\rho c^2 A_n}{\omega V}. \quad (2)$$

The resonance frequency (i.e., the frequency for which $X=0$) is given by

$$\omega_r = c \sqrt{\frac{A_n}{VL_n}}. \quad (3)$$

In the following, a nonlinear model for R is developed.

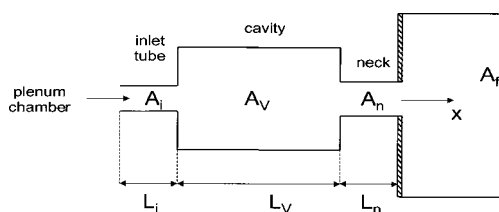


Fig. 2 Combustor damper

Neck and Inlet Tube. The flow in the neck and in the inlet tube may be assumed incompressible when the dimensions of the duct are small with respect to the wavelengths of interest ([2]). For the incompressible flow in a duct, the continuity and momentum equations integrated between the end sections 1 and 2 read, respectively, ([6]),

$$u_1 = u_2 = u, \quad (4)$$

$$L \frac{\partial u}{\partial t} + \frac{p_2 - p_1}{\rho} = - \left(\zeta_{\text{vis}} u + \frac{1}{2} \zeta_{\text{ac}} u |u| \right). \quad (5)$$

The viscous effects inside the duct are represented by the coefficient ζ_{vis} . The coefficient ζ_{ac} accounts for pressure losses occurring at duct ends because of area changes. In particular, for high Reynolds numbers one has ([7])

$$\zeta_{\text{ac}} = \begin{cases} (1 - A^-/A^+)^2 + (A^-/A^+)^2 \text{ sign}(u) & \text{for expansions,} \\ \frac{1}{2} (1 - A^+/A^-) - (A^+/A^-)^2 \text{ sign}(u) & \text{for contractions.} \end{cases} \quad (6)$$

Hence, the value of ζ_{ac} changes according to the sign of the velocity.

However, not only the fluid in the duct but also part of the fluid in the communicating volumes (e.g., outside the damper and inside the resonator cavity) participates in acoustic fluctuations. For long wavelengths, the air at the duct end may be modeled as a zero-mass solid piston fluctuating and then radiating acoustic energy outside the duct. For a tube terminating in a half-space (infinite flange) with $kD \ll 1$, the radiation reactance can be included by replacing the tube length with the "effective" length $l = L + 0.5D\Delta$, where ([2])

$$\Delta = \frac{8}{3\pi}. \quad (7)$$

An end-correction is applied at both ends of the duct and then in Eq. (5) the duct length L must be replaced by the effective length $l = L + D\Delta$. More accurate end-correction models include the effects due to: frequency dependency when kD is sufficiently large ([2]); detailed geometry of resonator cavity and neck flange ([8]); acoustic and bias flow velocity through the neck ([9]); wave propagation inside the cavity ([10]). In particular, when the wave propagation in the cavity is also modeled, Eq. (3) is valid for

$$A_v/A_n \geq 16V/(\lambda A_n). \quad (8)$$

By introducing the acoustic pressure perturbations $p' = p - \bar{p}$ and velocity perturbations $u' = u - \bar{u}$ in Eqs. (4) and (5) and subtracting the mean flow equations, one has

$$u'_1 = u'_2 = u', \quad (9)$$

$$l \frac{\partial u'}{\partial t} + \frac{p'_2 - p'_1}{\rho} + (\zeta_{\text{vis}} u)' + \Phi = 0. \quad (10)$$

The nonlinear pressure loss term is expressed as

$$\Phi = \frac{1}{2} \zeta_{\text{ac}} [(\bar{u} + u') | \bar{u} + u' | - \bar{u} | \bar{u} |], \quad (11)$$

where for simplicity we have assumed the same area jump at the neck ends. Equation (10) may be solved in the frequency domain. It writes

$$i \omega l \hat{u} + \frac{\hat{p}_2 - \hat{p}_1}{\rho} + (\widehat{\zeta_{\text{vis}} u}) + \hat{\Phi} = 0, \quad (12)$$

where the frequency domain viscous term is expressed as ([11])

$$(\widehat{\zeta_{\text{vis}} u}) = (1+i) \frac{L}{D} \sqrt{2\nu\omega} \left(1 + \frac{\gamma-1}{Pr^{1/2}} \right) \hat{u}. \quad (13)$$

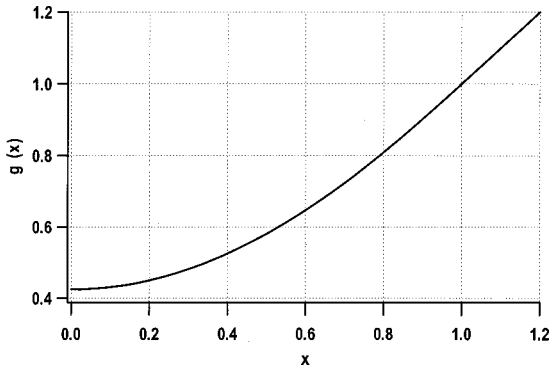


Fig. 3 $g(x)$ -function of nonlinear pressure loss

Equation (12) may be solved after the Laplace transform $\hat{\Phi}$ is obtained.

Nonlinear Pressure Loss Term. When $\bar{u} > 0$ and $|u'| < \bar{u}$, Eq. (11) reads at the first order $\Phi_{\text{lin}} = \zeta_{ac} \bar{u} u'$ and then

$$\hat{\Phi}_{\text{lin}} = \zeta_{ac} \bar{u} \hat{u}. \quad (14)$$

Equation (14) is valid within the linear acoustic assumption and leads to no pressure loss contribution without mean flow. However, for large u' (i.e., close to resonance) velocity perturbations may become of the same order of magnitude of \bar{u} and a nonlinear behavior of pressure losses arises. An analytic expression for nonlinear pressure losses is found in the frequency domain by differentiating Eq. (11) with respect to time ([12]). One has

$$\frac{\partial \Phi}{\partial t} = \zeta_{ac} |\bar{u} + u'| \frac{\partial u'}{\partial t}, \quad (15)$$

whose fundamental harmonic is given by

$$\hat{\Phi} = \zeta_{ac} g(\bar{u}/|\hat{u}|) |\hat{u}| \hat{u}, \quad (16)$$

where

$$g(x) = \begin{cases} \frac{2}{\pi} \left[x \arcsin(x) + \frac{\sqrt{1-x^2}}{3} (2+x^2) \right] & \text{if } x < 1, \\ x & \text{if } x > 1. \end{cases}$$

Figure 3 shows that without mean flow or for small $\bar{u}/|\hat{u}|$, linear pressure losses predict a smaller pressure loss term and then a larger $|\hat{u}|$.

Resonator Cavity. When in the resonator cavity Eq. (8) is satisfied, acoustic propagation may be neglected and isentropic transformations may be assumed. Then, $p_V V^\gamma = \text{const}$ and $p'_V = -\rho c^2 V'/V$ where the expression $\gamma \bar{p} = \rho c^2$ has been used and where the volume fluctuation is given by $V' = A_n x_n - A_i x_i$. By transforming to the frequency domain, the following relation is obtained:

$$\hat{p}_V = -i \frac{\rho c^2}{\omega V} (\hat{u}_i A_i - \hat{u}_n A_n). \quad (17)$$

Resonator Impedance and Power Absorption. When the end of the inlet tube on the plenum side is assumed to be an open boundary (zero acoustic pressure), the resonator model is completely described by Eq. (17) and by Eq. (12) written for the inlet duct and the neck. These three equations form a nonlinear system. The system with unknowns \hat{u}_i , \hat{u}_n , and \hat{p}_V is numerically solved for a certain value of \hat{p}_f . Due to the nonlinearity, Z is a function of \hat{p}_f .

When tuning the resonator decoupled from the combustor, the “relative attenuation” may be used to represent the resonator efficiency. The relative attenuation is defined as

$$a = W_f / W_{\text{ref}} \quad (18)$$

where W_f is the energy flux in the neck mouth and W_{ref} is the energy flux of a running plane wave which produces a pressure amplitude \hat{p}_f upon reflection at the rigid end A_f . The energy flux in the neck mouth is given by

$$W_f = \frac{1}{2} \Re(\hat{u}_n^* \hat{p}_f) A_n = \frac{1}{2} \Re(Z^{-1}) |\hat{p}_f|^2 A_n, \quad (19)$$

where

$$\Re(Z^{-1}) = \frac{R}{R^2 + X^2}. \quad (20)$$

The normalization power is

$$W_{\text{ref}} = \frac{1}{8} \frac{|\hat{p}_f|^2}{\rho c} A_f. \quad (21)$$

In both W_f and W_{ref} , the mean flow effects are neglected since by the Mach number is assumed to be small. The effect of ζ is to reduce \hat{u} and then to decrease the power absorption, as shown by Eq. (19). Thus, to maximize the relative attenuation is important to keep the pressure loss coefficients as small as possible.

Atmospheric Experiments on Resonators

The model presented in the above section is compared to experiments performed under atmospheric conditions. In the experiments, the combustion chamber was simulated by a cylindrical tube equipped with a loudspeaker at one end and with a Helmholtz resonator at the opposite end (Fig. 4). The tube cross section corresponds to the area of the flange the resonator is mounted on. The resonator was connected to a plenum which supplies the purging air. Three different experiments were performed: In Case A neither the inlet tube nor purging air are used; in Case B the inlet tube is added; in Case C purging air is also employed. In all tests, an average value of \hat{p}_f was used.

The relative attenuation was obtained by measuring the reflection coefficient at the resonator neck. In fact, the reflection coefficient is related to the impedance by

$$Z = \rho c \frac{1+r}{1-r}, \quad (22)$$

which substituted in Eq. (19) gives

$$W_f = \frac{1}{2} \Re \left(\frac{1-r}{1+r} \right) \frac{|\hat{p}_f|^2}{\rho c} A_n. \quad (23)$$

The experimental results are shown in Table 1, where the damper

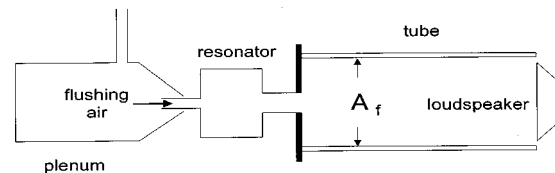


Fig. 4 Experimental setup

Table 1 Resonator experiments

| | Case A | Case B | Case C |
|------------------|--------|--------|--------|
| f_r [Hz] | 210 | 218 | 220 |
| a_{max} | 1.36 | 1.23 | 0.61 |

Table 2 Resonator model data

| | Case A | Case B | Case C |
|------------------|--------|--------|--------|
| $\Delta/2$ | 1.2 | 1.2 | 0.89 |
| $(\zeta_{ac})_n$ | 1.5 | 1.6 | 4.2 |
| $(\zeta_{ac})_i$ | - | 1.6 | 4.2 |

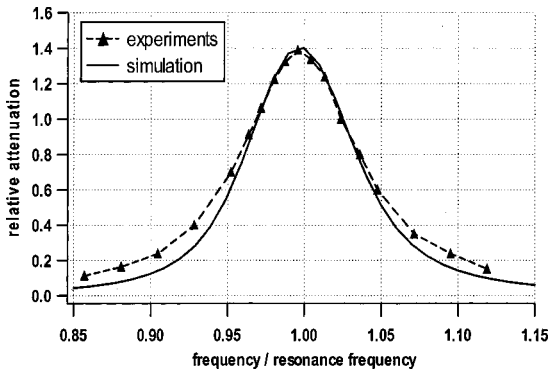


Fig. 5 Relative attenuation for Case A

resonance frequency f_r is that corresponding to the maximum relative attenuation a_{max} . The value of a_{max} in Case B is lower than in Case A, due to the reduction in \hat{u}_n related to the additional losses introduced by the presence of the inlet tube. The measured relative attenuation decreases significantly for Case C, due to mean flow effects.

The experimental resonance frequency and maximum relative attenuation are used to calibrate, respectively, the end-corrections $\Delta = \Delta_n = \Delta_i$ and the pressure loss coefficients presented in Table 2. For Case A, the experimental and computed relative attenuation values reported in Fig. 5 are in good agreement. The deviation of the model prediction from experiments for frequencies away from resonance is probably due to a frequency dependent behavior of ζ_{ac} . The end-corrections for Cases A and B have a value greater than $\Delta/2 = 0.85$ predicted by Eq. (7), being a possible explanation for the use of a constant average value \hat{p}_f instead of its frequency-dependent value related to the acoustic response of the test rig. Case C shows the end-correction decrease caused by the introduction of purging air ([9]). For Cases A and B, the values of pressure loss coefficients are consistent with $\zeta_{ac} = 1.5$ obtained from Eqs. (6). In Case C, the ζ_{ac} coefficients are a factor 2.8 greater than the values in the other two cases, a possible reason being the asymmetry of the flow.

Resonators Coupled to Combustor

The resonator model illustrated above is applied to the silo combustion chamber of an ALSTOM GT11N2 gas turbine. In the engine, pulsations occur at $St = 0.6$. An acoustic analysis of the combustion chamber is performed using the three-dimensional solver SYSNOISE [13]. The modal analysis performed neglecting mean flow effects and with a uniform temperature field gives a $St = 0.6$ acoustic mode characterized by a constant modal value in the silo (Fig. 6). In order to reduce the $St = 0.6$ peak, Helmholtz dampers tuned at the same frequency are designed using the non-linear model. No tuning of the resonator damping is done in order to maximize the pressure amplitude suppression. In the absence of direct experiments, the mouth impedance is computed using the end-correction of Eq. (7) and the pressure losses of Case C ($(\zeta_{ac})_n = (\zeta_{ac})_i = 4.2$). The resonators impedances are applied on the top of the silo. According to mechanical constraints, seven resonator are employed. The position of the dampers does not influence the sound reduction at $St = 0.6$, being the modal value constant on the top of the silo (Fig. 6).

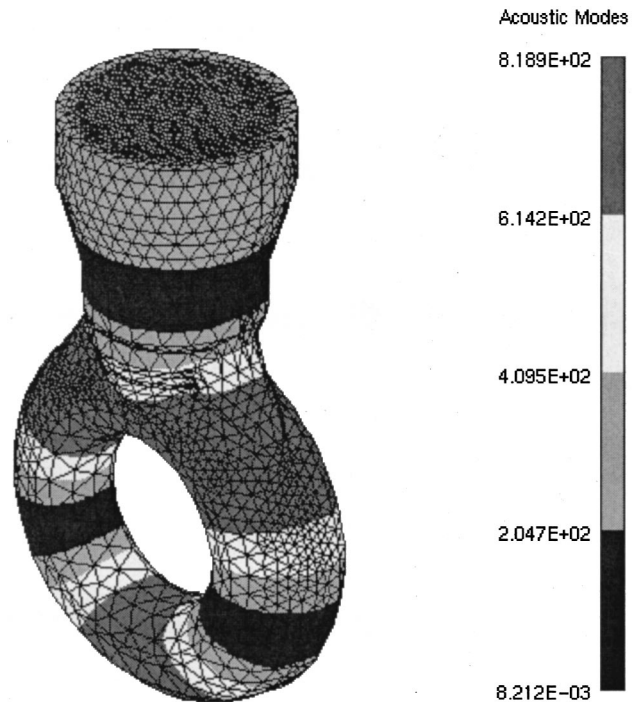


Fig. 6 Combustor eigenmode at $St = 0.6$

In order to compute the acoustic damping induced by the resonators, the frequency analysis of the combustion chamber is also performed. The excitation of the $St = 0.6$ mode may be due to the loudspeaker behavior of the flame or to a combustion instability where the mode has a time-growing amplitude saturated by nonlinearities ([14]). The pressure spectrum measured without dampers is then used to calibrate a sound source on the top of the silo. Figure 7 shows the calibration results for the spectrum normalized with the $St = 0.6$ peak amplitude. Far from $St = 0.6$, the agreement between measured and simulated spectra decreases due to the difficulty to model correctly the sound source over a wide frequency range.

A frequency analysis of the combustor with resonators is then performed using the same excitation of the case without resonators. The computed spectrum of Fig. 8 shows an amplitude reduction of 41% and suggested the use of the designed arrangement of dampers in the engine. The spectrum measured after the application of the designed arrangement of dampers in the engine is also reported in Fig. 8 and indicates a pressure damping of 53%. The

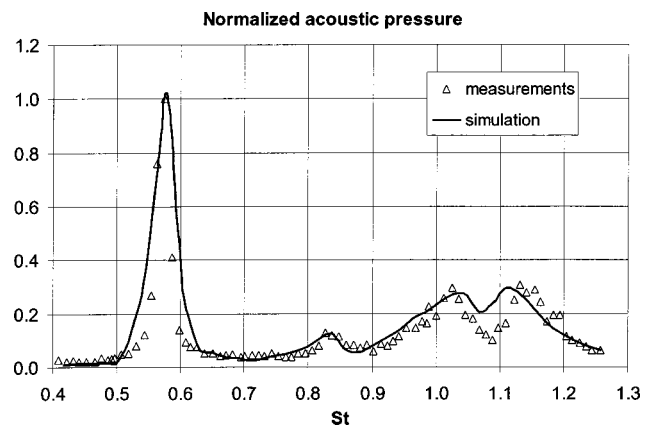


Fig. 7 Measured versus computed pressure spectrum without resonators

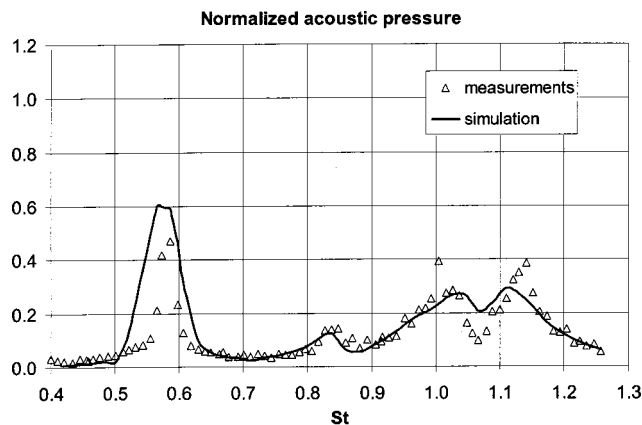


Fig. 8 Measured versus computed pressure spectrum with resonators

discrepancy between the computed and measured relative attenuation may be due to the resonator model (not directly calibrated on the employed dampers) and to the purging air flow that modifies the fluid dynamics and then the thermoacoustics of the system.

Conclusions

A model is presented to predict the acoustic response of two-throat resonators employed to damp pulsations in gas turbine combustion chambers. In order to accurately predict the resonator impedance and the acoustic power absorption, the model accounts for the purging air through the resonator and for the nonlinearity arising from the pressure loss term. Atmospheric experiments are used to calibrate the model, using the experimental resonance frequency and the maximum acoustic attenuation to define end-corrections and internal losses of the damper. The attenuation factor shows good agreement with experiments when nonlinear losses are included. The model reduces to the linear one when the acoustic velocity is smaller than the mean flow velocity. However, close to resonance, the nonlinear term is found to produce a significant increase of the pressure loss and then a decrease of the acoustic attenuation with respect to the linear model.

The nonlinear model is applied to resonators developed to suppress low-frequency pulsations in an ALSTOM GT11N2 gas turbine. The three-dimensional modal analysis of the combustion chamber is used to define the location of the dampers and the frequency analysis is performed in order to simulate the attenuation produced by resonators. The resonator arrangement so designed is implemented in the engine leading to an enhancement of the low-pulsation operating regime of the gas turbine.

Nomenclature

- $\overline{(\cdot)}$ = mean flow quantities
- $(\cdot)'$ = acoustic perturbations
- $(\hat{\cdot})$ = Laplace transform of acoustic perturbations
- a = relative attenuation
- A = cross-sectional area of resonator ducts
- c = speed of sound
- D = cross-sectional diameter
- f = frequency

- k = wave number ω/c
- l = effective length of resonator ducts
- L = length of resonator ducts
- p = pressure
- Pr = Prandtl number
- r = reflection coefficient
- R = resonator mouth resistance
- \Re = real part
- St = Strouhal number
- u = velocity
- V = volume of the resonator cavity
- W = acoustic energy flux
- x = coordinate of resonator axis
- X = resonator mouth reactance
- Z = resonator mouth impedance $= R + iX$
- γ = specific heat ratio
- Δ = end-correction
- ζ = pressure loss coefficient
- ζ_{ac} = area change loss coefficient
- ζ_{vis} = viscous loss coefficient
- λ = wavelength c/f
- ν = kinematic viscosity
- ρ = density
- Φ = pressure loss term
- ω = circular frequency $2\pi f$

Subscripts

- 1 = upstream duct section
- 2 = downstream duct section
- f = resonator flange
- i = resonator inlet tube
- n = resonator neck
- r = resonance quantities
- V = resonator cavity

References

- [1] von Helmholtz, H., 1860, *Theorie der Luftschwingungen in Rohren mit offenen Enden*, Crelle.
- [2] Morse, P. M., and Ingard, K., 1968, *Theoretical Acoustics*, McGraw-Hill, New York.
- [3] Fahy, F. J., and Schofield, C., 1980, "A Note on the Interaction Between a Helmholtz Resonator and an Acoustic Mode of an Enclosure," *J. Sound Vib.*, **72**, pp. 365–378.
- [4] Cummings, A., 1992, "The Effects of a Resonator Array on the Sound Field in a Cavity," *J. Sound Vib.*, **154**, pp. 25–44.
- [5] Gysling, D. L., Copeland, G. S., McCormick, D. C., and Proscia, W. M., 2000, "Combustion System Damping Augmentation With Helmholtz Resonators," *ASME J. Eng. Gas Turbines Power*, **122**, pp. 269–274.
- [6] Munjal, M. L., 1987, *Acoustics of Ducts and Mufflers*, John Wiley and Sons, Canada.
- [7] Batchelor, G. K., 1967, *An Introduction to Fluid Dynamics*, Cambridge University Press, Cambridge, UK.
- [8] Chanaud, R. C., 1994, "Effect of Geometry on the Resonance Frequency of Helmholtz Resonators," *J. Sound Vib.*, **178**, pp. 337–348.
- [9] Peters, M. C. A. M., Hirschberg, A., Reijnen, A. J., and Wijnands, A. P. J., 1993, "Damping and Reflection Coefficient Measurements for an Open Pipe at Low Mach and Low Helmholtz Numbers," *J. Fluid Mech.*, **256**, pp. 499–534.
- [10] Panton, R. L., and Miller, J. M., 1975, "Resonant Frequencies of Cylindrical Helmholtz Resonator," *J. Acoust. Soc. Am.*, **57**, pp. 1533–1535.
- [11] Kirchhoff, G., 1868, "Ueber den Einfluss der Wärmeleitung in einem Gase auf die Schallbewegung," *Poggendorfer Annalen*, **134**, pp. 177–193.
- [12] Keller, J. J., 1981, "Propagation of Simple Nonlinear Waves in Gas-Filled Tubes with Friction," *Z. Angew. Math. Phys.*, **32**, pp. 170–181.
- [13] LMS International, 1999, *SYSNOISE 5.4 Documentation*, Version 1.0, Brussels.
- [14] Culick, F. E., 1994, "Some Recent Results of Nonlinear Acoustics in Combustion Chambers," *AIAA J.*, **32**, pp. 146–169.

Flashback in a Swirl Burner With Cylindrical Premixing Zone

J. Fritz
M. Kröner¹
T. Sattelmayer

Lehrstuhl für Thermodynamik,
Technische Universität München,
85748 Garching, Germany

Flame flashback from the combustion chamber into the mixing zone is one of the inherent problems of lean premixed combustion and essentially determines the reliability of low NO_x burners. Generally, flashback can be initiated by one of the following four phenomena: flashback due to the conditions in the boundary layer, flashback due to turbulent flame propagation in the core flow, flashback induced by combustion instabilities and flashback caused by combustion induced vortex breakdown. In this study, flashback in a swirling tubular flow was investigated. In order to draw maximum benefit from the tests with respect to the application in gas turbines, the radial distribution of the axial and circumferential momentum in the tube was selected such that the typical character of a flow in mixing zones of premix burners without centerbody was obtained. A single burner test rig has been designed to provoke flashback with the preheating temperature, the equivalence ratio and the mean flow rate being the influencing parameters. The flame position within the mixing section is detected by a special optical flame sensor array, which allows the control of the experiment and furthermore the triggering of the measurement techniques. The burning velocity of the fuel has been varied by using natural gas or hydrogen. The characteristics of the flashback, the unsteady swirling flow during the flame propagation, the flame dynamics and the reaction zones have been investigated by applying high-speed video recordings, the laser Doppler anemometry and the laser induced fluorescence. The presented results show that a combustion induced vortex breakdown is the dominating mechanism of the observed flashback. This mechanism is very sensitive to the momentum distribution in the vortex core. By adding axial momentum around the mixing tube axis, the circumferential velocity gradient is reduced and flashback can be prevented. [DOI: 10.1115/1.1473155]

Flashback in Premixed Combustion Systems

In order to achieve low NO_x emissions, the lean premixed combustion is often used in stationary gas turbines. Because of their excellent flameholding, burnout and emission characteristics swirling flames are almost exclusively used in gas turbine combustion systems. The superior performance of swirling flames stems from the high turbulence level in the mixing zone and the generation of a radial pressure gradient in the burner exit, which leads to a stable recirculation zone with strong backflow of hot gases. Since both effects depend upon the swirl intensity, gas turbine burners are usually high swirl designs. An important upper limit for the aerodynamic design of the swirl generator is given by the transition of the vortex breakdown from the combustion chamber into the burner with the formation of recirculation zones in the mixing chamber. According to the usual design practice, the swirl number and the radial swirl distribution is selected such that for the nonreacting flow a sufficient margin against the propagation of the vortex breakdown in the core flow into the burner is obtained. The feedback of the chemical reaction on the flow field is usually not considered in the basic aerodynamic phase of the design procedure.

First of all, the reliability of swirl burners is determined by its capability to prevent flashback in normal operation. In addition, fail safe designs must be able to recover from flashback without damage due to thermal overheating. To date, a detailed understanding of the governing mechanisms for flashback in turbulent swirling flows has not been established, although the precise description of

the limits is a prerequisite for the design of reliable premix burners operating under severe pressure and temperature.

In general, four flashback causes can be distinguished:

- flashback in the boundary layer,
- turbulent flame propagation in the core flow,
- flashback due to combustion instabilities, and
- combustion induced vortex breakdown.

Flashback in the Boundary Layer. Low flow velocities in the boundary layer promote the upstream flame propagation whereas the heat loss to the wall can cause flame quenching. For laminar flows, Lewis and von Elbe [1] balance the velocity gradient g at the wall with the laminar flame speed S_L divided by the quenching distance d_q as the flashback criterion.

$$g = - \left. \frac{\partial u}{\partial r} \right|_R = \frac{S_L}{d_q} \quad (1)$$

According to Eq. (1) a critical velocity gradient $g < S_L/d_q$ leads to upstream flame propagation near the wall. In order to generalize the experimental results, a dimensionless relation was proposed as a flashback criterion ([2]). In this framework, the balance of the downstream convective transport and the upstream flame propagation with heat loss to the wall is expressed in terms of Peclet numbers. The velocity gradient is replaced by an average velocity and a characteristic length scale. Although the theories can also be formally applied to turbulent boundary layers, it is known that the same criteria do not apply in the turbulent case. The critical velocity gradient is much higher than the laminar one ([3]), since the axial turbulent diffusion above the laminar sublayer increases the flame speed.

This type of flashback is often predominant in nonswirling low-turbulence flows.

Turbulent Flame Propagation in the Core Flow. If the turbulent burning velocity exceeds the local flow velocity in the core

¹Current address: THERMOTEL, EEngineering Services GmbH, 85748 Garching, Germany.

Contributed by the International Gas Turbine Institute (IGTI) of THE AMERICAN SOCIETY OF MECHANICAL ENGINEERS for publication in the ASME JOURNAL OF ENGINEERING FOR GAS TURBINES AND POWER. Paper presented at the International Gas Turbine and Aeroengine Congress and Exhibition, New Orleans, LA, June 4–7, 2001; Paper 01-GT-054. Manuscript received by IGTI, December 2000, final revision, March 2001. Associate Editor: R. Natole.

flow, flashback is the consequence. The turbulent burning velocity depends on the chemical kinetics and the turbulence structure, i.e., the length scales and the local velocity fluctuations. Many studies on the correlation of the turbulent burning velocity with the turbulent velocity fluctuations in the flow have been published (e.g., [4–7]). However, the results obtained from different correlations scatter widely and the proper determination of turbulent flame velocities remains a challenging task because of the complex interaction of turbulence and chemistry.

Swirling flames have a highly wrinkled and corrugated structure, which increases the flame surface considerably above the surface of a laminar flame. Mainly this effect is responsible for the increase of the turbulent flame speed above the laminar value. Whether distributed reaction zones or even well stirred local zones are of strong significance under gas turbine conditions could not be demonstrated yet. If these effects exist, they have an additional effect on the turbulent flame propagation. Turbulent burning velocities show a correlation with the laminar flame speed. This implies that, while burning fuels with high laminar burning velocities, burners with a low turbulence level are more appropriate than high swirl designs in order to receive a sufficient margin against flashback ([8]).

For stable fuels like natural gas at moderate mixture temperatures, flashback in the core flow is less critical even in highly turbulent flows due to the low laminar flame speed. A simple design rule for the optimum safety against flame propagation in the main flow is to avoid local zones of low axial flow velocity and wake regions ([2]) in the mixing zone.

Flashback due to Combustion Instabilities. Combustion instabilities can be responsible for the upstream flame propagation, both in the boundary layer ([9]) and in the core flow. The driving force for noise and pulsations in gas turbine combustion systems is the fluctuating heat release of the reacting mixture in the primary zone. Four different mechanisms can contribute to the noise spectrum peaks ([10]). First of all, the turbulent noise produces a background noise level. This broad-band excitation can be considerably amplified at the eigenfrequencies of the combustion system so that they produce distinct pulsation. Swirling flows particularly tend to form natural coherent flow structures like precessing vortex cores ([11]) or vortices generated near the transition from the mixing section into the combustion chamber. This second physical phenomenon can result in flow oscillations at specific Strouhal numbers even in the isothermal flow and leads to an amplification of the combustion noise if the excitation meets an eigenfrequency of the system. The third driving mechanism are forced coherent flow structures. They are observed if the flow instabilities respond to the triggering by velocity perturbations with subsequent phase-locking. The classical mode of unstable self-excitation is the fourth potential cause of pulsations.

High amplitudes of periodic flow velocity fluctuations at the burner exit, as a result of the mentioned instability mechanisms, lead to a periodic displacement of the reaction zone. The consequence is a periodic variation of the burner pressure loss, which again incites the oscillations. This feedback loop finally leads to periodic flashbacks. Pulsation initiated flashback requires a high pulsation level to occur, which is far beyond the acceptable noise levels of combustion systems. This kind of flashback can be interpreted as the final terminating step of a highly unstable combustion process after sufficient amplification.

Combustion-Induced Vortex Breakdown. Many gas turbine burner designs follow the basic philosophy to stabilize the flame in the combustion chamber and to avoid reaction within the burner. Burners with a centerbody or fuel lance provide a recirculation zone on the axis even without swirl. However, imposing swirl on the main flow leads to a strong amplification of the back-flow of hot gases and a better flame stabilization. An advantage of designs with centerbody is that the swirl can be selected in a wide

window, which is primarily limited by the propagation of the vortex breakdown upstream and the formation of a recirculation zone around the centerbody.

The experimental flashback study is focused on burners without fuel lance in the center of the mixing zone. The design of swirlers without centerbody requires a thorough tailoring of the swirling flow, since the flameholding capability depends entirely on the vortex breakdown without the aid of a bluff body. It can be shown that in tubular flows axial profiles with a jet on the axis are required for a stable transition of the vortex flow into its annular form in the combustion chamber. It is well known that a reduction of the swirl around the vortex core by friction or an abrupt change in the cross section leads to a pressure rise on the axis. The positive pressure gradient reduces the axial velocity in the vortex core, which at the same time effects a radial transport of angular momentum. Therefore the vortex core grows and again supports the positive pressure gradient ([12]). These effects govern the transition of the vortex from its closed into its annular form.

The formation of the vortex breakdown strongly depends on the geometry and the distribution of the axial and circumferential velocity. If the swirl number exceeds a critical value, the recirculation zone is able to extend itself throughout the entire mixing section. It is shown subsequently for the first time that even if the swirl number is well adapted to prevent this effect in the isothermal flow, the chemical reaction can nevertheless lead to a breakdown of the flow, combined with an upstream flame propagation. This effect could be observed in the present work as a characteristic flashback mechanism in swirling flows and henceforth will be called combustion-induced vortex breakdown.

Experimental Facility

The experimental facility, as sketched in Fig. 1, is essentially made up by three parts, the fuel/air premixing section (A), the swirl generator followed by a mixing tube (swirl burner B), and the combustion chamber (C).

The combustion air is preheated by electrical air heaters. To avoid any influence of equivalence ratio fluctuations or the fuel/air mixing quality on the flashback behavior, a multistage premixing section has been installed. Gaseous fuel, natural gas or hydrogen, is added to the air in a swirl mixer and the mixture subsequently passes a static mixer for fine scale mixing. For the laser Doppler anemometry, scattering particles (TiO_2) can be added upstream of the fuel injector, in order to achieve an optimum dispersion of the seeding in the flow.

A swirler generates the desired flow profile with an axial jet. The actual object of interest, the cylindrical fused silica quartz glass mixing tube, is fixed between the swirler and the combustion chamber. The optical access to the mixing tube exit zone is pro-

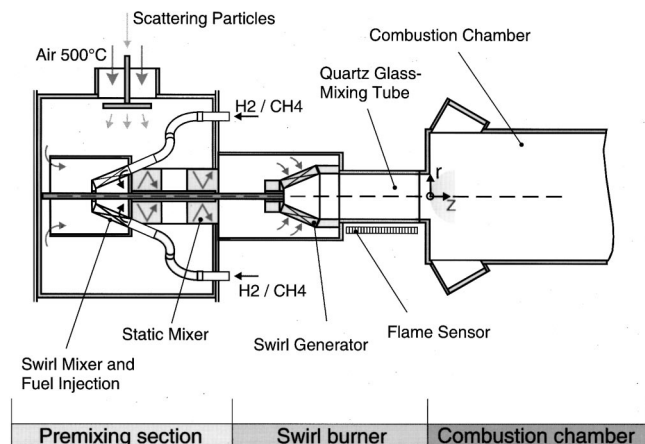


Fig. 1 Premixing section, swirl burner, and combustion chamber

vided by quartz windows. The combustion chamber itself is water-cooled and protected by ceramic flame tubes inside.

The rating of the experimental facility is as follows:

| | |
|----------------------|-----------------------|
| air mass flow: | 0.15 kg/s |
| pressure: | atmospheric |
| mixture temperature: | 30°C–500°C |
| rated thermal power: | 200 kW |
| fuel: | natural gas, hydrogen |

In the tests, flashback was initiated by a continuous increase of the fuel mass flow at a constant air mass flow, starting from a stable operating point. The increase of the equivalence ratio allows for the control of the density ratio over the flame front. Moreover, the turbulent burning velocity is influenced indirectly via the increase of the laminar flame speed. Both effects are of importance for the flashback limits of gas turbine burners. The position of the flame in the mixing tube is detected by an optical flame sensor which is described in detail below. After the flashback has propagated through the entire mixing tube, the sensor shuts off the fuel supply. With natural gas as the fuel, flashback could not be observed as long as the flow speed and the equivalence ratio were selected in the typical range of gas turbine burners. For this reason, the equivalence ratio in the tests had to be considerably increased over engine values in order to provoke flashback.

Optical Measurement Techniques

To classify the observed phenomena with respect to the mechanisms listed above, it is of prime importance to obtain simultaneously experimental data of the flow field and the flame front position. In addition, to avoid any impact on the flow and the reaction in the mixing tube during the flashback non-intrusive optical methods were applied.

Laser Doppler Anemometry (LDA). The laser Doppler anemometer used in the present experiments (two-dimensional Dantec LDA with BSA enhanced processors, 6 W Coherent Innova 90 argon ion laser, three-dimensional traverse system), was set up to measure coincidentally the axial and circumferential velocity components in a horizontal plane through the mixing tube axis with high spatial and temporal resolution. To reach a high flexibility, it was employed in its off-axis forward-scattering arrangement. The receiving optics could be adapted to the refraction conditions at the cylindrical interfaces dependant on the radial measuring point and a small effective measuring volume as well as a sufficiently high signal to noise ratio could be achieved. Unlike the laser beams, for the axial velocity component, the refraction of the laser beams for the circumferential velocity component depends on the radial position of the measuring volume. Both, the fringe spacing and the real measuring volume position are altered. To take this into account, a correction factor published by Broadway and Karahan [13] can be applied. With the described setup the stationary flow fields as well as the unsteady flow behavior during the flashback were obtained from the LDA measurements.

High Speed Video. A Kodak Ektapro Motion Analyzer 4540 high speed video camera was applied to visualize the unsteady flame propagation and to get the current flame front position and shape. The recordings have been made at a frame rate of 4500 pictures per second. In case of firing natural gas, the natural fluorescence, mainly emitted by the CH radicals in the flame front (blue-violet range), produce sufficient light for CCD chip recordings.

When combined with LDA measurements, the strong scattered laser light from the scattering particles deposited at the mixing tube wall makes the precise evaluation of the video sequences very difficult. For this reason it was necessary to improve the imaging technique. A major improvement was achieved through filtering the visible light using a Schott UG11 filter. In addition, a two-stage image intensifier (Proxitronic) was attached to the high

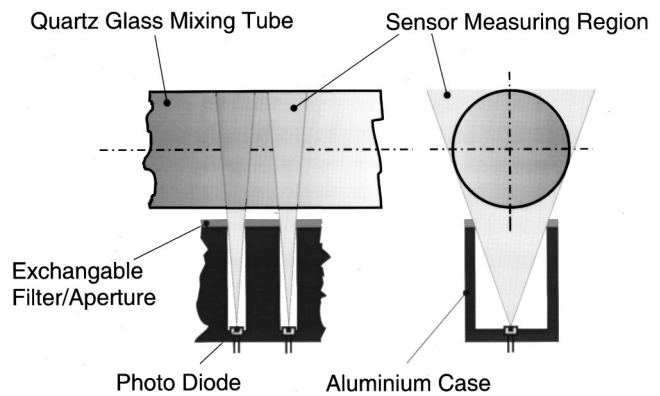


Fig. 2 Optical flame sensor for flashback detection

speed Camera. With this approach, effects of the scattered laser light and seeding could be completely eliminated and the natural flame fluorescence from the OH radicals could be recorded.

A software was developed to identify the flame front position automatically. Different digital image processing filters generate a binary picture from each video picture. For further data analysis, the flame front is identified and stored both as a function of the radial coordinate and time ([14]).

Optical Flame Sensor. The high speed video recordings give detailed information about the flame propagation, but unfortunately only over a limited time range of about 225 ms. For this reason, an optical flame sensor was developed for the observation of the flame dynamics over a longer measurement cycle with data rates up to 100 kHz (Fig. 2).

A row of photodiodes is placed along the mixing tube. The chosen photodiode is sensitive to radiation from the near UV to the blue-violet visible light. The analog output signals of all diodes are summed up to an analog signal, which is a measure for the current flame position. The sensor is calibrated by means of simultaneous recorded high speed video sequences. Furthermore the signal of each diode can be separately used to trigger other measurement techniques.

Laser-Induced Fluorescence (OH-LIF). The information provided by the high speed video recordings subsequently presented is always integrated over the depth of the mixing tube and this integration leads to a loss of the local flame structure. In order to obtain a better insight into the local structure of the flame during flashback, a triggered light sheet technique was applied in addition, which offers a spatially high resolution in two dimensions. The planar laser-induced fluorescence of the OH radicals in the reaction zone was selected to characterize the reaction zones of the flashback in great detail. The radicals were excited by a XeCl-excimer pumped dye laser (Lambda Physics EMG 201 and Scanmate 2 with Coumarin 153 dye) tuned to the $Q_1(6)$ line (283 nm) using the $A^2\Sigma^+ \leftarrow X^2\Pi(1,0)$ transition. This excitation has a better signal to noise ratio in comparison with the excitation in the region of 248 nm (KrF-excimer laser). This is of particular importance, since laser light scattering at the cylindrical mixing tube surface is difficult to avoid. The LIF images are recorded by an intensified CCD camera (LaVision Flamestar II). Laser light is cut off by a band pass mirror filter adjusted to 310 nm. During the OH-LIF measurements subsequently presented, the light sheet was located at an axial position of $-1.45D_i < z < -1.9D_i$. Therefore, a section of the flame front is depicted with a high optical resolution.

In the tests, either LDA or LIF have been combined with the optical flame sensor and the high speed camera in order to inves-

tigate the interaction between the flow field and the flame or between the structure of the flame front and the flame propagation, respectively.

Results and Discussion

Steady Swirling Flow Field. As will be shown later, it is advantageous to transfer the pressure loss of the swirler into a high axial velocity on the burner axis in order to prevent flashback. A special swirling flow with this attribute and a high circumferential velocity gradient in the vortex core has been used (burner configuration BC I, reference geometry). Figure 3 shows an example for the mean axial and circumferential velocity profile within the mixing tube (coordinate system see Fig. 1). The swirl generator is equipped with a variable orifice on the centerline, which allows the injection of an axial jet. As it is shown in Fig. 3, the axial and swirl momentum distribution near the axis can be influenced by opening the orifice (burner configuration BC II). This configuration leads to a lower mean circumferential velocity gradient in the vortex core. Simultaneously the axial momentum becomes slight higher at the axial position $z = -0.59 D_i$. The r.m.s. values of the velocity fluctuations u' and w' , normalized with the average velocity \bar{u}_a , show the high intensity of the turbulence in the swirling flow (Fig. 4). The abrupt increase of the velocity fluctuations towards the axis cannot be directly interpreted as turbulent fluctuations because of other influences such as the precessing vortex core. In the tests, the flashback limits of both configurations were investigated.

The velocity field was measured at different axial locations in the mixing tube. Figure 5 reveals a common characteristic property of tubular swirling flows: The changes of the velocity profiles in longitudinal direction is relatively weak, although a deteriora-

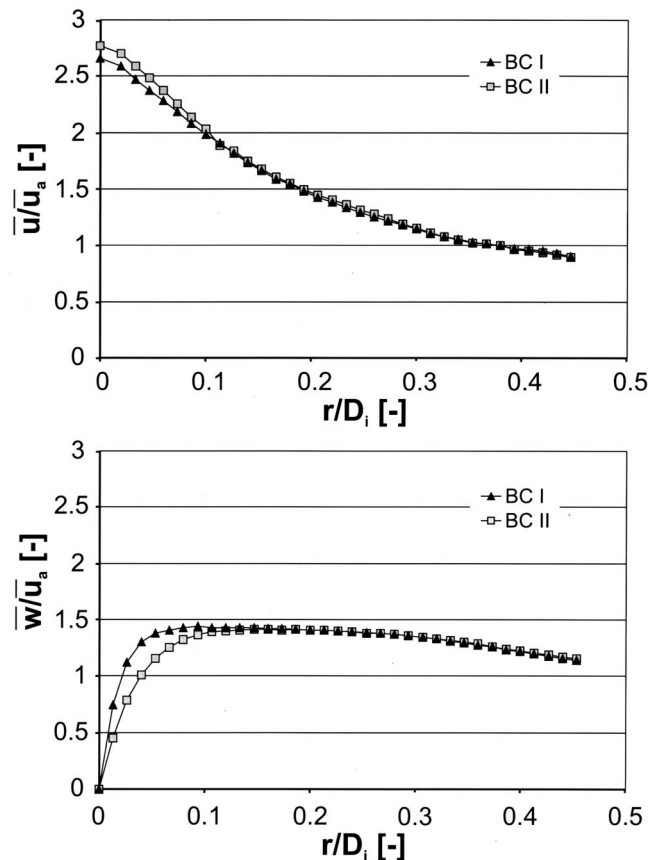


Fig. 3 Nondimensional mean axial and circumferential velocities \bar{u}/\bar{u}_a and \bar{w}/\bar{u}_a at $z = -0.59 D_i$

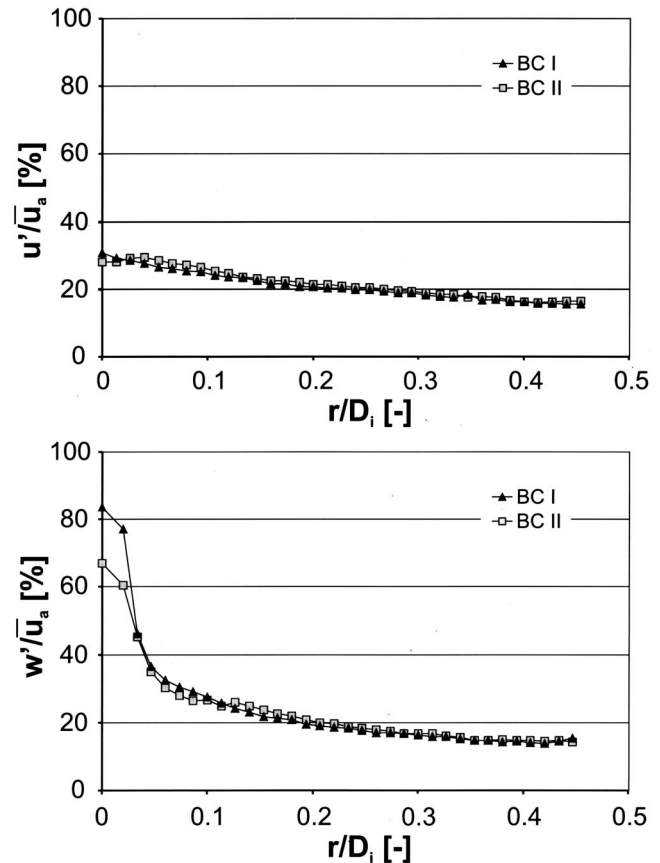


Fig. 4 Nondimensional r.m.s. of fluctuating axial and circumferential velocities u'/\bar{u}_a and w'/\bar{u}_a at $z = -0.59 D_i$

tion of the axial jet due to friction is clearly visible. From the axial velocity profile data, it can be seen in addition that the vortex breakdown in the isothermal flow is exactly located in the exit plane of the mixing tube.

Flashback Characteristics. Subsequently, the flashback behavior of burner configuration BC I will be discussed first. The data acquired by the simultaneous application of the optical flame sensor and the high speed video camera is especially qualified for illustrating the flame propagation process. The sensor signal in Fig. 6 shows the development of the flame position over a period of 900 ms. Obviously not a single flashback but rather numerous shiftings of the flame front characterize the flashback behavior. The extracted video sequences, presented in Figs. 7, 8, and 9 (cf. figure 6) show the flame propagation in the core flow with a high temporal resolution.

The propagation of the flame against the main flow direction starts with the formation of a flame needle near the axis. This needle penetrates the counterflow with a precessing motion (Figs. 7 B, C, D and 8 B, C). In some cases, vortices in the flow passing slightly off axis form a mushroom shaped flame tip (Fig. 8 D). This vortex interaction with the flame can lead to a separation of the flame tip from the downstream reaction zone (Fig. 8 E).

During the following flame evolution, a hot plug filled with combusting media is formed (Figs. 7 G, H and 8 G, H) and the flame propagation upstream either comes to rest or undergoes a further transition to a wedge shaped flame, which then propagates further upstream (Fig. 9). In the case of stagnation, the further process is not fully predetermined. The first mode is the repetition of the described process, which finally leads to a flashback through the entire tube. In contrast to this process, the second mode leads to the quenching of the reaction by the flow and to a

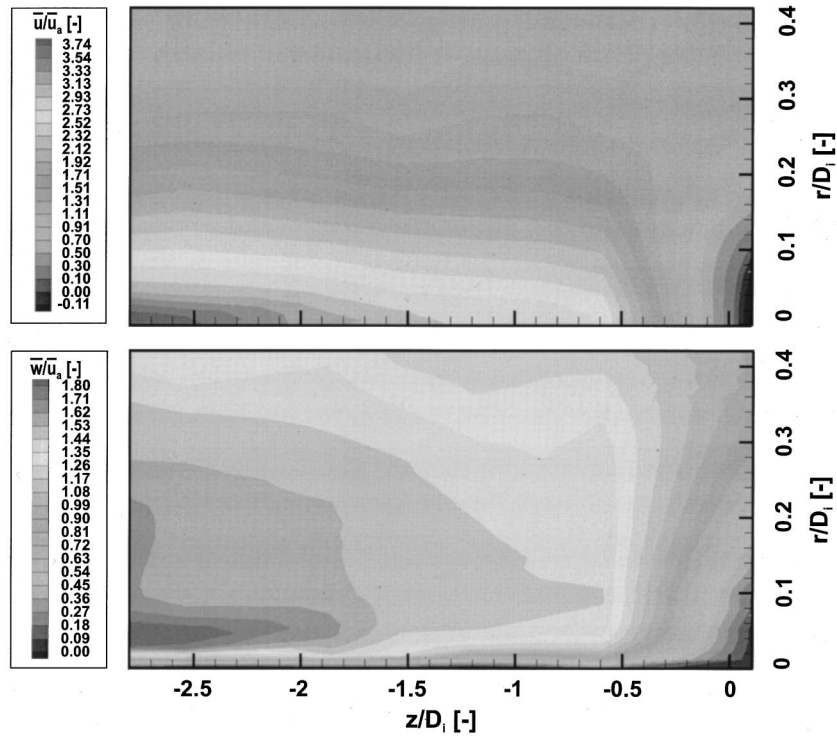


Fig. 5 Mean axial and circumferential velocity field \bar{u}/\bar{u}_a and \bar{w}/\bar{u}_a (BC I)

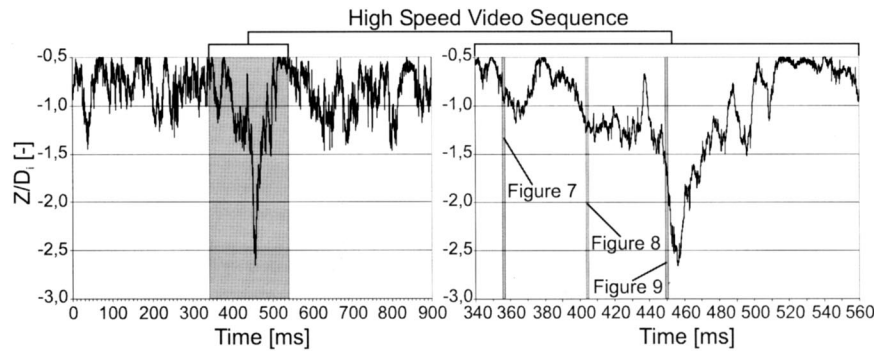


Fig. 6 Optical flame sensor signal during a flashback experiment. Methane-air mixture, $\phi=0.83$, $T=300^\circ\text{C}$, $Re=54763$.

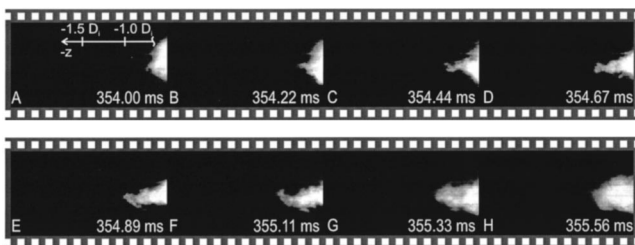


Fig. 7 UV-intensified high speed video sequence. Upstream flame acceleration by forming a flame needle (cf. Fig. 6)

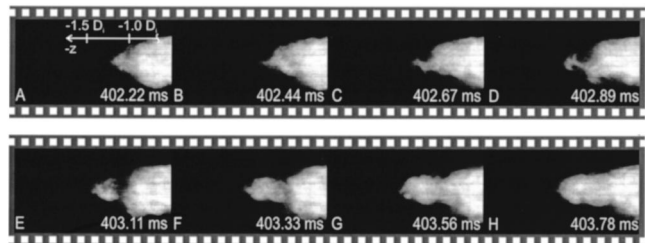


Fig. 8 UV-intensified high speed video sequence. A mushroom-shaped flame tip evolves a separated reaction zone (cf. Fig. 6).

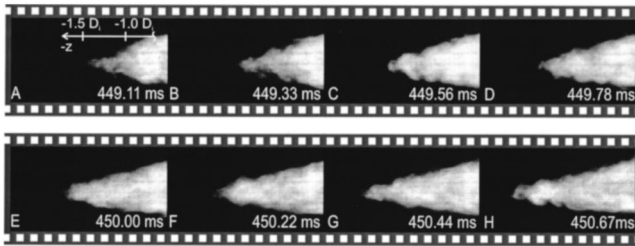


Fig. 9 UV-intensified high speed video sequence. Fast upstream moving wedge shaped flame (cf. Fig. 6).

subsequent shift of the flame back into the combustion chamber. This again leads to a recurrent flashback process as depicted in Fig. 6.

Due to the complicated dynamics of the flashback, it is insufficient to define the flashback limits as the point at which the flame propagates through the entire mixing tube. A statistical analysis of the signal of the optical flame sensor provides a better insight into the nature of the process. In Fig. 10 the histogram shows the influence of the equivalence ratio ϕ on the probability of the flame position. Starting with $\phi \leq 0.718$ the flame is stabilized at the combustion chamber inlet. For higher equivalence ratios ϕ , the probability of the flame appearing further upstream in the mixing tube increases. At $\phi \approx 0.83$ the flashback can partially propagate through the mixing tube up to $z = -2.25 D_i$. The lower probabilities of flame tip positions for the same case at $z > -0.25 D_i$ indicate that there is the tendency of a flame stabilization in the mixing tube. A further increase of the equivalence ratio leads to a final flashback throughout the entire mixing tube.

The experimental finding that the direct flashback through the entire mixing tube can be prevented within a very small window of the equivalence ratio can be explained by the higher jet velocity near the swirler (cf. Fig. 5).

The OH concentration distributions measured by LIF for selected cases fully support the findings obtained from the high speed video sequences. Of particular interest is the detailed information concerning the flame structure and the distribution of reactive species. An upstream propagating flame forms a sharp wedge or mushroom-shaped flame front (Figs. 11 and 12). The measurements reveal zones of high OH concentrations without distinct structures in the combusting sections downstream of the flame front. From the measurement it can be concluded that these zones are intensely stirred and represent a volume reaction zone.

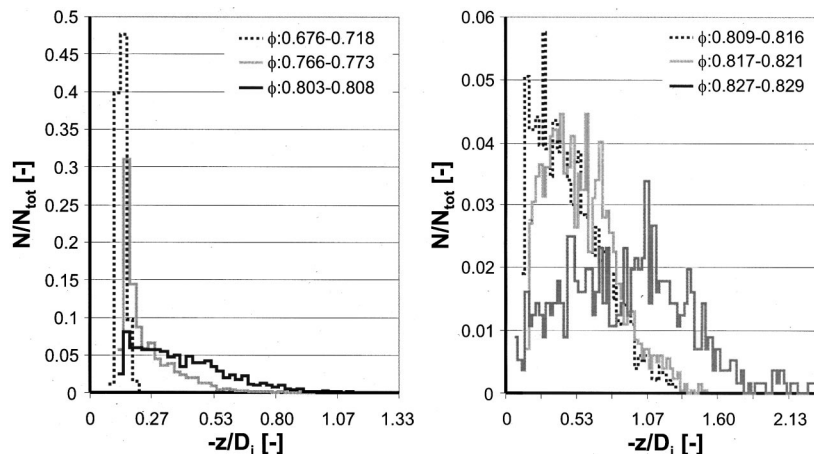


Fig. 10 Probability for flame position with equivalence ratio ϕ as parameter. Histogram at $T=250^\circ\text{C}$, $\text{Re}=73031$.

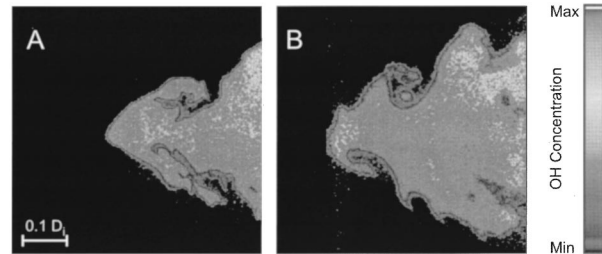


Fig. 11 OH concentration distribution during upstream flame propagation-wedge shaped flame. $\phi=0.83$, $T=300^\circ\text{C}$, $\text{Re}=54763$.

At the outer envelope of the flame, vortex structures are clearly visible. In some cases the flame tip almost completely detaches itself from its body (Figs. 13 A, confer 8 E). The transition from a fast upstream propagation into a temporarily constant flame position or even a reversal to a downstream propagation is mostly characterized by the breakdown of the volumetric reaction zone (Fig. 13). At the same time, flame structures suddenly appear, the flame becomes increasingly corrugated and quenched.

Unsteady Flow During Flashback. High speed sequences have shown that the upstream propagating flame tip is restricted to a region near the mixing tube axis. On the other hand, the profiles of the mean axial velocity (Fig. 3) show the highest values on the centerline and the velocity fluctuations are not high enough to explain the upstream flame propagation in the vortex core. Obviously, a feedback between the reaction and the velocity field must be present, in order to explain the observed phenomena qualitatively.

In this context, the unsteady flow near the mixing tube axis is of special interest and might provide the key for a better understanding of the flow-chemistry interaction. Hence, the high speed camera, the laser Doppler anemometer, and the optical flame sensor have been simultaneously applied in the flashback study to correlate the velocity data with the flame position data.

The right part of Fig. 14 shows a 900 ms sequence of the optical flame sensor signal, which was extracted from a longer 5 s measuring interval, in order to capture one single flashback. The sudden upstream flame propagation is clearly visible. The left part shows a magnified view of the flame position data during the flashback at $t = 600 - 640$ ms as well as the transient velocity data for one location slightly off the axis. An additional LDV measure-

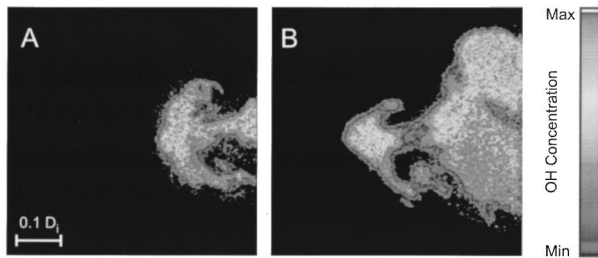


Fig. 12 OH concentration distribution during upstream flame propagation-mushroom shaped flame. $\phi=0.83$, $T=300^\circ\text{C}$, $\text{Re}=54763$.

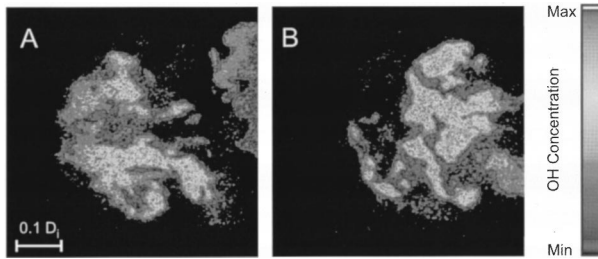


Fig. 13 OH concentration distribution in stagnating flames. $\phi=0.83$, $T=300^\circ\text{C}$, $\text{Re}=54763$.

ment (Fig. 15) provides data concerning the relationship between the velocity right on the axis and the flashback position. From the velocity data, it can be clearly seen that the upstream flame propagation is associated with a significant reduction of the axial velocity and with a distinct reverse flow on the axis. According to Fig. 15, the axial flow on the axis totally breaks down, before the flame tip reaches the LDA measuring volume. The location where the axial jet on the axis breaks down moves in counterflow direction, while the flame propagates upstream. It is of particular interest to note that the breakdown point is near to the position of the flame tip.

In the example shown in Fig. 15, the strong forward flow breaks down within approximately 2 ms. Within this extremely short time a significant reverse flow in the order of $1.5\bar{u}_a$ is developed. This leads to a very quick upstream transport of reaction products and intermediates. Since the characteristic time for this process is of the order of the characteristic time for the chemical reaction, the recirculation zone in the mixing tube appears as a highly stirred region (Fig. 11). Further LDA measurements at higher radii show that the extremely strong breakdown can only be observed near the mixing tube axis. At an off axis position of $r=0.13D_i$ (Fig. 14) for example, the decrease of the axial velocity is much weaker and does not approach negative values. The deceleration and the heat release near the axis leads to a radial transport of an angular momentum, which leads to a significant reduction of the circumferential velocity. Near the mixing tube wall the flow in the axial direction is accelerated during flashback.

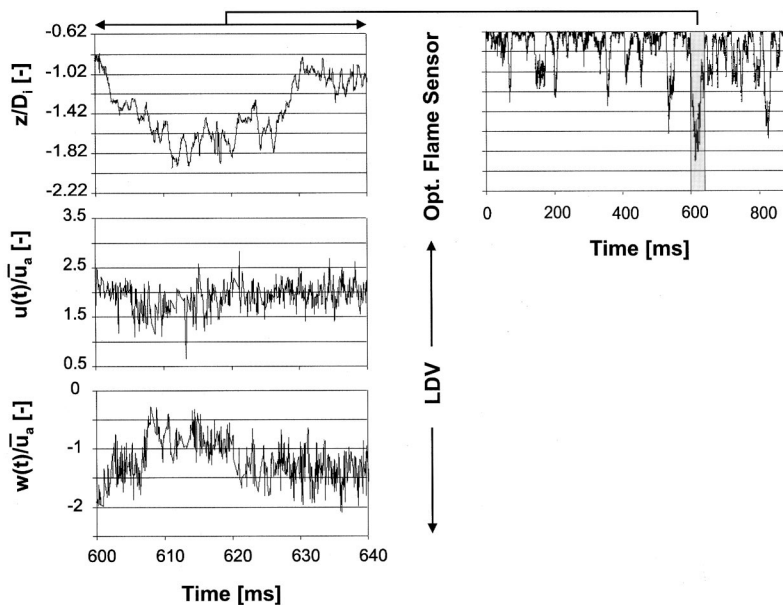


Fig. 14 Flame position and unsteady flow during a flashback. $\phi=0.83$, $T=300^\circ\text{C}$, $\text{Re}=54763$, measuring position $r=0.13D_i$, $z=-1.55D_i$.

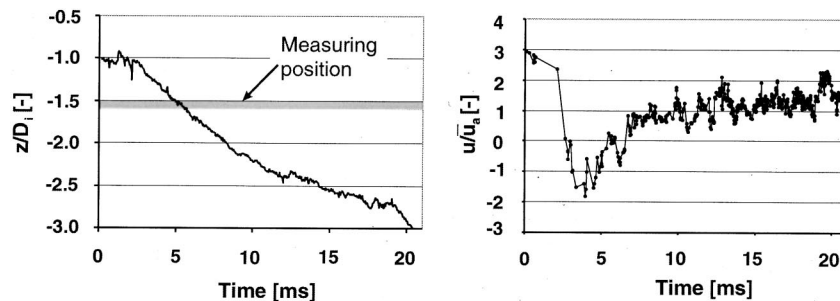


Fig. 15 Flame position (left) and unsteady flow during a flashback. $\phi=0.83$, $T=300^\circ\text{C}$, $\text{Re}=54763$, measuring position $r=0$, $z=-1.55D_i$.

From aerodynamic testing of tubular swirling flows, it is well known that small and lengthy cylindrical recirculation zones on the axis can be generated if the swirl number exceeds a certain maximum, if the radial distribution of the axial and tangential momentum is not properly tailored, or if the flow on the axis experiences a loss in total pressure during inflow through the swirler or due to the dissipation of kinetic energy in the vortex core. In the latter case, the loss of total pressure leads in a second step to lower axial velocities and a lower axial momentum on the axis. In our case, an analog effect occurs because the pressure distribution in the burner exit plane is influenced by the chemical reaction in the combustion chamber. For constant total pressure upstream of the swirler, the pressure on the axis rises at the burner exit with increasing thermal power. Consequently, this pressure rise leads to a reduction of the jet velocity near the burner outlet until the breakdown begins to propagate upstream. The associated shifting of the flame position with increasing equivalence ratio is depicted in Fig. 10.

Interestingly, the burner configuration II (cf. Fig. 3) showed a completely different flashback behavior, despite the relatively moderate differences of the two flow fields. Even with stoichiometric mixtures of natural gas and air, only a periodic displacement of the reaction was measured with the optical flame sensor. The flame did not propagate further upstream than to a position of $z = -0.8D_i$. Even in additional tests with hydrogen instead of natural gas, flashback could not be observed although the turbulent flame speed was much higher.

Apparently, the small additional overshoot of swirl free mixture around the axis can prevent the upstream propagation of vortex breakdown. The tests with hydrogen reveal in general that the combustion induced vortex breakdown is governed by additional parameters besides those responsible for the other flashback phenomena mentioned in the Introduction.

Concluding Remarks

From the experimental study on flashback in tubular swirling flows the following conclusions can be made:

- High speed video recordings and OH-LIF measurements show an upstream flame propagation in the core flow near the centerline. A flashback in the boundary layer could not be observed.
- The axial velocity of the steady flow field is too high to allow a turbulent flame propagation in the core flow without any additional driving forces. Therefore, flashbacks in the core require a breakdown of the axial velocity to occur first. This effect could be illustrated by LDA measurements.
- The propagation of the vortex breakdown into the mixing tube is obviously induced by changes of the pressure boundary condition at the combustion chamber inlet due to the chemical reaction. This propagation is the prerequisite for the start of the observed flashback process. The flame propagation is governed by the feedback between the chemical reaction and the flow in the mixing tube and vice versa.
- With small modifications of the axial and circumferential momentum in the vortex core, the flashback resistance can be considerably improved.
- The investigated burner configurations are able to arrest the flame within a narrow margin of the equivalence ratio. This can be explained by the increasing axial jet towards the swirler.
- Current paradigms concerning the appropriate swirl level of gas turbine burner should be reviewed, since designs with lower swirl exhibit advantages from the viewpoint of flashback safety.

Acknowledgment

It is gratefully acknowledged that the work presented in this paper has been supported by Alstom Power (CH) AG. The authors wish to thank T. Ruck and C. Steinbach for the useful discussions and their support.

Nomenclature

- D_i = inner mixing tube diameter (m)
 d_q = quenching distance (m)
 g = velocity gradient (1/s)
 u = instantaneous axial velocity (m/s)
 \bar{u} = mean axial velocity (m/s)
 u' = r.m.s. of fluctuating axial velocity (m/s)
 \bar{u}_a = mass mean axial velocity in the mixing tube (m/s)
 w = instantaneous circumferential velocity (m/s)
 \bar{w} = mean circumferential velocity (m/s)
 w' = r.m.s. of fluctuating circumferential velocity (m/s)
 Re = Reynolds number
 r = Radial coordinate (m)
 S_L = laminar burning velocity (m/s)
 T = fuel/air temperature in the mixing tube ($^{\circ}C$)
 t = time (s)
 z = axial coordinate (m)
 ϕ = equivalence ratio

References

- [1] Lewis, B., and von Elbel, G., 1987, *Combustion, Flames and Explosions of Gases*, Academic Press, New York.
- [2] Plee, S. L., and Mellor, A. M., 1978, "Review of Flashback Reported in Pre-vaporizing/Premixing Combustors," *Combust. Flame*, **32**, pp. 193–203.
- [3] Wohl, K., 1952, "Quenching, Flash -Back, Blow-Off—Theory and Experiment," *4th. Symposium (Int.) on Combustion*, The Combustion Institute, Pittsburgh, PA pp. 69–89.
- [4] Abdel-Gayed, R. G., and Bradley, D., 1989, "Combustion Regimes and Straining of Turbulent Premixed Flames," *Combust. Flame*, **76**, pp. 213–218.
- [5] Koroll, G. W., Kumar, R. K., and Bowles, E. M., 1993, "Burning Velocities of Hydrogen Air Mixtures," *Combust. Flame*, **94**, pp. 330–340.
- [6] Liu, Y., and Lenze, B., 1987, "Einflüsse der Frischgemisch-Turbulenzparameter auf die Flammengeschwindigkeit in turbulenten Vormischflammen, 3," *TECLAM Seminar*, Karlsruhe, Germany, pp. 77–86.
- [7] Gökalp, I., 1980, "On the Correlations of Turbulent Burning Velocities," *Combust. Sci. Technol.*, **23**, pp. 137–142.
- [8] Döbeling, K., Eroglu, A., Winkler, D., Sattelmayer, T., and Keppel, W., 1997, "Low NO_x Premixed Combustion of MBTu Fuels in a Research Burner," *ASME J. Eng. Gas Turbines Power*, **119**, pp. 553–558.
- [9] Guin, C., 1998, "Characterization of Autoignition and Flashback in Premixed Injection Systems," *AVT Symposium on Gas Turbine Engine Combustion, Emission and Alternative Fuels*, Lisbon, Portugal.
- [10] Sattelmayer, T., 2000, "Influence of the Combustor Aerodynamics on Combustion Instabilities From Equivalence Ratio Fluctuations," *ASME Paper 2000-GT-0082*.
- [11] Syred, N., and Beer, J. M., 1973, "Effect of Combustion Upon Precessing Vortex Cores Generated by Swirl Combustors," *14th Symposium (Int.) on Combustion*, The Combustion Institute, Pittsburgh, PA, **14**, pp. 537–549.
- [12] Hallett, W., 1981, "Zur Strömung und Mischung in einer eingeschlossenen Drallströmung mit Querschnittsänderungen," dissertation TU Karlsruhe, Germany.
- [13] Broadway, J., and Karahan, E., 1981, "Correction of Laser Doppler Anemometer Readings for Refraction at Cylindrical Interfaces," *DISA Information*, No. 26.
- [14] Fritz, J., Kröner, M., and Sattelmayer, T., 2000, "Simultaner Einsatz optischer Messmethoden zur Untersuchung der Flammenausbreitung in verdrahteten Rührströmungen," *Proceedings of the GALA 2000*, Freising, Germany.

Fuel-Cooled Thermal Management for Advanced Aeroengines

He Huang

Louis J. Spadaccini

David R. Sobel

United Technologies Research Center,
411 Silver Lane,
East Hartford, CT 06108

Fuel-cooled thermal management, including endothermic cracking and reforming of hydrocarbon fuels, is an enabling technology for advanced aero engines and offers potential for cycle improvements and pollutant emissions control in gas turbine engine applications. The successful implementation of this technology is, however, predicated on the use of conventional multicomponent hydrocarbon fuels and an understanding of the combustion characteristics of the reformed fuel mixture. The objective of this research is to develop and demonstrate the technologies necessary for utilizing conventional multicomponent hydrocarbon fuels for fuel-cooled thermal management, including the development of the endothermic potential of JP-7 and JP-8 + 100, a demonstration of the combustion of supercritical/endothermic fuel mixtures, and conceptual design of a fuel-air heat exchanger. The ability to achieve high heat sinks with existing jet fuels (e.g., JP-7 and JP-8 + 100) was demonstrated with a bench-scale test rig operating under flow conditions and passage geometries simulative of practical heat exchangers for aircraft and missile applications. Key measurements included fuel heat sink, reaction products, and extent of conversion. Full-scale sector rig tests were conducted to characterize the combustion and emissions of supercritical jet fuel, and demonstrate the safety and operability of the fuel system, including a fuel-air heat exchanger. [DOI: 10.1115/1.1689361]

Introduction

Thermal management is a significant challenge in advanced aircraft, rocket, and missile engines. As flight speeds increase to the high supersonic and hypersonic regime, the temperature of the ram air taken on board the vehicle becomes too high to cool the structure and, therefore, it is necessary to utilize the fuel as the primary coolant. Although cryogenic fuels, such as liquid methane and liquid hydrogen, can provide sufficient cooling, they require large vehicles (because of their low densities) and present cost, logistics, operational and safety problems. By contrast, conventional liquid hydrocarbon fuels may offer the required cooling capacity without the problems associated with cryogenic fuels. For example, paraffinic liquid hydrocarbon fuels have significant sensible heat sink capacities for supersonic aircraft applications and may undergo endothermic chemical cracking on a catalyst for hypersonic missile applications, [1].

Advanced gas turbine engines are more efficient and burn less fuel per pound of thrust, reducing the amount of cooling capacity available during operation; larger and more powerful avionics systems require significant cooling; and wings are now constructed largely of composite materials (instead of aluminum) that do not reject heat well to the atmosphere. Also, structural cooling may be incorporated to reduce the aircraft infrared (IR) signature, significantly increasing vehicle heat loads. Future aircraft are projected to operate at high Mach numbers, where aerodynamic heating becomes a design driver, and to be powered by engines that operate at high pressures and fuel/air ratios, thereby greatly increasing heat loads and exacerbating the thermal management task.

Vehicle waste heat can be rejected to either fuel or air. Taking advantage of the air heat sink involves relatively heavy heat exchangers and a vehicle drag penalty, while adding waste heat to the fuel can be done with a more compact and structurally inte-

grated heat exchanger and actually benefits the engine thermodynamic cycle by reducing the engine specific fuel consumption. Furthermore, increasing aircraft speed and engine thrust-to-weight ratio results in large simultaneous increases in heat load and temperature of the air available for cooling, thereby shifting the burden for engine and vehicle cooling to the fuel.

The total heat sink of a hydrocarbon fuel comes from the physical heating of the fuel (raising its temperature and thereby its sensible enthalpy) and a heat-absorbing (endothermic) chemical reaction. Nixon and his co-workers, [2,3], first demonstrated that the selective dehydrogenation of methylcyclohexane (MCH) on a platinum/alumina catalyst can provide a total heat sink of nearly 900 Btu/lb. MCH, the first-generation endothermic fuel, offers sufficient heat sink for cooling a Mach 4 to 6 aircraft, but is much more expensive than current aviation fuels and requires a very expensive platinum catalyst. On a practical path to realize the hydrocarbon fuel cooling technologies, Sobel and Spadaccini [1] first investigated the endothermic potential of liquid hydrocarbon fuels with inexpensive and readily available catalysts under operating conditions simulative of high-speed flight applications. High heat sink capacities and desirable reaction products were demonstrated in their study for pure paraffin (e.g., n-heptane) and blended normal paraffin (e.g., Norpar 12) fuels in coated-tube reactor configurations.

The current research is directed at developing the endothermic potential of JP-7 and JP-8 (including JP-8 + 100 and Jet A), i.e., conventional kerosene-base gas turbine fuels, using an inexpensive and readily available catalyst. Given the potential benefits of a fuel-cooled thermal management system, there are also many new technology issues that must be addressed. Structural integrity and safety of all components are considered to be paramount concerns. Operability issues in the supercritical regime and the capability to handle engine transients also pose serious challenges throughout the fuel system, including heat exchangers, control valves, and fuel injectors. Two-phase (i.e., liquid/vapor) fuel injection over a range of flight conditions presents combustor development challenges for efficiency, exhaust pattern factor, and emissions. In addition, combustion instability issues associated with the introduction of a compressible fuel must be addressed. Con-

Contributed by the International Gas Turbine Institute (IGTI) of THE AMERICAN SOCIETY OF MECHANICAL ENGINEERS for publication in the ASME JOURNAL OF ENGINEERING FOR GAS TURBINES AND POWER. Paper presented at the International Gas Turbine and Aeroengine Congress and Exhibition, Amsterdam, The Netherlands, June 3–6, 2002; Paper No. 2002-GT-30070. Manuscript received by IGTI, December 2001, final revision, March 2002. Associate Editor: E. Benvenuti.

sequently, it is also an objective to develop and demonstrate technology required for applying fuel cooling in thermal management systems for advanced gas turbines. The approach adopted in this study involves full-scale sector rig tests to (1) characterize the combustion and emissions of supercritical/reformed jet fuel, (2) demonstrate the safety and operability of the fuel system, and (3) evaluate the required component designs, such as a supercritical-fuel combustor with liquid/vapor fuel injectors, and fuel-air heat exchangers.

System Design Concepts

Supercritical/endothermic fuel cooling technology can be implemented in a practical aircraft thermal management system in two different ways: direct cooling, which refers to the incorporation of the heat exchanger into the structure of a hot component, such as a scramjet combustor, an augmentor, or a turbine exit guide vane; and indirect cooling, wherein ram air or compressor bleed air is cooled by the fuel in a nearby heat exchanger, and then used to cool the hot components. This indirect cooling, "cooled cooling air," allows a substantial increase in engine pressure ratio, with corresponding improvement in the thrust-to-weight ratio, [4,5], and thermal efficiency. In both ways, the cooling capacity of conventional hydrocarbon fuels is limited by a temperature constraint necessary to preclude coke deposition, [6,7]. For example, the cooling capacity of JP-8 or Jet A is limited to temperatures of approximately 325°F due to autoxidative coke deposition. Additives incorporated into JP-8+100 to suppress the autoxidative coke deposition permit extension of this limit to approximately 425°F, [8]. Higher fuel temperatures, and thereby higher sensible heat sinks, can be achieved through implementation of coke-mitigation strategies (e.g., operation at supercritical pressures, coke-tolerant designs, surface treatments, surface regeneration), [6,9]. Since the primary factor contributing to autoxidative coke deposition at temperatures up to approximately 700°F is oxygen dissolved in hydrocarbon fuels, techniques to remove that oxygen are particularly attractive. Spadaccini and Huang [10] first demonstrated the feasibility of an on-line deoxygenation concept for improving the fuel thermal-oxidative stability and thereby increasing the cooling capacity. The study established potential for realizing the thermal stability goals for JP-8+225/JP-900, [11], using a membrane-based deoxygenation technique. At temperatures above approximately 900°F, the sensible heat sink can be supplemented by a heat absorbing chemical reaction as the fuel undergoes thermal and catalytic cracking reactions that reform it into a mixture of lighter hydrocarbons and hydrogen, [1], which is then burned in the engine. The coke deposition mechanism in this high-temperature regime is characterized by pyrolysis. In this process, the catalyst can serve to enhance the endothermic reaction rate, improve the selectivity of the reaction for the preferred products that may have shorter ignition delay times and more rapid burning rates, and reduce the coke formation. The starting temperatures for the endothermic reactions depend primarily on the catalyst and the fuel composition. They are also a function of fuel flow rate and residence time.

In a hypersonic missile application where endothermic reactions are required, the transfer of heat into the fuel is accomplished in a catalytic fuel-air heat exchanger reactor (CHER). Within a reactor flow passage, the rate at which fuel is reformed depends on the balance among the heat transfer through the wall, the mass transfer of fresh reactant to the catalyst, and the chemical kinetics associated with both the thermal and catalytic reactions. Therefore, the reactor design requires (1) excellent structural integrity for safely implementing high-temperature air-fuel heat exchanger operation, (2) high convective heat transfer coefficients for rapid transfer of heat from air into the fuel, (3) minimum thermal resistance through the use of high conductivity materials and very thin (micron thickness) catalyst coatings bonded to the

Table 1 Jet fuel simulations

| Component | Molar Fraction | Component | Molar Fraction |
|-------------------|----------------|---------------------|----------------|
| JP-7 | | | |
| n-undecane | 0.122 | n-tetradecane | 0.031 |
| n-dodecane | 0.289 | n-pentadecane | 0.018 |
| n-tridecane | 0.368 | ethylcyclohexane | 0.172 |
| JP-8 | | | |
| methylcyclohexane | 0.075 | t-butylbenzene | 0.055 |
| meta-xylene | 0.070 | n-dodecane | 0.175 |
| n-octane | 0.130 | 1-methylnaphthalene | 0.052 |
| n-decane | 0.156 | n-tetradecane | 0.112 |
| butylbenzene | 0.055 | n-hexadecane | 0.065 |
| isobutylbenzene | 0.055 | | |

reactor walls, (4) high fuel-side mass transfer coefficient to enhance catalytic cracking reactions, and (5) lightweight and low cost.

Performance Characterization of Fuels

Compositions and Properties of Fuels. JP-7 and JP-8 (the more conventional gas turbine fuel) were chosen as the primary fuels in this study. These multicomponent hydrocarbon fuels are defined by their physical properties and broad composition guidelines (e.g., aromatics limits) rather than specific chemical compositions. Many of the defining characteristics can be found in the CRC Handbook for aviation fuels, [12]. JP-7 is a military jet fuel with high thermal stability. The fuel specifications for JP-7 require that aromatics comprise less than 5% of the fuel (as determined by ASTM D-1319), the remainder of the composition being saturated species, i.e., normal, iso, and cyclo-paraffins. JP-8, including Jet A, Jet A-1, and JP-8+100, represents a class of kerosene fuels. Of these gas-turbine fuels, JP-8+100 was the focus of the current effort; however, its similarity and relationship to the other fuels in this class warrant explanation. Jet A serves as the baseline commercial gas-turbine fuel within the U.S. Jet A-1, which differs from Jet A by having a prescribed freezing point of -53°F , instead of the -40°F associated with Jet A, is the primary commercial gas turbine fuel outside the U.S. JP-8 is the primary military gas turbine fuel and is essentially Jet A-1 with an additive package including icing and corrosion inhibitors and an antistatic component. A supplementary additive package was developed by the Air Force to extend the thermal stability limit of JP-8 ($\sim 325\text{ F}$) by 100°F . The additive package includes a dispersant, an antioxidant and a metal deactivator, and the resulting fuel is designated JP-8+100. Based on composition analyses of the jet fuels in this study and results reported by Heneghan et al. [13], 6-component and 11-component models, as listed in Table 1, were developed to simulate analytically the much more complex JP-7 and JP-8, respectively. These jet fuel simulations allow computations of the physical and thermodynamic properties of the jet fuels using the NIST SUPERTRAPP program, [14].

Test Apparatus and Analysis Procedures. The high-pressure bench-scale test apparatus is shown schematically in Fig. 1. Fuel is metered into the system at supercritical pressure using a positive-displacement pump. Fuel preheating to approximately 700°F (supercritical) was utilized for all tests involving endothermic reactions in order to reduce the reactor length requirement. Resistive heating was used to allow a direct measurement of the overall heat sink capacity of the fuels by performing an energy balance on the control volume depicted in Fig. 1. With this method, heat is supplied by the imposition of an electric current through the reactor tube itself. The electrical power input, Q_{in} , is converted to heat and transferred to the fuel on the inside of the reactor and, by natural convection, to the environment on the outside. The portion of heat lost to the environment through natural convection, Q_{env} , is minimized by insulation and accounted for

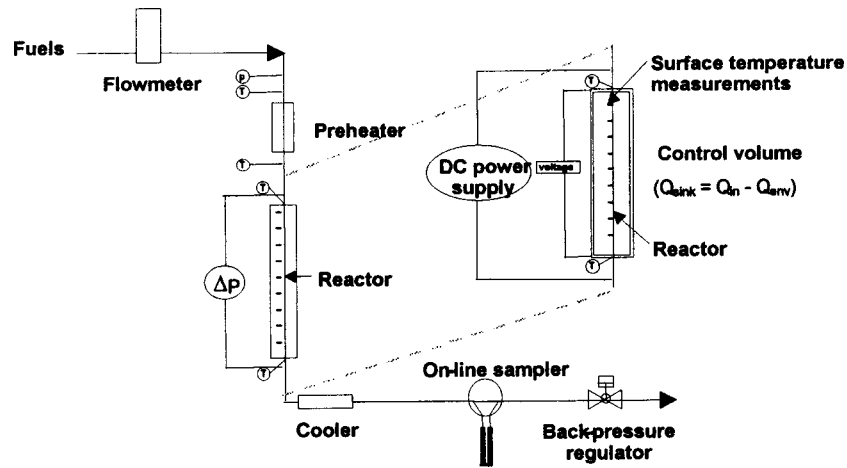


Fig. 1 Bench-scale reactor test rig

through multipoint calibrations without fuel flow prior to given tests. (The heat losses were in the range of 3 to 8% of the total power input, depending on the reactor wall temperatures and fuel flow rate.) The overall heat sink of the fuels, Q_{sink} can be computed by

$$Q_{\text{sink}} = Q_{\text{in}} - Q_{\text{env}} \quad (1)$$

Thermodynamically, the cooling capacity is defined as an enthalpy change of fuel between the inlet and exit. It can be calculated by

$$H_{\text{exit}} - H_{\text{inlet}} = \frac{Q_{\text{sink}}}{\dot{m}} \quad (2)$$

where H_{inlet} and H_{exit} are the fuel enthalpies at the reactor inlet and exit, respectively, and m the fuel mass flow rate. The overall heat sink of fuel (Q_{sink}) can be further divided into that which results in raising the temperature of the fuel/products (sensible heating, ΔH_{sens}) and that which is absorbed in the reaction (endotherm, ΔH_{endo}). The net endotherm can then be computed as

$$\Delta H_{\text{endo}} = (H_{\text{exit}} - H_{\text{inlet}}) - \Delta H_{\text{sens}} \quad (3)$$

and sensible heat sink computed as a function of the fuel temperatures measured at the reactor inlet (T_{inlet}) and exit (T_{exit}) by

$$\Delta H_{\text{sens}} = H(T_{\text{exit}}) - H(T_{\text{inlet}}) \quad (4)$$

For the purpose of sensible enthalpy calculation, the fuel composition remains constant.

All reactors were coated with an inexpensive zeolite cracking catalyst using a ceramic-like binder. In addition to the fuel temperature measurements at the reactor inlet and exit, the fuel pressures were also measured at the reactor inlet and exit to correlate reactor performance. A differential pressure gauge was used to measure and track in time the reactor pressure drop, which is indicative of coke deposition. Since the coated-wall reactor tubes were generally small diameter (<0.10 in.) to simulate practical heat exchanger reactor passages, only tube outer wall temperatures were measured along the reactor. Downstream of the reactor, the products were quenched in a water-cooled heat exchanger and the liquid and gaseous products were collected in an on-line bi-phase sample collector for compositional analysis. The liquid and gaseous components were separated and analyzed using both a cryocooled Hewlett Packard gas chromatograph/mass spectrometer (GC/MS) system and a fast-response MTI micro gas chromatograph. The extent of conversion of the fuel to gaseous products was determined by measuring the weight change in the on-line bi-phase sampler after collecting the gaseous products in an atmospheric pressure sample bag at ambient temperature.

Heat Sinks of Fuels. The results of the heat sink tests of a baseline fuel, n-octane, and primary fuels, JP-7 and JP-8 + 100 are shown in Figs. 2–4. The detailed testing conditions are described in Table 2. As mentioned above, the wall temperatures were measured along the reactor and the data showed similar wall temperature distributions for different fuels. The peak wall temperatures were located about 1 to 2 in. from the exit, and found to be 100 to 150°F higher than exit fuel temperatures, depending primarily on fuel flow rates. All the tests were run to the maximum operating temperatures, defined by the point where the reactors were plugged by coke deposition. The total heat sinks (i.e., physical + chemical) and estimated endotherms (chemical only) for n-octane, JP-7, and JP-8 + 100 are also depicted in Figs. 2 to 4. The physical heat sinks (sensible enthalpy differences) of the hydrocarbon fuels at the high temperatures (i.e., > ~1000 F) where chemical reactions occur are estimated using the NIST computer program SUPERTRAPP. The SUPERTRAPP computations were carried out based on the temperature measurements at the reactor inlet and exit, and the fuel simulations in Table 1. Comparison of the total heat sinks (on a mass basis) among these fuels at the flow conditions tested indicates that:

- there are insignificant differences in physical heat sink among these fuels;
- n-Octane and JP-7 have similar endotherms under the same temperatures. However, JP-7 has the lowest coke formation rate, probably due to its low olefin, low aromatics, low sulfur, and/or high cyclo-paraffin contents. Therefore, JP-7 can operate at higher temperature and provides higher heat sink; and
- JP-8 + 100 has slightly lower endotherm than those of n-octane and JP-7 under the same temperatures due to its higher aromatics content. Aromatics are not cracked (thermally or catalytically) under the conditions tested.

The chemical heat sink (endotherm) is a function of not only conversion but also product distribution. The change in JP-8 + 100 gaseous product composition with increasing temperature is shown in Fig. 5 and indicates a trend toward lower molecular weight species. Chromatographs of two JP-8 + 100 liquid product samples taken at temperatures of approximately 1100 and 1300°F indicate that the 1100°F sample was similar to that of unreacted JP-8 + 100, while at the higher temperature, nearly full conversion of paraffinic species and extensive side-chain cracking of aromatics to benzene and toluene were observed. To provide a more detailed analysis, liquid samples, corresponding to the gas samples in Fig. 5, were sent to a commercial laboratory. The analysis identified more than 400 separate peaks with no single peak accounting for more than approximately 5% of the liquid by

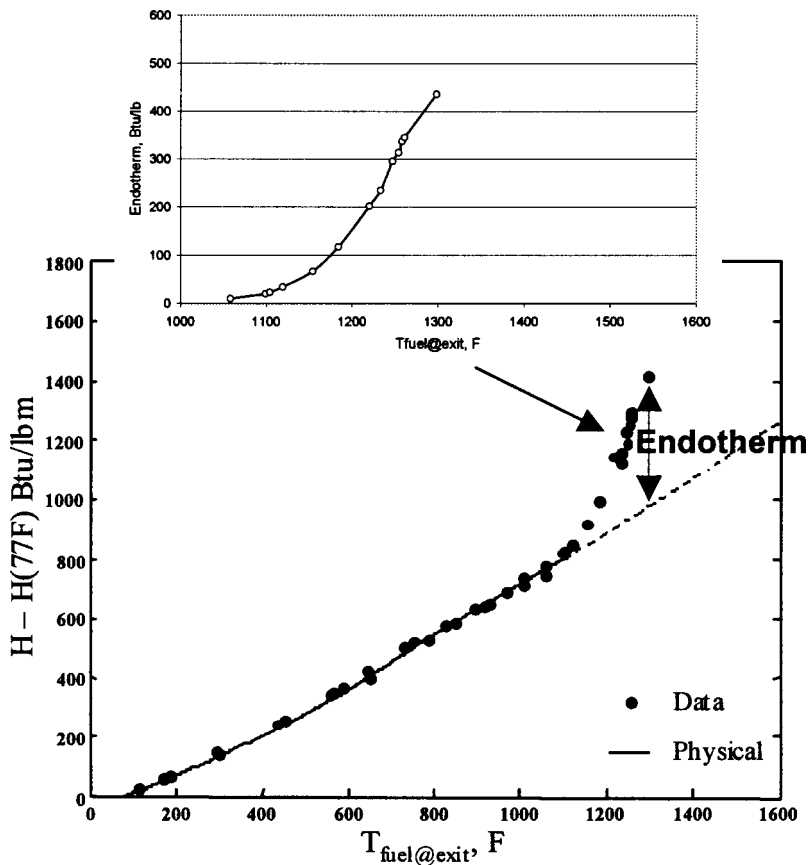


Fig. 2 Heat sink of n-octane

weight. The analysis, however, provided a distribution of the products both by carbon number and class, shown in Fig. 6. A comparison between the unreacted and reacted JP-8+100 liquid products indicates a substantial shift in the composition to lower molecular weight species, with the shift becoming more pronounced at higher reaction temperature. The analyses also indicated that no species with molecular weights higher than those of the unreacted fuel components were being formed as a result of the reaction (species up to C_{100} would have been detected with the analytical techniques used). Furthermore, the total amount of aromatics was unchanged through the reactor, indicating that the temperatures were not high enough to break the aromatic ring, nor were aromatics being created from non-aromatic compounds. It should be noted, however, that the amounts of simple aromatics (benzene and toluene) are increased, reflecting the stripping of side chains from alkylated aromatics. As expected for endothermic reactions, the analyses also proved high effectiveness in cracking normal paraffins and forming olefinic compounds in the liquid products.

There is an expected trend toward greater conversion to hydrogen and methane with increasing temperature for the JP-7 gaseous products. Although the primary species of gaseous products obtained are the same with JP-7 and JP-8+100, the JP-7 products have a significantly lower methane concentration. In addition, compared to JP-8+100, JP-7 demonstrates higher conversion and endotherm at a given temperature, because of its low aromatics content. Also, as was the case with the JP-8+100 liquid products, the chromatographs of unreacted and reacted (e.g., 1200°F) JP-7 indicate substantial reforming of the fuels in the liquid-product mixture.

To investigate possible differences in reaction performance, tests were run with Jet A and JP-8 allowing direct comparison with the tests of JP-8+100. The endotherms achieved with the

various fuels are very similar, indicating no significant effect attributable to the fuel additives. The effect of flow rate, in terms of liquid hourly space velocity (LHSV), was also investigated for JP-8+100 in the range of 500–3000 hr^{-1} . (LHSV is defined as the volumetric flow rate of the fuel in its liquid state divided by the volume of the reactor.) For a given reactor geometry, increasing the space velocity by a factor of two to six results in an increase in Reynolds number and decrease in residence time by essentially the same factor. The results indicate a lower conversion and correspondingly lower endotherm at the higher space velocity under these operating conditions.

Combustion Tests

A high-temperature moderate-pressure vitiated-air combustion test facility, shown schematically in Fig. 7, was used for developing technology required for demonstrating a high-heat-sink-fuel thermal management and combustion system. The apparatus consists of an air preparation section and separate airflow paths for a three-nozzle, arc-sector combustor test section and a catalytic heat exchanger reactor (CHER) test section. An electrically heated catalytic-tube reactor was used for preheating the fuel or supplying supercritical fuel for combustion tests conducted without a CHER.

Vitiated air heated to approximately 1200°F and 100 psia was used to simulate combustor-inlet/turbine-cooling air. The vitiated-air heater was designed (and has been demonstrated) to generate low nitric oxides emissions (emission index <1) at all operating conditions. It was supplied with nonvitiated air preheated to 800°F, and fired with natural gas. Gaseous oxygen was added downstream to restore the oxygen concentration to the atmospheric level of 21 mole percent.

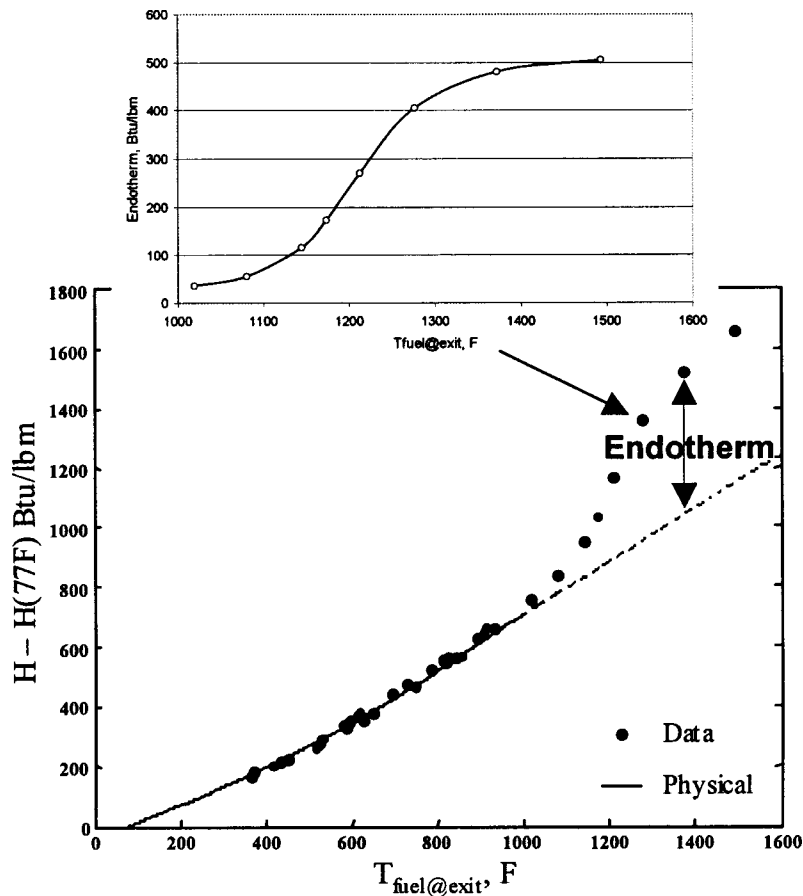


Fig. 3 Heat sink of JP-7

The liquid JP-8 + 100 fuel was preheated (as required) prior to entering the heat exchanger, where the temperature was increased to 800–1300°F (supercritical). Fuel pressure was maintained above critical in the CHERs (i.e., >340 psia) to preclude condensation and mixed-phase flow, and the flow rate was regulated using a high-temperature control valve and calibrated orifices.

The combustor assembly, shown in Fig. 8, comprised a 45-deg section of the pre-diffuser and combustor of a high-performance military engine. The prototype high-shear liquid/vapor fuel injection nozzle, shown in Fig. 9, contains three separate flow circuits for liquid and supercritical vapor fuel injection. Liquid fuel is injected through a single primary orifice in the center of the nozzle, and six secondary orifices in the inner annulus. Vapor fuel is injected through 12 orifices in the outer annulus. Air for atomizing and distributing the fuel is introduced around the nozzle through a large tailor-vortex radial-inflow swirler. The flow through each of the fuel circuits was metered continuously. The liquid fuel passages were thermally isolated from the hot fuel vapor and surrounding air stream to avoid coke formation. JP-8 + 100 fuel was used for all tests, and performance measurements were acquired for operation with all liquid fuel, and with liquid fuel and different percentages of vapor fuel. The composition of the combustor exhaust gases was determined by extracting gas samples at the exit plane of the combustor with a sampling-probe rake assembly. Five exhaust gas sampling rakes, with five probes each, were located directly downstream of the combustor. Measurements were made of the emissions of carbon monoxide, carbon dioxide, oxygen, nitric oxides, total unburned hydrocarbons, and smoke.

Combustion tests were performed with all liquid fuel and with different percentages of supercritical vapor fuel. A base-power inlet condition of 100 psia and 1200°F was selected, and tests

were conducted at progressively higher fuel/air ratios and with higher percentages of vaporized fuel injection. In these tests, the fuel was preheated electrically to approximately 700°F and then heated in the fuel-air heat exchanger to a supercritical injection temperature of approximately 900°F. Tests were conducted at $f/a=0.035$ to 0.055 (equivalence ratio 0.5 to 0.8) with 100% liquid fuel, and with 30, 38, and 52% vapor fuel injection. The results, shown in Fig. 10, present the combustion efficiency and smoke number as functions of the fuel/air ratios (calculated from the measured air and fuel flow rates).

The data demonstrate the ability to achieve efficient combustion (>99%) and good operability with a significant fraction (52%) of the fuel injected in the supercritical vapor state. The results also indicate that, as the fuel/air ratio is increased, the combustion efficiency decreases while the smoke and carbon monoxide emissions increased significantly and nitric oxides emissions remained nearly constant, suggesting that there is seemingly little effect on the peak combustion temperature. For the most part, the performance of the combustor was essentially unchanged by injecting a portion of the fuel as a supercritical vapor. Although there are some differences, they are small and the trends inconsistent, suggesting that there may be scatter in the data. The goal of efficient combustion with vaporized fuel was achieved without a significant increase in emissions, and the viability of the concept demonstrated. Although injection of low-density vapor fuel should enhance mixing, and thereby lower smoke emissions, the fuel must be effectively dispersed throughout the primary combustion zone in order to realize the benefit. In the present program, vapor fuel injection was not advanced to the extent possible, and would benefit from further development.

Injection of a compressible vapor fuel into a combustor will increase the potential for acoustic instability due to a coupling of

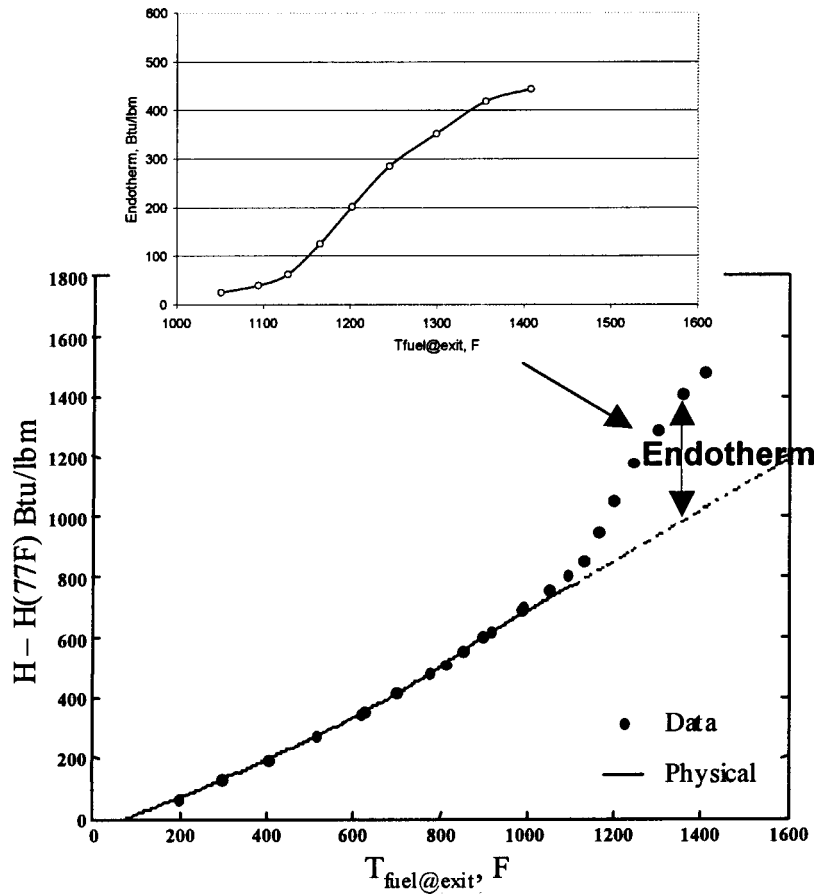


Fig. 4 Heat sink of JP-8+100

the resonant frequencies of the chamber and the fuel delivery system. Furthermore, the enhanced mixing and accelerated heat release anticipated from the use of supercritical/reformed fuel could either intensify or diminish this problem, depending upon the magnitude of the energy buildup prior to ignition.

The sensitivity of the combustor to potential acoustic instabilities was determined from pressure measurements in the injector and in the burner inlet cowl. High-frequency-response transducers were used to measure pressures in the liquid and vapor fuel manifolds, and to monitor the pressure in the combustor inlet cowl. To improve the combustor simulation and isolate measurements from rig-generated pressure disturbances in the exhaust ducting, water-cooled tubes were installed between each of the sampling probe rakes to increase the blockage and choke the flow, simulating the turbine guide vane of the engine.

Power spectral density plots for operation at the base-power inlet condition with fuel/air ratio 0.026 are given in Fig. 11. The zero-to-peak pressure fluctuation is plotted versus frequency. The effects of supercritical vapor injection on acoustic instability are determined by comparing the pressure response with and without vapor injection. The results indicate that the system operates es-

entially the same, with or without vapor injection, and that no new acoustic instabilities were introduced. The fuel manifold pressure measurements (i.e., primary, secondary, and vapor) indicate the same dominant frequencies of approximately 300 to 400 Hz, and pressure oscillations of approximately $\pm 0.2\%$.

Fuel-Air Heat Exchanger Design

Conceptual design studies have examined a wide range of potential fuel-air heat exchanger concepts for fuel-cooled thermal management system (e.g., cooled cooling air) and identified one

Table 2 Testing conditions

| Parameter | Condition |
|------------------|--|
| Tube size | 1/8" OD; 0.035" wall thickness; 24" length |
| Catalyst coating | P-octacat |
| Pressure | 600 psia |
| Mass flow rate | 4.8 lbm/hr |
| LHSV | 3000 1/hr |
| Fuel | JP-7, JP-8+100, and n-octane |

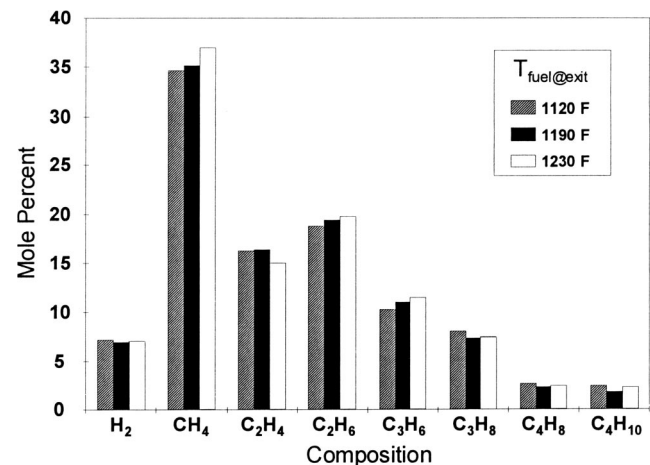


Fig. 5 JP-8+100 gaseous product composition

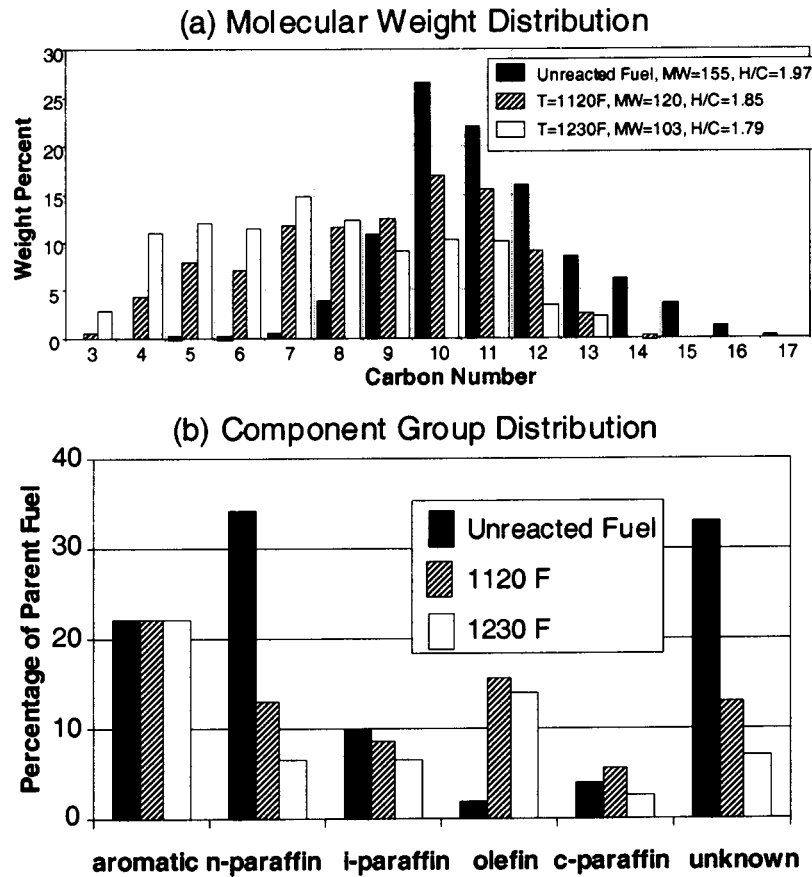


Fig. 6 JP-8+100 liquid products

design concept as an array of compact plate-fin heat exchangers constructed from high-temperature/strength super alloys for the combustion tests described above. The design consists of a multilayer plate-fin heat exchanger array, with the fuel and air flowing in a crossflow arrangement (see Fig. 12). A monolithic fuel passage construction was selected to satisfy safety and structural concerns. The design differs from conventional heat exchanger practice in that the fuel passages are formed by the chemical milling of semi-circular channels in solid facing plates, which are subsequently diffusion bonded into an integral structure. Corrugated fins and cover sheets are then brazed to the fuel plate to provide air passages. Although such a design concept was validated in the combustion tests reported above, it was heavy and expensive.

New technologies are needed in the development of lightweight, low cost, high temperature, and geometry-flexible fuel-air heat exchangers for fuel-cooled thermal management systems. One of the most promising designs to satisfy these requirements is

to use advanced metal foam structures. The foams have low density and high specific surface areas, enabling lightweight and high heat transfer, respectively. Furthermore, the three dimensionality of the open-cell foam structure minimizes the possibility for non-uniform flow in the airside. The foam can be bonded to metal tubes (fuel passages) forming an integral heat exchanger core that satisfies the structural and safety requirements (see Fig. 13).

Type 316 stainless steel was selected for making prototype metal foams and foam/tube elements because of its strength at the high temperatures required for advanced gas turbines. It will serve as a starting material for the manufacturing process development. Nickel was also selected for evaluation owing to its high thermal conductivity and moderate temperature capability. Several monolithic and bonded stainless steel and nickel foam-tube heat exchanger modules, shown typically in Fig. 13, have been fabricated and tested. In the sample shown in the figure, the bonding of tubes to the foam and the final sintering of foams were incorporated into one processing step, offering the potential for low-cost fabrica-

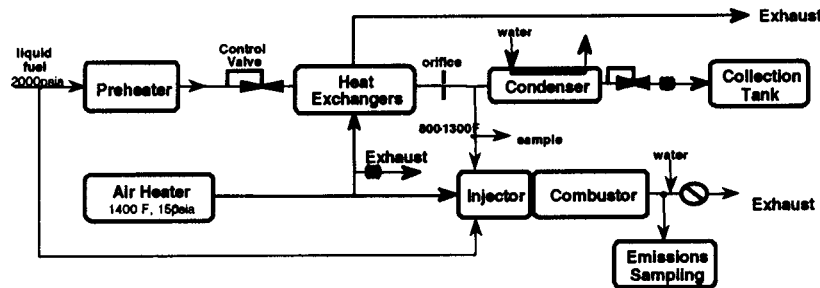


Fig. 7 Schematic of heat exchanger/combustor test facility

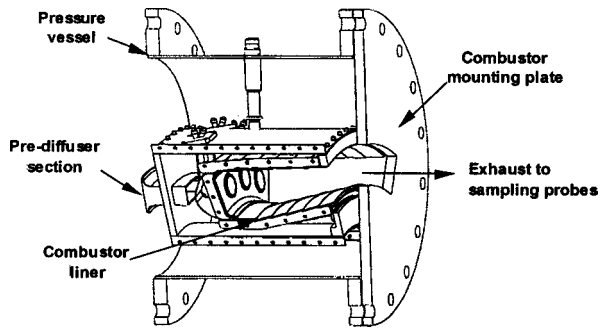


Fig. 8 Combustor sector

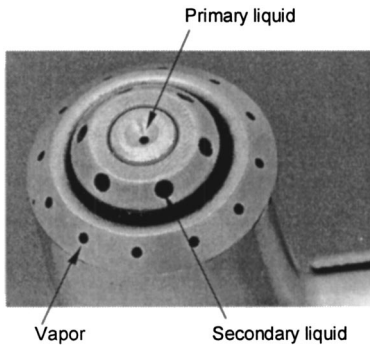


Fig. 9 Liquid/vapor fuel nozzle

tion. These modules have been assembled into a fuel-air heat exchanger performance characterization rig for assessing the effective thermal conductivity, pressure drop and heat transfer characteristics.

A CFD model was developed for assessing the conceptual design of a metal-foam fuel-air heat exchanger for a range of engine operating conditions. To optimize the overall performance, defined as a ratio of the temperature drop to the pressure drop in the airside, a cross-flow design, shown in Fig. 14, was developed in which the air and fuel make two passes through the metal foam; the fuel tubes are U-shaped. The bleed air first flows upward through the foam and across a bank of tubes containing the inlet fuel flow, and then is turned 180 deg and flows across a second bank of tubes through which the heated fuel exits. A full-size heat exchanger component based on this design will be fabricated and incorporated into a thermal management system of a demonstrator rig or engine. The test conditions and procedures will be specified, and a series of tests will be conducted to satisfy requirements for integrating the metal-foam heat exchanger into an engine thermal management system.

Conclusion

Key technologies necessary for utilizing the supercritical/endothermic heat sink capacity of current aircraft fuels in a fuel-cooled thermal management system were developed and demonstrated in this study. The endothermic heat sink capacities of the conventional hydrocarbon fuels (viz., JP-8 + 100 and JP-7) were demonstrated under operating conditions simulative of practical

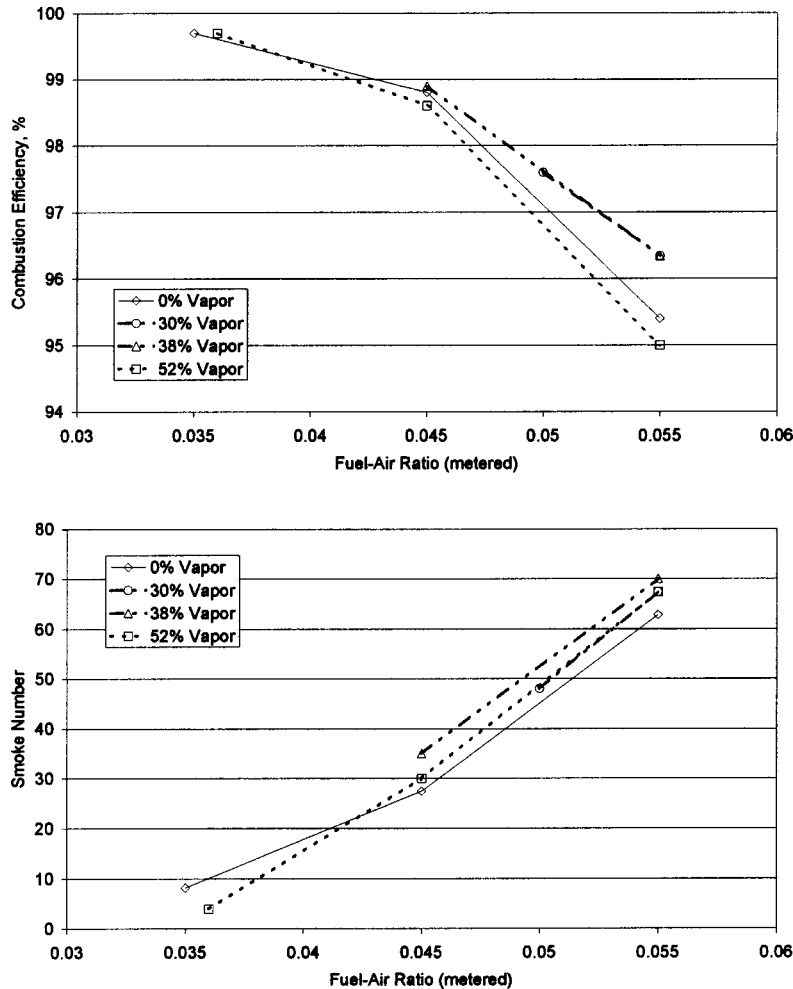


Fig. 10 Effect of vapor fuel on combustor performance

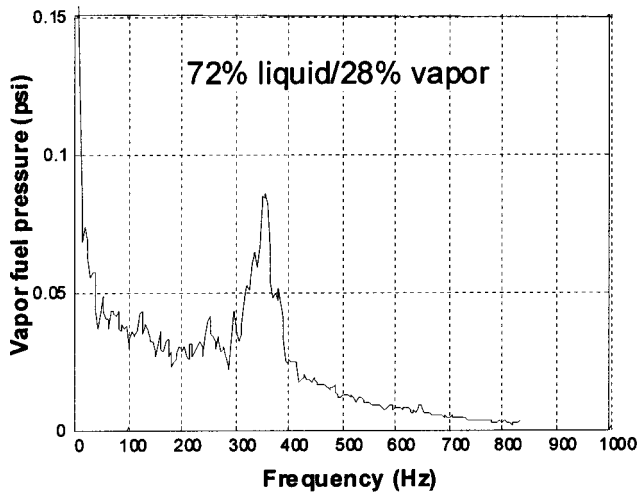
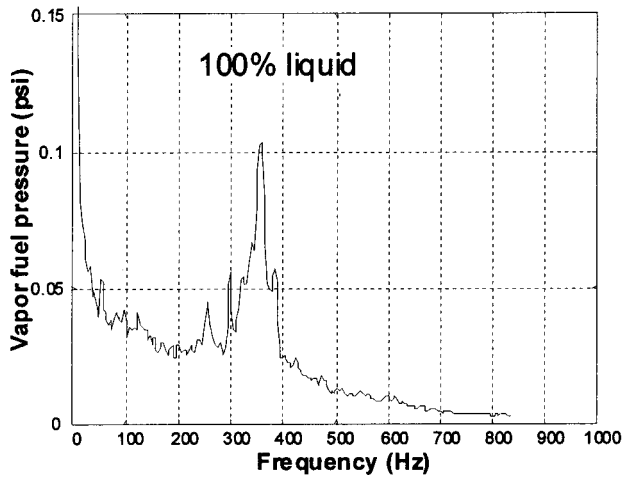


Fig. 11 Effect of vapor injection on combustor acoustics

applications. Performance evaluations were primarily based on overall heat sink (including endotherm) measurements and coke deposition. For the fuels studied, compositional analyses of both the parent fuel and processed fuel were performed and possible endothermic reforming/cracking reaction mechanisms identified. The results are directly applicable to the selection of fuels and the design of fuel-cooled thermal management systems for advanced aircraft engines and missile applications. The operability and performance characteristics of a supercritical-fuel combustor with liquid/vapor fuel injectors were demonstrated, and conceptual designs of fuel-air heat exchangers were developed for cooling compressor bleed air for turbine cooling.

Combustion tests were conducted on a full-scale sector rig to characterize the combustion and emissions of supercritical/

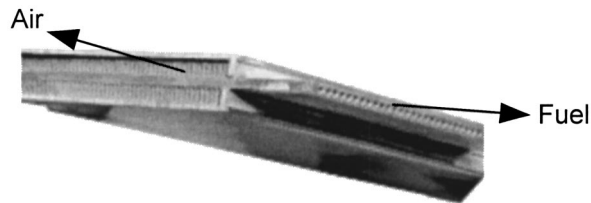


Fig. 12 Fuel-air plate-fin heat exchanger

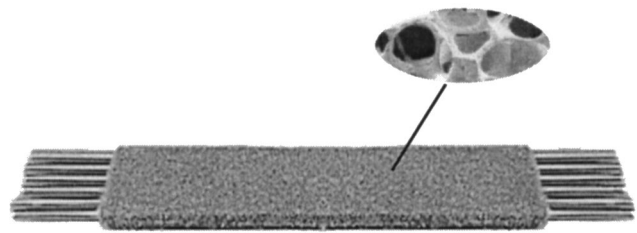


Fig. 13 Stainless steel foam-tube module

endothermic jet fuel, and the safety and operability of the fuel system. Combustion efficiency greater than 95% was achieved over a range of part to full-power conditions, with up to 55% of the fuel flow prevaporized in the heat exchanger. The combustor stability, efficiency, emissions, and pattern factor were found to be as good as the combustor operating on all-liquid fuel.

Based on the results of the current research, the following specific conclusions may be made:

- The cooled cooling air concept is feasible and can be implemented using conventional kerosene-base fuels as the heat sink.
- Substantial endotherms are achievable with JP-7 and JP-8 + 100 fuels using inexpensive zeolite catalysts in practical-geometry passages. With JP-8 + 100, endotherms of approximately 370–440 Btu/lbm were achieved at LHSV's of 3000 hr⁻¹ and fuel exit temperatures above 1300°F, corresponding to an overall available heat sink of approximately 1290–1480 Btu/lbm. JP-7, because of its low aromatics content, realized an endotherm of 420–500 Btu/lbm at similar temperatures and LHSV's, corresponding to an overall heat sink of 1420–1650 Btu/lbm. These heat sinks are very attractive for both gas turbine and hypersonic missile applications.
- There are insignificant differences in physical heat sink among the liquid hydrocarbon fuels, namely n-octane, JP-7, and JP-8 + 100.

The combustor performed as well with new liquid/vapor fuel injectors as with the current all-liquid fuel injectors. A desired reduction in smoke emissions was not achieved; however, the injector system was not developed to the maximum extent and appears to show room for further improvement.

The effects of fuel vapor injection and vapor temperature on the acoustic response of the combustor are very small.

Acknowledgments

This paper is based on research supported by the United Technologies Corporation, and work performed for the Air Force Re-

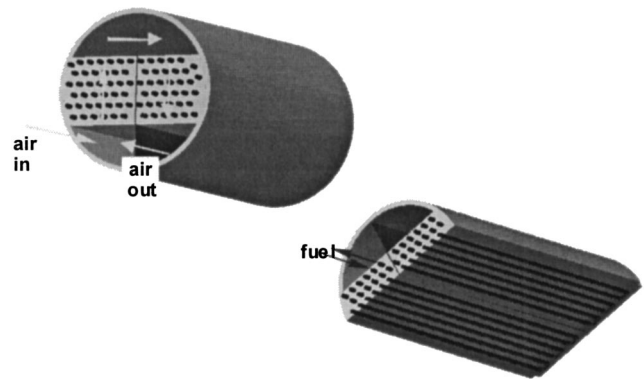


Fig. 14 Conceptual design of fuel-air metal foam heat exchanger

search Laboratory, Propulsion Directorate under Contracts F33615-92-C-2295 and F33615-97-D-2784, administered by Dr. Tim Edwards of the Fuels Branch, Turbine Engine Division, and Office of Naval Research under Contract N00014-00-2-0002, administered by Dr. Steven Fishman. The authors gratefully acknowledge the test support provided by Dr. Donald Hautman, Mr. David McHugh, Mr. Jay Borst, and Mr. John Hawkins.

References

- [1] Sobel, D. R., and Spadaccini, L. J., 1997, "Hydrocarbon Fuel Cooling Technologies for Advanced Propulsion," ASME J. Eng. Gas Turbines Power, **119**, pp. 344–351.
- [2] Nixon, A. C., Ackerman, G. H., Hawthorne, R. D., Ritchie, A. W., Henderson, H. T., and Bjorklund, I. S., 1964, "Vaporization and Endothermic Fuels for Advanced Engine Applications," AFAPL TDR 64-100, Parts I, II, and III.
- [3] Nixon, A. C., Ackerman, Faith, L. E., Hawthorne, R. D., A. W., Henderson, H. T., Rithie, A. W., Ryland, L. B., and Shryne, T. M., 1967, "Vaporization and Endothermic Fuels for Advanced Engine Applications," AFAPL TDR 67-114, Parts I, II, and III.
- [4] Bruening, G. B., and Chang, W. S., 1999, "Cooled Cooling Air Systems for Turbine Thermal Management," ASME Paper No. 99-GT-14.
- [5] Glickstein, M. R., and Spadaccini, L. J., 1998, "Applications of Endothermic Reaction Technology to the High Speed Civil Transport," NASA Contractor Report 207404.
- [6] Spadaccini, L. J., Sobel, D. R., and Huang, H., 2001, "Deposit Formation and Mitigation in Aircraft Fuels," ASME J. Eng. Gas Turbines Power, **123**(4), pp. 741–746.
- [7] Hazlett, R. N., 1991, *Thermal Oxidation Stability of Aviation Turbine Fuels*, ASTM Monograph 1, American Society for Testing and Materials, Philadelphia, PA.
- [8] Heneghan, S. P., Zabarnick, S., Ballal, D. R., and Harrison, W. E., 1996, "JP-8 + 100: Development of a Thermally Stable Jet Fuel," ASME J. Energy Resour. Technol., **118**, pp. 170–179.
- [9] Huang, H., and Spadaccini, L. J., 2001, "Coke Removal in Fuel-Cooled Thermal Management Systems," ASME Paper No. 2001-GT-0073.
- [10] Spadaccini, L. J., and Huang, H., 2002, "On-line Fuel Deoxygenation for Coke Suppression," ASME Paper No. GT-2002-30071.
- [11] Edwards, T., 1998, "Prospects for JP-8 + 225, A Stepping Stone to JP-900," AIAA Paper 98-3532.
- [12] Coordinating Research Council-SAE, 1983, *Handbook of Aviation Fuels*, CRC Report 530.
- [13] Heneghan, S. P., Locklear, S. L., Geiger, D. L., Anderson, S. D., and Schultz, W. D., 1993, "Static Tests of Jet Fuel Thermal and Oxidative Stability," J. Propul. Power, **9**(1), pp. 5–9.
- [14] Ely, J. F., and Huber, M. L., 1998, *NIST Standard Reference Database 4—NIST Thermo-physical Properties of Hydrocarbon Mixtures*.

Introduction and Performance Prediction of a Nutating-Disk Engine

T. Korakianitis

James Watt Professor of Mechanical Engineering,
University of Glasgow,
Glasgow G12 8QQ, UK
e-mail: t.alexander@mech.gla.ac.uk

L. Meyer

M. Boruta

Kinetic R&D, Inc.,
South Elgin, IL 60117

H. E. McCormick

C-K Engineering, Inc.,
Ballwin, MO 63011

A new type of internal combustion engine and its thermodynamic cycle are introduced. The core of the engine is a nutating nonrotating disk, with the center of its hub mounted in the middle of a Z-shaped shaft. The two ends of the shaft rotate, while the disk nutates. The motion of the disk circumference prescribes a portion of a sphere. A portion of the area of the disk is used for intake and compression, a portion is used to seal against a center casing, and the remaining portion is used for expansion and exhaust. The compressed air is admitted to an external accumulator, and then into an external combustion chamber before it is admitted to the power side of the disk. The accumulator and combustion chamber are kept at constant pressures. The engine has a few analogies with piston-engine operation, but like a gas turbine it has dedicated spaces and devices for compression, burning, and expansion. The thermal efficiency is similar to that of comparably sized simple-cycle gas turbines and piston engines. For the same engine volume and weight, this engine produces less specific power than a simple-cycle gas turbine, but approximately twice the power of a two-stroke engine and four times the power of a four-stroke engine. The engine has advantages in the 10 kW to 200 kW power range. This paper introduces the geometry and thermodynamic model for the engine, presents typical performance curves, and discusses the relative advantages of this engine over its competitors. [DOI: 10.1115/1.1635394]

Introduction

Demands for increased power density in uninhabited aerial vehicles (UAV), torpedoes, small automobiles, and other similar applications stress the design limits of internal combustion engines. In the power range of interest both gas turbines and piston engines have distinct drawbacks. The small size of piston engines coupled with heavy-fuel (diesel) flame-propagation space-and-speed limits introduce inherent problems with conventional diesel-fuel systems at all compression ratios. With continuous burning the combustion problem is less critical in turbine engines, but their performance is highly dependent on component efficiencies (compressor and turbine efficiencies, and pressure losses). Due to the large swallowing capacity of turbomachines, at the power range of interest the flow passages become small, and therefore dominated by boundary layer flows, so that components are small centrifugal compressors and radial turbines of comparatively low efficiency. Therefore there is a continuous need for small engines of low fuel consumption (high thermal efficiency) in small power ranges. This need exists for UAV, but also for several other portable-power needs of consumers (small electric generators) as well as the military (small underwater vehicles, UAV, etc). This is a niche market that cannot be met with conventional turbomachinery or piston-engine technology. There is huge potential of a new high-power-density engine concept in the small power range (10 to 200 kW) that combines the best advantages of piston engines and turbomachinery without compromising efficiency.

This paper introduces a novel engine, with a disk nutating around the rotating shaft. Various wobble-disk-type engines have been proposed before (Patten [1], Roseland [2], Wicha [3], Cohen [4], Nasvytis [5], Day and Koerner [6], Kreimeyer [7], Van Meejen [8], Wahl [9,10], Parker [11], Ziegler [12], and Kim, [13]), but

the disk was rotating as well as the shaft, thus creating friction and sealing problems along the disk perimeter. The most successful disk engine was built and tested by the National Gas Turbine Establishment in the UK and Caterpillar in the USA (Clarke et al. [14]). This engine had different arrangements, with complex gearing, and a rotating seal that resulted in high seal velocities (in the present engine the disk is nutating, not rotating, and the seal velocities are much lower). Clarke et al. [14] concluded that: (a) satisfactory seal designs, albeit of high wear rate due to their high velocity, were developed; (b) the engine produced the power predicted by theoretical calculations, which was lower than that of a highly boosted diesel; (c) the cost of production would be higher than that of diesels due to the complexity of the engine; and (d) Caterpillar did not have a financial or technical incentive to produce that engine. The engine described in this paper has some advantages over the Caterpillar approach (the disk does not rotate), while technology has advanced to the point where such an engine has potential applications.

Description of the Nutating Engine

A full description of the mechanical variations of the nutating engine was given by Meyer [15]. The concept is compared to gas turbines and piston engines and illustrated in Figs. 1–4. The disk is mounted at an angle to the shaft. As the shaft rotates the disk performs a nutating motion. The disk is separated into two parts, the intake/compression and power/exhaust sides. One set of seals on the perimeter of the disk wipe past the engine casing around it; a second set of seals wipe against the center of the housing between the compression and expansion sides of the disk. The interior of the engine casing is defined by the volume of revolution prescribed by the two nutating-disk segments. The major advantage of the nutating engine is that each side of the disk is used once per engine revolution. While one side (A) of the intake/compression performs part of the intake process, the other side (B) is compressing the working fluid admitted 90 deg shaft-angle earlier. Because of the nutating motion each process lasts for 270 deg crank angle, and the processes are 90 deg out of phase on each side of the disk. Similarly 270 deg crank angle power and

Contributed by the International Gas Turbine Institute (IGTI) of THE AMERICAN SOCIETY OF MECHANICAL ENGINEERS for publication in the ASME JOURNAL OF ENGINEERING FOR GAS TURBINES AND POWER. Paper presented at the International Gas Turbine and Aeroengine Congress and Exhibition, Indianapolis, IN, June 7–10, 1999; ASME Paper 99-GT-279. Manuscript received by IGTI, October 1998; final revision received by the ASME Headquarters, March 1999. Associate Editor: D. Wisler.

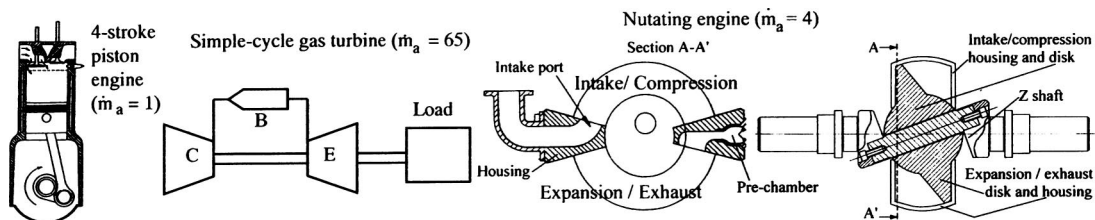


Fig. 1 Size and mass flow rate comparison of piston engine, simple-cycle gas turbine engine, and nutating engine

exhaust processes are concurrently occurring 90 deg out of phase from each other on the other side (C and D) of the disk, resulting in two intake and two power processes per shaft revolution. After compression, the working fluid is collected in the accumulator. At the outlet of the accumulator there is a pressure valve, feeding the

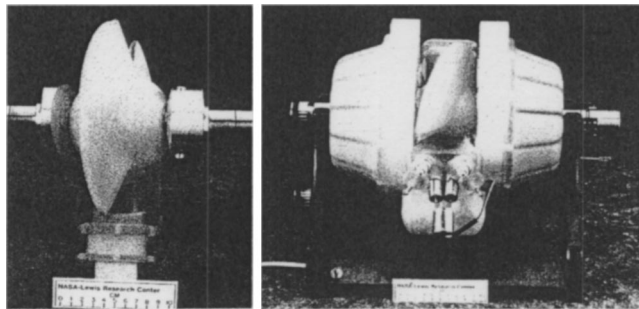


Fig. 2 Rapid-prototype models of the Meyer engine crankshaft and one-disk engine arrangements

compressed air to the combustion chamber. Fuel is admitted and partial combustion occurs in the combustion chamber, which acts as a pre-chamber. Ports admit the working fluid to the expansion/exhaust sides of the disk at the correct crank angles, and the remaining combustion occurs during the beginning of the expansion process.

Overall the Meyer nutating engine has some similarities to gas turbines, where the compressor, burner and expander each perform dedicated thermodynamic processes (Fig. 1), as opposed to piston engines where the same device (piston/chamber) is used for all processes; and it has some similarities to piston engine thermodynamic processes. It has several secondary advantages over conventional piston engines. For example, the thermodynamic processes last for 270 deg crank angle and overlap for 90 deg, so that the nutating engine has a smoother torque curve versus crank angle. The center of mass of the disk remains stationary, resulting in reduced bearing loads and sizes. There is considerable flexibility for alternative configurations. The compression and expansion sides may have different volumes. In one variation the intake volume is larger than the exhaust volume, thus "self-supercharging" the engine for high-altitude applications. In the opposite variation

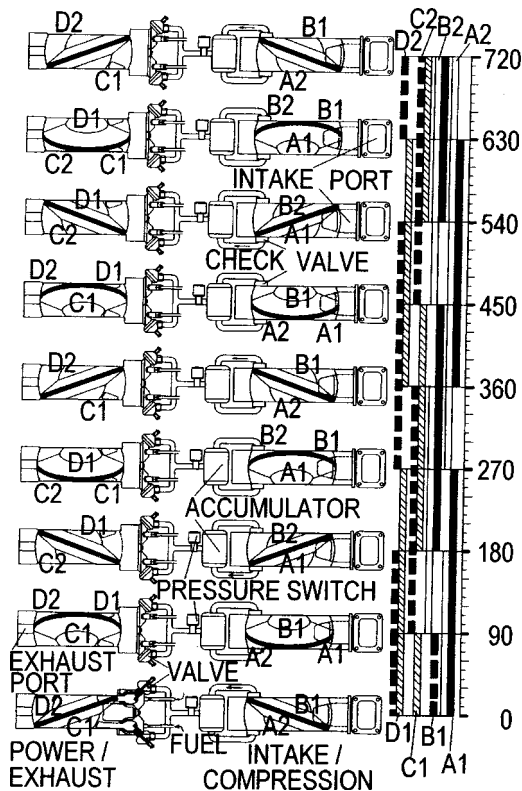


Fig. 3 Nutating-engine intake, compression, power, and exhaust processes

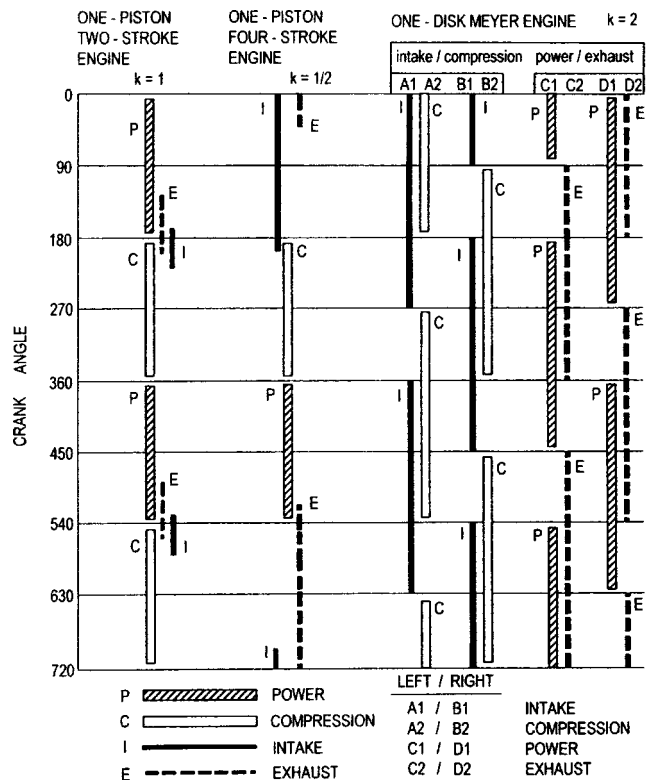


Fig. 4 Comparison of intake, compression, power, and exhaust processes with two-stroke and four-stroke piston engines

the intake volume is smaller than the exhaust volume, permitting more-efficient expansion than piston engines (to near ambient pressure). In a different configuration two disks can be mounted in series but with disks 180 deg out of phase, thus eliminating axial thrust. In yet a different configuration two disks can be mounted in series, one dedicated to intake on both sides, the second to exhaust on both sides, thus reducing thermal stresses in the casing and disks.

Thermodynamic-Cycle Comparisons

Thermal efficiency and specific power are two important non-dimensional internal combustion engine performance measures.

$$\eta_{th} \equiv \frac{\dot{W}}{\dot{E}_{in}} \approx \frac{\dot{W}}{\dot{m}_f \cdot L_{hv}} = \frac{\dot{W}}{\dot{m}_a (F/A) L_{hv}} \quad (1)$$

$$\dot{W}' \equiv \frac{\dot{W}}{\dot{m}_a C_p T_{01}} \quad (2)$$

where T_{01} is the temperature of the working fluid at engine inlet (atmospheric for conventional applications); and C_p in the last equation is C_p of the working fluid at T_{01} . \dot{W}' is a measure of the power density of the cycle.

Gas turbine η_{th} is a function of thermodynamic cycle (simple, regenerative, etc.), T_{mx} , component efficiencies (engine size), pressure losses, etc. Piston engine η_{th} (two or four stroke) is a function of size, power rating, compression ratio, amount of fuel added, throttling, turbocharging or supercharging, etc. For these engines η_{th} as a function of size, power, and speed is well established, and it depends on the level of technology.

In piston engines the volumetric efficiency is the ratio of swept volume to volume of incoming working fluid at inlet conditions.

$$\dot{m}_a = \eta_v \rho_{il} \dot{V} = k \eta_v \rho_{il} V_{sw} N_s \quad (3)$$

$$\dot{W} = \eta_{th} \dot{m}_a (F/A) L_{hv} = k \eta_{th} \eta_v \rho_{il} V_{sw} N_s (F/A) L_{hv} \quad (4)$$

The factor k denotes the number of power cycles per swept volume V_{sw} per engine revolution. For two-stroke engines $k=1$; for four-stroke engines $k=1/2$. Equation (4) shows the critical performance factors for piston engines, [16], which at full power run nearly stoichiometric. Given the type of fuel (L_{hv} and stoichiometric (F/A)), the determining parameters are η_{th} , η_v , ρ_{il} (increased by turbocharging or supercharging), N_s and V_{sw} . In piston engines the engine speed is proportional to mean piston speed $S=2lN_s$, which in turn is limited by lubrication considerations.

In gas turbines and in the nutating engine T_{mx} acts continuously on the hot parts (unlike in piston engines). Despite cooling arrangements, material temperature limits force gas turbines to run at (F/A) far below stoichiometric. The mass flow rate is

$$\dot{m}_a = \rho_{il} AC = \rho_{il} \dot{V}. \quad (5)$$

Because the product AC in gas turbines is much higher than that of comparatively sized (volume and weight) piston engines, the swallowing capacity of turbomachines is about 65 times that of piston engines (Wilson and Korakianitis [17,18]), so that \dot{W}' (Eq. (2)) of gas turbines is much higher than that of piston engines. However, in moderate power ranges, below 200 kW, gas turbine passages become small, favoring centrifugal components, of lower component efficiencies, lowering the η_{th} and \dot{W}' . Large simple-cycle gas turbines (compressor-burner-expander) approach $\eta_{th} \approx 0.4$; regenerative and intercooled-regenerative gas turbines have higher efficiencies but lower specific power. As engines become smaller, component efficiencies and the cycle thermal efficiency become lower.

Figure 1 illustrates a conceptual size, weight, mass and specific power comparison between conventional engines and the nutating engine. The three engines shown have about equal compression volume (gas turbine compressor volume), and about equal overall

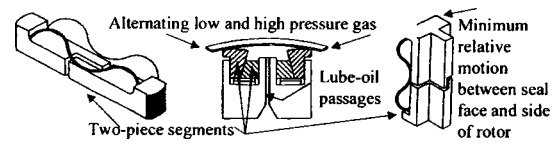


Fig. 5 Illustration of sealing arrangements: (a) left, disk end (center flat) surface to center housing; (b) center, disk tip (circumference) to outside-diameter housing; and (c) right, 6 to 12 radial seals on disk surface to flat end plate

engine volume and weight. The \dot{m}_a and therefore the power produced (Eq. (4)), are considerably different. If the mass flow rate through the four-stroke piston engine is $\dot{m}_a=1$, then for the simple-cycle gas turbine $\dot{m}_a \approx 65$ and as will be shown below for the nutating engine $\dot{m}_a \approx 4$. In piston engines V_{sw} is given by bore area times stroke (times the number of pistons). This swept volume provides one power stroke per engine revolution in two-stroke engines ($k=1$ in Eq. (3)), and one power stroke per two engine revolutions in four-stroke engines ($k=1/2$ in Eq. (3)). A comparable definition of the swept volume for the nutating engine is the volume of the intake casing minus the volume of the intake side of the disk. In addition to this swept volume, piston engines have the connecting rod and crank mechanism, gas turbines have the burner and expander, and the nutating engine has the expansion/exhaust side of the disk. All three engines have additional auxiliaries of similar sizes.

The major advantage of the nutating engine over the simple-cycle gas turbine is that for comparable engines in the 10–200 kW range the components of the gas turbine will be much smaller and therefore of lower efficiency. The major advantage of the nutating engine over the piston engine is that the swept volume is used twice per engine revolution, or in other words $k=2$ in Eq. (3). Since the thermodynamic processes of the nutating engine are similar to those of piston engines, its thermal efficiency is expected to be similar to that of comparably sized (physical volume) piston engines as well as simple-cycle gas turbines. In general the nutating engine will have additional pressure drops (corresponding to pressure drops in gas turbine components) associated with the flow of working fluid from intake to accumulator to combustion chamber to exhaust. On the other hand the average speed of the disk seals is much lower than that of comparable piston rings at the same engine rpm (or the nutating engine speed can be increased, increasing mass flow rate and power in proportion).

Sealing Arrangements

Three sets of seals are required in the nutating engine (Fig. 5). The first set is a wiping seal between the flat portion of the disk and the center housing, near and perpendicular to the shaft. The seal is split to accommodate thermal expansion, loaded by a spring, and energized by the pressure of the working fluid. The second seal is between the tip of the disk and the outside-diameter housing. This is a two-piece seal energized by metal springs and working-fluid pressures (alternating). Lubricating oil is supplied to this seal from the center of the disk. The third seal is a radial set of seals between the conical surface of the disk and the flat surface of the housing. Again this is a two-piece seal to accommodate thermal expansion, and it is energized by a metal spring and gas pressure. As the exhaust side of the disk opens, a number of several radial seals of the third type provide the same number of stepwise expansions. The mean speed of these seals is much lower than if the disk was rotating at engine rpm (the disk does not rotate), and therefore the wear rate of these seals is less than that on the rings of piston engines. Theoretical calculations of seal loads and required seal areas similar to those of Clarke et al. [14] show that a “figure of merit” of a seal design defined as a function of engine swept volume, component speed, and seal area is a function of the pressure drops across the seals integrated around

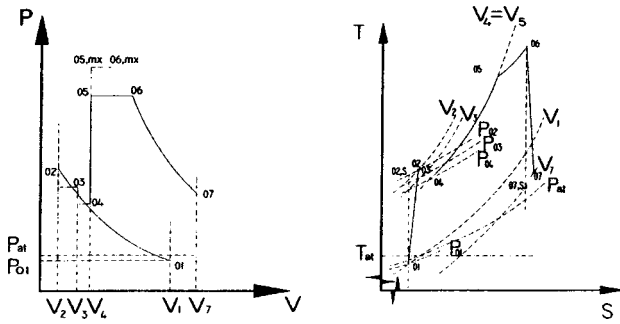


Fig. 6 Illustration of pressure-volume and temperature-entropy diagrams of thermodynamic models of the Meyer nutating engine

the thermodynamic cycle. Calculations of seal area required shows that the seals are feasible and technologically attainable.

Thermodynamic Model

The engine processes are modeled as follows. Every engine revolution two times the mass of working fluid that has been admitted to the swept volume V_{sw} is compressed to the compression ratio and admitted to the accumulator. From the accumulator the mass of air flows into the combustion chamber, where fuel is injected and combustion begins. From there the still burning mixture is admitted to the expansion volume. During the initial phases of expansion we have both burning and expansion. At the end of expansion valves or ports are opened, thus exhausting the products of combustion.

The thermodynamic model (Fig. 6) is based on nonisentropic compression from 1 to 2, expansions with pressure losses in the accumulator from 2 to 3 and in the combustion chamber from 3 to 4, burning partially at constant volume from 4 to 5, burning the remainder at constant pressure from 5 to 6 (while also expanding and producing power), and nonisentropic expansion from 6 to 7. The thermodynamic analysis models heat loss from the working fluid. The model calculates η_{th} and \dot{W} given appropriate inputs. These inputs are a function of engine size, speed, and several design details, and choosing them correctly requires experience with similar models. Several volume ratios are required inputs:

$$r_{12} \equiv r_c = \frac{V_1}{V_2} > 1 \quad (6)$$

$$r_{23} \equiv \frac{V_2}{V_3} \leq 1 \quad (7)$$

$$r_{34} \equiv \frac{V_3}{V_4} \leq 1 \quad (8)$$

$$r_{71} \equiv \frac{V_7}{V_1} \quad (9)$$

where V_7 can be smaller or larger than V_1 provided that $p_{07} > p_{at}$. It is assumed that the working fluid is air (\dot{m}_a) during intake, and a mixture of air and products of combustion during burning and expansion. The properties of these working fluids are evaluated by analytic polynomials as functions of temperature and (F/A) for air and products of combustion as described by Wilson and Korakianitis [17,18]. (The isobaric and isochoric specific heat capacities C_p and C_v are polynomial functions of T and (F/A) . The values of C_p and C_v shown in the equations below are not constant; they are the average values between the two temperature extremes, T_a and T_b of the process.)

$$C_p \equiv \overline{C_p} = C_p \left(\frac{T_a + T_b}{2}, (F/A) \right) \quad (10)$$

$$C_v \equiv \overline{C_v} = \overline{C_p} - R \quad (11)$$

At engine inlet friction drops the stagnation pressure (about 2%, $f_{pl,il} \equiv (p_{at} - p_{01})/p_{at}$) and the stagnation temperature is not affected. At the inlet the pressure, temperature and \dot{m}_a are

$$T_{01} = T_{at} \quad (12)$$

$$p_{01} = (1 - f_{pl,il}) p_{at} \quad (13)$$

$$\dot{m}_a = \eta_v \frac{p_{01} \dot{V}_1}{RT_{01}} = k \eta_v \frac{p_{01} V_{sw} N_S}{RT_{01}} \quad (14)$$

Isentropic compression would bring temperature to $T_{02,s}$ and pressure to p_{02} . The compression isentropic efficiency is used to evaluate T_{02} .

$$T_{02,s} = T_{01} \left(\frac{V_1}{V_2} \right)^{(R/\overline{C_v})} \quad (15)$$

$$p_{02} = \frac{mRT_{02,s}}{V_2} = p_{01} \frac{V_1}{V_2} \frac{T_{02,s}}{T_{01}} \quad (16)$$

$$\eta_{s,c} \equiv \frac{T_{02,s} - T_{01}}{T_{02} - T_{01}} \quad (17)$$

$$\dot{W}_c = \dot{m}_a [\overline{C_v} (T_{02} - T_{01})] > 0. \quad (18)$$

V_3 is used to evaluate the isentropic (maximum possible under perfect flow conditions) pressure at station 3, $p_{03,s}$. Then the pressure-loss (input) factor from 2 to 3 is used to evaluate the actual pressure at 3, p_{03} , and temperature T_{03} .

$$V_3 = V_2 / r_{23} \quad (19)$$

$$p_{03,s} = p_{02} \left(\frac{V_2}{V_3} \right)^{(\overline{C_p}/\overline{C_v})} \quad (20)$$

$$p_{03} = p_{03,s} (1 - f_{pl,23}) \quad (21)$$

$$T_{03} = T_{02} \frac{p_{03} V_3}{p_{02} V_2} \quad (22)$$

Similarly the volume at station 4 is then used to evaluate the isentropic (maximum possible under perfect flow conditions) pressure at station 4, $p_{04,s}$. Then the combustion chamber pressure-loss (input) factor $f_{pl,34}$ from 3 to 4 is used to evaluate the actual pressure at 4, p_{04} , and temperature T_{04} .

The maximum temperature of the cycle occurs at T_{06} ; however, this is lower than $T_{mx} = T_{06,mx}$, the maximum temperature that would have been obtained if there were no heat losses. Maximum material temperatures are far below T_{mx} . T_{mx} is present only instantaneously during the thermodynamic cycle, and there is continuous heat transfer out of the engine casing. This maximum temperature $T_{mx} = T_{06,mx}$ is an input to the calculations, and it is used to compute the fuel-air ratio and energy input to the cycle. The corresponding $T_{05,mx}$ is computed using input parameter θ_1 :

$$T' \equiv \frac{T_{mx}}{T_{at}} = \frac{T_{06,mx}}{T_{01}} \quad (23)$$

$$\theta_1 \equiv \frac{T_{06,mx} - T_{05,mx}}{T_{06,mx} - T_{04}} \quad (24)$$

The energy balance from 04 to 05,mx to 06,mx gives

$$\dot{E}_{in} = (\dot{m}_a + \dot{m}_f) [\overline{C_v} (T_{05,mx} - T_{04}) + \overline{C_p} (T_{06,mx} - T_{05,mx})] = \frac{\dot{m}_f \cdot L_{hv}}{\eta_{bu}} \quad (25)$$

$$(F/A) = \frac{\dot{m}_f}{\dot{m}_a} \quad (26)$$

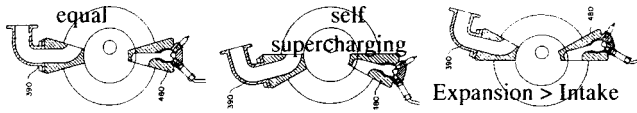


Fig. 7 The swept volume of intake and exhaust can be equal (left); or the intake volume may be bigger than the exhaust volume (“self-supercharging”) for high-altitude applications (center); or the exhaust volume may be bigger than the intake volume for higher on-ground efficiency (right)

where the left side of the energy equation is used to evaluate \dot{E}_{in} and the right side to evaluate (F/A) . Depending on cycle temperatures, this fuel-air ratio may approach, or be below stoichiometric.

Next heat losses out of the cycle drop the actual temperatures to T_{06} and T_{05} . These are computed using input parameters:

$$f_{ql,cy} \equiv \frac{T_{06,mx} - T_{06}}{T_{06,mx} - T_{at}} \quad (27)$$

$$\theta_2 \equiv \frac{T_{06} - T_{05}}{T_{06} - T_{04}} \quad (28)$$

A suitable value is $0.0 \leq f_{ql,cy} \leq 0.3$. This factor includes heat losses through the engine casing only. There are additional losses because of the effect of hot exhaust leaving the engine at station 07 at temperature (and pressure) higher than ambient. Input parameters θ_1 and θ_2 can simulate any range of burning rate, from constant volume to constant pressure combustion. Constant-volume combustion is represented by $\theta_2 = 0.0$ ($T_{06} = T_{05}$), while $\theta_2 = 1.0$ simulates constant-pressure combustion ($p_{04} = p_{05} = p_{06}$); and the values in between correspond to every combination between constant volume and constant pressure. The remaining pressures and volumes are now calculated by

$$V_5 = V_4 \quad (29)$$

$$p_{05} = p_{04} \left(\frac{V_4}{V_5} \right) \left(\frac{T_{05}}{T_{04}} \right) = p_{04} \left(\frac{T_{05}}{T_{04}} \right) \quad (30)$$

$$p_{06} = p_{05} \quad (31)$$

$$V_6 = V_5 \left(\frac{p_{05}}{p_{06}} \right) \left(\frac{T_{06}}{T_{05}} \right) = V_5 \left(\frac{T_{06}}{T_{05}} \right) \quad (32)$$

$$V_7 = \frac{V_7}{V_1} \frac{V_1}{V_2} \frac{V_2}{V_3} \frac{V_3}{V_4} V_4 = r_{71} r_c r_{23} r_{34} V_4 \quad (33)$$

Figure 7 illustrates an advantage of the Meyer nutating engine over piston engines. The compression ratio r_{12} need not be equal to the full expansion ratio r_{57} , allowing considerable flexibility depending on the application.

The constant-pressure expansion work is given by

$$\dot{W}_{e,56} = p_{05} (\dot{V}_6 - \dot{V}_5) = (\dot{m}_a + \dot{m}_f) R (T_{06} - T_{05}) > 0 \quad (34)$$

The expansion (volume) ratio is used to evaluate the isentropic temperature and pressure after isentropic expansion from p_{06} and T_{06} to p_{07} and $T_{07,s}$. The expansion isentropic efficiency is used to evaluate the temperature at the end of expansion T_{07} .

$$T_{07,s} = T_{06} \left(\frac{V_6}{V_7} \right)^{(R/\bar{C}_v)} \quad (35)$$

$$p_{07} = p_{06} \frac{V_6}{V_7} \frac{T_{07,s}}{T_{06}} \quad (36)$$

$$\eta_{s,e} = \frac{T_{06} - T_{07}}{T_{06} - T_{07,s}} \quad (37)$$

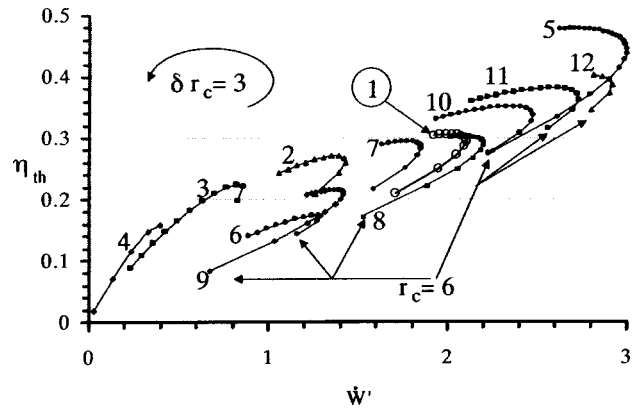


Fig. 8 Computed design-point thermal efficiency and specific power of several (total 162 shown) nutating engines using the inputs of Table 1

$$\dot{W}_{e,67} = (\dot{m}_a + \dot{m}_f) \bar{C}_v (T_{06} - T_{07}) > 0 \quad (38)$$

With mechanical efficiency η_{me} the power output is

$$\dot{W} = \eta_{me} (\dot{W}_{e,56} + \dot{W}_{e,67} - \dot{W}_c) \quad (39)$$

Thus the thermal efficiency and specific power of the cycle can now be evaluated using Eqs. (1) and (2).

Predicted Performance

A set of representative performance curves is shown in Fig. 8. Each line in Fig. 8 shows the design-point thermal efficiency and specific power of several nutating engines as function of compression ratio $r_c = r_{12}$ starting from $r_c = 6$ (which is the last clockwise point on each line) and moving counterclockwise with increment $\delta r_c = 3$. Line 1 (with open round symbols in Fig. 8) has been calculated with the input parameters shown on the left side of Table 1. With the standard inputs of line 1 the maximum power ($\dot{W}' = 2.10$) is obtained for $r_c = 18$ and the corresponding $\eta_{th} = 0.29$. The maximum thermal efficiency ($\eta_{th} = 0.31$) is obtained for $r_c = 27$ and the corresponding $\dot{W}' = 2.05$. Further increases in r_c result in reductions in both specific power and thermal efficiency. The remaining lines have been obtained by varying one input at a time from those of line 1, as indicated on the right column of Table 1. Several effects are illustrated by comparison of lines: lines 1, 2, 3 and 4 the effect of $T_{06,mx}$; lines 1, 5, and 6 the effect of heat losses; lines 1, 7, and 8 the effect of nearly constant volume versus nearly limited pressure cycle; and lines 1, 9, 10, 11, and 12 the effect of volume ratio r_{71} (limited by $p_{07} > p_{at}$). Similarly to the performance of simple-cycle gas turbine engines (Korakianitis and Wilson [17]) each line indicates that there is an optimum r_c for power and higher optimum r_c for thermal efficiency. In general the location of these lines is dependent on each

Table 1 Inputs for the predicted performance of Fig. 8

| Standard Inputs | Line/Input Variation |
|----------------------------------|---------------------------------|
| $T_{at} = 288$ K | 1: Standard |
| $p_{at} = 101.3$ kPa | 2: $T_{06,mx} = 2000$ K |
| $T_{06,mx} = 2400$ K | 3: $T_{06,mx} = 1600$ K |
| $f_{pl,il} = 0.02$ | 4: $T_{06,mx} = 1200$ K |
| $\eta_{s,c} = \eta_{s,e} = 0.90$ | 5: $f_{ql,cy} = 0.000$ |
| $f_{ql,cy} = 0.200$ | 6: $f_{ql,cy} = 0.400$ |
| $\theta_1 = \theta_2 = 0.50$ | 7: $\theta_1 = \theta_2 = 0.10$ |
| $r_{23} = r_{34} = 0.90$ | 8: $\theta_1 = \theta_2 = 0.80$ |
| $f_{pl,23} = f_{pl,23} = 0.050$ | 9: $r_{71} = 0.50$ |
| $r_{71} = 1.00$ | 10: $r_{71} = 1.50$ |
| $\eta_{bu} = 0.996$ | 11: $r_{71} = 2.00$ |
| $\eta_{me} = 0.98$ | 12: $r_{71} = 2.50$ |

cycle parameter and on component efficiencies. Just like in the prediction of thermodynamic performance of gas turbine engines, care must be taken so that these input parameters reflect the engine technology as a function of expense, size of flow passages, heat losses, mechanical losses, leakage, etc.

Using figures such as 8, a suitable cycle can be chosen for each application; η_{th} and \dot{W}' are read from the figure. The swept volume V_{sw} and speed $N_s = N_m/60$ are chosen, and \dot{m}_a is calculated or estimated. Then the equation for specific power gives the power delivered by the engine, and the corresponding torque

$$\dot{W} = \dot{m}_a (\dot{W}') C_p T_{01} \quad (40)$$

$$Q = \frac{\dot{W}}{\omega} = \frac{\dot{W}}{2\pi N_s} \quad (41)$$

For example using the information from line 1, a nutating engine with $r_c \approx 9$ would have $\eta_{th} \approx 0.23$ and $\dot{W}' \approx 1.97$. A 0.20 m disk would result in $V_{sw} = 0.377$ lt. Assuming $\eta_v = 0.90$ and 6,000 rpm, the resulting $\dot{m}_a = 0.476$ kg/s. Assuming that this engine runs stoichiometrically on heavy diesel and at standard atmospheric conditions, eqn. 4 results in $\dot{W} \approx 298$ kW, while the more-accurate estimate with Eq. (40) results in $\dot{W} \approx 284$ kW.

Preliminary calculations in several engine sizes comparing the torque computed from the last two equations to the torque computed from thermodynamically predicted pressure loads and structural geometry indicate satisfactory agreement. The torque delivered to the shaft assembly of the nutating engine is not as smooth as the (almost constant) torque of gas turbines, but it is much smoother than that of typical piston engines.

Conclusions

The thermal efficiency of the nutating engine is similar to that of gas turbines and piston engines of comparable technology and size. The power density (specific power) of gas turbines is higher than that of the nutating engine, except in low power ranges (10–200 kW) where the size of gas turbine components becomes too small thus reducing component efficiencies. In these power ranges and at 2000 to 10,000 shaft rpm the size of the nutating engine disk is between 0.10 to 0.30 m, making the component performance suitable for efficient power generation. The major advantage of nutating engines compared to piston engines of similar weight and volume is the higher power density. In the power range between 10 and 200 kW and where power density is essential, the nutating engine provides distinct advantages over simple-cycle gas turbines and piston engines. More-detailed models of the thermodynamic, dynamic, and heat transfer processes of nutating engines will not drastically change the expectations presented above.

It is fully expected that the challenges presented to the development of a nutating engine can be overcome. This confidence is based on the success of a prior related but different engine type at the National Engineering Laboratory in the UK and Caterpillar in the USA, [3]. The nutating engine does not require complex gearing, reducing production costs, and it is aimed at applications requiring a technical solution of higher power density in moderate power ranges.

Nomenclature

| | |
|--------------|---|
| A | = cross-sectional area of engine intake |
| C | = average axial velocity of working fluid at intake |
| C_p, C_v | = isobaric, isochoric specific heat capacities |
| E, \dot{E} | = energy, energy rate |

| | |
|------------------------|--|
| f | = heat-loss or pressure-loss factor |
| (F/A) | = fuel-to-air mass ratio |
| k | = volume sweeps (power strokes) per shaft rotation ($k=2$ for volume V_{sw} in the nutating engine) |
| l | = stroke of piston engine |
| L_{hv} | = lower heating value of the fuel |
| m, \dot{m} | = mass, mass flow rate |
| N_m, N_s | = revolutions per minute, per second, $N_s = N_m/60$ |
| p | = pressure |
| Q | = torque |
| r | = compression (volume) ratio, $r_{ij} \equiv V_i/V_j$, $i = 1, \dots, 7$ |
| r_d | = radius of disk of engine |
| R | = specific gas constant |
| T, T' | = temperature, temperature ratio |
| V | = volume |
| W, \dot{W}, \dot{W}' | = work, power, specific power |
| δr_c | = r_c increment (Fig. 8) |
| η | = efficiency |
| θ | = combustion-model factor |
| ρ | = density |
| ω | = angular velocity |

Subscripts

| | |
|----------|---------------------------------------|
| 01 to 07 | = thermodynamic cycle points (Fig. 6) |
| a | = air |
| at | = ambient (or atmospheric) |
| bu | = burner |
| c, e | = compression, expansion |
| f | = fuel |
| il | = engine inlet |
| me | = mechanical |
| mn, mx | = minimum, maximum |
| pl, ql | = pressure loss, heat loss |
| s | = isentropic |
| sw | = swept |
| th | = thermal |
| v | = volumetric |

References

- [1] Patten, J., 1882, Rotary engine. US patent no. 263,573.
- [2] Roseland, T. C., 1905, Rotary engine. US patent no. 790,264.
- [3] Wicha, A., 1935, Gas and vapor compressor. US patent no. 1,986,454.
- [4] Cohen, W. A., 1937, Rotary engine. US patent no. 2,069,646.
- [5] Nasvytis, A. L., 1961, Nutating disk motor. US patent 2,992,635.
- [6] Day, D. B., and Koerner, W. J., 1963, Nutating disk internal combustion engine. US patent no. 3,102,517.
- [7] Kreimeyer, H., 1970, Rotary nutating power device. US patent no. 3,492,974.
- [8] Van Meegen, H. A. B., 1974, An improved motor, pump or the like. Australian patent no. 67,511.
- [9] Wahl, R. H., 1975, Rotary nutating engine. US patent no. 3,895,610.
- [10] Wahl, R. H., 1976, Nutating engine. US patent no. 3,981,639.
- [11] Parker, 1982, Swashplate machines. US patent no. 3,942,384.
- [12] Ziegler, M., 1982, Die Erfindung betrifft einen Rotationskolbenverbrennungsmotor insbesondere für den Automobilbau. German patent no. 3,942,384.
- [13] Kim, J. D., 1992, Rotary wavy motion type engine. US patent no. 5,138,993.
- [14] Clarke, J. M., Walker, D. F., and Hamilton, P. H., 1972, "A New Class of Rotary Piston Machine Suitable for Compressors, Pumps and Internal Combustion Engines," Proc. Inst. Mech. Eng., **186**(62/72).
- [15] Meyer, L., 1993, Nutating internal combustion engine. US patent no. 5,251,594.
- [16] Korakianitis, T., and Sadoi, T., 1997, "Turbocharger-Design Effects on Gasoline-Engine Performance," ASME J. Eng. Gas Turbines Power, accepted for publication.
- [17] Wilson, D. G., and Korakianitis, T., 1998, *The Design of High-Efficiency Turbomachinery and Gas Turbines*, 2nd Ed., Prentice-Hall, Englewood Cliffs, NJ.
- [18] Korakianitis, T., and Wilson, D. G., 1994, "Models for Predicting the Performance of Brayton-Cycle Engines," ASME J. Eng. Gas Turbines Power, **116**, pp. 381–388.

Pre-integrated Nonequilibrium Combustion-Response Mapping for Gas Turbine Emissions

T. Korakianitis

James Watt Professor of Mechanical Engineering,
University of Glasgow,
Glasgow G12 8QQ, Scotland

R. Dyer

N. Subramanian

Mechanical Engineering Department,
Washington University,
Campus Box 1185,
1 Brookings Drive,
St. Louis, MO 63130

In gas turbine combustion the gas dynamic and chemical energy release mechanisms have comparable time scales, so that equilibrium chemistry is inadequate for predicting species formation (emissions). In current practice either equilibrium chemical reactions are coupled with experimentally derived empirical equations, or time-consuming computations are used. Coupling nonequilibrium chemistry, fluid dynamic, and initial and boundary condition equations results in large sets of numerically stiff equations; and their time integration demands enormous computational resources. The response modeling approach has been used successfully for large reaction sets. This paper makes two new contributions. First it shows how pre-integration of the heat release maps eliminates the stiffness of the equations. This is a new modification to the response mapping approach, and it performs satisfactorily for non-diffusion systems. Second the theoretical framework is further extended to predict species formation in cases with diffusion, which is applicable to gas turbine combustion systems and others. The methodology to implement this approach to reacting systems, and to gas turbine combustion, is presented. The benefits over other reaction-mapping techniques are discussed. [DOI: 10.1115/1.1688769]

Introduction

Conventional gas turbines use gaseous or liquid fuels. Fuel combustion generates pollutants like NO_x , CO, and unburned hydrocarbons (UHC). Modern pollution regulations demand reduction of these pollutants, thus paving the way for better and more sophisticated combustor designs, [1].

The formulation of most empirical models to predict emissions is based on the assumption that the exhaust concentrations are dependent on three main factors: (a) reaction rates; (b) mixing rates; and (c) mean residence time of working fluid in the combustion zone. The primary zone temperature and equivalence ratio determine reaction rates. The degree of homogeneity of the primary zone determines species mixing rates. The residence time of species in the primary zone determines the overall mean residence time in the combustion zone, and the wall quenching characteristics affect formation of species. Other secondary factors, depending on the combustor design, like mixing rate of secondary air, water injection etc., are sometimes included to improve the accuracy of the empirical models. Such models, [2], use expressions of the three factors identified above in terms of size of combustion zone, liner pressure loss, airflow proportions, and operating conditions such as pressure, temperature, and air mass flow rate. Empirical models have played an important role in the development of low emission combustors, and they have low computational overhead, but the increased demand for reduced gas turbine emissions is taxing the accuracy of these empirical models.

The alternative is the use of higher-fidelity numerical models (for example, such as those by Jones and Priddin, [3]). However, the accuracy of the numerical models is directly dependent on the model of the combustion process itself. In addition, use of these numerical models is case specific, because it requires extensive computations to derive sufficient combustion details for the specific combustor geometry and its species formation characteristics.

The precision of any detailed combustion modeling system de-

pends on the accuracy of the representation of chemical kinetics. Accurate representation requires large reaction mechanisms involving hundreds of chemical reactions and species. This increases the computational cost, as it involves solving hundreds of reactions at each temporal step. Thus full computation of gas turbine combustion reactions and formation of emissions is cumbersome because the unsteady Navier–Stokes equations must be coupled with the dozens to hundreds of species conservation equations and hundreds to thousands of reaction equations, [4], for chemical kinetics.

In order to overcome the problem, many combustion systems invoke the equilibrium assumption. However, the equilibrium assumption is not valid for all combustion systems. A classic example illustrating the deficiency of the equilibrium assumption is the prediction of NO_x emissions. For accurate predictions it is necessary to couple the thermal NO_x reactions to the reaction sequence describing the oxidation of the fuel. Most current equilibrium models follow the suggestion of Zelodovich et al. [5]. This assumes the rate of NO_x formation is slow compared to the fuel oxidation mechanisms, so that thermal NO formation reactions can be decoupled from the fuel oxidation process. This allows the calculation of NO assuming equilibrium values of temperatures and concentrations of O_2 , N_2 , O, and OH. As this assumption is not valid over the whole temperature range, significant errors emerge into the final result. This is illustrated for a methane-air oxidation in Fig. 1 (from [6]). The higher line is the ratio of the maximum NO formation rates calculated using the full chemical kinetics reaction mechanism divided by the initial NO formation rate calculated using Zeldovich's approximation. The lower line is the ratio of NO concentration at the time of maximum NO formation rate (calculated using detailed reaction mechanism) divided by the equilibrium NO concentration.

In order to continue meeting increasingly stringent emission regulations we need a more accurate computational method for complex combustion processes. However, solving the large set of stiff equations including interacting species and fluid dynamic equations is so time consuming that cannot be used for design predictions. One solution to obtaining reliable species-formation predictions is to reduce the reaction mechanism. Reduction techniques imply reduction in the complexity of the mathematical form of the chemical reactions. There are several types of reduc-

Contributed by the International Gas Turbine Institute (IGTI) of THE AMERICAN SOCIETY OF MECHANICAL ENGINEERS for publication in the ASME JOURNAL OF ENGINEERING FOR GAS TURBINES AND POWER. Paper presented at the International Gas Turbine and Aeroengine Congress and Exhibition, New Orleans, LA, June 4–7, 2001; Paper 2001-GT-0386. Manuscript received by IGTI, December 2000, final revision, March 2001. Associate Editor: R. Natole.

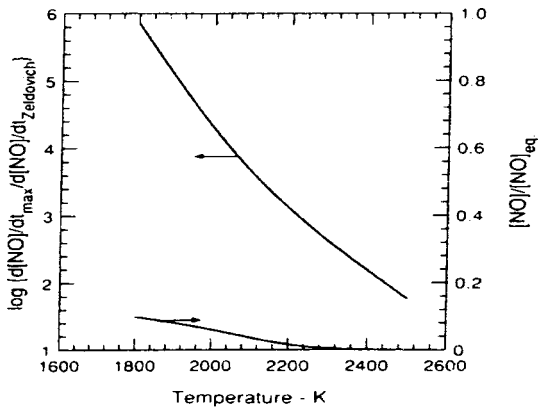


Fig. 1 NO prediction error

tion techniques, [7]. The subject of the current paper is a new reduction technique that falls under the general heading response modeling.

Response Modeling

Response modeling is the reduction of the reaction system using various techniques to maintain sufficient computational accuracy. The simplest reaction form used is the empirically calibrated, one-step global model of (for instance, heat release or NO_x concentration) where the equation coefficients are derived to fit a known quantity (for instance, reaction time) for a given chemical reaction system. A simple example of such a response map would consist of initial conditions (T , ρ , etc) of the mixture (pre-combustion) as inputs, and select species of interest (such as NO and NO_2) after combustion as outputs.

Westbrook and Dreyer [8] matched adiabatic flame speed using one and two-step methods. The addition of a second step permits an intermediate species to improve the predicted heat release. The simplified reaction sets must be calibrated to a specific physical situation (in this case adiabatic flame speed) thus compromising generality. Approximate systems, such as that presented by Jachimowski [9], still nearly tripled the number of equations required in a Navier-Stokes analysis of a reacting flow. Automated reduction methodologies, [10], simplify the tailoring of a reaction set to a desired set of conditions, but still require the same tradeoff between computational efficiency and model generality. Maas and Pope [11] and Blasenbrey et al. [14] have developed an approach based on intrinsic, low-dimensional manifolds present in the detailed reaction set. This assumes a rapid convergence of the reaction to the slowest (rate limiting) reaction paths, which are mapped by the method to as few as one or two parameters. The system reaction rates, as described by the rate of change of the mapping parameters, are tabulated as a function of the mapping parameters. Thus these parameters can be integrated along with the gas dynamic conservation variables and the system chemical state determined at the point corresponding on the low-dimensional manifold. A repro-model approach that parameterizes the chemical state in terms of an induction parameter was introduced by Korobienikov et al. [15] and later used by Taki and Fujiwara [16]. Oran et al. [17] developed a parameter for modeling the induction time in stoichiometric hydrogen-air and methane-air detonations. In these cases the induction parameter is integrated along with the gas dynamic variables to determine the time at which the heat release occurs.

Reduced mechanisms can greatly reduce the flux equations and source terms required for analysis. In general, however, the smaller the mechanism, the more closely it is calibrated to a specific circumstance and therefore the less generally applicable it is. The Intrinsic Low-Dimensional Manifolds and Repro-Models permit the mapping of the reaction space to a very few progress

variables, for example mole number of CO_2 and H_2O (Maas and Pope [11,12]). However, the progress variables must be integrated with the conservation variables, thus maintaining the stiffness of the equations. Therefore, integration of the resultant response-model equations with the fluid dynamic equations is still time consuming, as it maintains the high eigenvalue of these phenomena in the model equation set. Consequently, the numerical solution has accuracy and stability issues similar to those in the solutions of every stiff system of equations.

One significant contribution of the approach presented in this paper is that it avoids the above accuracy, stability and other stiff-equation concerns. Its conceptual roots are derived from the earlier work of Frenklach and Rabinowitz [18] Marsden, et al. [19]. In a significant variation from the above established methodology, Dyer and Korakianitis [20] developed hierarchical models of increased fidelity for chemical reaction response maps for a priori integration of the system of differential equations. These response maps are algebraic models capable of producing the state of the system as a function of the various system parameters, including chemical reaction time. The algebraic response model then takes the place of the set of differential equations to describe the response of the chemical system during the evolution of the flow field. This approach has several advantages. First, the detailed reaction system is integrated in a pre-process step, using detailed nonequilibrium chemical reaction species equations. This results in capturing all the nonequilibrium dynamic behavior of the chemical system, to the accuracy of the detailed chemical reaction models. The response model can also be derived directly from experimental data. Second, the resulting model is not an additional differential equation to be integrated. This means that the response model does not keep the high eigenvalues of the original species equations in the dynamic system, and it does not add stiffness to the numerical solution. Finally, the flow solver can advance the conserved variables at each time step and then use the response model to “decode” the chemical state into primitive variables such as pressure and temperature.

Reacting Flow Equations

The close coupling between the fluid dynamics and the chemical reaction is shown in the unsteady, compressible energy Eq. (1) and the unsteady, compressible species continuity Eq. (2).

$$\frac{\partial}{\partial t}(E_C) + \frac{\partial}{\partial x}(u[E_C + P]) - \frac{\partial}{\partial x} \left(\kappa \frac{\partial T}{\partial x} + \rho D \sum_{i=1}^{NS} \left[h_{i_0} \frac{\partial Y_i}{\partial x} \right] \right) = 0 \quad (1)$$

$$\frac{\partial}{\partial t}(\rho Y_i) + \frac{\partial}{\partial x}(\rho u Y_i) - \frac{\partial}{\partial x} \left(\rho D \frac{\partial Y_i}{\partial x} \right) = w_i \quad (2)$$

Frequently, the total enthalpy of the gas is described as in Eq. (3) to include the mixture heat of formation at reference state “ref” or “0” and the change in enthalpy from that state.

$$E_C = \frac{\rho u^2}{2} + \rho \sum_{i=1}^{NS} \left[h_{i_0} Y_i + \int_{T_0}^T C_p dT \right] = \frac{\rho u^2}{2} + \rho \sum_{i=1}^{NS} [h_i Y_i] \quad (3)$$

However, Eq. (2) can be scaled by the enthalpy for each species, summed over all species, and then subtracted from the energy equation to consolidate the interaction between the chemical reactions and the fluid dynamics (Eq. (4)).

$$\frac{\partial}{\partial t}(E_C) + \frac{\partial}{\partial x}(u(E_C + P)) - \left(\kappa \frac{\partial T}{\partial x} \right) = \sum_{i=1}^{NS} h_i \dot{w}_i = \dot{Q} \quad (4)$$

This reveals the chemical reactions as an energy source term to the fluid dynamic terms. Of course, this is merely a change in the bookkeeping of the energy storage modes of the system, placing the chemical potential on the side of the ledger not available to the fluid dynamic interactions until made available as thermal energy during the exothermic reaction. This bookkeeping then presents

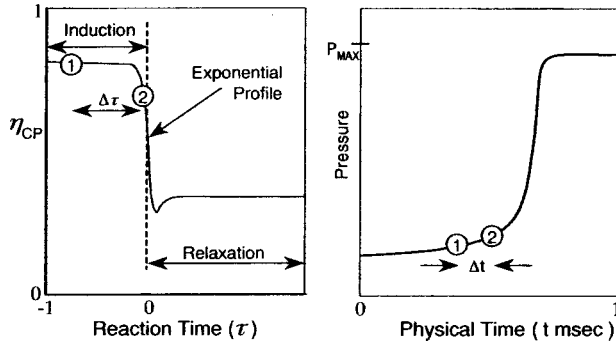


Fig. 2 Reaction profiles

the interaction question as: what are the minimum independent variables and functional form required to describe \dot{Q} ?

Response Modeling Equations

A typical heat release profile (illustrated on the left side of Fig. 2) is divided into the induction and relaxation phases, each described by an exponential profile. The abscissa is not to scale and represents time, and the ordinate represents any modeled parameter such as heat release, density, pressure, or concentration of one species. In each case we derive a mapping function, which represents the induction and relaxation phases of the reaction. The mathematical model results in coupled non-linear equations. For the induction and relaxation phases these equations are linearized about the beginning reactants and resultant products at equilibrium, respectively. Linearization is not possible for the exponential phase due to the non-equilibrium nature of the reaction during that phase. Instead the curve fits for the induction and relaxation phases are extended to the mid point of the reaction by treating the two curves as one continuous composite curve. Thus in Fig. 2, $-1 < \tau < +\infty$ and $0 < \eta_{CP} < 1.0$.

Each step in the solution process maps the chemical state at physical (solution) time t into the corresponding reaction time τ , which along with the system total energy and density determines the species. The model is advanced by Δt and the process is repeated. To each physical time t corresponds a chemical time τ (representing amounts of species).

Previous work, [20], established that this approach successfully represents a constant density process with fixed fuel-air ratio. Results indicated the initial system reactants, temperature and density are sufficient to predict the time evolution of the heat release profile, and detailed species concentration throughout the reaction. This approach is essentially limited to constant energy with no diffusion effects.

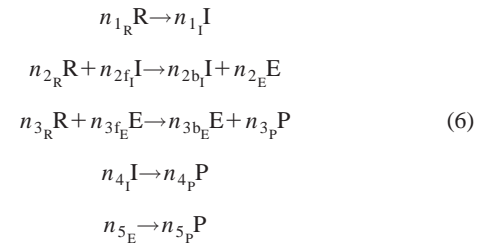
The detailed integration of the modeled reaction system requires two elements, the integrator, and the reaction rate set. Although not limiting, in this paper we used the Gear algorithm, [21], for integration of numerically stiff dynamic systems, and the detailed chemical-kinetics subroutines from the CHEMKIN, [22], library.

The following examples use the detailed propane-oxygen reaction set, [23]. This sample reaction set was selected due to its basic hydrocarbon structure and relatively smaller reaction set (isooctane has about 370 species and 1600 equations, and propane has about 54 species and 200 equations)

The normalized chemical potential energy (Eq. (5)) and nondimensional induction time τ are the basic parameters representing the heat release profile development. This focus is justified since the profile characterizes the heat release, and therefore the chemical state (species composition) of the gas.

$$\eta_{CP} = \frac{\sum_{\text{Reactants}} h_{i_0} Y_i - \sum_{\text{Products}} h_{i_0} Y_i}{\sum_{\text{Reactants}} h_{i_0} Y_i - \sum_{\text{Products}} h_{i_0} Y_i} \quad (5)$$

The profile shape for the heat release function is developed from a model system (represented by Eq. (6)) consisting of four species and five reactions. This is the minimum number required to represent reactants, products, and intermediate species. The model system is designed to mimic in outline form the features of the full combustion system. The first species P is used to represent all reactants, and a second model species II represents the products of the reaction at completion. It was determined that the model equation needs two types of intermediate (radical) species. The first, I, represents an induction species, which reflects the dissociation of fuel during the beginning stages of the reaction. The second intermediate species E represents the activity of the radical species, which dominate the vigorous, explosion phase of the reaction, such as the hydroxyl radical.



The first reaction in (6) represents the initiating reaction responsible for the initial population of the radical pool. The second and third reactions represent branching and propagating reactions responsible for the rapid growth of the radical pool. Finally, the fourth and fifth reactions terminate the reaction. The stoichiometric coefficients are included as parameters here since each of the reactions in this model system represents a set of reactions in a real system. The rate of growth of the radical populations is controlled by ratios n_{2b_1}/n_{2f_1} , n_{2E}/n_{2f_1} , and n_{3b_E}/n_{3f_E} . The reaction equations are formulated in standard Arrhenius form, and coupled with the energy equation. This is given by the sum of the energies of the species, each computed by the mass-averaged energy for a Gibbs-Dalton mixture of semi-perfect gases. The resulting set of highly non-linear differential equations cannot be integrated. Therefore, perturbations are taken about the initial conditions, producing the following set of linear differential equations.

$$\frac{d}{dt} \begin{Bmatrix} \delta R \\ \delta I \\ \delta E \end{Bmatrix} = \begin{bmatrix} a_{RR} & a_{RI} & a_{RE} \\ a_{IR} & a_{II} & a_{IE} \\ a_{ER} & a_{EI} & a_{EE} \end{bmatrix} \begin{Bmatrix} \delta R \\ \delta I \\ \delta E \end{Bmatrix} + \begin{Bmatrix} b_R \\ b_I \\ b_E \end{Bmatrix} \quad (7)$$

This resulting set of three linear differential equations has three characteristic roots (eigenvalues) resulting in the functional form:

$$\begin{aligned} \delta R &= a_{R1} e^{\Lambda_{R1} t} + a_{R2} e^{\Lambda_{R2} t} + a_{R3} e^{\Lambda_{R3} t} \\ \delta I &= a_{I1} e^{\Lambda_{I1} t} + a_{I2} e^{\Lambda_{I2} t} + a_{I3} e^{\Lambda_{I3} t} \\ \delta E &= a_{E1} e^{\Lambda_{E1} t} + a_{E2} e^{\Lambda_{E2} t} + a_{E3} e^{\Lambda_{E3} t} \end{aligned} \quad (8)$$

Thus, the expression for the chemical potential Eq. (5) takes a form similar to Eq. (9). A similar expression is derived for the relaxation phase of the reaction, but with the equations linearized around the equilibrium state of the mixture of products. The heat release and heat-release rate are made continuous at the midpoint of the reaction. The top expression in Eq. (9) applies to the induction phase, and the bottom expression applies to the relaxation phase. Here, τ is the reaction time normalized by the induction time.

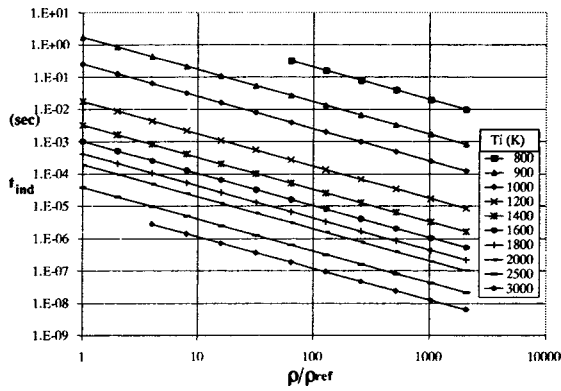


Fig. 3 Induction time

$$\begin{aligned}
 c_P &= a_{L0} + a_{L1}e^{\Lambda_{L1}\tau} + a_{L2}e^{\Lambda_{L2}\tau} + a_{L3}e^{\Lambda_{L3}\tau} \\
 &= a_{R0} + a_{R1}e^{\Lambda_{R1}\tau} + a_{R2}e^{\Lambda_{R2}\tau} + a_{R3}e^{\Lambda_{R3}\tau} \quad (9)
 \end{aligned}$$

The resulting three exponential profiles in Eq. (9) are based on the key parameters of the induction time and the equilibrium heat release, plus an additional five parameters to determine the profile shape on each side (induction and relaxation) of the reaction midpoint. For the induction phase expression, the five parameters consist of three eigenvalues and the time and magnitude of the minimum heat release. This minimum heat release accounts for the reduction in the sensible energy of the system as the reactants begin to dissociate into radicals (which have higher heats of formation).

Figures 3 and 4 show the induction time and equilibrium heat release for select sample cases of propane-oxygen mixtures. Each point represents different initial temperature-density conditions. The reference density is the minimum value considered in the parametrics, $\rho_{ref} = 2 \times 10^{-5}$ gm/cc.

Computation of the three eigenvalues is based on matching conditions at: the reaction start; at 10%, and 50% of the heat release reaction; and at the minimum reaction heat release. The heat release profile slope was set to zero at the point of minimum reaction heat release, and an additional matching point was chosen mid way between the initial time and the time at minimum reaction heat release. For illustration, Figs. 5 and 6 show the major (largest) eigenvalues for the induction (Λ_{L1}) and relaxation (Λ_{R1}) phases.

Figure 7 is a comparison of results from the full integration using CHEMKIN and the response modeling technique. The initial conditions were 2.56×10^{-3} gm/cc and 2500 K. The time scale here is expanded around the midpoint of the reaction heat

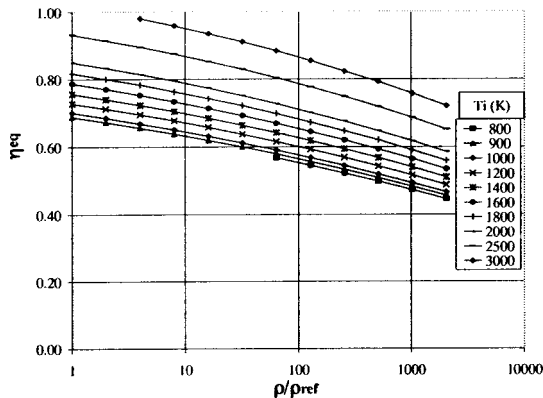


Fig. 4 Equilibrium heat release

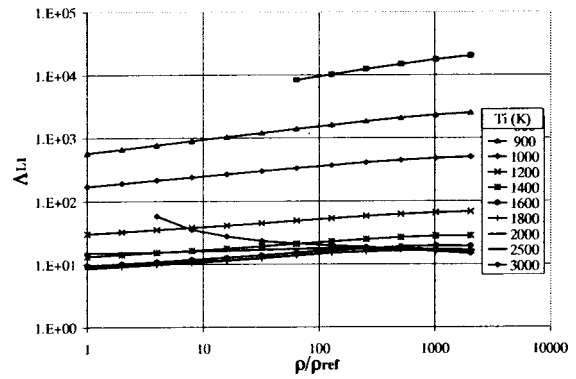


Fig. 5 First induction characteristic

release (defined as $\tau=0$). Even at this expanded scale, it can be seen that the model is capturing the heat release quite accurately.

Theoretical Approach for Gas Turbines

Figure 8 shows the parallel advance of the gas dynamic and chemical state during the solution process. The system starts from state 1 at time t_1 and the gas dynamic variables are advanced to time t_2 . In parallel, the chemical state is mapped through a reaction profile whose coefficients are mapped by a neural network to obtain the reaction time τ . The solution is advanced $\Delta\tau$ and the map is reversed to provide the chemical state at time τ_2 , corre-

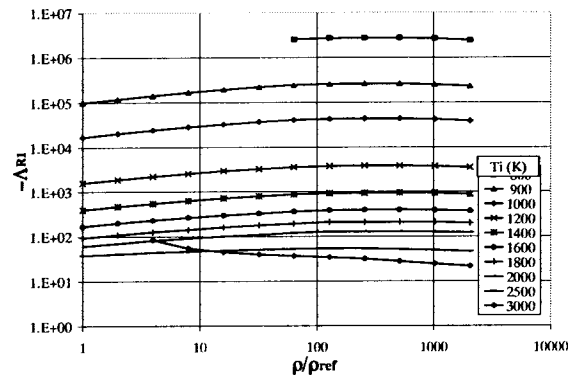


Fig. 6 First relaxation characteristic

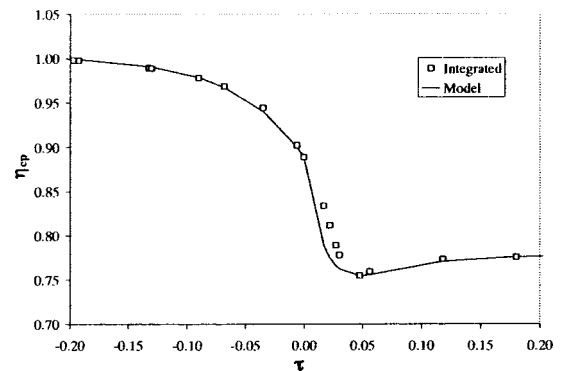


Fig. 7 Chemical potential

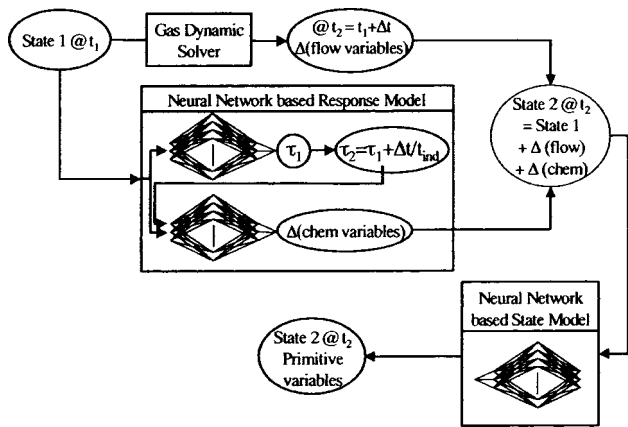


Fig. 8 Response map with neural networks

sponding to t_2 . The final step uses a separate neural network to “decode” the conservation variables at t_2 into the corresponding primitive variables.

Figure 9 illustrates the application of response mapping to gas turbines. In a pre-processor step, the response of the chemical system is mapped parametrically starting from various temperatures and densities. The results (pressure, temperature, and selected species) are mapped into a response model. These mapped results are coupled to a CFD solver.

The preceding method is limited to reactions without diffusion. Extrapolation of the foregoing to combustion with diffusion is relatively straightforward. The method is extended to include a diffusion parameter for gas turbine combustion. The diffusion parameter enables parametric modeling of the reaction rate as a function of fundamental diffusion phenomena.

Implementation for Diffusion

Consider a fluid element as a thermodynamic system in a Lagrangian frame of reference. If the density is held constant, the total energy E_C of the element is constant except for the effects of diffusion, which is accounted for as explained below.

At a given condition of temperature, pressure etc as specified at any point in the reaction, and in the absence of work, Eq. (1) is reduced to Eq. (10).

$$-C_p L_E \frac{\partial T}{\partial x} = \sum_{i=1}^{NS} \left[h_{i0} \frac{\partial Y_i}{\partial x} \right] \quad (10)$$

where L_E is the Lewis number, defined as the ratio of chemical diffusion divided by molecular diffusion ($L_E = \kappa/D$). The Lewis number represents the balance of energy flux between thermal diffusion and the diffusion of mixture heat of formation, and it is

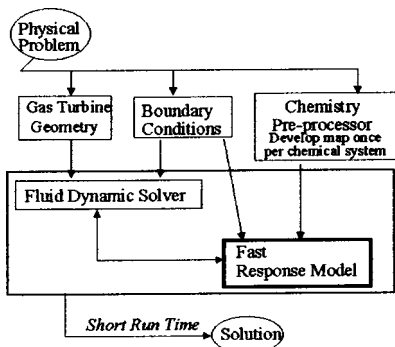


Fig. 9 Application of response mapping to gas turbines

the energy constraint on the system. We can thus diffuse species into the reaction and calculate the energy change due to diffusion at different points in the reaction. In addition to temperature and density we can now add diffusion as a new variable in the mapping process.

Consider the fluid element in the induction phase interacting with another (neighboring) element, which is in the heat release phase of the reaction. In this case, thermal energy is conducted from the second into the first element. At the same time, however, species at high chemical potential energy (reactants) are diffusing from the first to the second element and species with lower chemical potential energy (more products) are diffusing into the first element. This represents a net diffusion of chemical potential energy in the direction opposite to the thermal diffusion. If these two fluxes balance, the fluid element remains at constant energy.

A straightforward way to match the thermal energy and the heat of formation fluxes is to determine the equilibrium state for the given initial conditions and then mix the equilibrium species into the reacting system at a specified rate. If this is done at constant system energy E_C , the effect is the same as specifying the thermal energy diffusion required to satisfy Eq. (10). Thus, the source term for the detailed integration is modified to include a diffusion term to the equilibrium state:

$$\dot{w}'_i = \dot{w}_i + \delta_{EQ}(Y_{iEQ} - Y_i) \quad (11)$$

where for the purpose of generating a response model, δ_{EQ} is a chosen parameter signifying the rate of diffusive exchange between the fluid element undergoing reaction and a reservoir at the equilibrium condition for the same constituents, energy and density.

An illustration of the use of such a parameter using CHEMKIN is shown in Fig. 10. The reaction in this case is for propane air at an initial temperature of 950 K and constant density of 3.0×10^{-4} gm/cc. The reaction was started with a species distribution reflecting reaction progress of 2%. That is, 2% of the total heat release from pure reactants to the equilibrium state has taken place at time zero. The time scale in Fig. 8 is normalized by the induction time of the slowest reaction ($\delta_{EQ} = 0$).

As expected, the increase in diffusion parameter increases the effective reaction rate. Therefore such a parameter can model the effects of a diffusion-dominated reaction on the reaction. The selection of the equilibrium state as the reference reservoir for the diffusion has the property that all of the reaction traces converge to the same final state (products). That is, they converge to equilibrium. This would not be the case for a diffusion reference reservoir selected at a different point along the reaction path. For example, if the reference is chosen as the reaction midpoint, reac-

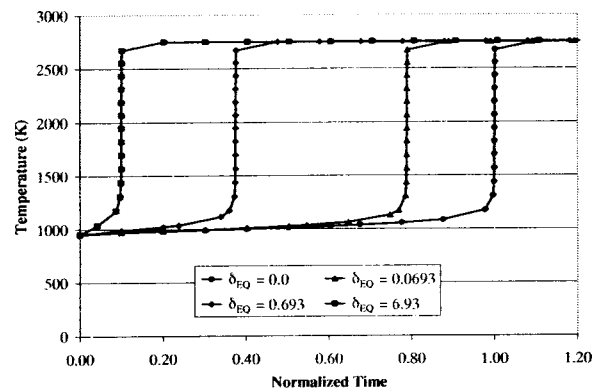


Fig. 10 Effect of species diffusion

tions with large, constant diffusion parameters would continuously be pushed away from equilibrium as they approached that state.

Summary and Conclusions

Response modeling can represent chemical systems consisting of large reaction sets. Pre-integrated response mapping presented here has the additional benefit of removing the stiffness from the dynamic system of equations. This approach is shown to work satisfactorily for reacting systems without diffusion, and the method is further extended for use in reacting systems with diffusion, such as gas turbine combustion.

The reaction mechanisms are pre-integrated with a detailed method. The integration is done for different representative mixture densities, temperatures and diffusion parameters. A sample parametric map derived for a given reaction set with known products of combustion (which serves as the reservoir reference state) models the effect of diffusion.

The methodology presented provides the means to couple these pre-integrated model equations with traditional Navier-Stokes CFD solvers to predict the formation of species in gas turbine combustors. The information from the high eigenvalues of formation of species have been included in the pre-integrated maps, but the linearized model equations are not stiff, thus permitting quicker computation of the effect of design changes on pollutant formation in gas turbine engines. This representation, coupled with the equation of state, produces a system capable of accurately replacing the detailed reaction integration in the analysis of a coupled gas dynamic system with nonequilibrium chemistry.

Nomenclature

| | |
|----------------------|---|
| C_p | = specific heat at constant pressure |
| D | = molecular diffusivity coefficient |
| E | = model explosion species concentration |
| δE | = normalized change in E |
| E_C | = total energy including heat of formation |
| η_{EQ} | = potential at equilibrium |
| η_{CP} | = normalized chemical potential |
| h_i | = enthalpy of species i |
| h_{i0} | = heat of formation of species i |
| I | = model induction species concentration |
| δI | = normalized change in I |
| κ | = thermal diffusivity coefficient |
| L_E | = Lewis number |
| Λ_{Li} | = induction characteristic for species i |
| Λ_{Ri} | = relaxation characteristic for species i |
| $n_{1i} - n_{5i}$ | = stoichiometric coefficients |
| NS | = number of species |
| P | = pressure |
| \mathcal{P} | = model products |
| $\delta \mathcal{P}$ | = normalized change in \mathcal{P} |
| \dot{Q} | = heat release rate |
| ρ | = density |
| ρ_{ref} | = reference density (2×10^{-5} gm/cc) |
| R | = model reactants concentration |
| δR | = normalized change in R |
| t | = time |
| t_{ind} | = induction time (sec) |
| τ | = time normalized by induction time |
| T | = temperature |
| T_0 | = reference temperature |
| u | = flow velocity in the x -direction |

| | |
|--------------|---|
| \dot{w}_i | = rate of formation of species i |
| \dot{w}'_i | = modified rate of formation of species i |
| x | = spatial variable |
| δ | = diffusion parameter |
| Y_i | = mass fraction of species i |

References

- [1] Lefebvre, A. H., 1995, "The Role of Fuel Preparation in Low-Emission Combustion," *ASME J. Eng. Gas Turbines Power*, **117**, pp. 617–654.
- [2] Rizk, N. K., and Mongia, H. C., 1994, "Emissions Predictions of different Gas Turbine Combustors," AIAA Paper No. 94-0118.
- [3] Jones, W. P., and Priddin, C. H., 1978, "Predictions of the Flow Field and Local Gas Composition in Gas Turbine Combustors," *Proceedings of the 17th International Symposium on Combustion*, The Combustion Institute, Pittsburgh, PA, pp. 399–409.
- [4] Smith, G. P., Golden, D. M., Frenklach, M., Moriarty, N. W., Eiteneer, B., Goldenberg, M., Bowman, C. T., Hanson, R. K., Song, S., Gardiner, W. C., Jr., Lissianski, V. V., and Qin, Z., GRI-Mech 3.0 http://www.me.berkeley.edu/gri_mech/
- [5] Zeldovich, Ya. B., Sadovnikov, P. Ya., and Frank Kamnetskii, D. A., 1947, "Oxidation of Nitrogen in Combustion," Academy of Sciences of the USSR, Moscow.
- [6] Miller, J. A., and Bowman, C. T., 1989, "Mechanism and Modeling of Nitrogen Chemistry in Combustion," *Prog. Energy Combust. Sci.*, **15**, pp. 287–338.
- [7] Frenklach, M., 1991, "Reduction of Chemical Reactions," AIAA Conference on Combustion Modeling, Chap. 5.
- [8] Westbrook, C. K., and Dryer, F. L., 1981, "Simplified Reaction Mechanisms for the Oxidation of Hydrocarbon Fuels in Flames," *Combust. Sci. Technol.*, **27**, pp. 31–43.
- [9] Jachimowski, C. J., 1985, "A Simplified Hydrocarbon Reaction Mechanism for Combustion Applications," *J. Propul. Power*, **1**(5).
- [10] Montgomery, C. J., Cremer, M. A., Heap, M. P., Chen, J. Y., Westbrook, C. K., and Maurice, L. Q., 1999, "Reduced Chemical Kinetic Mechanisms for Hydrocarbon Fuels," AIAA-99-2220.
- [11] Maas, U., and Pope, S. B., 1992, "Simplifying Chemical Kinetics: Intrinsic Low-Dimensional Manifolds in Composition Space," *Combust. Flame*, **88**, pp. 239–264.
- [12] Maas, U., and Pope, S. B., 1992, "Implementation of Simplified Chemical Kinetics Based on Intrinsic Low-Dimensional Manifolds," *Twenty-Fourth Symposium (International) on Combustion*, The Combustion Institute, Pittsburgh, PA, pp. 103–112.
- [13] Maas, U., and Pope, S. B., 1994, "Laminar Flame Calculations Using Simplified Chemical Kinetics Based on Intrinsic Low-Dimensional Manifolds," *Twenty-Fifth Symposium (International) on Combustion*, The Combustion Institute, Pittsburgh, PA, pp. 1349–1356.
- [14] Blasenbrey, T., Schmidt, D., and Maas, U., 1998, "Automatically Simplified Chemical Kinetics and Molecular Transport and Its Applications in Premixed and Non-Premixed Laminar Flame Calculations," *Twenty-Seventh Symposium (International) on Combustion*, The Combustion Institute, Pittsburgh, PA, pp. 505–511.
- [15] Korbenikov, V. P., Lenen, V. A., Markov, V. V., and Chernyi, G. G., 1972, "Propagation of Blast Waves in a Combustible Gas," *Acta Astronautica* **529**.
- [16] Taki, S., and Fujiwara, T., 1981, "Numerical Simulation of Triple Shock Behavior of Gaseous Detonation," *Eighteenth Symposium (International) on Combustion*, The Combustion Institute, Pittsburgh, PA, pp. 1671–1681.
- [17] Oran, E. S., Boris, J. P., Young, T., Flanigan, M., Burks, T., and Picone, M., 1981, "Numerical Simulations of Detonations in Hydrogen-Air and Methane-Air Mixtures," *Eighteenth Symposium (International) on Combustion*, The Combustion Institute, Pittsburgh, PA, pp. 1641–1649.
- [18] Frenklach, M., and Rabinowitz, M. J., 1988, "Optimization of Large Reaction Systems," *Proceedings of 12th IMACS World Congress on Scientific Computations*, **3**, pp. 602–604.
- [19] Marsden, Jr., A. R., Frenklach, M., and Reible, D. D., 1987, "Increasing the Computational Feasibility of Urban Air Quality Models that Employ Complex Chemical Mechanisms," *J. Air Pollut. Control Assoc.*, **37**(4), pp. 370–376.
- [20] Dyer, S. R., and Korakianitis, T., 2000, "Hierarchical development of Heat Release Profiles for Non Equilibrium Detonation Models," submitted to Combustion and Flame, Washington University, ICE lab report 2000-ICE-03, May.
- [21] Shampine, L. F., and Gear, C. W., 1979, "A User's View of Solving Stiff Ordinary Differential Equations," *SIAM Rev.*, **21**(1).
- [22] Kee, R. J., Miller, J. A., and Jefferson, T. H., 1980, "CHEMKIN: A General-Purpose, Problem-Independent, Transportable," FORTRAN Chemical Kinetics Package, Sandia National Laboratory, SAND 80-8003.
- [23] Westbrook, C. K., and Pitz, W. J., 1983, "A Comprehensive Chemical Kinetic Reaction Mechanism for Oxidation and Pyrolysis of Propane and Propene," *Combust. Sci. Technol.*, **37**, pp. 117–152.

Degradation Effects on Combined Cycle Power Plant Performance— Part III: Gas and Steam Turbine Component Degradation Effects

A. I. Zwebek
P. Pilidis

Department of Power Engineering and
Propulsion,
School of Engineering,
Cranfield University,
Bedford MK43 0AL, UK

This paper presents an investigation of the degradation effects that gas and steam turbine cycles components have on combined cycle (CCGT) power plant performance. Gas turbine component degradation effects were assessed with TurboMatch, the Cranfield Gas Turbine simulation code. A new code was developed to assess bottoming cycle performance deterioration. The two codes were then joined to simulate the combined cycle performance deterioration as a whole unit. Areas examined were gas turbine compressor and turbine degradation, HRSG degradation, steam turbine degradation, condenser degradation, and increased gas turbine back pressure due to HRSG degradation. The procedure, assumptions made, and the results obtained are presented and discussed. The parameters that appear to have the greatest influence on degradation are the effects on the gas generator. [DOI: 10.1115/1.1639007]

Introduction

The rapid improvement of gas turbine technology in the 1990s drove combined cycle thermal efficiency to nearly 60% with natural gas as a fuel (Briesch and Bannister [1]). It will probably go even higher in the future. This high plant efficiency along with low emissions and competitive capital and running costs made the combined cycle gas turbine (CCGT) plant a very popular prime mover for electricity generation.

This interest increase in the CCGT plants led to the users of such plants to become more concerned about the plant's behavior after running for long times. As a result, simulation codes are developed to predict the behavior of such power plants and their subsystems on a thermo-fluid dynamic basis (Erbes and Gay [2], Roy-Aikins [3], and Thermoflow [4]).

This is the third in a series of three technical papers looking at the degradation effects that different components of combined cycle have on the plant's performance.

The first paper (Zwebek and Pilidis [5]) presented the effects that gas turbine components degradation have on gas turbine and hence on the overall CCGT plant, the second paper (Zwebek and Pilidis [6]) discussed the steam (bottoming) cycle component degradation effects have on CCGT plant. The conclusion of the two papers mentioned above is summarized herein. In the first paper, [5], it was concluded that the GT turbine degradation has the utmost effect on gas turbine as well as on steam turbine cycles performances compared to GT compressor. Also, it was shown that the GT exhaust temperature has a predominant effect on steam cycle efficiency over the GT exhaust mass flow. Because the CCGT plant is more dependent on the gas turbine, and as it was expected, the CCGT plant performance was more sensitive to change in gas turbine cycle conditions than to the changes in steam turbine cycle conditions.

The conclusion from the second paper, [6], was that, within the HRSG unit, the evaporator degradation is the utmost effecting fault on steam turbine cycle performance compared to superheater and economizer. Also concluded that, the steam turbine isentropic

efficiency as a performance parameter has the uppermost effect on steam turbine cycle power and efficiency. Finally, the effects of HRSG and condenser degradations on steam cycle and hence on CCGT plants performance is very low compared to the steam turbine unit components degradation.

Gas/Steam Turbine Performance Deterioration. Even under normal engine operating conditions, with good inlet filtration systems, and using a clean fuel, the gas turbine engine flow path components will become fouled, eroded, corroded, and covered with rust scale, (Diakunchak [7], Lakshminarasimha et al. [8], Tabakoff [9], and Tabakoff et al. [10], and others). The results will then be an engine performance deterioration. Since the gas turbine, in this case, is connected to another plant (steam cycle) which is entirely dependent on it, then the concern due to performance deterioration will increase. This is due to the fact that any failure or malfunctioning within the gas turbine will be magnified as it would be affecting the two (CCGT) plants at the same time.

This paper explores different component degradation effects on a simple combined cycle (CCGT) plant of Fig. 1. The plant under consideration is composed of a single-shaft industrial gas turbine coupled with a single-pressure HRSG steam (bottoming) cycle.

The (design point) specifications of both gas and steam turbine plants used with this unfired cycle were chosen in such a way that they represent an existing typical real cycle, as follows:

Gas Turbine Specifications

inlet mass flow=408.6 kg/sec
compressor pressure ratio=15.2
turbine entry temperature=1697.80 K
exhaust mass flow=419.4 kg/sec
exhaust temperature=871.24 K
power=165.93 MW
thermal efficiency=35.57%

Steam Turbine Specifications

live steam pressure=65.4 bar
live steam temperature=537.8°C
steam mass flow=67 kg/sec
steam turbine isentropic effc.=89.48%
superheater surface area=8424.8 m²
evaporator surface area=29315.6 m²
economizer surface area=38004.1 m²
condenser surface area=3942.9 m²

Contributed by the International Gas Turbine Institute (IGTI) of THE AMERICAN SOCIETY OF MECHANICAL ENGINEERS for publication in the ASME JOURNAL OF ENGINEERING FOR GAS TURBINES AND POWER. Paper presented at the International Gas Turbine and Aeroengine Congress and Exhibition, Amsterdam, The Netherlands, June 3–6, 2002; Paper No. 2002-GT-30513. Manuscript received by IGTI, Dec. 2001, final revision, Mar. 2002. Associate Editor: E. Benvenuti.

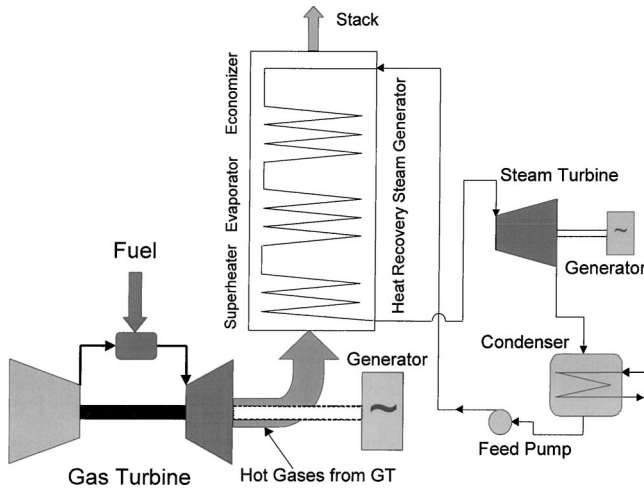


Fig. 1 Schematic diagram of a single pressure CCGT power plant

HRSG efficiency=81.11%
 steam turbine plant power output=76.4541 MW
 steam turbine plant efficiency=33.97%

The effects of the gas turbine degradation on steam cycle, and hence on the CCGT plants performance as whole was investigated. The faults investigated were the following:

- i. compressor isentropic effc. degradation,
- ii. turbine isentropic efficiency degradation,
- iii. compressor and turbine fouling,
- iv. compressor and turbine erosion,
- v. economizer degradation,
- vi. evaporator degradation,
- vii. superheater degradation,
- viii. steam turbine fouling,
- ix. steam turbine erosion,
- x. ST isentropic efficiency degradation,
- xi. condenser degradation,
- xii. combination of all faults mentioned above, and
- xiii. gas turbine back pressure increase due to heat exchanger (HRSG) surfaces fouling.

The terms fouling and erosion are used in the context of other work, (Diakunchak [7] and Lakshminarasimha et al. [8]). In the case of gas turbine unit, because the combustion system is not likely to be a direct cause of gas turbine performance deterioration (Diakunchak [7]) it was assumed not to degrade for the following reasons:

- i. Combustion chamber faults that affect GT overall performance are rare in comparison to those faults that may occur in the compressor and turbine.
- ii. Any malfunctioning in the combustion chamber would mean increased emissions, which is not allowed by environmental laws in many places.

Fault Representation

In order to investigate the effects of faults mentioned in previous section on the Gas/steam turbine plants performance as a standing alone units, and hence on CCGT plant as a whole, these faults were fed into the program as a percent reduction of the original design point value (shown 0.0 in Table 1). This is done as follows:

Fouling: GT compressor, GT turbine, and ST turbine fouling is represented by reduced flow capacity at the inlet of the component plus a reduction in the component isentropic efficiency. By doing so, it is assumed that there is a blockage in the inlet area of the

Table 1 Representation of component degradation

| Fault | Represented By | Range |
|---------------------------|-----------------------|-------------|
| Compressor fouling | Drop in Γ | 0.0–(–5.0%) |
| Compressor erosion | Drop in η_C | 0.0–(–2.5%) |
| | Drop in Γ | 0.0–(–5.0%) |
| Turbine fouling | Drop in η_C | 0.0–(–2.5%) |
| | Drop in Γ | 0.0–(–5.0%) |
| Turbine erosion | Drop in η_T | 0.0–(–2.5%) |
| | Rise in Γ | 0.0–(+5.0%) |
| FOD | Drop in η_T | 0.0–(–5.0%) |
| Gas turbine back pressure | GT Back pressure rise | 0.0–(+3.0%) |
| Economizer degradation | Drop in U | 0.0–(–5.0%) |
| Evaporator degradation | Drop in U | 0.0–(–5.0%) |
| Superheater degradation | Drop in U | 0.0–(–5.0%) |
| Condenser degradation | Drop in U | 0.0–(–5.0%) |
| Steam turbine fouling | Drop in Γ | 0.0–(–5.0%) |
| | Drop in η_T | 0.0–(–2.5%) |
| Steam turbine erosion | Rise in Γ | 0.0–(+5.0%) |
| | Drop in η_T | 0.0–(–2.5%) |
| FOD | Drop in η_T | 0.0–(–5.0%) |

component due to fouling along with a decrease in the component's isentropic efficiency due to surface roughness, for example.

Erosion: Compressor erosion is represented by a lower inlet mass flow capacity and a reduction in compressor isentropic efficiency. On the other hand, GT and ST turbines erosion is represented by an increased flow capacity plus a reduction in the turbine isentropic efficiency (Lakshminarasimha et al. [8]).

These two phenomena are represented by changing the so-called nondimensional mass flow (Eq. (1)) of the component maps (Table 1).

$$\frac{\dot{W}\sqrt{T_i}}{PA} \text{ is increased or reduced} \quad (1)$$

Component Efficiency Degradation: This is modeled by reducing the component isentropic efficiency of the appropriate map and keeping all other parameters at their design point (DP) levels. In this case, it was assumed that the component isentropic efficiency might decrease from its DP value due to any reason, such as blade tip rubs or FOD.

Heat Exchanger Degradation: The degradation of either of the heat exchangers (economizer, evaporator, superheater, and condenser) was simulated by assuming a percent reduction in the original DP value of the overall heat transfer coefficient of the heat exchanger in concern.

Gas Turbine Back Pressure: The increased back pressure at the gas turbine exhaust is represented as an increase in the GT exhaust outlet pressure.

The above-mentioned faults are applied to different components of the plant in different values. Table 1 summarizes these faults and their ranges at which they were applied to each component.

Therefore, throughout this study, it was assumed that there was no component washing or any type of maintenance carried out on the gas and steam turbine plants until the deterioration reached 5% from the original design point performance.

Combined Cycle Degradation Simulation

Before starting any degradation simulations it was necessary to establish a datum working line (design point performance) of both plants. This base line performance point is represented by (0.0) value in Table 1 above and on all deterioration graphs shown below. Once the design point performance has been identified, then the magnitude of faults representing a physical fault of the component in consideration, (see "faults representation"), to be implanted on each component has to be established.

Unfortunately, although there is a lot of work published on the subject of gas turbine performance deterioration (Tabakoff [9],

Table 2 Component isentropic efficiency variation with degradation

| Physical Fault | Nondimensional Mass Flow Change (A) | Isentropic Efficiency Change (B) | Ratio A:B |
|-----------------------|---|----------------------------------|--------------|
| Compressor fouling | $\Gamma_c \downarrow$ | $\eta_c \downarrow$ | $\sim 1:0.5$ |
| Compressor erosion | $\Gamma_c \downarrow$ | $\eta_c \downarrow$ | $\sim 1:0.5$ |
| Compressor corrosion | $\Gamma_c \downarrow$ | $\eta_c \downarrow$ | $\sim 1:0.5$ |
| Turbine fouling | $\Gamma_T \downarrow$ | $\eta_T \downarrow$ | $\sim 1:0.5$ |
| Turbine erosion | $\Gamma_T \uparrow$ | $\eta_T \downarrow$ | $\sim 1:0.5$ |
| Turbine corrosion | $\Gamma_T \downarrow$ | $\eta_T \downarrow$ | $\sim 1:0.5$ |
| Foreign object damage | $\Gamma_{C/T} \downarrow$ | $\eta_{C/T} \downarrow$ | $\sim 1:2.0$ |
| Thermal distortion | $\Gamma_T \uparrow \downarrow$ | $\eta_{C/T} \downarrow$ | $\sim 1:2.0$ |
| Blade rubbing | $\Gamma_C \downarrow$ & $\Gamma_T \uparrow$ | $\eta_{C/T} \downarrow$ | $\sim 1:2.0$ |

Tabakoff et al. [10], Diakunchak [7], and Lakshminarasimha et al. [8], and others), the applied degradation magnitude to each component, when simulating gas turbines deterioration performance, in most cases is either arbitrary or based on some published experimental results. Therefore, in present study the values mentioned by Diakunchak [7] and Escher [11] were taken as a guidelines from which the implanted faults were estimated. Table 2 (Zwebek and Pilidis [5]) shows a summary of how component isentropic efficiency changes vary with degradation. These values were applied in all calculations to the appropriate components.

Based on what is mentioned above, in the case of steam turbine plant, it was also assumed that every 1.0% deterioration in mass flow capacity (fouling or erosion) would result in a deterioration of (0.50%) in steam turbine isentropic efficiency.

Unfortunately, not much literature was found on the subject of CCGT plant degradation, or on modeling of this problem, including the effect of GT back pressure rise. Therefore to simulate the effect of back pressure on gas turbine performance, due to HRSG degradation some assumptions have been made. An increase in back pressure by ≈ 0.0025 atm results in a reduction in gas turbine power by $\approx 0.3\%$. Typical back pressure ranges from 0.025 to 0.037 atm above the design value. Because of the inherent problems which accompanies the increase of back pressure, e.g., high

Table 3 GT back pressure distribution along with other components degradation

| GT Back Pressure | GT Fouling | GT Erosion |
|------------------|------------|------------|
| +1.0% | -1.0% | +1.0% |
| +1.5% | -2.0% | +2.0% |
| +2.0% | -3.0% | +3.0% |
| +2.5% | -4.0% | +4.0% |
| +3.0% | -5.0% | +5.0% |

torque on the shaft, coupling forces on thrust bearing, and vibration, it was assumed that maximum it can go up to 0.03 atm over the DP value.

It is worth reminding the reader here that the values in Fig. 3 and in the following successive figures are also including the gas turbine back pressure rise due to HRSG degradation. This is accomplished by implanting a value of GT exhaust back pressure rise with a corresponding GT degradation (fouling/erosion) value as shown in Table 3.

Gas Turbine Degradation Simulation Results

Due to its working nature and depending on the place where it is installed, it was assumed that the gas turbine might foul or erode. Therefore, the simulation strategy of the gas turbine was divided into two different categories. The first strategy was to assume that the gas turbine will foul up (-5.0%) from its original DP performance. On the other hand, the second strategy assumes an erosion in gas turbine gas path components up to (+5.0%) from their DP performance. In parallel with each of the cases mentioned above, an amount increase in gas turbine back pressure due to degraded HRSG was assumed as shown in Table 3.

As Fig. 2 shows, a back pressure increase of (3.0%) resulted in a reduction in gas turbine thermal efficiency and power by (-2.0%) approximately. While the exhaust mass flow was almost constant, the exhaust temperature increased by about (0.75%) from its original DP value.

Figure 3 summarizes the main performance parameters of gas turbine and how they vary with degradation. As it can be seen, it

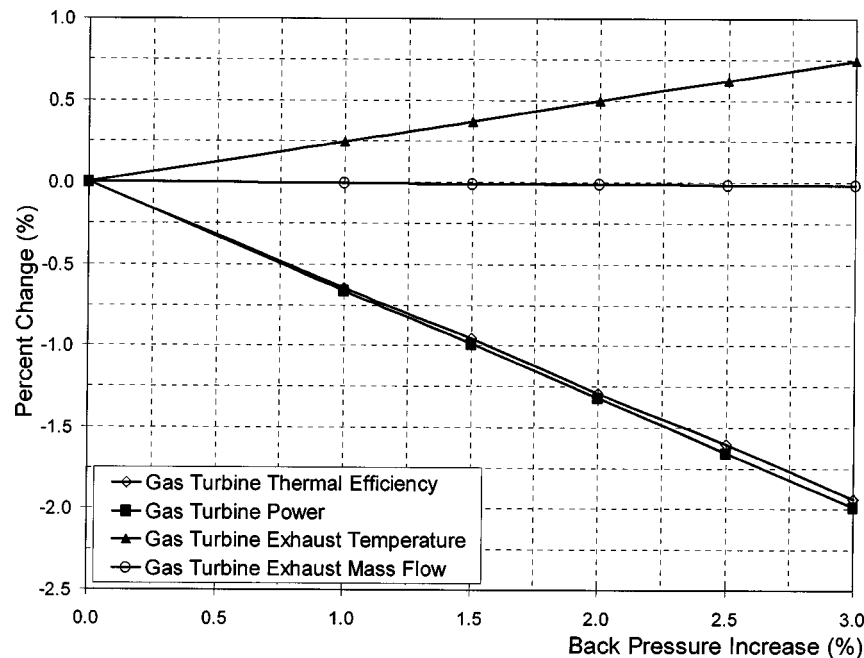


Fig. 2 Back pressure effects on GT performance

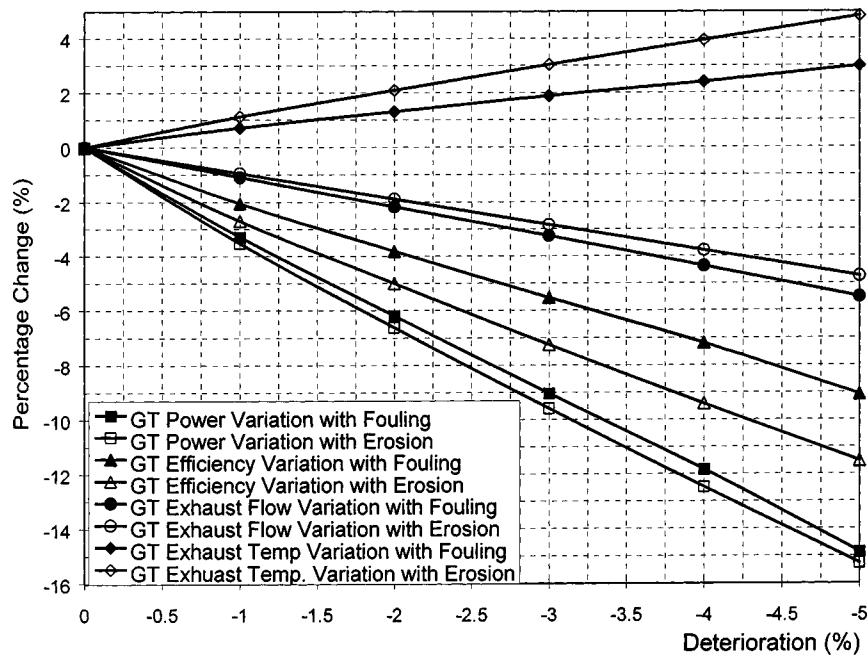


Fig. 3 GT performance parameters variation with gas turbine cycle component degradation

seems that the effect of either fouling or erosion is tending to have a similar curvature trend, but the magnitude is different.

As this figure shows, the maximum degradation consequence was encountered with gas turbine power deterioration due to GT component erosion. This was around (-15.2%) from the original DP value. The corresponding plant thermal efficiency drop was about (-11.5%) .

The combination of decreased compressor mass flow with an increased turbine flow capacity, due to erosion by 5%, led to a higher (about 2.5%) reduction in the plant's overall efficiency in comparison to the case where both components are experiencing fouling. This is due to the fact that the decreased pressure ratio through the turbine due to erosion resulted in a lower power output of the turbine, and hence a reduced overall power output of the engine which then reflected on the engine's overall efficiency. This shows that the erosion effect of gas turbine gas path components on the gas turbine performance is higher than the fouling effect.

Steam Cycle Degradation Simulation Results

As it was explained above, since the trend of the GT degradation due to either fouling or erosion is the same, and they only differ in the magnitude, and due to the limited space (page numbers allowed for this paper) it was decided to discuss only the fault which gave the higher impact on GT performance when simulating the bottoming cycle. Therefore, as already showed, since the GT erosion effects were predominant over the effect of fouling, it was decided to use its values when simulating steam cycle performance degradation.

The most important steam turbine cycle performance deterioration simulation results are represented graphically in Figs. 4 through 8. It is worth reminding the reader here that the values in these figures are including also the gas turbine degradation (erosion) and GT exhaust back pressure rise effects due to HRSG degradation as shown in Fig. 3.

The GT degradation effects on ST as well as on CCGT plants was plotted within the graphs showing those plants degradation. Figure 4 shows the effects of degraded topping (GT) as well as bottoming (ST) cycles on the steam flow through the bottoming cycle. As this figure shows, the increase in steam mass flow (about

8.3%) was at its highest value with superheater degradation by 5%. Although the expectation was to see the highest change in mass flow variation with GT degradation, the results came up with different values. In reality, this increase in mass flow was not due to degraded superheater. In fact as Zwebek and Pilidis [6] showed, the effect of degraded superheater alone on steam mass flow (with out gas turbine degradation) is almost negligible $(+0.51\%)$. Therefore, as Eq. (1) shows, the inlet conditions at the ST inlet are controlled by the so-called nondimensional mass flow (Eq. (1) above). Now by comparing the superheater degradation effects in Figs. 4, 7, and 8 with GT degradation effects it will be observed that while steam live pressure is almost constant (Fig. 7), there was an increase in steam mass flow. Now to fulfil the conditions of Eq. (1), then the live steam temperature must increase. This is the result obtained (as Fig. 8 shows). The same discussion is almost applicable to all other conditions.

It is well known from the very basics of steam turbine cycle theory that the steam turbine power is a function of steam mass flow and its enthalpy. Now by comparing Fig. 5 with Fig. 4 it would be observed that the steam turbine power is more or less following the mass flow behavior.

The effects of degraded topping as well as bottoming cycle components on steam turbine power plant are illustrated in Fig. 5. As this figure shows, the largest displacement of ST turbine power from its original DP value was encountered with superheater as well as condenser degradations. Again as stated above, this increase in ST power is merely due to increased gas turbine exhaust temperature due to GT degradation which led to increase steam mass flow and hence to increase the ST power. On the other hand, the lowest effect on ST power resulted from GT degradation along with ST turbine isentropic efficiency degradation; this was around $+4.2\%$.

One of the very important results obtained from this study is that, unlike the case with GT or ST degradations alone where the relationship between performance parameter variation (ST power, ST Rankine, etc.) and deterioration is linear, in the case of both plants deteriorated the relationship obtained was also nearly linear.

Cerri [12] stated that the maximal CCGT efficiency is reached when the GT exhaust temperature is higher than the one corre-

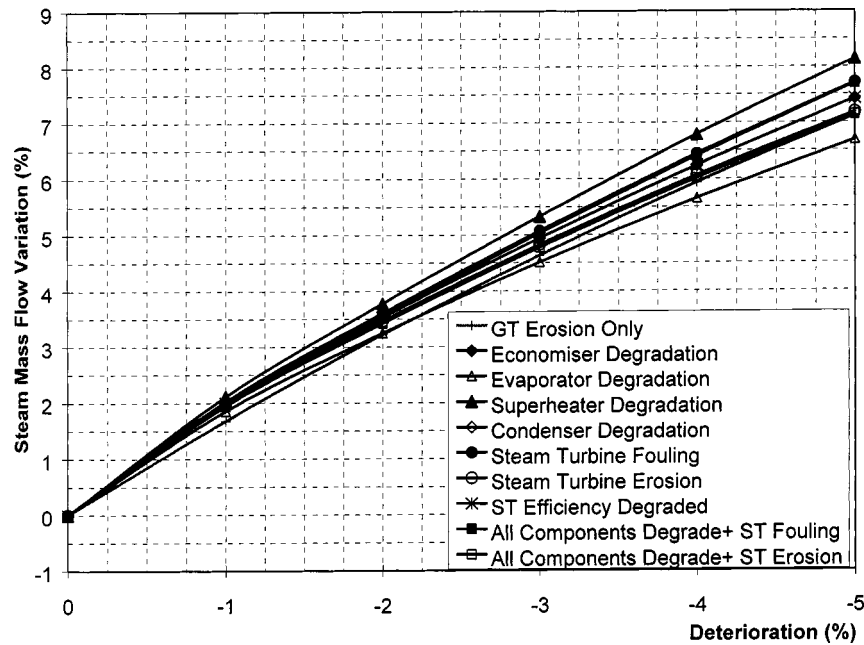


Fig. 4 ST steam mass flow variation with gas and steam cycles component degradation

sponding to the maximum GT efficiency; i.e., as GT exhaust temperature goes up, the CCGT efficiency goes up. Since gas turbine efficiency is already at its maximum, and still by increasing GT exhaust temperature (due to any reason) the CCGT will increase. This would then implicitly indicate that this increase is gained by increased steam turbine plant's power due to the increased steam turbine inlet conditions as explained above. This exactly coincides with the results obtained in the current study (see Fig. 5).

The next important performance parameter to discuss here is the steam turbine plant (Rankine) efficiency variation with degra-

dation, which is illustrated in Fig. 6. The thermal efficiency definition of steam turbine (bottoming) plant is given by

$$\eta_R = \frac{W_{SC}}{Q_{HRSG}} \quad (2)$$

This equation shows that the steam turbine (bottoming) cycle efficiency is a function of steam turbine net power output and the heat transferred in the HRSG (Q_{HRSG}), which is representing the heat input to the steam cycle. Now by looking at Fig. 9 it will be

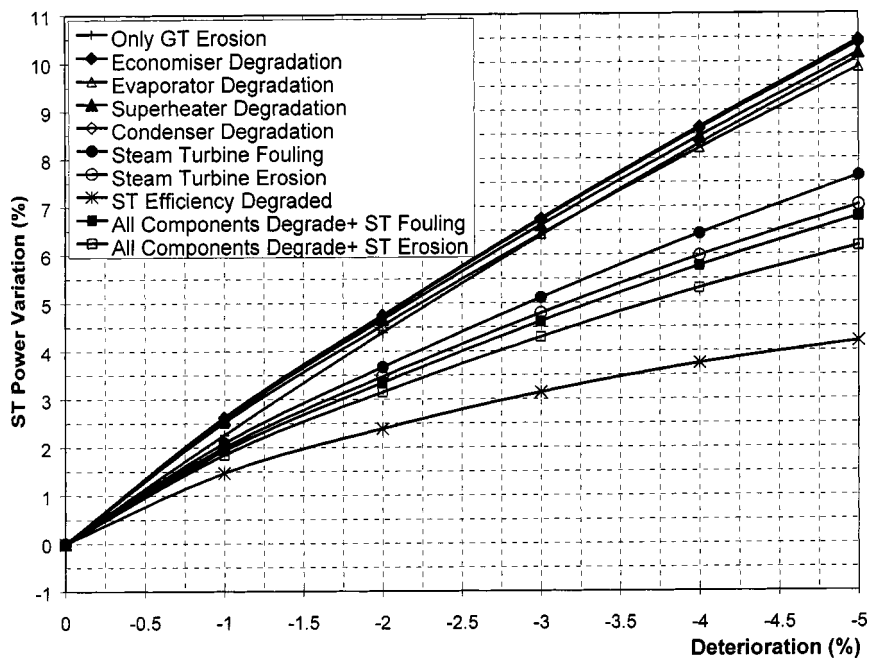


Fig. 5 Steam turbine power variation with gas and steam cycles component degradation

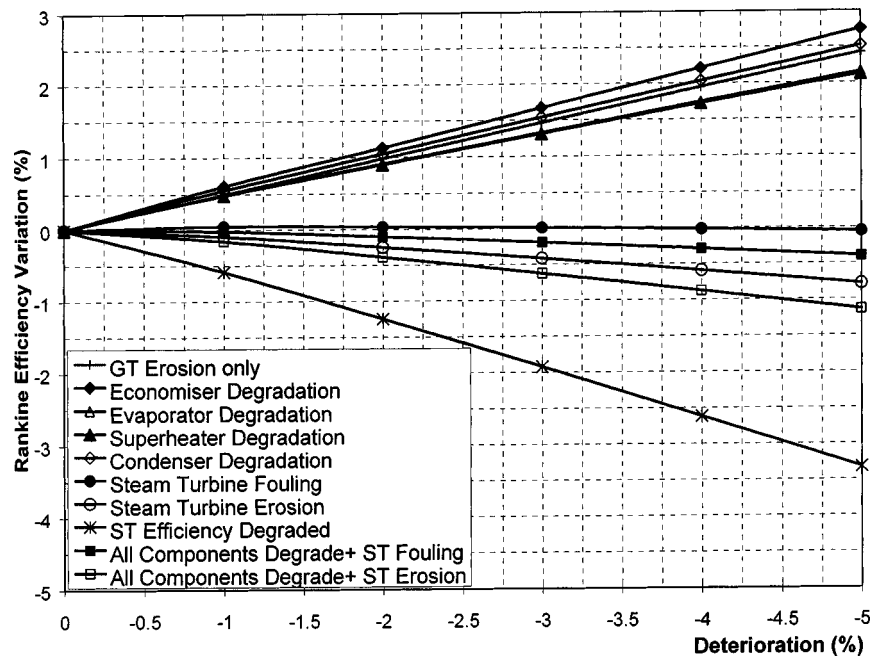


Fig. 6 Rankine efficiency variation with gas and steam cycles component degradation

seen that all types of degradations resulted into an increase in the HRSG efficiency, i.e., increased Q_{HRSG} . As Fig. 5 shows, although ST power increased with all types of degradation as well, yet the increase in the Q_{HRSG} (relative to DP value) in some cases was higher than the increase in ST power. This led to the ST efficiency to fall with such cases. This can be clearly seen in the case of ST turbine isentropic degradation. In this case, the increase in ST power was around 4.2% with 5% degradation. Although (as Fig. 9 shows) there was an increase in HRSG efficiency by about 4.2% (for the same magnitude of degradation) as

well, nevertheless, the increase in Q_{HRSG} was predominant and hence resulted in decreasing the ST turbine efficiency by approximately 3.3%.

As Figs. 5 and 6 show, the ST turbine isentropic efficiency has a predominant effect over all other types of ST cycle degradations. This is in agreement with the conclusion established by Zwebek and Pilidis [6].

The degradation effects of gas and steam plants on live steam pressure and temperature are expressed on Figs. 7 and 8, respectively. As Fig. 7 shows, the blockage of the steam turbine inlet due

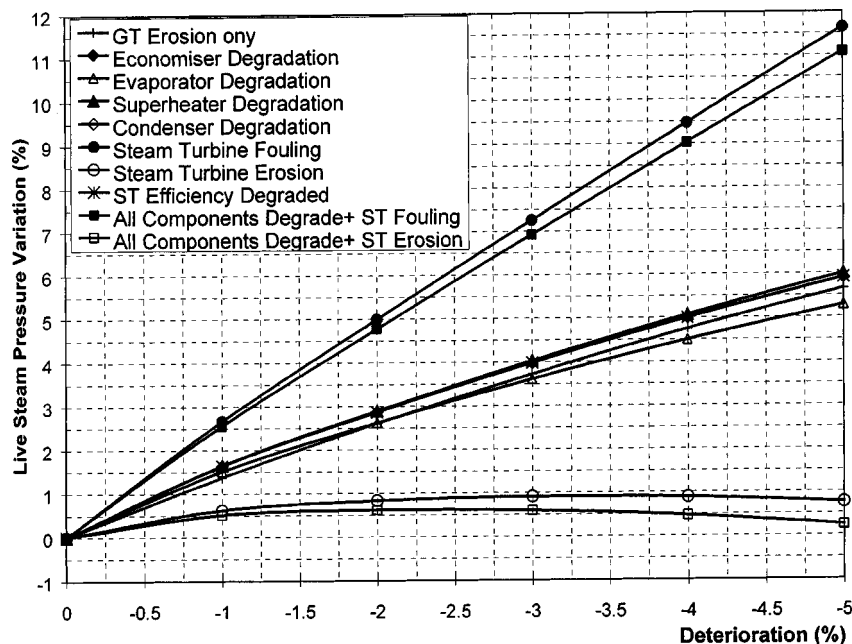


Fig. 7 Live steam pressure variation with gas and steam cycles component degradation

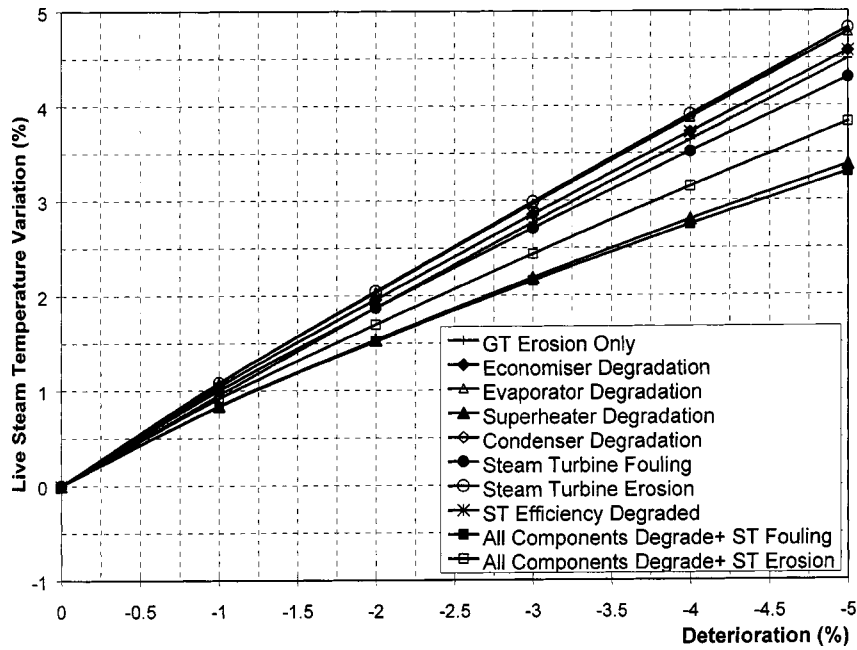


Fig. 8 Live steam temperature variation with gas and steam cycles component degradation

to fouling by 5.0% resulted in about 11.6% increase in live steam pressure at the ST turbine inlet. The combination of all other types of degradation with steam turbine fouling reduced the inlet pressure to about 11.0%. On the other hand, the degradation of all components along with steam turbine erosion by 5.0% resulted in only 0.3% (approximately) reduction in live steam pressure.

In the case of live steam temperature, as Fig. 8 shows, the effect of different components degradation on live steam temperature is mostly controlled by increased gas turbine exhaust temperature. As already shown above (see Fig. 3) the effect of gas turbine

components degradation was to increase the GT exhaust temperature. This, then by itself, led the live steam temperature to increase (see explanation above).

Combined Cycle Degradation Results

The degradation results have been explained in part by addressing the two cycles separately. Figure 10 shows the whole CCGT plant's power and how it varies with GT and ST plants degradation.

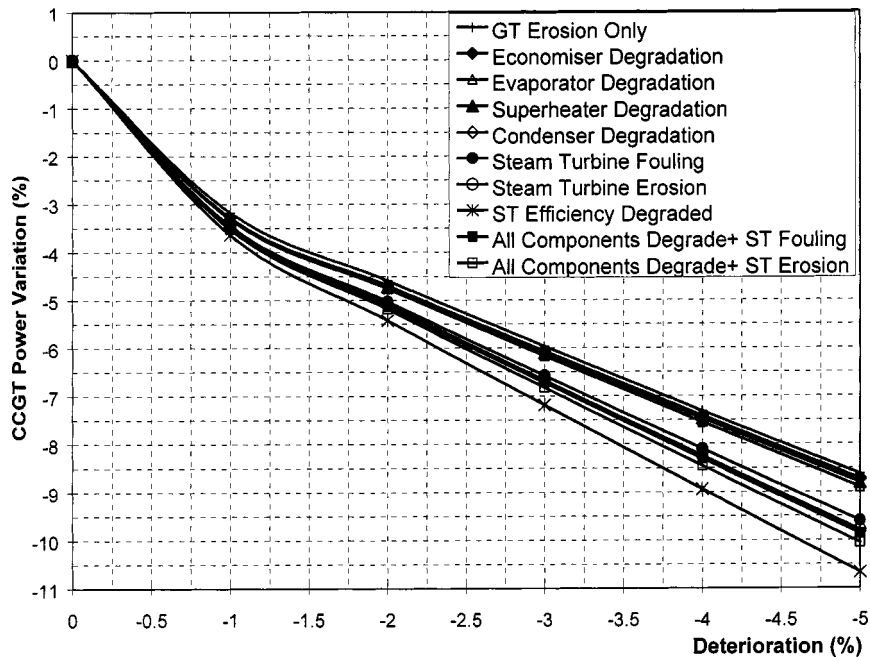


Fig. 9 HRSG efficiency variation with gas Steam cycles component degradation

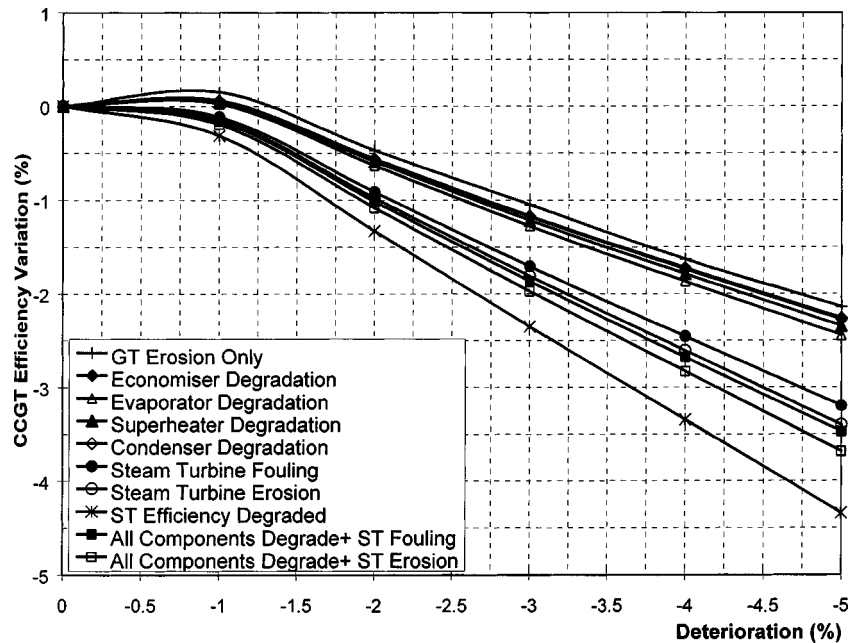


Fig. 10 CCGT power variation with gas and steam cycles component degradation

As this figure shows, although there was an increase in ST power (see Fig. 5), the decrease that was caused by GT power (see Fig. 3) was predominant. This actually is a straightforward result since GT power counts for the two thirds of the total amount of CCGT power. Figure 11 is a reproduction of Fig. 9 showing the CCGT efficiency is actually following the behavior of CCGT power.

As the two previous figures showed, the GT turbine degradation alone was having the least effect on CCGT plant power and efficiency. On the other hand, when the ST component effects were included in the degradation, the outcome deterioration results started to increase. As these two figures show, the largest degra-

degradation effect was due to the ST turbine isentropic efficiency degradation along with GT degradation. This was about -10.7% and -4.3% deterioration in CCGT power and efficiency respectively with -5.0% degradation.

Figures 9 and 12 illustrate the degradation effects of both plants on HRSG efficiency (η_{HRSG}) and stack temperature, respectively. The stack temperature is mainly a measure of the amount of gas turbine exhaust heat utilization by the bottoming cycle. Also, by definition, HRSG efficiency is a function of stack temperature and HRSG exhaust inlet temperature for a given ambient temperature (Eq. (3))

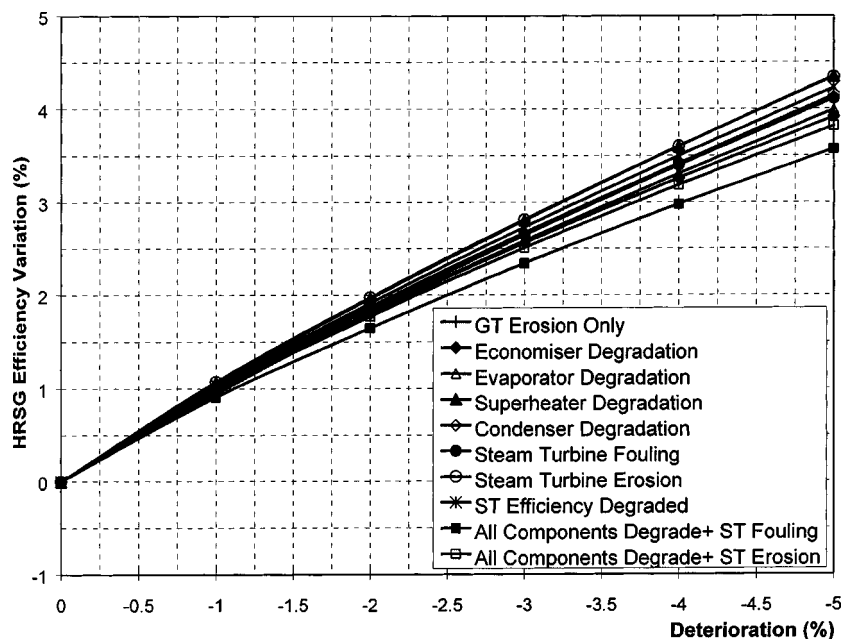


Fig. 11 CCGT efficiency variation with gas steam cycles component degradation

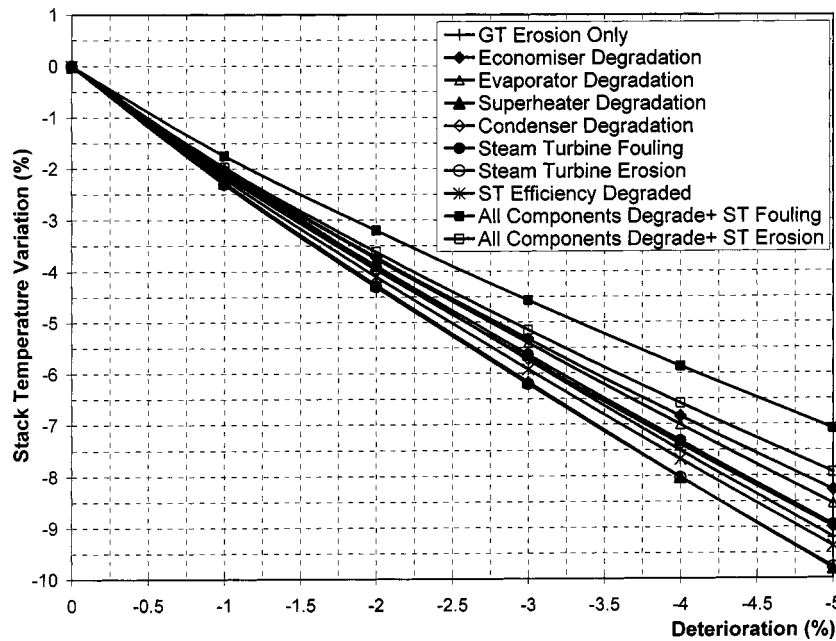


Fig. 12 Stack temperature variation with gas and steam cycles component degradation

$$\eta_{\text{HRSG}} = \frac{T_{\text{Gin}} - T_{\text{Stack}}}{T_{\text{Gin}} - T_{\text{amb}}} \quad (3)$$

This equation shows that, for a given HRSG inlet exhaust and ambient temperatures, the HRSG efficiency increases with decreased stack temperature (T_{Stack}) and vice versa.

While, as Zwebek and Pilidis [5] showed, the effects of GT component degradation resulted in decreasing T_{Stack} , the effects of ST component degradation Zwebek and Pilidis [6] came up (somewhat) with opposite results. Now, as Fig. 12 shows, although in this case both plants were degraded, all types of degradation led to decreasing T_{Stack} and hence increasing the η_{HRSG} (see Fig. 11). This leads us to a conclusion that the effects of GT degradation on η_{HRSG} are predominant over the effect ST component degradation.

Conclusions

The results obtained showed that the erosion of gas turbine gas path components has a predominant effect on its performance over the effect of fouling.

The results obtained are in agreement with those found in the literature. The combination of the two (upper and bottoming) cycle's degradations leads to a nearly linear behavior of the deterioration results.

The obtained degradation effects of GT plant on steam cycle plant's performance are in agreement with the published data that the authors found in open literature, [12].

The combination of GT component degradation with ST turbine isentropic efficiency degradations led to the highest deterioration of CCGT plant power and efficiency.

The combination of both plant component degradation led to decreasing the stack temperature (T_{Stack}). This shows that the effects of GT degradation on T_{Stack} and hence on η_{HRSG} are predominant over the effect ST component degradation.

Nomenclature

atm = atmospheric pressure
 CCGT = combined cycle gas turbine plant
 DP = design point
 GT = gas turbine

HRSG = heat recovery steam generator
 Q = heat transfer
 ST = steam turbine
 T = temperature
 Γ = nondimensional mass flow
 η = efficiency
 U = heat transfer coefficient

Subscripts

C = GT compressor
 CC = combined cycle
 GT = gas turbine
 ST = steam turbine
 i = inlet
 G_{in} = HRSG inlet
 SC = steam cycle
 T = turbine
 Stack = HRSG exit

References

- [1] Briesch, M. S., and Bannister, R. L., 1995, "A Combined Cycle Designed to Achieve Greater Than 60 Percent Efficiency," ASME J. Eng. Gas Turbines Power, **117**.
- [2] Erbes, M. R., and Gay, R. R., 1989, "Gate/Cycle Predictions of the Off-Design Performance of Combined-Cycle Power Plants," Winter Annual Meeting of the ASME, San Francisco, CA.
- [3] Roy-Aikins, J. E. A., 1995, "BRAKINE: A Programming Software for the Performance Simulation of Brayton and Rankine Cycle Plants," Proc. Inst. Mech. Engrs., Part A, J. Power Energy, **209**.
- [4] ThermoFlow, 1999, *Thermoflex[®], Fully Flexible Heat Balance Modelling-Users Manual*.
- [5] Zwebek, A. I., and Pilidis, P., 2001, "Degradation Effects on Combined Cycle Power Plant Performance, Part I: Gas Turbine Cycle Component Degradation Effects," ASME Paper 2001-GT-388.
- [6] Zwebek, A. I., and Pilidis, P., 2001, "Degradation Effects on Combined Cycle Power Plant Performance, Part II: Steam Turbine Cycle Component Degradation Effects," ASME Paper 2001-GT-389.
- [7] Diakunchak, I. S., 1992, "Performance Deterioration in Industrial Gas Turbines," ASME J. Eng. Gas Turbines Power, **114**.
- [8] Lakshminarasimha, A. N., Boyce, M. P., and Meher-Homji, C. B., 1994, "Modelling and Analysis of Gas Turbine Performance Deterioration," ASME J. Eng. Gas Turbines Power, **116**.
- [9] Tabakoff, W., 1986, "Compressor Erosion and Performance Deterioration," AIAA/ASME 4th Joint Fluid Mechanics, Plasma Dynamics, and Laser Conference, Atlanta, GA, May 12-14.

- [10] Tabakoff, W., Lakshminarasimha, A. N., and Pasin, M., 1990, "Simulation of Compressor Performance Deterioration due to Erosion," *ASME J. Eng. Gas Turbines Power*, **112**.
- [11] Escher, P. C., 1995, "Pythia: An Object-Oriented Gas Path Analysis Computer Program for General Applications," Ph.D. thesis, School of Mechanical Engineering, Cranfield University, UK.
- [12] Cerri, G., 1987, "Parametric Analysis of Combined Gas-Steam Cycles," *ASME J. Eng. Gas Turbines Power*, **109**.

Inherent CO₂ Capture Using Chemical Looping Combustion in a Natural Gas Fired Power Cycle

Ø. Brandvoll
O. Bolland

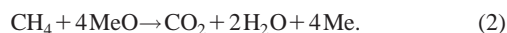
The Norwegian University of Science
and Technology,
N-7491 Trondheim, Norway

In this paper an alternative to the so-called “oxy-fuel” combustion for CO₂ capture is evaluated. “Chemical looping combustion” (CLC), is closely related to oxy-fuel combustion as the chemically bound oxygen reacts in a stoichiometric ratio with the fuel. In the CLC process the overall combustion reaction takes place in two reaction steps in two separate reactors. In the reduction reactor, the fuel is oxidized by the oxygen carrier, i.e., the metal oxide MeO. The metal oxide is reduced to a metal oxide with a lower oxidation number, Me, in the reaction with the fuel. In this manner, pure oxygen is supplied to the reaction with the fuel without using a traditional air separation plant, like cryogenic distillation of air. The paper presents a thermodynamic cycle analysis, where CLC is applied in a humid air turbine concept. Main parameters are identified, and these are presented and compared to other CO₂ capture options. Further, an evaluation of the oxygen carrier, metals/oxides, is presented. An exergy analysis is carried out in order to understand where losses occur, and to explain the difference between CLC and conventional combustion. The oxidation reactor air inlet temperature and the oxidation reactor exhaust temperature have a significant impact on the overall efficiency. This can be attributed to the controlling effect of these parameters on the required airflow rate. An optimum efficiency of 55.9% has been found for a given set of input parameters. Crucial issues of oxygen carrier durability, chemical performance, and mechanical properties have been idealized, and further research on the feasibility of CLC is needed. Whether or not the assumption 100% gas conversion holds, is a crucial issue and remains to be determined experimentally. Successful long-term operation of chemical looping systems of this particular type has not yet been demonstrated. The simulation points out a very promising potential of CLC as a power/heat generating method with inherent capture of CO₂. Exergy analysis show reduced irreversibilities for CLC compared to conventional combustion. Simulations of this type will prove useful in designing CLC systems in the future when promising oxygen carriers have been investigated in more detail. [DOI: 10.1115/1.1615251]

Introduction

Originally proposed by Richter and Knoche [1] in 1983, the main idea of chemical looping combustion (CLC) is to split combustion of natural gas into separate oxidation and reduction reactions by introducing a suitable metal oxide as an oxygen carrier to circulate between the two reactors, as indicated in Fig. 1.

The oxide is reduced to metal in the presence of hydrocarbons, and reformed by oxidation with air. The reaction for methane and a metal oxide can be formulated as follows:



The oxidation is highly exothermic ($\Delta H_{\text{OX}} = -959 \text{ kJ/mol}$) and provides high temperature exhaust gas for power production (or as a heat source), and metal oxide which supply heat to the exhaust stream from the reduction reactor in a gas-solid heat exchange reactor, thus increasing the power generating potential of this exhaust, as well as supplying heat to the endothermic reduction reaction ($\Delta H_{\text{RED}} = 156 \text{ kJ/mol}$). CLC is a method for reducing the

exergy loss associated with the highly irreversible combustion of a fuel. This reduction is, however, dependent upon the degree of conversion in the two reactors. The advantage of inherent CO₂ separation without severe energy penalties has drawn increased attention in light of the current global warming debate, [2]. Formation of NO_x is also very low by virtue of the relatively low temperature conditions in the reactors. Current literature directly related to CLC is sparse. An overview of current CLC research is summarized in Table 1.

Procedure

This paper presents the results of a simulation of a CLC power plant. The simulations were performed in Matlab 5.0. The applied

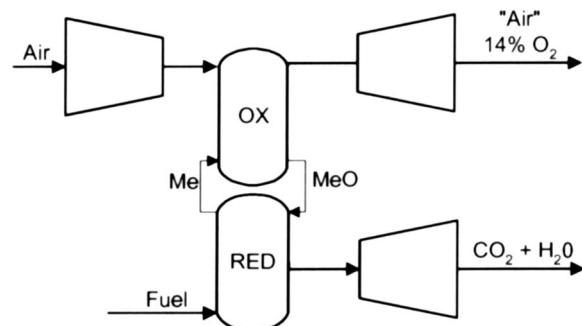


Fig. 1 The chemical looping combustion principle

Contributed by the International Gas Turbine Institute (IGTI) of THE AMERICAN SOCIETY OF MECHANICAL ENGINEERS for publication in the ASME JOURNAL OF ENGINEERING FOR GAS TURBINES AND POWER. Paper presented at the International Gas Turbine and Aeroengine Congress and Exhibition, Amsterdam, The Netherlands, June 3–6, 2002; Paper No. 2002-GT-30129. Manuscript received by IGTI, Dec. 2001, final revision, Mar. 2002. Associate Editor: E. Benvenuti.

Table 1 Published work on CLC power generation systems

| Authors | Studied Area | Results |
|--|---|---|
| Ishida et al. [2,10,11] Anheden [9] Mattison and Lyngfeldt [5] | Thermodynamics, exergy analysis Reaction characteristics of different types of ferrous (III) oxides | Reduced exergy loss compared to conventional combustion, as a result of reaction splitting Reactions rates (red/ox) are sufficient for power generating applications |
| Ishida et al. [6,7,12–17] Lyngfeldt et al. [8] | Oxygen carriers: reduction/oxidation rates, synthesis, mechanical properties, carbon deposition, kinetics Reactor design and technical feasibility | Several promising oxygen carriers have been investigated, reaction rates are sufficiently large Circulating fluidized bed concept discussed as a suitable reactor set up |
| Hatanaka et al. [18] | Reaction kinetics | Reaction rates are sufficiently large |

process schematic is shown in Fig. 2. This is essentially similar to that proposed by Ishida et al. [2]. The model is made up from the mass and energy balances for the six main component types in the flowsheet: turbine, compressor, pump, reactors, heat exchangers, and condensers. Standard equations for compressor and turbine work, required pump power and heat exchange calculations have been used. Turbine cooling efficiency penalty is not included in the present work. The heat losses in both reactors are set to 1% of the inlet stream enthalpies. The CLC system could be integrated in various power cycles. In the present study it was chosen to use the humid air turbine (HAT) principle. A humidifying tower is used to saturate the incoming air, before entering the oxidation reactor. Thermochemical data from Barin [3] and Kotas [4] are used throughout the calculation, and heat capacities for mixtures of gases have been estimated by assuming ideal-gas behavior. Power requirements to circulate the oxygen carrier, besides reactor pressure drop, are considered negligible.

Key parameters employed in calculations on this system are the degree of oxidation (X) and the conversion factor or Gas Yield (γ_{red}):

$$X = 1 - \frac{m_{oxd} - m}{m_{oxd} - m_{red}} = \frac{m - m_{red}}{m_{oxd} - m_{red}} \quad (3)$$

$$\gamma_{red} = \frac{P_{CO_2, out}}{P_{CH_4, out} + P_{CO_2, out} + P_{CO, out}} \quad (4)$$

X describes the state of the oxygen carrier at a given point in the process, and is defined as the fraction of the oxygen carrier material that is oxidized at a given time. γ_{red} , which has been used by some authors, [5], is here assumed to be unity. The *conversion difference* ΔX per unit time between initial and current degree of oxidation of the carrier material, is also a measure of the reaction efficiency.

Choice of Oxygen Carrier. A number of promising oxygen carriers have been found, of which NiO/NiAl₂O₄ is perhaps the most interesting, [6]. Based on previous experiments; [7], and availability of thermodynamical data, NiO/YSZ on a 3:2 mass basis was selected as oxygen carrier. The degree of oxidation X_o

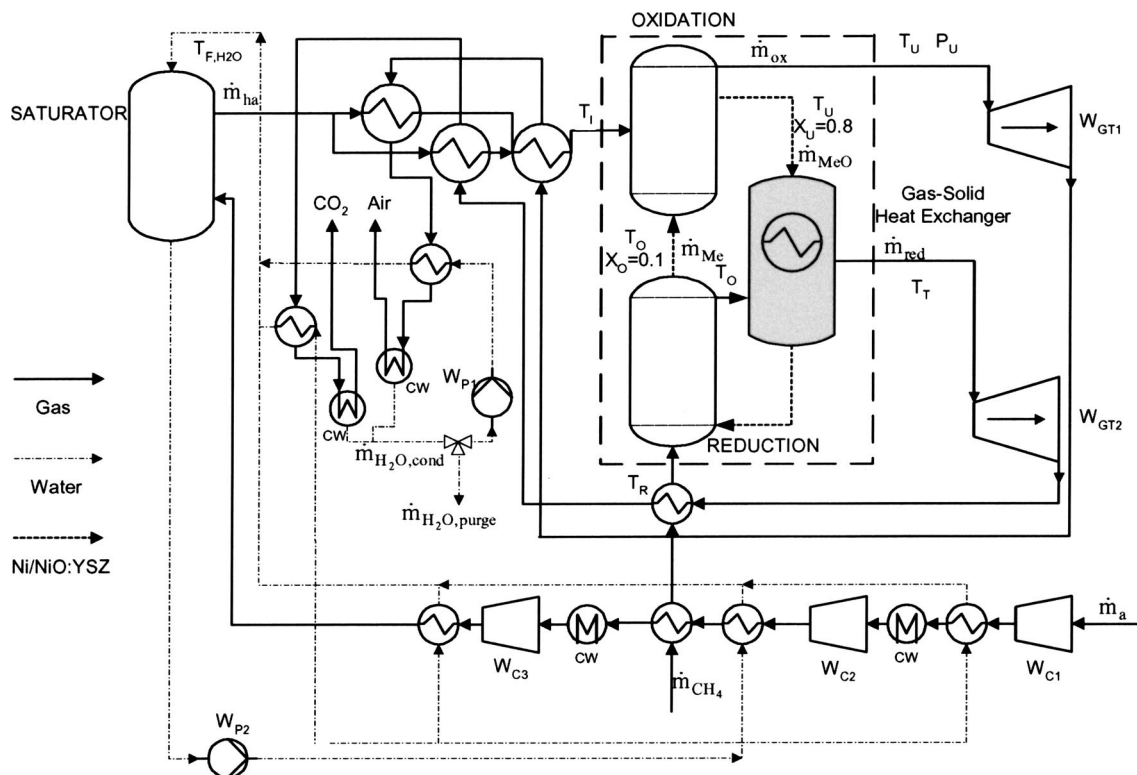


Fig. 2 Process flowsheet. A gas turbine with compressor intercooling and air saturation. The CLC system is shown within the dashed box.

Table 2 Summary of simulation results

| Base Case | 520 | 465 | 1200 | 900 | 560 | 20 | 55.3 |
|------------|----------------|----------------|-----------------|-----------------|-----------------|--------------|--------------|
| PARAMETERS | | | | | | | Response |
| CASES # | T_I [°C] | T_R [°C] | T_U [°C] | T_T [°C] | T_O [°C] | P_U [Bar] | η_{TOT} |
| 1 | <i>400–520</i> | 465 | 1200 | 900 | 560 | 20 | 50.2–55.3 |
| 2 | <i>522–519</i> | <i>375–465</i> | 1200 | 900 | 548 | 20 | 55.2–55.3 |
| 3 | <i>349–519</i> | 465 | <i>900–1200</i> | 900 | 257 | 20 | 45.1–55.3 |
| 4 | <i>519–527</i> | 681 | 1200 | <i>900–1200</i> | <i>485–560</i> | 20 | 55.3–55.9 |
| 5 | 519 | 465 | 1200 | 900 | <i>224–1067</i> | 20 | 55.4–54.0 |
| 6 | <i>633–505</i> | 549 | 1200 | 900 | 573 | <i>10–20</i> | 54.6–55.3 |

is set to 0.1 at the oxidation reactor entrance, and $X_U=0.8$ at the reduction reactor entrance. These values have been selected (instead of 0.0 and 1.0) in order to decrease the reactor volumes (and residence times) necessary for complete transformation of the material, while maintaining a relatively low mass-flow of the oxygen carrier.

Results and Discussion

Six process parameters that are believed to affect the overall efficiency were identified: oxidation reactor air inlet temperature T_I , fuel inlet temperature T_R , oxidation reactor exhaust temperature T_U , primary reduction exhaust temperature T_O , were varied in turn, and their influence on important process parameters and ultimately on the overall efficiency was calculated. The efficiency is defined as the ratio of net shaft power output (work of turbines minus work of compressors and pumps) to the lower heating value of CH_4 . The basis of the simulation is a fuel consumption rate of 1.0 kg CH_4 /s. Table 2 presents the main results in a highly compressed form. Variation of primary parameters is shown in italics, and gives rise to degrees-of-freedom in other process parameters, in addition to the primary sought effect on total efficiency.

(1) **Oxidation inlet temperature, T_I .** The temperature of the air as it enters the oxidation reactor will affect the power production of W_{GT1} , as it determines the airflow rate through the process when reactor outlet temperature and heat exchanger duties are given. An increase in total efficiency is observed due to a proportionally larger turbine output gain as the airflow rate increases when going from $T_I=400–520^\circ C$, than the rise in required compressive work. T_I will also affect the water temperature in the saturator, as more high temperature heat is available at low T_I . T_I is found to have significant impact on η_{TOT} ,—about 5.1% over the temperature range. The temperature T_I is set as high as possible, limited by the ΔT_{min} requirements in the preheating exchangers. Based on this result, the following simulations use all available high-temperature heat to increase T_I to optimize efficiency.

(2) **Fuel inlet temperature, T_R .** With given outlet conditions and fuel flow, lowering the fuel inlet temperature allows more heat to be transferred in the air-preheaters thus allowing a further increase in T_I . The amount of fuel entering the system is much lower than the amount of air. Subsequently, the total energy influx to the reactors remains constant, and little effect is observed in η_{TOT} . A slight increase is observed, however. Maximum fuel inlet temperature, limited by ΔT_{MIN} requirements in the heat exchangers, is therefore chosen in the following simulations.

(3) **Oxidation reactor outlet temperature, T_U .** Lowering the turbine inlet temperature T_U , immediately lowers the GT1 turbine power output. Turbine outlet temperature also decreases, and less energy is available for air preheating. On the other hand, the airflow can be increased, and the need for costly turbine and reactor cooling might be eliminated. The increased airflow cancels the effect of the temperature decrease and the power output W_{GT1} remains constant, but the required compressor power increases

significantly, as can be seen in Fig. 3(b). The power generating potential of GT1 is unaffected and a significant effect on total efficiency is thus observed.

(4) **Turbine GT2 inlet temperature, T_T .** Increasing T_T is possible by increasing the mean residence time of the particles in the gas-solid heat exchanger, thus transferring more energy. Less energy is thus available when the oxygen carrier enters the oxidation reactor. Consequently the airflow must be reduced to maintain constant outlet conditions. Increased power in turbine GT2 comes at the cost of lowering the power in turbine GT1 and η_{TOT} is relatively unaffected. Economical considerations with regard to turbine GT2 imply that a low inlet temperature is desirable to avoid cooling of the turbine.

(5) **Reduction reactor outlet temperature, T_O .** By increasing the carrier mass flow rate, while maintaining a constant volume in the gas-solid heat exchanger, the oxygen carrier will have a higher temperature as it enters the reduction reactor. This will lead to an increase in T_O . Additionally a change in X_U (after oxidation) and X_O (after reduction) is observed as the reactor volumes are considered to be constant and the mean residence times (τ_{ox}, τ_{red}) decreases. This leads to a slight change in the energy balance for the reduction reactor, the net result being a small decrease in efficiency. This observation is important because of the implication that T_O can be chosen to optimize the kinetics of the reduction reaction, without significant losses in efficiency.

(6) **Reactor pressure.** Reduced pressure invariably leads to reduced power generation in both turbines, along with a reduction in required compressor work. The airflow rate will increase, however, and only a slight net effect is observed. When going from 10 to 20 bars, there is a slight increase in compressor work while W_{GT1} remains constant. η_{TOT} increases, however, due to the increased contribution from turbine GT2. The total efficiency rises slightly for pressures up to 20 bar, where the increase in compressor work exceeds the increase in W_{GT2} . 20 bars therefore seem to be an optimal operating pressure for the reactor system.

In Fig. 3(a), T_I and T_U are plotted against total efficiency, assuming constant fuel input. Note that changing T_U also leads to a change in T_I due to the heat integration of the two streams. Figure 3(b) shows the effect on airflow rate when reducing T_U from 1200 to 900°C.

Reactor System

A key issue in CLC considerations is the type of reactor system chosen. The concept of a *circulating fluidized bed* (CFB) has been proposed, [8], and is believed to be the most promising setup for successful long-term operation. The basis for the simulation is a CFB ($\epsilon=0.95$) for oxidation, and a fluidized bed ($\epsilon=0.45$) for reduction. It is assumed that the oxygen carrier transport is gravity-driven in the reduction reactor. Key parameters are shown in Table 3. The flow of metal/metal oxide between the reactors is about 1.4–1.5 kg per MJ of net plant power output. The specific work (net plant power output per kg of air) is about $1/1.78=0.56$ MJ/kg, which is somewhat higher (20–30%) than that of a gas turbine. The oxidation reactor volume is around 1.1 m³/MW of net plant power output, which is below that of a conventional CFB combustion plant.

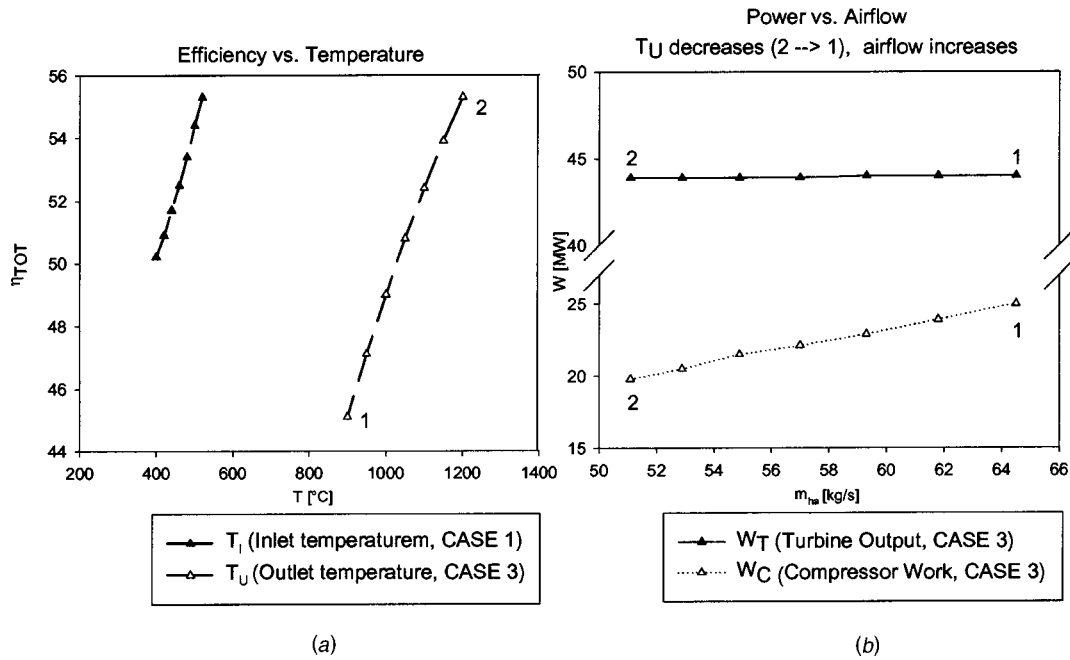


Fig. 3 (a) $T-\eta$ diagram for T_1 and T_U . (b) $W-m_{ha}$ diagram, ($900 < T_U < 1200$).

Table 3 Reactor key parameters (28 MW power output, 50 MW fuel lower heating value, $X_O=0.1$, $X_U=0.8$)

| | kg/s | kg/MJ _{el} | kg/MJ _{LHV} |
|---------------------------|----------------|----------------------------------|----------------------|
| MeO | 43.9 | 1.57 | 0.88 |
| Me | 39.3 | 1.40 | 0.79 |
| Oxidation reactor airflow | 49.8 | 1.78 | 1.0 |
| | m ³ | m ³ /MW _{el} | kg/MW _{LHV} |
| Oxidation reactor (CFB) | 31.2 | 1.11 | 155 |
| Reduction reactor (FB) | 3.3 | 0.12 | 141 |

Exergy Considerations

Thermodynamics states that the maximum amount of mechanical energy from transformation of a chemical compound is obtained when the conversion is reversible, i.e., occurs at a state of equilibrium. Due to material limitations in the combustor and turbine of a gas turbine, combustion is carried out at temperatures far below that of the equilibrium temperature associated with the oxidation of fuel with oxygen. The reaction is thus highly irreversible with considerable entropy generation. Exergy is also destroyed by irreversibilities in process components such as turbines and heat exchangers.

In order to compare CLC with conventional combustion with respect to irreversibilities, it is assumed that the process in Fig. 2 can either use CLC or have a conventional combustor within the dashed box shown in Fig. 2. The intention of this comparison is to show that the chemical conversion of fuel in CLC is done with reduced exergy loss compared to traditional combustion processes. The process would be the same with these two combustion systems, except that a conventional combustion system would have one hot pressurized gas stream to expand through a turbine, whereas for the CLC system there are two separate streams expanded through two separate turbines. It is for the exergy consideration assumed that the system outside the dashed box in Fig. 2 is the same so that the difference in irreversibilities for the whole process is related to the combustion block, see Fig. 4.

In the following it is assumed that the irreversibilities outside

the reactor are similar in CLC and conventional combustion, although the proposed use of a CFB indicates a slightly higher pressure loss in the CLC combustion block.

Fundamentally, the exergy balance for a control volume at steady state can be formulated as follows:

$$E_D = \sum_{cv} E_Q - W_{cv} + \left(\sum_i \dot{m}_i e_i - \sum_e \dot{m}_e e_e \right) \quad (5)$$

where

$$\sum_{cv} E_Q = \sum_{cv} \left(1 - \frac{T_0}{T_j} \right) \quad (6)$$

The first and second terms of Eq. (5) are exergy transfer associated with heat transfer and work. Adiabatic conditions are assumed and the work term is not considered since the control volume does not include the turbines. The specific exergy terms e_i and e_e for process streams at inlet (i) and exit (e) (n components), can be further decomposed into physical (e^P) and chemical (e^{CH}) exergy, assuming mechanical exergy to be negligible:

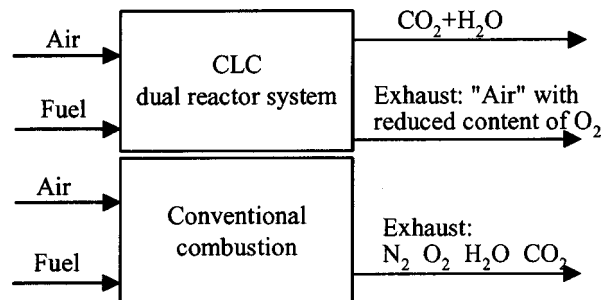


Fig. 4 Comparison of two combustion principles

Table 4 Exergy considerations (T,P)

| | Exergy [kW] | | |
|--|-------------|--------------------------|-----------|
| | e^P | e^{CH} | e^{TOT} |
| CLC: | | | |
| Fuel (T=681°C, 21 bar) | 1,599 | 52,080 | 53,679 |
| Air (527,21.3) | 27,849 | 1,441 | 29,290 |
| CO ₂ + H ₂ O (1200,19.4) | 8,214 | 2,347 | 10,562 |
| Exhaust (1200,20) | 58,713 | 1,900 | 60,613 |
| | | $\dot{E}_D = 11,789$ | |
| | | $1 - \eta_{ex} = 22.6\%$ | |
| Conventional combustion: | | | |
| Fuel (681,21) | 1,599 | 52,080 | 53,679 |
| Air (527,21) | 27,757 | 1,441 | 29,198 |
| Exhaust (1200,20.5) | 66,746 | 3,057 | 69,803 |
| | | $\dot{E}_D = 13,074$ | |
| | | $1 - \eta_{ex} = 24.4\%$ | |

$$e^P = (h - h_0) - T_0(s - s_0) \quad (7)$$

$$e^{CH} = \sum_n y_n e_n^{CH} + \bar{R} T_0 \sum_n y_n \ln y_n \quad (8)$$

The rate of exergy destruction in the reactor can thus be estimated from the difference in exergy content in the streams at the volume boundary. Exergetic efficiency is defined accordingly as

$$\eta_{ex} = 1 - \frac{E_D}{E_F} \quad (9)$$

Using stream data from the simulation with the highest overall efficiency (case 4, 55.9%), an exergy balance for a control volume over the reactor section (indicated with a dashed box in Fig. 2) has been considered. For comparison, the same process streams are applicable in a conventional humid air gas turbine in order to estimate the difference in exergy loss associated with reaction splitting. The results are shown in Table 4 and are consistent with other studies, [2,9].

The exergy loss of CLC is about 2%—points less compared to conventional combustion. The reduced exergy loss in CLC becomes even more evident considering that a conventional combustion cycle will need a CO₂ separation unit.

Conclusions

The oxidation reactor air inlet temperature (T_I) and the oxidation reactor exhaust temperature (T_U) have a significant impact on the overall efficiency. This can be attributed to the controlling effect of these parameters on the required airflow rate. An optimum efficiency of 55.9% has been found for $T_I = 527^\circ\text{C}$, $T_U = T_T = 1200^\circ\text{C}$, $T_O = 485^\circ\text{C}$, and $\dot{m}_a = 49.3 \text{ kg/s}$. The captured CO₂ is at atmospheric pressure. If taking into account the compression of CO₂ 1–100 bar, the efficiency would be lowered by 2% points, to about 54%. Crucial issues of oxygen carrier durability, chemical performance, and mechanical properties have been highly idealized, and further research on the feasibility of CLC is needed. Whether or not the assumption of $\gamma_{red} \sim 1$ holds, is a crucial issue and remains to be determined experimentally. Results of previous studies on chemical kinetics are used directly in the simulations, under conditions quite different from the original study, and thus introduce uncertainties in the calculations, as successful long-term operation of chemical looping systems of this particular type has not yet been demonstrated. The simulation points out a very promising potential of CLC as a power/heat generating method with inherent capture of CO₂. Exergy analysis show reduced irreversibilities for CLC compared to conventional combustion. Simulations of this type will prove useful in designing CLC systems in the future when promising oxygen carriers have been investigated in more detail.

Acknowledgments

This study was funded by the Norwegian Research Council program—Energy for the Future.

Nomenclature

| | |
|-----------------|--|
| e^{CH} | = specific chemical exergy (kJ/kg) |
| e^P | = specific physical exergy (kJ/kg) |
| E_D | = exergy destruction rate (kW) |
| E_F | = exergy supplied from fuel (kW) |
| E_L | = exergy loss (kW) |
| E_Q | = exergy transfer due to heat transfer (kW) |
| \bar{h} | = specific enthalpy (kJ/kg) |
| ΔH_{rx} | = heat of reaction (kJ/kmol) |
| m | = instantaneous mass of oxygen carrier (kg) |
| \dot{m} | = mass flow rate (kg/s) |
| m_{oxd} | = mass of oxygen carrier when 100% oxidized (kg) |
| m_{red} | = mass of oxygen carrier when 100% reduced (kg) |
| P_i | = partial pressure of component i (bar) |
| \bar{R} | = gas constant (kJ/K kmol) |
| s | = entropy (kJ/kg K) |
| T | = temperature ($^\circ\text{C}$) |
| V | = volume (m^3) |
| W | = work (MW) |
| X | = degree of oxidation |
| y_i | = molar fraction of component i |
| Y | = absolute humidity |
| ε | = bed void |
| γ_{red} | = gas yield |
| η | = efficiency |
| ρ | = particle density (kg/m^3) |
| τ | = mean residence time (s) |

References

- [1] Richter, H. J., and Knoche, K., 1983, "Reversibility of Combustion Processes," *Efficiency and Costing—Second Law Analysis of Processes* (ACS Symposium Series 235), ACS, Washington, DC, pp. 71–85.
- [2] Ishida, M., and Jin, H., 1994, "A New Advanced Power-Generation System Using Chemical-Looping Combustion," *Energy*, **19**(4), pp. 415–422.
- [3] Barin, I., 1995, *Thermochemical Data of Pure Substances*, 3rd Ed., VCH Verlagsgesellschaft.
- [4] Kotas, T. J., 1995, *The Exergy Method of Thermal Plant Analysis*, Krieger, Melbourne, FL.
- [5] Mattisson, T., Lyngfelt, A., and Cho, P., 2000, "Possibility of Using Iron Oxide as an Oxygen Carrier for Combustion of Methane With Removal of CO₂—Application of Chemical-Looping Combustion," [HTTP://www.entek.chalmers.se/~anly/co2/ghgt5.pdf](http://www.entek.chalmers.se/~anly/co2/ghgt5.pdf).
- [6] Jin, H., Okamoto, T., and Ishida, M., 1999, "Development of a Novel Chemical-Looping Combustion: Synthesis of a Solid Looping Material of NiO/NiAl₂O₄," *Ind. Eng. Chem. Res.*, **3**, pp. 126–132.
- [7] Ishida, M., and Jin, H., 1994, "A Novel Combustor Based on Chemical-Looping Reactions and Its Reaction Kinetics," *J. Chem. Eng. Jpn.*, **27**(3), pp. 296–301.
- [8] Lyngfelt, A., Leckner, B., and Mattisson, T., 2000, "A Fluidized-Bed Combustion Process With Inherent CO₂ Separation," *Chem. Eng. Sci.*, submitted for publication.
- [9] Anheden, M., 2000, "Analysis of Gas Turbine Systems for Sustainable Energy Conversion," doctoral thesis, Department of Chemical Engineering and Technology Energy Processes, Royal Institute of Technology, Stockholm, Sweden.
- [10] Ishida, M., Zheng, D., and Akehata, T., 1987, "Evaluation of a Chemical-Looping-Combustion Power-Generation System by Graphic Exergy Analysis," *Energy*, **12**, pp. 147–154.
- [11] Ishida, M., and Jin, H., 1993, "Graphical Exergy Analysis of Complex Cycles," *Energy*, **18**(3), pp. 615–625.
- [12] Ishida, M., and Jin, H., 1996, "A Novel Chemical-Looping Combustor Without NO_x Formation," *Research Notes, Ind. Eng. Chem.*, **35**, pp. 2469–2472.
- [13] Ishida, M., Jin, H., and Okamoto, T., 1996, "A Fundamental Study of a New Kind of Medium Material for Chemical-Looping Combustion," *Energy Fuels*, **10**, pp. 923–963.
- [14] Ishida, M., Jin, H., and Okamoto, T., 1998, "Kinetic Behavior of Solid Particle in Chemical-Looping Combustion: Suppressing Carbon Deposition in Reduction," *Energy Fuels*, **12**, pp. 223–229.
- [15] Ishida, M., Jin, H., and Okamoto, T., 1998, "Development of a Novel Chemical-Looping Combustion: Synthesis of a Looping Material With a

Double Metal Oxide of CoO-NiO," *Energy Fuels*, **12**, pp. 1272–1277.

- [16] Ishida, M., and Jin, H., 1997, "CO₂ Recovery in a Power Plant With Chemical Looping Combustion," *Energy Convers. Manage.*, **38**, Suppl., pp. 187–192.
- [17] Ishida, M., and Jin, H., 1998, "Greenhouse Gas Control by a Novel Combustion: No Energy Penalty and No CO₂ Separation Equipment," *Greenhouse Gas Control Technologies*, Proceedings of the 4th International conference on Greenhouse Gas Control Technologies, Aug. 30–Sept. 2, Interlaken, Switzerland, pp. 627–632.
- [18] Hatanaka, T., Matsuda, S., and Hatano, H., 1997, "A New-Concept Gas-Solid Combustion System 'MERIT' for High Combustion Efficiency and Low Emissions," *Proceedings of the 32nd Intersociety Energy Conversion Engineering Conference*, pp. 944–947.

Carbon Dioxide Emission Analysis With Energy Payback Effect

Motoaki Utamura

Alstom K. K.,
3-4, Minatojima-Nakamachi 2-chome,
Chuo-ku, Kobe[6]50-0046, Japan
e-mail: utasan@asp1.ijsnet.ne.jp

Analytical model is proposed to account for carbon emission behavior during replacement of power source from fossil to renewable energy in which sustainability of energy supply is stressed. Analyses show that energy payback time (EPT) should be much shorter than the doubling time of manufacturing cycle to secure adequate available energy during as well as after the replacement. Nuclear, small hydropower, and photovoltaic cell are taken as representative candidates and investigated as an option to replace fossil power until mid-century. Nuclear and small hydropower can be promising candidates but photovoltaic cell needs further development efforts to reduce EPT to avoid energy expense after the replacement. [DOI: 10.1115/1.1691442]

Introduction

The global warming rate has recently been more rapidly than ever observed in the past. According to climate model simulation by IPCC, [1], this warming cannot be accounted for without the increase of the concentration of carbon dioxide (CO₂) in the atmosphere. In order to stabilize the CO₂ concentration in the air within an allowable limit at the beginning of the next century, drastically low carbon future would be envisaged. For example, DNE21 model, [2], warned annual carbon emissions should start decreasing in 2040 and eventual CO₂ emission cuts of more than half of today's level should be reached. To achieve the goal, efforts should be focused on the exploitation of carbon-free renewable energy. Its energy density, however, is generally low and thus consumes energy as well as requires investment per unit of energy produced by itself more than that of fossil fuel, to install its power source.

It is common to evaluate initial cost, transportation cost and running cost to judge whether a new power generation system should be introduced. Energy balance considerations, however, are much more fundamental to determine if a certain system may be an effective measure to reduce CO₂ emissions. In fact, the introduction of the renewable energy is not carbon free when it is undergoing to substitute for fossil fuel because its manufacturing consumes fossil fuel. Less work, however, has been done so far on systematic approach to macroscopic energy system based on energy balance. Both energy payback time and life cycle time of a certain power generation system are key concepts to judge whether the introduction of the system is proper or not.

A simple analytical model was proposed to predict carbon emissions sent to the atmosphere as function of time during introducing renewable energy. Also, based on calculation result restrictions regarding both the energy payback and the life cycle times were discussed on photovoltaic cells.

Sustainability of Energy Supply

Steady-State Conditions. Rebirth scenarios in general illustrate future such as global primary energy supply becomes saturated while end demand increases depending on population growth.

Some fundamental inequalities are discussed below for the sustainability of electric power supply.

Contributed by the International Gas Turbine Institute (IGTI) of THE AMERICAN SOCIETY OF MECHANICAL ENGINEERS for publication in the ASME JOURNAL OF ENGINEERING FOR GAS TURBINES AND POWER. Paper presented at the International Gas Turbine and Aeroengine Congress and Exhibition, Amsterdam, The Netherlands, June 3–6, 2002; Paper No. 2002-GT-30448. Manuscript received by IGTI, December 2001, final revision, March 2002. Associate Editor: E. Benvenuti.

(1) *Effectiveness of Power Source.* It is apparent that in any meaningful electric power source energy required to manufacture itself must not exceed total energy produced in its life. This condition leads to $b < c\tau_1$ that reduces to using energy payback time ε

$$\varepsilon/\tau_1 < 1. \quad (1)$$

(2) *Retention of a Given Energy Supply K.* Suppose a group of electric power sources that continue to supply annual constant energy K where successive dieback and reproduction occur. Then energy requirement similar to the above holds to the group, i.e., $Nb/\tau_1 < K$ that reduces again to Eq. (1). Thus, Eq. (1) is a necessary condition to sustain energy system as well.

(3) *Availability Consideration.* Left-hand side of Eq. (1) may be understood as dimensionless energy payback time (DEPT) and is denoted by β . Here, coefficient of availability (COA) α is defined as the ratio of net available energy produced in life time (total energy produced minus production energy) to the total energy produced. Then, from the definition, α is related to β as follows:

$$\alpha = 1 - \beta. \quad (2)$$

Dynamic Conditions. In order to be able to replace a conventional power source (CPS) by a new one (NPS), the amount of electricity generated by an active new power source a year must exceed the energy required to manufacture itself per year.

To meet the requirement with death as well as birth of power source considered, the following inequality must hold regardless of time

$$cX \geq bf'(t) \quad (3)$$

where

$$X = f(t) - f(t - \tau_1). \quad (4)$$

With the assumption that $f(t)$ is of exponential type function being $2^{t/\tau_2}$ applied to Eqs. (3) and (4), we can reduce

$$\gamma(1 - e^{-1/\gamma}) \geq \beta \quad (5)$$

where

$$\gamma = \tau_2 / (\tau_1 \ln 2). \quad (6)$$

It is seen that to create available energy doubling time τ_2 must have a lower limit value as function of τ_1 , ε and α_0 .

This restriction guarantees the condition that replacement of power source, say from fossil to renewable should take place.

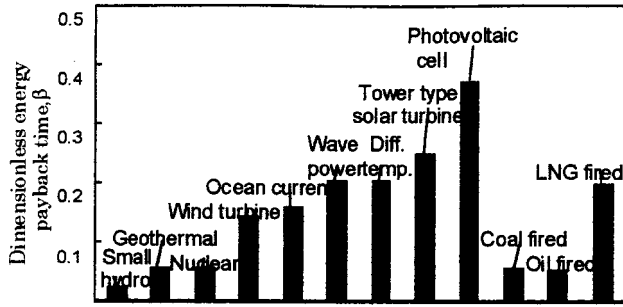


Fig. 1 Dimensionless energy payback time of various power sources

In case that $\tau_1 \gg \tau_2$, the value of bracket on the left hand side of Eq. (5) approaches unity. Equations (2) and (5) are useful to select appropriate candidate among various carbon-free renewable energies and establish their production schedule.

Figure 1 shows DEPT of various renewable power sources reduced from Ref. [3] in comparison with fossil fired current power source which covers 95% of primary energy supply of the world at present. For example, DEPT of photovoltaic cell is 0.37 from Fig. 1 and then Eq. (2) yields $\alpha = 0.63$.

This means maximum achievable COA is 0.63 that is much smaller than that of fossil power source.

Analysis of Carbon Emissions From Mixed Power Sources During Replacement

CO₂ emission from power plants result from three ways, i.e., (1) manufacturing and installations of facility, (2) operation and maintenance (O & M), and (3) fuel combustion. Fossil power meeting 95% of world electricity demand at the moment emits most CO₂ due to the fuel combustion. On the other hand, natural energy as an alternative to fossil energy for CO₂ abatement is not necessarily free from CO₂ emission because fossil energy is consumed during its manufacturing and installations until replacement completes. Its portion is reported almost 100% for small hydropower and more than 90% for both photovoltaic cell and wind power, [3].

From the above, following assumptions are imposed in analysis for simplicity.

1. Power sources can be divided into two categories, conventional (fossil) and new (renewable) ones. Suppose the former is replaced by the latter with time.
2. Conventional power source (CPS) is represented by coal fired plant and emits most CO₂ in the process of fuel combustion.
3. New power source (NPS) emits CO₂ during manufacturing and installation only and none of CO₂ in its operation.

Constant Gross Energy Supply Scheme (Model A). Total carbon emitted from power sources is the sum of contributions from both the conventional and the renewable.

Assuming mixed power is unchanged during replacement by the new power and maintained to be equal to K , then carbon mass balance may be expressed by

$$KA_m = A_0(K - c\Delta X) + A_m bf'(t). \quad (7)$$

Incorporating Eq. (4) and referring to the definition of ΔX , Eq. (7) can be rewritten as

$$a \equiv \frac{A_m}{A_0} = \frac{1 - (f(t) - f(0))/N + (f(t - \tau_1) - f(-\tau_1))/N}{1 - \varepsilon f'(t)/N} \quad (8)$$

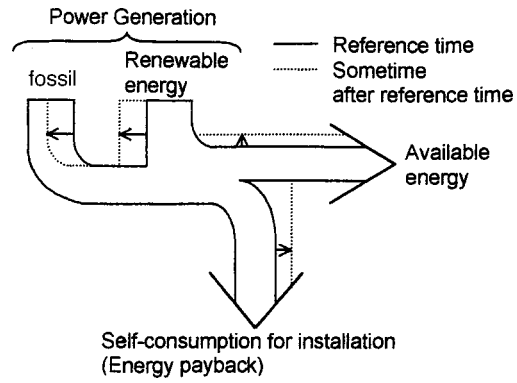


Fig. 2 Electric energy balance

where $f(t)$ is the cumulative number of the renewable power sources manufactured until time t that is assumed to be doubled in every τ_2 years giving

$$f(t) = f(0)2^{t/\tau_2}. \quad (9)$$

Then using dimensionless time $\phi (= t/\tau_1)$, Eq. (8) leads to

$$a = \frac{1 - G(\phi)}{1 - J(\phi)} \quad (10)$$

where

$$G(\phi) = (e^{\phi/\gamma} - 1)/N$$

$$J(\phi) = \beta e^{\phi/\gamma} / (\gamma N (1 - e^{-1/\gamma})). \quad (11)$$

The time of complete replacement τ_f is expressed with dimensionless form δ_A from solving the equation $K = c\Delta X$ with respect to ϕ

$$\delta_A = \gamma \ln(N + 1). \quad (12)$$

Energy balance of a mixed power system follows (see Fig. 2). In this model total production energy is constant equal to K and then by definition,

$$\sigma = 1. \quad (13)$$

Energy consumption for manufacturing power sources is $(1 - \alpha_0)(K - c\Delta X) \equiv B$ for conventional power (CPS) and $bf'(t) \equiv C$ for a new one (NPS). Then, available energy may be expressed by $K - B - C$ and the coefficient of availability (COA) α_m for the mixed power system yields

$$\alpha_{mA}(\phi) = (1 - \alpha_0)G(\phi) + \alpha_0 - J(\phi) \quad (14)$$

and becomes at $\phi = \delta_A$ when replacement completes

$$\alpha_{mA}(\delta_A) = 1 - \beta(N + 1) / (\gamma N (1 - e^{-1/\gamma})). \quad (15)$$

Increased Available Energy Supply Scheme (Model B). Here the energy supply is assumed to be increased by those required for manufacturing new renewable power sources. Then noting that energy supply due to conventional and new power sources become $K - (c\Delta X - bf'(t))$ and $c\Delta X$, respectively, the carbon balance of mixed power system yields

$$A_m(K + bf'(t)) = A_0(K - (c\Delta X - bf'(t))) + A_m bf'(t) \quad (16)$$

under the condition that $cX \geq bf'(t)$ (Eq. (3)). This reduces to

$$KA_m = A_0(K - c\Delta X) + A_0 bf'(t).$$

Following the precedent procedure, we have

$$a = 1 - G(\phi) + J(\phi). \quad (17)$$

The total production energy is $K + bf'(t)$ and then expressed by

$$\sigma = 1 + J(\phi).$$

Table 1 Summary of expressions of models

| Item Model | Energy production, σ | Available energy, α_m | Carbon emission ratio, a | Time of completion of replacement, δ |
|--------------------------------------|--|---|---|---|
| A. Constant gross energy supply | 1 | $(1-\alpha_0)G(\phi) + \alpha_0 J(\phi)$ | $\frac{1-G(\phi)}{1-J(\phi)}$ | $\gamma \ln(N+1)$ |
| B. Increased available energy supply | $1+J(\phi)$ | $\alpha_0 + (1-\alpha_0) \cdot (G(\phi)-J(\phi))$ | $1-G(\phi)+J(\phi)$ | $\gamma \ln((N+1)(1-e^{-1/\gamma}) / (1-\beta/\gamma \cdot e^{-1/\gamma}))$ |
| C. Constant available energy supply | $1 - \left(\frac{1}{\alpha_0} - 1\right)G(\phi) + \frac{1}{\alpha_0}J(\phi)$ | α_0 | $\frac{\alpha_0 - G(\phi) + J(\phi)}{\alpha_0 - (1-\alpha_0)(G(\phi)-J(\phi))}$ | $\gamma \ln(\alpha_0(N+1)(1-e^{-1/\gamma}) / (1-\beta/\gamma \cdot e^{-1/\gamma}))$ |

Note: $G(\phi) = (e^{\phi/\gamma} - 1)/N$
 $J(\phi) = \beta e^{\phi/\gamma} / (\gamma N(1 - e^{-1/\gamma}))$

Full replacement occurs at the time τ_f when

$$K - (c\Delta X_f - bf'(t)) = 0$$

holds. Then dimensionless form δ_B for τ_f becomes

$$\delta_B = \gamma \ln((N+1)(1 - e^{-1/\gamma}) / (1 - \beta/\gamma \cdot e^{-1/\gamma})). \quad (18)$$

It is seen that δ_B is larger than δ_A in the precedent model of constant K .

Available energy supply is $K\alpha_0 + (1 - \alpha_0)(c\Delta X - bf'(t))$ and COA α_m can be written as

$$\alpha_{mB}(\phi) = \alpha_0 + (1 - \alpha_0)(G(\phi) - J(\phi)). \quad (19)$$

When replacement completes, $\alpha_{mB}(\delta_B)$ becomes unity as is expected from the assumption.

Constant Available Energy Supply Scheme (Model C). In this model, energy would be supplied by a new renewable power source so that available energy remains unvaried with the value $\alpha_0 K$ at any time. Thus, $\alpha_{mc} = \alpha_0$.

Based on this assumption, energy balance becomes with unknown parameter η

$$\alpha_0 [K - \eta(c\Delta X - bf'(t))] + c\Delta X - bf'(t) = \alpha_0 K. \quad (20)$$

This reduces to

$$(1 - \alpha_0 \eta)(c\Delta X - bf'(t)) = 0.$$

The condition that Eq. (20) be identity with respect to t yields

$$\eta = \frac{1}{\alpha_0}. \quad (21)$$

Then, carbon balance becomes

$$\begin{aligned} A_m \left[K - \frac{1}{\alpha_0}(c\Delta X - bf'(t)) + c\Delta X \right] \\ = A_0 \left[K - \frac{1}{\alpha_0}(c\Delta X - bf'(t)) \right] + A_m bf'(t). \end{aligned} \quad (22)$$

This reduces to

$$a = \frac{\alpha_0 - G(\phi) + J(\phi)}{\alpha_0 - (1 - \alpha_0)(G(\phi) - J(\phi))}. \quad (23)$$

and

$$\sigma = 1 - \left(\frac{1}{\alpha_0} - 1\right)G(\phi) + \frac{1}{\alpha_0}J(\phi).$$

Replacement of power source ends at the time τ_f when

$$K - \frac{1}{\alpha_0}(c\Delta X - bf'(t)) = 0$$

holds. Normalized expression δ_c for τ_f becomes

$$\delta_c = \delta_B + \gamma \ln \alpha_0. \quad (24)$$

This model coincides with model B in extremity when α_0 approaches unity.

Model Comparison. Table 1 summarizes expressions among models described in the above sections and Fig. 3 shows samples calculations of them with parameter values $\alpha_0 = 0.95$, $\beta = 0.1$, $\gamma = 0.19$, and $N = 2300$. These are derived from those of coal fired thermal power plant (α_0) and photovoltaic cell (β, γ, N), [4], related to the development undergoing in Japan. As shown in Fig. 3(c) the expression of energy produced by new power is $G(\phi)$ and common to all models. Since α_0 is close to unity, simulation results by model B and C behave similarly. From Fig. 3(a) it is seen that these models yield production of total energy at the end of power source replacement almost two times larger than the initial value.

This comes from the fact that $G(\delta_B) \cong 1/(1 - \beta/\gamma)$ and $\beta/\gamma \cong 0.5$. These are equipped with active renewable power sources whose number is two times more than that of model A as shown in Fig. 3(c). The amount of carbon emission is least in the model A at the expense of available energy as shown in Figs. 3(b) and 3(d). Once the replacement is completed, energy production rate thereafter may be constant, i.e., $J(\phi) = G(\delta)$, ($\phi \geq \delta$). Hence, such a power source as having either small value of $G(\delta)$ or high available to total energy ratio would be preferred in the choice of new power source.

Gross Carbon Emissions. Using the model B, the amount of carbon release in the air during the course of time of replacement is evaluated by the following integral:

$$l = \int_0^{\delta_B} a \sigma d\phi. \quad (25)$$

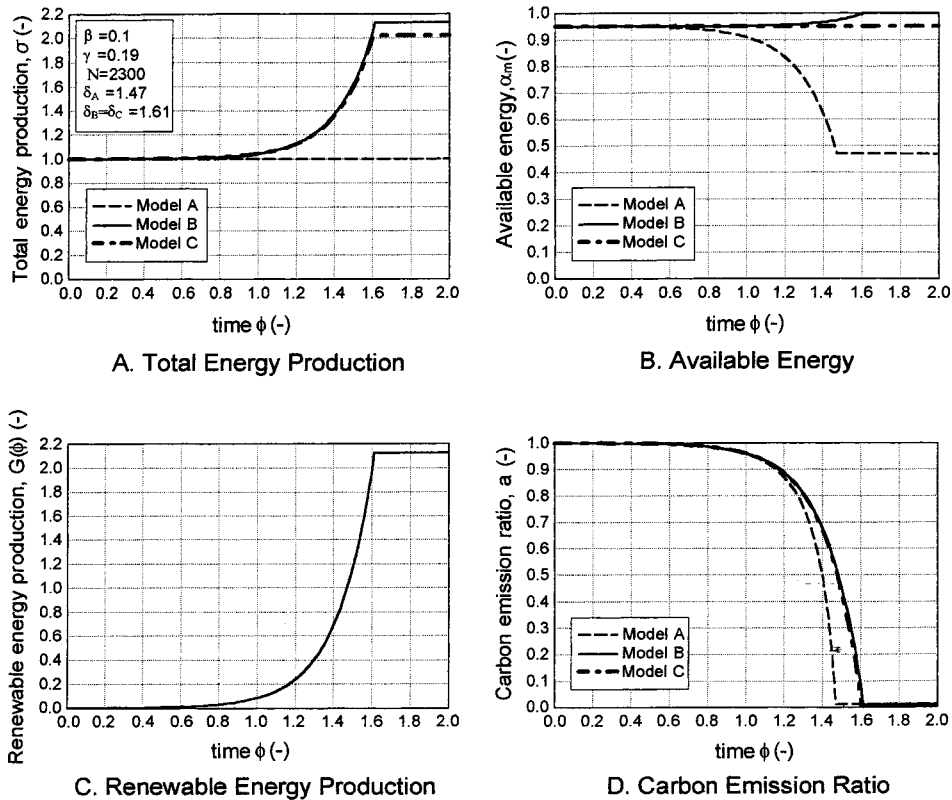


Fig. 3 Energy production and carbon emission during replacement of coal-fired power source by renewable one

Initial value of unit carbon emission per unit time is due to the old power source. Then, $1 \times \delta_B$ would be understood to be its contribution. A product $l\tau_1$ is a measure of the amount of carbon release.

Results and Discussions

Prediction of Power Conversion Time and Carbon and Emissions for Representative Carbon Free Energy Sources. Among candidates for renewable power source, nuclear, small hydropower and photovoltaic cell were chosen and analyzed. They are representative because nuclear is already prevailed, small hydropower has a large amount of resources to be exploited with smallest energy payback time (EPT) and photovoltaic cell is easy to be installed anywhere on the earth but has the biggest EPT at present as shown in Fig. 1.

Adopting model B in the precedent section, where increased available energy is guaranteed, time of complete replacement and carbon release was analyzed.

Calculation procedure follows:

1. Specify renewable energy and obtain β from Fig. 1.
2. Input K and $cX(0)$, and calculate $N(=K/cX(0))$.
3. Guess permissible γ considering Eq. (5).
4. Calculate δ using Eq. (18).
5. Calculate τ_f and compare with target value.
6. Calculate σ_f from $\sigma = 1 + J(\phi)$ using Eq. (11).

Results are given in Table 2 and Fig. 4.

K value of 600TWh/y was electric energy produced by burning fossil fuel in Japan in 1996 which is to be replaced by carbon-free energy. Photovoltaic cell power capacity reached about 200 MW

in 1999 in Japan, which is the largest in the world, [4]. The value of $cX(0)$ were determined assuming 90% availability for nuclear and 60% for small hydropower, and 15% for photovoltaic cell, [4,5]. As mentioned earlier, carbon release in the air should start decreasing until mid-century in order to stabilize the concentration of carbon dioxide at the beginning of the next century so as to reach the value two times larger than that of pre-industrial era. Considering this situation, results show that nuclear and small hydropower, having tolerable value of τ_f , may be a good candidate in terms of CO_2 abatement. Here, we have to care about it that nuclear is not a renewable but an exhaustible energy resource, and not reputable among natural resources. Also, hydropower may affect ecosystem around river during and after exploitation.

Photovoltaic cell, however, requires 97 years from 1999 for complete replacement according to the present performance characteristics, which is too long to realize the rebirth scenario. Besides, σ_f is very large. This means the present specifications i.e., 20 years of average life and 7.4 years of energy payback time (EPT) need improved. Then, these were modified to be three years for EPT and 30 years for life respectively within a range under controversy and calculated again. It is seen result was much improved in terms of replacement time. In view of energy, however, total power σ_f required in this case is seen to result in still two times larger than those required following the analysis given in the preceding section. This means half of energy is consumed to make photovoltaic cells themselves. Out of scope of this study though, it might probably raise a serious cost issue. On the other hand, in the cases of nuclear and small hydropower, excess power is estimated to be about 14% and 6%, respectively, both of which are very small.

In these new power sources, longer replacement completion tactics look tolerable even at the expense of allowance of a bit

Table 2 Assessment of renewable energy candidates

| Parameter | Power source | Nuclear | Small hydropower | Photovoltaic cell | |
|-----------|----------------|---------------|------------------|-------------------|-----------------|
| | | | | Present spec. | Target spec. |
| Input | K (TWh /y) | 600 | 600 | 600 | 600 |
| | cX(0) (TWh /y) | 330 (41GW) | 82 (15GW) | 0.26 (200MW) | 0.26 (200MW) |
| | β | 0.06 | 0.02 | 0.37 | 0.1 |
| | τ_1 (y) | 30 | 30 | 20 | 30 |
| | N | 1.8 | 7.3 | 2300 | 2300 |
| Output | γ | 1.5 | 0.5 | 0.5 | 0.19 |
| | δ_B | 1.67 | 1.08 | 4.84 | 1.61 |
| | τ_2 (y) | 31 | 10 | 7 | 4 |
| | τ_f (y) | 50 | 32 | 97 | 48 |
| | σ_f | 1.14 | 1.06 | 6.9 | 2.1 |

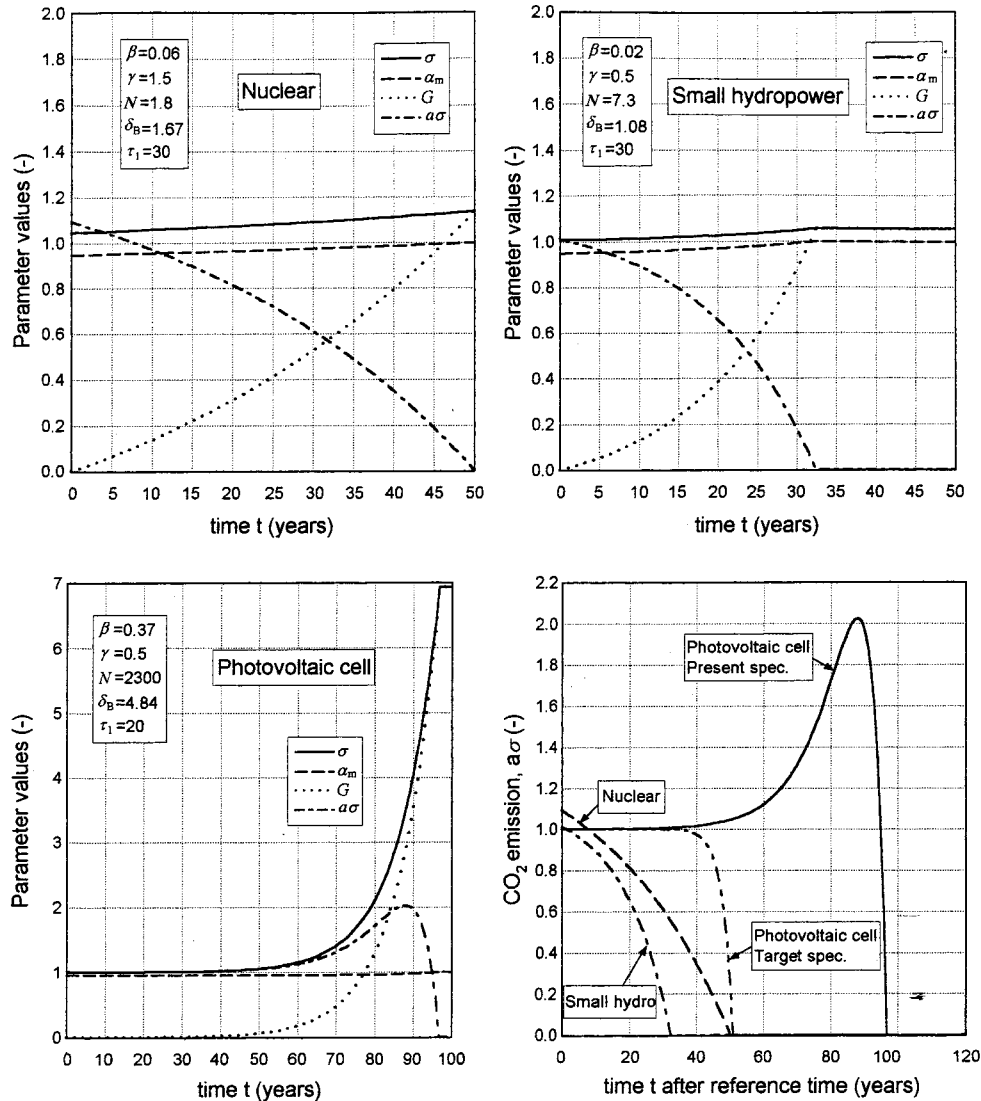


Fig. 4 Energy production and carbon emission during replacement of coal-fired power source by various nonfossil power source

$$\varepsilon \ll \tau_2 \ll \tau_1. \quad (30)$$

This yields optimal choice of parameter range for τ_2 , which serves in planning manufacturing scheme for NPS.

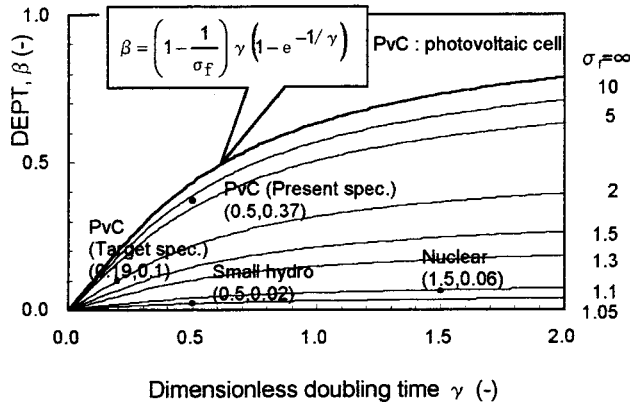


Fig. 5 Capacities of various nonfossil power sources at complete replacement

more release of carbon. It is important to note that once complete replacement reached, power generation scale cannot be reduced without loss of available energy.

In the case of photovoltaic cell, the amount of carbon release exceeds unity, which results from increased manufacturing rate. However, it is seen that it is improved in the case of target spec. of photovoltaic cell.

Restrictions on the Energy Payback, Average Life, and Doubling Time in Manufacturing Renewable Power Source.

Preferable design and manufacturing conditions are discussed in this section, which serves to determine the goal of renewable energy resource development. In view of energy saving, an energy strategy to maximize the available energy as well as to minimize the number of installations of new power sources is desired. Its dominant parameters are sought.

(1) The number of installations of new power sources. Using the relation $\sigma_f = 1 + J(\delta) = G(\delta)$, the number of active power sources at the end of replacement σ_f is expressed by

$$1/\sigma_f = 1 - \beta(N+1)/\gamma(N(1 - e^{-1/\gamma}) + \beta/\gamma). \quad (26)$$

With $N \gg 1$, this expression can be approximated by

$$1/\sigma_f = 1 - \beta/\gamma(1 - e^{-1/\gamma}) \quad (27)$$

which strongly depends on the value β/γ . Under the condition $\gamma \ll 1$, Eq. (27) may be further simplified to $1/\sigma_f = 1 - \beta/\gamma$. It is important to note that $1 - \beta/\gamma$ is independent of life time τ_1 . The inequality

$$\beta/\gamma \ll 1 \quad (28)$$

is desirable from the standpoint of energy saving. This implies that power source manufacturing rate ($1/\gamma$) of the next generation should have an allowable higher limit as function of energy payback time β .

Figure 5 shows the relation between β and γ with σ as a parameter. Calculation results for nonfossil energy in Table 2 are also plotted. It is interesting to note that the envelope line corresponding to $\sigma_f = \infty$ coincides with Eq. (5).

In view of energy saving, smaller value of σ_f is desirable, which, it is seen, primarily influenced by β in the range $\gamma > 0.5$. However, the effect of γ becomes significant as well in the range

$$\gamma \ll 1. \quad (29)$$

Coincident realization of Eqs. (28) and (29) is equivalent to

Conclusions

Carbon dioxide (CO_2) abatement by the introduction of renewable energy in place of fossil fuel was modeled and analyzed with overall energy balance taken into account. Limited operation time of new power source was considered. Exponential function of time was assumed as a trial function to express the number growth of new power sources during replacement.

1. Several useful inequalities and relations among characteristic parameters have been obtained in dimensionless forms of energy payback time (EPT), average life (τ_1) and manufacturing doubling time (τ_2).
2. Energy payback time should be controlled much shorter than doubling time in order to obtain sufficient available energy on completion of replacement.
3. Nuclear and small hydropower can be a promising candidate but photovoltaic cell needs further development efforts to reduce EPT to avoid energy expense after the replacement.
4. Energy balance issue should be considered prior to economic one in determining energy option for CO_2 abatement. Present model may be useful in solving inverse problem to determine target specification for developing power sources of renewable energy. Future research task is to involve energy flow model using more realistic trial function of new energy production.

Acknowledgments

Author is indebted to Prof. P. Pilidis, Cranfield University, UK, for his kind recommendation of paper submission on this theme. He also expresses his sincere thanks to Prof. Emeritus H. Yoshiki, Tokyo University, for his kind disclosure of information necessary to conduct this work.

Nomenclature

- A = carbon sent to the atmosphere per unit electric energy produced
- a = normalized value of carbon emissions ($\equiv A_m/A_o$)
- b = energy required to manufacture a new electric power source (NPS)
- c = electric energy produced by NPS per year
- $f(t)$ = cumulative number of NPSs installed after reference time ($t=0$) until time t
- $f'(t)$ = derivative of $f(t)$ with respect to t
- $G(\phi)$ = normalized energy production by NPSs per year
- $J(\phi)$ = normalized introduction rate of NPSs
- K = a fraction of primary electric energy supply per year to be replaced by NPSs
- N = the number of NPSs equivalent to K ($\equiv K/cX(0)$)
- t = time (year)
- X = the number of active NPSs ($\equiv f(t) - f(t - \tau_1)$)
- ΔX = increment of the number of active NPSs after reference time ($t=0$) ($\equiv X - X(0)$)

Greek

- α = coefficient of availability (COA) ($\equiv 1 - \beta$)
- β = dimensionless energy payback time (DEPT) ($\equiv \varepsilon/\tau_1$)
- γ = dimensionless doubling time ($\equiv \tau_2/(\tau_1 \ln 2)$)
- δ = dimensionless form of τ_f ($\equiv \tau_f/\tau_1$)
- ε = energy payback time (EPT) ($\equiv b/c$)

σ = energy production normalized by K
 τ_1 = life time of NPS
 τ_2 = doubling time in production of NPSs
 ϕ = dimensionless time $t(\equiv t/\tau_1)$

Suffices

o = reference time
 m = mixed state of conventional and new power sources
 f = time when conventional power sources (CPSs) are fully replaced by NPSs

References

- [1] Godrej, D., 2001, *Climate Change*, Verso, London.
- [2] Kaya, Y., 2000, "Carbon Dioxide Abatement Strategy (in Japanese)," *Nikkan-Kogyo*, Aug. pp. 179–217.
- [3] Uchiyama, Y., and Yamamoto, H., 1991, "Energy Analysis of Various Electric Power Plants for CO₂ Emission Evaluation (in Japanese)," *Electric Economy Research*, (29), June, p. 7.
- [4] Kando, M., 2001, "Photovoltaic Power Generation (in Japanese)," *Journal of Thermal and Nuclear Power*, **52**(10), Oct.
- [5] Hondo, H., et al., 2000, "Evaluation of Power Generation Technologies Based on Life Cycle CO₂ Emissions (in Japanese)," CRIEPI Report No. Y99009, Mar.

Small-Scale Well-Proven Inherently Safe Nuclear Power Conversion

G. A. K. Crommelin

Captain (E) RNLN (ret),
Huzarenlaan 15,
7215 ED Joppe, The Netherlands
e-mail: gulian.crommelin@tip.nl

Over the last few years a number of papers have discussed the progress on studies and thoughts on small-scale nuclear power, especially nuclear power conversion systems aiming at the nonutility markets, such as the stand-alone heat generation, combined heat and power production, stand-alone electricity conversion, and ship propulsion. The design of these installations must fully comply with the philosophies as are common in these markets, where the expression “the engine is a means to an end” applies. So design to cost, design to be operated by non professional energy producers, to be managed by a pool-management system, maintained, repaired and overhauled by replacement, etc. The paper will discuss such a design. So far all papers mentioned have discussed the gas turbine directly coupled to the heat source. However, the helium turbine is considered quite a challenge for the gas turbine industry, so alternatives had to be found. At the moment the possibilities of gas turbines with an indirect heat source (to burn refuse, wood, refinery waste, etc.) are getting much more attention. The paper therefore will discuss how an inherently safe, well proven, nuclear heat source can be coupled by an intermediate heat exchanger to a recuperative, existing but adapted gas turbine. [DOI: 10.1115/1.1691946]

Introduction

There seem to be two reasons and two facts requesting for timely innovation of the small-scale energy conversion units.

First, recent studies about the expected growth of the world population indicate a slowing down (World Energy Council), but still a doubling is expected by the middle of this century. In addition it can be expected that on average the world economy will continue to grow and it is predicted too that the increase of the shortage of fresh water will continue to grow. (Figs. 1 and 2).

This will result in a very impressive growth in the demand for energy in general, including transport and industry. For example: between 1960 and 2000 the world population doubled from 2.5 to 5 billion. During the same period the tonnage of shipping worldwide went from 100 million brute tonnage to nearly 500 million BRT (partly as a result of the number of oil tankers, but also because of the growth of the world economy) (Aalders TU-Delft, [1]).

Secondly, to convert enough energy to fulfil these needs all existing energy conversion units must be ready to be used, where and when they are most effective. The possibilities of the two existing energy producers used in the markets of small-scale energy requirements (diesel and gas turbine) have reached their technical optimum and are increasingly put under pressure to cut emissions from the environmental organisations and political parties all over the world. For example, a recent study of the scientific bureau of a leading political party in the Netherlands stated, based upon statistics, “most of the polluting emissions leading to acidification, take place in the maritime environment.” The reasons are the gaseous emissions, which contain not only CO₂, but also a combination of NO_x (nitrogenoxide), SO₂ (sulphur dioxide) and NH₃ (ammonia). The example used is: shipping controlled by Dutch companies, is held responsible for 23% of the acidification

(agriculture—43%, the other branches—less than on average, 6%).

So the awareness of this kind of pollution has reached politics. It therefore seems logical that the pressure will increase on the shipping branch to comply with the intentions and the rules regarding the environment. The only way the shipping branch can stand up to these challenges is by (timely) innovation. And part of that innovative effort should be looking for better propulsion plants that keep the price per transport at the same level and is more environmentally friendly than today’s propulsion plants. Although the price per kWh of the fossil-fired propulsion plant is still attractive for the owners, the thinking about the next step should start now. Because of an another old law: “Timely innovation is a necessity for a company to survive.”

The first fact is an old one. New technologies have never waited until the old version was worn out, or the fuel had run out, etc.

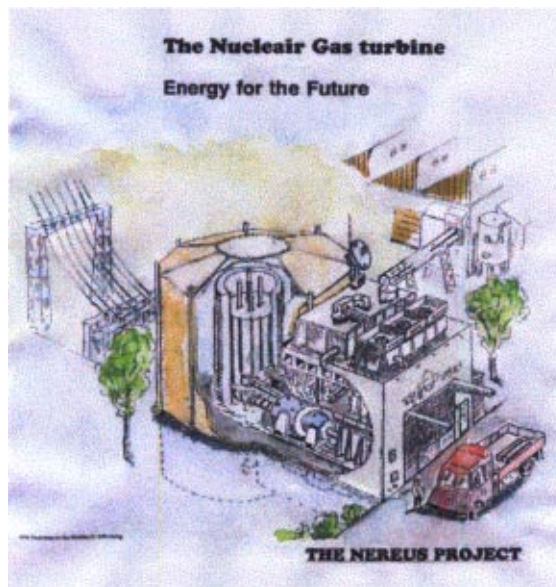


Fig. 1 An artist impression of a nuclear gas turbine plant

Contributed by the International Gas Turbine Institute (IGTI) of THE AMERICAN SOCIETY OF MECHANICAL ENGINEERS for publication in the ASME JOURNAL OF ENGINEERING FOR GAS TURBINES AND POWER. Paper presented at the International Gas Turbine and Aeroengine Congress and Exhibition, Amsterdam, The Netherlands, June 3–6, 2002; Paper No. 2002-GT-30509. Manuscript received by IGTI, Dec. 2001, final revision, Mar. 2002. Associate Editor: E. Benvenuti.

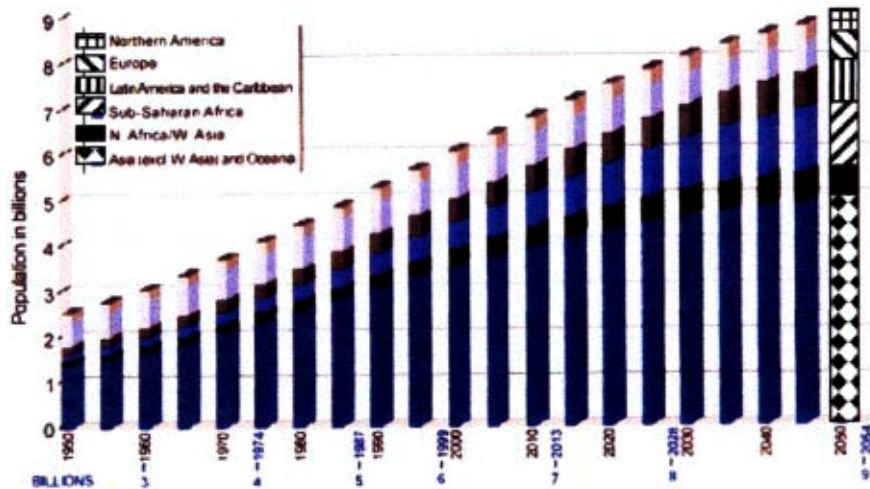


Fig. 2 Regional distribution of the world population (1950–2050)

Also known as the law: “the Stone Age was not over because humanity could not find stones anymore, but because new technologies and tooling became available.”

The second fact. The capacity of the “green energy sources” are limited. Hydropower is increasingly considered “nongreen,” because of the effect of the big mass of water on the local climate. Solar power is still very expensive and most people do not want a windmill in their back yard. But most importantly: energy is electricity and/or heat and fresh water. In the Netherlands electricity is only 30% of the total energy demand. And none of the green power systems delivers actual heat.

The Solutions? There is a well-proven, demonstrated, documented, inherently safe nuclear technology in the cupboard of several scientific institutions and organisations waiting to be used. It is called the “HTR-GT,” which stands for high temperature reactor with a gas turbine as energy conversion unit.

The reaction of most owners of ships on presentations of the possibilities of the inherently safe nuclear reactor in combination with a gas turbine is very much the same and representative for the markets as mentioned:

“We had never heard of this possibility, but we agree with the arguments. We foresee for the near future problems with passengers taking a cruise on board a nuclear powered ship, or entering certain harbors. However, shipping will not go back to sails or even rowing. Solar power is no option either. So we have to take “nuclear” on board”.¹ (See Refs. [2–11]).

The NEREUS Project

The project, mentioned in the abstract, is called “The NEREUS project.” In this case “NEREUS” stands for: a Naturally safe, Efficient, Reactor, Easy to operate, Ultimately simple and Small. This describes very well the aims of the design team and the only way in which a nuclear plant will be technically acceptable for the markets of stand-alone heat generation, Combined heat and power production, stand-alone electricity conversion and as prime mover on board ships with an all-electric propulsion system. In other words the markets of the nonprofessional energy producers. (Haverkate et al. [12]).

The correct way to preserve the environment is not to disturb it at all. And when you have to disturb it, because of activities necessary to your way of life, be certain that the disturbance is as minimal as possible. The best way of doing that is expressed by

¹It is possible to make a cruise to the North Pole on board Russian nuclear icebreakers.

the following expression in the Dutch language: “Do not, by way of thanks for the pleasant stay, leave the owner of the woods the empty bags and bottles.”

For shipping this means:

- no oil pollution and a minimum of wave disturbance as result of bow wave and wash,
- a minimum of gaseous and waste heat emissions, and
- a minimum of noise and vibrations.

And this must, for financial reasons, be combined with a minimum of costs.

History

The step towards nuclear power conversion is a logical one in the history of mankind. Figure 3 shows, in an artistic way, the history of the way in which the human race has produced energy. The way this energy was converted into useful energy can also be analyzed. It is beyond discussion that the attainments related to the availability to mankind of cheap energy will never be given up. Human beings are somewhat reluctant to accept new developments, but when they have learned the advantages they will only give it up when further improvements are available. Only in difficult times, as during a war, will achievements and goods considered as luxuries (temporarily) be set aside. As far as the subject of “energy” is concerned, the availability of cheap and reliable en-



Fig. 3 “Combustion” over the centuries

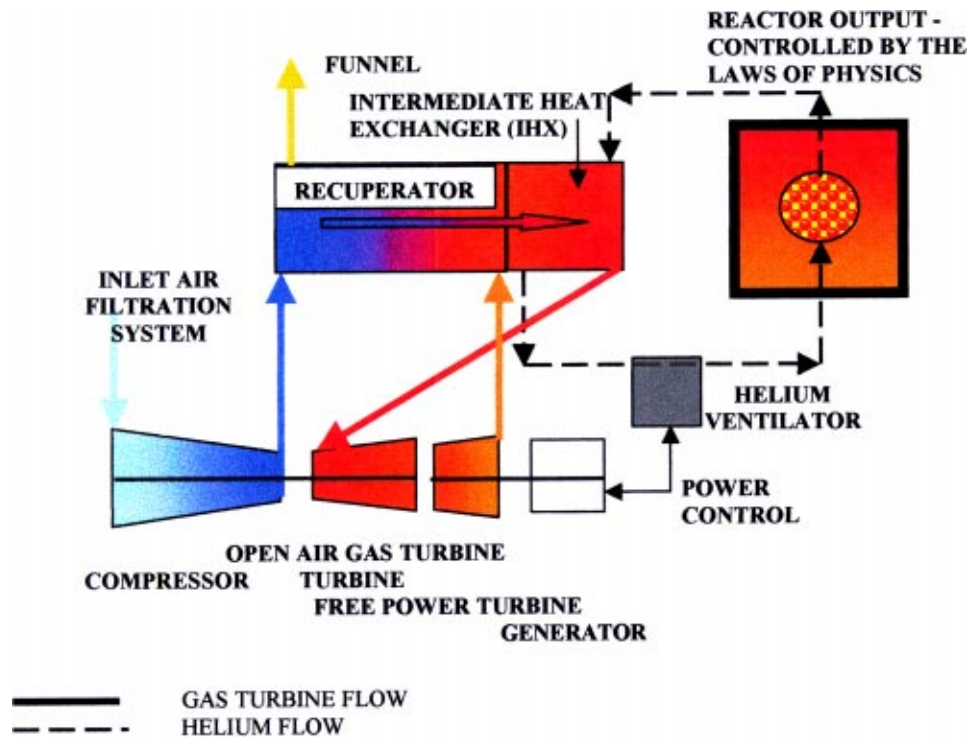


Fig. 4 Open-cycle gas turbine “burning uranium”

ergy, good medical care and clean potable water within a manageable environment are the building stones of our prosperity and welfare. The human race has sometimes tried to turn back history, even at great costs, but it has always been in vain.

The Trends in Energy Production. “We celebrate the past, to awaken the future”—John F. Kennedy

- The amount of energy per kg fuel increases.
- The combustion unit decreases in size per kW.
- Emissions change from “deluted and dispersed” (uncontrollable) to “confined and controlled” (manageable).
- The medium for transportation increases in purity, causing less corrosion and erosion.
- The energy transport system starts as an open (dirty) cycle, but becomes a closed (clean) cycle.
- The rotating energy conversion unit becomes standard.
- The complexity of the installations increases during its usage period due to a constant.
- Stream of modifications and improvements.
- The number of people to control and maintain the installations decreases.
- The weight and volume per produced KW decreases.
- The total process efficiency increases constantly.
- New systems never appear as a result of a shortage of a type of fuel, but because better systems became available. The end is always a very complex engine trying to fight off, in vain, the new systems coming along.

Conclusion 1: This results in energy conversion systems with lower through life costing per kWh.

Conclusion 2: Nuclear power conversion is the logical next step in the ways humanity produces energy.

Conclusion 3: The (closed-cycle) gas turbine with an inherently safe, well-proven, nuclear heat source seems to be the next logical step in the history of energy conversion.

So far all studies on gas turbines with a nuclear heat source

have connected the heat source to the energy conversion unit by a closed-cycle system consisting of a helium gas turbine. A logical thought, because it seems undoubtedly to lead to the highest efficiency and compactness. However, helium gas turbines are not proven technology yet. It seems to become an expensive operation to design, construct and test such a machine.

On the other hand, many studies and tests are going on to design different external heat sources for gas turbines. Heat sources which are able to burn, in a controllable and effective way, waste of refineries, biomass, industrial waste gases, pulverised coal, etc. So it seems logical to investigate whether uranium could be added to this list of fuels.

From the publications on the closed-cycle nuclear gas turbine (HTR-GT) one learns that the nuclear fuel is cooled by helium, pumped around by a recuperative gas turbine. However, the test reactor in Jülich worked with a two-loop system. The reactor was cooled by helium pumped around by a so-called helium ventilator. The heat was transported to a steam cycle via an Intermediate Heat Exchanger. So this test bed was actually a standard (Rankine) pressurized water reactor power plant, with a new nuclear heat source.

The logical next thought is why not change in the Jülich concept the Rankine-type secondary water-steam closed cycle into a Brayton-type open cycle and see how these systems compare with the Brayton-type open cycle for small (circa 20 MWth) plants.

For the open-cycle loop Fig. 4 has been the subject of a preliminary study.

Reactor construction, size and shape, cooling, internal power control, both gas turbines use a recuperator, industrial heat exchanger can be applied, both systems can use a free power turbine, the same nuclear reactor control by the negative temperature coefficient, both fit into a space of $10 \times 10 \times 10$ meters, both can have a one spool or two spool turbine with a free power turbine (the PBMR Co (SA) project uses a two spool helium turbine with a free power turbine) and for logistic support both are suitable for a pool-management system.

| Differences: | Closed Cycle | Open Cycle |
|--------------------------------|--|--|
| 1. Gas turbine | helium | air |
| 2. Gas turbine | new design | adapted existing gas turbine |
| 3. Generator | helium cooled | air cooled |
| 4. Heat dump in cycle | yes | open air |
| 5. Intermediate heat exchanger | No | yes |
| 6. Control of the installation | mass flow | Revolutions of the helium ventilator |
| 7. Efficiency calculated by | 30°C | 15°C |
| 8. Efficiency | higher | lower due to pressure losses |
| 9. Efficiency at 15°C | | comparable |
| 10. Pressure losses | the IHX increases the pressure losses versus | the closed-cycle |
| 11. Magnetic bearings | compulsory | advisable |
| 12. Amount of helium | more | less |
| 13. Number of rotating seals | none | at least one (helium ventilator) |
| 14. Inlet air | only for reactor cooling | for GT and reactor cooling |
| 15. Funnel arrangements | reactor cooling | outlet reactor cooling and GT outlet, but no gaseous emissions, only hot air |
| 16. Starting | using generator | using existing starting system of the gas turbine (pneumatic, hydraulic or electric starting motor on the HP spool) or the generator probably slower |
| 17. Response to power changes | | comparable |
| 18. Weight total installation | | comparable |
| 19. Volume total installation | | comparable |
| 20. Vibrations | | comparable |

Ad 1 and 2—As said the open cycle could be more easily realised, using existing but adapted gas turbines using the results of studies for gas turbines with an external heat source.

Ad 3—Air-cooled generators are available.

Ad 4—no comment

Ad 5—Intermediate heat exchanger. The existing recuperator designs must be studied for a suitable design. The possibility of radioactive dust entering the helium circuit and through a leak in the gas flow of the gas turbine is always mentioned, however the helium ventilator which was used in Jülich, never showed radioactive contamination.

Ad. 6—The demanded electricity on the generator must be transmitted to the control of the electro motor of the helium ventilator. This will result in a reduction of the helium mass flow, but as has been explained, not in the temperature. This, due to the negative temperature coefficient, will stay at 800°C. This will lead to a reduction of the temperature of the air flow from the IHX to the inlet of the turbine. So the gas turbine will slow down.

Ad 7, 8, and 9—There is always a lot of attention paid to the efficiency of an energy conversion unit. In this case the efficiency of the open air cycle gas turbine will be reduced due to the increase of the resistance in the system caused by the IHX. Any efficiency calculations considering gas turbines depend heavily on the inlet temperature of the compressor. In the case of the closed-cycle system this is dictated by the temperature of the air or water used in the heat dump. Most calculations use 30°C, being the temperature of the sea and rivers in the tropics. For an open cycle, the ISO norm applies for the inlet conditions, being 15°C and 1013 mbar pressure.

Ad 10—It is obvious we have to study and to work out the effects of adding an IHX and taking away the heat dump and the cooling of the generator.

Ad 11—Magnetic bearings are a well-proven technology nowadays. The usage is compulsory in the case of a helium closed-cycle system, because of the effects of lubrication oil entering the helium system and so the nuclear fuel. For an open air cycle this seems unnecessary, although to reduce maintenance it is still advisable.

Ad 12—Helium is an expensive gas. It is also not common

knowledge that, due to the importance of this gas for Zeppelins for military applications, there are still restrictions on the procurement.

Ad 13—Helium is a one atomic gas, so it is difficult to seal. This especially applies to rotating seals. As has been explained in the case of a closed-cycle helium system, rotating seals to the open air can be prevented. In the case of the indirect cycle there is at least one rotating seal, the seal between the electromotor of the helium ventilator and the actual ventilator.

Ad 14—In the case of the closed-cycle helium HTR-GT the reactor cooling is driven by natural draft. In case of the open air cycle the gas turbine needs filtrated air as transport medium to bring the reactor energy from the IHX to the turbines.

Ad 15—In addition to the reactor outlet cooling construction, the gas turbine will have a funnel construction as well.

Ad 16—No remarks.

Ad 17—This seems logical in view of the extra weight of the intermediate heat exchanger.

Conclusions

- In view of the predicted doubling of the world population, the doubling of the energy consumption per capita and the further increase in the shortage of fresh water in the next 50 years, the search for more environmentally friendly and controllable energy conversion systems is a necessity.
- “Burning” uranium is the next logical step in combustion.
- “Burning” uranium in an inherently safe way and, indirectly in an open-cycle adapted gas turbine, is possible.
- Timely innovation is a necessity for a company or industrial branches to survive.
- All technologies required are available. However, study and engineering by all parties involved are needed to find the optimal solutions.

The next logical step for small-scale inherently safe nuclear energy conversion can be taken!

General Information

World population (2050)—www.worldenergy.org
Availability of potable water (2025)—www.worldwatercouncil.org

These websites give further information about studies and projects regarding small-scale nuclear power:

IAEA <http://www.iaea.org/inis/aws/htgr/>
South-Africa <http://www.pbmr.co.za> and http://id.inel.gov/Pebble_Bed/mpbr.htm
Japan <http://www.jeeri.go.jp/english/temp.html>
China <http://www.inet.tsinghua.edu.cn/English/>
United States <http://www.ga.com/gtmhr.html>, <http://atomicinsights.com> and <http://atomicengines.com>
The Netherlands <http://www.romawa.nl>

References

- [1] Aalders, 2000,
[2] Wallerbos, E. J. M., 1998, "Reactivity Effects in a Pebble-Bed Type Nuclear Reactor. An Experimental and Calculational Study," Ph.D. thesis, Delft University of Technology, The Netherlands.
[3] van Bende, E. E., 2000, "Plutonium Burning in a Pebble-Bed Type High Temperature Nuclear Reactor," Ph.D. thesis, Delft University of Technology, The Netherlands.
[4] Verkerk, E. C., 2000, "Dynamics of the Pebble-Bed Nuclear Reactor in the Direct Brayton Cycle," Ph.D. thesis, Delft University of Technology, The Netherlands.
[5] Kikstra, J. F., 2001, "Modelling, Design and Control of a Cogenerating Nuclear Gas Turbine Plant," Ph.D. thesis, Delft University of Technology, The Netherlands.
[6] Op het Veld, R., and van Buijtenen, J. P., 1998, "An Empirical Approach to the Preliminary Design of a Closed Cycle Gas Turbine," ASME Paper No. 98-GT-393.
[7] Crommelin, G. A. K., 1999, "The NEREUS Installation—The Nuclear Part," ASME Paper No. 99-GT-88.
[8] Crommelin, G. A. K., 1999, "The NEREUS Installation—The Non-Nuclear Part," ASME Paper No. 99-GT-87.
[9] Crommelin, G. A. K., van der Hagen, T. H. J. J., and van Buijtenen, J. P., 2001, "The Next Logical Step in Prime Movers on Board Ships," 2001-GT-
[10] Hagen, T. H. J. J., van der Buijtenen, J. P., and Crommelin, G. A. K., 2001, "The Next Logical Step in Prime Movers on Board Ships—The Nuclear Part," ASME Paper No. 2001-GT.
[11] van Buijtenen, J. P., Crommelin, G. A. K., and Crommelin, W. F., 2001, "The Design of Closed Cycle Gas Turbines for HTR and Other Heat Sources," ASME Paper No. 2001-GT.
[12] Haverkate et al., 1997,

Gas Turbine Test Parameters Corrections Including Operation With Water Injection

K. Mathioudakis

Associate Professor
Laboratory of Thermal Turbomachines,
National Technical University of Athens,
P.O. Box 64069,
Athens 15710, Greece

Methods for correcting data from gas turbine acceptance testing are discussed, focusing on matters which are not sufficiently covered by existing standards. First a brief outline is presented of the reasoning on which correction curves are based. Typical performance correction curves are shown together with the method of calculating mass flow rate and turbine inlet temperature from test data. A procedure for verifying guarantee data at a specific operating point is then given. Operation with water injection is then considered. Ways of correcting performance data are proposed, and the reasoning of following such a procedure is discussed. Corrections for water amount as well as power and efficiency are discussed. Data from actual gas turbine testing are used to demonstrate how the proposed procedure can be applied in actual cases of acceptance testing.

[DOI: 10.1115/1.1691443]

Introduction

The performance of turbomachines depends strongly on the properties of the medium flowing through them. In order to compare performances at different inlet conditions or with different media, it is necessary to apply corrections and refer performance parameters to certain reference conditions. The gas turbine being an engine whose major components are turbomachines (compressors and turbines), also needs the application of such corrections.

The corrections usually applied on gas turbine performance quantities to refer them to typical operating conditions can be found in many references. A very good presentation and a derivation of such formulas has been given by Volponi [1].

In gas turbine applications a very important matter, concerning the verification of performances of a given engine, is the execution of its acceptance tests and the subsequent evaluation of the obtained data. The purpose is to verify that the performance specified and guaranteed by the engine manufacturer is met by a particular gas turbine put in operation. A widely accepted procedure for performing such tests is the procedure described by the International Standard ISO 2314, [2]. The standard specifies, among other things, the typical "standard day" conditions, to which performance have to be referred. It also provides formulas for referring certain parameters to operation at these standard conditions. Performance Test Code PTC22, [3], also specifies test procedures for gas turbines.

In order to derive performance at standard day conditions from test data at some other ambient conditions, the correction of measured performances has to be performed through "correction curves," provided by the engine manufacturer. The typical form of such curves has been discussed in the paper of Cloyd and Harris [4]. They have also presented the basic reasoning and the principles behind these curves and their application. Matters related to the correction of data, by the procedure of the ISO standard have been discussed by Kampf [5] and Lorisika [6].

As will become evident farther in the present paper, simple application of the typical set of correction curves may not allow the verification of certain specified performance figures. The situation becomes more complex when operation with injection of

other fluids is considered. Water injection is a means for reducing NO_x emissions, while steam may be injected for emissions reduction or power augmentation. Correcting data coming from operation of this later type is not a procedure specified by standards, while it has not been discussed in open publications, even though individual engine manufacturers have their own procedures.

Methods to cover for these inadequacies are presented in the present paper. The methods presented are useful not only for the user (acceptance testing), but also for the engine manufacturer, when testing is done for establishing the performances of an engine.

Factors Determining Performance—Correction Curves

The two main performance parameters used for gas turbine rating are power output and efficiency (or equivalently, heat rate), as for example specified in ANSI Standard B133.6, [7]. Other parameters that may also be of interest are EGT and exhaust gases flow rate, when exhaust heat is further exploited, as for example in combined cycles or for cogeneration.

The factors influencing power output can be understood from the formula expressing power in function of the main operating parameters. Power output is evaluated by subtracting the power consumed by the compressor and the parasitic losses from the power produced by the turbine:

$$P = \dot{m}_g c_{pg} T_4 \left(1 - \frac{1}{\pi_T^{\frac{\gamma_g - 1}{\gamma_g}}} \right) \eta_{Tis} - \dot{m}_a c_{pa} T_2 \frac{1}{\eta_{Cis}} \left(\pi_c^{\frac{\gamma_a - 1}{\gamma_a}} - 1 \right) - P_L \quad (1)$$

Out of all variables contained in this formula, turbine inlet temperature T_4 is the most crucial. It is desirable to have as high values as possible, because of the beneficial effect it has on power (but also on efficiency). It is, however, restricted to remain below certain limits, imposed by materials strength and cooling technology.

On the other hand, Eq. (1) shows that the power produced, when T_4 has a certain value, will be influenced by:

- *Ambient pressure.* It influences density and therefore mass flow rate for given rotational speed

Contributed by the International Gas Turbine Institute (IGTI) of THE AMERICAN SOCIETY OF MECHANICAL ENGINEERS for publication in the ASME JOURNAL OF ENGINEERING FOR GAS TURBINES AND POWER. Paper presented at the International Gas Turbine and Aeroengine Congress and Exhibition, Amsterdam, The Netherlands, June 3–6, 2002; Paper No. 2002-GT-30466. Manuscript received by IGTI, December 2001, final revision, March 2002. Associate Editor: E. Benvenuti.

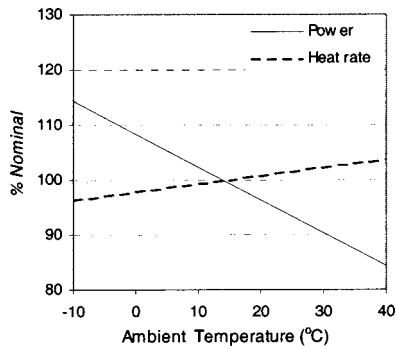


Fig. 1 Power and heat rate dependence on ambient temperature

- *Ambient temperature* T_2 . It influences (a) density and therefore mass flow rate, (b) power absorbed by the compressor for a certain pressure ratio π_C .
- *Humidity*. It influences (a) density and thus mass flow rate, (b) gas properties, namely the specific heats included in the above relation.

Changes in these quantities also influence power through the change in *pressure ratio*, resulting from a shift of engine operating point. Such a shift occurs due to a change of the matching conditions between engine compressor and turbine, resulting in different operating points on their corresponding performance characteristics. Out of all factors ambient temperature is the one that mostly influences performance, while it exhibits significant variations for different times of the year. Ambient pressure can vary significantly with elevation, but it does not usually exhibit large variations at a certain location. The influence of humidity is important only at high ambient temperatures.

Equation (1) shows that power output is also influenced by other factors: A change in fuel may lead to a change of gas composition and thus specific heat C_{pg} , as well as of the proportion of m_g to m_a . Injection of water or steam in the combustion chamber (for example for NO_x reduction) changes C_{pg} and the gas mass flow rate m_g .

Changes in power output are, in general, expected to imply changes in thermal efficiency as well, efficiency being defined as the ratio of power output to heat input:

$$\eta_{th} = \frac{P}{Q_{in}} \quad (2)$$

From this expression it is expected that the factors influencing power will also influence efficiency. It is known (see, for example, [7]) that efficiency does not depend on ambient pressure while it has a strong dependence on T_4 .

Because of the importance of T_4 , engine manufacturers will try to keep it as high as possible. On the other hand, engine control systems will operate so that T_4 remains constant at full load conditions. (It must be noted that some manufacturers may reduce T_4 for operation with steam or water injection, to compensate for increased heat transfer due to increased C_p of the hot gases). It is ensured in this way that maximum performances are achieved, while the engine is protected from over-temperature. For a particular rating, it is thus of interest to know what the performance is when T_4 is kept fixed, independently of ambient conditions. If testing occurs at conditions other than the ISO standard day, it is desirable to derive the performance that the engine would have at ISO conditions, from the test values at current conditions. Performance quantities derived from such a procedure are termed "corrected" quantities and are produced with the help of the correction curves provided by the engine manufacturer. Typical form of curves expressing performance dependence on ambient conditions are shown in Figs. 1–4, below (sample such curves can be found

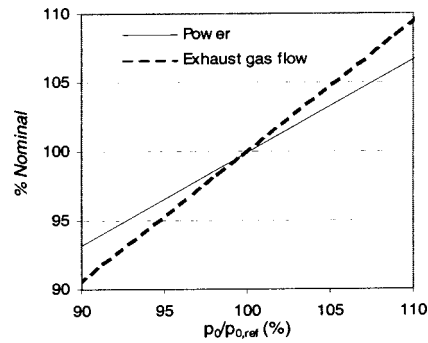


Fig. 2 Power and exhaust gases mass flow rate. Dependence on ambient pressure.

in Walsh and Fletcher [8], Cloyd and Harris [4], and Brooks [9]).

These curves usually are used to determine the values of correction factors which can be applied on test data. Since they represent relatively small deviations around a certain operating condition, their form is almost linear. Since the behavior of a gas turbine over its entire operating range includes clearly nonlinear parameter interrelations, one set of curves is valid for operating conditions in the vicinity of one load setting. It is therefore usual to have a set of curves for each major load setting considered: full load 75%, 50%, etc.

Calculation of Main and Auxiliary Quantities

When the value Y_{test} of a performance parameter of interest is derived from quantities measured during a test, the corresponding value for standard ambient conditions is calculated using correction factors:

$$Y_{cor} = Y_{test} \cdot K_1 \cdot K_2 \cdots K_n \quad (3)$$

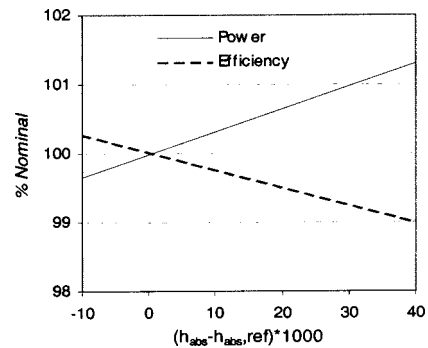


Fig. 3 Dependence of power and efficiency on ambient humidity

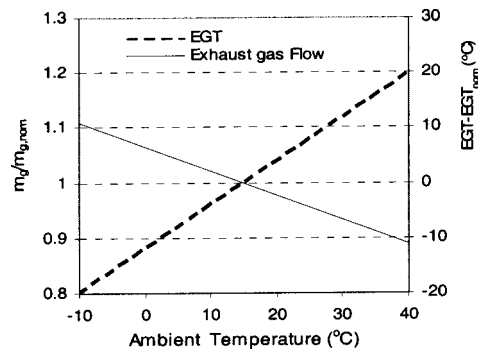


Fig. 4 Dependence of EGT and exhaust gases mass flow rate on ambient temperature

K_1, K_2, \dots, K_n are correction factors, each one representing the effect of one ambient parameter. The values of the factors are directly deduced from curves such as the ones shown in Figs. 1 through 4. This formula assumes that individual corrections are of small magnitude and can thus be superimposed. This is why the effect of each parameter is included by multiplying by the corresponding factor.

Corrected quantities can be used for comparison to guarantee values of performance ratings. Two quantities which are not usually included in the guaranteed performance but are nevertheless very useful to obtain are inlet air mass flow rate and turbine inlet temperature. Since both of these quantities are very difficult to measure, especially for testing on site, procedures for their calculation from values of other measured quantities are used. For example, ISO 2314, [2], specifies such a procedure for a simple gas turbine configuration. A similar type of approach, extended to include operation with water injection in the combustion chamber and external cooling of turbine cooling flows, is presented in Appendix A of the present paper.

Turbine inlet temperature is useful to calculate, because it is the quantity that is considered to be kept constant when correction curves are derived. Since the actual temperature at turbine inlet is difficult to be evaluated, unless details about cooling flows are known, the temperature usually employed is the one defined by the ISO standard, which assumes that all cooling flows are mixed at the inlet to the first-stage turbine rotor. This temperature is also termed stator outlet temperature. As will become apparent later, knowledge of this temperature is a key factor for referring quantities derived from measurement data at certain testing conditions to reference conditions.

Referring Values to Specific Conditions

As mentioned previously, the two main performance parameters that have to fulfill guarantees are power output and heat rate (or equivalently efficiency). Power output at full load is usually specified in conjunction with some control parameter. A usual way is to specify a power that should be achieved without exceeding a given value of exhaust gas temperature (EGT).

At this point it should be commented that when testing of a particular turbine occurs and the data are referred to standard day inlet conditions, the corrected values do not necessarily coincide to specified ones. To make this point clear consider the following example: Testing at nonstandard ambient conditions gives a measured power P_{test} which produces a corrected power P_{corr} , via Eq. (3). P_{corr} is in general different from the full load power output P_{nom} . If test data come only from this power setting, it is not possible to check if EGT has remained within limits, since the test gives EGT at P_{corr} and not at P_{nom} .

A way to solve this problem is to acquire data at several operating conditions, in the vicinity of the operating point tested. Such operating conditions are, for example, produced by setting small load variations around one operating point. The data collected at these conditions can then be used to interpolate and find values at the precise specified conditions. An example of application of this concept is shown in Fig. 5. Data used to verify base load is achieved while remaining well below an EGT limit are shown. The test data come from the actual acceptance testing of a utility gas turbine (Mathioudakis, [10]). The verification is done for base load and peak load conditions. It is shown that interpolation through the test data allows the comparison at precisely the specified conditions, even though there is no test point at exactly the specified load. A straight line fitted through the test data is sufficient, since the small deviations around the operating point considered justify the linear behavior, as mentioned previously.

Coming to efficiency, usually an efficiency value that should be achieved is specified for a specific power output. For the same reason as before, obtaining data at more than one operating points, in the vicinity of the point of interest, allows the verification of values at precisely the specified conditions. An example of com-

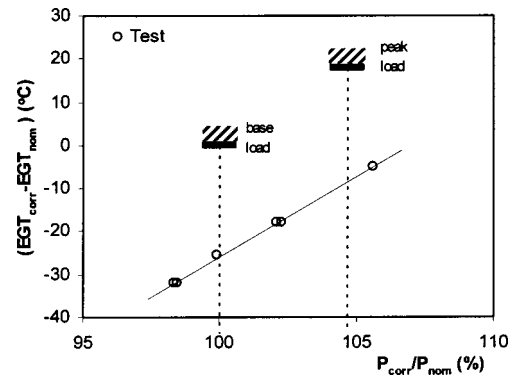


Fig. 5 Use of test data to verify base load and peak load conditions. (/// indicates specified limit values).

parison of data obtained from testing to specified limits of efficiency is shown in Fig. 6. In this figure operating points of full load and partial loads are included. Lines are fitted in the vicinity of each operating point.

An alternative to testing at several points is to use additional correction curves that would allow correction for deviations from the specified operating condition. A type of such curves that may be supplied is dependence of power and efficiency on turbine inlet temperature, which should be evaluated according to a predefined procedure. This approach still requires data from more than one points, in order to calibrate the turbine inlet temperature evaluation. Use of corrections of this type is a matter of agreement between user and manufacturer. Testing, however, and proceeding as presented above has the advantage that it leaves no doubt about their precise values.

Operation With Water Injection

When water injection at the compressor outlet is used to reduce NO_x emissions power output increases, for a given TIT. The additional fuel needed is proportionally larger than the power increase, resulting in a drop of thermal efficiency. A typical form of the power and efficiency deviations in function of the amount of injected water is shown in Fig. 7. For these reasons, separate guaranties are usually specified for operation with water injection. In addition to power and efficiency, water amount is also specified. We will see now how corrections can be done.

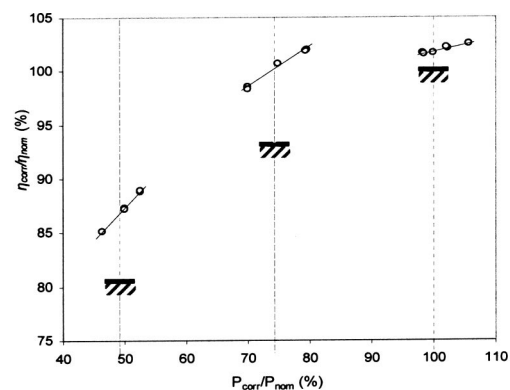


Fig. 6 Efficiency versus power, to check values at a specific load. Dry operation. (/// indicates specified lower limit values).

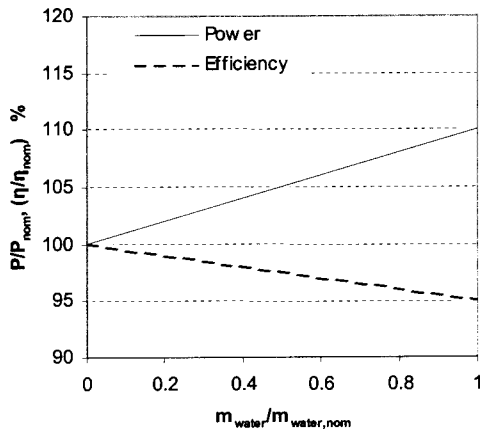


Fig. 7 Typical form of power and efficiency variations in function of the amount of injected water

Water Flow Rate. First the quantity of water necessary to achieve a predefined level of emissions has to be verified. Desired emissions levels should be achieved by injecting an amount of water less than a specified value.

Corrections have to be done by keeping appropriate parameters constant. TIT has to be kept constant, on the basis of the same reasoning as for dry operation. An additional quantity that has to be kept constant is water to fuel ratio w , namely the ratio of water mass flow rate to fuel mass flow rate.

The reason that water to fuel ratio should be maintained the same is that this quantity determines the level of NO_x emissions reduction, for a given TIT. This fact has been established and discussed by several authors as, for example, Shaw [11], Koch and Felix [12], Schetter [13], and Pavri and Moore [14], while Lefebvre [15] reports analytical relations for estimating emissions reduction as a function of water/fuel ratio. This means that if testing has shown certain levels of emissions at some operating conditions, when data are referred to another condition keeping water-to-fuel ratio the same, the same level of emissions will be observed. The immediate implication is that if a certain amount of water has been measured, then the amount that would be needed in order to have the same effect on emissions, for constant TIT, can be evaluated through the following expression:

$$\dot{m}_{w,\text{corr}} = \dot{m}_{w,\text{meas}} \frac{\dot{m}_{f,\text{corr}}}{\dot{m}_{f,\text{meas}}} \quad (4)$$

The corrected fuel flow rate $\dot{m}_{f,\text{corr}}$ is the one that would be consumed, if the gas turbine was operating with the same TIT, at standard ambient conditions. It can be evaluated from corrected power output and efficiency:

$$\dot{m}_{f,\text{corr}} = \frac{P_{\text{corr}}}{\eta_{\text{corr}} \text{LHV}} \quad (5)$$

In order to verify values of water flow they should thus be corrected by means of Eq. (4). In this case too, in order to compare precisely at specified power output levels, test data from several operating points should be used. An example of using such data, from different loads, is shown in Fig. 8. For operation at full load conditions, two level of power output are considered, connected to two levels of emissions reduction. The larger amounts of water gives to a more drastic reduction of emissions, compared to the smaller one.

Power and Efficiency. Power and efficiency can be referred to standard conditions by using dry operation corrections curves, unless large deviations are considered, as shown in Appendix B. In order to compare efficiency at a certain load it is again necessary to use data from neighboring operating points. An example of

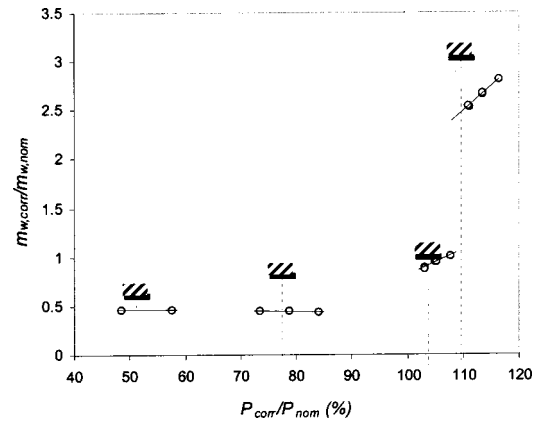


Fig. 8 Comparing water flow rates to guaranteed values. Load points A–50%, B–75%, C–100%(1), D–100%(2). (Hatched rectangle indicates specified limit values).

data from testing and their comparison to specified values is shown in Fig. 9. The two groups of points, representing two levels of efficiency decrease, correspond to the two different levels of water injection, mentioned above.

The actual water-to-fuel ratio for these load points, expressed in function of TIT, is shown in Fig. 10 (w is evaluated from measured water and fuel flow rates). It is observed that this quantity slightly varies with load. This is because the engine control system adjusts the amount of injected water such that emissions remain under a certain limit. Load increase is linked to turbine inlet temperature, which in turn increases NO_x production, and thus the amount of water needed increases.

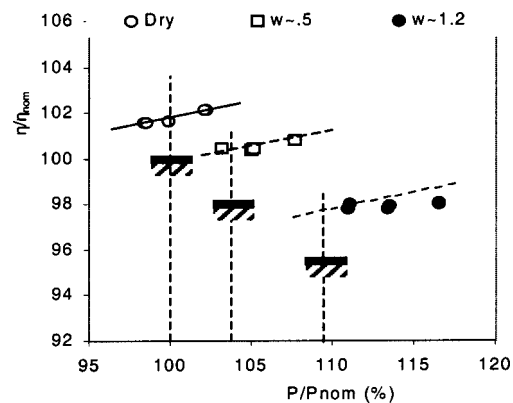


Fig. 9 Efficiency versus power for different amounts of injected water. (Hatched rectangle indicates specified lower limit values).

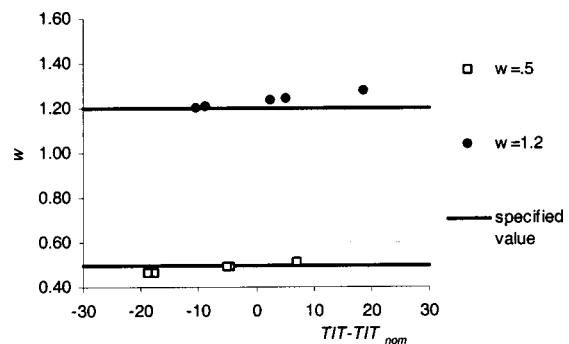


Fig. 10 Water-to-fuel ratio for the points of Fig. 9

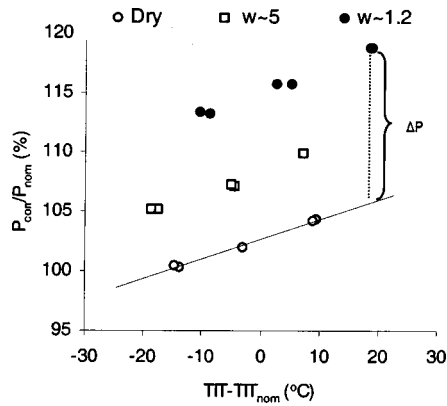


Fig. 11 Power output versus TIT for different amounts of injected water

Although comparison to reference values can be done by interpolating for the specified load, for more accurate comparison the same water-to-fuel ratio has to be considered. The comparison at the same w is done by drawing a line parallel to the line fitted through the data for dry operation, between the points from testing for the w of interest. This is shown in Fig. 9, where the lines are drawn to correspond to the specified values of Fig. 10. The theoretical basis allowing to draw this lines is the fact that the slope of the power-efficiency curve remains the same for dry or wet operation.

Effect of Water Amount on Power and Efficiency. The effect of water injection can be assessed from test data, which have to be referred so that quantities are compared for the same turbine inlet temperature. It is thus essential to evaluate TIT from test data and compare points with the same TIT. In order to be able to refer all values to the same TIT, several individual operating conditions will have to be tested around one operating point.

Power output variation around the full load operating point, for different amounts of injected water is shown in Fig. 11. The operating points correspond to two levels of water injection, as mentioned previously. Power output increases more for larger amount of injected water. TIT has been calculated by using Eq. (A3), (A5) and the test data come from the gas turbine layout shown in Appendix A. In Fig. 11 it is shown that once a baseline is established for power versus TIT for dry operation, then the deviation for each test point with water injection is estimated by subtracting the corresponding test value from the one for dry operation. In a similar way deviations of thermal efficiency are derived, as shown in Fig. 12. Larger efficiency drops are observed for larger amount of injected water.

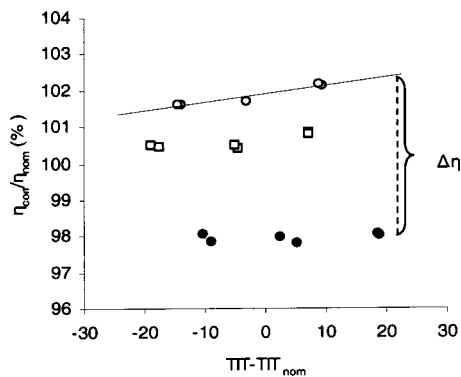


Fig. 12 Efficiency versus TIT for different amounts of injected water

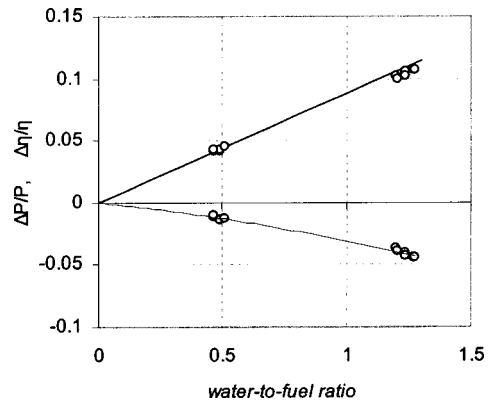


Fig. 13 Power output and efficiency variation in function of water-to-fuel ratio, at full-load turbine inlet temperature

Once data have been presented in the form shown in Figs. 11 and 12, the relationship between power and efficiency deviations and water to fuel ratio can be established. This dependence for the data of the previous figures is shown in Fig. 13. The deviations are functions of water to fuel ratio, a fact that can be established by means of theoretical analysis, as shown by Mathioudakis [10].

Conclusions

Correction of gas turbine test data to refer them to operation with standard day inlet conditions have been discussed. It was shown that when specific values of performance parameters have to be used for comparisons, test data have to be collected at operating points in the vicinity of the ones initially specified. Interdependence of parameters can then be established from the tests and precise information can be derived for comparisons.

Operation with water injection was considered in more detail, in view of the fact that existing standards do not provide for this particular case. The method of correcting various performance parameters of interest was presented, including correction for the amount of injected water. The way of using test data for deducing performance parameter deviations to quantify the effect of water injection was presented. The theoretical basis for calculating auxiliary performance quantities, such as TIT and air mass flow rate, for this type of operation was presented. Small deviation analysis was also shown to support aspects of the approach proposed for corrections.

Data from tests on a particular gas turbine have been used to demonstrate implementation of the correction procedures proposed in this paper.

Acknowledgments

The author would like to thank Public Power Corporation (Greece) for allowing the inclusion of the test data in the present paper.

Nomenclature

- b = compressor external air bleed as a fraction of inlet mass flow
- c_p, c_v = specific heat for constant pressure, volume
- EGT = exhaust gas temperature
- f = fuel/air ratio $f = \dot{m}_f / \dot{m}_a$
- h = specific enthalpy
- IGV = inlet guide vane
- K_b = total pressure loss in burner
- LHV = fuel lower heating value
- \dot{m} = mass flow rate
- \dot{m}_b = mass flow of bleed air
- \dot{m}_{ex} = mass flow rate of bleed air for external use

- P = gas turbine power output
 P_{booster} = power input to cooling air from booster compressor (Fig. A1)
 P_L = parasitic power loss
 P_T = power produced by turbine
 p = pressure (total)
 q = reduced (normalized) mass flow rate
 $q = \dot{m} \sqrt{(RT/\gamma)/p}$
 R = gas constant
 T = temperature (total)
TIT = turbine inlet temperature
 w = water/fuel ratio $w = m_w/m_f$
 Y = isentropic exponent $Y = C_p/C_v$
 η_{th} = gas turbine efficiency, Eq. (2)
 η_{Cis} = compressor isentropic efficiency
 η_{Tis} = turbine isentropic efficiency
 π_C = compressor pressure ratio $\pi_C = p_3/p_2$
 π_T = turbine pressure ratio $\pi_T = p_4/p_5$

Subscripts

- 0 = condition at which LHV was evaluated
2,3,4,5,
31,32 = position along the gas turbine, Fig. (A1)
amb = ambient condition
a = quantity related to air
C = Compressor
corr = quantity corrected to standard day conditions
f = fuel
g = quantity related to the combustion gases
nom = nominal, refers to full load operation
s = quantity related to steam
T = turbine
test = quantity coming from testing
w = quantity related to injected water

Appendix A

Calculation of Air Mass Flow Rate and Turbine Inlet Temperature. The air mass flow into the gas turbine can be evaluated from measured quantities, by applying heat balance over the components of the turbine and combining the resulting equations. The overall layout, the numbering of the different positions as well as the quantities measured and their location along the gas path, are shown in Fig. A1. This layout includes external cooling and subsequent pressure boosting, and it is general enough to cover simpler configurations (for example, no external bleed cooling). The particular engine from which data have been included in the present paper is the model V64.3 manufactured by Siemens.

The heat balance equations are written for each individual component, Fig. A2. The formulation used here for turbine and combustor it is found to be easier to consider the change of properties of individual components of the mixture of gases flowing through them. In a mixture all substances are at the same temperature. Pressure is of interest for calculating steam properties. The partial pressure of steam, when needed, is evaluated from its molar fraction.

Compressor.

$$P_c = m_{a2}(h_{a3} - h_{a2}) \quad (A1)$$

Turbine.

$$P_T = m_{a32}h_{a32} + m_{g4}h_{g4} + m_w h_{s4} - m_{a32}h_{a5} - m_{g5}h_{g5} - m_w h_{s5} \quad (A2)$$

Combustion Chamber.

$$\begin{aligned}
& m_f(h_f - h_{f0}) + m_f \text{LHV} + (m_{a3} - m_{ex} - m_{a31})(h_{a3} - h_{a0}) \\
& = m_{g4}(h_{g4} - h_{g0}) + m_w(h_{s4} - h_w) \quad (A3)
\end{aligned}$$

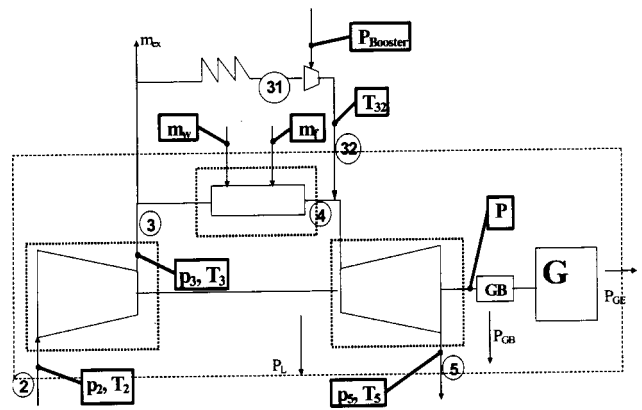


Fig. A1 Layout of gas turbine for heat balance calculations. Quantities measured during performance testing are contained in boxes with callouts at measuring location.

Enthalpy of water and steam in this equation are calculated with the same reference, and therefore their difference contains the latent heat.

Subtracting compressor and turbine powers and using Eq. (A3) gives the following equation for gas turbine power output:

$$\begin{aligned}
P &= m_f \text{LHV} + m_f(h_f - h_{f0}) + (m_{a3} - m_{ex} - m_{a31})(h_{a3} - h_{a0}) \\
&\quad - m_{a32}(h_{a5} - h_{a32}) - m_{a2}(h_{a3} - h_{a2}) - m_w(h_{s5} - h_w) \\
&\quad - m_{g4}(h_{g5} - h_{g0}). \quad (A4)
\end{aligned}$$

Using the combustor heat balance and the mass flow balances of the components gives finally the following equation for the mass flow rate into the gas turbine:

$$m_{a2} = \frac{A}{B}, \quad (A5)$$

where

$$\begin{aligned}
A &= P - Q_f - Q_w - (m_f - m_{a31})(h_{g0} - h_{g5}) - P_{\text{booster}} \\
&\quad - m_{a31}(h_{a31} - h_{a5} - h_{a3} + h_{a0})
\end{aligned}$$

$$B = (1 - b)(h_{g0} - h_{g5}) + (h_{a2} - h_{a0}) - b(h_{a3} - h_{a0})$$

$Q_f = m_f \text{LHV} + m_f(h_f - h_{f0})$, heat flow provided by the fuel, $Q_w = m_w(h_w - h_{s5})$, heat flow absorbed by the injected water

External bleed flows are expressed as a fraction of inlet air flow: $b = m_{ex}/m_{a2}$.

Turbine inlet temperature can be calculated once air mass flow rate is known, using combustion chamber heat balance, Eq. (A3). All terms are known, apart from h_{g4} and h_{s4} , which are single

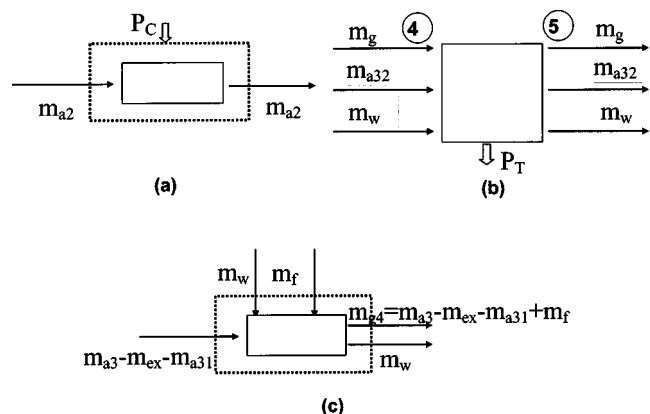


Fig. A2 Block diagram for writing equations (a) compressor, (b) turbine, (c) combustor

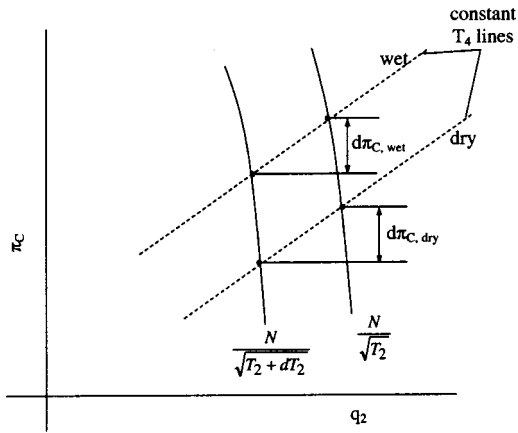


Fig. B1 Compressor operating point for dry and wet operation and its movement for a change in ambient temperature (constant mechanical speeds)

value functions of temperature T_4 . T_4 is thus evaluated from this equation by applying an iterative numerical scheme.

TIT evaluated from such a procedure will be known with an uncertainty that depends on the uncertainties of the measured quantities used for its derivation. An example of calculation of the propagation of measurement uncertainties to the evaluated turbine inlet temperature has been given by Mathioudakis et al. [16].

Appendix B

Parameter Deviations for Ambient Temperature Changes.

Changes in power output when ambient temperature changes can be derived from Eq. (1). Power changes can be related to the changes of all parameters determining it, by applying differentiation on the relations expressing the interdependence of different parameters. Starting from Eq. (1), we obtain

$$\frac{dP}{P} = \frac{dP_T}{P_T} \cdot \frac{P_T}{P} - \frac{dP_c}{P_c} \cdot \frac{P_c}{P}. \quad (B1)$$

The fractional changes dP_c/P_c and dP_T/P_T can be evaluated by taking logarithms and then differentiating. We consider variations for T_2 changing and turbine inlet temperature T_4 , remaining constant. It is reasonable to assume that gas properties do not change, while isentropic efficiencies of compressor and turbine also do not change. With these assumptions we obtain:

$$\frac{dP}{P} = \lambda \left(\frac{dm_g}{m_g} + B \frac{d\pi_T}{\pi_T} \right) - (\lambda - 1) \left(\frac{dm_a}{m_a} + \frac{dT_2}{T_2} + A \frac{d\pi_c}{\pi_c} \right) \quad (B2)$$

where

$$\lambda = \frac{P_T}{P}, \quad A = \frac{\gamma_{\alpha-1}}{\gamma_{\alpha}} \cdot \frac{\pi_c^{\gamma_{\alpha}}}{\pi_c^{\gamma_{\alpha}-1} - 1},$$

$$B = \frac{\gamma_g - 1}{\gamma_g} \cdot \frac{1}{\pi_T^{\gamma_g} - 1}.$$

Since inlet, combustion chamber, and exit losses remain practically unaltered, it can easily be deduced that

$$\frac{d\pi_c}{\pi_c} = \frac{d\pi_T}{\pi_T}. \quad (B3)$$

Hot gases flow rate and inlet air flow rate are related through the relation:

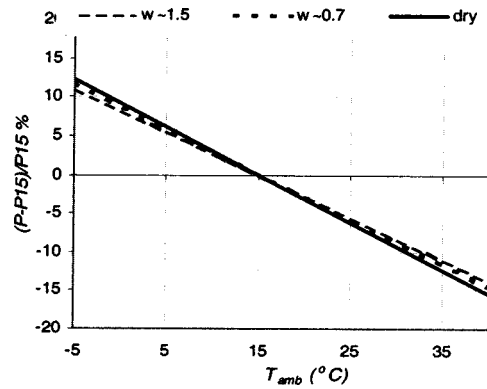


Fig. B2 Fractional change of power and efficiency for dry and wet operation of a single-shaft gas turbine

$$m_g = m_a(1-b)(1+f(1+w))$$

which gives

$$\frac{dm_g}{m_g} = \frac{dm_a}{m_a} - \frac{db}{1-b} + \frac{f}{1+f(1+w)} \frac{df}{f}.$$

For values usually encountered, the terms containing db and df can be assumed to be of higher order and therefore

$$\frac{dm_g}{m_g} = \frac{dm_a}{m_a}. \quad (B4)$$

From the definition of compressor flow function we obtain

$$q_2 = \frac{m_a}{p_2} \sqrt{\frac{R_2 T_2}{\gamma_2}} \Rightarrow \frac{dm_a}{m_a} = \frac{dq_2}{q_2} - \frac{1}{2} \frac{dT_2}{T_2}. \quad (B5)$$

We can use the compressor turbine mass flow compatibility equation to relate compressor flow function, pressure ratio and T_2 . The equation writes:

$$q_4 = q_2(1-b)(1+f(1+w)) \sqrt{\frac{R_4}{R_2} \frac{\gamma_2}{\gamma_4} \frac{1}{\pi_c}} (1-K_b) \sqrt{\frac{T_4}{T_2}}. \quad (B6)$$

For a choked turbine ($q_4 = \text{constant}$), if we assume that properties do not change and use the assumptions for Eq. (B3) we obtain

$$\frac{dq_2}{q_2} - \frac{d\pi_c}{\pi_c} - \frac{1}{2} \frac{dT_2}{T_2} = 0. \quad (B7)$$

Using Eqs. (B3), (B4), (B5), (B7), Eq. (B2) gives

$$\frac{dP}{P} = (\lambda B - (\lambda - 1)A + 1) \frac{d\pi_c}{\pi_c} - (\lambda - 1) \frac{dT_2}{T_2}. \quad (B8)$$

Quantities a , b , λ do not change significantly for small changes of T_2 . On the other hand, for a change in inlet temperature the movements of compressor operating point is as shown in Fig. B1. Since the operating points with and without water injection, for given ambient temperature, are not very far apart proportional changes of pressure ratio are approximately the same for the same change in T_2 . They will differ if constant speed lines are further apart, namely if large temperature differences are considered.

In view of these arguments, Eq. (B8) implies that dependence of fractional change in power on T_2 can be considered to be the same, whether the gas turbine operates without or with water injection. Deviations should be expected to be larger for larger temperature differences. To demonstrate the validity of this conclusion, correction curves derived by an engine performance model have been produced for dry and wet operation and are shown in Fig. B2.

It is observed that the presence of water has only a marginal effect on the form of the correction curves. For larger amounts of water and large deviations from standard day temperature, deviations between dry and wet operation correction curves may rise to the order of one percentage point. If such situations are expected to be encountered, the different correction curves should be taken into account.

References

- [1] Volponi, A., 1998, "Gas Turbine Parameter Corrections," ASME Paper No. 98-GT-347.
- [2] ISO 2314, 1989, Gas Turbine Acceptance Tests.
- [3] ASME PTC22-1997, Performance Test Code for Gas Turbines.
- [4] Cloyd, S. T., and Harris A. J., 1995, "Gas Turbine Performance. New Application and Test Correction Curves," ASME Paper No. 95-GT-167.
- [5] Krampf, F. M., 1992, "A Practical Guide for Gas Turbine Performance Field and Test Data Analysis," ASME Paper No. 92-GT-427.
- [6] Lorisika, G., 1985, "Gas Turbine Performance and Efficiency Test ISO Standard and Measuring Tolerances," *Swiss Gas Turbine Engineering Handbook*, Vol. III, Turbomachinery International Publications.
- [7] ANSI B 133.6, 1976, Procurement Standard for Gas Turbine Ratings and Performance.
- [8] Walsh, P. P., and Fletcher, P., 1998, *Gas Turbine Performance*, Blackwell Science, Ltd., London.
- [9] Brooks, F. J., "GE Gas Turbine Performance Characteristics," GE Reference Library, publication GER 3567H.
- [10] Mathioudakis, K., 2002, "Analysis of the Effects of Water Injection on the Performance of a Gas Turbine," *ASME J. Eng. Gas Turbines Power*, **124**, pp. 489–495.
- [11] Shaw, H., 1974, "The Effects of Water, Pressure, and Equivalence Ratio on Nitric Oxide Production in Gas Turbines," *ASME J. Eng. Gas Turbines Power*, **96**, pp. 240–246.
- [12] Koch, H., and Felix, P., 1977, "Exhaust Gas Emissions of Brown Boveri Gas Turbines," *Brown Boveri Rev.*, **64**, pp. 27–33.
- [13] Schetter, B., 1993, "Gas Turbine Combustion and Emission Control," *Combined Cycles for Power Plants*, Von Karman Institute Lecture Series 1993-08.
- [14] Pavri, R., and Moore, G. D., "Gas Turbine Emissions and Control," GE Reference Library, publication GER 4211.
- [15] Lefebvre, A. H., 1995, "The Role of Fuel Preparation in Low Emission Combustion," *ASME J. Eng. Gas Turbines Power*, **117**, pp. 617–654.
- [16] Mathioudakis, K., Stamatis, A., Tsalavoutas, A., and Aretakis, N., 2001, "Performance Analysis of Industrial Gas Turbines for Engine Condition Monitoring," *Proceedings Of The Institution of Mechanical Engineers, Part A*, Journal of Power and Energy, **215**(A2), Mar. pp. 173–184.

H. Nakane
A. Maekawa
E. Akita
K. Akagi
T. Nakano
S. Nishimoto
S. Hashimoto
T. Shinohara
H. Uehara

Mitsubishi Heavy Industries, Ltd.,
2-2-2 Shinhama Arai-cho, Takasago,
Hyogo 676-8686, Japan

The Development of High-Performance Leaf Seals

Recently, from the environmental point of view, demand for a combined cycle plant is increasing, and superior gas turbine performance is being rapidly promoted at the same time. As one of the key technologies for superior performance, reduction of secondary air leakage, which is necessary for blade cooling and bearing sealing, is required. Especially, reduction of air leakage through rotating parts and stationary parts clearance is critical. [DOI: 10.1115/1.1615257]

Introduction

Hitherto, a noncontact type labyrinth seal has been widely used as a seal between rotating parts and stationary parts. However, this seal requires a large clearance to avoid contact, and this causes reduction of performance due to the large amount of air leakage. Currently, application of brush seals is rapidly increasing as an improvement, however, a brush seal maintains contact not only at shut down, but also during operation, thereby wear of wire is accelerated during prolonged operation, reducing the sealing performance. In addition, since stiffness of the wire itself is low, differential sealing pressure is also low, [1–3].

In order to overcome these short comings, a so-called “leaf seal” has been developed over the years. The leaf seal has a structure in which multi layered flexible leaves are arranged in the circumferential direction. In this seal, the tip of the leaf is lifted up from the rotor surface by the hydrodynamic effect as the rotating speed is accelerated. As a result of this mechanism, wear of the seal is reduced during operation. The clearance generated by the leaf tip lifting up is negligibly small and, therefore, sealing performance is better. Moreover, because the leaf has an axial width, it can endure seal differential pressure several times that of the brush seal.

The effect of the leaf lifting up and the leakage air amount were verified by rig tests. After these verification tests, this leaf seal is now being used in Mitsubishi M501G gas turbine, installed at an in-house power station located at the Takasago machinery works, in order to confirm sealing performance and durability. The leaf seal can sustain high differential pressure even if it is used in single stage, and has very good durability. To conclude it can be said that the leaf seal is the next generation seal replacing the brush seal.

Characteristics of Leaf Seal

The structure of the leaf seal is shown in Fig. 1. The leaf seal has a structure of multiple leaf plates of 5 to 10 mm width arranged in the circumferential direction. The leaf seal is designed to have minimal gap between each leaf plate to prevent leaves

from restricting their behavior with respect to each other. Furthermore the rigidity is optimized by selecting proper plate thickness, length, width, and gap between leaf plates. A leaf plate is attached to the housing with a sharp angle between the leaf plate and the surface of the rotor in the rotating direction. The tips of leaf plates are in contact with the rotor at shut down of the gas turbine. On the other hand, the tips of leaf plates are lifted up by hydrodynamic lifting force by rotation during operation. Through this mechanism, a noncontact condition with the rotor can be obtained. The characteristics of the leaf seal are summarized as follows:

1. Because the leaf plate has a specified axial width and the gap between leaf plates is very small, leakage air flow is laminar between leaf plates. As a result, the amount of leakage can be reduced.
2. The noncontact condition with the rotor due to the hydrodynamic lifting force by rotation and differential pressure of the seal can prevent heating and wear of the leaf seal.
3. Sealing at high differential pressures can be done even with one stage of leaf seal because the leaf plate has an axial width and rigidity in the direction of differential pressure.

The comparison of conventional seals with the leaf seal is shown in Table 1, [4,5]. Additionally, other new seals technologies are shown in Table 2.

From the viewpoint of the structure of multiple leaf plates arranged in the circumferential direction and the concept of using the hydrodynamic force by rotation to keep the noncontact condition with the rotor, the leaf seal is very unique.

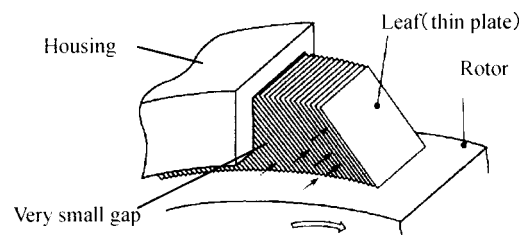


Fig. 1 Structure of the leaf seal

Contributed by the International Gas Turbine Institute (IGTI) of THE AMERICAN SOCIETY OF MECHANICAL ENGINEERS for publication in the ASME JOURNAL OF ENGINEERING FOR GAS TURBINES AND POWER. Paper presented at the International Gas Turbine and Aeroengine Congress and Exhibition, Amsterdam, The Netherlands, June 3–6, 2002; Paper No. 2002-GT-30243. Manuscript received by IGTI, December 2001, final revision, March 2002. Associate Editor: E. Benvenuti.

Table 1 Comparison of conventional seals and the leaf seal

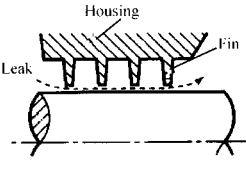
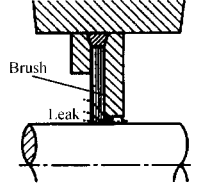
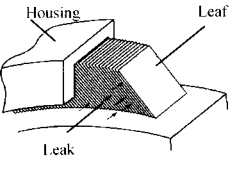
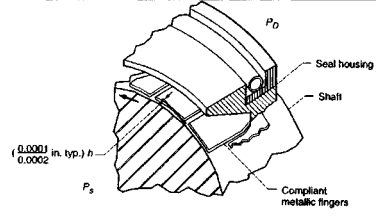
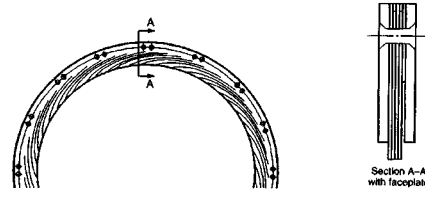
| | Labyrinth seal | Brush seal | Leaf seal |
|-----------------------|---|--|---|
| Conceptual figure |  |  |  |
| Relative leak amount | 100 % (gap 0.5mm, 4 stage) | 40 % (1 stage) | 30 % (1 stage) |
| Seal type | Non-Contact | Contact | Non-Contact at Operation Contact at Shut Down |
| Differential pressure | - | Max. 0.5 MPa | Max. 1.0 MPa |
| Wear | No wear | Wear | Negligibly small wear |

Table 2 New seals technology

| Compliant metallic hydrodynamic shaft seal [4] | Laminated finger seal [5] |
|---|--|
|  |  |
| In the compliant shaft seal, shingled sealing elements float on an elastohydrodynamic film, virtually eliminating seal wear and operating within design limits. | The laminated finger seal is constructed of a stack of laminations; each lamination consists of multiple fingers on flexure elements. The fingers allow the seal to follow radial movement of the rotor. Layers are indexed such that axial openings between elements are covered by the succeeding layer. |

Leaf Seal Design Sequence

First of all, the operating condition and the size of the portion to which the leaf seal is attached are determined as the design inputs. Based on these inputs, rigidity of the leaf plate, lifting characteristics, and leakage amount are calculated, and parameters of the configuration of the leaf plate shown in Fig. 2 are determined to

satisfy the required specification. Since sealing ability depends on these parameters, it is important to determine the design point.

Therefore, the following points are considered as the target of the leaf seal design:

1. The leakage amount should be 1/3 or less than that of the labyrinth seal.

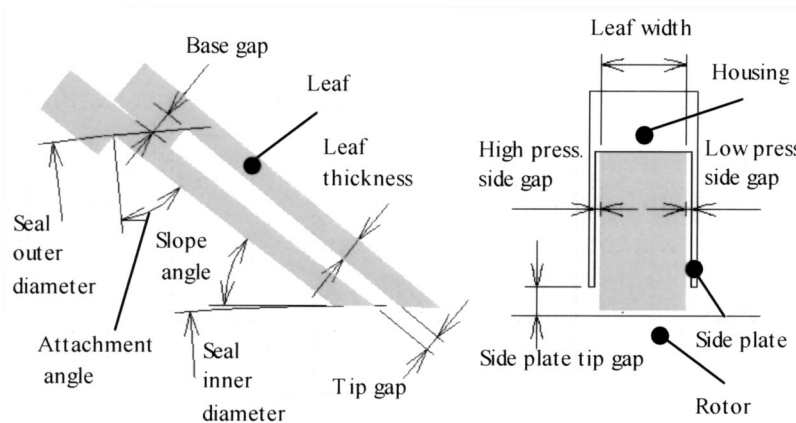


Fig. 2 Parameters of the configuration of the leaf plate

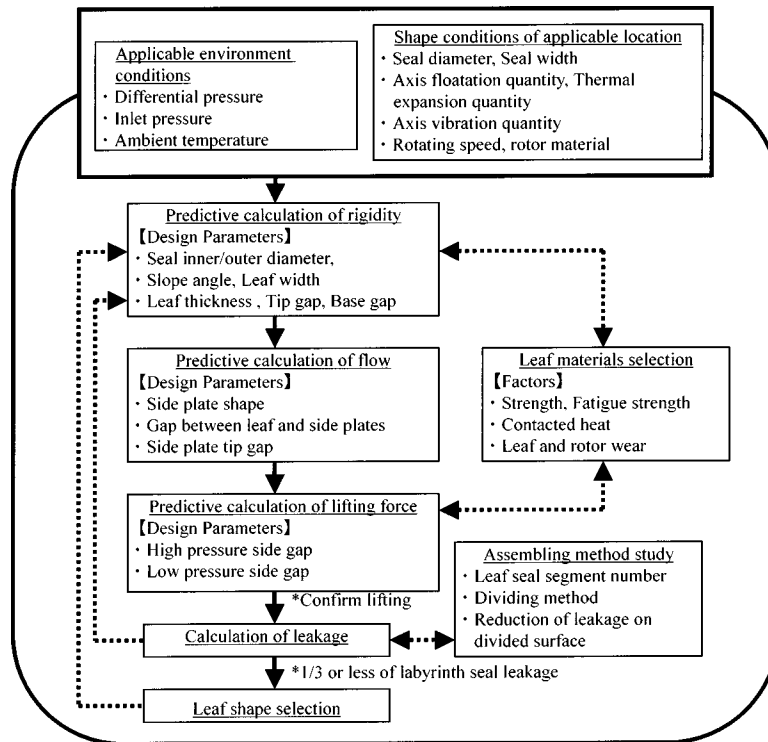


Fig. 3 Process for selecting the configuration of leaf plate

2. The noncontact condition between leaf plates and the rotor should be kept during operating condition.

Fig. 3 shows the process for selecting the configuration of leaf plate based on the above targets.

Estimation of Rigidity Characteristics

The lifting of the leaf plates by hydrodynamic lifting force due to rotation and seal differential pressure during rated operation is one of the characteristics of the leaf seal. The rigidity of the leaf seal is an essential parameter to determine the lifting characteristics. In addition, rigidity significantly influences heating and wear by rotor interference force, so configuration of leaf plate should be designed in order that the specified rigidity can be obtained.

Since the leaf seal has a circumferential layer of multiple leaf plates as explained, when the radial displacement of the leaf seal is increased, leaf plates are restricted with each other by their deformation and the rigidity of the leaf plate is increased in comparison with the rigidity of one isolated leaf plate. During prediction of rigidity, this phenomenon should be taken into consideration.

Figure 4 shows the concept of the rigidity measuring test. Table 3 shows the parameters of tested leaf seal and Fig. 5 shows the rigidity measuring test device. In this test, the inner housing is fixed and the load is added to the leaf seal. From the measurement of load and the displacement, the rigidity of the leaf seal is evaluated based on the relation between the load and the rigidity of one leaf plate. The relation between the load and radial displacement of the leaf seal is shown in Fig. 6 as a comparison of the calculated values and the actual measurement. From the result, although the measured force is larger than the calculated values because of friction between leaf plates, it was confirmed that the calculation value is appropriate for estimating the rigidity from the viewpoint of qualitative and quantitative.

Estimation of Flow Characteristics

The flow of fluid in the leaf seal consists of flows through each gap (1) between leaves and (2) between the leaf plate and the rotor

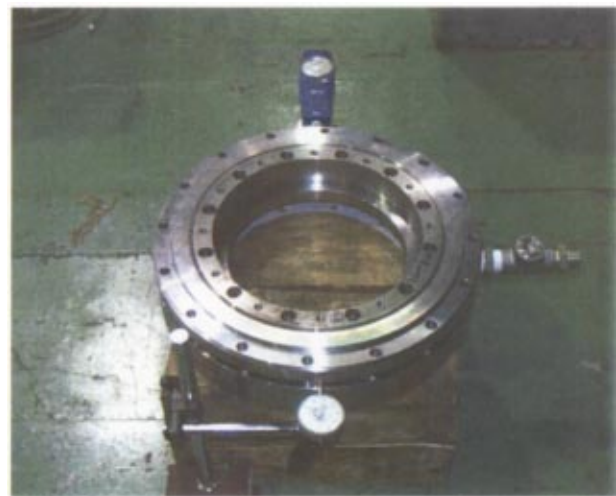
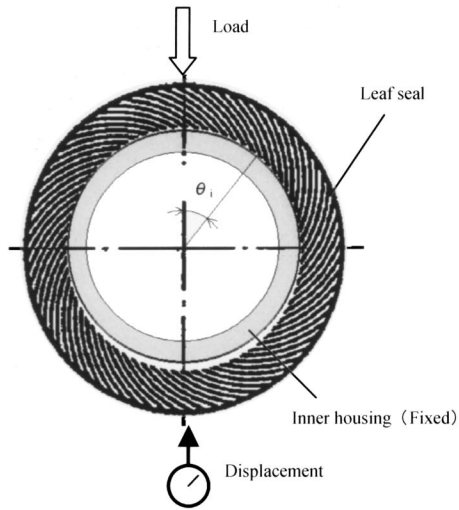


Fig. 4 Concept of the rigidity measuring test

Table 3 Parameters of tested leaf seal

| | |
|---------------------|-------------|
| Seal outer diameter | 390 mm |
| Seal inner diameter | 350 mm |
| Slope angle | 37.5 deg |
| Seal width | 5.0 mm |
| Leaf thickness | 70 μ m |
| Tip gap | 8 μ m |
| Number of leaves | 8581 leaves |



| Relation between the load and the rigidity of one leaf | |
|---|--|
| $W = K_{180} \cdot \delta$ | |
| $K_{180} = k \cdot 2 \cdot \sum_{i=1}^m \cos(\theta_i)^2$ | |
| W | : Load |
| K_{180} | : Rigidity of 1/2 arc of the leaf seal |
| δ | : Displacement |
| k | : Rigidity of one leaf plate ($k = f/y$) |
| m | : Number of leaves in 1/4 arc of the leaf |

Fig. 5 Rigidity measuring test device

as shown in Fig. 7. However, flow (2) between leaf plate and rotor is negligible because the lifting amount of leaf is very small (0 to $10 \mu\text{m}$).

The flow (1) consists of (1)a and (1)b. The flow calculation is done by the finite difference method using (1)a as two-dimensional compressible laminar flow and (1)b as compressible flow symmetrical about the one-dimensional axis. Through this

calculation, convergence solution which satisfies the condition of continuity of flow is obtained.

Moreover, it was confirmed that the flow calculation result of the finite difference method almost corresponds with CFD result. Figure 8 shows the flow pattern in the leaf seal analyzed using

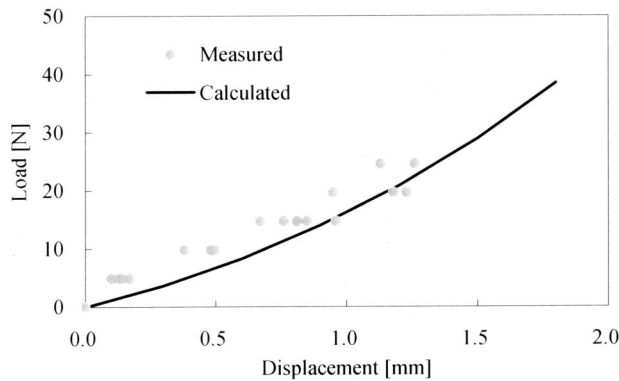


Fig. 6 Relation between the load and radial displacement

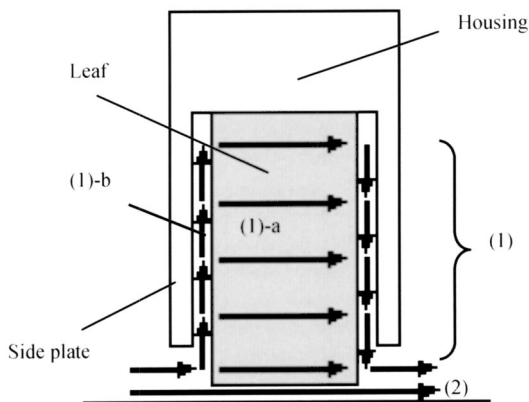


Fig. 7 Flow of fluid in the leaf seal

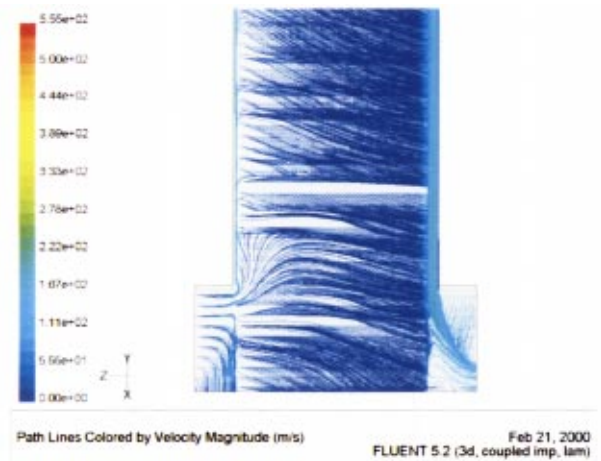


Fig. 8 Flow pattern in the leaf seal (CFD)

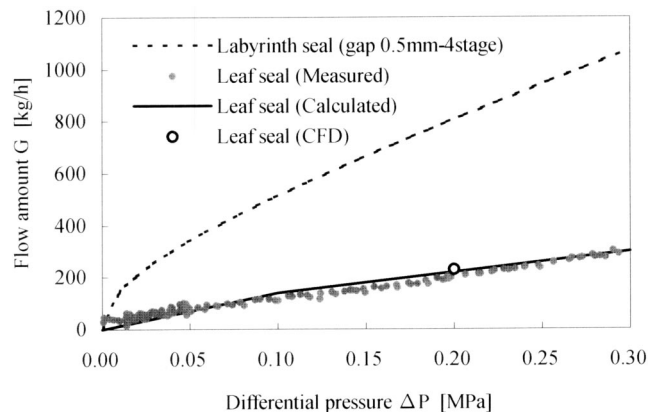


Fig. 9 Correlation between pressure ratio and flow amount

Table 4 Test condition

| | |
|-------------------|------------------|
| Fluid | Air |
| Rotor speed | 5000 rpm |
| Seal diameter | 350 mm |
| Inlet temperature | Room temperature |
| Inlet pressure | 0.1~0.4 MPa |
| Outlet Pressure | 0.1 MPa |

Table 5 Parameters of tested leaf seal

| | |
|------------------------|-------------|
| Seal outer diameter | 390 mm |
| Seal inner diameter | 350 mm |
| Slope angle | 37.5 deg |
| Attachment angle | 45.4 deg |
| Seal width | 5.0 mm |
| Leaf thickness | 70 μm |
| Tip gap | 8 μm |
| Base gap | 30 μm |
| Number of leaves | 8581 leaves |
| Side plate tip gap | 1.5 mm |
| High pressure side gap | 0.05 mm |
| Low pressure side gap | 0.15 mm |
| Radial interference | 0.6 mm |

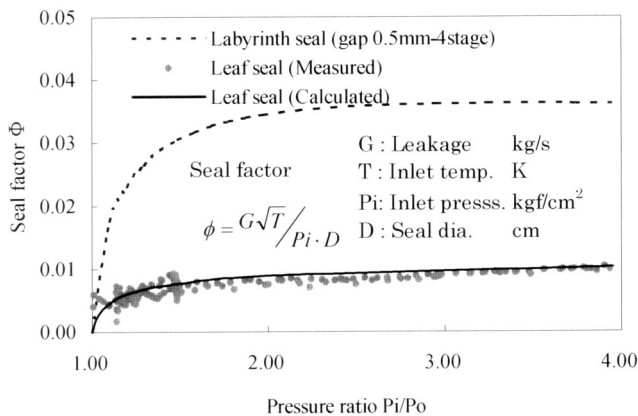


Fig. 10 Correlation between pressure ratio and seal factor

CFD. The total estimated flow through leaf seal is calculated by these flows, adding the estimated amount due to flow through segmented portion.

Figure 9 shows the flow characteristic test result of a two-segment leaf seal using a seal rotation test device. The amount of leakage is reduced to 1/3.2 compared with a labyrinth seal (gap 0.5 mm, 4-stage). The test condition is shown in Table 4. The tested leaf seal has a structure which is shown in Table 5.

Figure 10 shows the seal factor of leaf seal and labyrinth seal. The seal factor indicates constant value “0.01” with pressure ratio over 2. From the test result, the choked flow is observed as was observed in the labyrinth seal. In addition, it is also confirmed that the test result almost corresponds with the estimated figure. Table 5 and Fig. 11 show the parameters and the appearance of the leaf seal. Figure 12 shows the seal rotation test device used for the flow characteristic test.

Estimation of Lifting Characteristics

The amount of leaf lifting is calculated by balance of forces working on a leaf plate. The forces working on a leaf plate include (1) rotor interference force, (2) hydrodynamic lifting force, and (3) force generated by differential pressure, as shown in Fig. 13.

The rotor interference force (1) is the contact force between the leaf plate and the rotor at setting. This force is determined by the configuration of a leaf (length, thickness, and width). The hydrodynamic lifting force (2) is determined by tip configuration of a leaf plate, that is, thickness and width of a leaf. In the design stage, the configuration of a leaf plate is optimized in order that these forces can maintain lifting clearance. In addition to these forces, the force generated by differential pressure (3) also affects the lifting characteristics determined by the above-mentioned leaf seal configuration.

Hydrodynamic Lifting Force. In order to confirm the hydrodynamic effect, the lifting characteristic test was carried out using a seal rotation test device with an electrical contact check device shown in Fig. 12. In this test, the leaf lifting is confirmed by the electricity discontinuity. Figure 14 shows the contact check test result. From the result, it was confirmed that leaf lifting occurs with the rotating speed over 1500 rpm.

Moreover, the measurement result of rotating torque of the leaf seal is shown in Fig. 15. The rotation torque is determined by deducting the base torque, which is measured before installing the leaf seal, from overall torque. In this test, the rotating torque corresponds to friction torque according to the amount of radial interference at startup. On the other hand, it is considered to correspond with shear resistance of the air layer at the gap between the leaf plate and rotor during rotation. In Fig. 15, the relation between rotating speed and friction torque of the leaf seal and the calculated rotating torque due to shear resistance by the air layer at gap 1 to 10 μm are shown.

At the rotating speed 0 rpm, the rotating torque corresponds with the friction torque due to interference force with radial inter-

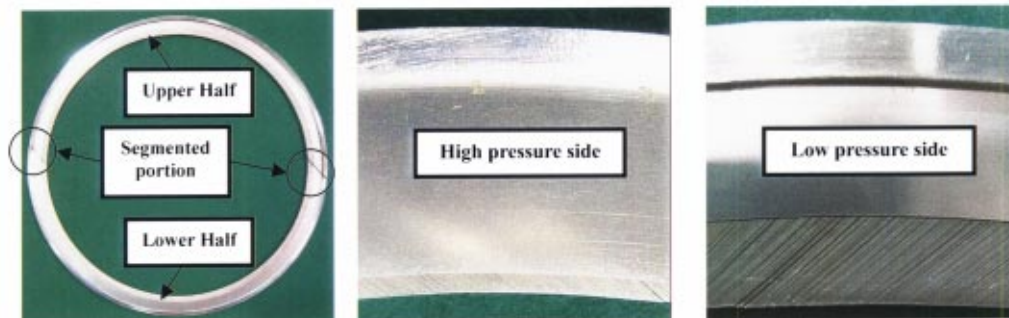


Fig. 11 Appearance of the leaf seal (2-segment)

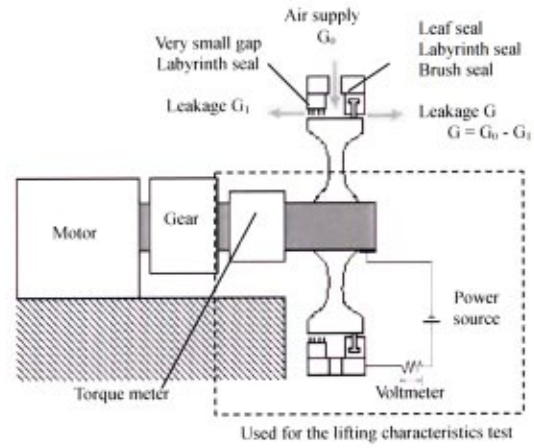


Fig. 12 Seal rotation test device

ference. When accelerating the rotating speed, the rotating torque decreases from 0 to 2000 rpm. This phenomenon is caused by reduction of contact pressure because of lifting force of the leaf plate generated by hydrodynamic lifting force during rotation. On the other hand, the friction torque trend of the leaf seal is changed from decreasing to increasing from 2000 to 5000 rpm. This result means that the tip of the leaf plate is lifted up completely and corresponds to the electricity check test result. The rotating torque of the leaf seal is almost equal to the torque due to the shearing force of the air layer at the rotating speed over 2000 rpm. Figure 16 shows the relation between tangential speed of the rotor surface and the lifting amount of leaf plates which is estimated from the rotating torque.

Force Generated by Differential Pressure. The force generated by the differential pressure can be the lowering force or the lifting force. In order to obtain the lifting characteristics, the effect of this force must be minimized to be negligibly small. In the leaf seal, the specified force can be generated with control of pressure distribution by the configuration of the high/low pressure side gap.

Figure 17 shows the relation between the pressure distribution in the leaf seal and the high/low pressure side gap. From the result of CFD analysis, it is confirmed that the characteristic of the pressure distribution does not depend on the differential pressure.

In the case that the high-pressure side gap is wider than the low-pressure side gap, the pressure distribution in the leaf seal is

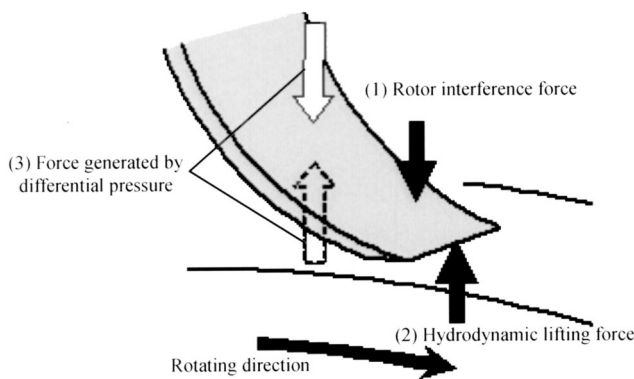


Fig. 13 Balance of forces working on a leaf plate

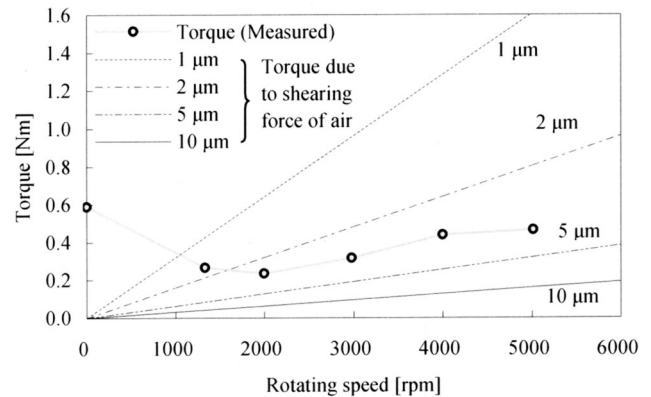


Fig. 15 Rotating torque of the leaf seal

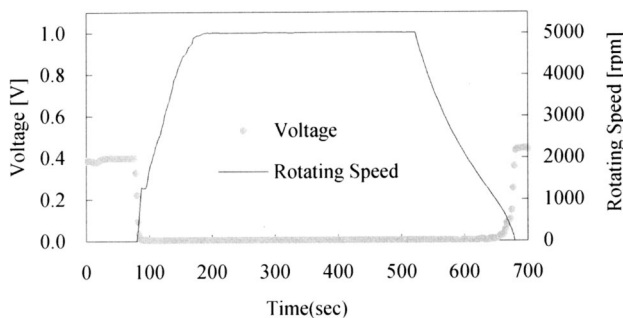


Fig. 14 Electricity check test result

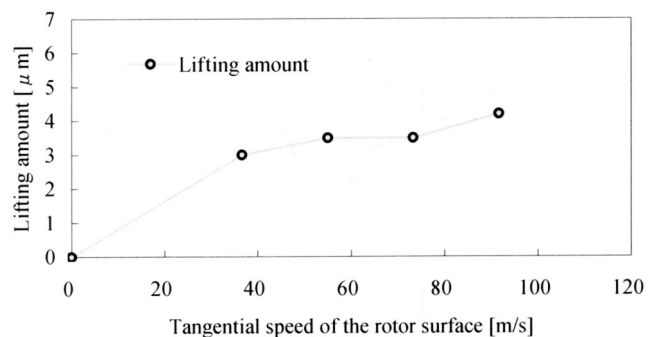


Fig. 16 Lifting amount of leaf plates

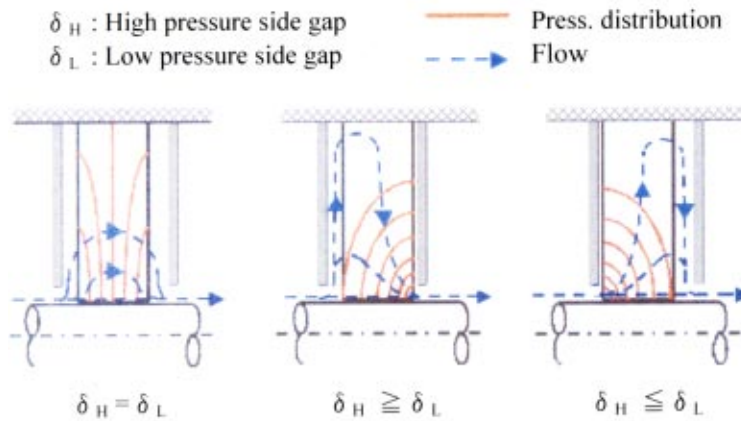


Fig. 17 Relation between the pressure distribution and the high/low pressure side gap

high at the outer side and low at inner side. This phenomenon causes the lowering force as shown in Fig. 18. On the other hand, opposite phenomenon is caused in the case that the low-pressure side gap is wider than the high-pressure side gap. In this case the lifting force acts on the leaf plate as shown in Fig. 19. Thus it is possible to control this force by selecting optimized high/low pressure side gaps in the design stage.

On the other hand, in the brush seal, it is difficult to control this force, [2]. Since the rigidity of the brush is very low, the low-pressure side gap cannot be increased to prevent the deformation of the brush caused by the differential pressure.

Figure 20 shows the measurement result of the turning torque by changing the differential pressure with very slow turning speed. In the leaf seal, since the change of the turning torque is very small, the effect of the force generated by the differential

pressure can be negligible. However, in the brush seal, the lowering force is increased with differential pressure, so the working differential pressure is limited.

Verification Result in an Actual Engine

In order to verify the sealing performance and the durability of the leaf seal, the prototype leaf seal is applied to a M501G gas turbine installed at T-Point¹ as an in-house verification test plant. The leaf seal is located between the compressor and the turbine section as shown in Fig. 21.

From the measurement result of the inlet/outlet pressure and temperature, it was confirmed that the sealing performance of the leaf seal was equivalent to the brush seal.

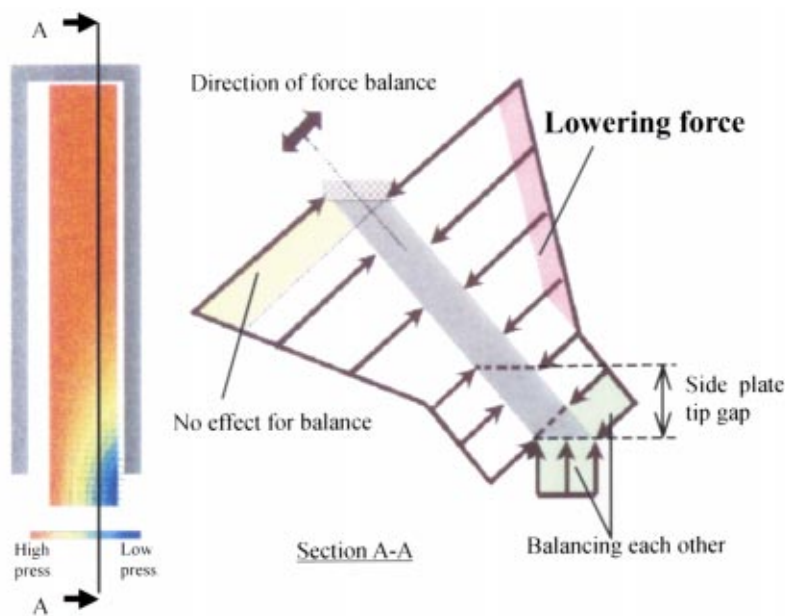


Fig. 18 Force balance on the leaf seal ($\delta_H \geq \delta_L$)

¹Mitsubishi Heavy Industries (MHI) constructed the long-term in-house verification plant known as T-Point for verifying new gas turbine technology prior to commercialization. The facility at T-Point consists of a M501G gas turbine, steam turbine, HRSG (heat recovery steam generator) and associated controls. The output of the M501G gas turbine at T-Point is 225 MW.

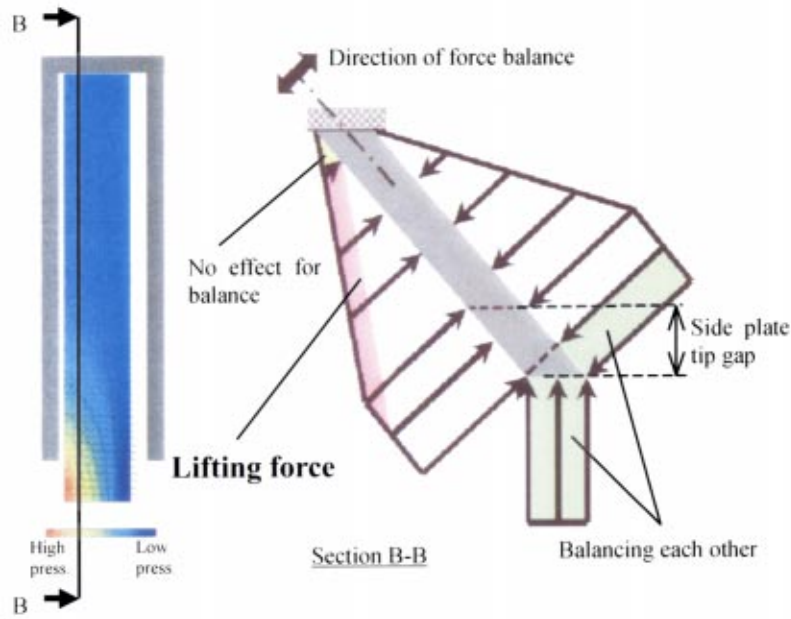


Fig. 19 Force balance on the leaf seal ($\delta_H \cong \delta_L$)

Moreover, from the inspection result after the operation (start: over 50 times, operating hours: over 1000 hr), the durability of the leaf seal was verified as follows:

1. Loss of leaves and cracked leaves were not observed.

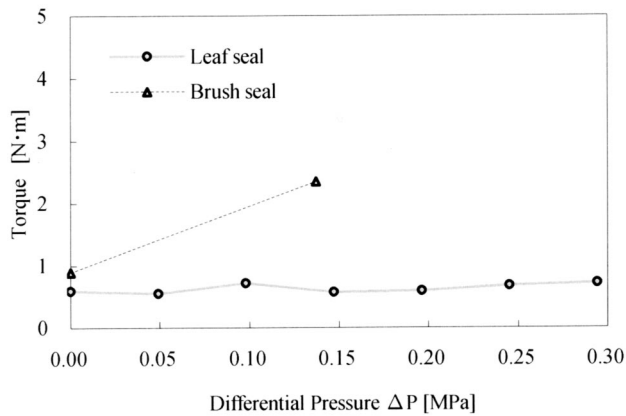


Fig. 20 Relation between the differential pressure and the rotating torque

2. Although rust was observed around the leaf seal, no rust adhered to the gap between the leaves, and the leaf plates did not stick to each other.

3. Although the tip of the leaf plates was slightly polished, the wear of the leaf plates was negligibly small.

Figure 22 shows the appearance of the leaf seal. Since the inspection result of the leaf seal was good, the verification of the leaf seal in M501G has been continued.

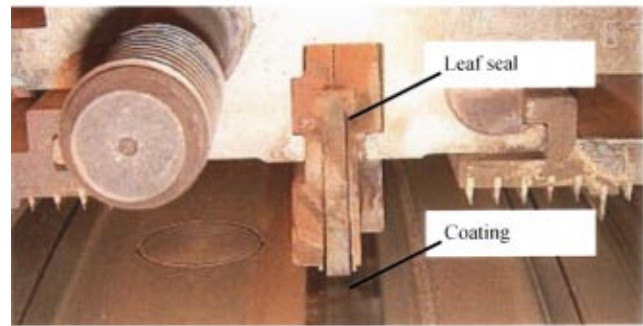


Fig. 22 Appearance of the leaf seal after operation

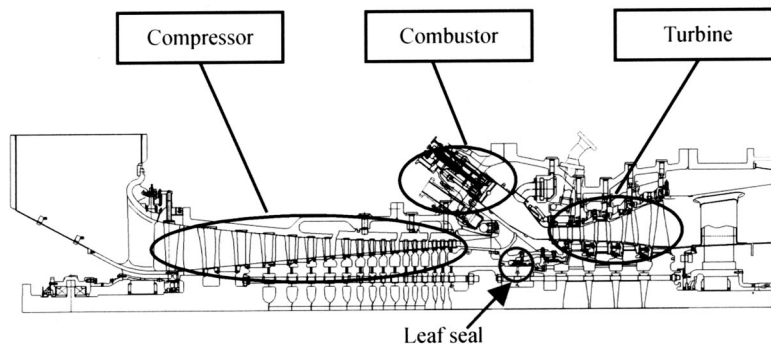


Fig. 21 Location of the leaf seal

Conclusions

We have developed the leaf seal that can considerably reduce the amount of leakage, compared with the conventional labyrinth seal. The leaf seal is superior to the brush seal that is now increasingly utilized in gas turbines, because the leaf seal has a longer life and can be utilized in the high differential pressure areas. Through the estimation of characteristics and the characteristics test of the leaf seal, the following results were obtained:

1. It is confirmed that the amount of leakage could be reduced to 1/3 compared to the conventional labyrinth seal (4 stages with 0.5 mm gap).
2. It is confirmed that the tip of a leaf plate could be lifted up during operation due to hydrodynamic lifting force by rotation. In addition, it is confirmed that lifting force can be controlled by seal differential pressure with setting of high/low pressure side gap as determined in the design stage.
3. The estimation of rigidity and leakage amount almost correspond with the test result. Therefore, it can be concluded that the design sequence is established.

4. For further reduction of leakage amount, it is essential to reduce leakage at the segmented portion.

5. Since the inspection result of the prototype leaf seal is good, in the future, we will expand the application of leaf seal to the seal portions of large capacity gas turbines.

References

- [1] Wolfe, C. E., et al., 1997, "Brush Seals in Industrial Gas Turbines," Paper No. AIAA-97-2730.
- [2] Chupp, R. E., et al., 1997, "Advanced Seal Development for Large Industrial Gas Turbines," Paper No. AIAA-97-2731.
- [3] Aksit, M. F., et al., 1996, "A Computational of Brush Seal Bristle Deflection," Paper No. AIAA-96-2909.
- [4] Gardner, J., Basu, P., and Dutta, A., 1992, "A New Compliant Seal Concept for Aerospace Applications," *Fourth International Symposium on Transport Phenomena and Dynamics of Rotating Machinery*, preprint, Vol. A., pp. 593–612.
- [5] Johnson, M. C., and Medlin, E. G., 1992, "Laminated Finger Seal With Logarithmic Curvature," U.S. Patent 5,108,116.

Effect of Inlet Air Cooling by Ice Storage on Unit Sizing of a Gas Turbine Cogeneration Plant

Ryohei Yokoyama

Associate Professor,
Mem. ASME
e-mail: yokoyama@ese.energy.osakafu-u.ac.jp

Koichi Ito

Professor,
Fellow ASME,

Department of Energy Systems Engineering,
Osaka Prefecture University,
1-1 Gakuen-cho,
Sakai, Osaka 599-8531, Japan

In the commercial sector, heat and power demands peak in the summer daytime because of high space cooling demands, and cogeneration plants are required to produce maximum heat and power to meet their demands. However, gas turbine cogeneration plants have the disadvantage of decreases in maximum power output in the summer daytime, which reduces the availability of gas turbines. One of the ways to avoid the aforementioned disadvantage is to cool inlet air and augment maximum power output. In addition, one of the ways for inlet air cooling is to make ice by driving electric compression refrigerators using off-peak power generated during the nighttime, store it in ice banks, and use its heat for inlet air cooling during the on-peak period. The objective of this paper is to investigate the effect of inlet air cooling by ice storage on the unit sizing and cost of a gas turbine cogeneration plant. An optimal unit sizing method based on the mixed-integer linear programming is used to rationally determine equipment capacities and operational strategies of the plant. A numerical study is conducted, in which the gas turbine cogeneration plants with and without inlet air cooled by ice storage are compared with each other, and the effect of inlet air cooling on the equipment capacities as well as the annual total cost and its items is clarified. [DOI: 10.1115/1.1692011]

Introduction

Because of their potential of high economic and energy saving characteristics by energy efficient utilization, cogeneration plants with gas turbines as prime movers have been installed increasingly into industrial and commercial sectors in Japan. In the commercial sector, heat and power demands peak in the summer daytime because of high space cooling demands, and cogeneration plants are required to produce maximum heat and power to meet their demands. However, gas turbine cogeneration plants have the disadvantage of decreases in maximum power output in the summer daytime, which reduces the availability of gas turbines. This is because high ambient air temperature makes the density of air low, and resultant low mass flow rates of air into gas turbines reduce maximum power output.

From the viewpoint of power producers, power augmentation is important for the purpose of using gas turbine generators to provide on-peak power. One of the ways to avoid the aforementioned disadvantage is to cool inlet air and augment maximum power output. Several technologies for inlet air cooling are considered: evaporative cooling, thermal energy storage using ice or cold water, indirect cooling using absorption or mechanical refrigerators, etc., [1]. One of the successful technologies for inlet air cooling is to make ice by driving electric compression refrigerators using off-peak power generated during the nighttime, store it in ice banks, and use its heat for inlet air cooling during the on-peak period. This technology has been introduced into some gas turbine power generation plants, [2,3]. In addition, modeling and evaluation of inlet air cooling by ice storage have been conducted to investigate its effect on the performance of power generation, [4].

On the other hand, from the viewpoint of power consumers who operate gas turbine generators and purchase electricity from electric power companies, power augmentation is important for the purpose of reducing demand and energy charges of electricity

purchased. In Japan, to levelize the daily profile of electricity consumption, the spread of thermal storage systems has been promoted by electric power companies, and discounted rates for energy charge of electricity consumed for thermal storage during the nighttime are provided. Therefore, power augmentation through inlet air cooling by ice storage has the advantage of utilizing these discounted rates for energy charge of electricity consumed to drive electric compression refrigerators during the nighttime.

In cogeneration applications, ice storage is considered as one of the coadunate technologies of cogeneration and thermal storage, [5], and it has been introduced into gas turbine cogeneration plants for power augmentation through inlet air cooling. However, the situation may be complicated for cogeneration plants in the commercial sector. For example, the following questions occur: Which is more advantageous to use ice storage for supplying cold water to space cooling demand or for cooling inlet air? Which is more advantageous to make ice using electricity purchased from electric power companies or generated by gas turbine generators? Thus, it is an important subject to investigate the effect of inlet air cooling by ice storage on the performance and cost of cogeneration in consideration of the aforementioned questions. The effect has been investigated in terms of operational performance, [6]. However, no investigation has been made in terms of unit sizing.

The objective of this paper is to investigate the effect of inlet air cooling by ice storage on the unit sizing and cost of a gas turbine cogeneration plant. An optimal unit sizing method based on the mixed-integer linear programming is used to rationally determine equipment capacities and operational strategies of the plant. First, a typical configuration of a gas turbine cogeneration plant with inlet air cooled by ice storage is presented, which is followed by a brief description for the formulation of an optimal unit sizing problem. Finally, a numerical study is conducted, in which the gas turbine cogeneration plants with and without inlet air cooled by ice storage are compared with each other, and the effect of inlet air cooling on the equipment capacities as well as the annual total cost and its items is investigated.

Plant Configuration

A gas turbine cogeneration plant shown in Fig. 1 is considered in this paper. This plant is composed of a gas turbine generator

Contributed by the International Gas Turbine Institute (IGTI) of THE AMERICAN SOCIETY OF MECHANICAL ENGINEERS for publication in the ASME JOURNAL OF ENGINEERING FOR GAS TURBINES AND POWER. Paper presented at the International Gas Turbine and Aeroengine Congress and Exhibition, Amsterdam, The Netherlands, June 3–6, 2002; Paper No. 2002-GT-30484. Manuscript received by IGTI, December 2001, final revision, March 2002. Associate Editor: E. Benvenuti.

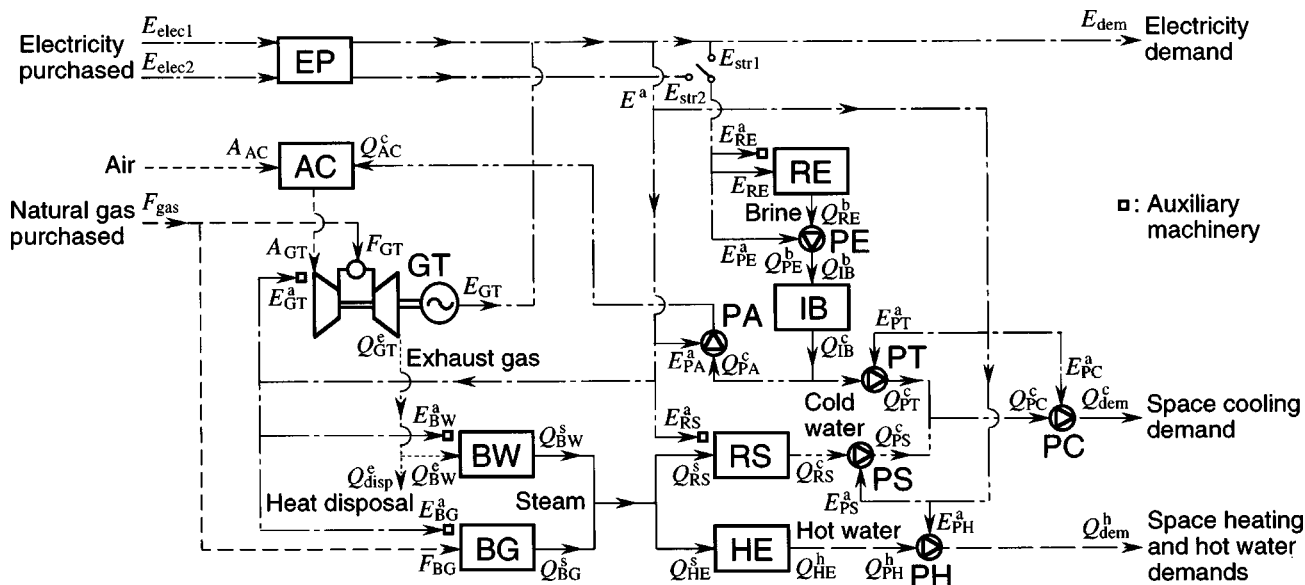


Fig. 1 Configuration of gas turbine cogeneration plant with inlet air cooled by ice storage

(GT), an air cooler (AC), a waste heat recovery boiler (BW), a gas-fired auxiliary boiler (BG), a steam absorption refrigerator (RS), a heat exchanger (HE), an electric compression refrigerator (RE), an ice bank (IB), a device for receiving electricity (EP), which includes the equipment for converting voltage, etc., and pumps (PA, PC, PE, PH, PS, and PT). Electricity is supplied to customers by operating the gas turbine generator and by purchasing electricity from an outside electric power company. Heat of exhaust gas generated from the gas turbine is recovered by the waste heat recovery boiler to produce steam, and it is used for heat supply. An excess of exhaust gas is disposed of through an exhaust gas dumper. A shortage of steam is supplemented by the gas-fired auxiliary boiler. Steam is used by the steam absorption refrigerator and heat exchanger to supply cold water for space cooling, and hot water for space heating and hot water supply, respectively. The electric compression refrigerator supplies brine to make ice in the ice bank. Cold water retrieved from the ice bank is supplied to the air cooler and space cooling demand. The air cooler cools air supplied to the gas turbine.

Electricity purchased is divided into two kinds: one is purchased at a standard rate for energy charge, and the other at a discounted rate for energy charge, which can be applied to the electricity consumed for ice storage during the nighttime. When the latter is used, the heat stored using electricity purchased at the discounted rate cannot be retrieved from the ice bank. On the other hand, the heat stored using electricity generated by the gas turbine generator or purchased at the standard rate can be retrieved from the ice bank at any time. A switch is drawn to show this selection of electricity.

Optimal Unit Sizing Method

An optimal unit sizing method based on the mixed-integer linear programming is used to determine capacities of equipment and maximum demands of utilities rationally in consideration of their operational strategies for seasonal and hourly changes in energy demands.

Fundamental Optimization Model. To consider seasonal and hourly changes in energy demands, a typical year is divided into M representative days with average and peak energy demands, and the index for the representative days is designated by m , i.e., $m = 1, 2, \dots, M$. Furthermore, each representative day is

divided into K sampling times with a period of Δt , i.e., $\Delta t = 24/K$, and the index for the sampling times is designated by k , i.e., $k = 1, 2, \dots, K$.

Continuous variables for equipment capacities and utility maximum demands are considered as design variables. In addition, continuous variables for flow rates of input and output energy of equipment are considered as operation variables. These variables are determined to minimize a specified objective function. Here, the annual total cost is adopted as the objective function, and is composed of capital costs of equipment, and demand and energy charges of utilities. The operation and maintenance costs are not considered explicitly. Since they are small as compared with the demand and energy charges of utilities, they are assumed to be included in the capital costs of equipment. As constraints to be satisfied, performance characteristics of equipment and energy balance relationships of energy flows are considered.

At the first step of the research, the following first-order approximation is used for performance characteristics and capital costs of equipment to solve the optimization problem exactly. Without this approximation, the optimization problem becomes too difficult to solve exactly, and an approximate solution may not indicate the effect of inlet air cooling on the unit sizing reasonably.

First, the relationship between the flow rates of input and output energy of each piece of equipment is assumed to be expressed by a linear equation, which means that the thermal efficiency or coefficient of performance is constant regardless of capacity and part load. In addition, the maximum flow rate of input or output energy of each piece of equipment is assumed to be in proportion to its capacity. These are expressed as follows:

$$\left. \begin{aligned} v(m, k) &= pu(m, k) \\ 0 &\leq u(m, k) \leq \bar{u} \eta \end{aligned} \right\} (m = 1, 2, \dots, M; k = 1, 2, \dots, K) \quad (1)$$

where u and v are the continuous variables for the flow rates of input and output energy, respectively, p is the constant thermal efficiency or coefficient of performance, η is the continuous variable for the capacity, and \bar{u} is the upper limit for u in case of unit capacity, i.e., $\eta = 1$. Second, the capital cost of each piece of equipment is assumed to be in proportion to its capacity as follows:

$$C = Y \eta \quad (2)$$

where C is the capital cost, and Y is the unit capital cost.

Modified Optimization Model. As for the operation, since the gas turbine cogeneration plant includes the ice bank which stores cooling heat, the operational strategy cannot be determined independently for each sampling time, but should be determined for a period within which energy demands change cyclically. Here, on the assumption that energy demands change cyclically with a period of 24 hours on each representative day, the daily cyclic operation is considered.

The aforementioned fundamental optimization model cannot incorporate the selection of inlet air cooling as well as that of electricity as to which electricity is selected, purchased at the discounted rate, or generated by the gas turbine generator or purchased at the standard rate. Here, binary variables are introduced to express the selection of inlet air cooling and electricity.

Therefore, as operation variables, the selection of inlet air cooling and electricity, the flow rates of input and output energy of each piece of equipment, and the storage level of the ice bank are determined. In the following, the formulation of the performance characteristics of only the gas turbine generator, air cooler, and ice bank is given as examples.

For the gas turbine generator, the relationships among the natural gas consumption F_{GT} , the electric power generated E_{GT} , the heat flow rate of exhaust gas Q_{GT}^e , the electric power consumed for auxiliary machinery E_{GT}^a , and the mass flow rate of air A_{GT} are expressed as follows:

$$\left. \begin{aligned} E_{GT}(m,k) &= p_{GT}(T(m,k))F_{GT}(m,k) + p_{GT}(T')F'_{GT}(m,k) \\ Q_{GT}^e(m,k) &= q_{GT}(T(m,k))F_{GT}(m,k) + q_{GT}(T')F'_{GT}(m,k) \\ E_{GT}^a(m,k) &= r_{GT}(F_{GT}(m,k) + F'_{GT}(m,k)) \\ A_{GT}(m,k) &= s_{GT}F_{GT}(m,k) \\ A'_{GT}(m,k) &= s_{GT}F'_{GT}(m,k) \\ F_{GT}(m,k) &\leq \bar{F}_{GT}(T(m,k))\eta_{GT}(1 - \delta_{GT}(m,k)) \\ F'_{GT}(m,k) &\leq \bar{F}_{GT}(T')\eta_{GT}\delta_{GT}(m,k) \\ \delta_{GT}(m,k) &\in \{0,1\} \end{aligned} \right\} \quad (m=1,2,\dots,M;k=1,2,\dots,K) \quad (3)$$

where δ_{GT} is the binary variable for the selection of inlet air cooling, and $()'$ means a quantity in case that inlet air is cooled. The parameters p , q , r , and s are performance characteristic values, and p and q are expressed as functions with respect to the inlet air temperature. Here, T is the ambient air temperature, which varies with season and time, and T' is the temperature of air cooled by the air cooler, which is assumed to be constant. \bar{F}_{GT} is the upper limit for the natural gas consumption in case of unit capacity, and is also expressed as a function with respect to the inlet air temperature.

For the air cooler, the relationship between the mass flow rate of air A_{AC} and the cooling heat consumption Q_{AC}^c is expressed as follows:

$$\left. \begin{aligned} Q_{AC}^c(m,k) &= p_{AC}(x(m,k), T(m,k), T', \phi')A_{AC}(m,k) \\ 0 &\leq Q_{AC}^c(m,k) \leq \bar{Q}_{AC}\eta_{AC} \end{aligned} \right\} \quad (m=1,2,\dots,M;k=1,2,\dots,K) \quad (4)$$

where p is the cooling heat consumed for the unit mass of air, and is expressed as a function with respect to the conditions of air, i.e., temperature and humidity, before and after it is cooled. As arguments of p , x is the absolute humidity of ambient air, and ϕ' is the relative humidity of air after it is cooled. The cooling heat is composed of the sensible heat due to decreases in the temperature of air and water vapor, the latent heat due to the condensation of water vapor, and the sensible heat due to a decrease in the temperature of condensed water. The first one is evaluated using the average specific heats and temperature differences of air and water

Table 1 Definition of representative days

| Day No. m | Name of Day | Number of Days per Year d/y |
|-------------|----------------|-----------------------------|
| 1 | Summer average | 82 |
| 2 | Winter average | 80 |
| 3 | Midseason 1 | 91 |
| 4 | Midseason 2 | 92 |
| 5 | Summer peak | 10 |
| 6 | Winter peak | 10 |

vapor. The second and third ones are evaluated using the average latent heat of water vapor, and the average specific heat and temperature difference of condensed water.

For the ice bank, the relationships among the storage level of heat stored in the bank R_{IB} , the flow rates of heat stored into and retrieved from the bank, Q_{IB}^b and Q_{IB}^c , respectively, are expressed as follows:

$$\left. \begin{aligned} (R_{IB^l}(m,k) - R_{IB^l}(m,k-1))/\Delta t \\ = Q_{IB^l}^b(m,k) - Q_{IB^l}^c(m,k) - \zeta R_{IB^l}(m,k) \\ R_{IB^l}(m,k) \geq 0 \\ Q_{IB^l}^b(m,k) \geq 0 \\ Q_{IB^l}^c(m,k) \geq 0 \end{aligned} \right\} (l=1,2)$$

$$\left. \begin{aligned} R_{IB}(m,k) &= \sum_{l=1}^2 R_{IB^l}(m,k) \leq \bar{R}_{IB}\eta_{IB} \\ Q_{IB}^b(m,k) &= \sum_{l=1}^2 Q_{IB^l}^b(m,k) \leq \bar{Q}_{IB}^b\eta_{IB} \\ Q_{IB}^c(m,k) &= \sum_{l=1}^2 Q_{IB^l}^c(m,k) \leq \bar{Q}_{IB}^c\eta_{IB} \end{aligned} \right\} \quad (m=1,2,\dots,M;k=1,2,\dots,K) \quad (5)$$

where the heat balance relationship in the ice bank is expressed by a finite difference equation, and ζ is the heat loss coefficient. In addition, the subscript l is used to distinguish the heat stored using electricity generated by the gas turbine generator or purchased at the standard rate ($l=1$) from that using electricity purchased at the discounted rate ($l=2$). Furthermore, the following constraint is considered for the daily cyclic operation:

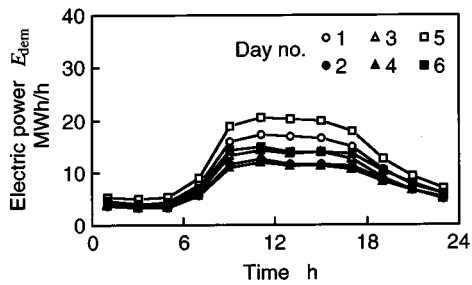
$$R_{IB^l}(m,0) = R_{IB^l}(m,K) \quad (m=1,2,\dots,M;l=1,2). \quad (6)$$

Solution Method. Although there exists the nonlinear term $\eta_{GT}\delta_{GT}$ in Eq. (3), it can be linearized exactly by replacing it with a continuous variable and introducing relevant constraints, [7]. As a result, the optimal unit sizing problem is formulated as a mixed-integer linear programming one. Here, the branch and bound method combined with the simplex method is used as a solution algorithm. This method searches the optimal solution by repeating the branching and bounding operations which divides the whole feasible region into smaller ones, and removes ones where it turns out that there exists no optimal solution, respectively. GAMS/CPLEX is used as a concrete solver, [8].

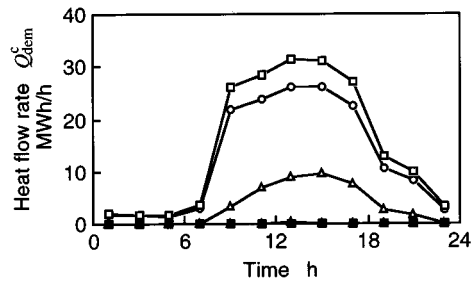
Numerical Study

A numerical study is carried out using the aforementioned optimization model to investigate the effect of inlet air cooling on the unit sizing and cost of a gas turbine cogeneration plant for district heat and power supply.

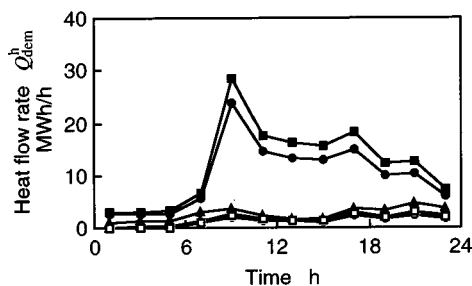
Input Data. The district in Osaka, Japan under consideration has four office buildings and two hotels to which heat and power are supplied. Energy demands are estimated for six representative days, i.e., $M=6$, as shown in Table 1. Figures 2(a) to 2(c) show electricity, space cooling, and space heating and hot water de-



(a) Electric power



(b) Space cooling



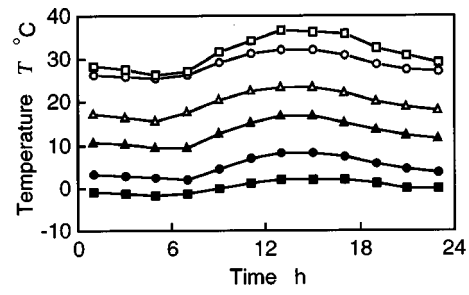
(c) Space heating and hot water

Fig. 2 Energy demands; (a) electric power, (b) space cooling, (c) space heating and hot water

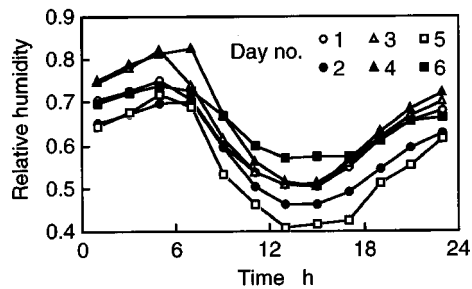
mands, respectively. Daily changes in energy demands are drawn for the representative days. Each day is divided into twelve sampling times, i.e., $K=12$ and $\Delta t=2$ h.

As ambient conditions, the temperature and humidity of ambient air are given. Figure 3(a) shows daily changes in air temperature T for the representative days. Since the absolute humidity of air x does not significantly change during a day, it is assumed to be constant during each representative day, as shown in Table 2. The relative humidity of air is calculated from its temperature and absolute humidity, and its daily changes are shown for the representative days in Fig. 3(b). The temperature of air after it is cooled by the air cooler is assumed to be $T'=7^\circ\text{C}$, in consideration of the temperature of cold water for space and inlet air cooling as well as the temperature difference in the air cooler, and without consideration of the condition of inlet icing. The relative humidity of air after it is cooled by the air cooler is assumed to be saturated at $\phi'=0.9$ with the condensation of water vapor.

The performance characteristic values of equipment, the unit capital costs of equipment, and the rates for demand and energy charges of utilities are given in Tables 3 and 4. The power generating and exhaust heat efficiencies of the gas turbine generator at the inlet air temperature of 0°C are shown as their reference values. Here, the dependence of the performance characteristic values p_{GT} and q_{GT} , and the upper limit for the natural gas consumption in case of unit capacity \bar{F}_{GT} in Eq. (3) on the inlet air temperature T is assumed as follows:



(a) Temperature



(b) Relative humidity

Fig. 3 Temperature and relative humidity of ambient air; (a) temperature, (b) relative humidity

$$\left. \begin{aligned} p_{GT}(T) &= 3.21 - 0.0049T \\ q_{GT}(T) &= 6.79 + 0.0255T \\ \bar{F}_{GT}(T) &= 1.22 - 0.0060T \end{aligned} \right\} \quad (7)$$

where the units of p_{GT} , q_{GT} , \bar{F}_{GT} , and T are kWh/m^3 , kWh/m^3 , m^3/h , and $^\circ\text{C}$, respectively. The thermal efficiency of the heat exchanger is not based on the inlet and outlet temperatures but the heat exchanged, and it is assumed that the heat loss from the heat exchanger is zero. It is assumed that the capacity of the device for receiving electricity is equal to the maximum demand of electricity purchased. All values of costs are stated in yen, which is equivalent to about 8.0×10^{-3} dollars on the recent exchange rate.

The following two plants are investigated:

- Plant A: The inlet air cooling by ice storage is not adopted.

Table 2 Absolute humidity of ambient air

| Day No. m | Absolute Humidity x |
|-------------|-----------------------|
| 1 | 0.0152 |
| 2 | 0.0031 |
| 3 | 0.0091 |
| 4 | 0.0060 |
| 5 | 0.0155 |
| 6 | 0.0025 |

Table 3 Performance characteristic values of equipment

| Equipment | Item | Value |
|------------------------------|-----------------------------|------------------------|
| Gas turbine generator* | Power generating efficiency | 0.278 |
| | Exhaust heat efficiency | 0.588 |
| Air cooler | Thermal efficiency | 1.00 |
| | Thermal efficiency | 0.780 |
| Gas-fired auxiliary boiler | Thermal efficiency | 0.920 |
| Steam absorption refrig. | Coefficient of performance | 1.25 |
| Heat exchanger | Thermal efficiency | 1.00 |
| Electric compression refrig. | Coefficient of performance | 3.57 |
| Ice bank | Heat loss coefficient | 0.005 h^{-1} |
| Device for receiving elec. | Efficiency | 1.00 |

*Inlet air temperature is assumed to be 0°C

Table 4 Unit capital costs of equipment, and rates for demand and energy charges of utilities

| Equipment/Utility | | Unit Cost |
|------------------------------|---------------|------------------------------------|
| Gas turbine generator | | 230.0×10^3 yen/kW |
| Air cooler | | 20.0×10^3 yen/kW |
| Waste heat recovery boiler | | 9.6×10^3 yen/kW |
| Gas-fired auxiliary boiler | | 6.6×10^3 yen/kW |
| Steam absorption refrig. | | 30.1×10^3 yen/kW |
| Heat exchanger | | 8.6×10^3 yen/kW |
| Electric compression refrig. | | 34.4×10^3 yen/kW |
| Ice bank | | 1.9×10^3 yen/kWh |
| Electricity | Demand charge | 1740 yen/(kW·month) |
| | Energy charge | 10.77 yen/kWh (summer) |
| | | 9.79 yen/kWh (other seasons) |
| Natural gas | Demand charge | 4.50 yen/kWh (thermal storage) |
| | Energy charge | 2033 yen/(m ³ ·h·month) |
| | | |

- Plant B: The inlet air cooling by ice storage is adopted.

Plant A is a conventional gas turbine cogeneration plant combined with ice storage. The electric compression refrigerator and ice bank are installed only to supply cold water for space cooling. Plant B is the plant under investigation in this paper. The comparison of these two plants clarifies the effect of inlet air cooling by ice storage on the unit sizing and cost of the plant.

Results and Discussion. Table 5 shows the optimal values of equipment capacities and utility maximum demands for plants A and B. The power generating capacity of the gas turbine generator at the inlet air temperature of 0°C is shown as its reference value. The arrows in the table show the increases and decreases in equipment capacities and utility maximum demands from plants A to B. The adoption of inlet air cooling increases the capacities of the gas turbine cogeneration and ice storage units, and decreases the capacities of the conventional equipment such as the gas-fired auxiliary boiler, steam absorption refrigerator, and device for receiving electricity. The increase in the capacity of the gas turbine generator and the adoption of inlet air cooling decreases the maximum demand of electricity, while it increases that of natural gas.

Table 6 shows the annual total cost and its items for plants A and B. As for the energy charge, its values for the representative days and their annual sum are included in the table. The arrows in the table show the increases and decreases in costs from plants A to B, and the values in the right-end column show the increase and decrease rates in costs from plant A to B. The increase in the annual capital cost is mainly because the capacities of the gas turbine cogeneration and ice storage units increase. The decrease in the annual demand charge is mainly because the maximum demand of electricity decreases. The decrease in the annual energy charge is small as compared with that in the annual demand charge. The decreases in the energy charge for the representative day Nos. 2 and 6 are due to the increase in the capacity of the gas

turbine cogeneration unit, because these days correspond to winter, and the inlet air and space cooling is unnecessary. The decreases in the energy charge for the representative day Nos. 1 and 5 are due to the increases in the capacities of the gas turbine cogeneration and ice storage units as well as the adoption of inlet air cooling. However, the effect of inlet air cooling may be smaller than that of the increases in the capacities of the cogeneration and storage units. This is because that the decrease rates in the energy charge for the representative day Nos. 1 and 5 do not significantly differ from those for the representative day Nos. 2 and 6. The energy charges for the representative day Nos. 3 and 4 almost remain constant. This is because these days correspond to midseason, thermal energy is unnecessary, and the operation of the gas turbine cogeneration unit may not be advantageous.

From the aforementioned results, the largest effect of the inlet air cooling by ice storage on the unit sizing of the gas turbine cogeneration plant is to decrease the maximum demand of electricity, and consequently its demand charge. The decrease in the annual total cost is about 1.1%, and may be small. However, the decrease in the annual total cost by installing the gas turbine cogeneration and ice storage units is about 3.8% as compared with the conventional plant without those units. Therefore, the adoption of inlet air cooling is meaningful.

Figures 4 and 5 show the optimal operational strategies of plant B for the representative day Nos. 5 and 1, respectively. In these figures, Figs. 4(a) and 5(a) shows the allocation of electricity supply, i.e., the electric power purchased at the standard and discounted rates, E_{elec1} and E_{elec2} , respectively, and the electric power generated by the gas turbine generator E_{GT} . Figures 4(b) and 5(b) shows the allocation of cold water supply to space cooling demand, i.e., the flow rate of heat retrieved from the ice bank Q_{PT}^c , and the flow rate of heat generated by the steam absorption refrigerator Q_{RS}^c . Figures 4(c) and 5(c) show the heat stored in the ice bank R_{IB} , which is divided into the heat stored using

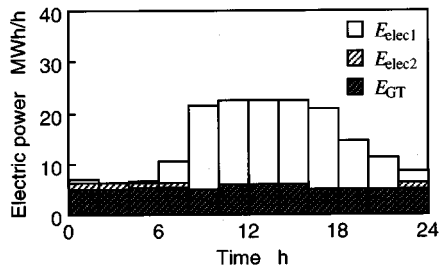
Table 5 Optimal values of equipment capacities and utility maximum demands

| Equipment/Utility | | Plant A | | Plant B |
|------------------------------|---------------------------------|---------|---|---------|
| Gas turbine generator* | MW | 5.72 | ↑ | 6.23 |
| Air cooler | MW | 0.00 | ↑ | 1.40 |
| Waste heat recovery boiler | MW | 11.98 | ↑ | 13.05 |
| Gas-fired auxiliary boiler | MW | 28.70 | ↓ | 26.96 |
| Steam absorption refrig. | MW | 25.07 | ↓ | 23.99 |
| Heat exchanger | MW | 28.44 | → | 28.44 |
| Electric compression refrig. | MW | 2.26 | ↑ | 3.59 |
| Ice bank | MWh | 28.25 | ↑ | 42.38 |
| Device for receiving elec. | MW | 17.88 | ↓ | 16.48 |
| Electricity | MW | 17.88 | ↓ | 16.48 |
| Natural gas | $\times 10^3$ m ³ /h | 2.70 | ↑ | 2.86 |

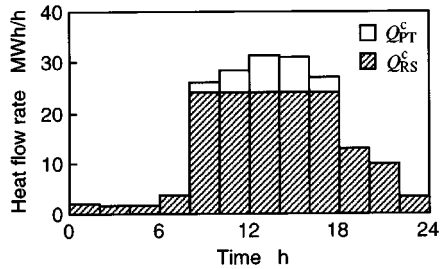
*Maximum power output in case that inlet air temperature is 0°C

Table 6 Annual total cost and its items (Unit: $\times 10^6$ yen/y)

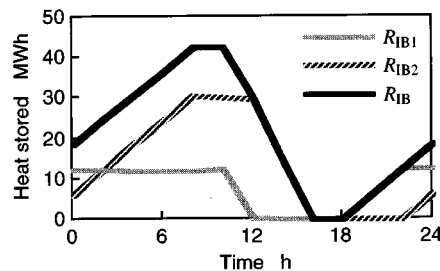
| Item | Plant A | | Plant B | Inc./dec. |
|----------------------|---------|---|---------|-----------|
| Annual capital cost | 495.1 | ↑ | 509.0 | +2.81% |
| Annual demand charge | 439.1 | ↓ | 414.0 | -5.72 |
| Annual energy charge | 859.9 | ↓ | 852.1 | -0.91 |
| 1 | 261.8 | ↓ | 258.0 | -1.45 |
| 2 | 171.1 | ↓ | 168.0 | -1.81 |
| Energy charge 3 | 195.4 | → | 195.4 | 0.00 |
| Day No. m 4 | 165.4 | → | 165.3 | -0.06 |
| 5 | 39.7 | ↓ | 39.2 | -1.26 |
| 6 | 26.5 | ↓ | 26.2 | -1.13 |
| Annual total cost | 1794.1 | ↓ | 1775.1 | -1.06 |



(a) Electricity supply

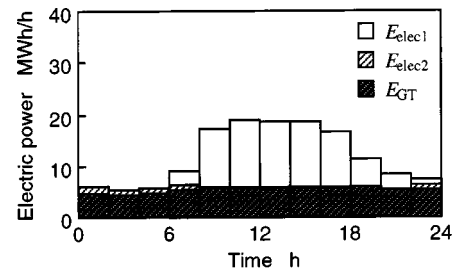


(b) Cold water supply

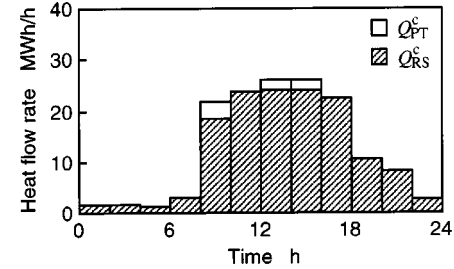


(c) Heat stored in ice bank

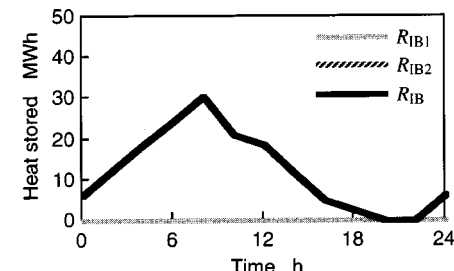
Fig. 4 Optimal operational strategy (plant B, day No. 5); (a) electricity supply, (b) cold water supply, (c) heat stored in ice bank



(a) Electricity supply



(b) Cold water supply



(c) Heat stored in ice bank

Fig. 5 Optimal operational strategy (plant B, day No. 1); (a) electricity supply, (b) cold water supply, (c) heat stored in ice bank

electricity generated by the gas turbine generator or purchased at the standard rate R_{IB1} and the heat stored using electricity purchased at the discounted rate R_{IB2} .

On the representative day No. 5, as shown in Fig. 4(a), the inlet air cooling is conducted only for a peak period, i.e., from 10:00 to 16:00. This can trim the maximum demand of electricity. As shown in Fig. 4(b), the ice storage is used not only for inlet air cooling but also for space cooling. This reduces the capacity of the steam absorption refrigerator. As shown in Fig. 4(c), the heat stored in the ice bank is generated by the electric compression refrigerator using not only the electricity purchased at the discounted rate during the nighttime but also the electricity purchased at the standard rate during the daytime. This is because the availability of the electric compression refrigerator can be increased.

On the representative day No. 1, as shown in Fig. 5(a), the inlet air cooling is conducted for a longer period, i.e., from 8:00 to 20:00. In addition, as shown in Fig. 5(c), the heat stored in the ice bank is generated by the electric compression refrigerator using only the electricity purchased at the discounted rate during the nighttime. This is because the representative day No. 1 has a smaller space cooling demand than No. 5, the steam absorption refrigerator can supply most of cold water for space cooling, and the ice storage unit can supply more cold water for inlet air cooling. These can be understood from Fig. 5(b).

Conclusions

The effect of inlet air cooling by ice storage on the unit sizing and cost of a gas turbine cogeneration plant has been investigated using an optimal unit sizing method based on the mixed-integer linear programming. A numerical study has been conducted for a gas turbine cogeneration plant for district heat and power supply. The gas turbine cogeneration plants with and without inlet air cooled by ice storage have been compared with each other, and the effect of inlet air cooling on the equipment capacities as well as the annual total cost and its items has been investigated. The following main results have been obtained:

- The inlet air cooling increases the capacities of the gas turbine cogeneration and ice storage units, and decreases the capacities of the conventional equipment.
- The largest effect of inlet air cooling is to decrease in the demand charge of electricity at the sacrifice of the increases in the capital cost of equipment and the demand charge of natural gas.
- The energy charge can be decreased by the increase in the capacities of the gas turbine cogeneration and ice storage units, but the effect of inlet air cooling on the decrease in the energy charge may be small.
- The effect of inlet air cooling on the decrease in the annual total cost may also be small, but it is meaningful as compared with that of installing the gas turbine cogeneration and ice storage units.

Nomenclature

A = mass flow rate of air (kg/h)
 C = capital cost of equipment (yen)
 E = electric power (kWh/h)
 F = natural gas consumption (m³/h)
 K = number of sampling times
 k = index for sampling times
 M = number of representative days
 m = index for representative days
 p, q, r, s = performance characteristic values (kWh/m³, kg/m³, kWh/kg)
 Q = heat flow rate (kWh/h)
 R = heat stored (kWh)
 T = air temperature (°C)
 Δt = sampling time interval (h)
 u = flow rate of input energy of equipment
 v = flow rate of output energy of equipment
 x = absolute humidity
 Y = unit capital cost of equipment (yen/kW, yen/kWh)
 δ = binary variable
 ζ = heat loss coefficient (h⁻¹)
 η = equipment capacity (kW, kWh)
 ϕ = relative humidity
 $(\)'$ = inlet air cooling
 $(\)$ = upper limit

Subscripts

dem = demand
disp = disposal
elec = electricity purchased
gas = natural gas purchased
 l = index for selection of electricity
str = ice storage

Subscripts (Equipment)

AC = air cooler
BG = gas-fired auxiliary boiler

BW = waste heat recovery boiler
EP = device for receiving electricity
GT = gas turbine generator
HE = heat exchanger
IB = ice bank
PA, PC, PE, PH, PS, PT = pumps
RE = electric compression refrigerator
RS = steam absorption refrigerator

Superscripts

a = auxiliary power
 b = brine
 c = cold water
 e = exhaust gas
 h = hot water
 s = steam

References

- [1] Lukas, H., 1997, "Power Augmentation Through Inlet Cooling," *Global Gas Turb. News*, **37**(3), pp. 12–15.
- [2] Ebeling, J. A., Halil, R., Bantam, D., Bakenhus, B., Schreiber, H., and Wendland, R., 1992, "Peaking Gas Turbine Capacity Enhancement Using Ice Storage for Compressor Inlet Air Cooling," ASME Paper No. 92-GT-265.
- [3] Ebeling, J. A., Balsbaugh, R., Blanchard, S., and Beaty, L., 1994, "Thermal Energy Storage and Inlet Air Cooling for Combined Cycle," ASME Paper No. 94-GT-310.
- [4] Cross, J. K., Beckman, W. A., Mitchell, J. W., Reindl, D. T., and Knebel, D. E., 1995, "Modeling of Hybrid Combustion Turbine Inlet Air Cooling Systems," ASHRAE Trans., Paper No. SD-95-19-3, pp. 1335–1341.
- [5] Somasundaram, S., Drost, M. K., Brown, D. R., and Antoniuk, Z. I., 1996, "Coadunation of Technologies: Cogeneration and Thermal Energy Storage," ASME J. Eng. Gas Turbines Power, **118**, pp. 32–37.
- [6] Yokoyama, R., and Ito, K., 2000, "Evaluation of Operational Performance of a Gas Turbine Cogeneration Plant With Intake Air Cooled by Ice Storage," ASME Paper No. 2000-GT-304.
- [7] Yokoyama, R., Hasegawa, Y., and Ito, K., 2002, "A MILP Decomposition Approach to Large-Scale Optimization in Structural Design of Energy Supply Systems," *Energy Convers. Manage.*, **43**, pp. 771–790.
- [8] Brooke, A., Kendrick, D., and Meeraus, A., 1996, *GAMS Release 2.25 a User's Guide*, GAMS Development Corp.

Sangkyun Kang

Samsung Advanced Institute of Technology,
MEMS Laboratory,
SAIT P.O. Box 111,
Suwon 440-600, Korea
e-mail: sangkyun.kang@samsung.com

James P. Johnston

Department of Mechanical Engineering,
Stanford University,
Stanford, CA 94305

Toshiyuki Arima

Minoru Matsunaga

Hideaki Tsuru

Wako Research Center,
Honda R&D Company, Ltd.,
Saitama, Japan

Friedrich B. Prinz

Department of Mechanical Engineering,
Stanford University,
Stanford, CA 94305

Microscale Radial-Flow Compressor Impeller Made of Silicon Nitride: Manufacturing and Performance

A microscale, high-speed compressor impeller (12 mm diameter, 800,000 rpm) was tested for feasibility in regard to aerodynamic performance. The compressor was designed for application in a first-sized gas turbine generator. To survive high stresses at such high temperatures, the rotor was manufactured as a single turbine/compressor/shaft unit in silicon nitride, by the Mold SDM process. Performance testing was conducted in a cold-flow rig at reduced speed of 420,000 rpm. Results from a CFD code compared favorably to measured data at this speed. Extrapolation from test conditions to full design speed was accomplished by application of CFD applied at both speeds. [DOI: 10.1115/1.1739246]

Introduction

The need for a portable microsized power source is increasing with the development of unmanned aerial vehicles, autonomous robots and other mobile devices. Since it is known that the power density of a gas turbine engine is inversely proportional to its length scale, a gas turbine engine with a rotary generator was chosen over other possible devices, [1,2]. In this paper, the compressor for the gas turbine engine is the principal object of investigation.

Preliminary design analysis showed that a gas-turbine-generator based on a simple Brayton cycle with a cycle pressure ratio of 3:1 could produce the desired power in a fist-sized package, excluding fuel tank and controls. The largest component is a reverse flow annular combustion chamber. The radial flow compressor and turbine rotors are much smaller. They are mounted back-to-back in an overhung configuration on the shaft, ahead of the rear bearing. The generator, mounted between the front and rear bearings, is the second largest component of the package.

With rotors of 12 mm diameter, the shaft must spin at 800,000 rpm (500 m/s tip speed) to achieve the design pressure ratio of 3:1 using a radial flow compressor impeller with backward leaning blades. To withstand the high stresses at high temperature without the need for auxiliary cooling, a ceramic material was chosen for the rotors and shaft. Also, to achieve the desired performance levels, the turbine and compressor were designed with the fully three-dimensional geometry obtained in conventional turbomachines. These geometric criteria were achieved by the use of Mold SDM process, developed in the Rapid Prototyping Laboratory at

Stanford University, to produce very small, intricate, three-dimensional rotors and shafts out of silicon nitride.

The compressor rotor, Fig. 1, was designed to be about 12 mm in diameter with unshrouded blades. It had six full blades and six partial blades (splitters) which inclined backwards at approximately 50° at the tip. The hub-to-shroud depth at the tip, diffuser inlet, was about 1 mm, and the axial tip clearance was $76 \mu\text{m}$. At design point flow rate of 2.38 g/s, a work input coefficient ($Vt_{\text{tip}}/U_{\text{tip}}$) of about 0.7 was utilized so that the impeller would have enough pressure rise to produce a stage pressure ratio of 3.0 and efficiency of 65%. Loss estimates used in the preliminary design included low Reynolds number effects plus a tip clearance leakage loss of 4%.

Downstream of the impeller, a thin-vaned, radial flow diffuser, preceded by a short vaneless space, was designed for use in the actual engine. In the study presented here, a vaneless diffuser (1 mm deep with a radius ratio of 2:1) ahead of an exit dump chamber was used for the experiments and for the computational fluid dynamics (CFD) which were intended to explore the performance of the impeller.

Many technical hurdles remain in the design of the final power plant. For example, the type of bearings is a major issue. Air journal and thrust bearings were employed in the 4 mm diameter rotors of the 10 Watt micro gas turbine generator developed at the MIT Gas Turbine Laboratory, [2]. They were also used in the 10 mm rotors of the 100 Watt engine design by IHI and Tohoku University, [3]. Modern developments in ball bearings for high speeds and small sizes, such as those used in air turbines for dental drills, may also offer an option. For our work, we employed ball bearings for the compressor impellers which were tested up to 420,000 rpm (260 m/s tip speed). In separate tests in a special, small bearing test stand which utilized a 5 mm diameter air turbine, stable runs at 830,000 rpm were achieved. This paper concentrates on the design and manufacturing of the turbine/

Contributed by the International Gas Turbine Institute (IGTI) of THE AMERICAN SOCIETY OF MECHANICAL ENGINEERS for publication in the ASME JOURNAL OF ENGINEERING FOR GAS TURBINES AND POWER. Paper presented at the International Gas Turbine and Aeroengine Congress and Exhibition, Atlanta, GA, June 16–19, 2003, Paper No. 2003-GT-38933. Manuscript received by IGTI, October 2002, final revision, March 2003. Associate Editor: H. R. Simmons.

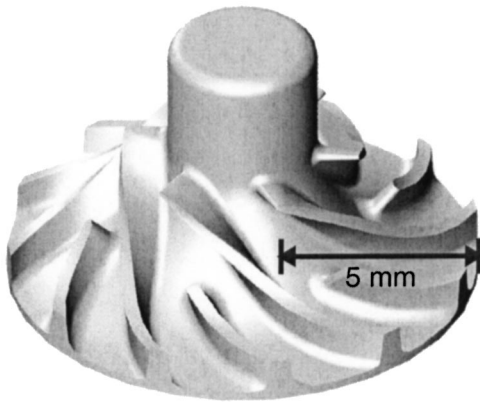


Fig. 1 CAD model of compressor

compressor/shaft assembly, and the evaluation of the compressor impeller performance by both experiment and from the results of CFD.

Some Design and Aerodynamic Performance Issues Related to Compressor and Turbine Size. Low Reynolds number, surface roughness, tip clearances, and minimum feature size are all important issues when one considers the design and performance of any miniaturized turbomachine. All four items can lead to reduced levels of performance, and thus require some discussion. Some guidance is found in the literature, [4], concerning Reynolds number and surface roughness effects. Also, some very useful information may be obtained from papers on an earlier microcompressor (4 mm diameter at 500 m/s tip speed) even though the radial flow path is unusual: flat and two-dimensional, [2,5].

Scaling of efficiency for shrouded, radial flow compressor impellers, typical of narrow industrial compressor stages, was established, [4]. He used a Reynolds number based on tip speed, U_{tip} ; blade height at the tip, b_{tip} ; and kinematic viscosity at impeller inlet, which is $1.5 \times 10^{-5} \text{ m}^2/\text{s}$ for air at room temperature and atmospheric pressure in the cases considered here. The method appears to work well when the flow through the impeller blade passages approximates turbulent flow in smooth and rough ducts.

The scale ratio is about 25:1 between this case, where $b_{tip} = 1 \text{ mm}$, and a large scale, geometrically similar, high Reynolds number impeller where b_{tip} is approximately 25 mm. When Casey's scaling method is applied to impellers with tip speeds of 500 m/s, a reduction in stage efficiency by 11% is obtained for hydraulically smooth surfaces. If the surface roughness height is $1 \mu\text{m}$, an additional three points is lost.

It is noted that the Reynolds number for the small impeller is 3.35×10^4 , which indicates that the flow in the impeller is turbulent, not laminar as it would be if the size were reduced by another factor of 10. The losses would increase catastrophically if the flow were laminar, [5], and one may justifiably conclude that an impeller with a diameter of 1 to 2 mm may represent a lower limit, if efficiency is an important design criterion as it is here.

The current impeller does not have a rotating shroud like the impellers investigated by Casey. Here, there is no shroud cover, but an open clearance over the blade tips which is approximately 10% of the blade height, b_{tip} . Thus the losses predicted above are not going to be better than rough estimates. Probably, the friction losses will be smaller, but there may be an additional loss due to leakage over the blade tips, which should increase as the clearance increases. This added loss, which is assumed to be independent of scale, was originally estimated to be four points in addition to other losses. Adding all losses together and assuming the design point efficiency of the micro compressor is 65% says that a stage which is 25 times larger should have an efficiency of 83%, a value

in the expected range for this type of radial flow compressor. An attempt was made to determine the effects of change of axial clearance in the experimental program.

Finally, the effects of minimum feature size need to be discussed. Here, 0.3 mm (30% of b_{tip}) was chosen as the blade thickness and the blade leading edges were not sharp as is the case in large high Mach number compressors of similar geometric shape. These effects will tend to increase blockage at both blade leading edges (inducer region) and at the trailing edges. There is currently no way to accurately estimate the added losses and separate them from the flow distribution (thicker boundary layers) blockage due to low Reynolds numbers. Blockage has several effects: (a) It reduces the flow area compared to the available geometric area and thus limits the through flow. This effect may be accounted for in design by an increase in dimensions such as b_2 when a particular mass flow rate is required. (b) Blocked area represents flow distortion which, compared to uniform flow, increases the mass-flow-average kinetic energy leaving the impeller. The downstream diffuser must cope with this non-uniformity as it reduces the kinetic energy and recovers it as static pressure rise. It is well known that increase of inlet blockage (flow distortion) leads to decrease in diffuser pressure recovery and consequently a loss in stage efficiency. In any case, the relatively large minimum feature size in the microscale compressor impeller is expected to have a negative influence on efficiency.

Microscale Ceramic Components and Their Fabrication

Ceramics, especially silicon nitride, can have exceptional high temperature strength properties in a material of low density which makes them attractive for gas turbine applications where highly stressed turbines and other components must survive in contact with very hot gasses. In large turbines, vanes and blades are large enough to be manufactured with internal and film cooling which allows high temperature metals to be used in most cases. However, in the case of microscale turbines (diameter $< 100 \mu\text{m}$), the limits of scale preclude active blade cooling, and thus the blades must be solid which makes ceramics desirable, if they can be produced.

Two major issues have blocked application of ceramics to gas turbines, rotors in particular. The first is reliability and second is the lack of the shaping techniques. This project was able to avoid the reliability issue by noticing the increased reliability of the small sized ceramic components. The second issue has been overcome by the use of Mold SDM process with the application of gelcasting.

Reliability of Ceramic Components in Microscale Gas Turbine Engines. The reliability issue is rooted on the brittle nature of the material. Figure 2 illustrates two characteristics of the fracture behavior of ceramic specimen under identical loading conditions. First, failure is sudden and complete, which is different

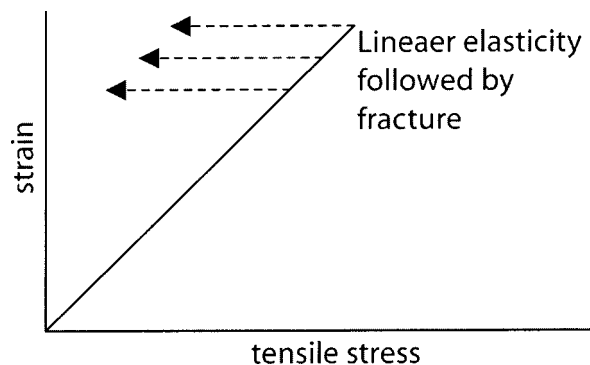


Fig. 2 Fracture behavior of ceramic specimens under the identical loading conditions

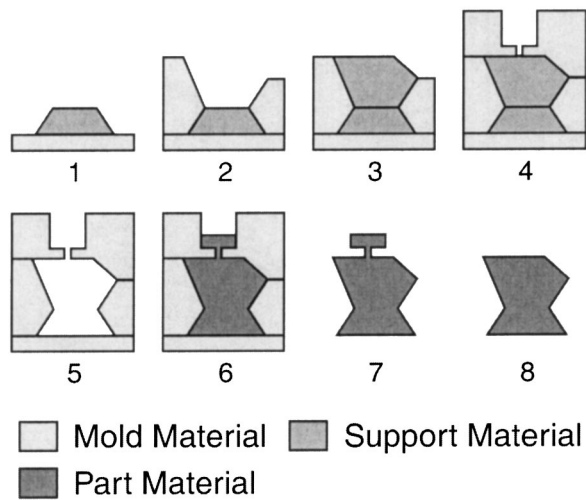


Fig. 3 Mold SDM process build sequence example

from metal. Second, the maximum strength of each sample varies significantly in nominally identical specimens where Young's modulus is nearly constant. This characteristic, among others, points to flaws as the source of failure. Considering the brittle (sudden) failure mode, the biggest flaw contained in a specimen is responsible for the failure of the whole part.

Since the pore sizes follow a particular distribution, the size of the largest flaw tends to increase as the volume of the specimen increases under the same material and process condition. This property, accounted for in Weibull statistics, results in Eq. (1). Here, V is the volume of the part of interest. The argument, m , of the function $f(m)$ is a parameter referred to as the Weibull modulus. σ_0 is a characteristic stress value for fracture obtained by a statistical treatment, [6]. The actual form of $f(m)$ varies according to the loading conditions. For example, $f(m) = 2(m+1)^2$ for three-point bending and $f(m) = 2(m+1)$ for four-point bending. In the actual design of a ceramic part, Eq. (1) is used to calculate the allowable stress σ_{max} so that the part can have survival probability of P_s .

$$P_s = \exp \left[- \left(\frac{\sigma_{max}}{\sigma_0} \right)^m \frac{V}{f(m)} \right] \quad (1)$$

Since the argument of the exponential is negative, decreasing V (smaller volume) increases the P_s . A Taylor expansion of P_s around $P_s=1$ shows that the failure probability P_f , which is defined as $P_f = 1 - P_s$, is proportional to V . This suggests that the smaller the ceramic part, the more reliable, [1].

Mold SDM Process. The mold SDM process, a derivative of shape deposition manufacturing (SDM), [7], combined with gelcasting one has the capability to fabricate silicon nitride components with full three-dimensional geometry containing features (e.g., blades) as small as $200 \mu\text{m}$. It is even possible to achieve a complex monolithic geometry in a single part that is not possible with the conventional ceramic processes such as injection molding and green machining.

In the mold SDM process, the fugitive mold of the final geometry is fabricated by SDM. SDM combines a material addition and material removal process to achieve both shape complexity and superior surface finish compared to the other rapid prototyping processes such as three-dimensional printing (3DP), stereolithography (SLA), selective laser sintering (SLS), and fused deposition manufacturing (FDM). Superior surface finish is particularly important in the fabrication of ceramic components since the strength of ceramic parts is highly sensitive to the surface smoothness due to the brittleness of ceramics.

Table 1 The average strength values of Mold SDM silicon nitride measured in four point bending at room temperature, [8]

| Material | Strength (MPa) |
|------------------------------------|----------------|
| Si3N4 unpolished | 414 |
| Si3N4 polished | 950 |
| Si3N4 pressure sintering, polished | 983 |

Gelcasting is a ceramic forming process developed by Oak Ridge National Laboratory and is compatible with mold SDM. Gelcasting slurry is a mixture of ceramic powder, monomers (chain former and branch former) and solvent. Usually, gelcasting slurries have low viscosity. Right before casting, an initiator system (a set of chemicals that initiates and propagates polymerization) is added. Then, the chain former and branch former contained in the slurry are transformed into polymer chains, which hold the ceramic particles in position and gives strength to the green part which is eventually sintered at high temperature to become the final, strong ceramic part.

Steps 1 to 4 of Fig. 3 show the mold fabrication using SDM process. The mold and support materials are deposited by casting and shaped by machining. Since all the surfaces are directly shaped by machining or replicated from the machined surfaces, all the final geometry has the characteristic surface quality, which is about $1 \mu\text{m}$ RMS. Machinable waxes are used for the mold material and Aqua-Sol soldermask (Advanced Ceramics Research, Tucson, AZ) is used for the support material. Since the soldermask is UV curable liquid, it can be deposited into any shape. The solidified soldermask is dissolved in water leaving the cavity for the final geometry, as shown in step 5.

Silicon nitride gelcasting slurry is cast into the mold and cured (step 6) at an elevated temperature. Then follows the removal of the wax mold (step 7) by melting and removal of the casting features (step 8) completes the green part. The green part goes through ceramic processing such as drying (evaporation of the solvent) and removal of polymer chains and, finally, sintering at high temperature. During the sintering, the part densifies and obtains its full strength.

Properties of Mold SDM Silicon Nitride. The strength of sintered ceramic components without any finishing (as-sintered strength) is smaller than that of the ground parts. The maximum strength of the sintered parts is achieved by grinding surface (polished strength) since it removes the surface layer and rough surfaces. Grinding, however, is not applicable to the Mold SDM ceramic parts due to their shape complexity. Thus, the as sintered strength, rather than the polished strength is more important to the Mold SDM ceramic parts. The Mold SDM silicon nitride specimens show mean strength higher than 400 MPa as long as the machined scallop height of the mold is under $5 \mu\text{m}$, [8]. The test sample size was $3 \times 4 \times 45 \text{ mm}$ and the silicon nitride composition was $8.6\text{Y}_2\text{O}_3 - 3\text{Al}_2\text{O}_3 - 88.4\text{Si}_3\text{N}_4$. (See Table 1.)

Verification of the Design by CFD and Experimental Methods

The aerodynamic performance of a compressor in a rotor group was "tested" by two independent methods; (i) by direct measurements in a specially designed test facility, and (ii) by CFD analysis. The performance objective was to determine if the pressure ratio and efficiency at the design flow rate satisfied the requirements for ultimate, successful application in the gas turbine.

Test Facility and Procedures. The general goal was to verify the functionality of the compressor impeller at the highest possible rotor speed. No attempt was made to model the vaned diffuser planned for the gas turbine itself. The shaft of the rotor group fabricated with the Mold SDM process was mounted on two miniature ball bearings (3.175 mm ID) in an overhung posi-

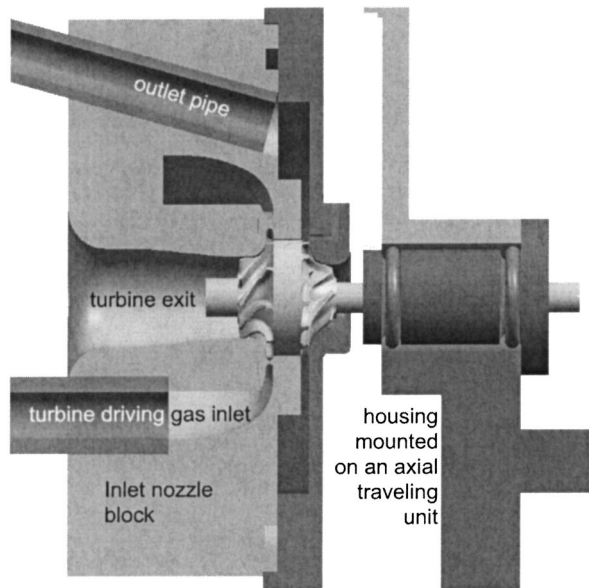


Fig. 4 Cross section of inlet nozzle block, rotor group, bearings, and mounting unit

tion. The bearings were then mounted in a cartridge, held in an axial traversing unit that was actuated by a micrometer. Thus, the rotor group could be moved along the axis to vary the axial clearance between the blades and the fixed aluminum shroud, which also formed one wall of the radial vaneless diffuser. The opposite side of the diffuser and a downstream flow collection chamber were integral with a turbine inlet nozzle block, which included the turbine shroud and exit duct. This complex part was fabricated in Ciba TDT 205-3 polyurethane by the SDM method, see Fig. 4.

Flow entered the compressor impeller through a smooth bell mouth in the shroud wall. The four outlet pipes (only one shown above) from the collection chamber, downstream of the vaneless diffuser, were connected to a common tube. This tube passed into a flow meter (Sierra Instruments: Top-Trak 280 series, 0-150 SLPM) and a flow control valve which acted as throttle before the compressed air discharged to the atmosphere. Uncertainty of the flow measurement was ± 0.05 g/s.

The turbine was driven by compressed, room temperature nitrogen supplied through four tubes inserted into a plenum chamber in the inlet nozzle block (only one shown in Fig. 4). The turbine exit was to the atmosphere through a diffusing duct. Rotor speeds up to 500,000 rpm could be obtained with this system. Thus, testing at the design speed of 800,000 rpm was not feasible.

Rotational speed, N , was measured by a Fourier analysis of light reflected from one end of the shaft. The light was converted by an Optiphase Model V500 analog receiver. A National Instrument data acquisition board (PCI-MIO-16E-4) installed in a PC received the signal and the frequency was obtained by Fourier transformation performed with LabView software. Control of N to an accuracy of $\pm 1,200$ rpm was provided by regulation of the nitrogen pressure entering the turbine.

The densification of the silicon nitride during the sintering process is accompanied by linear shrinkage $19 \pm 1\%$ in this case). This shrinkage is accounted for in the design before the molds are made. To satisfy final accuracy requirements, certain surfaces such as turbine and compressor blade-shroud-contour profiles, the outer tip diameter and the shaft of the rotor were ground to fine tolerances. The ground rotor was mounted on two bearings (hidden inside the cartridge) as shown in Fig. 5. The rotor blades are

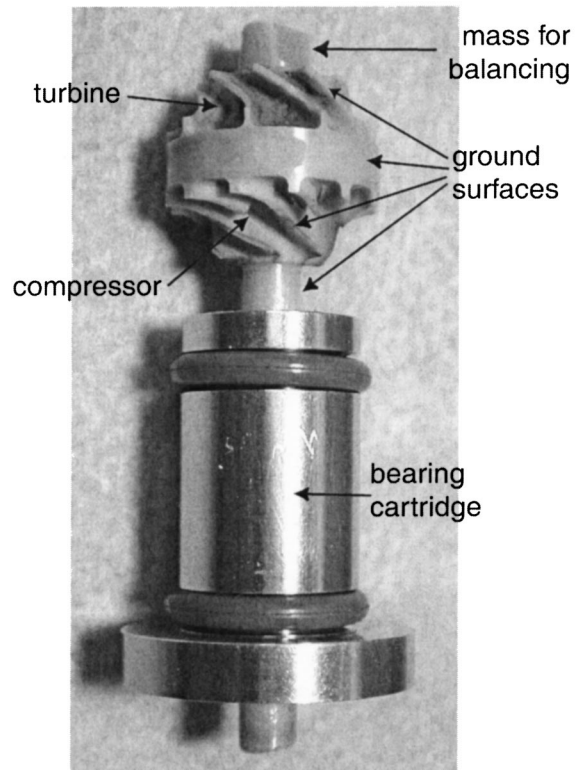


Fig. 5 Rotor group mounted on ball bearings

much thicker compared to their span compared to those on larger rotors. No noticeable sagging of blades during sintering was observed.

The finite element analysis of the rotor at 800,000 rpm predicted that the maximum stress of 290 MPa will occur at the root of the compressor blade near the exducer. In this study, the life prediction using probabilistic code was not performed. Further investigation such as strength measurement at operating temperature is required to ensure a life time of rotor.

The rotor was balanced while mounted on the bearings to a residual unbalance of 0.003 g-mm static, 0.003 g-mm dynamic at 1500 rpm. A combination of minute errors in rig machining and assembly combined with rotor vibrations when the rotor spins at high speed caused the speed limit of the rig to be 420,000 rpm to avoid short term mechanical failure. Since the test speed is only about a half of the design speed and the average strength value is higher than the predicted maximum value at design speed, proof tests were omitted.

Performance of this compressor rotor was therefore determined at a speed of 420,000 rpm by measuring the pressures and temperatures at inlet and exit versus the mass flow rate, and by comparison to the results obtained by CFD. The small scale of the apparatus didn't permit detailed examination of the flow field leaving the impeller; only single point data at the exit (2) were possible. As a result, the mass flow average results obtainable from the CFD had to be compared to experimental results obtained using the assumption of one-dimensional, uniform flow at the exit (2) in the data analysis.

A cross section of the test rig is provided in Fig. 6. This drawing is roughly to scale except for the collection chamber which is larger in the actual apparatus. The turbine rotor and nozzles, to the left, are not shown, nor are the bearings, which are to the right in the Fig. 6. Atmospheric air at (1) enters the inlet bell at very low speed, from the right. The exit state (2) for the impeller is measured at $R_2 = 6.9$ mm, a radius slightly larger than the tip radius of the impeller.

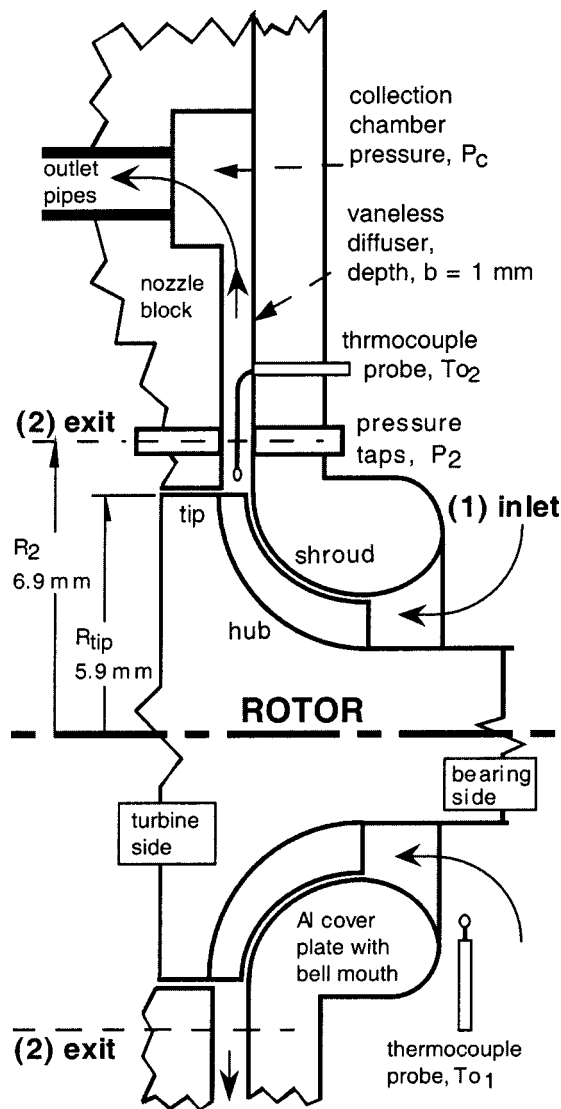


Fig. 6 Compressor rotor in test rig showing measurement stations and instruments

Four static pressures were measured: P_2 , the exit static pressure, is the average of the pressures from the two wall taps at the exit station, (2). Only small pressure differences were observed between these taps. The pressure in the collection chamber, P_c , was indicated by pressure measured upstream of the metering valve. Pressure was also recorded from a forth wall tap (not shown) installed on the shroud side at $R=6.185$ mm, but data from this tap was not considered reliable since a tap could not be installed at the same radius on the hub side. These pressures were measured to an estimated uncertainty of ± 6 kPa, on gauge pressure sensors by Omega (PX139-015D4V). Inlet pressure, P_{o1} , was taken to be 101.4 kPa, atmospheric pressure.

Temperature was measured at inlet (1) and exit (2) using type K thermocouples by Omega (5SC-TT-K-36-7-2), an ice reference and a precision multimeter. T_{o1} was obtained from a thermocouple placed near the inlet bell. At the exit station, the bare wires (0.127 mm dia.) were inserted through the a hole in the aluminum cover which forms the shroud wall, bent over in the radial direction with the junction set as close to the tip as possible, Fig. 6. Between the hole in the cover and the junction, the bare wires comprised a 3 mm long stem. This was found necessary to avoid substantial conduction cooling of the junction by the Al cover which was always at about room temperature. To avoid aerody-

dynamic interference, the radial thermocouple probe was displaced by 90° relative to the circumferential location of the two wall static taps at (2). The overall uncertainty of the measured temperatures was estimated to be $\pm 1^\circ\text{C}$. Finally, data for each run was obtained only after the thermocouple readings had stabilized.

Special consideration was needed to obtain the stagnation temperature, T_{o2} , at (2) because of the high speed of the flow (order 100 m/s) over the thermocouple probe. The raw readings were corrected by use of an aerodynamic recovery factor of 0.66 based on the tangential speed, V_t , in the location of the junction, which was very close to the tip of the impeller. The accuracy of this procedure is addressed below in the results section.

The desired final results, pressure ratio, (P_{o2}/P_{o1}), and the adiabatic efficiency, η , require the estimation of the exit stagnation pressure, P_{o2} , by application of the measured data. The assumptions are that air is a simple perfect gas, the velocity profiles at exit are uniform, and the flow fills the exit (no flow blockage). The flow speed at the inlet is nearly zero, so static and stagnation states are equal at (1).

The equations that were solved for the estimation of P_{o2} are as follows:

Conservation of mass:

$$Mg = \rho_2(2\pi R_2 b_2) V r_2. \quad (2)$$

Perfect gas equation of state:

$$\rho_2 = P_2 / (RT_2). \quad (3)$$

Euler's turbine equation work=adiabatic, steady flow energy equation work input:

$$U_{tip} V t_{tip} = Cp(T_{o2} - T_{o1}). \quad (4)$$

Definition of stagnation temperature:

$$T_{o2} = T_2 + (V t_2^2 + V r_2^2) / (2Cp). \quad (5)$$

Estimation of $V t_2$ by angular momentum conservation:

$$V t_2 = V t_{tip} (R_{tip} / R_2). \quad (6)$$

The solving these equations, after inserting the data, gives ρ_2 , T_2 , $V r_2$, $V t_{tip}$, and $V t_2$, and thus:

$$P_{o2} = P_2 \left(\frac{T_{o2}}{T_2} \right)^{k/(k-1)} \quad (7)$$

$$\eta = \frac{T_{o1}}{T_{o2} - T_{o1}} \left[\left(\frac{P_{o2}}{P_{o1}} \right)^{(k-1)/k} - 1 \right]. \quad (8)$$

Outline of the CFD Method. The CFD code used here is based on a compressible-flow, Reynolds-averaged, Navier-Stokes method developed for computation of turbine and compressor rotor flows, [9]. A low Reynolds number k - ϵ turbulence model is incorporated, and the code uses structured, nonorthogonal, body-fitted meshes. For this case, one blade-to-blade passage was divided by the splitter into two primary streamtubes, which extended from inlet to just downstream of the exit in the vaneless space. The mesh sizes for the streamtubes were $196 \times 94 \times 49$. A clearance gap of 0.1 mm (10% of b_{tip}) was incorporated in the computation. Computations were carried out at 800,000 rpm, the design condition, and at test conditions, 420,000 rpm, so that direct comparison to the experimental results would be possible. Values of the properties at the exit (2) were obtained by mass flow averaging the detailed results.

Experimental and CFD Results

Pressure ratios and temperature differences were examined for consistency, and to check that the experimental results were reasonable because of the simplifying assumptions involved in arriving at the final results from the raw data. Figure 7 shows both data and CFD results for two pressure ratios, the static pressure ratio, P_2/P_{o1} , and the stagnation pressure ratio, P_{o2}/P_{o1} , plotted

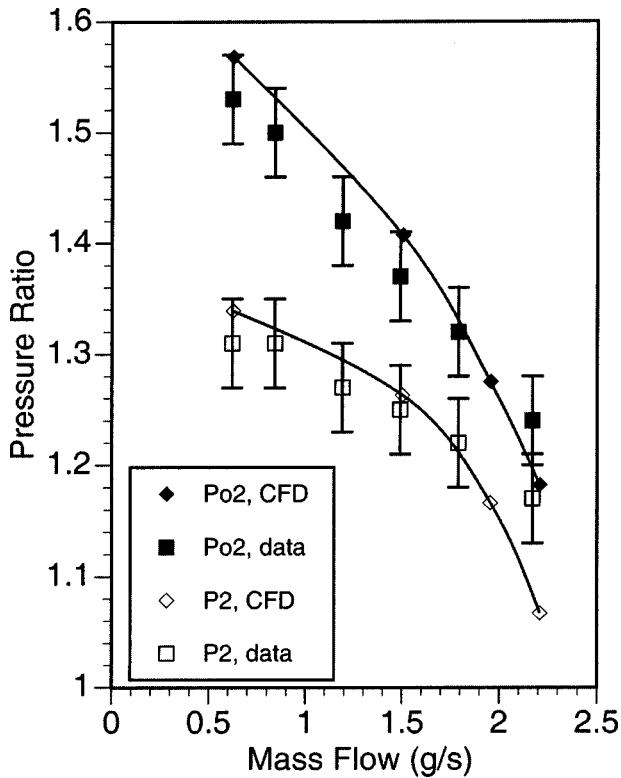


Fig. 7 Pressure ratio at 420,000 rpm

versus the mass flow rate at 420,000 rpm. The data based on the static pressure, P_2 , is independent of the temperature data, and is shown in the lower set of points (open squares). The scatter in these points is less than with an estimate of the uncertainty, [10], in the pressure ratio data, ± 0.06 . The CFD results based on P_2 , except for the point at highest flow rate, are in fairly close agreement with the measured results. The same conclusion may be drawn on comparison of the data and CFD results for P_{O_2} , the solid points and curve in the upper portion of the graph. The

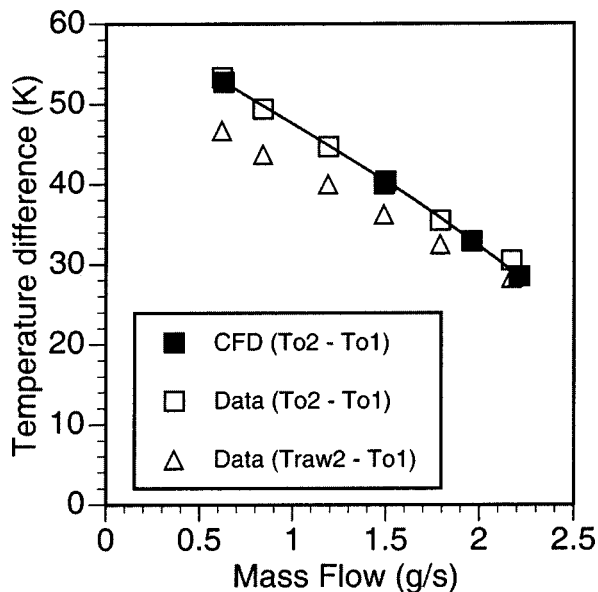


Fig. 8 Temperature rise at 420,000 rpm

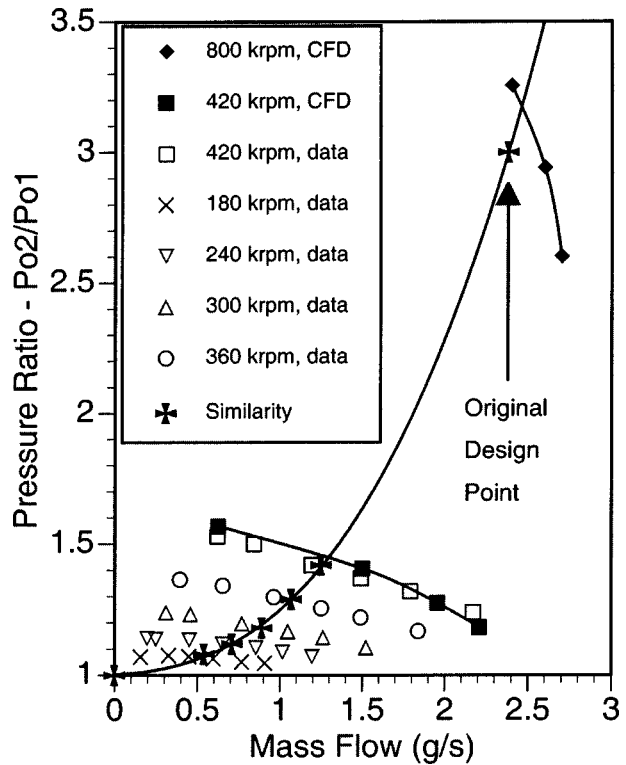


Fig. 9 Pressure ratio at various rotor speeds with a curve of flow similarity

method used to compute P_{O_2} from the raw data also appears to be reasonable, but it also may contribute a small error to final results. It can't be concluded that either result is more accurate than the other because of significant differences between the two methods. For example, surface roughness effects, accuracy of blade angle

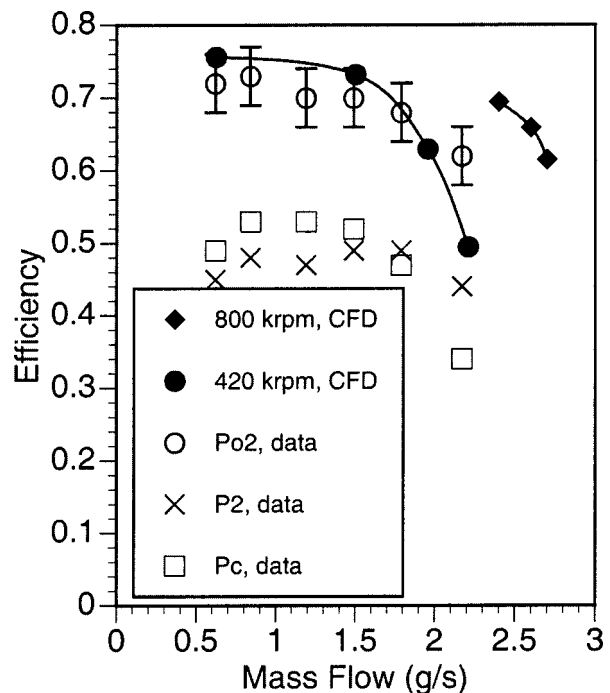


Fig. 10 Adiabatic efficiency at 800 krpm and 420 krpm based on three pressures

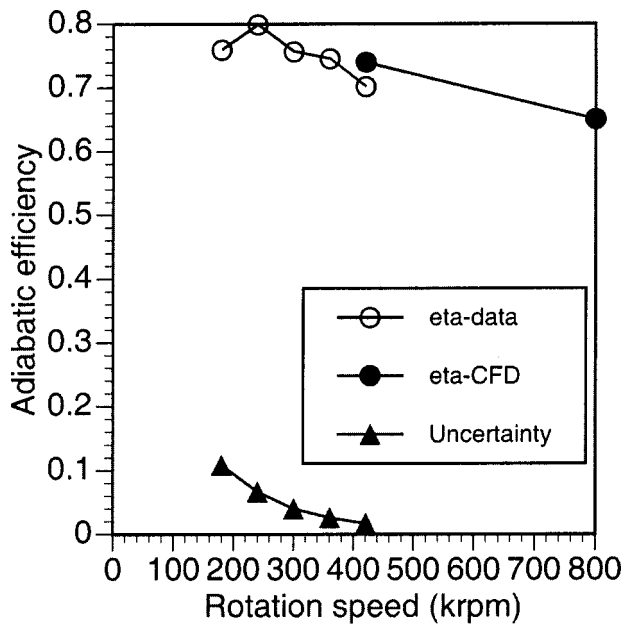


Fig. 11 Adiabatic efficiency and its uncertainty versus rotor speed along a trajectory of flow rate similitude

settings at leading edges, axial tip clearances may all lead to small differences between experimental and CFD results.

Measured temperatures at the exit (2) and inlet (1) not only enter the estimation of P_{O_2} from the raw data, but they also are needed in the calculation of the adiabatic efficiency. The temperature rise (difference) enters directly in the denominator of the efficiency and its estimated uncertainty is about $\pm 1.5^\circ\text{C}$ if proper corrections are made in the raw temperature readings. Figure 8 shows several results including probe data corrected for nonadiabatic effects. These data were very well correlated with the CFD results. $T_{\text{raw}2} - T_{O_1}$, based on direct, raw readings from the thermocouple at (2), gave low temperature rise values. Such low values led to efficiencies that were unbelievably high. Preliminary experiments with an exit thermocouple placed in the collection chamber gave even lower readings. This was thought to be the result of significant heat losses to the walls of the vaneless diffuser. Heat transfer effects can be a significant issue in a microscopic devices, [2], and this is the reason that the exit thermocouple was placed as close to the impeller tip as possible.

Scaling of the pressure ratio results between different rotor speeds, in the case of slightly compressible flow, is accomplished by use of a dimensionless parameter, the flow coefficient, which in our case looks like, $Mg/(\rho_1 R_{\text{tip}}^3 \omega)$. For our purposes the inlet density and impeller tip speed are constant so a line of similarity which scales the mass flow rate, Mg , through the design point is

$$Mg = Mg_{dp} [\omega / \omega_{dp}] \quad (9)$$

The similarity line drawn on Fig. 9 passes through the original design point at a pressure ratio of 3 and mass flow rate of 2.38 g/s for 800,000 rpm. It passes through the data for 420,000 rpm at pressure ratio of 1.42 and mass flow of 1.25 g/s. Data for a number of lower speeds are also shown on the graph. The shape of the CFD curve at design speed has a slightly different shape from the curves at 420,000 rpm. This is because compressibility is much more important in this case, and simple similarity scaling cannot be expected to be exact. In particular, at the highest flow rate, local choking effects near the blade leading edges will cause a sharper downturn in the pressure ratio and efficiency.

The adiabatic efficiencies for 800,000 rpm and 420,000 rpm are compared in Fig. 10. At the test conditions, the measured efficiency is about 0.04 points lower than the CFD results around the

design point similarity flow rate of 1.25 g/s. This could be significant even accounting for the estimated uncertainty. At high flow rate, the CFD result drops to lower values than is suggested by the data. Reasons for this are not known.

Two other sets of data were used in the calculation of the efficiency for 420,000 rpm to illustrate the need for an effective diffuser design. The first is based on the measured static pressure ratio, (P_2/P_{O_2}) , at the exit station, and the second on the pressure ratio from the downstream collection chamber (P_c/P_{O_1}) . Both these results show adiabatic efficiencies that are 0.24 and 0.18 points lower than the total-to-total (P_{O_2}/P_{O_1}) efficiency. To reduce the significant diffuser losses implied here, a very effective vane diffuser design will be required for the actual compressor stage, not a simple vaneless space, [5].

The efficiency was measured for a range of speeds from 420,000 rpm down to 180,000 rpm and it was found that the efficiency, in the region of the design point, at each speed increased, down to 420,000 rpm. Figure 11 illustrates this point and it includes the CFD results which end at the real design condition, 800,000 rpm. Also shown in the figure is the experimental uncertainty for the data. This indicates that the scatter indicated in the three low rpm points can be attributed to error in the data.

The uncertainty analysis used here, [10], gives an estimate for single sample experiments based on a 95% confidence limit. In the adiabatic efficiency, see Eq. (8), the major contributions to error are the temperature rise $T_{O_2} - T_{O_1}$ and the pressure ratio P_{O_2}/P_{O_1} . The error in temperature at (2) is the major contributor to overall error at all speeds, but more so at lower speeds. In spite of the possible errors, a decrease in efficiency with increase in speed is a trend for this compressor impeller believed to relate to the increased sensitivity of the flow to compressible flow effects as rotor speed increases.

Conclusions

An essential element of a fist-sized, micro-scale, gas turbine engine, a monolithic, silicon nitride rotor (turbine compressor shaft), has been built successfully. The functionality of the compressor was confirmed by measurement of pressure ratio and adiabatic efficiency at 420,000 rpm and various flow rates. The successful test of the rotor group at high speed indicates the usefulness of mold SDM process as the manufacturing process for the rotating components of micro gas turbine engines.

The good match of experimental and CFD results suggests that current, preliminary design methods adapted to low Reynolds number conditions and combined with CFD techniques can be used to develop a microscale gas turbine engine with full three-dimensional shaped turbine and compressor impellers. However, tests confirming predicted performance at full operating speed, 800,000 rpm in this case, are still to be desired.

With the proper development of high-speed bearing technology, and the application of mold SDM process for manufacture of the hot rotating elements in silicon nitride, a fist-sized microscale gas turbine engine appears to be a possibility.

Acknowledgment

We recognize Frank Holman and his team at M-Dot Aerospace in Phoenix, AZ, for their contributions in the preliminary design phases of this study. The contributions of Tibor Fabian, Tom Halser and Bernard Liu of Rapid Prototyping Laboratory at Stanford University in test rig design, assembly and rotor sintering are gratefully acknowledged. The support for ceramic processing by Atsushi Koizumi of Honda R&D Co., Ltd., is also greatly appreciated. Finally, we thank Prof. Robert Moffat of Stanford University for his analysis and suggested solution for the temperature measurement problem.

Nomenclature

b_2 = hub to shroud distance at exit station
 b_{tip} = hub to shroud distance at blade tip. Here, $b_2 = b_{tip}$.
 C_p = specific heat at constant pressure. Here,
 $C_p = 1005 \text{ (m}^2/\text{s}^2\text{-K)}$.
 k = ratio of specific heats. Here $k = 1.4$.
 Mg = mass flow rate
 N = rotating speed (rpm)
 P_c = collection chamber pressure
 P_s = probability of survival of a ceramic specimen under specified loads
 P_f = probability of failure of a ceramic specimen. Here,
 $P_f = 1 - P_s$.
 P_2 = static pressure at (2)
 P_{O1} = inlet total and static pressure. Here, 1 atm. = 101.4 kPa.
 P_{O2} = total pressure at (2)
 R = gas constant. Here, $R = 287 \text{ (N-m/kg-K)}$
 R_2 = radius of exit station (6.9 mm)
 R_{tip} = radius of the rotor at tip
 ω = rotating speed (1/sec)
 T_2 = static temperature at (2)
 T_{O1} = total temperature at (1). Range = 289 to 296 K.
 T_{O2} = total temperature at (2)
 U_{tip} = rotor tip speed: ωR_{tip}
 V_{r2} = radial flow speed at (2)
 V_{t2} = tangential flow speed at (2)
 $V_{t_{tip}}$ = tangential flow speed at tip

η = adiabatic efficiency, see Eq. (8)
 ρ_2 = static density at (2)
 σ_{max} = maximum stress

References

- [1] Kang, S., 2002, "Fabrication of Ceramic Components for a Micro Gas Turbine Engine," Ph.D. thesis, Stanford University, Stanford, CA.
- [2] Epstein, A. H. et al., 2000, "Shirtbutton-Sized Gas Turbines: The Engineering Challenges of Micro High Speed Rotating Machinery," Proceedings, 8th Int'l Symposium on Transport Phenomena and Dynamics of Rotating Machinery, Honolulu, HI.
- [3] Isomura, K. et al., 2002, "Design of a Micromachined Gas Turbine With 3-Dimensional Impeller," Proceedings, The 9th of International Symposium on Transport Phenomena and Dynamics of Rotating Machinery, Honolulu, HI.
- [4] Casey, M. V., 1985, "The Effects of Reynolds Number on the Efficiency of Centrifugal Compressor Stages," ASME J. Eng. Gas Turbines Power, **107**, pp. 541–548.
- [5] Jacobson, S. A., 1998, "Aerothermal Challenges in the Design of a Microfabricated Gas Turbine Engine," Proceedings, 29th AIAA fluid Dynamics Conference, Albuquerque, NM.
- [6] Wachtman, J. B., 1996, *Mechanical Properties of Ceramics*, John Wiley & Sons, New York.
- [7] Cooper, A. G. et al., 1999, "Automated Fabrication of Complex Molded Parts Using Mold Shape Deposition Manufacturing," Mater. Des., **20(2/3)**, pp. 83–89.
- [8] Stampfl, J. et al., 2002, "Rapid Prototyping and Manufacturing by Gelcasting of Metallic and Ceramic Slurries," Mater. Sci. Eng., A, **334**, pp. 187–192.
- [9] Arima, T. et al., 1999, "A Numerical Investigation of Transonic Axial Compressor Rotor Flow Using a Low Reynolds Number k - ϵ Turbulence Model," ASME J. Eng. Gas Turbines Power, **121**, pp. 45–58.
- [10] Kline, S. J., and McClintock, F., 1953, "Describing Uncertainties in Single Sample Experiments," Mech. Eng. (Am. Soc. Mech. Eng.), pp. 3–8.

On the Control of Synchronous Vibration in Rotor/Magnetic Bearing Systems Involving Auxiliary Bearing Contact

P. S. Keogh

M. O. T. Cole

M. N. Sahinkaya

C. R. Burrows

Department of Mechanical Engineering,
Faculty of Engineering and Design,
University of Bath,
Bath BA2 7AY, UK

During the normal operation of rotor/magnetic bearing systems, contacts with auxiliary bearings or bushes are avoided. However, auxiliary bearings are required under abnormal conditions and in malfunction situations to prevent contact between the rotor and stator laminations. Studies in the open literature deal largely with rotor drop and the requirements of auxiliary bearings design parameters for safe rundown. Rotor drop occurs when the rotor is delevitated and no further means of magnetic bearing control is available. This paper considers the case when full control is still available and rotor/auxiliary bearing contact has been induced by an abnormal operating condition or a temporary fault. It is demonstrated that events leading to contact from a linearly stable rotor orbit can drive the rotor into a nonlinear vibratory motion involving persistent contacts. Furthermore, the phase of the measured vibration response may be changed to such an extent that synchronous controllers designed to minimize rotor vibration amplitudes will worsen the rotor response, resulting in higher contact forces. A modified controller design is proposed and demonstrated to be capable of returning a rotor from a contacting to a noncontacting state. [DOI: 10.1115/1.1689362]

Introduction

It is common practice in rotor/magnetic bearing systems to incorporate auxiliary bearings that prevent damage to the rotor and stator laminations. In many applications the auxiliary bearings consist of simple bushes or rolling element bearings. Foil bearings (Heshmat [1]) offer an alternative compliant landing system. Another novel design has been proposed by Chen, et al. [2] in which the rotor runs with a nominal clearance. When a rotor drop occurs a system of rollers closes in and recenters the rotor.

Most of the work in the open literature has dealt with the rotor dynamics following a drop condition of the rotor. Essentially all control capability associated with the magnetic bearings is considered to no longer exist. Early studies from Johnson [3] and Black [4] considered the use of receptance techniques to analyze behavior. Subsynchronous vibrations induced by rotor/stator clearance were investigated by Childs [5], Muszynska [6], and Ehrich [7]. Kim and Noah [8] established bifurcation boundaries for the onset of possible chaotic rotor motion. Further developments in this area have been covered by Wang and Noah [9] and Gonsalves et al. [10].

A number of experimental studies have been directed specifically towards auxiliary bearings in magnetic bearing applications. Fumagalli, et al. [11] and Fumagalli and Schweitzer [12] present measured rotor vibration and contact forces. Papers by Kirk et al. [13,14] and Schmied and Pradetto [15] consider the interaction of realistic turbomachinery rotors with auxiliary bearings and investigate the influential parameters on the system dynamics following rotor drop. A primary concern is the selection of auxiliary bearings that inhibit the onset of damaging backward whirl. The work of Flowers, et al. [16–18] focuses on the synchronous dynamics to establish system parameters that may be varied to reduce shaft vibration.

To date, there is a lack of published work relating to rotor/auxiliary bearing contact when magnetic bearings still possess control capability. It can be envisaged that a transient event may lead to the rotor making repeated contacts with one or more auxiliary bearings. The question that arises is whether existing control strategies will alleviate this situation or induce even harder contacts. This paper presents an investigation into the use of synchronous harmonic controllers that are designed to minimize measured rotor vibration amplitudes. A rotor with residual unbalance may be driven into contact with auxiliary bearings and exhibit a synchronous whirl component if:

- it is subject to a change in direct lateral forcing (e.g. valve closure, mass loss, mass deposition),
- the system experiences sudden base motion (transport applications, seismic motions), and
- an intermittent fault leads to temporary loss of control.

There may be eventualities such as friction induced backward whirl on auxiliary bearings during which the synchronous component is dominated by higher frequency rotor vibration involving large contact forces (Kirk [14]). If this occurs the limited load capacity of magnetic bearings is likely to prevent effective vibration control. This paper focuses on the case when a sizeable synchronous vibration component is still present and it is feasible to recover control of the rotor. The main results are obtained experimentally from a flexible rotor/magnetic bearing facility. It is demonstrated that it is feasible to restore normal rotor motion within the clearance space from a persistent contacting state using a modified controller gain matrix.

Experimental Facility

The experimental flexible rotor/magnetic bearing facility is shown in Fig. 1. The rotor is horizontally mounted on two radial magnetic bearings, each capable of delivering radial forces of amplitude 1700 N at 100 Hz before roll off. The rotor shaft is 2 m long with four 10 kg disks of radii 10 cm mounted on it to provide added inertia, giving a total mass of 100 kg. The rotor is driven through a universal coupling at speeds up to 6000 rev/min. Aux-

Contributed by the International Gas Turbine Institute (IGTI) of THE AMERICAN SOCIETY OF MECHANICAL ENGINEERS for publication in the ASME JOURNAL OF ENGINEERING FOR GAS TURBINES AND POWER. Paper presented at the International Gas Turbine and Aeroengine Congress and Exhibition, Amsterdam, The Netherlands, June 3–6, 2002; Paper No. 2002-GT-30292. Manuscript received by IGTI, December 2001, final revision, March 2002. Associate Editor: E. Benvenuti.

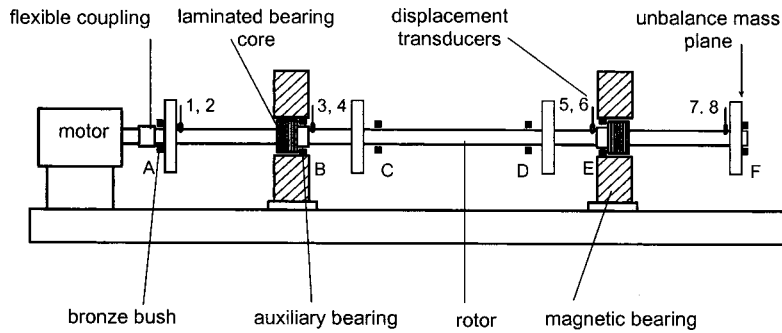


Fig. 1 Schematic layout of flexible rotor/magnetic bearing facility showing sensors (1–8), auxiliary bearings and bushes (A–F)

iliary rolling element bearings (B, E) of nominal radial clearance 0.7 mm prevent contact between the magnetic bearing and rotor laminations, which have a radial clearance of 1.2 mm. Additionally, a number of bronze bushes (A, C, D, F) of nominal radial clearance 0.8 mm are located close to the rotor disks to prevent further rotor excursions. Rotor lateral displacement could be measured using eight eddy current displacement sensors in four axial planes. Each sensor pair was arranged at ± 45 deg either side of the vertical line.

Rotor Dynamic Assessment

Under steady synchronous vibration excitation a finite element model of the rotor with linearized magnetic bearings may be represented in the form

$$-\Omega^2 \mathbf{M} \mathbf{x} + i \Omega \mathbf{C} \mathbf{x} + \mathbf{K} \mathbf{x} = \mathbf{f} + \mathbf{B}_u \mathbf{u} \quad (1)$$

where all vectors are synchronous components. Here \mathbf{f} is a disturbance vector of steady synchronous force components and \mathbf{B}_u is a matrix that distributes the synchronous control force components in \mathbf{u} to the full force vector. For the experimental system under consideration, \mathbf{u} is a four-element vector. The system matrices \mathbf{M} , \mathbf{C} , and \mathbf{K} embody the rotor dynamic characteristics and additional stiffness and damping associated with local proportional and derivative (PD) feedback at the magnetic bearings. The additional synchronous control force components in \mathbf{u} are intended to minimize synchronous vibration.

It is evident from the Appendix that the synchronous response of the rotor may be expressed in terms of system eigenvalues and eigenvectors by

$$\mathbf{x} = [\mathbf{I} \quad \mathbf{0}] \mathbf{V} (i \omega \mathbf{I} - \mathbf{\Lambda})^{-1} \mathbf{V}^{-1} \mathbf{B} (\mathbf{f} + \mathbf{B}_u \mathbf{u}). \quad (2)$$

This expresses resonant amplification that occurs close to critical speeds through terms in the diagonal matrix $(i \omega \mathbf{I} - \mathbf{\Lambda})^{-1}$. Mode shape information contained in \mathbf{V} also determines the predicted response of the rotor to the disturbance and control force components. Large rotor responses around critical speeds can be produced by relatively small disturbance forces, which may be compensated by control forces that are within the magnetic bearing capacity. Away from critical speeds, rotor excursions that cause auxiliary bearing contact may occur due to large disturbance forces and the required control forces could exceed the magnetic bearing capacity. For a rigid rotor, the magnetic bearings should be capable of compensating the unbalance forces associated with the rotor in a synchronous whirl of radius equal to the auxiliary bearing radial clearance.

The rotor considered in the present paper is flexible over the speed range 0–32 Hz. Using a finite element model with 52 degrees-of-freedom, critical speed modes were predicted at 13 Hz, 21 Hz, and 30 Hz with damping ratios of 0.18, 0.12, and 0.10, respectively. The first mode is dominantly conical whirl while the second and third involve combinations of translatory whirl and rotor bending.

Results Without Vibration Control

The rotor synchronous vibration component appropriate to a sensor measuring a displacement $y(t)$ is defined over the k th time interval by

$$q_k = \frac{1}{T} \int_{(k-1)T}^{kT} y(t) e^{-i \Omega t} dt = r_k e^{i \phi_k} \quad (3)$$

where $T = 2\pi/\Omega$. Under steady-state conditions q_k will attain a constant complex value. Initially the rotor was stabilized in levitation using standard PID control local to each magnetic bearing. The linearized magnetic bearing characteristics then corresponded to centralizing spring/damper systems of radial stiffness 1×10^6 N/m and damping 5000 Ns/m. Without additional vibration control ($\mathbf{u} = \mathbf{0}$), the rotor was slowly run up in speed with two separate unbalance masses of 260 gcm and 480 gcm, tied to the nondriven end disk. Without these masses the rotor residual vibration was relatively small. Figures 2 and 3 show the variation of synchronous vibration components from two of the sensors against running speed. These sensors were positioned in the two axial planes on the nondriven end of the rotor at 45 deg to the

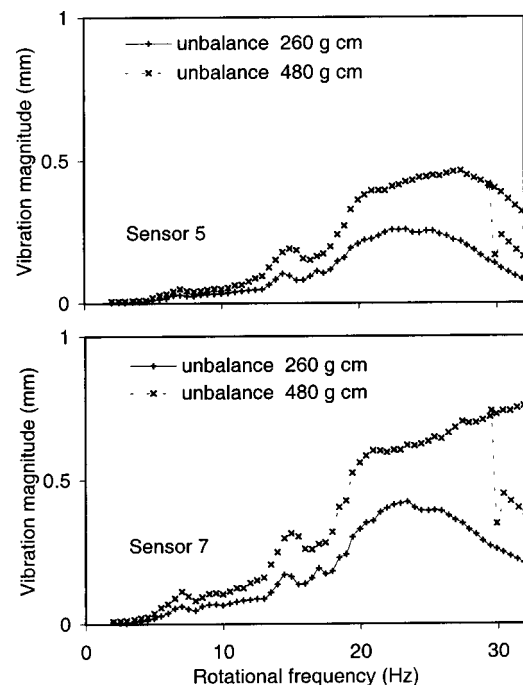


Fig. 2 Magnitudes of measured synchronous vibration components at selected sensors

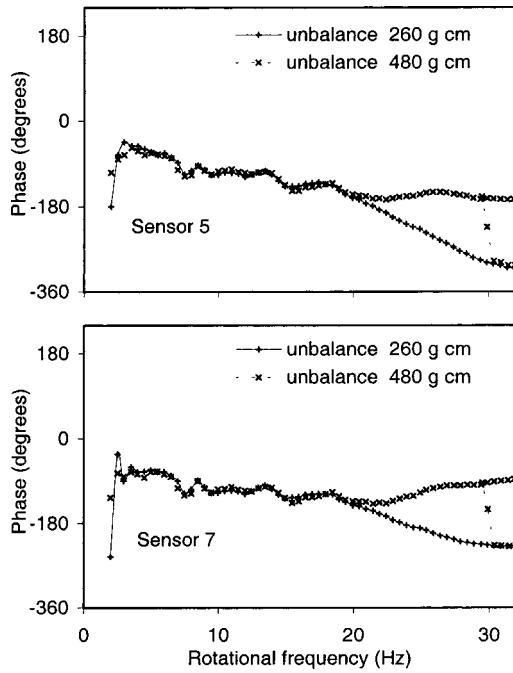


Fig. 3 Phases of measured synchronous vibration components at selected sensors

vertical. Figure 2 shows the magnitudes (r_k) and Fig. 3 shows the phases (ϕ_k) after steady state conditions had been attained.

In the case of the 260 gcm unbalance, the rotor did not make contact with any auxiliary bearing or bush. The rotor response is seen to exhibit critical speeds in the 10–32 Hz speed range, as predicted by the rotor dynamic modeling. With the 480 gcm unbalance the rotor made audible and repeated contacts with the nondriven and bronze bush at speeds above 19 Hz. This behavior was confirmed by the rotor orbit measurements. Figure 2 shows that the 480 gcm unbalance causes proportionately larger response magnitudes than the 260 gcm unbalance, though the speed associated with the onset of contacts is difficult to identify. However, this becomes clear when the phases of the synchronous components are compared. For running speeds below 19 Hz, the phases of the synchronous response components are similar, which is consistent with linear rotor dynamic behavior. However, as the rotor speed moved above 19 Hz the severity of the rotor contacts increased for the 480 gcm unbalance and the corresponding phases deviate from those obtained with the 260 gcm unbalance. This is a nonlinear effect and the phase deviation was similar for all sensors. At a running speed of 32 Hz the phase deviation is around 160 deg. As the speed was slowly increased further a point (35 Hz) was reached when the rotor returned to a steady noncontacting orbit. This was attributed to the decrease in rotor modal response on passing through the bending critical speed around 30 Hz. When the speed was slowly reduced the noncontacting orbit was maintained until, at around 30 Hz, the rotor amplitude was large enough to again cause contact with the nondriven end bush. This hysteretic effect was possible because the rotor was able to vibrate in two states involving a steady synchronous component. The noncontacting state corresponds to the usual steady unbalance response of the rotor with the magnetic bearings under PID control. In the persistent contacting state, the disturbance force \mathbf{f} of Eq. (1) is changed and includes an additional synchronous amplitude dependent term arising from the contact forces. The change in \mathbf{f} is such that stability of the larger orbit is maintained.

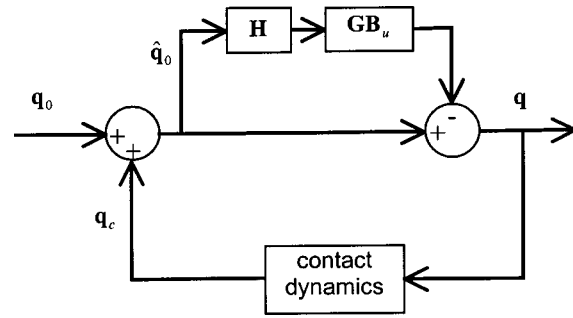


Fig. 4 System structure with contact dynamics

Vibration Control Implications

A synchronous vibration controller that is commonly applied in the open loop is now considered. Let the vector of measured steady-state synchronous vibration components be denoted by $\mathbf{q} = (q^1, \dots, q^8)^T$ where the superscript indicates the sensor number. A linear form is assumed for the system dynamics:

$$\mathbf{q} = \mathbf{G}(\Omega)(\mathbf{f} + \mathbf{B}_u \mathbf{u}) \quad (4)$$

where \mathbf{G} is a speed dependent influence coefficient matrix (Appendix). Without vibration control the measured synchronous vibration components are given by $\mathbf{q}_0 = \mathbf{G}(\Omega)\mathbf{f}$. Control forces that minimize \mathbf{q} in a least squares sense are given by $\mathbf{u} = \mathbf{u}_0$ with

$$\mathbf{u}_0 = -\mathbf{H}(\Omega)\mathbf{q}_0 \quad (5)$$

where $\mathbf{H} = ((\mathbf{G}\mathbf{B}_u)^H \mathbf{G}\mathbf{B}_u)^{-1} (\mathbf{G}\mathbf{B}_u)^H$ is the pseudo-inverse of $\mathbf{G}\mathbf{B}_u$. The minimized synchronous components are then given by

$$\mathbf{q} = (\mathbf{I} - \mathbf{G}(\Omega)\mathbf{B}_u\mathbf{H}(\Omega))\mathbf{q}_0 \quad (6)$$

The controller gain matrix \mathbf{H} may be established from on-line measurements and application of appropriate trial forces to estimate the influence coefficient matrix $\mathbf{G}\mathbf{B}_u$. Alternatively, a theoretical rotor model may be used to obtain \mathbf{H} . The controller will then minimize rotor vibration, provided that the linear system structure given by Eq. (4) does not change significantly.

If an event occurs that leads to the rotor making repeated contacts with an auxiliary bearing, the synchronous responses satisfy

$$\mathbf{q} = \mathbf{G}(\Omega)(\mathbf{f} + \mathbf{B}_c \mathbf{f}_c + \mathbf{B}_u \mathbf{u}) \quad (7)$$

where \mathbf{f}_c is a vector of synchronous components of the contact forces. In real time the contact forces will result from short duration impacts and longer duration rubs. Strictly, the synchronous components of these forces will not be steady if the rotor motion is chaotic or exhibits bifurcation. If open-loop synchronous control is attempted when the rotor is in the contacting condition the evaluated control forces will be

$$\mathbf{u} = \mathbf{u}_0 + \mathbf{u}_c \quad (8)$$

where

$$\mathbf{u}_c = -\mathbf{H}(\Omega)\mathbf{q}_c \quad (9)$$

$$\mathbf{q}_c = \mathbf{G}(\Omega)\mathbf{B}_c \mathbf{f}_c$$

The controlled synchronous response components will be given by

$$\mathbf{q} = (\mathbf{I} - \mathbf{G}(\Omega)\mathbf{B}_u\mathbf{H}(\Omega))\hat{\mathbf{q}}_0 \quad (10)$$

where $\hat{\mathbf{q}}_0 = \mathbf{q}_0 + \mathbf{q}_c$.

The control system structure with the inclusion of rotor contact dynamics is shown in Fig. 4. The feedback path introduced by the contact dynamics compromises the feedforward control path. The contact dynamics block will be nonlinear, with an overall gain determined by the physical restriction imposed by the auxiliary bearings or bushes. In view of the results presented in Figs. 2 and

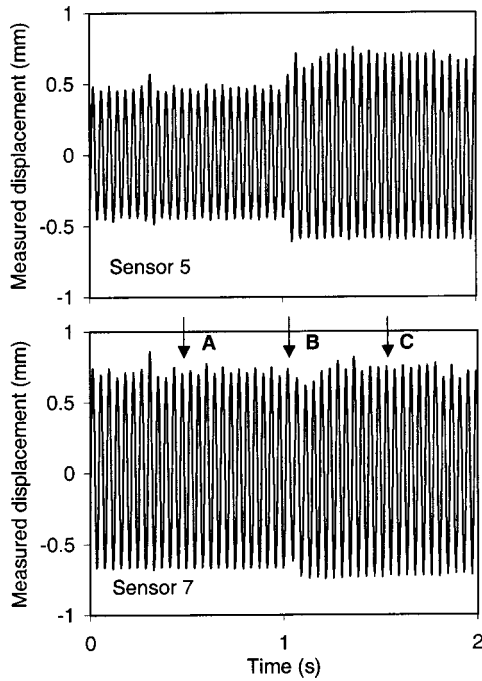


Fig. 5 Synchronous control with rotor contact (rotor speed 24 Hz, 480 gcm unbalance)

3, the main nonlinear influence will be evident through phase shifting of the measured synchronous vibration components (Eq. (9)). In fact, when the phase shifts exceed 90 deg the control forces specified by Eqs. (8) and (9) will tend to increase rotor vibration \mathbf{q} with corresponding increases in contact force levels.

Figure 5 shows experimentally the effect of attempting synchronous feedforward control when the rotor is in a persistent contacting state with the nondriven end bush indicated by F in Fig. 1. The rotor speed was 24 Hz and the 480 gcm unbalance mass was attached. The controller gain matrix \mathbf{H} was determined from the identification procedure involving trial forces applied by the magnetic bearings to the rotor in a well-balanced noncontacting state. In Fig. 5, control forces evaluated according to Eq. (8) are applied at $t=1$ s (indicated by arrow B) and seen to be ineffective. The rotor orbits at the nondriven end disk are shown in Fig. 6, before and during control force application. Changes in rotor vibration are difficult to distinguish since the levels do not change greatly in the contacting state. However, there was a significant increase in audible noise arising from the contacts following application of the control forces, which was a qualitative indication of higher contact forces.

Modified Controller Design

An advantage of using synchronous vibration controllers is that they can be designed entirely from on-line measurements. There is a range of alternative controllers that can be designed using optimally based techniques to minimize vibration levels. However, these would require a nonlinear plant model for the rotor in a contacting state, which is not presently available. The main purpose of this paper is to demonstrate that it is possible to restore a rotor from a dynamic contacting state to a noncontacting state using a modified synchronous vibration controller.

The behavior of the measured steady synchronous vibration components during an unbalance induced contacting state is evident from Figs. 2 and 3. The basic concept behind the modified controller design is to allow the control action to operate in an attenuating manner on either the contacting or noncontacting rotor

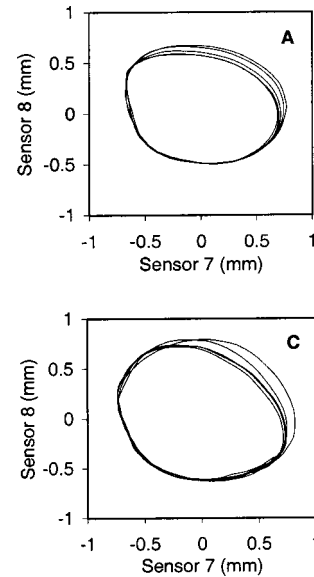


Fig. 6 Rotor orbits before and after synchronous control force application (rotor speed 24 Hz, 480 gcm unbalance)

vibration. Recall that the measured synchronous amplitudes are $\hat{\mathbf{q}}_0$ in the contacting state and \mathbf{q}_0 in the noncontacting state. For a given operating condition these are related by

$$\hat{\mathbf{q}}_0 = \mathbf{Z}\mathbf{q}_0 \quad (11)$$

where \mathbf{Z} is a complex diagonal matrix that reflects the amplitude and phase differences between the sensor measurements in the two states. The open-loop synchronous control forces required to minimize synchronous vibration should be independent of the rotor contact condition:

$$\mathbf{u} = \begin{cases} -\mathbf{H}(\Omega)\mathbf{q}_0 & \text{if noncontacting} \\ -\mathbf{H}(\Omega)\mathbf{Z}^{-1}\hat{\mathbf{q}}_0 & \text{if contacting.} \end{cases} \quad (12)$$

In practice the sensor measurements will not make any distinction between contacting or noncontacting states so let \mathbf{q}_m denote either $\hat{\mathbf{q}}_0$ or \mathbf{q}_0 as appropriate. An averaged form of Eq. (12) is

$$\mathbf{u} = -\frac{1}{2}\mathbf{H}(\Omega)(\mathbf{I} + \mathbf{Z}^{-1})\mathbf{q}_m. \quad (13)$$

These control forces will not minimize synchronous vibration, but they should attenuate synchronous vibration from either state, the controlled response being given by

$$\mathbf{q} = \left(\mathbf{I} - \frac{1}{2}\mathbf{G}(\Omega)\mathbf{B}_u\mathbf{H}(\Omega)(\mathbf{I} + \mathbf{Z}^{-1}) \right) \mathbf{q}_m \quad (14)$$

The averaged control proposed in Eq. (13) relies on identification of \mathbf{Z} for the given operating condition. This may be inferred by simulation of rotor dynamic response in a contacting state or from on-line measurements. The former is preferable for design purposes provided a validated simulation model exist. The latter may be feasible for a class of machines for which a test prototype is available.

In this paper, test results are used since the intention is to demonstrate the potential of the control procedure. The test facility is representative of a machine with an overhung disk having a bush positioned to prevent excessive rotor flexure. The results corresponding to the 480 gcm unbalance in Fig. 2 indicate that the phase change induced by contacts is relatively consistent between different sensors for a given operating condition. Let this phase change be denoted by θ . The synchronous amplitude changes induced by contact were only slightly different at each sensor and a good approximation was found to be of the form

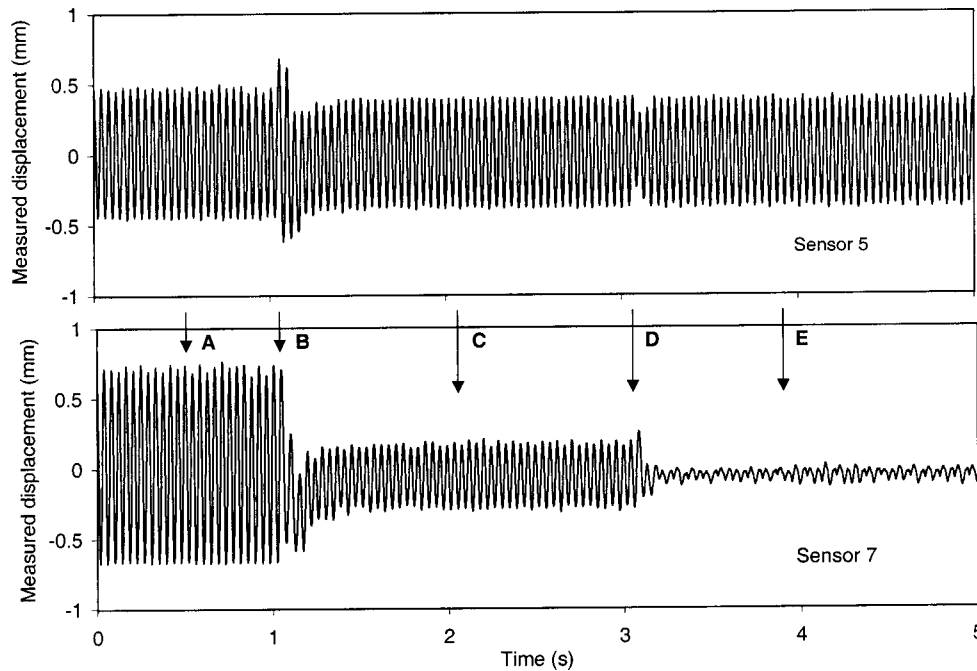


Fig. 7 Modified synchronous vibration control with rotor contact (rotor speed 24 Hz, 480 gcm unbalance)

$$\mathbf{Z} = x e^{i\theta} \mathbf{I} \quad (15)$$

where x is positive real. In deriving this equation the nominal noncontacting synchronous responses were inferred by scaling the synchronous responses due to the 260 gcm unbalance. Hence the control forces proposed in Eq. (13) reduce to

$$\mathbf{u} = -\alpha e^{i\beta} \mathbf{H}(\Omega) \mathbf{q}_m \quad (16)$$

where

$$\alpha e^{i\beta} = \frac{1}{2} (1 + x^{-1} e^{-i\theta}). \quad (17)$$

Contact could occur between the rotor and non-driven end bush with the 480 gcm disk unbalance at any speed between 19 Hz and 32 Hz (Figs. 2 and 3). A speed of 24 Hz was selected for demonstration purposes and the required controller parameters were obtained from the identification of $x = 0.57$, $\theta = 1.155$ rad:

$$\alpha = 1.17, \quad \beta = -0.753 \text{ rad.} \quad (18)$$

The results of applying the modified controller at $t = 1$ s (indicated by arrow B) are shown in Fig. 7. The controller successfully removed the rotor from the contacting state. The noncontacting orbit was then minimized, through subsequent application of the standard feedforward controller of Eq. (5) at a time indicated by arrow D. Corresponding orbit motions at selected time points (A, C, E) are shown in Fig. 8 to demonstrate the success of the procedure.

An assessment of the nondriven end magnetic bearing synchronous forces was also undertaken. For time point A, which arises purely from PID control, the total synchronous magnetic bearing force had an amplitude of 570 N. At time point C the total magnetic bearing force is a superposition of the PID and open loop synchronous components given by Eq. (16). The maximum synchronous magnetic bearing force at this time was less than 200 N, indicating that control force levels needed to be reduced to return the rotor to a noncontacting state. At time point E, when the optimal synchronous control has been applied (Eq. (5)), the maximum synchronous magnetic bearing force was reduced to be less

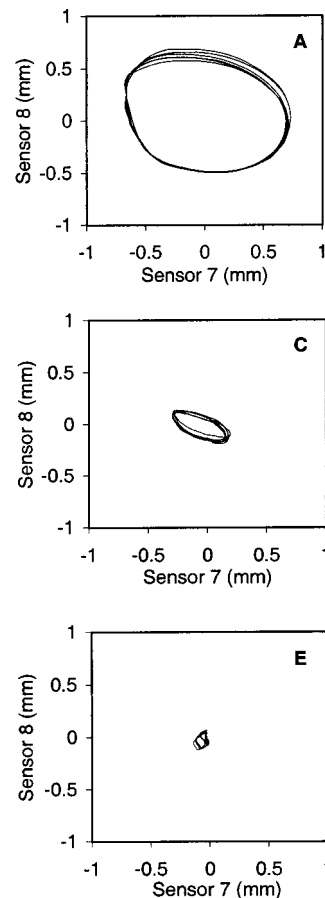


Fig. 8 Rotor orbits at selected times (see Fig. 7, rotor speed 24 Hz, 480 gcm unbalance). A—before vibration control, C—after modified synchronous vibration control, E—following final synchronous vibration control.

than 140 N. In general, control force levels will need to be increased or decreased depending on the operating speed and unbalance distributions.

These results indicate the difficulties that may be experienced if PID control alone is used to return the rotor to a noncontacting state. It could be argued that variations of PID gains can produce similar synchronous force components, but this may compromise system stability or lead to saturation problems.

Conclusions

An experimentally based investigation has been made into the dynamics and control of rotor vibration when contact with auxiliary bearings or bushes has been induced. If the vibration is forced synchronously, as in the case of unbalance, synchronous vibration components provide a useful measure of the rotor vibration. Furthermore, they also provide a means of deriving synchronous control forces in a widely used class of harmonic controller. The application of a suitably large unbalance mass showed that if the rotor is driven to make persistent contacts, significant phase changes in the measured vibration components may occur when compared to the non-contacting case. The phase shifts were similar in each sensor measurement and could be up to 180 deg at certain speeds. The implication for established controllers based on the linear noncontacting system is that application of the control forces would be ineffective and significantly worsen the rotor dynamic condition.

A modified controller was derived that was able to return the rotor from a contacting to a noncontacting state. The modified controller parameters were derived using measured data, namely amplitude and phase changes of the synchronous vibration components. In future, model based techniques could also be used to derive the controller coefficients and avoid the need to induce rotor contacts as part of the measurement process.

Acknowledgment

The authors gratefully acknowledge the support of the Engineering and Physical Sciences Research Council of the U.K. in supporting this work through grant GR/R45277/01.

Nomenclature

| | |
|---|--|
| A , B | = state space matrices (Appendix) |
| B_c , B_u | = force distribution matrices |
| C | = rotor system damping matrix |
| C_q | = transformation matrices |
| f | = vector of synchronous force components (N) |
| f_c | = vector of synchronous contact force components (N) |
| G | = influence coefficient matrix |
| H | = controller gain matrix |
| I | = identity matrix |
| K | = rotor system stiffness matrix |
| M | = rotor mass matrix |
| q_k | = complex synchronous vibration component (m) |
| q | = vector of synchronous vibration components (m) |
| \hat{q}_0 | = $q_0 + q_c$ (m) |
| q_m | = vector of measured synchronous components (m) |
| r_k | = magnitude of q_k (m) |
| t | = time variable (s) |
| T | = synchronous period ($2\pi/\Omega$) (s) |
| u | = vector of synchronous control force components (N) |
| V | = eigenvector matrix |
| w | = state vector (Appendix) |
| x | = rotor synchronous component vector |
| x | = amplitude factor |
| y | = general displacement signal (m) |
| Z | = complex diagonal matrix |
| α , β | = modified synchronous controller parameters |

| | |
|-----------|-------------------------|
| θ | = phase change (rad) |
| ϕ_k | = phase of q_k (rad) |
| Λ | = eigenvalue matrix |
| Ω | = running speed (rad/s) |

Subscripts

| | |
|---|--|
| 0 | = derived from an uncontrolled vibration state |
| c | = derived from a rotor in a contacting state |

Appendix

Equation (1) may be transformed to

$$i\Omega \mathbf{w} = \mathbf{A}\mathbf{w} + \mathbf{B}(\mathbf{f} + \mathbf{B}_u \mathbf{u}) \quad (A1)$$

where

$$\mathbf{w} = \begin{bmatrix} \mathbf{x} \\ i\Omega \mathbf{x} \end{bmatrix}, \quad \mathbf{A} = \begin{bmatrix} \mathbf{0} & \mathbf{I} \\ -\mathbf{M}^{-1}\mathbf{K} & -\mathbf{M}^{-1}\mathbf{C} \end{bmatrix}, \quad \mathbf{B} = \begin{bmatrix} \mathbf{0} \\ \mathbf{M}^{-1} \end{bmatrix}. \quad (A2)$$

Solving the eigenvalue problem for **A** yields

$$\mathbf{A}\mathbf{V} = \mathbf{V}\mathbf{\Lambda} \quad (A3)$$

where $\mathbf{\Lambda}$ is the diagonal matrix of eigenvalues and \mathbf{V} is the eigenvector matrix. It now follows from Eqs. (A1) and (A2) that

$$\mathbf{w} = \mathbf{V}(i\Omega \mathbf{I} - \mathbf{\Lambda})^{-1} \mathbf{V}^{-1} \mathbf{B}(\mathbf{f} + \mathbf{B}_u \mathbf{u}). \quad (A4)$$

If a set of displacement sensor measurements **q** coincide with particular elements of **x** they may be extracted using a suitable matrix transformation $\mathbf{q} = \mathbf{C}_q \mathbf{w}$. In other words

$$\mathbf{q} = \mathbf{G}(\Omega)(\mathbf{f} + \mathbf{B}_u \mathbf{u}) \quad (A5)$$

where

$$\mathbf{G}(\Omega) = \mathbf{C}_q \mathbf{V}(i\Omega \mathbf{I} - \mathbf{\Lambda})^{-1} \mathbf{V}^{-1} \mathbf{B}. \quad (A6)$$

References

- [1] Heshmat, H., 1991, "Analysis of Compliant Foil Bearings with Spatially Variable Stiffness," AIAA Paper No. AIAA-91-2103.
- [2] Chen, H. M., Walton, J., and Heshmat, H., 1997, "Zero Clearance Auxiliary Bearings for Magnetic Bearing Systems," ASME TURBO EXPO 97, Orlando, FL.
- [3] Johnson, D. C., 1962, "Synchronous Whirl of a Vertical Shaft Having Clearance in One Bearing," J. Mech. Eng. Sci., **4**(1), p. 85.
- [4] Black, H. F., 1968, "Interaction of a Whirling Rotor With a Vibrating Stator Across a Clearance Annulus," J. Mech. Eng. Sci., **10**(1), pp. 1–12.
- [5] Childs, D. W., 1979, "Rub Induced Parametric Excitation in Rotors," ASME J. Mech. Des., **10**, pp. 640–644.
- [6] Muszynska, A., 1984, "Partial Lateral Rotor to Stator Rubs," Paper C281/84, Proceedings, 3rd International Conference on Vibrations in Rotating Machinery, University of York, York, U.K., IMechE, London, pp. 327–335.
- [7] Ehrich, F. F., 1988, "High Order Subharmonic Response of High Speed Rotors in Bearing Clearance," ASME J. Vib., Acoust., Stress, Reliab. Des., **110**, pp. 9–16.
- [8] Kim, Y. B., and Noah, S. T., 1990, "Bifurcation Analysis for a Modified Jeffcott Rotor With Bearing Clearances," Nonlinear Dyn., **1**, pp. 221–241.
- [9] Wang, X., and Noah, S. T., 1998, "Nonlinear Dynamics of a Magnetically Supported Rotor on Safety Auxiliary Bearings," ASME J. Vib. Acoust., **120**, pp. 596–606.
- [10] Gonsalves, D. H., Neilson, R. D., and Barr, A. D. S., 1995, "A Study of the Response of a Discontinuously Nonlinear Rotor System," Nonlinear Dyn., **7**, pp. 451–470.
- [11] Fumagalli, M., Varadi, P., and Schweitzer, G., 1994, "Impact Dynamics of High Speed Rotors in Retainer Bearings and Measurement Concepts," Proceedings, 4th International Symposium on Magnetic Bearings, ETH Zurich, Zurich, Switzerland, pp. 239–244.
- [12] Fumagalli, M., and Schweitzer, G., 1996, "Measurements on a Rotor Contacting Its Housing," Paper C500/085/96, Proceedings, 6th International Conference on Vibrations in Rotating Machinery, University of Oxford, Oxford, U.K., IMechE, London, pp. 779–788.
- [13] Kirk, R. G., Swanson, E. E., Kavarana, F. H., and Wang, X., 1994, "Rotor Drop Test Stand for AMB Rotating Machinery, Part 1: Description of Test Stand and Initial Results," Proceedings, 4th International Symposium on Magnetic Bearings, ETH Zurich, Zurich, Switzerland, pp. 207–212.
- [14] Kirk, R. G., 1999, "Evaluation of AMB Turbomachinery Auxiliary Bearings," ASME J. Vib. Acoust., **121**, pp. 156–161.
- [15] Schmied, J., and Pradetto, J. C., 1992, "Behavior of a One Ton Rotor Being

Dropped into Auxiliary Bearings,” *Proceedings, 3rd International Symposium on Magnetic Bearings*, Alexandria, VA, Technomic Publishing, Lancaster, PA, pp. 145–156.

- [16] Lawen, J. L., and Flowers, G. T., 1997, “Synchronous Dynamics of a Coupled Shaft/Bearing/Housing System With Auxiliary Support from a Clearance Bearing,” *ASME J. Eng. Gas Turbines Power*, **119**, pp. 430–435.
- [17] Lawen, J. L., and Flowers, G. T., 1999, “Interaction Dynamics Between a Flexible Rotor and an Auxiliary Clearance Bearing,” *ASME J. Vibr. Acoust.*, **121**, pp. 183–189.
- [18] Xie, H., Flowers, G. T., Feng, L., and Lawrence, C., 1999, “Steady-State Dynamic Behavior of a Flexible Rotor With Auxiliary Support from a Clearance Bearing,” *ASME J. Vibr. Acoust.*, **121**, pp. 78–83.

Neural Network Emulation of a Magnetically Suspended Rotor

A. Escalante

V. Guzmán

M. Parada

L. Medina

e-mail: usb-ldm@usb.ve

S. E. Diaz

Universidad Simon Bolivar,
Decanato de Investigacion y Desarrollo,
Caracas 1080-A, Venezuela

The use of magnetic bearings in high speed/low friction applications is increasing in industry. Magnetic bearings are sophisticated electromechanical systems, and modeling magnetic bearings using standard techniques is complex and time consuming. In this work a neural network is designed and trained to emulate the operation of a complete system (magnetic bearing, PID controller, and power amplifiers). The neural network is simulated and integrated into a virtual instrument that will be used in the laboratory both as a teaching and a research tool. The main aims in this work are: (1) determining the minimum amount of artificial neurons required in the neural network to emulate the magnetic bearing system, (2) determining the more appropriate ANN training method for this application, and (3) determining the errors produced when a neural network trained to emulate system operation with a balanced rotor is used to predict system response when operating with an unbalanced rotor. The neural network is trained using as input the position data from the proximity sensors; neural network outputs are the control signals to the coil amplifiers. [DOI: 10.1115/1.1689363]

Introduction

The use of active magnetic bearings (AMB) in high-speed/low-friction applications is increasing in industry, at present in those special applications where performance is the most important design consideration and the drawbacks caused by high cost and increased complexity can be tolerated. Magnetic bearings are complex electromechanical systems in which the rotating shaft is kept suspended by an array of electromagnets. The mechanical advantages are multiples when using AMB, since there is no mechanical contact between the moving and the static parts, and hence no friction forces and no running losses. On the other hand, the electromagnetic energy conversion process is highly nonlinear and is neither self-generated nor self-regulated. An external power amplifier is required to feed current into the electromagnets, and a sensor array is necessary to measure the rotor displacement from its intended equilibrium point; this information is used by an electronic controller to dynamically adjust the force generated by the amplifier in the magnetic circuit, compensating the previously measured displacement and returning the rotor to its equilibrium point. Since the operating shaft speed and hence the required frequency response is high, the tolerable position error is small and the energy available from the electromagnets is limited to a value not much higher than the nominal maximum load, a high performance controller, one with a very fast and accurate response, and a very precise system model, are fundamental requirements.

Our group, formed by mechanical, power electronics, and control engineers from the Departments of Mechanical Engineering and Electronic and Circuits at Simon Bolivar University, is interested in improving magnetic bearing performance and reducing system complexity by working in three related areas: system modeling, actuator topology, and control strategies; efforts that are concentrated in a long-term research project that aims to the development of an artificial neural network controller for magnetic bearings.

Artificial neural networks (ANN) have recently become a very active research field with general applications in dynamic systems

identification and control, [1–3], and also in the field of magnetic bearings, [4–6]. An ANN implementation has two advantages over the standard methods:

1. The ANN-based model is developed by training the ANN network using a training algorithm and training data sets. These data sets, measured in the real system, provide the input/output information required to represent system behavior. Hence, only information that can be directly measured as system inputs and outputs is required.
2. Usually the ANN configuration is simple, requiring only a small number of artificial neurons in the network. Hence, if the ANN is implemented in hardware, the control circuitry may be simpler and smaller, less expensive and more reliable than the standard PID controllers now in use.

Training defines the weights associated with the different synaptic connections linking the artificial neurons in the network, enabling the ANN to emulate the system used to generate the training data set. This process is equivalent to the development of a mathematical description of the system, and hence can be analyzed as a problem in system identification, [7]. This is a great advantage, since it makes possible the direct application of all the fundamental results worked out in Estimation Theory to the study of ANN performance, [8–10].

Previous works, [1,11], have proved the ANN strength in modeling complex nonlinear mechanical systems, but they have not used estimation theory to analyze the obtained results.

System identification has usually been done estimating coefficients for linear models with either a least squares or maximum likelihood algorithms, [9,10], but the fundamental concept of estimation through output prediction and model validation is applicable to many problems, including ANN, [7].

In this work, system identification techniques applied to ANN were used in two different stages. First, they were used to select network inputs and to choose an optimum training data set. Afterwards, once the ANN was trained, they were used to analyze simulation performance, taking into account the effect of external elements, such as rotor load unbalance, upon the model's error prediction capability.

Two training algorithms were considered in this work: an extension of the Levenberg-Marquardt method, [12,13], applied to ANN, [14], and the back-propagation algorithm, [15]. Their efficiency was determined experimentally, comparing the results produced by two identical ANN, one trained using the extended

Contributed by the International Gas Turbine Institute (IGTI) of THE AMERICAN SOCIETY OF MECHANICAL ENGINEERS for publication in the ASME JOURNAL OF ENGINEERING FOR GAS TURBINES AND POWER. Paper presented at the International Gas Turbine and Aeroengine Congress and Exhibition, Amsterdam, The Netherlands, June 3–6, 2002; Paper No. 2002-GT-30294. Manuscript received by IGTI, December 2001, final revision, March 2002. Associate Editor: E. Benvenuti.

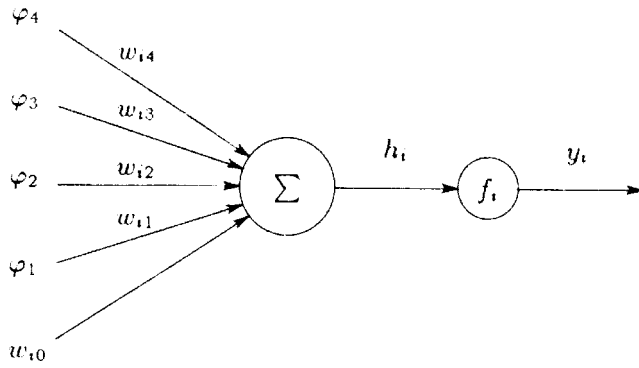


Fig. 1 Node or artificial neuron

Levenberg-Marquardt method and the other trained with the back-propagation algorithm. Both ANN were used to simulate the behavior of a magnetic bearing system when it is accelerated from rest to a set speed using a constant acceleration ramp, both with balanced and unbalanced rotor loads. After comparing the results, the extended Levenberg-Marquardt method was selected as the more efficient way to modify the network weight matrix since it produced better convergence results.

The experimental work was performed using a commercially available magnetic bearing test system, with a PID control system able to control two radial and one axial magnetic bearings. The work presented here is the initial validation test for the ANN modeling techniques, performed using the minimum setup with only one radial magnetic bearing, controlled in close loop by the PID controller. In order to keep the comparison variables to a minimum, only the input and output variables (shaft position and coil currents) used by the PID controller were considered in this initial ANN model. Since the results were good, work is continuing, the next step will be a ANN model of the basic setup operating in open loop, that is, without the PID controller. This model will then be the base from which the ANN controller will be developed.

Neural Networks Basics

A neural network is a set of basic processing units called “nodes” assembled in a highly interconnected network representing a function in an input space $I \in R^{NI}$ to an output space $Y \in R^{NY}$, where NI and NY are integers, indicating respectively the input and output space dimensions.

A node or neuron (Fig. 1) is a processing element that weights its inputs, adds them and uses the result as the argument of an output function, called “activation function.” In Fig. 1:

- w_{ij} , is the weight associated with input j .
- w_{i0} is the neuron’s polarizing weight. It can be considered as the weight applied to a pseudo-input having a fixed input value, usually 1.
- h_i is the result of the weighted sum of all the inputs.
- $f(h_i)$ is the neuron activation function.
- y_i is the neuron output, given by

$$y_i = f_i(h_i) = f_i \left[\sum_{j=1}^n (\varphi_j \cdot w_{ij} + w_{i0}) \right]. \quad (1)$$

Activation Functions. In principle, the function $f_i(h_i)$ producing the neuron output may have any arbitrary form, but the more widely used functions are: linear, hyperbolic tangent, sigmoid, and step function.

In this work the only activating functions used are the linear and the hyperbolic tangent, since all other activating functions can be derived from these two basic ones.

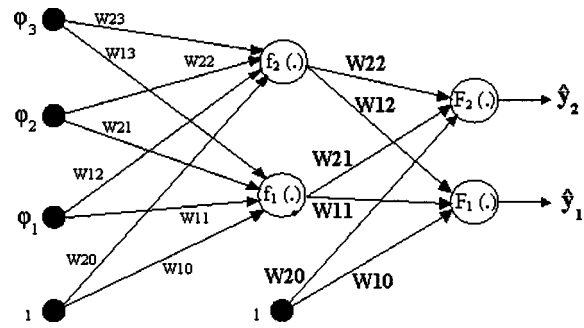


Fig. 2 The multilayer perceptron

Multilayer Perceptron (MLP). The individual neurons can be combined in many different ways called network topologies, [16].

In the basic multilayer perceptron (MLP) network topology, presented in Fig. 2, the neurons are arrayed in layers; the outputs of all neurons in one layer connect exclusively to the inputs of the neurons in the next layer, and the connection is complete, that is, all units in layer “ n ” are connected to all units in layer “ $n + 1$.”

The second layer in Fig. 2 is called the “output layer,” since the output of the unit in this layer are the network outputs. The first layer in the figure is the “hidden layer,” since the elements in this layer lay “hidden” between the network inputs (ϕ_1, ϕ_2, ϕ_3) and the network outputs. An ANN with “ n ” layers will have “ $n - 1$ ” hidden layers. The mathematical expression giving the value of any particular output in a two-layer MLP network is

$$\hat{y}_i(t) = g_i[\varphi, \theta] = F_i \left[\sum_{j=1}^{n_h} W_{i,j} f_j \left(\sum_{l=1}^{n_\varphi} w_{jl} \varphi_l + w_{j,0} \right) + W_{i,0} \right] \quad (2)$$

where θ is the “parameters vector,” containing all adjustable parameters in the network, such as synaptic connections weights and polarization values. Since polarizations can be interpreted as weights applied to constant value inputs, the term “weights” is commonly used to cover both weights and polarizations.

The multilayer perceptron (MLP), also known as the “feed-forward topology” is the more commonly used ANN, since it is capable of modeling both simple and complex relationships in a simple and easy to implement way, [15]. Due to these reasons, the MLP is the topology chosen in the present work.

System Identification With Neural Networks

The identification process aims to produce a mathematical description of the dynamic system being considered, based on a series of measurements taken from the system. Based upon previous knowledge the designer may have about the system, the identification problem may be approached in many ways. In this work, a black-box approach will be used, since it suits the ANN working characteristics and it greatly simplifies the design problem.

The Procedure. Figure 3 shows the standard system identification procedure.

Experiment. The experiment provides a data sequence describing system behavior either in all or in some part of the system operating range. In the experiment, inputs are varied and resulting output values are recorded.

The data sequence formed by paired input/output sets is represented as

$$Z^N = \{[u(t), y(t)], T = 1, \dots, N\}. \quad (3)$$

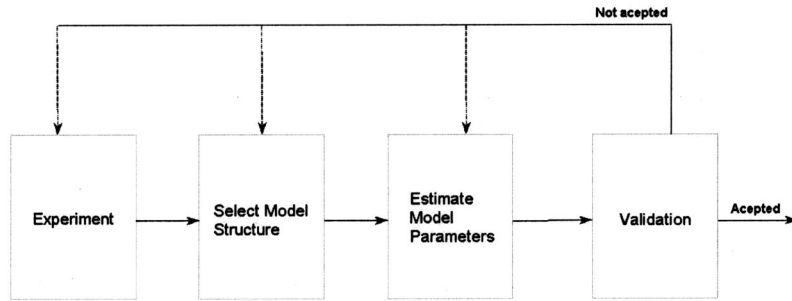


Fig. 3 System Identification procedure

These data sequences will then be used to produce a system model. If the system is unstable, it will be necessary to gather the data working in close loop, either using a feedback control system or a human operator.

Some important aspects that must be taken into account when designing the experiments are:

- sampling frequency selection,
- input signal set selection, and
- output data preprocessing, which includes such things as non-linearity testing, perturbation removal, noise filtering, etc., required to eliminate unwanted effects.

Select Model Structure. In this stage the designer follows his previous experience (or that presented in previous works) either to select a candidate model from those that are already in use, or to propose a completely new one.

In this work a nonlinear model based on multilayer perceptron is to be used, since this family of models has previously proved to be a good choice due to:

- the resulting model is a natural extension of linear model structures,
- internal network topology can be gradually expanded if required to model more complex nonlinear relationships, and
- the complexity of structural design choices is kept at a reasonable level.

The design process is adjustable to control system requirements.

Nonlinear Model Structures Based on Neural Networks. In general, as in the linear situation, the system output, $y(t)$, can be presented as

$$y(t) = g[\varphi(t, \theta)] + e(t) \quad (4)$$

and the predicted output is given by

$$\hat{y}(t|\theta) = g[\varphi(t, \theta)] \quad (5)$$

where

- $\varphi(t, \theta)$ is the regressor vector: that is, the ANN input vector,
- θ is weight vector,
- g is the neural network function, or predictor, and
- $e(t)$ is the prediction error.

The regressor vector used defines the specific type of nonlinear model implemented by the neural network, [17].

In this work the NNARX (nonlinear autoregressive, external input model) will be used to identify the model. This configuration does not have internal feedback (its regressor vector does not include any neuron output). Due to this, the predictor is stable, which is a natural requirement in the magnetic bearing application.

Figure 4 shows the NNARX Model structure. The NNARX vector regressor is

$$\varphi(t) = [y(t-1) \dots y(t-n_a) u(t-n_k) \dots u(t-n_k-n_b+1)]^T \quad (6)$$

where u and y are, respectively, the network inputs and outputs.

The associated predictor is

$$\hat{y}(t|\theta) = \hat{y}(t|t-1, \theta) = g(\varphi(t), \theta). \quad (7)$$

Estimate Model Parameters. This requires fixing all the ANN input weights. To do this, two elements must be selected:

- The criteria specifying how the weights relate with the training, and
- The training algorithm.

Formally, the training problem can be presented as follows: Given a data sequence

$$Z^N = \{[u(t), y(t)], T = 1, \dots, N\} \quad (8)$$

and a possible ANN model, training the ANN aims to achieve

$$Z^N \rightarrow \hat{\theta}. \quad (9)$$

That is, to produce a trained model whose outputs to a given input sequence are “close” to the outputs produced by the real system when the same input sequence is applied to it. Usually the “closeness” criteria applied is the one defined by means of the quadratic error:

$$V_N(\theta, Z^N) = \frac{1}{2N} \sum_{t=1}^n [y(t) - \hat{y}(t|\theta)]^2 = \frac{1}{2N} \sum_{t=1}^n \varepsilon^2(t, \theta). \quad (10)$$

The synaptic connection weights can be determined using a number of methods, [14,15]; the more used methods are

- the back-propagation algorithm and
- the Levenberg-Marquardt method.

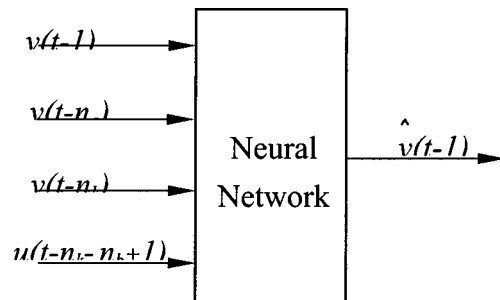


Fig. 4 NNARX model structure

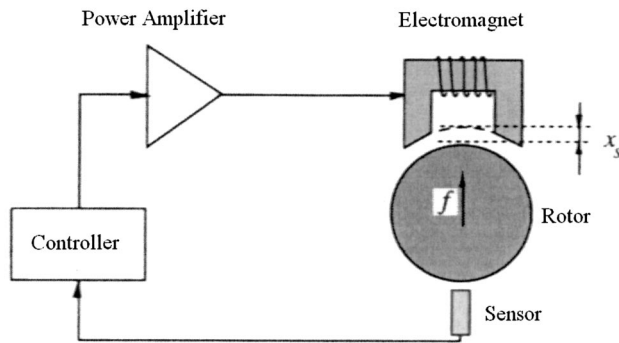


Fig. 5 Magnetic bearing working principle

Both methods were used in the present work; the results obtained proved that in this application the Levenberg-Marquardt was better.

Validation. In this stage the estimated model is tested to verify if it represents adequately the system under study, [18]. The input sets used in the validation tests must be different from those used in the training process. In principle each model should be tested according to its proposed application (simulation, prediction, control, fault prediction, etc.).

In practice a number of more or less standard tests are commonly used comparing with statistical tools how the predicted and real outputs are related, and how the outputs are related to the previous data (and with linear and non-linear combinations of the previous data). To perform a complete test of all possible data combinations will be a very long and difficult task; it is also unnecessary since adequate tests can be performed using a reduced set of auto and cross correlations carefully selected, [7,19].

The Mechanical System

Principles of Magnetic Bearing Operation. Figure 5 shows the general working principle used in basic magnetic bearing system. The rotor is kept suspended by the force generated by the magnetic circuit. A sensor measures the rotor displacement from its intended equilibrium point (x_s); this information is used by the controller to dynamically adjust the force generated by the amplifier in the magnetic circuit, compensating the previously measured displacement and returning the rotor to its equilibrium point. In practice, more than one amplifier and one magnetic circuit will be required to keep a rotating axis in place.

Experimental Setup

Figure 6 shows the experimental magnetic bearing test rig used in this work.

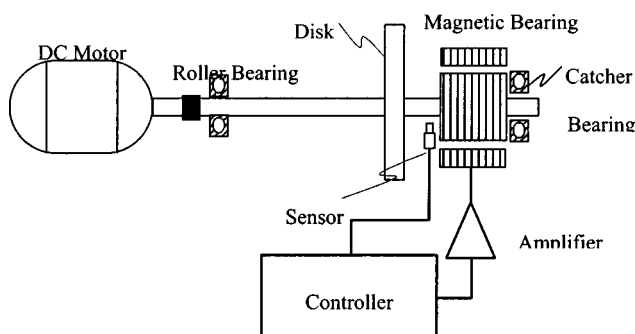


Fig. 6 Experimental setup lock diagram

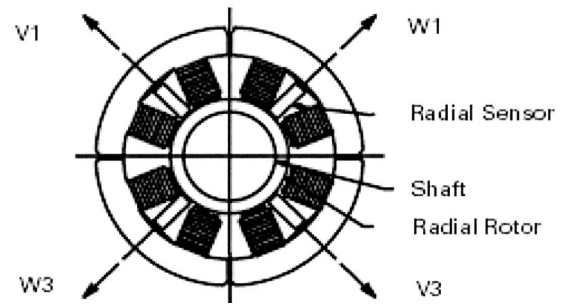


Fig. 7 w and v-axis identification

To simplify the problem at this stage, only one magnetic bearing was included; the 12" shaft was supported at one end by a magnetic bearing and at the other by a conventional ball bearing. Work is being done to extend the model, including a second magnetic radial bearing to fully support the axis, and one axial bearing at the shaft end, to limit longitudinal displacements.

Load unbalance can be included by adding masses to the inertia disk. Both balanced and unbalanced tests were performed using the system.

Figure 7 shows in schematic form the array of sensors and magnetic coils used in the magnetic bearing. The control system considers two perpendicular axis, W and V that are 45 deg displaced from the vertical. Two position sensors and four actuator windings are used in relation with each axis.

Figure 8 shows one of the two identical control loops used to balance the rotor in the two axes. Basic sensor sensitivity is 100 $\mu\text{m/volt}$.

Process Identification

The process presented in Fig. 4 was followed to produce an ANN model of the magnetic bearing system. Since this system is unstable, the data gathering was done operating the standard setup in close-loop configuration, where one PID controller is in charge of magnetic bearing regulation, and another PID controller sets DC motor speed. The neural network then simulates the complete system response (plant plus PID controller). This implies that model will be useful only to validate the ANN modeling techniques, and not in the design of a practical control system.

Data Gathering Experiment

The magnetic bearing system has two inputs and four outputs, as follows:

1. rotor position relative to the stator in the two axes (W, V): PW, PV (inputs). Note that the ANN implemented is autoregressive, using a total of three states (the current and the two previous ones) as inputs, and thus is able to internally generate the required information about the derivative displacements (velocity and or acceleration).
2. currents in the two upper actuator coils in each axis (W, V): TCW, TCV (outputs).
3. currents in the two lower actuator coils in each axis (W, V): BCW, BCV (outputs).

This set is complete, since the model should be able to predict the currents required to levitate the rotor (the four outputs) using only the rotor position (the two inputs) and the system past history (as given by the model memory).

The data sets required first to train the ANN and then to validate the model were taken from measurements in the experimental setup. The data sets cover the complete speed range in which the model must be valid representing the mechanical system behavior. Prescribed constant acceleration speed ramps, set on the motor controller, were used for the construction of the ANN training data

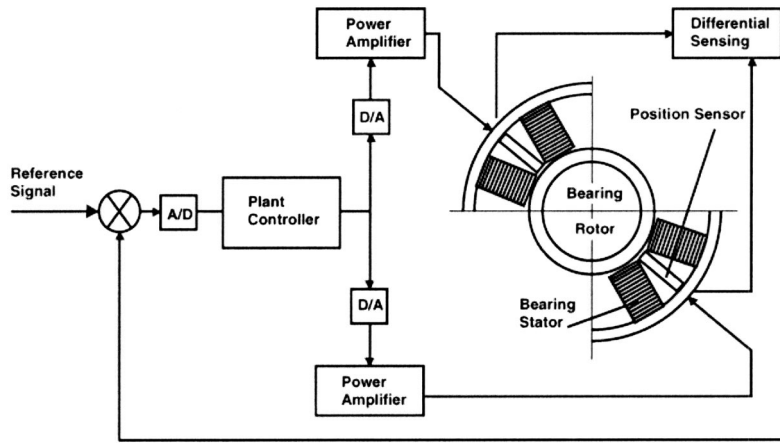


Fig. 8 Single axis control scheme

sets. The use of speed ramps allows for compact, easy to generate, training data sets that contain information about the variation of system parameters with speed (or frequency), such as gyroscopic effects, transient behavior, controller response, etc. The ANN (trained with the ramps) is validated against data sets taken at constant speeds (covering the whole speed range), which better resemble common operating conditions. The result is that a single data set taken during an acceleration ramp (rather than several sets taken at different speeds) can be used to train the ANN over the whole speed range.

Four training sequences were defined, as shown in Table 1. All sequences were acceleration runs having the same final motor speed (5000 rpm.), but the constant acceleration was varied, in order to change the amount of data available for training the network.

The test ramps were produced as startup ramps, changing the PID parameters in the DC motor speed controller. Table 2 shows the PID values used in the motor speed control loop to produce the four acceleration ramps.

If the magnetic bearing system is properly isolated from external vibrations, the variations present in the rotor position are mainly sinusoidal, due to the excitation provided by shaft rotation and the presence of unavoidable intrinsic unbalances in the rotating system (DC motor rotor, shaft, ball-bearing, and inertia disk). The maximum excitation frequency will be the maximum rotor speed, that is 5000 rpm (83.3 Hz).

A sampling rate of 1 K sample per second will be used to ensure that more than 10 points per cycle are taken even when the rotor operates at maximum speed. This will ensure that all data can be represented in either the time or frequency domains without accuracy loss.

Table 1 Time (in seconds) required to complete the speed ramp in each data gathering sequence

| Speed Range in rpm | Ramp1 | Ramp2 | Ramp3 | Ramp4 |
|--------------------|-------|-------|-------|-------|
| 0–5000 | 25 s | 70 s | 120 s | 170 s |

Table 2 PID settings required to produce the training ramps

| Constant Value | Ramp1 | Ramp2 | Ramp3 | Ramp4 |
|----------------|-------|-------|-------|-------|
| P | 0.085 | 0.090 | 0.050 | 0.050 |
| I | 0.070 | 0.005 | 0.001 | 0.005 |
| D | 0.005 | 0.007 | 0.007 | 0.007 |

To standardize the data sets, all measures are scaled to achieve a “0” mean and the same variance, [15], and they are represented in graphical form versus number of samples.

Figure 9 shows the data sets taken in one training session with ramp No. 2 (Ramp2).

The validation data sets were acquired with the rotor operating at constant speed (3000 rpm) with three different unbalances:

- no unbalance,
- “unitary” unbalance (a single peg in the inertia disk), and
- “double” unbalance (two pegs in the inertia disk).

Figure 10 shows the data taken when the system was operated with double unbalance at 3000 rpm.

Model Configuration

As mentioned previously, in order to accommodate the highly nonlinear magnetic bearing system a NNARX (nonlinear autoregressive, external input model) was selected as the preferred ANN configuration. The neural network regressor vector will be defined by Eq. (6), and the predictor by Eq. (7).

The output set, Y , will be formed by the four coil currents, TCW, TCV, BCW, BCV, and the inputs will be the two position variables: PW and PV.

The values of n_a , n_b , and n_k where empirically set, respectively, at 2, 2, 1; in order to use a second-order regressor vector. This choice is based on the fact that, at least in a first approximation, the magnetic bearing can be modeled by a second-order (mass-spring-damper) mechanical system, [20]. This is the only information about the magnetic bearing internal behavior used in setting up the neural network model; all other information is produced using a black-box approach taking into account only measured input/output data. Figure 11 shows the model structure used in this application.

The ANN was implemented using a multilayer perceptron (MLP) topology. This configuration was selected due to its simplicity, easy computational implementation and its ability to model dynamical systems with good accuracy. Figure 12 shows the neural network internal structure.

Model Parameters Estimation. In order to complete the model, the following parameters must be set:

- number of hidden layers: N^{ch} .
- number of neurons in the hidden layers: N_h .
- quadratic error tolerated in each output prediction: E .

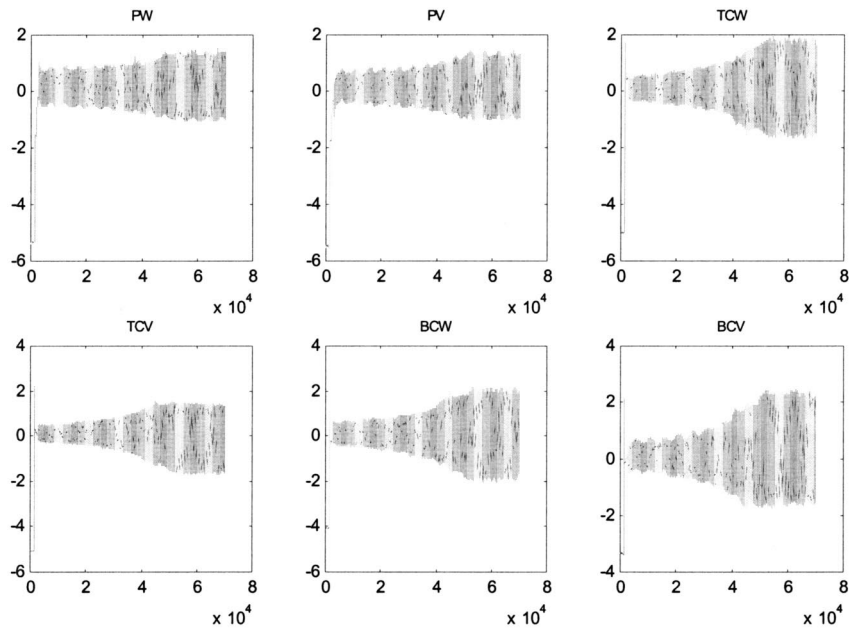


Fig. 9 Ramp No. 2 training sequence (normalized amplitude versus number of samples)

- weight matrix.
- number of iterations (epochs) used in the training: Max-iter.
- weight decay factor: D (only for the Levenberg-Marquardt method).
- Levenberg-Marquardt initial parameter: λ .
- step size (back-propagation): μ .

Parameter selection was a two step process. Initially the parameters listed in Table 3 were set empirically, taking into account factors such as predefined network structure, available computer power, number of tests to be performed and previous experience. The choices were validated by the overall ANN performance reported in the next section.

Experimental Results

The experimental work performed with the ANN model was done in two stages: First, the “training quality” of the different training sequences was analyzed. Once the “best” performing ANN was selected, the ANN model was validated applying the three validating data sets to the selected ANN and comparing its outputs with those measured in the mechanical system in the validation sequences.

Training Results. Initially, using the values presented in Table 3, the weight matrix was evaluated using the Levenberg-Marquardt and the back-propagation algorithm.

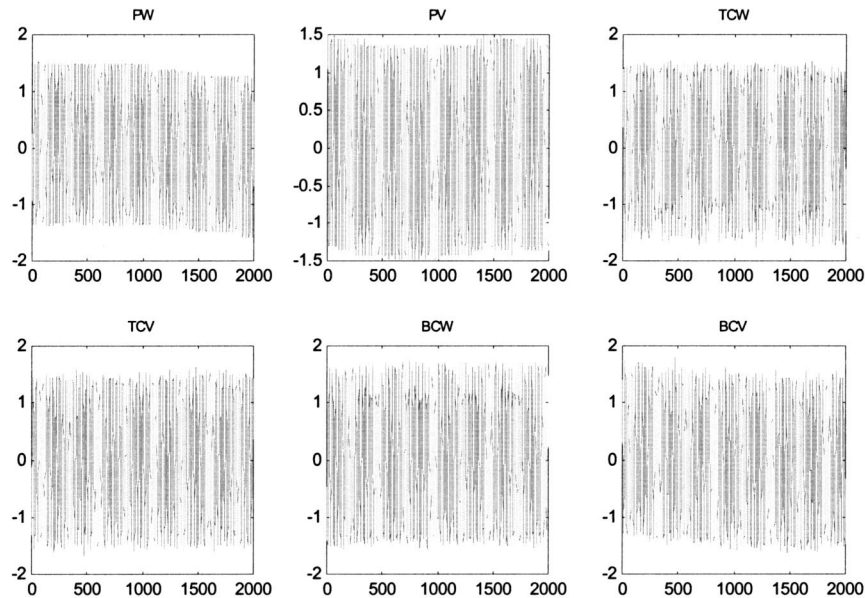


Fig. 10 Validation sequence, 2000 samples per channel, with “double unbalance” and running at 3000 rpm. (3000 rpm2d) (normalized amplitude versus number of samples).

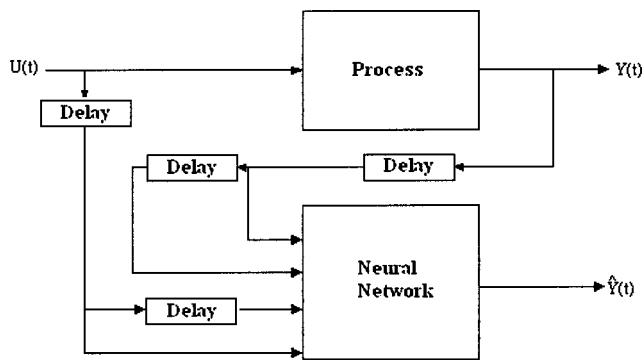


Fig. 11 Model structure

Four ANN were trained using the Levenberg-Marquardt method, one for each speed ramp. Back propagation was used to train only one ANN, using speed ramp No. 2, the ramp that produced the best results using the Levenberg-Marquardt method.

Each trained ANN was tested with the same validation data set, the first sequence taken with the magnetic bearing system running at 3000 rpm, with no additional unbalance. Three figures of merit were considered: the calculated auto-correlation function for the predicted error in the trained ANN BCV output, and the two cross correlation functions between the BCV output and the inputs PV and PW (due to symmetry, the four outputs behave in very similar ways both in the real and the simulated system; results from only one output variable will be shown from here onwards in order to save space).

As can be seen by comparing the results shown in Figs. 13 and 14, the results obtained with training ramps Ramp1 and Ramp2 are not similar. The main difference is that the autocorrelation in Fig. 13, Ramp1 is very close to "1" in the whole range, showing that the predicted error in any time instant is influenced by previous errors, indicating that the training performed with Ramp1 is not acceptable.

The training results obtained using Ramp2 and Ramp3 can be seen in Figs. 14 and 15. The differences are very few and the autocorrelation is close to zero in both cases, showing that both training sequences are adequate.

Figure 16 shows the results produced by training the ANN with Ramp4 sequence. As can be seen, the autocorrelation function is higher than in the two previous cases.

From the error point of view, both Ramp1 and Ramp4 must be rejected. Both Ramp2 and Ramp3 give adequate error levels.

Table 3 ANN parameters: initial selection

| Parameter | N_{ch} | N_h | Maxiter | D | λ | μ |
|-----------|----------|-------|---------|--------------------|-----------|--------------------|
| Value | 1 | 5 | 100 | 1×10^{-5} | 1 | 1×10^{-4} |

Since Ramp2 is much shorter than Ramp3 (70 s instead of 120 s) it is the one to be preferred in order to reduce the computational power required.

Once Ramp2 was selected as the best from both the error and the length points of view, another ANN was trained using this training sequence and the back-propagation algorithm in order to compare training results.

Figures 17 and 18 shows the results produced by the ANN network trained using the Levenberg-Marquardt method; Figs. 19 and 20 shows the results produced by the ANN network trained using the back-propagation algorithm.

As can be seen comparing Figs. 17 and 19 the prediction error (real system output less ANN predicted output) is lower in all the test range in the ANN trained using the Levenberg-Marquardt method.

This is also evident when comparing Figs. 18 and 20. In these figures, the autocorrelation function calculated for ANN trained using the Levenberg-Marquardt method falls to zero long before the one calculated for the ANN trained using the back-propagation algorithm, and it is closer to zero in the complete range; the values of the two cross-correlation functions calculated between the output TCV and the inputs PW and PV calculated for ANN trained using the Levenberg-Marquardt method are always within in the ± 0.1 range, in the other hand the cross-correlation functions values calculated for the ANN trained using the back-propagation algorithm are much higher, going in some cases outside the ± 0.2 range.

Since the ANN trained using the Levenberg-Marquardt method clearly outperform the ANN trained using the back-propagation algorithm, the Levenberg-Marquardt training method was selected as the more adequate in this application.

Table 4 shows a summary of the results obtained in the training using the Levenberg-Marquardt method. The best result, a quadratic error of 3.02×10^{-2} was obtained with ramp No. 2. The error using the back-propagation algorithm was 40% bigger (4.28×10^{-2}).

Validation. Once the ANN trained with Ramp2 sequence and using the Levenberg-Marquardt method was selected, the magnetic bearing system model was validated testing it under unbalanced conditions not present in the training data sets, to see how

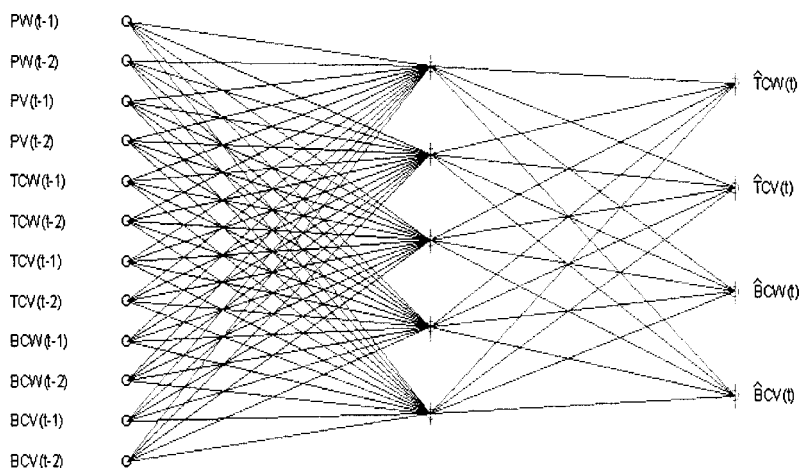


Fig. 12 Artificial neural network structure

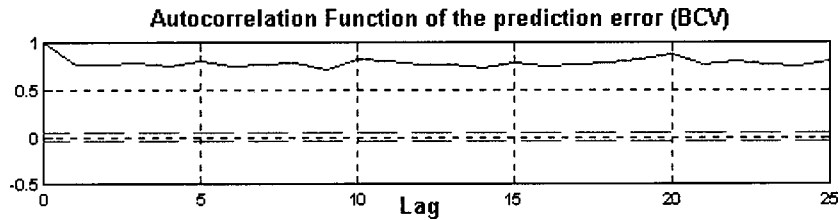


Fig. 13 Autocorrelation functions, ANN trained with Ramp1 and tested with 3000 rpm validation sequence (correlations values versus number of delayed samples)

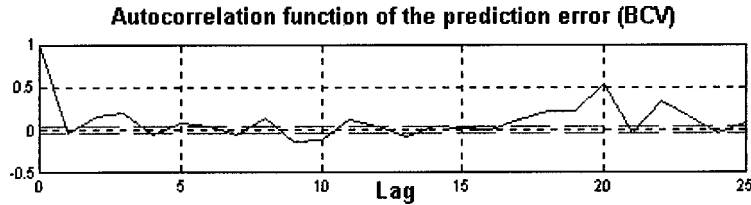


Fig. 14 Autocorrelation functions, ANN trained with Ramp2 and tested with 3000 rpm validation sequence (correlations values versus number of delayed samples)

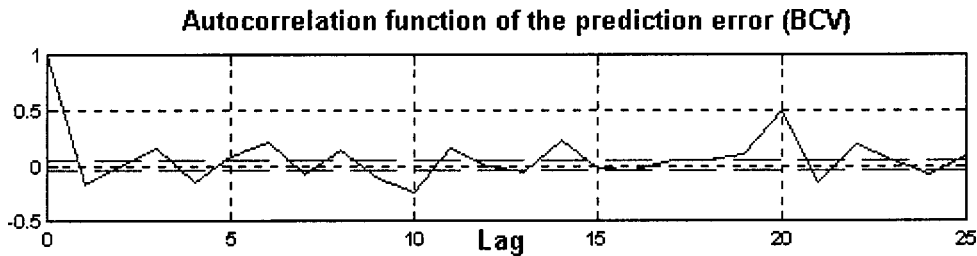


Fig. 15 Autocorrelation functions, ANN trained with Ramp3 and tested with 3000 rpm validation sequence (correlations values versus number of delayed samples)

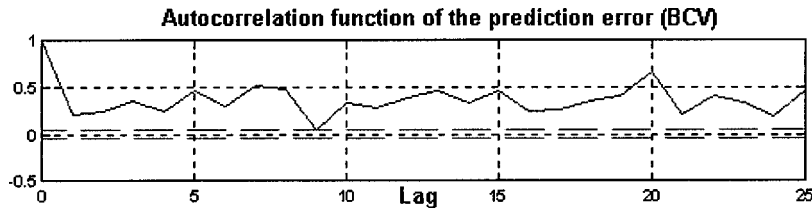


Fig. 16 Autocorrelation function, ANN trained with Ramp4 and tested with 3000 rpm validation sequence (correlations values versus number of delayed samples)

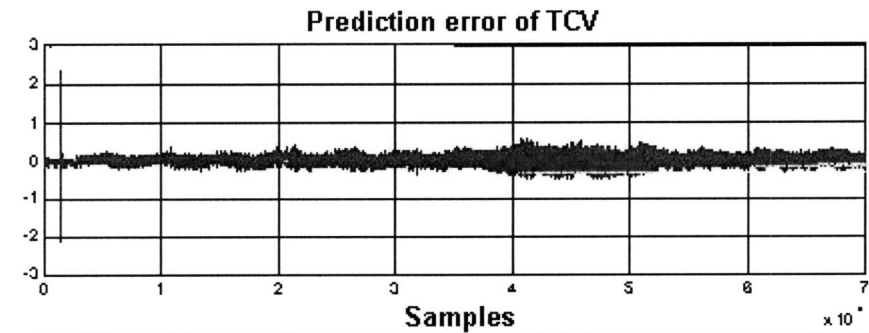


Fig. 17 TCV prediction error ANN trained with Ramp2 using the Levenberg-Marquardt method (currents values in A. versus number of samples).

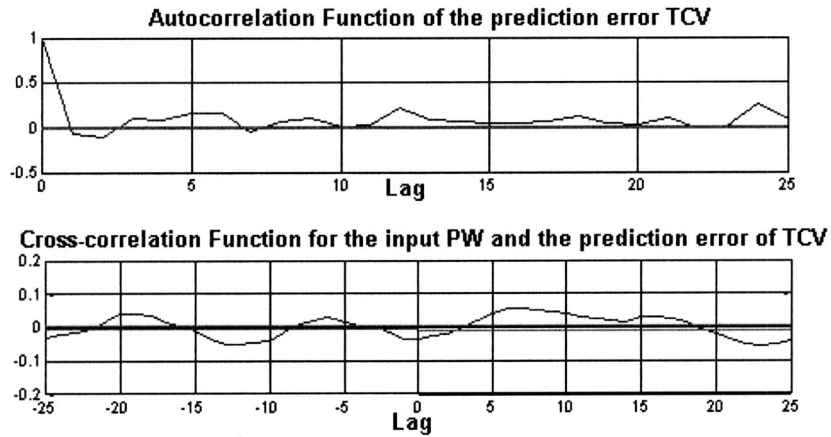


Fig. 18 TCV correlation functions. ANN trained with Ramp2, using the Levenberg-Marquardt method (correlations values versus number of delayed samples).

well the ANN model will represent the magnetic bearing system under load conditions not considered in the training sessions. Three validation sequences were used:

- “3000 rpm:” Motor running at constant speed (3000 rpm), no additional unbalance in the system.
- “3000 rpm d:” Motor running at constant speed (3000 rpm), one “unitary” unbalance mass in the system.
- “3000 rpm 2d:” Motor running at constant speed (3000 rpm), two “unitary” unbalance masses in the system.

The “3000 rpm” sequence is the base reference since the system was trained with no unbalance, but using a different speed stimulus (a speed ramp from 0 to 5000 rpm).

Figure 21 upper shows superimposed the real output and simulated one step ahead prediction. They are very similar and the error (real system output less ANN predicted output) is better seen in Fig. 21 (lower). The predicted error lays almost continuously within the ± 0.2 range, with isolated error spikes ranging up to the ± 0.3 range.

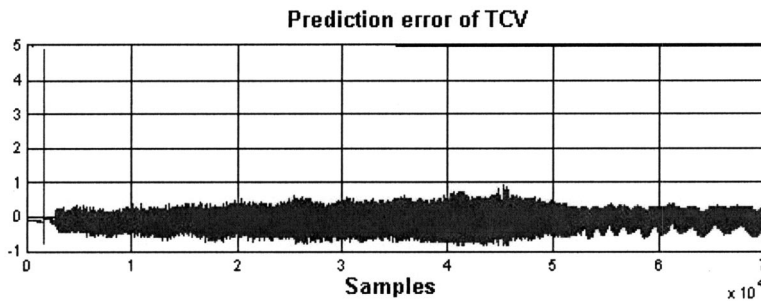


Fig. 19 TCV output. ANN trained with Ramp2, using the back-propagation algorithm (currents values in A. versus number of samples).

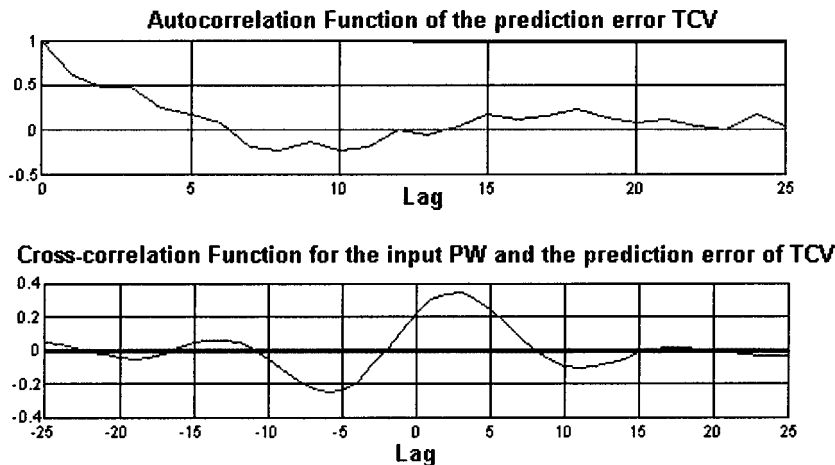


Fig. 20 TCV correlation functions. ANN trained with Ramp2, using the back-propagation algorithm (correlations values versus number of delayed samples).

Table 4 ANN output mean quadratic error. ANN trained using the Levenberg-Marquardt method.

| Mean Quadratic Error (E) | Ramp1 | Ramp2 | Ramp3 | Ramp4 |
|--------------------------|-----------------------|-----------------------|-----------------------|-----------------------|
| | 5.08×10^{-2} | 3.02×10^{-2} | 3.14×10^{-2} | 5.25×10^{-2} |

The output autocorrelation function, shown in Fig. 22 falls quickly to zero and remains at a low value in almost all the test range, with only one region in which it raises to a peak value of 0.5, showing that the predicted error is random and is not a function of previous error values.

The two crosscorrelation functions (Fig. 22) show an oscillation frequency equal to excitation frequency (50 Hz), with peak values in the ± 0.2 range, showing that the error is associated in frequency with the input and that the output function estimated by

the ANN has the same fundamental frequency than the real signal.

Once unbalance is present the predicted error waveform locks in shape with the excitation waveform (Figs. 23 through 25), having clearly defined peaks rising to 0.3 with unitary unbalance, Fig. 23, and 0.4 with double unbalance, Fig. 25.

In Figs. 24 and 25 the correlation between the predicted error and the input variable is a very well-defined sinusoidal function oscillating at the input excitation frequency (50 Hz).

No fundamental change is appreciable in the autocorrelation function, the peak observed in the unloaded test (Fig. 22) is still present at the same position, with some increment in its magnitude, changing from over 0.5 (no additional unbalance, Fig. 22) to 0.8 (double unbalance, Fig. 26).

The observed output behavior is coherent with the physical situation: an unbalance load producing an oscillating position error which forces periodic increases in the control current; it is evident that the model is working, but is unable to fully compensate the unbalanced load.

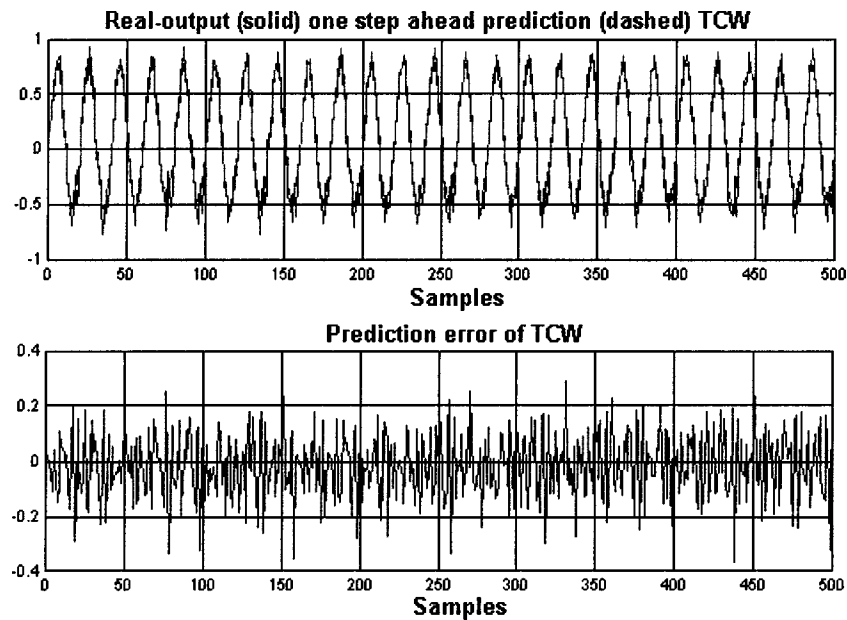


Fig. 21 TCW output, testing done with 3000 rpm sequence (currents values in A. versus number of samples)

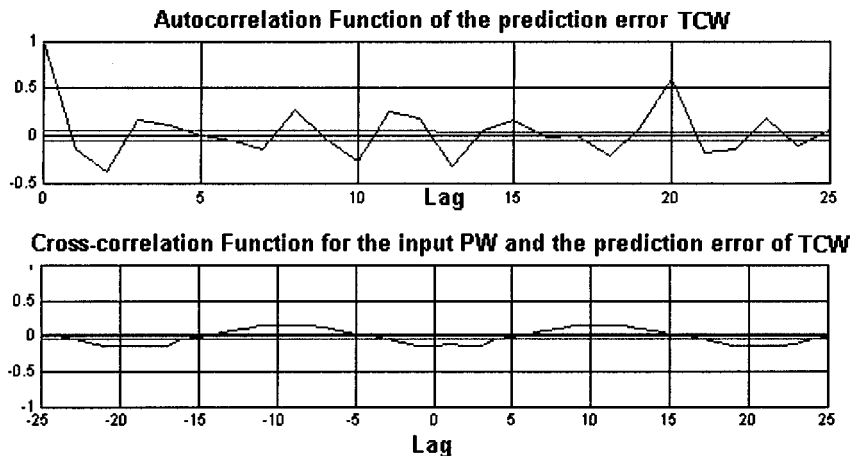


Fig. 22 Correlation functions, TCW output, testing done with 3000 rpm sequence (correlations values versus number of delayed samples)

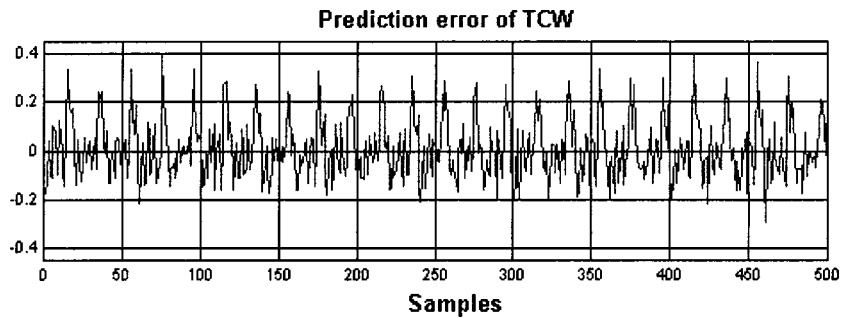


Fig. 23 TCW output, testing done with 3000 rpmd sequence (currents values in A. versus number of samples)

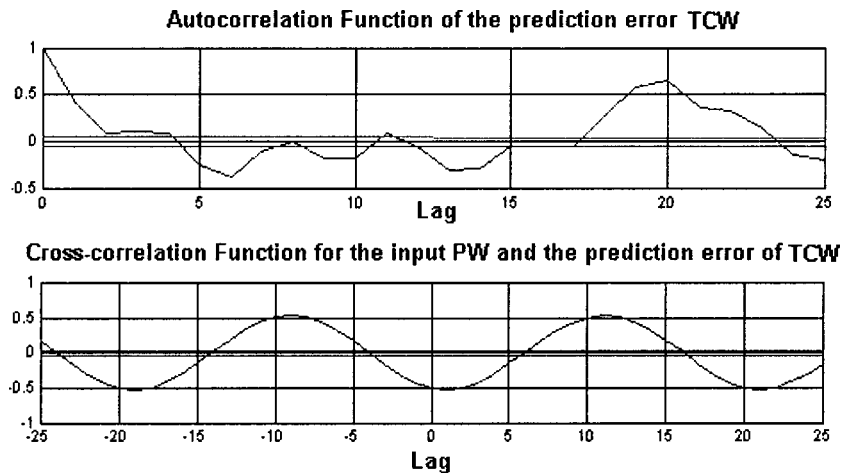


Fig. 24 Correlation functions, TCW output, testing done with 3000 rpmd sequence (correlations values versus number of delayed samples)

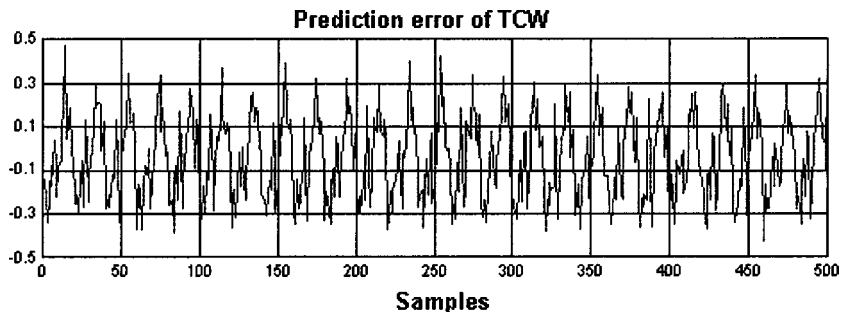


Fig. 25 TCW output, testing done with 3000 rpm2d sequence (currents values in A. versus number of samples)

Conclusions

- A simple ANN with just one hidden layer and five neurons can be used to model the magnetic bearing system under consideration.
- A relatively short training data sequence (70 seconds, 70,000 samples per channel) is enough to train the ANN-based model.
- An ANN-based model trained with a training data sequence taken when the mechanical system operates in transient mode (acceleration ramp) can simulate steady-state constant speed operation.
- The Levenberg-Marquardt method gives the best training performance in this application.
- The ANN-based model trained with a data sequence taken from the mechanical system operating with balanced load is

able to predict the mechanical system output when it is operated with unbalanced loads, though with a higher predicted error.

Further work must be done with the ANN-based model in order to:

- determine the highest shaft speed that can be accurately modeled.
- compare the performances achieved when it is trained with training data sequences taken at different operating modes (steady run, decelerating ramps, sinusoidal speed variations, etc.), and with balanced and unbalanced loads.
- determine an ANN-based model of the magnetic bearing system working in open loop, that is, without the PID controller.

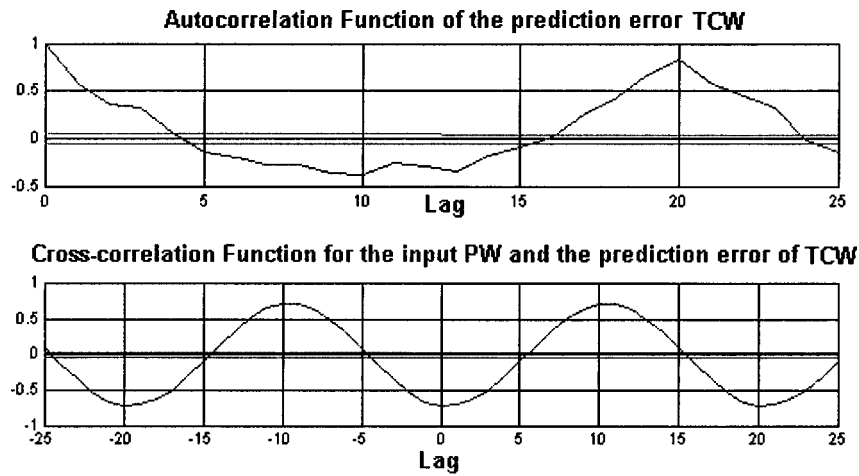


Fig. 26 Correlation functions, TCW output, testing done with 3000 rpm2d sequence (correlations values versus number of delayed samples)

Acknowledgments

The authors want to express their gratitude to CONICIT (S1-98003728) and to the Dean of Research and Development Bureau of the Simón Bolívar University for the financial support required to perform this work.

References

- [1] Bhat, N. V., Minderman, Jr., P. A., McAvoy, T., and Wang, N. S., 1990, "Modeling Chemical process System Via Neural Computation," *IEEE Control Syst. Mag.*, Apr.
- [2] Chen, S., Billings, S. A., and Grant, P. M., 1990, "Non-Linear Systems Identification using Neural Networks," *Int. J. Control*, **51**, pp. 1191–1214.
- [3] Nguyen, D., and Widrow, B., 1990, "Neural Networks for Self-Learning Control Systems," *IEEE Control Syst. Mag.*, Apr.
- [4] Chen, H., and Lewis, P., 1992, "Rule-Based Damping Control for Magnetic Bearings," *Proc. 3rd International Symposium on Magnetic Bearings*, Technomic, Lancaster, PA, pp. 25–32.
- [5] Fittro, R., 1993, "Magnetic Bearing Control Using Artificial Neural Networks," *MAG'93 Magnetic Bearings, Magnetic Drives and Dry Gas Seals Conference*, Alexandria, VA, Technomic, Lancaster, PA, pp. 201–210.
- [6] Choi, B. B., Brown, G., and Johnson, D., 1997, "Neural Network Control of a magnetically Suspended Rotor System," *MAG'97, Magnetic Bearings, Magnetic Drives and Dry Gas Seals Conference*, Alexandria, VA, Technomic, Lancaster, PA, pp. 281–289.
- [7] Billings, S. A., Jamaludin, H. B., and Chen, S., 1992, "Properties of Neural Networks With Application to Modeling Non-linear Dynamical System," *Int. J. Control*, **55**, pp. 194–224.
- [8] Nahi, N. E., 1969, *Estimation Theory and Applications*, Krieger, New York.
- [9] Goodwing, G. C., and Payne, R. L., 1977, *Dynamic System Identification: Experiment Design and Data Analysis*, Academic Press, San Diego.
- [10] Ljung, L., and Soderstrom, T., 1983, *Theory and Practice of Recursive Identification*, M.I.T. Press, Cambridge, MA.
- [11] Narendra, K. S., and Parthasarathy, K., 1990, "Identification and Control of Dynamical System Using Neural Networks," *IEEE Trans. Neural Netw.*, **1**, pp. 4–27.
- [12] Levenberg, K., 1944, "A Method for Solution of Certain Nonlinear Problems in Least Squares," *Q. Appl. Math.*, **2**, pp. 164–168.
- [13] Marquardt, D., 1963, "An Algorithm for Least Squares Estimation of Nonlinear Parameters," *SIAM (Soc. Ind. Appl. Math.) J. Appl. Math.*, **11**(2), pp. 164–168.
- [14] Hagan, M. T., and Menhaj, J. B., 1994, "Training Feedforward Networks With the Marquardt Algorithm," *IEEE Trans. Neural Netw.*, **5**(6), pp. 989–993.
- [15] Norgaard, M., Ravn, O., Poulsen, N. K., and Hansen, L. K., 2000, *Neural Networks for Modeling and Control of Dynamic System*, 1st Ed., Springer-Verlag, Berlin.
- [16] Haykin, S., 1998, *Neural Networks: A Comprehensive Foundation*, 2nd Ed., Prentice-Hall, Englewood Cliffs, NJ.
- [17] Ljung, L., 1999, *System Identification-Theory for the User*, 2nd Ed., Prentice-Hall, Englewood Cliffs, NJ.
- [18] Margaglio, E., 1998, "Recurrent Neural Networks Applied to Non-linear System Identification," Internal Report, Simón Bolívar University (in Spanish).
- [19] Billings, S. A., and Zhu, Q. M., 1994, "Nonlinear Model Validation Using Correlation Test," *Int. J. Control*, **60**(6), pp. 1107–1120.
- [20] Sweitzer, G., Bleuler, H., Traxler, A., 1994, *Active Magnetic Bearings: Basics, Properties, and Applications of Actives Magnetic Bearing*, 1st Ed., v/d/f Hochschulverlag AG an der ETH Zurich, Zurich.

P. T. Rajeev
 GE Superabrasives,
 6325 Huntley Road,
 Worthington, OH 43085
 e-mail: Rajeev.pakalapati@gesm.ge.com

H. Murthy

T. N. Farris¹

e-mail: farrist@purdue.edu

School of Aeronautics & Astronautics,
 Purdue University,
 315 North Grant Street,
 West Lafayette, IN 47907-2023

Load History Effects on Fretting Contacts of Isotropic Materials

The load history that blade/disk contacts in jet engine attachment hardware are subject to can be very complex. Using finite element method (FEM) to track changes in the contact tractions due to changing loads can be computationally very expensive. For two-dimensional plane-strain contact problems with friction involving similar/dissimilar isotropic materials, the contact tractions can be related to the initial gap function and the slip function using coupled Cauchy singular integral equations (SIEs). The effect of load history on the contact tractions is illustrated by presenting results for an example fretting "mission." For the case of dissimilar isotropic materials the mission results show the effect of the coupling between the shear traction and the contact pressure.
 [DOI: 10.1115/1.1689364]

1 Introduction

The study of fretting fatigue in laboratory typically involves nominally clamping two materials under the action of a constant normal load (P) and subjecting the contact interface to an oscillatory shear load (Q) under conditions of partial slip, [1]. A study of local contact stresses is paramount to understanding the nucleation and growth of cracks caused by fretting, [2]. Assuming two-dimensional plane-strain conditions the contact tractions can be related to the initial gap and the relative slip functions by means of a pair of coupled singular integral equations (SIEs). A numerical method, exploiting the fast Fourier transform (FFT) technique, can be devised to obtain the contact traction very quickly, when both the contacting bodies are made from the same isotropic materials, [3]. For the case of dissimilar materials a different numerical technique, but nevertheless faster than finite element method (FEM), can be used to obtain the contact tractions, [4]. Additionally, for cases where the contact region can be divided into a central stick zone with two slip zones on either side, a few simple rules describe the direction of the slip. First, if only normal load is applied then the directions of relative slip in the two slip zones will be opposite to one another and whether this slip is directed "inward" or "outward" will depend on relative stiffness of the two contacting bodies. Secondly, if a shear load is applied then the direction of relative slip in both the slip zones will be in the direction of the change in the shear load (ΔQ).

In gas turbine applications, however, contacting components are subjected to very complex load histories. Figure 1(a) shows a typical variation of the normal and shear loads between the blade and disk of a jet engine stage during operation. In principle such a "mission" can be simulated with the finite element method to obtain a history of the contact tractions. However, this process is computationally expensive and complicated to implement. One difficulty is that for a given load step (from an equilibrium position) there are no clear rules on how to establish the direction of slip in both the slip zones. In fact, it is not clear if the applied load increment will only produce one stick zone. Also, the load history cannot be discretized in time too finely because very small load increments might produce small stick or slip zones and this will require an impractically high number of node points to accurately resolve the contact tractions. The computational speed and mini-

mal pre-processing required of the SIE method make it eminently suitable for analysis of load history effects in fretting.

2 Governing Singular Integral Equations

A schematic of two elastic bodies in contact is shown in Fig. 2. The surface displacement components of each body are given by u_x and u_y (where $i=1,2$ refers to the two bodies). Relative slip between the two bodies, $s(x)$, and the initial gap function, $H(x)$, in the contact zone are related to the displacements as

$$s(x) = {}_2u_x - {}_1u_x \quad (1)$$

$$H(x) + C_1x = {}_2u_y - {}_1u_y + H_0 \quad (2)$$

where H_0 is a constant and C_1 is a rotation term. Equation (1) defines slip as difference in tangential surface displacement of the two bodies. Equation (2) states that the normal displacement of the bodies must lead to continuity between the two bodies without interpenetration. Using equations of elasticity for plane-strain half-spaces, the contact pressure, $p(x)$, and the shear traction, $q(x)$, can be related to $H(x)$ and $s(x)$ as, [5],

$$\frac{\partial s}{\partial x} = \frac{k_2}{\pi} \int_{a_1}^{a_2} \frac{q(t)}{t-x} dt + k_1 p(x) \quad (3)$$

$$\frac{\partial H}{\partial x} + C_1 = -k_1 q(x) + \frac{k_2}{\pi} \int_{a_1}^{a_2} \frac{p(t)}{t-x} dt \quad (4)$$

where the Dundurs constants, [6], k_1 and k_2 are obtained from the Young's modulus (E) and Poisson's ratio (ν) of the two bodies as

$$k_1 = \frac{(1-2\nu_2)(1+\nu_2)}{E_2} - \frac{(1-2\nu_1)(1+\nu_1)}{E_1} \quad (5)$$

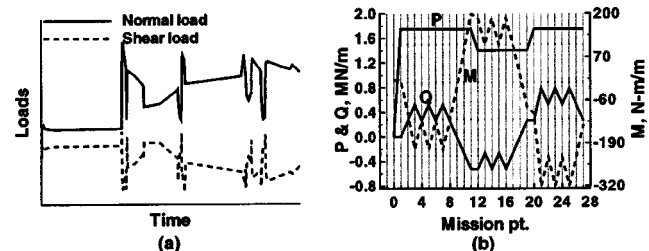


Fig. 1 (a) Typical attachment load history, (b) example load history

¹To whom correspondence should be addressed.

Contributed by the International Gas Turbine Institute (IGTI) of THE AMERICAN SOCIETY OF MECHANICAL ENGINEERS for publication in the ASME JOURNAL OF ENGINEERING FOR GAS TURBINES AND POWER. Paper presented at the International Gas Turbine and Aeroengine Congress and Exhibition, Amsterdam, The Netherlands, June 3–6, 2002; Paper No. 2002-GT-30297. Manuscript received by IGTI, December 2001, final revision, March 2002. Associate Editor: E. Benvenuti.

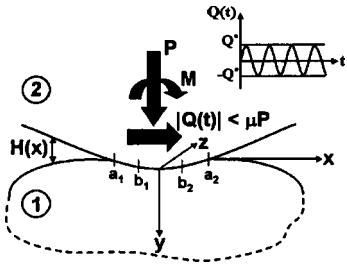


Fig. 2 Schematic of two elastic bodies in partial slip contact. a_1 and a_2 denote the ends of the contact zone and b_1 and b_2 denote the end of the stick zones.

$$k_2 = -\frac{2(1-\nu_2^2)}{E_2} - \frac{2(1-\nu_1^2)}{E_1}. \quad (6)$$

Please note that $k_1 = 0$ when both the contacting bodies are made from similar isotropic materials which means that Eqs. (3) and (4) are decoupled so that the contact pressure is independent of the tangential load. If the initial gap function and the slip function are known, Eqs. (3) and (4) can be solved for the contact tractions. The initial gap function, $H(x)$, can be obtained from a knowledge of the undeformed geometry of the contacting bodies but the slip function, $s(x)$, is more complicated.

For partial slip contact problems ($Q < \mu P$) Dundurs and Comninou [6] deduced that in order for Coulomb's law of friction to be obeyed at the edge of contact and for there not to be any interpenetration of the contacting surfaces, there has to be some amount of relative sliding between the contacting surfaces. The most common scenario is that there is a central "stick" zone in which no relative slip takes place surrounded by a "slip" zone in

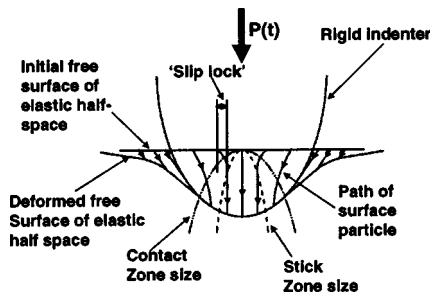


Fig. 3 The evolution of the contact and stick zones and the "slip lock" phenomenon that occurs during the incremental indentation of an elastic half-space by a rigid surface

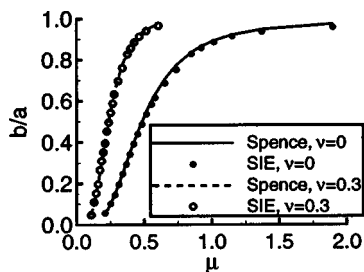


Fig. 4 Stick zone size as a function of the coefficient of friction. The values of b/a obtained by solving the coupled singular integral equations incrementally are in good agreement to those obtained by Spence [7] using a self-similar analysis.

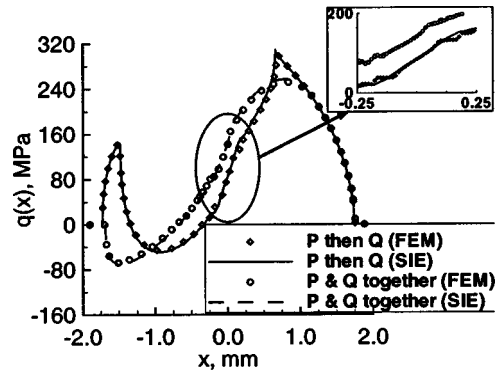


Fig. 5 Shear traction results when a rigid cylinder is brought into contact with a Ti-6Al-4V half-space for two different load histories ($P = 1.75 \text{ MN/m}$, $Q = 0.35 \text{ MN/m}$)

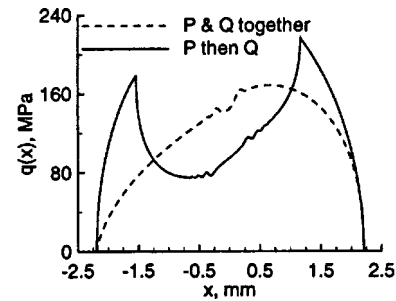
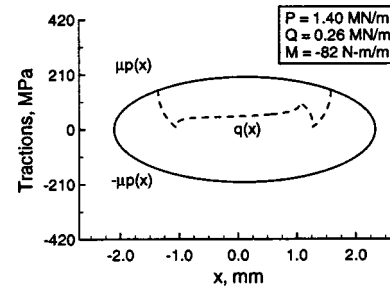
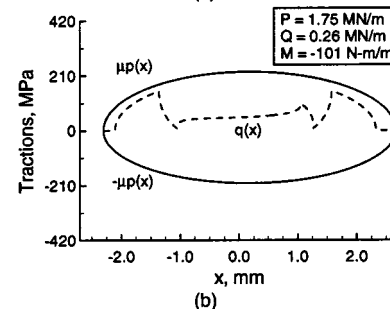


Fig. 6 Shear traction results when a cylinder made from Inco718 alloy is brought into contact with a Ti-6Al-4V half-space for two different load histories ($P = 1.75 \text{ MN/m}$, $Q = 0.53 \text{ MN/m}$)



(a)



(b)

Fig. 7 Mission points 19, and 20 with Ti-6Al-4V cylinder contacting Ti-6Al-4V half-space

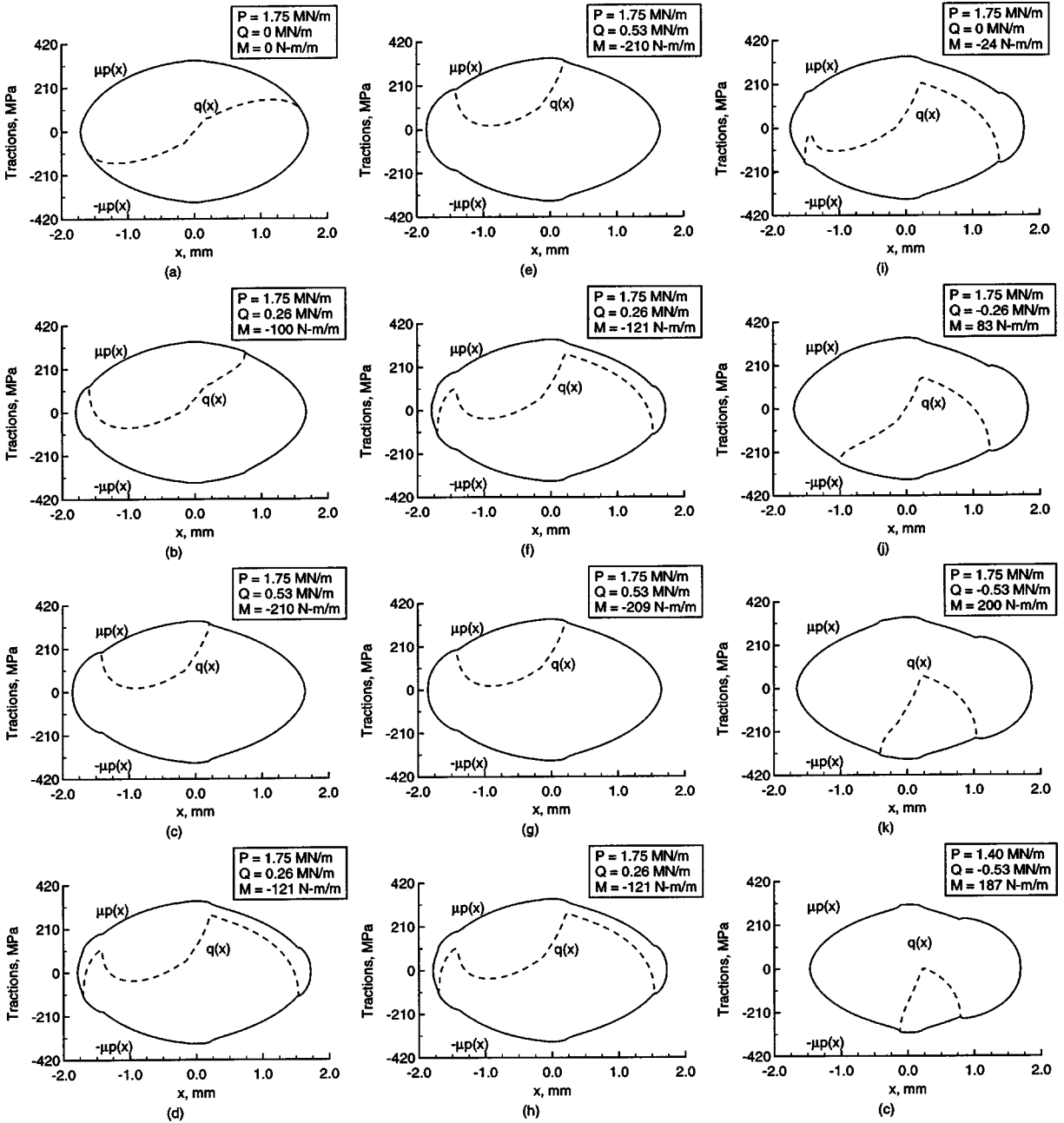


Fig. 8 Mission points, 1, 2, 3, 4, 5, 6, 7, 8, 9, 10, 11, and 12

which the tangential traction is limited by the available friction. In a given load increment, these conditions can be written as

$$\frac{\partial s(x,t)}{\partial t} = 0 \quad x \in (b_1, b_2) \quad (7)$$

$$|q(x)| = \mu |p(x)| \quad x \in \{(a_1, b_1) \cup (b_2, a_2)\} \quad (8)$$

where b_1 and b_2 are the ends of the stick zone and a_1 and a_2 are the ends of the contact zone as shown in Fig. 2. If the next load increment at a given instant in time is such that the size of the stick zone grows into the slip zone then the accumulated slip in the newly added regions to the stick zone gets “locked in.” Thus, the contact pressure and shear stress distribution are load path or history dependent.

This point is illustrated in Fig. 3 for the case of normal indentation ($Q=0$) of an elastic half-space by a rigid punch. As the applied load, P , increases the point A on the surface of the half-

space slips against the rigid surface until the stick zone extends to include that point. From that time onward any increase in the load does not result in additional slip, i.e., the slip is locked in. To solve Eqs. (3) and (4) for the contact tractions, we need to have knowledge of the accumulated slip function, $s(x,t)$, at the current instant of time. For the most general loading/unloading paths there is no way of knowing the slip function a priori. Hence Eqs. (3) and (4) have to be solved incrementally.

The governing singular integral equations (Eqs. (3) and (4)) are solved numerically using the method described in an earlier paper, [4]. The numerical implementation is verified by comparing to a solution available in the literature. Spence [7] gives the contact tractions and the size of the stick zone when an elastic half-space is indented by a rigid power-law indenter ($H(x) = Ax^n$) under the influence of normal load alone, i.e., $Q=0$. Under such conditions the solution is symmetric w.r.t contact pressure and antisymmetric w.r.t the shear traction. Hence the ends of the contact zone and the

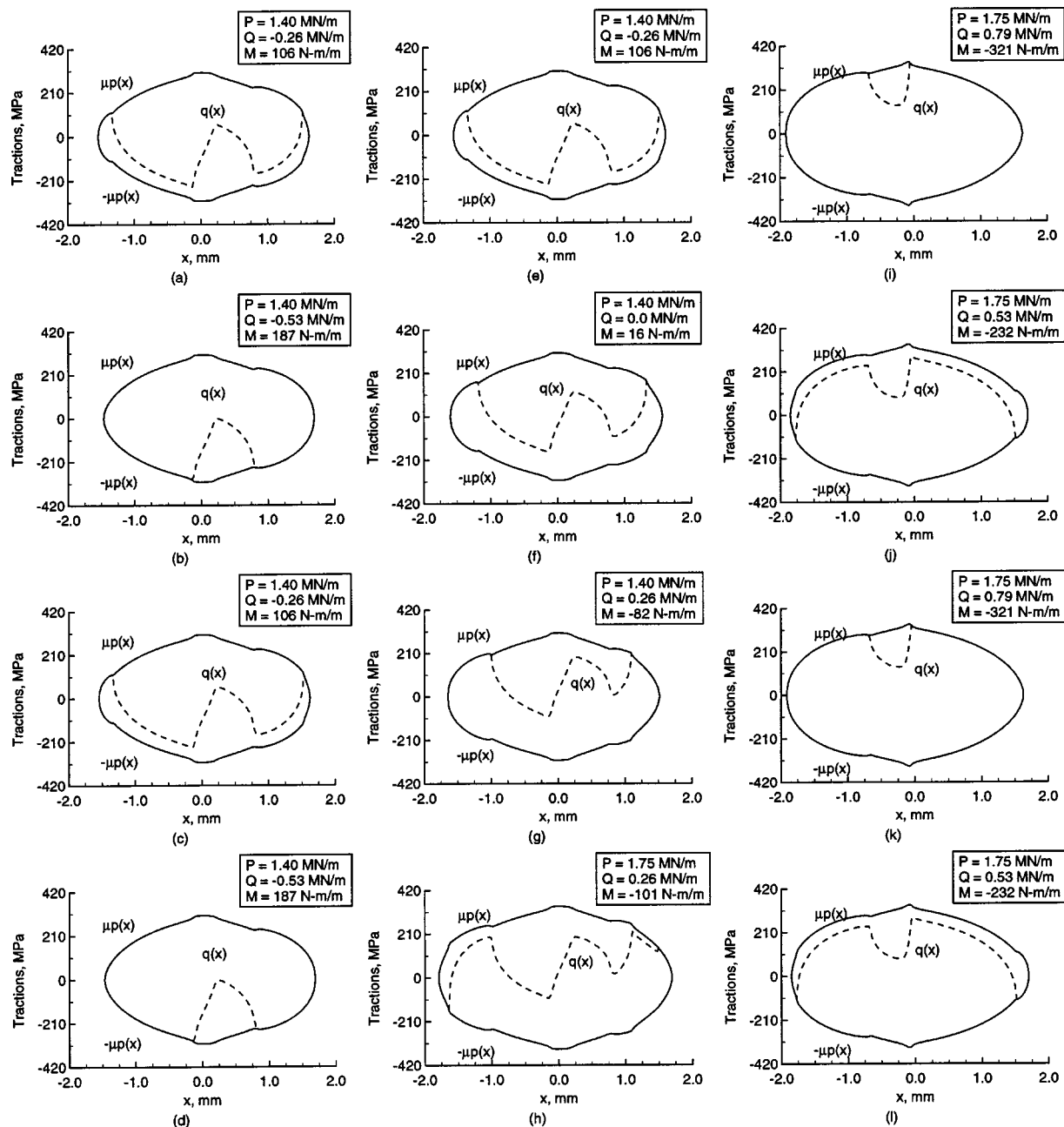


Fig. 9 Mission points 13, 14, 15, 16, 17, 18, 19, 20, 21, 22, 23, and 24

ends of the stick zone will be located symmetrically about the origin, i.e., $a_2 = -a_1 = a$ and $b_2 = -b_1 = b$. Exploiting the self-similarity of the problem Spence reasoned that the ratio of the size of the stick zone to the size of the contact area remains fixed irrespective of the shape, given by the index n , of the power law indenter. Moreover this ratio depends only on the Poisson's ratio (ν) of the half-space and the coefficient of friction (μ).

The present analysis technique is applied to this problem by incrementally indenting an elastic half-space by a rigid parabolic punch ($n=2$). The indentation is continued until the contact size $a=1$. Normal load is applied incrementally using 40 load steps of equal magnitude with the relative slip function calculated at the end of current step used as input to the next step. Slip function in the very first step is assumed to be zero within the stick zone. The analysis is performed for different values of μ and two different values of ν ($=0.0, 0.3$). Results of the current analysis (Fig. 4) are in good agreement with Spence's results for this reduced problem

providing partial justification of numerical convergence. Further details on numerical implementation and convergence are given by Rajeev and Farris [8].

3 Load History Effects

Consider the following two scenarios: (1) a cylindrical punch with a radius (R) of 177.8 mm is brought in contact with a half-space under the action of a normal load, P , and then a shear load, Q ($< \mu P$), is applied to the punch, and (2) the cylindrical punch is brought in contact with the half-space by applying P and Q together, i.e., an oblique load. If the punch and the half-space are made from similar isotropic materials, a central stick zone is produced in the first case whereas the entire contact is in stick in the second case, [5].

For the case of dissimilar materials the contact tractions for the above two load histories have to be obtained numerically. The

Table 1 Contact zones and stick zones for different mission points

| Pt. | a_1 (mm) | a_2 (mm) | b_1 (mm) | b_2 (mm) | Pt. | a_1 (mm) | a_2 (mm) | b_1 (mm) | b_2 (mm) |
|-----|---------------|---------------|---------------|---------------|-----|---------------|---------------|---------------|---------------|
| 1 | -1.714 | 1.714 | -1.608 | 1.607 | 15 | -1.545 | 1.623 | -1.341 | 1.530 |
| 2 | -1.792 | 1.679 | -1.598 | 0.762 | 16 | -1.468 | 1.691 | -1.341 | 1.426 |
| 3 | -1.854 | 1.653 | -1.421 | 0.208 | 17 | -1.545 | 1.623 | -1.341 | 1.530 |
| 4 | -1.788 | 1.722 | -1.706 | 1.540 | 18 | -1.601 | 1.567 | -1.184 | 1.333 |
| 5 | -1.853 | 1.650 | -1.697 | 1.540 | 19 | -1.650 | 1.517 | -0.999 | 1.095 |
| 6 | -1.788 | 1.722 | -1.706 | 1.540 | 20 | -1.794 | 1.696 | -1.643 | 1.498 |
| 7 | -1.853 | 1.650 | -1.689 | 1.540 | 21 | -1.915 | 1.632 | -0.677 | -0.058 |
| 8 | -1.788 | 1.722 | -1.706 | 1.540 | 22 | -1.851 | 1.701 | -1.776 | 1.517 |
| 9 | -1.735 | 1.775 | -1.524 | 1.405 | 23 | -1.912 | 1.628 | -1.773 | 1.517 |
| 10 | -1.692 | 1.822 | -1.004 | 1.249 | 24 | -1.851 | 1.701 | -1.776 | 1.517 |
| 11 | -1.659 | 1.870 | -0.415 | 1.046 | 25 | -1.912 | 1.628 | -1.774 | 1.518 |
| 12 | -1.471 | 1.692 | -0.120 | 0.793 | 26 | -1.851 | 1.701 | -1.776 | 1.518 |
| 13 | -1.545 | 1.623 | -1.341 | 1.530 | 27 | -1.800 | 1.754 | -1.612 | 1.382 |
| 14 | -1.468 | 1.692 | -1.340 | 1.265 | | | | | |

shear traction results when a rigid cylinder is brought into contact with a Ti-6Al-4V half-space ($E=115.8$ GPa, $\nu=0.32$) are presented in Fig. 5. The coefficient of friction is $\mu=0.5$ and cylinder radius is $R=177.8$ mm in these and subsequent calculations unless otherwise indicated. Note that the SIE results are in good agreement with the FEM results. Figure 6 presents the shear traction results when a cylindrical punch made from Inco718 alloy ($E=208.2$ GPa, $\nu=0.31$) is brought into contact with a Ti-6Al-4V half-space. The “kinks” in the central region of the shear traction distributions are a result of assuming that the relative slip function is identically zero in the stick zone in the very first load increment. They can be confined to smaller regions by increasing the number of load increments. It must be noted that, for the same reason, these “kinks” exist in FEM analyses as well (Fig. 5). Small slip zones are present near the edges of contact that are not present in the similar material case.

To demonstrate the ability of the SIE method to analyze complex fretting missions a rigid cylinder and a Ti-6Al-4V half-space subjected to the example load history of Fig. 1(b) are considered. The mission points are numbered 1 through 27. Results for a Ti-6Al-4V cylinder indenting a Ti-6Al-4V half space are shown in Fig. 7 for comparison with two of the dissimilar material load steps. Initially the rigid cylinder is brought in contact with the half-space under the action of normal load alone ($P=1.75$ MN/m, $Q=0$). The contact tractions are shown in Fig. 8(a). Note that the slip in both the slip zones is in opposite directions. Next a shear load of 0.53 MN/m is applied keeping the normal load constant. The distribution of the contact tractions are shown in Fig. 8(c). The shear load is then cycled between 0.53 MN/m and 0.26 MN/m (Figs. 8(c)–8(h)). Notice that the slip at the edges is in the direction of the negative x -axis whenever $\Delta Q < 0$. The shear load is then unloaded to zero (Fig. 8(i)) and loaded in the opposite direction to -0.53 MN/m (Fig. 8(k)). At this point, keeping shear load at -0.53 MN/m, the normal load is decreased from 1.75 MN/m to 1.40 MN/m (Fig. 8(l)). Note that this causes a reduction in the size of the stick zone as can be expected from the

increased ratio of Q/P . Figures 9(a)–(e) show the effect of cycling the shear load between -0.53 MN/m and -0.26 MN/m. Notice that the slip at the edges is in the direction of the positive x -axis whenever $\Delta Q > 0$. The shear load is then increased to 0.26 MN/m (Fig. 9(g)) and keeping the shear load constant the normal load is increased from 1.40 MN/m to 1.75 MN/m (Fig. 9(h)). Very interestingly, even though the shear load is not zero, this causes slip in opposite directions in both the slip zones. Figures 9(i)–10(c) show the effect of increasing the shear load to 0.79 MN/m cycling it between 0.79 MN/m and 0.53 MN/m and finally decreasing it to 0.26 MN/m. The ends of contact zone and the ends of stick zones are presented in Table 1.

A similar load history is applied to the case of a Ti-6Al-4V cylinder contacting a Ti-6Al-4V half-space. While the complete set of results are not reproduced here, it is interesting to make the comparison for the load step between mission points 19 and 20 (Fig. 7). As the normal load is increased with constant tangential load, the dissimilar material results illustrate slip in opposite directions near the edge of the contact. The similar material results show that the new contact region at the edges are stuck together. It is evident from all of the plots of the contact pressure distribution that coupling between the shear traction and the pressure in the governing equations (Eqs. (3) and (4)) is quite significant for the dissimilar material cases.

Figures 8–10 clearly show the effect load history has on contact tractions in partial slip contact problems. Using the SIE method, in theory, it is possible to track the changes in contact tractions due to changes in applied loads no matter how small. However, if the changes in applied loads are too small, the changes in contact tractions are either also very small or limited to very small regions. Consider the following scenario: (1) apply the load history shown in Fig. 1(b) from mission points 1 through 3, and (2) keeping $Q(=0.53$ MN/m) and $M(=-210$ N-m/m) constant increase the normal from 1.75 MN/m to 1.79 MN/n. At the end of step 1 the contact traction are shown in Fig. 8(c). As has

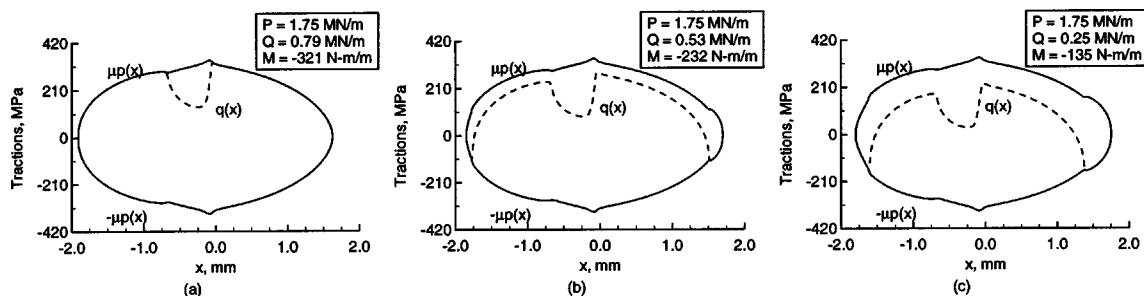


Fig. 10 Mission points 25, 26, and 27

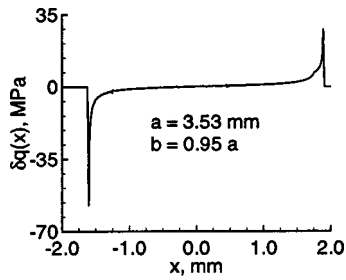


Fig. 11 Change in shear traction due to a 2% increase in normal load and keeping the shear load and moment constant. The initial distribution of the shear traction is shown in Fig. 8(c). Note that a and b denote the size of the contact zone and the size of the stick zone, respectively.

been noted in the previous section increasing the normal load alone, by say δP , will cause relative slip in opposite directions in the two slip zones. In this particular case the δP is so small that the two slip zones are limited to very small regions at the ends of the contact zone. In fact, the stick zone is $\approx 95\%$ of the contact zone. The effect of this change in normal load on the shear stress is shown in Fig. 11. To capture this level of detail, the computational resolution must be increased significantly, [8]. If both of the contacting bodies were deformable, then the slip zones will be confined to even smaller regions requiring even more resolution. The computational expense required to accurately analyze such contacts using FEM can be prohibitively high whereas the SIE method is more amenable to such analyses.

4 Conclusions

A technique capable of analyzing arbitrary load histories in fretting contact is presented. Sample results illustrate the importance of the effect of dissimilar material properties. The resulting local stresses are useful for predicting fretting fatigue lives in labora-

tory conditions for simple load histories, [9]. Current efforts are aimed at conducting experiments with more complicated load histories.

Acknowledgment

This work was supported under U.S. Air Force Contract No. F49620-99-C-0007, "Advanced High Cycle Fatigue Life Assurance Methodologies," Dr. J. R. Calcaterra, AFRL/MLLN as Project Monitor, through the University of Dayton Research Institute under subcontract #RSC99010, Dr. J. P. Gallagher as Project Monitor.

References

- [1] Farris, T. N., Szolwinski, M. P., and Harish, G., 2000, "Fretting in Aerospace Structures and Materials," *Fretting Fatigue: Current Technology and Practices*, D. Hoepfner, V. Chandrasekaran, and C. Elliott, eds., American Society for Testing and Materials, Philadelphia, ASTM STP 1367.
- [2] Murthy, H., Farris, T. N., and Slavik, D. C., 2001, "Fretting Fatigue of Ti-6Al-4V Subjected to Blade/Disk Contact Loading," *Developments in Fracture Mechanics for the New Century, 50th Anniversary of Japan Society of Materials Science*, pp. 41–48.
- [3] Murthy, H., Harish, G., and Farris, T., 2002, "Efficient Modeling of Fretting of Blade/Disk Contacts Including Load History Effects," *ASME J. Tribol.*, in press.
- [4] Rajeev, P. T., and Farris, T. N., 2001, "Two Dimensional Contact of Dissimilar/Anisotropic Materials," *Proc. of 42nd AIAA/ASME/ASCE/AHS/ASC Structures, Structural Dynamics and Materials Conference*, Seattle, WA, AIAA, Washington, DC, **1**, pp. 515–522.
- [5] Hills, D. A., and Nowell, D., 1994, *Mechanics of Fretting Fatigue*, Kluwer, Dordrecht, The Netherlands.
- [6] Dundurs, J., and Comninou, M. J., 1979, "Some Consequences of the Inequality Conditions in Contact and Crack Problems," *J. Elast.*, **9**, pp. 71–82.
- [7] Spence, D. A., 1973, "An Eigenvalue Problem for Elastic Contact With Finite Friction," *Proc. Cambridge Philos. Soc.*, **73**, pp. 249–268.
- [8] Rajeev, P., and Farris, T., 2002, "Numerical Analysis of Fretting Contacts of Dissimilar Isotropic and Anisotropic Materials," *J. Strain Anal.*, **37**(6) pp. 503–507.
- [9] Murthy, H., Rajeev, P. T., and Farris, T. N., 2002, "Fretting Fatigue of Ti-6Al-4V/Ti-6Al-4V and Ti-6Al-4V/In718 Subjected to Blade/Disk Contact Loading," *Proc. of 8th International Fatigue Congress, EMAS, Stockholm*, in press.

Critical Plane Fatigue Modeling and Characterization of Single Crystal Nickel Superalloys

Rajiv A. Naik

Daniel P. DeLuca

Dilip M. Shah

Pratt & Whitney
400 Main Street
East Hartford, CT 06108

Single crystal nickel-base superalloys deform by shearing along $\langle 111 \rangle$ planes, sometimes referred to as “octahedral” slip planes. Under fatigue loading, cyclic stress produces alternating slip reversals on the critical slip systems which eventually results in fatigue crack initiation along the “critical” octahedral planes. A “critical plane” fatigue modeling approach was developed in the present study to analyze high cycle fatigue (HCF) failures in single crystal materials. This approach accounted for the effects of crystal orientation and the micromechanics of the deformation and slip mechanisms observed in single crystal materials. Three-dimensional stress and strain transformation equations were developed to determine stresses and strains along the crystallographic octahedral planes and corresponding slip systems. These stresses and strains were then used to calculate several multiaxial critical plane parameters to determine the amount of fatigue damage and also the “critical planes” along which HCF failures would initiate. The computed fatigue damage parameters were used along with experimentally measured fatigue lives, at 1100°F, to correlate the data for different loading orientations. Microscopic observations of the fracture surfaces were used to determine the actual octahedral plane (or facet) on which fatigue initiation occurred. X-ray diffraction measurements were then used to uniquely identify this damage initiation facet with respect to the crystal orientation in each specimen. These experimentally determined HCF initiation planes were compared with the analytically predicted “critical planes.”

[DOI: 10.1115/1.1690768]

Introduction

High cycle fatigue (HCF) is one of the major causes of component failures in gas turbine aircraft engines, [1]. Some of the fatigue failures in today's aircraft and spacecraft propulsion systems are found in components made from single crystal nickel-base alloys. These alloys provide superior creep and thermomechanical fatigue capabilities over polycrystalline alloys for use in high-temperature turbine components. However, single crystal materials are much more difficult to fabricate, characterize, and model than polycrystalline materials due to their highly anisotropic properties. The orientation of the crystal lattice with respect to the component geometry needs to be accounted for in the design of all single crystal components. Characterization of these materials also needs to be performed along the different crystallographic planes. Modeling of their material and failure response requires the appropriate use of three-dimensional, anisotropic constitutive models and failure theories. Modeling and characterization of the fatigue response of these materials also needs a new paradigm which is based on the observed crystallographic slip mechanisms. The traditional uniaxial Goodman diagram approach can no longer be used effectively to describe the complex fatigue response of these materials.

Single crystal nickel-base superalloys are essentially two-phase materials consisting of a large volume fraction (60%–65%) of intermetallic γ' precipitates, based on the intermetallic compound Ni_3Al , interspersed in a coherent face-centered cubic γ matrix comprised of nickel with cobalt, chromium, and tungsten in solid solution. This structure results in highly orthotropic material properties. Single crystals deform by shearing along $\{111\}$ planes,

sometimes referred to as “octahedral” planes. For temperatures below 1250°F, this shearing occurs in the $\langle 110 \rangle$ family of directions. The four octahedral $\{111\}$ planes and the twelve corresponding $\langle 110 \rangle$ slip directions (three on each plane) are shown in Figs. 1 and 2. The direction of load application with respect to the crystal orientation (1-2-3 axes in Fig. 1) determines the resolved shear stress for each of the $\{111\}\langle 110 \rangle$ slip plane/slip direction sets (or slip systems). When the resolved shear stress on any slip system is sufficiently high it will cause slip along that “critical” slip system. Under fatigue loading, cyclic stress produces alternating slip reversals on the critical slip systems which eventually results in fatigue crack initiation along those “critical” octahedral planes, [2].

A critical plane fatigue modeling approach is ideally suited for such a fatigue failure mechanism. Such an approach was used by Walls [3] and Arakare and Swanson [4] to analyze low cycle fatigue (LCF) in single crystal materials. Under fatigue loading, the orientation of the single crystal axes in three-dimensional space will, in general, be different than the loading axis (Fig. 3). This necessitates the use of appropriate three-dimensional transformation equations for the stress and strain tensors to determine the stresses and strains along the crystallographic axes. Further stress and strain transformation is then required to determine stresses and strains on the crystallographic octahedral planes and along the corresponding slip systems. Using these stresses and strains in the crystal coordinate system, it is possible to calculate multiaxial critical plane parameters to determine the amount of fatigue damage under a given set of applied cyclic stresses and strains.

The objectives of this study were to develop a consistent HCF fatigue modeling approach that accounts for the effects of crystal orientation and the micromechanics of the deformation and slip mechanisms observed in single crystal materials. Several multiaxial critical plane parameters, which use the resolved shear stresses and strains along the slip directions, were used to determine the amount of fatigue damage and also the “critical planes”

Contributed by the International Gas Turbine Institute (IGTI) of THE AMERICAN SOCIETY OF MECHANICAL ENGINEERS for publication in the ASME JOURNAL OF ENGINEERING FOR GAS TURBINES AND POWER. Paper presented at the International Gas Turbine and Aeroengine Congress and Exhibition, Amsterdam, The Netherlands, June 3–6, 2002; Paper No. 2002-GT-30300. Manuscript received by IGTI, Dec. 2001, final revision, Mar. 2002. Associate Editor: E. Benvenuti.

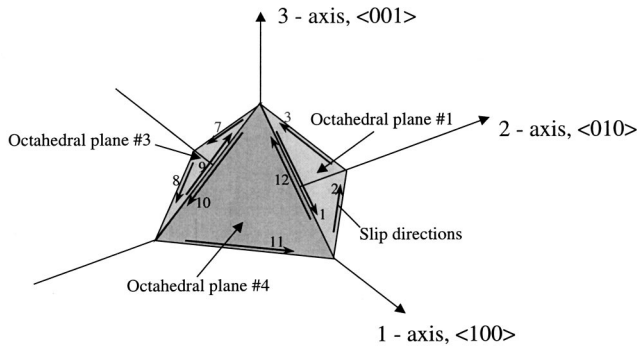


Fig. 1 Octahedral $\langle 111 \rangle$ planes and $\langle 110 \rangle$ family of slip directions for a single crystal

along which HCF failures would initiate. These fatigue damage parameters were used to correlate experimentally measured HCF lives at 1100°F. Three different loading orientations were used in the test program. Microscopic observations of the fracture surfaces were used to determine the actual octahedral plane (or facet) on which fatigue initiation occurred. X-ray diffraction measurements were then used to uniquely identify this damage initiation facet with respect to the crystal orientation in each specimen. These experimentally determined HCF initiation planes were compared with the analytically predicted “critical planes.” The fatigue modeling approach presented in this paper provides a consistent method to account for the effects of single crystal anisotropy and also for the micromechanical preferred slip deformation mechanisms operative in a single crystal material.

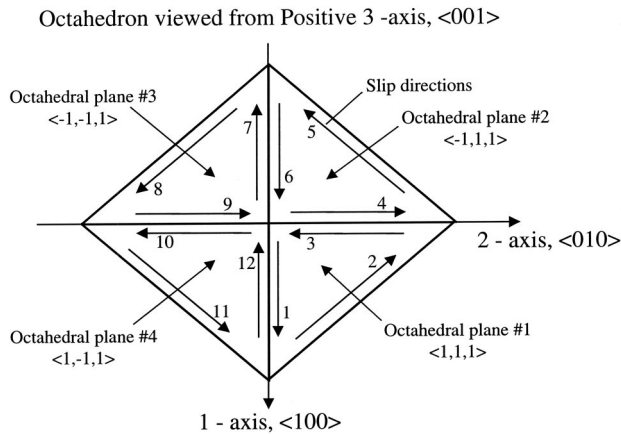


Fig. 2 Plan view of octahedral $\langle 111 \rangle$ planes and $\langle 110 \rangle$ family of slip directions

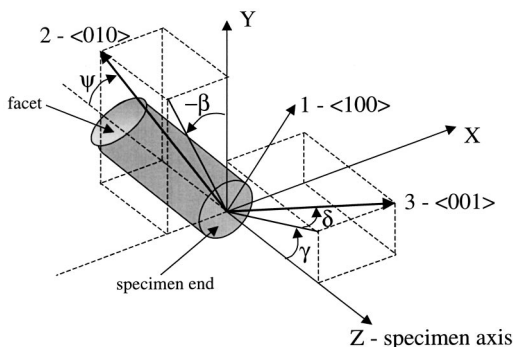


Fig. 3 Definition of Laue angles δ , β , γ , and ψ

Testing

The material used in the present study was PWA 1484, which was cast in the $\langle 001 \rangle$ directions in either a rectangular slab or a cylindrical bar form. The specimens designated by $\langle 001 \rangle$ were machined from cylindrical bars. The specimens designated by $\langle 010 \rangle$ were machined from rectangular slabs. The specimens designated by $\langle 001 + 15 \rangle$ were machined at an off-axis angle of nominally 15° from the primary direction of the rectangular slabs. The secondary orientation was not controlled in the casting of the slabs and the bars.

Cylindrical specimens (3.5 in. long and 0.5 in. in diameter) were machined from the slabs and the bars. The specimens had a gage section that was 0.32 in. long and 0.16 in. in diameter.

All the specimens were tested in a servo-hydraulic machine under load control at 30 Hz and a fatigue stress ratio (R-ratio) of 0.1. Table 1 summarizes the specimens, their orientations, the maximum cyclic stress levels, and the fatigue lives (Nf). Only the specimens that failed were considered in the present study. Note that the actual crystallographic orientations based on the measured Laue angles are different from the nominal orientations in Table 1. The $\langle 010 \rangle$ and the $\langle 001 \rangle$ orientations were treated separately in this paper due to observed crack propagation differences, [2], along and across the dendrites.

Failure Characterization

The fracture surfaces of all the specimens were studied using optical and scanning electron microscopy (SEM) to determine the failure mechanism. In all cases, octahedral slip was identified as the mode of failure based on the faceted appearance of the failure surface. The fatigue initiation site and the facet on which it occurred was identified and marked for each specimen. A laser location technique was used to locate and orient the initiation facet of each specimen in the vertical direction such that the normal to the facet plane and the specimen axis were in the same vertical (Y-Z)-plane (see Fig. 3). The specimen X-Y-Z-axes were defined with respect to the specimen axis and one end face of the specimen. The specimen Z-axis was drawn along the specimen axis with the positive Z-direction as shown in Fig. 3. The specimen Y-axis was defined to be vertically upwards after locating the initiation facet in the vertically upward direction. The specimen X-axis was drawn in the horizontal direction such that the X-Y-plane was normal to the specimen Z-axis. Thus, the X-Y-plane was along the specimen end face.

The laser location technique consisted of projecting a laser beam, aligned at a fixed angle to the specimen axis, on to the initiation facet. The specimen was rotated about the Z-axis until the reflection of the laser beam, off the facet, was in the same vertical plane (Y-Z-plane) as the specimen axis. The specimen was fixed in this orientation in a V-block after this laser location procedure. This procedure fixed the orientation of the initiation facet of each specimen in the Y-Z-plane and also provided a fixed reference frame for defining the orientation of the crystallographic axes with respect to the specimen X-Y-Z-axes.

The orientations of the crystallographic axes were determined using Laue X-ray diffraction techniques. Using the Laue techniques, the orientation of the $\langle 001 \rangle$ axis was determined by measuring the orientation angles δ and γ (see Fig. 3). The angle δ is defined as the angle between the $\langle 001 \rangle$ axis and its projection on the Y-Z-plane. The angle γ is defined as the angle between the projection of the $\langle 001 \rangle$ axis on the Y-Z-plane and the Z-axis (or specimen axis). The positive direction for both these angles is indicated in Fig. 3.

In order to completely define the orientation of the crystallographic axes in three-dimensional space, one more angle needs to be measured. The angle β shown in Fig. 3 was also measured by observing the pattern of the dendrites on the end of the specimen. As shown in Fig. 3, the angle β was defined as the angle between the projection of the $\langle 010 \rangle$ axis on the X-Y-plane and the Y-axis (β is positive in the clockwise direction from the Y-axis). Based

Table 1 Summary of specimens, cyclic stresses, fatigue lives, and Laue angles

| Orientation | Specimen ID | Max. Stress (ksi) | Nf (cycles) | Laue Angles, deg | | |
|-------------|-------------|----------------------|----------------|------------------|----------|---------|
| | | | | δ | γ | β |
| <001+15> | T20WX-1 | 125 | 2.29E+04 | -21.1 | -13.2 | 29.2 |
| <001+15> | T20WX-2 | 130 | 6.72E+04 | 26.4 | 2.1 | -19.4 |
| <001+15> | T20WX-3 | 120 | 5.94E+04 | 25.5 | -3.1 | -24.7 |
| <001+15> | T20WX-4 | 115 | 1.69E+05 | -22.3 | -5.5 | 27.6 |
| <001+15> | T20WX-5 | 135 | 1.39E+04 | 23.8 | -9.4 | -25.9 |
| <001+15> | T20WX-6 | 125 | 3.62E+04 | -23.1 | -4.3 | 25.6 |
| <001+15> | A2LLL-1 | 115 | 7.80E+04 | 11.1 | -11.2 | -38.5 |
| <001+15> | A2LLL-2 | 112.5 | 6.97E+04 | -9.9 | -9.3 | 39.0 |
| <010> | A2LKP-1 | 140 | 3.27E+04 | 0.9 | 1.8 | 44.3 |
| <010> | A2LKP-2 | 130 | 1.77E+05 | 1.2 | -0.6 | -43.3 |
| <010> | A2LKP-3 | 120 | 3.27E+05 | -1.6 | -1.5 | 45.4 |
| <010> | A2LKP-4 | 125 | 6.66E+04 | -1.6 | -1.5 | 44.0 |
| <010> | A2LKP-5 | 130 | 7.05E+04 | 1.5 | 1.1 | -41.2 |
| <010> | A2LKP-6 | 135 | 2.99E+04 | 0.5 | 2.4 | 41.4 |
| <010> | A2LKP-7 | 120 | 6.26E+06 | -0.1 | -1.3 | -36.4 |
| <010> | A2LKP-8 | 117.5 | 7.54E+06 | -1.9 | 0.1 | -43.6 |
| <001> | K1L1U-1 | 140 | 3.20E+04 | 1.3 | 6.3 | 42.6 |
| <001> | K1L16-2 | 120 | 2.38E+05 | 1.6 | -0.6 | -42.6 |
| <001> | K1L1H-1 | 130 | 9.86E+04 | -2.4 | -2.8 | 41.5 |
| <001> | K1L1H-2 | 110 | 7.98E+06 | 2.3 | -2.3 | -40.7 |
| <001> | K1L1V-1 | 120 | 1.73E+06 | -2.9 | 6.2 | -44.6 |

on the measured angles δ , γ , and β , it is possible to derive an expression for the angle ψ (Fig. 3) which is the angle between the (010) orientation and the negative Z-axis. These angles were used to completely define the orientation of the crystal axes in three-dimensional space using direction cosines (described in the next section).

Furthermore, based on the measured angles δ , γ , and β , it was possible to use classical stereographic projection techniques to uniquely identify the octahedral plane on which fatigue initiation occurred. This initiation plane was fixed for each specimen to be in the vertical orientation using the laser location technique before the measurement of the Laue angles. The octahedral planes were identified as, 1, 2, 3, or 4 using the convention shown in Fig. 2. The identification number of the octahedral plane on which fatigue initiation occurred was determined using the measured Laue angles and the stereographic projection technique for each specimen and is given in Table 2.

Analysis

The three Laue angles δ , γ , and β , measured in the failure characterization of each specimen formed the basis of the present analysis. These three angles provided the relationship between the loading axis (Z-axis or specimen axis) and the orientation of the single crystal axes in three-dimensional space. Using the applied fatigue stresses along the Z-axis, the stresses and strains in the crystal coordinate system were determined using three-dimensional transformation equations, which were based on the direction cosines derived from the three Laue angles. The stresses and strains in the crystal coordinate system were then resolved on the octahedral planes and along the 12 slip directions (Figs. 1, 2) using a second set of transformation equations. The direction cosines and the transformation equations are presented in the following sections.

Direction Cosines. As mentioned earlier, the three Laue angles δ , γ , and β , were used to define the direction cosines between the loading axes (X-Y-Z) and the crystal axes (1-2-3). The direction cosines between the loading coordinate system X-Y-Z with respect to the crystal coordinate system 1-2-3 are given in Table 3. The notation used for the direction cosines was of the form a_{ij} , $i=1, 3$, and $j=1, 3$. Thus, a_{11} =cosine (angle between

the 1-axis and the X-axis), a_{23} =cosine (angle between the 2-axis and the Z-axis), etc. Once the orientations between the two coordinate systems are described, mathematically, in terms of the direction cosines (Table 3), it is possible to proceed with the transformation of the stresses and strains between the two axes.

The angle ψ in Table 3 is derived in terms of the angles δ , γ , and β , and is given by

$$\tan(\psi) = \frac{\cos(\delta)\cos(\gamma)}{\sin(\delta)\sin(\beta) + \cos(\beta)\cos(\delta)\sin(\gamma)} \quad (1)$$

The direction cosines, a_{11} , a_{12} , and a_{13} , can be determined using classical properties and relationships of direction cosines, [5], and the known direction cosines in Table 3. Thus, $a_{11}=a_{22}^*a_{33} - a_{23}^*a_{32}$, $a_{12}=a_{23}^*a_{31} - a_{21}^*a_{33}$, and $a_{13}=a_{21}^*a_{32} - a_{22}^*a_{31}$.

Three-Dimensional Stress and Strain Transformation. The symmetry in the stress and strain tensors can be exploited to express these tensors in the “contracted” notation, thereby, simplifying the resulting mathematical description of the transformation equations. The following notation is used for the stresses and engineering strains in the two coordinate systems: $\{\sigma_{XYZ}\} = \{\sigma_X, \sigma_Y, \sigma_Z, \tau_{XY}, \tau_{YZ}, \tau_{XZ}\}$ and $\{\epsilon_{XYZ}\} = \{\epsilon_X, \epsilon_Y, \epsilon_Z, \gamma_{XY}, \gamma_{YZ}, \gamma_{XZ}\}$; $\{\sigma_{123}\} = \{\sigma_1, \sigma_2, \sigma_3, \tau_{12}, \tau_{23}, \tau_{31}\}$ and $\{\epsilon_{123}\} = \{\epsilon_1, \epsilon_2, \epsilon_3, \gamma_{12}, \gamma_{23}, \gamma_{31}\}$.

The transformation of the elastic stresses, $\{\sigma_{XYZ}\}$, and strains, $\{\epsilon_{XYZ}\}$, in the loading coordinate system to the stresses, $\{\sigma_{123}\}$, and strains, $\{\epsilon_{123}\}$, in the crystal coordinate system, is given by the following matrix equations:

$$\{\sigma_{123}\} = [P]^{-1}\{\sigma_{XYZ}\}, \quad \{\epsilon_{123}\} = [Q]^{-1}\{\epsilon_{XYZ}\} \quad (2)$$

where the transformation matrices, [P], and [Q] are given in terms of the direction cosines as, [5]:

Table 3 Direction cosines between X-Y-Z and 1-2-3-axes

| | X | Y | Z |
|---|-------------------------|----------------------------|----------------------------|
| 1 | a_{11} | a_{12} | a_{13} |
| 2 | $\sin(\psi)\sin(\beta)$ | $\sin(\psi)\cos(\beta)$ | $-\cos(\psi)$ |
| 3 | $\sin(\delta)$ | $\cos(\delta)\sin(\gamma)$ | $\cos(\delta)\cos(\gamma)$ |

Table 2 Observed and predicted critical octahedral planes

| Orientation | Specimen ID | Observed and Predicted Critical Octahedral Planes | | | | | | |
|-------------|-------------|---|------|-------|------|---------|------|---------|
| | | Observed | FIN | WALLS | FSK | SSR | CCB | McD |
| <001+15> | T20WX-1 | 3 | 3 | 3 | 3 | 2 | 3 | 2 |
| <001+15> | T20WX-2 | 1 | 1 | 1 | 1 | 4 | 1 | 4 |
| <001+15> | T20WX-3 | 1 | 4 | 1 | 4 | 1 | 1 | 1 |
| <001+15> | T20WX-4 | 3 | 3 | 3 | 3 | 2 | 3 | 2 |
| <001+15> | T20WX-5 | 1 | 4 | 1 | 4 | 1 | 1 | 1 |
| <001+15> | T20WX-6 | 3 | 3 | 3 | 3 | 2 | 3 | 2 |
| <001+15> | A2LLL-1 | 1, 2 | 4 | 4 | 4 | 1, 3 | 1, 4 | 1, 3 |
| <001+15> | A2LLL-2 | 3 | 3 | 3 | 3 | 2 | 3 | 2 |
| <010> | A2LKP-1 | 4 | 1 | 1, 2 | 1 | 1, 2 | 2 | 1, 2 |
| <010> | A2LKP-2 | 1, 2 | 4 | 1, 4 | 4 | 1, 4 | 1 | 1, 4 |
| <010> | A2LKP-3 | 3, 4 | 3 | 3 | 3 | 2, 3, 4 | 3 | 2, 3, 4 |
| <010> | A2LKP-4 | 3 | 3 | 3 | 3 | 2, 3, 4 | 3 | 2, 3, 4 |
| <010> | A2LKP-5 | 1, 2 | 1 | 1 | 1 | 1, 2, 4 | 1 | 1, 2, 4 |
| <010> | A2LKP-6 | 3, 4 | 1 | 1, 2 | 1, 2 | 1, 2 | 2 | 1, 2 |
| <010> | A2LKP-7 | 1 | 3, 4 | 3, 4 | 3, 4 | 3, 4 | 4 | 3, 4 |
| <010> | A2LKP-8 | 1, 2, 3 | 2, 3 | 3 | 2, 3 | 2, 3 | 3 | 2, 3 |
| <001> | K1L1U-1 | 4 | 1 | 2 | 1 | 1, 2 | 2 | 1, 2 |
| <001> | K1L16-2 | 1 | 4 | 1, 4 | 4 | 1, 4 | 1 | 1, 4 |
| <001> | K1L1H-1 | 3, 4 | 3 | 3 | 3 | 2, 3, 4 | 3, 4 | 2, 3, 4 |
| <001> | K1L1H-2 | 1 | 4 | 4 | 4 | 1, 3, 4 | 4 | 1, 3, 4 |
| <001> | K1L1V-1 | 2 | 2 | 2 | 2 | 1, 2 | 2 | 1, 2 |
| | | % Correlation: | 50.0 | 68.2 | 50.0 | 54.5 | 68.2 | 54.6 |
| | | Curve-fit, R² | 0.53 | 0.52 | 0.60 | 0.67 | 0.48 | 0.54 |

$$[P] = \begin{bmatrix} a_{11}^2 & a_{12}^2 & a_{13}^2 & 2a_{11}a_{12} & 2a_{12}a_{13} & 2a_{11}a_{13} \\ a_{21}^2 & a_{22}^2 & a_{23}^2 & 2a_{21}a_{22} & 2a_{22}a_{23} & 2a_{21}a_{23} \\ a_{31}^2 & a_{32}^2 & a_{33}^2 & 2a_{31}a_{32} & 2a_{32}a_{33} & 2a_{31}a_{33} \\ a_{11}a_{21} & a_{12}a_{22} & a_{13}a_{23} & a_{11}a_{22} + a_{12}a_{21} & a_{12}a_{23} + a_{13}a_{22} & a_{13}a_{21} + a_{11}a_{23} \\ a_{21}a_{31} & a_{22}a_{32} & a_{23}a_{33} & a_{22}a_{31} + a_{21}a_{32} & a_{23}a_{32} + a_{22}a_{33} & a_{21}a_{33} + a_{23}a_{31} \\ a_{11}a_{31} & a_{12}a_{32} & a_{13}a_{33} & a_{11}a_{32} + a_{12}a_{31} & a_{12}a_{33} + a_{13}a_{32} & a_{13}a_{31} + a_{11}a_{33} \end{bmatrix} \quad (3)$$

$$[Q] = \begin{bmatrix} a_{11}^2 & a_{12}^2 & a_{13}^2 & a_{11}a_{12} & a_{12}a_{13} & a_{11}a_{13} \\ a_{21}^2 & a_{22}^2 & a_{23}^2 & a_{21}a_{22} & a_{22}a_{23} & a_{21}a_{23} \\ a_{31}^2 & a_{32}^2 & a_{33}^2 & a_{31}a_{32} & a_{32}a_{33} & a_{31}a_{33} \\ 2a_{11}a_{21} & 2a_{12}a_{22} & 2a_{13}a_{23} & a_{11}a_{22} + a_{12}a_{21} & a_{12}a_{23} + a_{13}a_{22} & a_{13}a_{21} + a_{11}a_{23} \\ 2a_{21}a_{31} & 2a_{22}a_{32} & 2a_{23}a_{33} & a_{22}a_{31} + a_{21}a_{32} & a_{23}a_{32} + a_{22}a_{33} & a_{21}a_{33} + a_{23}a_{31} \\ 2a_{11}a_{31} & 2a_{12}a_{32} & 2a_{13}a_{33} & a_{11}a_{32} + a_{12}a_{31} & a_{12}a_{33} + a_{13}a_{32} & a_{13}a_{31} + a_{11}a_{33} \end{bmatrix} \quad (4)$$

The elastic strains in the loading coordinate system were calculated using, $\{\epsilon_{XYZ}\} = [S_{eff}]\{\sigma_{XYZ}\}$, where $[S_{eff}]$ is the transformed compliance matrix in the X-Y-Z-coordinate system (see Appendix A).

Stresses and Strains on Octahedral Planes and Along Slip Directions. The stresses, $\{\sigma^{oct}\}$, and strains, $\{\epsilon^{oct}\}$, normal to the four octahedral planes and the resolved shear stresses, $\{\tau^s\}$, and strains, $\{\gamma^s\}$, along the twelve slip directions (see Figs. 1, 2) were described using the following notation: $\{\sigma^{oct}\} = \{\sigma_1^{oct}, \sigma_2^{oct}, \sigma_3^{oct}, \sigma_4^{oct}\}$ and $\{\epsilon^{oct}\} = \{\epsilon_1^{oct}, \epsilon_2^{oct}, \epsilon_3^{oct}, \epsilon_4^{oct}\}$, where the subscripts, 1, 2, . . . , 4 refer to the four octahedral planes shown in Figs. 1, 2. The following notation is used for the resolved shear stresses and strains along the twelve primary slip

directions: $\{\tau^s\} = \{\tau_1^s, \tau_2^s, \tau_3^s, \tau_4^s, \tau_5^s, \tau_6^s, \tau_7^s, \tau_8^s, \tau_9^s, \tau_{10}^s, \tau_{11}^s, \tau_{12}^s\}$ and $\{\gamma^s\} = \{\gamma_1^s, \gamma_2^s, \gamma_3^s, \gamma_4^s, \gamma_5^s, \gamma_6^s, \gamma_7^s, \gamma_8^s, \gamma_9^s, \gamma_{10}^s, \gamma_{11}^s, \gamma_{12}^s\}$, where, the subscripts, 1, 2, . . . , 12 refer to the 12 primary slip directions shown in Figs. 1, 2.

The octahedral stresses, $\{\sigma^{oct}\}$, and strains, $\{\epsilon^{oct}\}$, can be determined using the known stresses, $\{\sigma_{123}\}$, and strains, $\{\epsilon_{123}\}$, in the crystal coordinate system, by the following matrix equations:

$$\{\sigma^{oct}\} = [R]\{\sigma_{123}\}, \quad \{\epsilon^{oct}\} = [S]\{\epsilon_{123}\} \quad (5)$$

where the transformation matrices, $[R]$, and $[S]$ are given by

$$[R] = \frac{1}{3} \begin{bmatrix} 1 & 1 & 1 & 2 & 2 & 2 \\ 1 & 1 & 1 & -2 & 2 & -2 \\ 1 & 1 & 1 & 2 & -2 & -2 \\ 1 & 1 & 1 & -2 & -2 & 2 \\ 1 & 1 & 1 & 1 & 1 & 1 \\ 1 & 1 & 1 & -1 & 1 & -1 \\ 1 & 1 & 1 & 1 & -1 & -1 \\ 1 & 1 & 1 & -1 & -1 & 1 \end{bmatrix}, \quad (6)$$

The resolved shear stresses, $\{\tau^s\}$, and strains, $\{\gamma^s\}$, along the slip directions, can be determined using the known stresses, $\{\sigma_{123}\}$, and strains, $\{\varepsilon_{123}\}$, in the crystal coordinate system, by the following matrix equations:

$$\{\tau^s\} = [T]\{\sigma_{123}\}, \quad \{\gamma^s\} = [U]\{\varepsilon_{123}\} \quad (7)$$

where the transformation matrices, $[T]$, and, $[U]$, are given by

$$[T] = \frac{1}{\sqrt{6}} \begin{bmatrix} 1 & 0 & -1 & 1 & -1 & 0 \\ -1 & 1 & 0 & 0 & 1 & -1 \\ 0 & -1 & 1 & -1 & 0 & 1 \\ 0 & 1 & -1 & -1 & 0 & 1 \\ 1 & -1 & 0 & 0 & -1 & -1 \\ -1 & 0 & 1 & 1 & 1 & 0 \\ 1 & 0 & -1 & 1 & 1 & 0 \\ -1 & 1 & 0 & 0 & -1 & 1 \\ 0 & -1 & 1 & -1 & 0 & -1 \\ 0 & 1 & -1 & -1 & 0 & -1 \\ 1 & -1 & 0 & 0 & 1 & 1 \\ -1 & 0 & 1 & 1 & -1 & 0 \end{bmatrix}, \quad (8)$$

$$[U] = \frac{1}{\sqrt{6}} \begin{bmatrix} 2 & 0 & -2 & 1 & -1 & 0 \\ -2 & 2 & 0 & 0 & 1 & -1 \\ 0 & -2 & 2 & -1 & 0 & 1 \\ 0 & 2 & -2 & -1 & 0 & 1 \\ 2 & -2 & 0 & 0 & -1 & -1 \\ -2 & 0 & 2 & 1 & 1 & 0 \\ 2 & 0 & -2 & 1 & 1 & 0 \\ -2 & 2 & 0 & 0 & -1 & 1 \\ 0 & -2 & 2 & -1 & 0 & -1 \\ 0 & 2 & -2 & -1 & 0 & -1 \\ 2 & -2 & 0 & 0 & 1 & 1 \\ -2 & 0 & 2 & 1 & -1 & 0 \end{bmatrix}$$

Critical Plane Models. Using these computed stresses and strains in the crystal coordinate system, it is possible to calculate multi-axial critical plane parameters to determine the amount of fatigue damage under a given set of applied cyclic stresses and strains. Six different critical plane models were evaluated in the present study. These were the Findley (FIN) [6], Walls [3], Fatemi-Socie-Kurath (FSK) [7,8], shear stress range (SSR), Chu-Conle-Bonnen (CCB) [9], and McDiarmid (McD) [10] parameters. The Walls and SSR parameters had shown good correlation with single crystal LCF data in earlier studies, [3,4].

The FIN parameter was calculated using the maximum shear stress amplitude, τ_a , and the maximum normal stress, σ_{\max} , on the critical slip plane:

$$\text{FIN} = \tau_a + k \sigma_{\max} \quad (9)$$

where, k is a fitting parameter. In the present study, $k=1$ was used for all the calculations of the FIN parameter.

The FSK parameter was calculated using the maximum shear strain amplitude, γ_a , and the maximum normal stress, σ_{\max} , on the critical slip plane:

$$\text{FSK} = \gamma_a \left(1 + k \left(\frac{\sigma_{\max}}{\sigma_{\text{yield}}} \right) \right) \quad (10)$$

where, σ_{yield} , is the yield strength and k is a fitting parameter. In the present study, $k=1$ was used for all the calculations of the FSK parameter.

The Walls parameter was derived by considering the mode mixity of the normal and shear strains on an octahedral plane. It is calculated using the maximum shear strain, γ_{\max} , and the maximum normal strain, ε_{\max} , on the critical slip plane:

$$\text{Walls} = 50 \gamma_{\max} \varepsilon_{\max} \left(\frac{\pi}{\arctan(\gamma_{\max}/\varepsilon_{\max}) + \pi/2} \right)^{0.5} \quad (11)$$

The SSR parameter was calculated using the maximum shear stress range along a “critical slip direction” during the fatigue cycle. The CCB parameter was calculated as the sum of two products: (i) the product of the maximum shear strain amplitude, γ_a , and the maximum shear stress, τ_{\max} , on the critical slip plane; and (ii) the product of the maximum normal strain amplitude, ε_a , and the maximum normal stress, σ_{\max} , on the critical slip plane:

$$\text{CCB} = 2 \gamma_a \tau_{\max} + \varepsilon_a \sigma_{\max}. \quad (12)$$

The McD parameter was calculated as the sum of the maximum shear stress amplitude, τ_a , along a “critical slip direction” and the maximum normal stress, σ_{\max} , on the critical slip plane:

$$\text{McD} = \tau_a + k \sigma_{\max} \quad (13)$$

where k is a curve-fit parameter. In the present study, $k=0.1$ was used for all the calculations of the McD parameter. Although the McD parameter looks similar to the FIN parameter, it differs in the critical plane search algorithm as described in the next section.

Critical Plane Search Algorithms. The critical plane was determined by first computing each of the critical plane parameters along each of the 12 slip directions throughout the fatigue cycle. The max normal stresses and strains (computed normal to the octahedral plane) and the max shear stress and strain amplitudes, along each slip direction, required to compute the different parameters, were determined by scanning through all the computed stresses and strains at all the time steps of the fatigue cycle. The “critical slip direction” for the FIN, Walls, FSK, SSR and CCB parameters was determined as the slip direction on which the damage parameter was a maximum during the fatigue cycle. For the McD parameter, the “critical slip direction” was determined as the slip direction along which the shear stress amplitude, τ_a , was a maximum during the fatigue cycle. The McD parameter (Eq. (13)) was then determined along this critical slip direction.

Results and Discussion

All the calculations were performed using the following elastic constants, measured along the primary $\langle 001 \rangle$ orientations, for PWA 1484 at 1100°F: $E=15.69$ msi, $\nu=0.3995$, $G=15.93$ msi. The critical planes determined by the different critical plane parameters are given in Table 2 along with the octahedral plane IDs on which fatigue initiation was actually observed. The four different octahedral planes are identified using the convention indicated in Figs. 1 and 2. Some specimens exhibited fatigue initiations along the ridge formed by adjacent octahedral planes (Fig. 4). Two or more octahedral initiation planes were reported for such specimens.

The specimens for which the predicted critical plane correlated with the observed plane have been highlighted for each different



Fig. 4 SEM photo showing ridge HCF initiation

damage parameter in Table 2. Depending on the resolved stress and strain states on the octahedral planes, sometimes the parameters were found to be critical along more than one plane. The SSR and McD parameters had a greater tendency to become critical on multiple planes. The percent correlation for each parameter is indicated at the bottom of the table. All parameters had a correlation of at least 50% with the observed critical planes. The highest correlation was obtained using the CCB parameter, which uses an energy based formulation, followed by the Walls parameter, which tries to capture the mode mixity of the normal and shear strains on the octahedral planes. Both the SSR and McD parameters, which rely on the shear stress range along the slip directions were equally successful in predicting the critical planes. Note that the McD parameter calculated using $k=0.1$ was numeri-

cally very similar to the SSR parameter. The FIN and the FSK parameters, which use a combination of the shear stress range or shear strain range and the normal stress to determine the critical plane were only 50% successful in predicting the observed critical planes.

The degree of correlation of the “predicted” and the “actual” critical planes is also a function of the statistical distribution of defects and their propensity to initiate fatigue damage on a certain octahedral plane. In the above correlation it is assumed that only defects along the “predicted” critical planes lead to fatigue damage initiation. However, this approach neglects the statistical nature of the defect distributions. In Table 3, for example, the observed critical planes for three specimens (A2LKP-1, A2LKP-6, and KILIU-1) were not predicted by any of the models. A com-

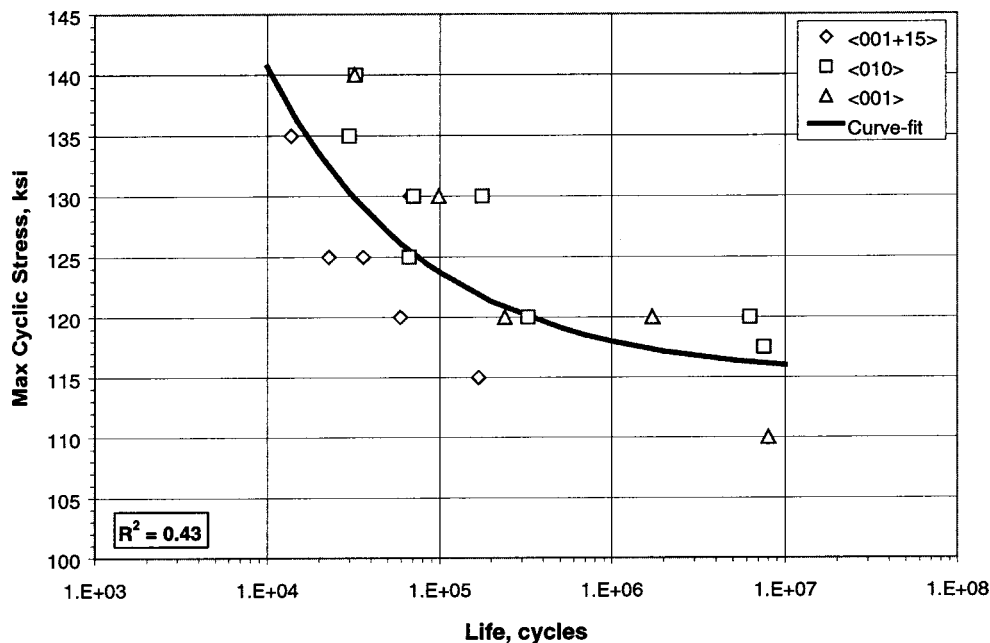


Fig. 5 Max cyclic stress versus life, 1100°F and $R=0.1$

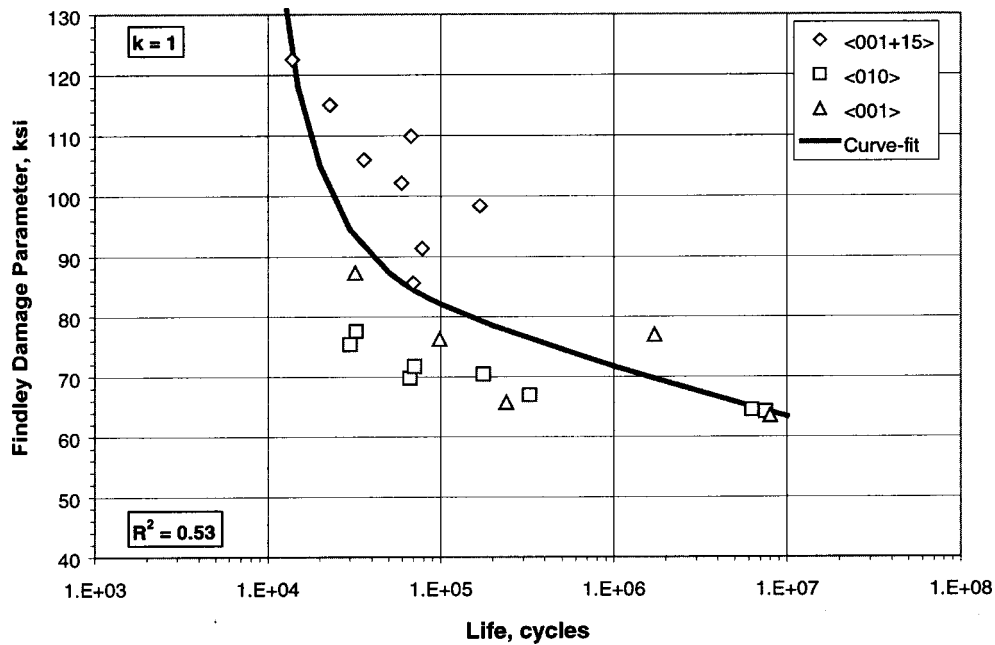


Fig. 6 Findley parameter versus life, 1100°F and $R=0.1$

bined statistical and micromechanical approach might be able to better capture the “actual” phenomenon that leads to fatigue initiation in a single crystal material.

The different parameters were also evaluated by determining how well they were able to correlate the fatigue data for the different specimen orientations. Figure 5 graphically shows the HCF data in Table 1 as an S-N plot. Figure 5 clearly indicates that the traditional S-N approach cannot be used to correlate the fatigue data for the different specimen and loading orientations. The curve-fit has a very low correlation coefficient, $R^2=0.43$.

Figures 6–11 show plots of the calculated damage parameters versus life for all the specimens using the applied cyclic stresses and the actual measured (not nominal) crystal orientations (Table

1) for each specimen. The curve-fit correlation coefficient, R^2 , was used as a measure of how well the damage parameter correlated the fatigue data for the different specimen orientations. These values of R^2 for the different damage parameters are also included at the bottom of Table 2.

From an inspection of the results in Figs. 6–11, it appears that the SSR and the FSK parameters were most successful in correlating the fatigue data for the different specimen orientations. Considering the variability that is usually associated with single crystal fatigue data, R^2 values around 0.6 are assumed to indicate data correlations that are quite good.

Both the FIN and McD damage parameters seemed to be highly

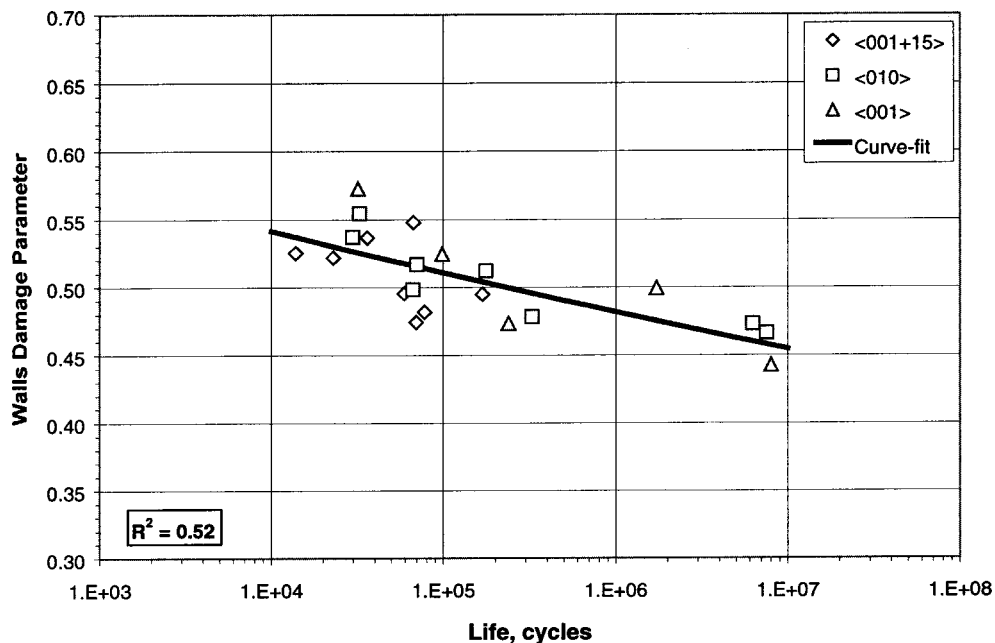


Fig. 7 Walls parameter versus life, 1100°F and $R=0.1$

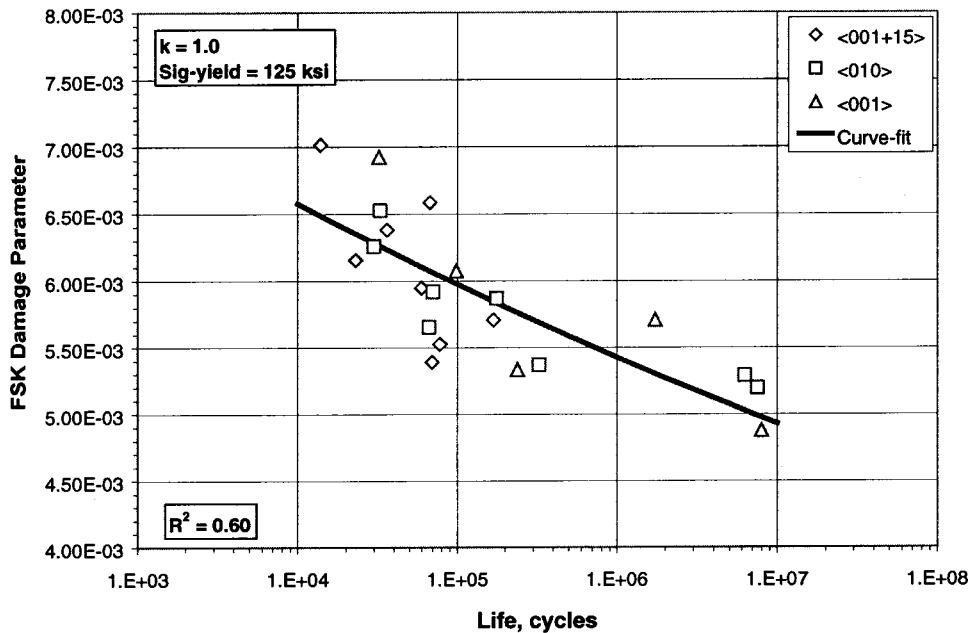


Fig. 8 Fatemi-Socie-Kurath parameter, 1100°F, $R=0.1$

dependent on choice of the fitting parameter, k . They were able to correlate the current fatigue data well when $k \cong 0$ was used. In this case these parameters were similar to the SSR parameter.

Based on how well the different damage parameters (i) correlated with the observed critical planes and (ii) correlated the fatigue data for the different specimen orientations, it appears that the SSR, Walls, and CCB damage parameters are well suited for the HCF analysis of single crystal materials.

Summary

A “critical plane” fatigue modeling approach was developed in the present study to analyze the HCF failures in single crystal materials. This approach accounted for the effects of crystal ori-

entation and the micromechanics of the deformation and slip mechanisms observed in single crystal materials. Several multi-axial critical plane parameters were evaluated using experimentally measured fatigue lives and HCF initiation sites, at 1100°F. Microscopic observations of the fracture surfaces and X-ray diffraction were used to determine the actual octahedral plane (or facet) on which fatigue initiation occurred. These experimentally determined HCF initiation planes were compared with the analytically predicted “critical planes.” The different parameters were also evaluated by determining how well they were able to correlate the fatigue data for the different specimen orientations.

Based on the present evaluation, the shear stress range, Walls and Chu-Conle-Bonnen damage parameters, were found to be

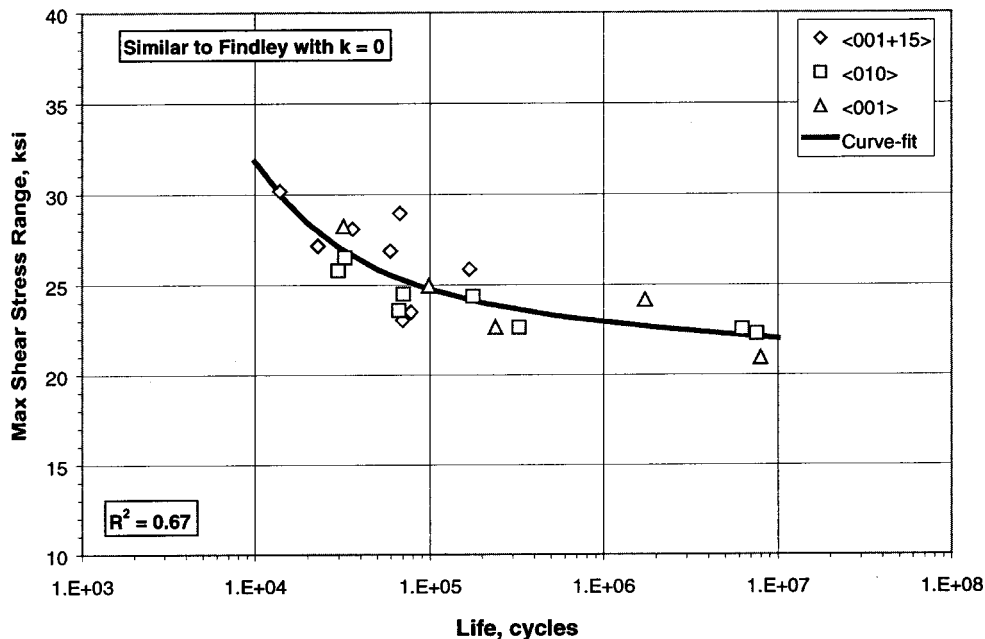


Fig. 9 Max shear stress range, 1100°F and $R=0.1$

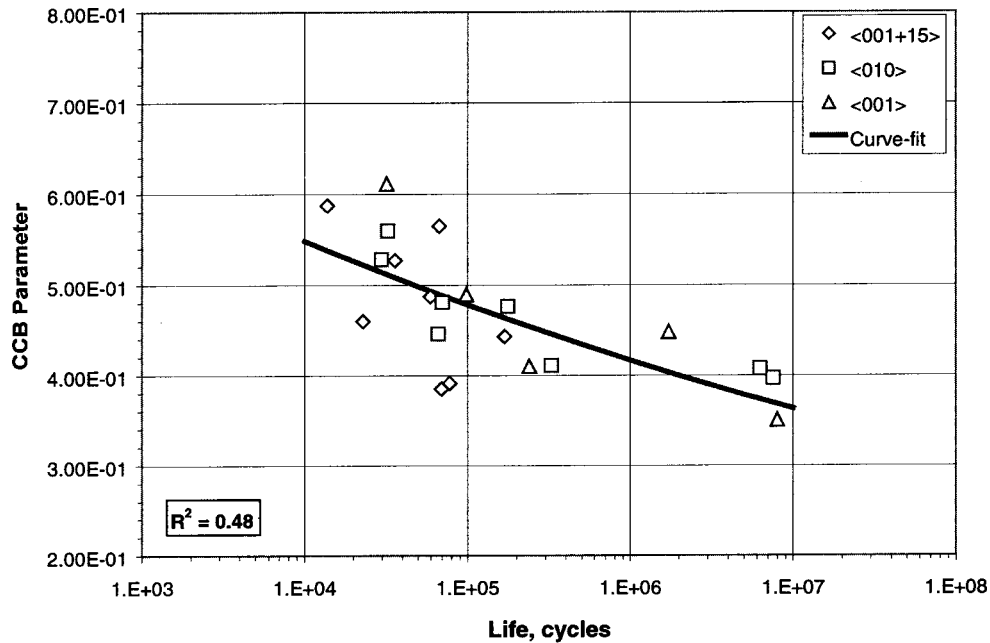


Fig. 10 Chu-Conle-Bonnen parameter, 1100°F and $R=0.1$

well suited for the HCF analysis of single crystal materials. The fatigue modeling approach presented in this paper provides a consistent method to account for the effects of single crystal anisotropy and also for the micromechanical preferred slip deformation mechanisms operative in a single crystal material.

Acknowledgments

This work was sponsored by the US Air Force under UDRI contract number RSC 99009. The authors also appreciate the contributions of Pratt & Whitney colleagues, Mr. Keith Kersey and Mr. David Gibbons, Mr. David Roe, and Mr. Bruce Hockaday in this study.

Appendix A

The strains, $\{\varepsilon_{XYZ}\}$, in the loading (X - Y - Z)-coordinate system are calculated using the given stresses, $\{\sigma_{XYZ}\}$, as

$$\{\varepsilon_{XYZ}\} = [S_{\text{eff}}]\{\sigma_{XYZ}\} \quad (A1)$$

where $[S_{\text{eff}}]$ is the transformed compliance matrix which can be determined using the procedure described below.

For a single crystal material, which exhibits cubic symmetry, the generalized Hooke's law can be expressed using only three independent elastic constants: the Young's modulus, E , the Poisson's ratio, ν , and the shear modulus, G . The strains, $\{\varepsilon_{123}\}$, in the

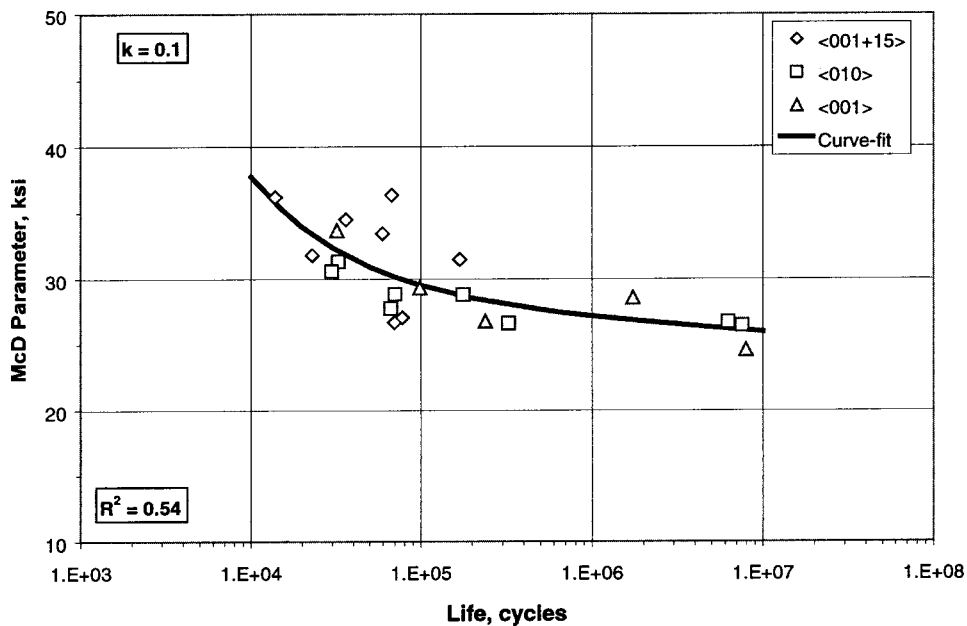


Fig. 11 McDiarmid parameter, 1100°F and $R=0.1$

crystal coordinate system (1-2-3) can be related to the stresses, $\{\sigma_{123}\}$, using the compliance matrix, $[S_c]$ as, [5]:

$$\{\varepsilon_{123}\} = [S_c]\{\sigma_{123}\}$$

$$\text{where, } [S_c] = \begin{bmatrix} \frac{1}{E} & -\frac{\nu}{E} & -\frac{\nu}{E} & 0 & 0 & 0 \\ -\frac{\nu}{E} & \frac{1}{E} & -\frac{\nu}{E} & 0 & 0 & 0 \\ -\frac{\nu}{E} & -\frac{\nu}{E} & \frac{1}{E} & 0 & 0 & 0 \\ 0 & 0 & 0 & \frac{1}{G} & 0 & 0 \\ 0 & 0 & 0 & 0 & \frac{1}{G} & 0 \\ 0 & 0 & 0 & 0 & 0 & \frac{1}{G} \end{bmatrix} \quad (A2)$$

Using Eqs. (2) and (A2) we have

$$\{\varepsilon_{XYZ}\} = [Q][S_c][P]^{-1}\{\sigma_{XYZ}\}. \quad (A3)$$

By comparing Eqs. (A1) and (A3), the transformed compliance matrix $[S_{\text{eff}}]$ can be expressed as

$$[S_{\text{eff}}] = [Q][S_c][P]^{-1}. \quad (A4)$$

Thus, the transformed compliance matrix $[S_{\text{eff}}]$ can be determined from Eq. (A4) when the elastic constants, E , ν , and G are known

in the crystal coordinate system and the direction cosines (see Table 3) between the crystal (1-2-3)-coordinate system and the loading (X - Y - Z)-coordinate system are known.

References

- [1] Cowles, B. A., 1996, "High Cycle Fatigue Failure in Aircraft Gas Turbines: An Industry Perspective," *Int. J. Fract.*, **80**, pp. 147–163.
- [2] Deluca, D. P., and Annis, C., 1995, "Fatigue in Single Crystal Nickel Superalloys," Final Technical Report, Office of Naval Research Contract No. N00014-91-C-0124, Department of the Navy, FR23800, Aug.
- [3] Walls, D., 1997, "Shear-Based Fatigue Failure Criteria for PWA 1480 Single Crystal," Pratt & Whitney internal document.
- [4] Arakare, N. K., and Swanson, G., 2000, "Effect of Crystal Orientation on Fatigue Failure of Single Crystal Nickel Base Turbine Blade Superalloys," *Proceedings of the International Gas Turbine & Aeroengine Congress & Exhibition*, Munich, Germany, May 8–11.
- [5] Lekhnitskii, S. G., 1963, *Theory of Elasticity of an Anisotropic Elastic Body*, Holden-Day, Oakland, CA.
- [6] Findley, W. N., 1959, "A Theory for the Effect of Mean Stress on Fatigue of Metals Under Combined Torsion and Axial Load or Bending," *Trans. ASME, J. Eng. Ind.*, **81**, pp. 301–306.
- [7] Fatemi, A., and Socie, D. F., 1988, "A Critical Plane Approach to Multiaxial Fatigue Damage Including Out-of-Phase Loading," *Fatigue Fract. of Eng. Mater.*, **11**(3), pp. 149–165.
- [8] Fatemi, A., and Kurath, P., 1988, "Multiaxial Fatigue Life Predictions Under the Influence of Mean-Stresses," *Trans. ASME J. Eng. Mater. Technol.*, **110**, pp. 380–388.
- [9] Chu, C.-C., Conle, F., and Bonnen, J. J., 1993, "Multiaxial Stress-Strain Modeling and Fatigue Life Prediction of SAE Axle Shafts," *Advances in Multiaxial Fatigue*, D. L. McDowell and R. Ellis, eds., ASTM, Philadelphia, PA, ASTM STP 1191, pp. 37–54.
- [10] McDiarmid, D. L., 1991, "A General Criterion for High Cycle Multiaxial Fatigue Failure," *Fatigue Fract. Eng. Mater. Struct.*, **14**, 429–453.

T. N. Shiau
Professor

W. C. Hsu
Graduate Student

Department of Mechanical Engineering,
National Chung Cheng University,
621 Chia Yi,
Taiwan, ROC

J. R. Chang
Assistant Professor,
Department of Aircraft Engineering,
Air Force Institute of Technology,
820 Kaohsiung County,
Taiwan, ROC

Dynamic Response of a Hydrodynamic Thrust Bearing-Mounted Rotor

For investigating the dynamic response of a hydrodynamic thrust bearing-mounted flexible rotor, the dynamic characteristic data of thrust bearings for high surface velocities are applied for constructing the equation of motion for the rotor system, which is modeled with the finite element method. Based on the short bearing approximation and the π film cavitation model of the nonlinear oil-film forces, the dynamic responses are investigated using direct numerical integration with a variable order solver based on the numerical differentiation formulas. Harmonic, quasi-periodic, and chaotic motions are predicted for a range of spin speeds of the rotor. Poincaré maps of predicted rotor trajectories are also examined. It shows that spin speeds of the rotor and the oil film force coefficient might promote undesirable nonsynchronous vibrations. [DOI: 10.1115/1.1690769]

Introduction

For safe operation of high-speed turbomachinery, it is common practice to install squeeze film dampers to reduce the vibrations caused by unbalanced forces, [1]. There has been much research focusing on the stability of the unbalanced response of rotors mounted in journal and squeeze film bearings. A nonsynchronous mode of operation was mentioned by Mohan and Hahn [2]. Zhao et al. [3] had studied the stability of unbalanced responses of a squeeze film damped flexible rotor.

A high-speed rotor is usually equipped with a thrust bearing with two hydrodynamic oil films. Due to the relative motion of the thrust collar, both oil-films have a considerable effect on the lateral vibrations of the rotor-bearing system as presented by Mittwollen et al. [4]. The dynamic characteristics of hydrodynamic thrust bearing were presented by Storteig and White [5]. Jiang and Yu [6] provided an extensive theoretical investigation into the dynamic behavior of a rotor-bearing system equipped with a hydrodynamic thrust bearing.

Since axial thrust forces may be potentially damaging on the rotor-bearing system, it becomes necessary to consider these effects via thrust bearing on the rotor system motion. In this study, the effects of thrust bearing on shaft vibration are considered and applied to the system equation of motion. Harmonic, quasi-periodic, and chaotic motions, [7], are predicted for a range of spin speeds of the rotor by direct numerical integration. These motions can also be examined by Poincaré maps of the return points on the phase plane.

Hydrodynamic Thrust Bearing

The design of a hydrodynamic thrust bearing is shown in Fig. 1. Approximating the circular pad as a rectangle with length l and width b , as shown in Fig. 2, the dimensionless static and dynamic oil film forces in axial and circumferential directions are functions of the dimensionless displacement of the thrust collar and can be represented as

$$\bar{F}_a = \bar{F}_{a,stat} + \Delta\bar{F}_a \quad (1)$$

$$\bar{F}_c = \bar{F}_{c,stat} + \Delta\bar{F}_c \quad (2)$$

Contributed by the International Gas Turbine Institute (IGTI) of THE AMERICAN SOCIETY OF MECHANICAL ENGINEERS for publication in the ASME JOURNAL OF ENGINEERING FOR GAS TURBINES AND POWER. Paper presented at the International Gas Turbine and Aeroengine Congress and Exhibition, Amsterdam, The Netherlands, June 3–6, 2002; Paper No. 2002-GT-30314. Manuscript received by IGTI, Dec. 2001, final revision, Mar. 2002. Associate Editor: E. Benvenuti.

where $\Delta\bar{F}_a = \gamma_{aa}^* \Delta\bar{u} + \beta_{aa}^* \Delta\bar{u}'$, $\Delta\bar{F}_c = \gamma_{ca}^* \Delta\bar{u}'$ ($' = \partial/\partial\Omega t$). The coefficients, γ_{aa}^* , β_{aa}^* and γ_{ca}^* , and dimensionless forces, $\bar{F}_{a,stat}$ and $\bar{F}_{c,stat}$, have been determined by Mittwollen et al. [4].

For an axial displacement u_o of the thrust collar caused by an axial thrust force applying on the shaft, the static and dynamic oil film forces exerted on each side of the thrust collar, as shown in Fig. 3, can be represented as

$$F_a^r = F_{a,stat}^r + \Delta F_a^r \quad (3)$$

$$F_a^l = F_{a,stat}^l + \Delta F_a^l \quad (4)$$

Thus the total axial oil film forces acting on the thrust collar can be arranged as

$$F_x = F_a^l - F_a^r = -F_{a,stat} - k_a u - c_a \dot{u} \quad (5)$$

where $F_{a,stat}$, k_a , and c_a are functions of axial displacement u_o of the thrust collar as given in Appendix A.

A change of the tilting angles (B, Γ) of the thrust collar changes the film thickness h_o of the single pad and therefore alters the axial and circumferential forces. Excluded the negligible reacting forces and momenta due to the radial movement of the thrust collar, as shown in Fig. 3, the reacting forces and momenta caused by the tilting angles (B, Γ) and tilting angular velocities ($\dot{B}, \dot{\Gamma}$) can be determined. Combining the axial oil film force (F_x) and lateral nonlinear forces (f_v, f_w) caused by the radial oil film forces, the total reacting forces and momenta exerted on the thrust collar can be represented as

$$\begin{Bmatrix} F_x \\ F_y \\ F_z \end{Bmatrix} = \begin{bmatrix} -c_a & 0 & 0 \\ 0 & 0 & 0 \\ 0 & 0 & 0 \end{bmatrix} \begin{Bmatrix} \dot{u} \\ \dot{B} \\ \dot{\Gamma} \end{Bmatrix} + \begin{bmatrix} -k_a & 0 & 0 \\ 0 & k_{yB} & 0 \\ 0 & 0 & k_{yB} \end{bmatrix} \begin{Bmatrix} u \\ B \\ \Gamma \end{Bmatrix} + \begin{Bmatrix} F_{a,stat} \\ 0 \\ 0 \end{Bmatrix} + \begin{Bmatrix} 0 \\ f_v \\ f_w \end{Bmatrix} \quad (6)$$

$$\begin{Bmatrix} M_B \\ M_\Gamma \end{Bmatrix} = \begin{bmatrix} -k_{BB} & 0 \\ 0 & -k_{BB} \end{bmatrix} \begin{Bmatrix} B \\ \Gamma \end{Bmatrix} + \begin{bmatrix} -c_{BB} & 0 \\ 0 & -c_{BB} \end{bmatrix} \begin{Bmatrix} \dot{B} \\ \dot{\Gamma} \end{Bmatrix} \quad (7)$$

where k_{yB} , k_{BB} , and c_{BB} are functions of axial displacement u_o of the thrust collar as given in Appendix A. Ω is the spin speed of the rotor. And the lateral nonlinear oil film forces (f_v, f_w) are

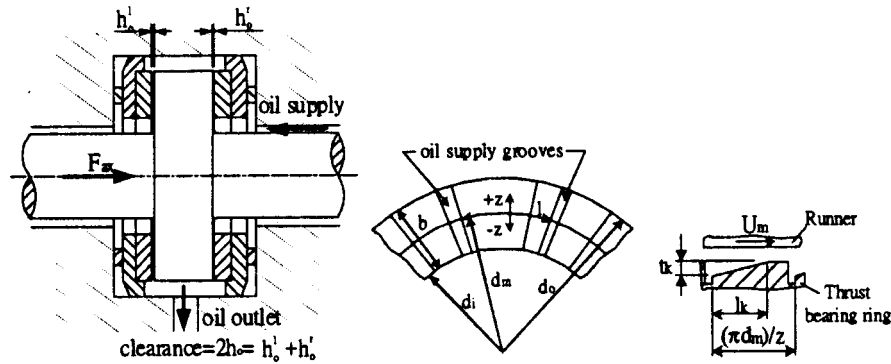


Fig. 1 Thrust bearing configuration, [4]

$$f_v = -B \int_{\theta_1}^{\theta_2} \frac{(\dot{v} \cos \theta + \dot{w} \sin \theta)/C_r}{(1 - v \cos \theta/C_r - w \sin \theta/C_r)^3} \cos \theta d\theta \quad (8)$$

$$f_w = -B \int_{\theta_1}^{\theta_2} \frac{(\dot{v} \cos \theta + \dot{w} \sin \theta)/C_r}{(1 - v \cos \theta/C_r - w \sin \theta/C_r)^3} \sin \theta d\theta \quad (9)$$

where $B = \eta r L^3 / C_r^2$ and C_r is the radial clearance of the squeeze film damper. Using π film theory, $\phi = \tan^{-1}(w/v)$, $\theta_2 = \tan^{-1}(-\dot{v}/\dot{w})$, and $\theta_2 = \theta_1 + \pi$.

System Equations of Motion

The rotor system considered here, as shown in Fig. 4, consists of the following components: flexible shaft, unbalanced rigid disk, journal bearing and hydrodynamic thrust bearing. The system equations of motion are formulated by the finite element method and obtained by assembling the equations of motion of each component. They are given as follows:

$$[M]\{\ddot{q}\} + ([C] - \Omega[G])\{\dot{q}\} + [K]\{q\} = \{F^L\} + \{F^N\} \quad (10)$$

where $[M]$, $[C]$, $[G]$, $[K]$ are the mass, damping, gyroscopic and stiffness matrices of the system, respectively. $\{F^L\}$ and $\{F^N\}$ represent the system linear and nonlinear force vector, respectively. The nonlinear forces only act on the nonlinear supports where journal bearing and thrust bearing are installed. These coefficient matrices are as given in Appendix B.

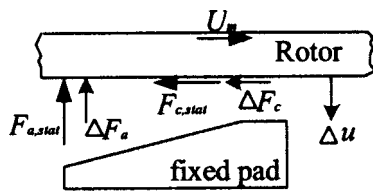


Fig. 2 Static and dynamic oil film forces, [4]

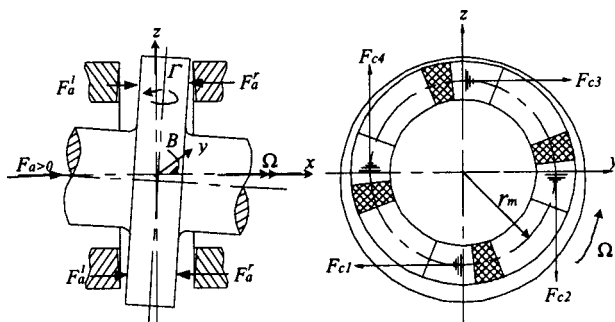


Fig. 3 Thrust bearing, [4]

Bifurcation Diagram

A Poincaré section is a stroboscopic picture of a motion on a phase plane and it consists of the time series at a constant interval of T ($T = 2\pi/\Omega$). The point on the Poincaré section is referred to as the return point. For the numerical computation of a bifurcation diagram, the rotor speed is increased in a constant step and the state variables at the end of the integration are used as initial values for the next speed. After reaching the steady state, the Z-coordinates ($W_1(nT)$, $W_2(nT)$, and $W_3(nT)$ for $n=1$ to 300) of the return points of consecutive 300 cycles at each node in the Poincaré section are then plotted versus the rotor speed.

Numerical Examples and Results

A high-speed rotor system, as shown in Fig. 4, is employed to demonstrate the performance of the method. The corresponding configuration data of the thrust pad, rotor shaft and the disk are $t_k = 4.8 \times 10^{-5}$ m, $h_o = 10^{-4}$ m, $b = 2.5 \times 10^{-2}$ m, $d_m = 7.5 \times 10^{-2}$ m, $z = 4$, $l = \pi d_m/4$, $\rho = 7680$ kg/m³, $L_1 = L_2 = 200$ mm, $E = 2.07 \times 10^{11}$ N/m², $G = 7.96 \times 10^{10}$ N/m², $m_d = 22$ kg, $e = 10^{-4}$ m, $I_d = 0.031$ kgm², $I_p = 0.062$ kgm², $C_r = 1$ mm. Due to the relative motion of the thrust collar, the effect of both oil-films on the lateral vibrations of the rotor-bearing system is first investigated. The coefficients of the thrust bearing are determined using various applied axial forces shown in Figs. 5–9. These results show that the stiffness coefficients k_a and k_{BB} increase as spin speed of the rotor increases and are independent of axial force, whereas k_{yB} increases as axial force increases and is independent of spin speed of the rotor. On the contrary, the damping coefficients c_a and c_{BB} decrease as spin speed of the rotor and little difference is observed with axial force variation. The results also show that the thrust bearing has little effect on the lateral damping coefficients.

Since the dynamic response will change with various oil film force coefficients B and different disk locations, these effects are first investigated by the bifurcation diagrams. The dimensionless displacement of response is defined as the radius of the orbit divided by radial clearance C_r of the bearing. The dimensionless Z-coordinates ($W_1(nT)$, $W_2(nT)$, and $W_3(nT)$) denote the return points at nodes where the journal bearing, disk and thrust bearing are located, respectively. They are plotted in the Poincaré section

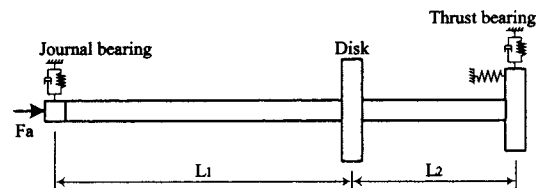


Fig. 4 Configuration of a high-speed rotor system

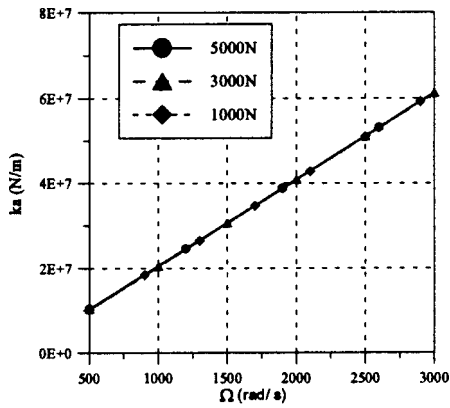


Fig. 5 Stiffness coefficients k_a versus Ω

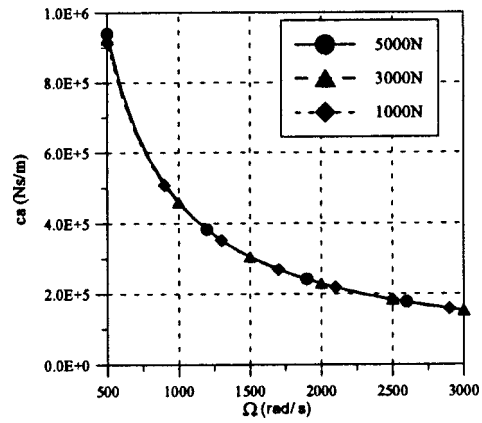


Fig. 8 Damping coefficients c_a versus Ω

versus the rotor speeds with various oil film force coefficients B and different disk locations as shown in Figs. 10–21.

The distances of lengths are $L_1=200$ mm, $L_2=200$ mm for the case when the disk is located at the middle of the rotor. The bifurcation diagrams with $B=100$ and $B=200$ are plotted in Figs. 10–12 and 13–15, respectively. The results show that chaotic motion occurs at higher spin speed and the spread of the return points is depressed when oil film force coefficient B gets larger. The distances of lengths are $L_1=100$ mm, $L_2=300$ mm and $L_1=300$ mm, $L_2=100$ mm for the cases when the disk is located near the left and right of the rotor, respectively. The bifurcation diagrams with various disk location when $B=100$ are plotted in Figs. 13–21, respectively. As compared from the results, the

spread of the return points is depressed for the case when the disk is located near the right of the rotor where the thrust bearing is installed.

For the case when the disk is located at the middle of the rotor and the oil film force coefficient B is 200, the dynamic response is also examined. Harmonic, chaotic and quasi-periodic motions are predicted from the phase diagrams of the return points as shown in Figs. 22(a)–(d). For a harmonic motion, there will be only one mark on the phase diagram as shown in Fig. 22(a). By increasing the spin speed of the rotor further to 2270 rad/s and 2430 rad/s the responses tend to become chaotic as shown in Figs. 22(b) and (c). The quasi-periodic response results in closed orbits on Poincaré map as shown in Fig. 22(d).

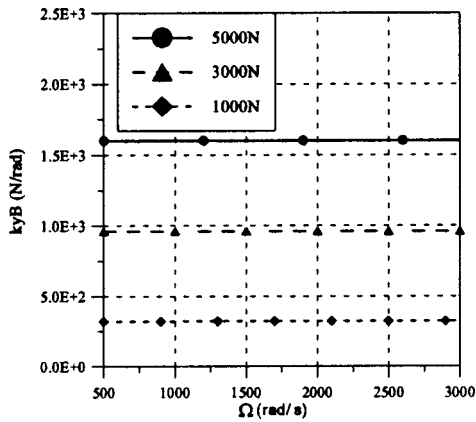


Fig. 6 Stiffness coefficients k_{yB} versus Ω

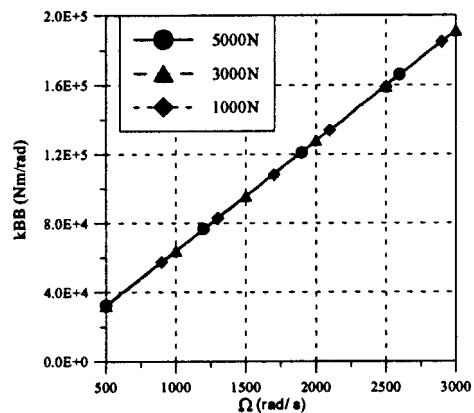


Fig. 7 Stiffness coefficients k_{BB} versus Ω

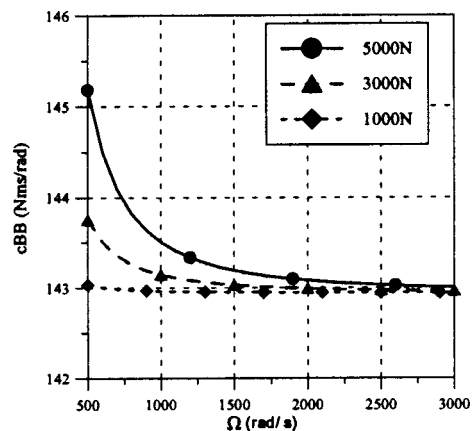


Fig. 9 Damping coefficients c_{BB} versus Ω

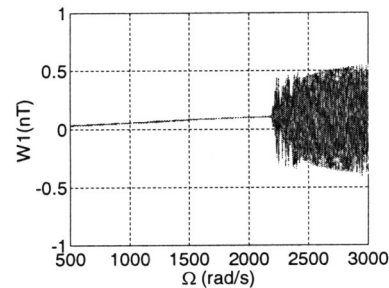


Fig. 10 Bifurcation diagram $W_1(nT)$ at $B=200$, $L_1=200$

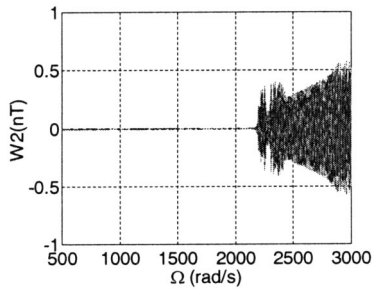


Fig. 11 Bifurcation diagram W_2 (nT) at $B=200, L_1=200$

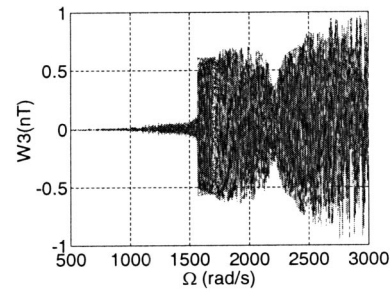


Fig. 15 Bifurcation diagram W_3 (nT) at $B=100, L_1=200$

Conclusions

In this paper, effects of a hydrodynamic thrust bearing on shaft vibration are employed to study the dynamic behavior of the rotor system. The results can be summarized as follows:

1. The stiffness coefficients k_a and k_{BB} increase as spin speed of the rotor increases and are independent of axial force, whereas k_{yB} increases as axial force increases and is independent of spin speed of the rotor.

2. The damping coefficients c_a and c_{BB} decrease as spin speed of the rotor and little difference is observed with axial force variation.

3. The thrust bearing has more effects on the lateral stiffness coefficients than the lateral damping coefficients.

4. Chaotic motion occurs at higher spin speed and the spread of the return points is depressed when oil film force coefficient B gets larger.

5. The spread of the return points can be depressed when the disk is located near the thrust bearing.

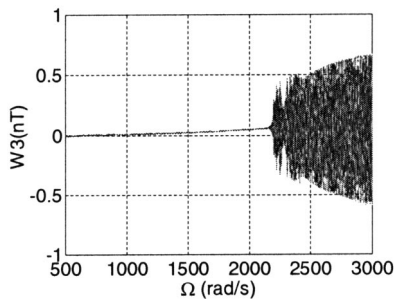


Fig. 12 Bifurcation diagram W_3 (nT) at $B=200, L_1=200$

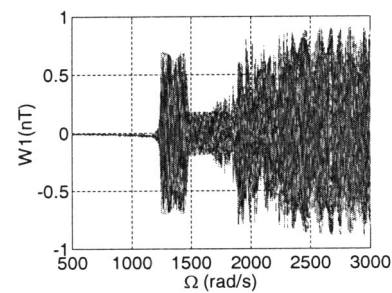


Fig. 16 Bifurcation diagram W_1 (nT) at $B=100, L_1=100$

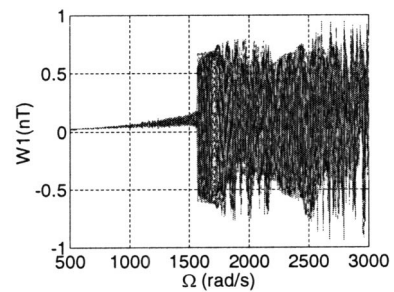


Fig. 13 Bifurcation diagram W_1 (nT) at $B=100, L_1=200$

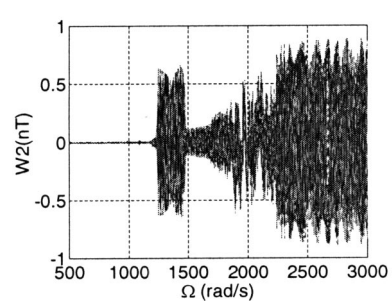


Fig. 17 Bifurcation diagram W_2 (nT) at $B=100, L_1=100$

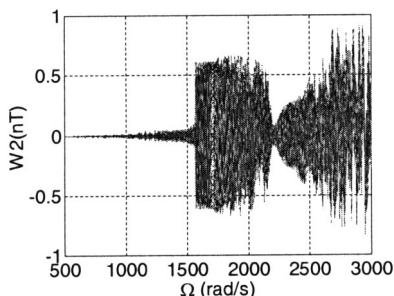


Fig. 14 Bifurcation diagram W_2 (nT) at $B=100, L_1=200$

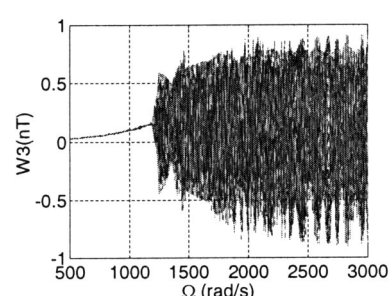


Fig. 18 Bifurcation diagram W_3 (nT) at $B=100, L_1=100$

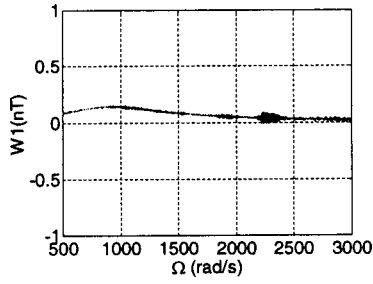


Fig. 19 Bifurcation diagram W_1 (nT) at $B=100$, $L_1=300$

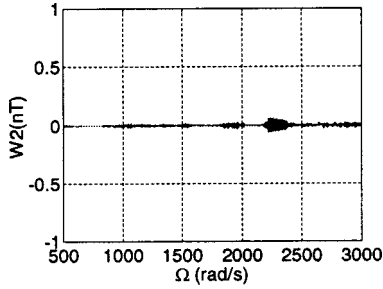


Fig. 20 Bifurcation diagram W_2 (nT) at $B=100$, $L_1=300$

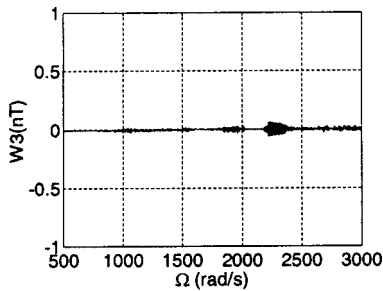


Fig. 21 Bifurcation diagram W_3 (nT) at $B=100$, $L_1=300$

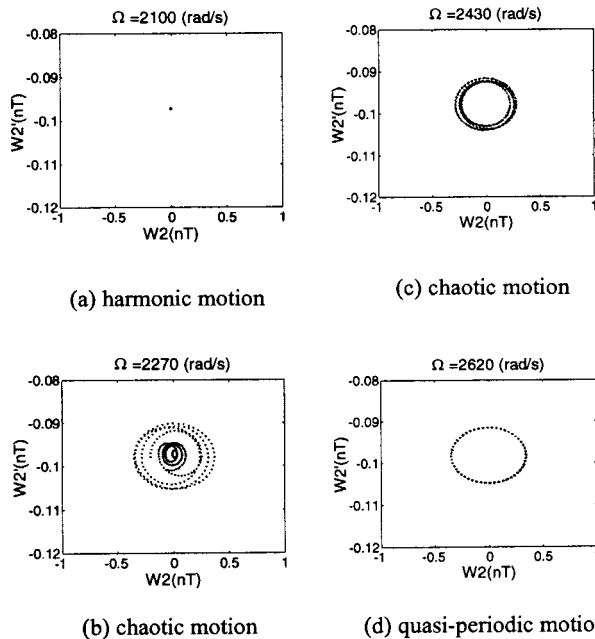


Fig. 22 Phase diagram of W_2 (nT) at various Ω ; (a) harmonic motion, (b) chaotic motion, (c) chaotic motion, (d) quasi-periodic motion

6. Harmonic, quasi-periodic, and chaotic motions are predicted for a range of spin speeds of the rotor.

Nomenclature

- A = cross section area of the rotor
- $B = B = \eta r L^3 / C_r^2$, oil film force parameter
- $[C]$ = damping matrix of the system
- C_r = clearance of the bearing
- E = Young's modulus of rotor shaft
- $[F^L], [F^N]$ = System linear and nonlinear force vectors
- $\bar{F}_{a,stat}, \bar{F}_{c,stat}$ = dimensionless static oil film forces on thrust pad on normal and tangential directions, respectively
- F_x, F_y, F_z = oil film forces on x , y , and z -directions, respectively
- $[G]$ = gyroscopic matrix of the system
- G = shear modulus
- I, I_d, I_p = area moment of inertia of cross section of rotor and diametrical and polar mass moment of disk inertia, respectively
- $[K]$ = stiffness matrix of the system
- L = thrust collar width
- L_1, L_2 = length of each rotor element
- $[M]$ = mass matrix of the system
- M_B, M_Γ = moments caused by oil film forces about y and z -axes, respectively
- $[Q(T)]$ = Floquet transition matrix
- T = a period T is $2\pi/\Omega$ when spin speed is Ω
- V, W = nodal dimensionless translation displacements
- $W_i(nT), i=1-3$ = the return points of nodes where the journal bearing, disk and thrust bearing are located
- b = thrust pad width
- c_a, c_{BB} = damping coefficients of thrust bearing
- d_m = mean diameter of thrust bearing
- e = disk eccentricity
- f_v, f_w = radial oil film forces acting on the bearing
- h_o = thrust oil film thickness
- k_a, k_{yB}, k_{BB} = stiffness coefficients of thrust bearing
- m_d = mass of disk
- l = thrust pad length
- $\{q\}$ = coordinate vectors for the system
- r = thrust collar radius
- u, v, w, B, Γ = nodal translation and rotation displacements
- u_o = static oil film thickness
- z = number of thrust pad
- Λ_i = eigenvalue of Floquet transition matrix
- Ω = spin speed of rotor
- $\beta_{\alpha\alpha}^*, \gamma_{\alpha\alpha}^*, \gamma_{c\alpha}^*$ = the dimensionless static and dynamic oil film force coefficients in axial and circumferential directions
- η = viscosity of lubricant

Appendix A

The Static Force and Coefficients for Thrust Bearing.

$$F_{a,stat} = \Omega \left(\frac{\bar{F}_{a,stat}^l \left(\frac{h_o + u_o}{t_k} \right)}{(h_o + u_o)^2} - \frac{\bar{F}_{a,stat}^r \left(\frac{h_o - u_o}{t_k} \right)}{(h_o - u_o)^2} \right) b l^2 \frac{d_m}{2} \eta + \Omega k_a u_o \quad (11)$$

$$k_a = \Omega \left(\frac{\gamma_{aa}^* \left(\frac{h_o - u_o}{t_k} \right)}{(h_o - u_o)^3} + \frac{\gamma_{aa}^* \left(\frac{h_o + u_o}{t_k} \right)}{(h_o + u_o)^3} \right) b l^2 \frac{d_m}{2} \eta \quad (12)$$

$$c_a = \left(\frac{\beta_{aa}^* \left(\frac{h_o - u_o}{t_k} \right)}{(h_o - u_o)^3} + \frac{\beta_{aa}^* \left(\frac{h_o + u_o}{t_k} \right)}{(h_o + u_o)^3} \right) bl^3 \eta \quad (13)$$

$$k_{yB} = \Omega \left(\frac{\gamma_{ca}^* \left(\frac{h_o - u_o}{t_k} \right)}{(h_o - u_o)^2} - \frac{\gamma_{ca}^* \left(\frac{h_o + u_o}{t_k} \right)}{(h_o + u_o)^2} \right) \frac{bl \eta z (d_m^2 + b^2)}{8} \quad (14)$$

$$k_{BB} = \Omega \left(\frac{\gamma_{aa}^* \left(\frac{h_o - u_o}{t_k} \right)}{(h_o - u_o)^3} + \frac{\gamma_{aa}^* \left(\frac{h_o + u_o}{t_k} \right)}{(h_o + u_o)^3} \right) \frac{d_m bl^2 \eta z (d_m^2 + b^2)}{16} \quad (15)$$

$$c_{BB} = \left(\frac{\beta_{aa}^* \left(\frac{h_o - u_o}{t_k} \right)}{(h_o - u_o)^3} + \frac{\beta_{aa}^* \left(\frac{h_o + u_o}{t_k} \right)}{(h_o + u_o)^3} \right) \frac{bl^3 \eta z (d_m^2 + b^2)}{8} \quad (16)$$

Appendix B

Coefficient Matrices of the System.

$$\{q\} = \{u_1 \ v_1 \ w_1 \ B_1 \ \Gamma_1 \ u_2 \ v_2 \ w_2 \ B_2 \ \Gamma_2 \ u_3 \ v_3 \ w_3 \ B_3 \ \Gamma_3\}^T \quad (17)$$

$$\{F^L\} = \{F_a \ 0 \ 0 \ 0 \ 0 \ 0 \ m_d e \cos \Omega t \ m_d e \sin \Omega t \ 0 \ 0 \ -F_a \ 0 \ 0 \ 0 \ 0\}^T \quad (18)$$

$$\{F^N\} = \{0 \ f_{v1} \ f_{w1} \ 0 \ 0 \ 0 \ 0 \ 0 \ 0 \ 0 \ 0 \ f_{v3} \ f_{w3} \ 0 \ 0\}^T \quad (19)$$

$$[M] = [M_{i,j}] = [M_{j,i}],$$

where

$$M_{1,1} = 2M_{6,1} = \rho A L_1 / 3, \quad M_{6,6} = \rho A (L_1 + L_2) / 3 + m_d,$$

$$M_{11,11} = 2M_{11,6} = \rho A L_2 / 3,$$

$$M_{2,2} = M_{3,3} = m_{11}, \quad M_{5,2} = -M_{4,3} = -m_{21}, \quad M_{4,4} = M_{5,5} = m_{31},$$

$$M_{7,2} = M_{8,3} = m_{41}, \quad M_{7,5} = -M_{8,4} = M_{9,3} = -M_{10,2} = m_{51},$$

$$M_{9,4} = M_{10,5} = -m_{61}, \quad M_{7,7} = M_{8,8} = m_{11} + m_{12} + m_d,$$

$$M_{9,9} = M_{10,10} = m_{31} + m_{32} + I_d, \quad M_{9,8} = -M_{10,7} = m_{21} - m_{22},$$

$$M_{12,7} = M_{13,8} = m_{42}, \quad M_{12,10} = -M_{13,9} = M_{14,8} = -M_{15,7} = m_{52},$$

$$M_{14,9} = M_{15,10} = -m_{62}, \quad M_{12,12} = M_{13,13} = m_{12},$$

$$M_{14,13} = -M_{15,12} = m_{22},$$

$$M_{14,14} = M_{15,15} = m_{32}, \quad \text{others} = 0. \quad (20)$$

$$[C] = [C_{i,j}], \quad C_{11,11} = c_a, \quad C_{14,14} = c_{BB},$$

$$C_{15,15} = c_{BB}, \quad \text{others} = 0. \quad (21)$$

$$[G] = [G_{i,j}] = -[G_{j,i}],$$

where

$$G_{3,2} = G_{7,3} = -G_{8,2} = g_{11},$$

$$G_{4,2} = G_{5,3} = G_{7,4} = G_{8,5} = G_{9,2} = G_{10,3} = g_{21},$$

$$G_{5,4} = g_{31}, \quad G_{9,5} = -G_{10,4} = g_{41}, \quad G_{8,7} = g_{11} + g_{12},$$

$$G_{9,7} = G_{10,8} = -g_{21} + g_{22},$$

$$G_{10,9} = g_{31} + g_{32} - I_p, \quad G_{12,8} = -G_{13,7} = g_{12}, \quad (22)$$

$$G_{12,9} = G_{13,10} = G_{14,7} = G_{15,8} = -G_{14,12} = -G_{15,13} = g_{22},$$

$$G_{14,10} = -G_{15,9} = g_{42}, \quad G_{13,12} = g_{12}, \quad G_{15,14} = g_{32}, \quad \text{others} = 0.$$

$$[K] = [K^1] + [K^2] \quad (23)$$

$$[K^1] = [K_{i,j}^1] = [K_{j,i}^1],$$

where

$$K_{1,1}^1 = -K_{6,1}^1 = EA/L_1, \quad K_{6,6}^1 = EA/L_1 + EA/L_2,$$

$$K_{11,11}^1 = -K_{11,6}^1 = EA/L_2,$$

$$K_{2,2}^1 = K_{3,3}^1 = -K_{7,2}^1 = -K_{8,3}^1 = k_{11},$$

$$K_{5,2}^1 = -K_{4,3}^1 = -K_{7,5}^1 = K_{8,4}^1 = -K_{9,3}^1 = K_{10,2}^1 = k_{31},$$

$$K_{4,4}^1 = K_{5,5}^1 = k_{21}, \quad K_{9,4}^1 = K_{10,5}^1 = k_{41},$$

$$K_{7,7}^1 = K_{8,8}^1 = k_{11} + k_{12},$$

$$K_{9,9}^1 = K_{10,10}^1 = k_{21} + k_{22},$$

$$K_{12,12}^1 = K_{13,13}^1 = -K_{12,7}^1 = -K_{13,8}^1 = k_{12},$$

$$K_{9,8}^1 = -K_{8,7}^1 = k_{31} - k_{32},$$

$$K_{15,7}^1 = -K_{14,8}^1 = K_{13,9}^1 = K_{14,13}^1 = -K_{15,12}^1 = k_{32},$$

$$K_{14,9}^1 = K_{15,10}^1 = k_{42}, \quad K_{14,14}^1 = K_{15,15}^1 = k_{22}, \quad \text{others} = 0.$$

$$[K^2] = [K_{i,j}^2],$$

where

$$K_{11,11}^2 = k_a, \quad K_{12,14}^2 = -k_{yB}, \quad K_{13,15}^2 = -k_{yB},$$

$$K_{14,14}^2 = k_{BB}, \quad K_{15,15}^2 = k_{BB}, \quad \text{others} = 0. \quad (25)$$

where $i = 1, 2$ for each following term.

$$\Phi_i = \frac{12EI}{kGAL_i^2}, \quad \Xi_{1i} = \frac{\rho AL_i}{420(1 + \Phi_i)^2},$$

$$\Xi_{2i} = \frac{\rho Al}{30L_i(1 + \Phi_i)^2}, \quad \Xi_{3i} = \frac{-\rho l}{15L_i(1 + \Phi_i)},$$

$$\Xi_{4i} = \frac{F_a}{30L_i(1 + \Phi_i)^2}, \quad \Xi_{5i} = \frac{EI}{L_i^3(1 + \Phi_i)}.$$

$$m_{1i} = (156 + 294\Phi_i + 140\Phi_i^2)\Xi_{1i} + 36\Xi_{2i}$$

$$m_{2i} = (22 + 38.5\Phi_i + 17.5\Phi_i^2)L_i\Xi_{1i} + (3 - 15\Phi_i)L_i\Xi_{2i}$$

$$m_{3i} = (4 + 7\Phi_i + 3.5\Phi_i^2)L_i^2\Xi_{1i} + (4 + 5\Phi_i + 10\Phi_i^2)L_i^2\Xi_{2i}$$

$$m_{4i} = (54 + 126\Phi_i + 70\Phi_i^2)\Xi_{1i} - 36\Xi_{2i}$$

$$m_{5i} = (13 + 31.5\Phi_i + 17.5\Phi_i^2)L_i\Xi_{1i} - (3 - 15\Phi_i)L_i\Xi_{2i}$$

$$m_{6i} = (3 + 7\Phi_i + 3.5\Phi_i^2)L_i^2\Xi_{1i} + (1 + 5\Phi_i - 5\Phi_i^2)L_i^2\Xi_{2i}$$

$$g_{1i} = 36\Xi_{3i}, \quad g_{2i} = (-3 + 15\Phi_i)L_i\Xi_{3i},$$

$$g_{3i} = (4 + 5\Phi_i + 10\Phi_i^2)L_i^2\Xi_{3i}$$

$$g_{4i} = (1 + 5\Phi_i - 5\Phi_i^2)L_i^2\Xi_{3i},$$

$$k_{1i} = (36 + 60\Phi_i + 30\Phi_i^2)\Xi_{4i} + 12\Xi_{5i}$$

$$k_{2i} = (4 + 5\Phi_i + 2.5\Phi_i^2)L_i^2\Xi_{4i} + (4 + \Phi_i)L_i^2\Xi_{5i},$$

$$k_{3i} = 3L_i\Xi_{4i} + 6L_i\Xi_{5i}$$

$$k_{4i} = (-1 - 5\Phi_i - 2.5\Phi_i^2)L_i^2\Xi_{4i} + (2 - \Phi_i)L_i^2\Xi_{5i}.$$

References

- [1] Holmes, R., 1985, "The Control of Engine Vibration Using Squeeze Film Dampers," *ASME J. Eng. Gas Turbines Power*, **105**, pp. 525–529.
- [2] Mohan, S., and Hahn, E. J., 1974, "Design of Squeeze-Film Damper Supports for Rigid Rotors," *J. Eng. Ind.*, **96**, pp. 976–982.
- [3] Zhao, J. Y., Linnett, I. W., and McLean, L. J., 1994, "Stability and Bifurcation of Unbalanced Response of a Squeeze Film Damped Flexible Rotor," *ASME J. Tribol.*, **116**, pp. 361–368.
- [4] Mittwollen, N., Hegel, T., and Glienicke, J., 1991, "Effect of Hydrodynamic Thrust Bearings on Lateral Shaft Vibrations," *ASME J. Tribol.*, **113**, pp. 811–818.
- [5] Storteig, E., and White, M. F., 1999, "Dynamic Characteristics of Hydro-Dynamically Lubricated Fixed-Pad Thrust Bearing," *Wear*, **232**, pp. 250–255.
- [6] Jiang, P. L., and Yu, L., 1999, "Dynamics of a Rotor-Bearing System Equipped With a Hydrodynamic Thrust Bearing," *J. Sound Vib.*, **227**, pp. 863–872.
- [7] Shiau, T. N., Rao, J. S., Chang, J. R., and Choi, S. T., 1999, "Dynamic Behavior of Geared Rotors," *ASME J. Eng. Gas Turbines Power*, **121**, pp. 494–503.

Dynamic Response of Squeeze Film Dampers Operating With Bubbly Mixtures

Luis San Andres

Professor

Oscar C. De Santiago

Research Assistant

Mechanical Engineering Department,
Texas A&M University,
College Station, TX 77843-3123

Squeeze film dampers (SFDs) aid to attenuate vibrations in compressors and turbines while traversing critical speeds. In actual applications, gas ingestion from the environment may lead to the formation of a foamy lubricant that degrades the rotor/bearing system dynamic performance. Impact and imbalance response tests conducted on a rigid rotor supported on SFDs, and aimed to emulate the pervasive effect of air ingestion into the damper film lands, are reported. Two types of squeeze film damper support the test rotor, one is a conventional cylindrical design with a squirrel cage-type elastic support, and the other is a compact four-pad damper with integral wire EDM elastic supports. Both dampers have identical diameter and radial clearance. Controlled (air in oil) mixtures ranging from pure oil to all air conditions are supplied to the SFDs, and measurements of the transient rotor response to calibrated impact loads are conducted. System damping coefficients, identified from acceleration/load transfer functions, decrease steadily as the air content in the mixture increases. However, measurements of the rotor synchronous imbalance response conducted with a lubricant bubbly mixture (50% air volume) show little difference with test results obtained with pure lubricant supplied to the dampers. The experimental results show that air entrainment is process and device-dependent, and that small amounts of lubricant enable the effective action of SFDs when the rotor traverses a critical speed. [DOI: 10.1115/1.1690770]

Introduction

Squeeze film dampers (SFDs) are customarily used in aircraft gas turbines and process compressors to attenuate rotor vibration amplitudes and reduce forces transmitted from the rotating assembly to the support structure. SFDs derive their behavior from a lubricant being squeezed in the annular space between a nonrotating journal and a bearing housing. The journal, typically mounted on the outer race of rolling element bearings, whirls due to the forces exerted on the rotating shaft, and the squeeze fluid film generates reaction forces opposing the dynamic rotor motions. In modern rotor-bearing systems, integral squeeze film dampers (ISFDs) generate significant damping forces to traverse safely critical speeds, [1]. The advantages of integral dampers over conventional cylindrical SFDs include a shorter axial span, less weight and number of parts, and easiness of installation.

Operation of squeeze film dampers induces air ingestion from the surroundings if there is not enough lubricant flow through the film lands. Lubricant cavitation affects the forced performance of SFDs by creating stiffening (centering) forces which may produce severe system non linearities, [2]. Sustained air entrainment, on the other hand, can dramatically reduce the film forces and limit the damping capability. Air entrainment is more prevalent while a rotor traverses a critical speed with large amplitude of motion and at high rotational speeds.

Diaz and San Andrés [3] advance a model for prediction of the forced response of SFDs operating with bubbly mixtures. Tangential forces decrease rapidly as the air content increases in the bubbly mixture. Figure 1 shows a comparison between experimental and predicted tangential (damping) forces at a fixed whirl frequency of 8.3 Hz, [4]. The measurements and predictions show a quick drop in damping force for very small air volume fractions,

and then a steady linear decrease towards a null force at 100% volume fraction (pure air within the damper clearance). The experiments suggest a simple formula that accounts for the effect of air content on the damping coefficient (C_β), i.e.,

$$C_\beta = C_L(1 - \beta) \quad (1)$$

where C_L is the damping coefficient obtained for a damper filled with lubricant and submerged within an oil bath, and β is the (usually unknown) air volume fraction in the bubbly mixture. A feed-squeeze flow parameter (γ) relates the lubricant feed flow rate (\dot{V}_L) to the dynamic change in volume within the squeeze film gap, i.e.,

$$\gamma = \frac{\dot{V}_L}{\pi D L e \omega} \quad (2)$$

where (ω, e) are the frequency and amplitude of journal motion; and (D) and (L) denote the diameter and length of the damper film lands, respectively. If $\gamma > 1$ then no air entrainment occurs, i.e. the through flow is sufficient to fill the volume change caused by the journal whirl motion. On the other hand, air ingestion and entrapment will occur if $\gamma < 1$ and the damper will then operate with a bubbly lubricant mixture. Reference [3] details a cumbersome formula relating the air volume fraction (β) to the feed parameter (γ). Equation (1) may be used for quick estimation of damping forces during a preliminary SFD design. Reference [3] advances a comprehensive computational analysis, albeit more complex, but validated by extensive experimentation.

Note that (\dot{V}_L) is a function of the supply and discharge pressures and of the flow resistances through the film lands and feed ports. These resistances depend on the damper clearance and feed characteristics, lubricant and mixture viscosities, etc. Thus, air entrainment is device dependent and increases with the amplitude and frequency of motion. Providing enough external pressurization can prevent air entrainment by ensuring a sufficiently large through lubricant flow rate. This condition may not be readily available in practice nor may be desirable in terms of performance, and weight and volume of auxiliary equipment.

Contributed by the International Gas Turbine Institute (IGTI) of THE AMERICAN SOCIETY OF MECHANICAL ENGINEERS for publication in the ASME JOURNAL OF ENGINEERING FOR GAS TURBINES AND POWER. Paper presented at the International Gas Turbine and Aeroengine Congress and Exhibition, Amsterdam, The Netherlands, June 3–6, 2002; Paper No. 2002-GT-30317. Manuscript received by IGTI, Dec. 2001, final revision, Mar. 2002. Associate Editor: E. Benvenuti.

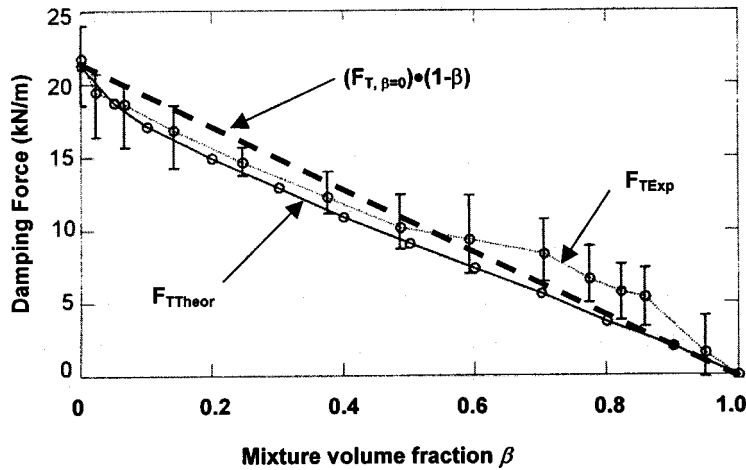


Fig. 1 Experimental and predicted damping force versus air content in a lubricated mixture. Whirl frequency=8.33 Hz, vertical bars denote experimental uncertainty. Source [1].

San Andrés et al. [5] estimate damping coefficients on a small squeeze film damper subjected to unidirectional sine sweep load excitations and operating with controlled bubbly mixtures. For these periodic motions, damping coefficients remain constant for air volume fractions as high as 80%. In contrast, damping coefficients from impact excitations, [6], first increase for volume contents up to 50% and then present a drastic reduction for higher volume fractions. Periodic journal motions in the sweep sine tests expel the air from the lubricant mixture thus rendering constant damping forces, whereas in the impact tests the journal motions of small amplitude and short duration cause the mixture to behave as a fluid of larger viscosity.

The objective of the current experiments is to forward further evidence on the effects of controlled mixtures of air and oil on the dynamic response of a larger rotor mounted on a pair of hydrodynamic bearings in series with SFDs. Rotor responses to impact loads under stationary conditions and rotor imbalance synchro-

nous responses are detailed; and system damping coefficients are estimated from frequency domain transfer functions and peak responses to imbalances, respectively.

Test Rig and Lubrication System

Figure 2 depicts the test rotor supported on two bearing arrangements. A 7.5 kW (10 HP) power supply and DC motor drive the rotor through a flexible coupling. The rotor assembly consists of a shaft (673 mm long and 76.2 mm in diameter) and three disks (25.4 mm thick) shrunk fitted at evenly spaced intervals of 63.5 mm. The two disks closer to the motor end are 279.4 mm in diameter, and the third disk has a diameter of 228.6 mm. The rotor (shaft and disks) including part of the coupling weighs 45.7 kg.

The bearing span is 406 mm with the rotor middle disk located halfway between the two bearing supports. The drive end support comprises a flexure pivot tilting pad journal bearing (FPJB) in

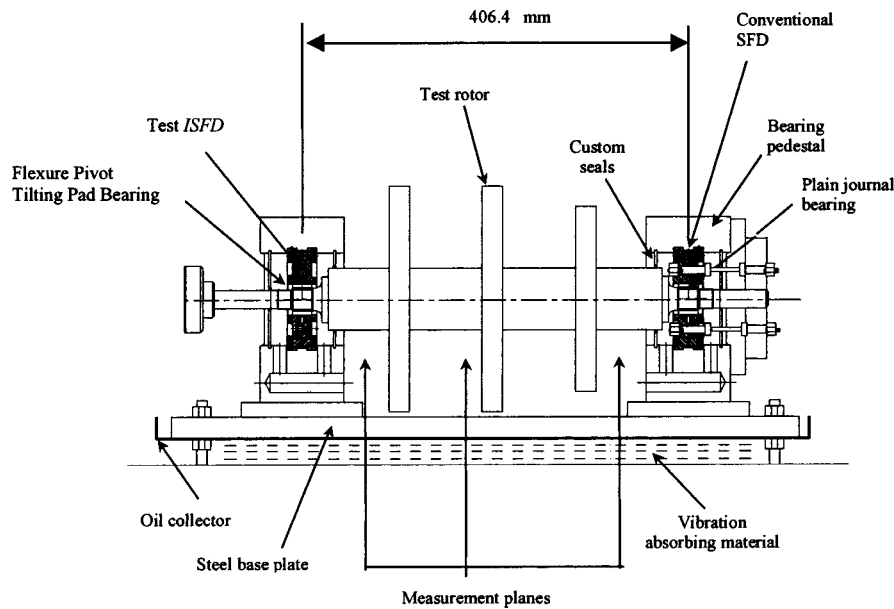


Fig. 2 Test rig for measurements of imbalance response of rotor supported on hydrodynamic bearings and squeeze film dampers

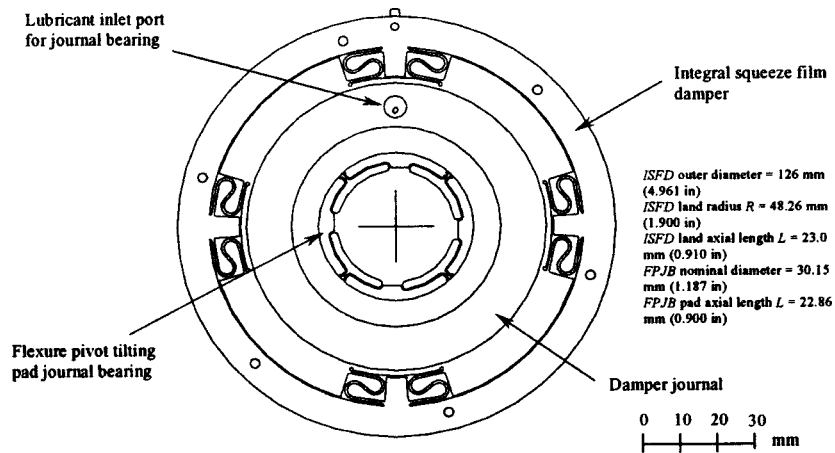


Fig. 3 Configuration of integral squeeze film damper and flexure pivot tilting pad journal bearing

series with an integral SFD (see Fig. 3). The free-end support accommodates a plain journal bearing in series with a cylindrical SFD, as shown in Fig. 4. The bearing pedestals are split elements with a 36 mm wide groove at mid-length of their inner bore. The damper housings rest on this section, and after their installation, the groove becomes a circumferential lubricant feed chamber into the SFDs lands.

A lubrication system delivers oil to the bearing housings, dampers and hydrodynamic bearings, from a 151 liter reservoir through a variable speed gear pump. Turbine flow meters monitor the flow rate supplied to the bearings and dampers, and pressure gauges indicate the static supply pressure into each bearing support element. The average residence time of the oil in the main tank is about 30 minutes, which is considered enough to free the lubricant from any remaining air. A sparger element generates a bubbly mixture (air in oil) supplied to the damper elements *only*. The sparger consists of a porous material cylinder encased in a metallic pipe. Air flows within the inner cylinder, and forced through the porous media, emerges as small bubbles mixing with the up-coming oil stream, thus forming a bubbly mixture. The air supply pressure must be slightly higher than the oil pressure to avoid reverse flow, but not too high that it blocks the lubricant flow. All lubricant lines purged prior to the experiments allow accurate measurements of oil flow rate, and thus better estimates of the air volume fraction in the mixture.

The lubricant used in the experiments is an ISO VG 10 oil (viscosity of 18 cPoise at 21°C). The air volume fraction (β) in the bubbly mixture is determined from

$$\beta = \frac{\dot{V}_A}{\dot{V}_A + \dot{V}_L} \quad (3)$$

where $\dot{V}_A = \dot{m}_A / \rho_A$ is the air volumetric flow rate at the sparger inlet and \dot{V}_L is the lubricant flow rate measured with a turbine flow meter. The air density (ρ_A) follows from the thermostatic relationship for an ideal gas, $\rho_A = P/R_d T$, with P and T as the absolute pressure and temperature at the sparger inlet.

The lubricant feed port is located on the side (horizontal plane) of each bearing housing support. Drain ducts at their bottom collect the oil discharge from the hydrodynamic bearings and squeeze film dampers. An independent circuit feeds the tilting pad bearing through one of the sides of the integral damper. Small orifices located between the bearing pads serve as lubricant feeding ports. The plain hydrodynamic journal bearing at the free end receives some lubricant from the squeeze film damper journal and through a single feeding port located on the upper half of the bearing.

Three pairs of noncontact eddy-current displacement sensors installed in the bearing pedestals measure relative rotor displacements at locations next to the bearing (inboard side) on the motor drive end, the middle disk, and the bearing at the rotor free end. An optical keyphasor facing the motor coupling provides a pickup signal for measurement of the rotor speed and reference timing for rotor response phase angles. Several type-K thermocouples record temperatures of the lubricant at the inlet and discharge ports, drive motor, and ambient temperatures.

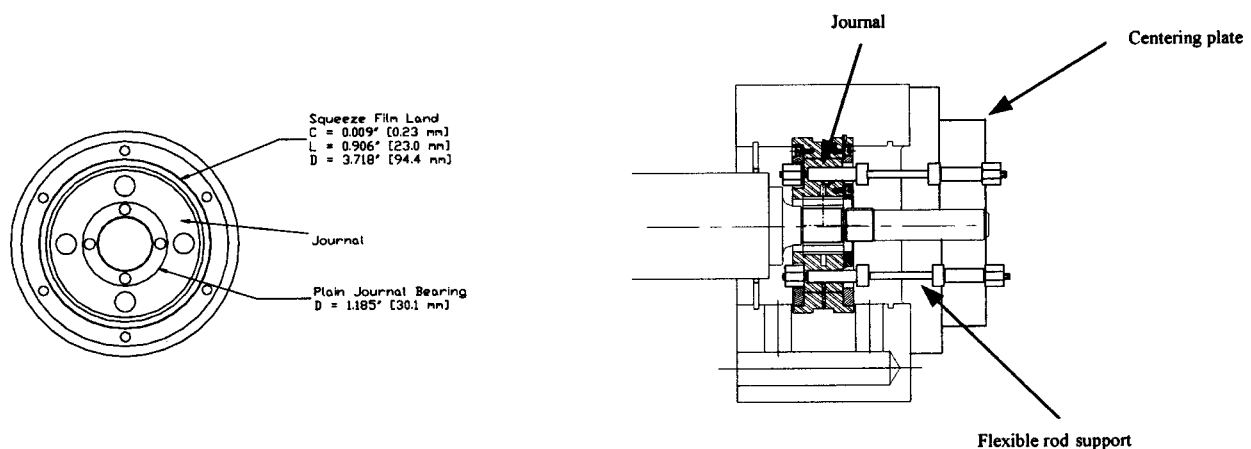


Fig. 4 Configuration and main dimensions of cylindrical squeeze film damper and plain journal bearing

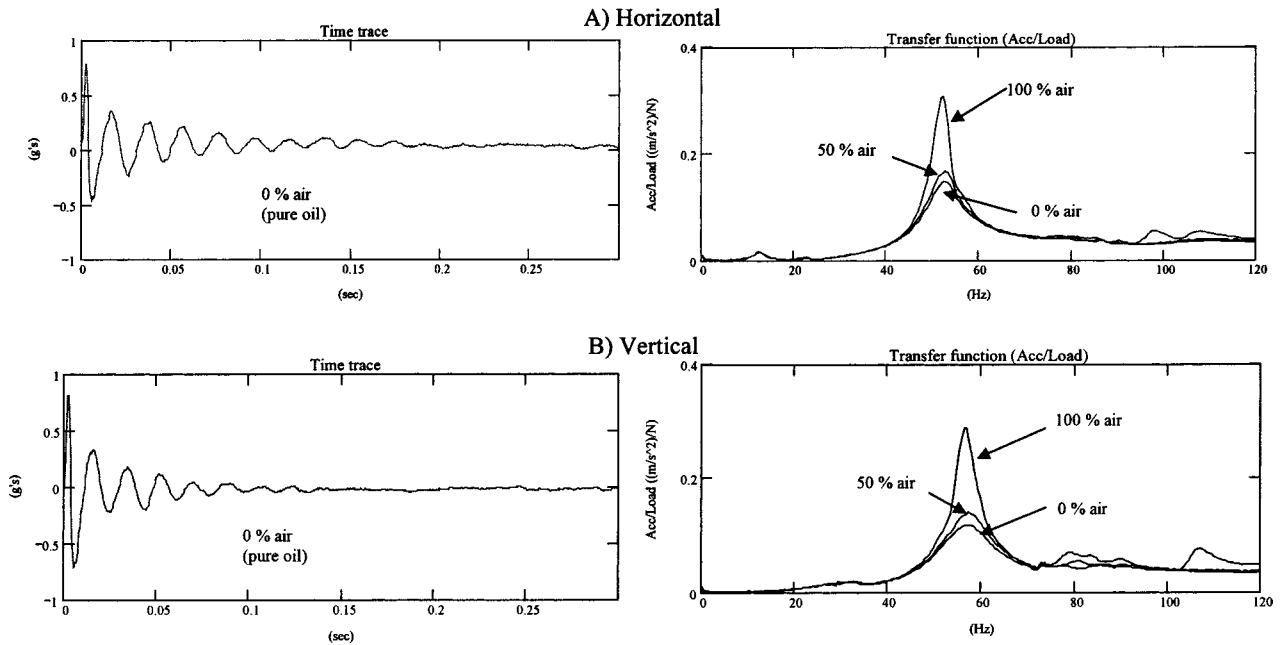


Fig. 5 Response of test rotor to impacts exerted on middle disk. Dampers operating with 100% (dry lands), 50%, and 0% air content (pure oil). (a) horizontal, (b) vertical motions.

Description of Test Dampers and Hydrodynamic Bearings

The integral squeeze film damper consists of an outer ring with a circumferential groove for lubricant supply and an inner ring (damper journal) on which a tilting pad bearing fits, as shown in Fig. 3. Four pairs of S-shaped thin webs connect the outer and inner rings, and a small clearance of 0.229 mm (9 mils) separates the two rings into four film lands (pads) where hydrodynamic pressure generates the damping forces. The measured radial stiffness of the damper springs is ~ 3.5 MN/m, [1]. In operation, the series stiffness of the journal bearing contributes modestly since it is about four times the structural stiffness of the damper springs at the system critical speed (~ 3000 rpm).

The clearance around the damper journal (in the film lands) is manufactured uneven so that the journal becomes centered under the webs deflection due to the shaft weight. The damper film lands have an arc extent (θ_p) of 52 deg, axial length (L) of 23 mm and a diameter (D) of 96.3 mm. The outer ring has four holes, 1.6 mm in diameter, serving as inlet lubricant ports to the squeeze film lands from the external groove. The inner ring has a lateral feeding port and an internal groove for oil supply into the tilting pad bearing. A flexible hose connection provides the lubricant to the tilting pad bearing through the damper journal from an independent supply line.

Figure 4 depicts the cylindrical SFD with the squirrel cage-type elastic support, namely four steel rods connected to ground. The rods deflect under the static and dynamic loads and have a combined radial stiffness of 3.5 MN/m identical to the integral damper stiffness. A centering mechanism positions the damper journal within the film clearance through the elastic bars. The damper housing contains six feed holes, 1.6 mm in diameter, that connect the circumferential groove to the damper film land (360 deg in extent). The journal has diameter and length equal to 95 mm and 23.0 mm, respectively. The journal inner bore holds a plain cylindrical hydrodynamic bearing. The nominal radial clearance on the damper film lands (c) is equal to 0.229 mm, identical on both dampers. The nominal radial clearance for the hydrodynamic journal bearing is 0.051 mm.

Impact Response Experiments

Impact response tests are a common procedure for identification of modal parameters in many types of vibrating structures, [7]. While the rotor is stationary, a calibrated hammer impacts the middle disk (very close to the rotor CG) and excites the first (cylindrical) mode of vibration. A small accelerometer fixed on the outer diameter of the middle disk records the ensuing rotor vibration.

The measurements serve to identify system damping coefficients at the first natural frequency using a one-degree-of-freedom model representing planar motions of the test rotor. No oil is purposely fed through the fluid film bearings and the dampers operate with open ends in all cases. In the frequency domain, the transfer function (H) of acceleration (a) over load (F) is

$$H = \frac{a}{F} = \frac{-\omega^2}{(\omega^2 M + j\omega C + K)} \quad (4)$$

where M is the total vibrating mass, C is the system direct damping coefficient, and K is the equivalent stiffness. At the system natural frequency ($\omega = \omega_n = \sqrt{K/M}$), Eq. (4) renders a simple expression for estimation of the damping coefficient, i.e.,

$$C = \frac{\omega_n}{|H(\omega_n)|} \quad (5)$$

This estimation relies on a single measurement at the appropriate frequency. A second method utilizes the magnitude of Eq. (4) to fit a curve on the acceleration (H) over a frequency range, thus rendering all parameters (K, C, M).

Figure 5 displays typical transient rotor accelerations and the magnitude of the acceleration/load frequency responses resulting from impacts in the horizontal and vertical directions. The time responses correspond to tests with pure oil in the dampers. The rotor acceleration remains less than 1g in the vertical direction ensuring that the rotor is always in contact with the journal bearings. The transfer functions correspond to frequency averages of 16 consecutive impacts. Transfer function measurements show

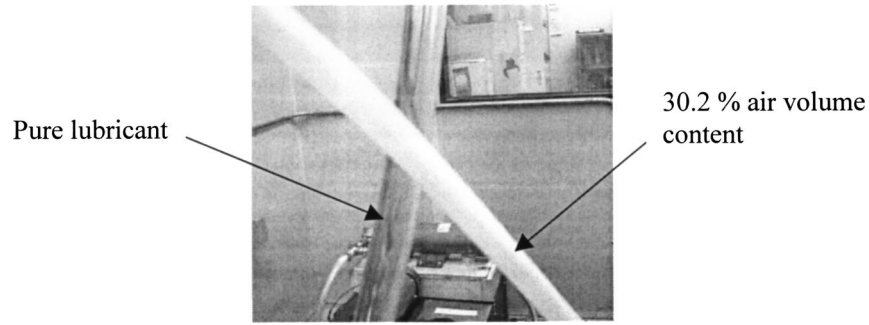


Fig. 6 Appearance of lubricant mixture supplied into squeeze film dampers. 30.2% air volume fraction.

large values of coherence (very close to one) in a broad range around the first natural frequency. Note that the system has little damping for the experiments without lubricant. The system damping readily increases for bubbly mixtures, and is the largest for a pure oil condition.

The system natural frequencies are 56 Hz and 52 Hz in the horizontal and vertical directions, respectively; and from these, equivalent system stiffness of 5.63 MN/m and 4.86 MN/m result for $M = 45.7$ kg. These stiffnesses are the effective values provided by the two dampers and the support structure.

Impact response tests were performed with a stationary rotor for eight bubbly mixtures. The air volume fractions correspond to 9.7, 17.8, 30.2, 42.0, 50.4, 59.9, 71.0, and 80.1% at a nearly uniform lubricant temperature (20.6–22.2°C). The gas mass fraction in the mixture is quite small since the air supply pressure into the sparger is relatively low, below 1 bar in all instances. To generate uniform bubbly mixtures, the oil flow rate was maintained at 3.5 liters/minute and the gas flow rate varied. The lubricant flow rate ensures the damper lands will not starve, even for the largest journal motions excited at the fundamental natural frequency (~52–56 Hz). Pressure gauges and flow meters show little variability for air-oil mixtures of up to 80% of air volume fraction. Higher air content mixtures are very difficult to control.

The air in oil mixtures generated seemed homogeneous with bubbles of very small size (<1 mm) traveling from the sparger element into the bearing housings. The sparger is located in a vertical position, directly above the test rig and very close to the final supply line, to reduce the deleterious effect of natural buoyancy tending to separate the gas from the liquid. Figure 6 shows a photograph comparing the lubricant aspect before and after air is injected into the oil for a volume fraction of 30%. The air and oil flows, as well as the visual aspect of the mixture remain constant for the entire duration of each test.

The uncertainty in the estimated air volume content (β) is determined for each mixture using standard procedures for single sample experiments. The uncertainty of the measured variables (air and oil flow rates) includes the resolution and uncertainty of the instruments, as well as the observed fluctuations occurring for mixtures with more than 50% of air. Uncertainties for air volume fractions equal to 9.7, 42, and 80% are 1.4, 1.0 and 4.8%, respectively.

Equivalent damping coefficients with *dry* damper lands (i.e. no lubricant) represent the contribution of the structural components such as custom-made seals and others, and acting in parallel with the damping from the damper film lands when lubricated. From single-point identification, *dry* damping coefficients are 1232

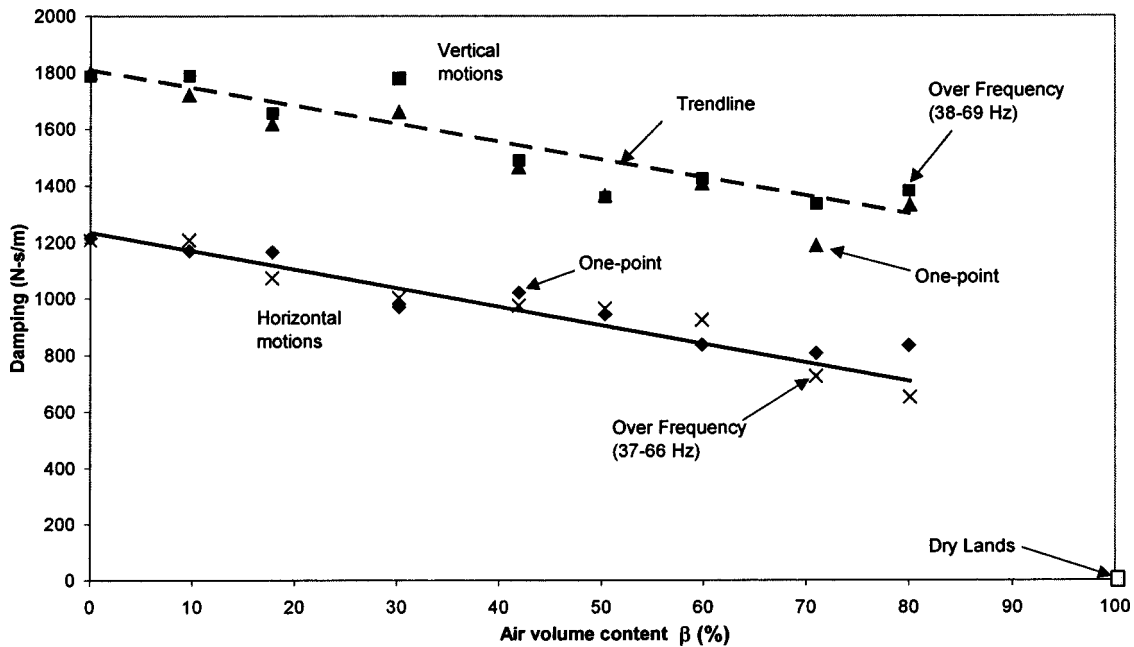


Fig. 7 Damping coefficients versus air volume fraction as derived from impact responses. Estimates from single point and over a frequency range. Contribution of two dampers after subtraction of structural (dry) damping.

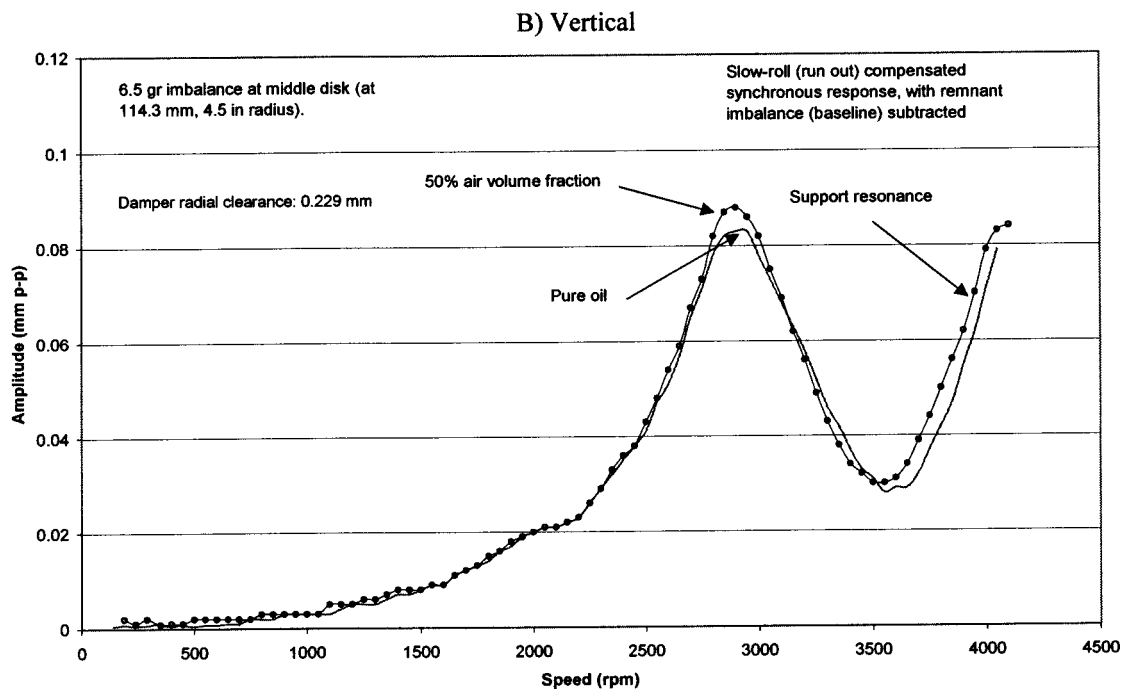
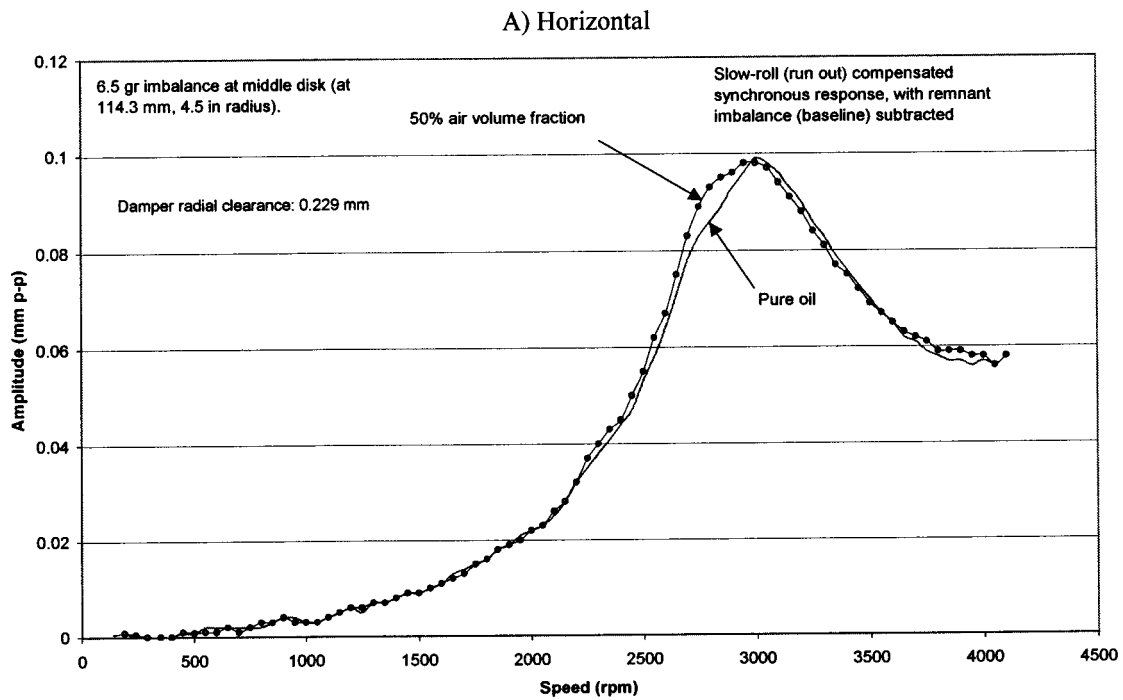


Fig. 8 Imbalance response of test rotor close to the middle disk for pure oil and 50% air volume fraction (a) horizontal, (b) vertical.

N-s/m and 1,036 N-s/m, for motions in the vertical and horizontal directions, respectively. The difference between these values is due in part to the pedestal asymmetry.

Figure 7 shows the estimated damping coefficients of both SFDs from rotor responses to vertical and horizontal impacts for increasing air volume fractions (β). The experimental values refer to the dampers alone since the damping coefficients under dry

conditions have been subtracted. The figure includes damping parameters obtained from the single-point estimation procedure and a curve fit over a frequency range (37–69 Hz). In general, damping coefficients estimated from single-point measurements and identified over a frequency range are in very close agreement. Damping coefficients steadily decrease for increasing values of air volume in the mixture. However, in spite of the apparent rotor

bearing symmetry, damping coefficients estimated from vertical motions are larger than those derived from horizontal rotor motions.

Damping coefficients derived from vertical rotor motions decrease linearly as the air volume fraction increases to 70%, and then show a small increment for $\beta=0.80$. The damping coefficients decrease rapidly for larger air volume fractions. Note that the rate of decay for the test damping coefficients, ~ -625 Ns/m/100% air content, is similar for the impact tests conducted along the vertical and horizontal directions. The largest amplitudes of motion recorded in the tests are of 20% relative to the damper clearance.

The present test results differ from those reported in [5] for similar experiments conducted on a smaller size test rig. On that occasion, estimated damping coefficients for mixtures with up to 50% in air volume were larger than for the pure lubricant condition since, as explained in [5], the bubbles in the mixture did not readily compress and behaved as rigid particles, increasing the mixture effective viscosity and rendering larger damping coefficients. Presently, viscous damping coefficients under pure lubricant conditions equal 1804 N-s/m in the vertical direction and 1209 N-s/m in the horizontal direction.

Predictions of squeeze film damper coefficients using a finite length full-film SFD model [1] render a magnitude of 2310 N-s/m for both dampers acting in parallel (1660 Ns/m from the cylindrical damper and 650 Ns/m from the integral damper). These predictions for unidirectional loading take into account actual manufacturing tolerances and operating temperatures.

Imbalance Response Experiments

Coast down rotor imbalance response measurements provide further assessment on the effect of air content in the lubricant mixture flowing through the squeeze film dampers. Prior measurements on the same test rig supported on ISFDs in series with ball bearings and flexure pivot bearings are given in [1] and [8], respectively. The rotor amplitude responses evidenced a linear rotor-bearing system, even for large imbalance displacements. Imbalance response measurements also provide a means for estimating system damping coefficients from the amplification factor (Q) at the critical speed.

Figure 8 depicts coast down (peak to peak) rotor amplitudes of synchronous motion recorded at the middle disk from a top speed of 4000 rpm. A 6.5 gram imbalance mass is attached to the middle disk at a radius of 114.3 mm, and corresponds to an imbalance distance (u) of 16.3 μ m. There are two curves in the figures, one for pure oil flowing through the damper lands and the other for a bubbly mixture with 50% in air volume content. The critical speeds in the vertical and horizontal directions occur at 2900 rpm (48.3 Hz) and 3000 rpm (50 Hz), respectively. Recall that the system natural frequencies are 56 and 52 Hz for the vertical and horizontal directions, respectively. Thus a remarkable reduction in vertical stiffness is evident, lowering the natural frequency by almost 8 Hz, and associated to a support resonance that begins to appear at ~ 3700 rpm. The largest magnitude of response occurs in the horizontal direction (0.10 mm p-p) and corresponds to rotor motions of about 22% of the damper clearance.

Most remarkably, however, is the minimal effect of the bubbly mixture on the amplitudes of the rotor synchronous response. The experimental results evidence a minute increase in the amplitude of vibration in the vertical direction while traversing the critical speed. The rotor responses to impacts and lubricated mixtures contrast notably with the rotor responses to imbalances. Recall that in the former tests, system damping drops by almost 20% for a 50% air volume content.

The apparent contradiction is easily resolved when realizing that pure lubricant exiting the hydrodynamic bearings inevitably leaks along the damper lateral faces. It is likely that some pure lubricant, rather than air, is drawn into the damper lands during the rotor orbiting motions, thus maintaining its damping ability.

Table 1 Estimates of system stiffness and damping coefficients from imbalance responses

| Speed Range: 2.1–3.4 krpm | |
|--|---------------------------------------|
| Pure oil | 50% air volume fraction |
| $C = 4968$ N-s/m | $C = 4860$ N-s/m |
| $K = 4.32$ MN/m | $K = 4.2$ MN/m |
| $\xi = 0.178$ | $\xi = 0.177$ |
| $r = 0.997$ (correlation factor) | $r = 0.967$ |
| One-point estimates of system damping from amplification factor (Q): | |
| Pure Oil \rightarrow Horizontal: 4916 N-s/m | 50% air volume fraction |
| | \rightarrow Horizontal: 4,964 N-s/m |

San Andrés and Lubell [9] report measurements of hydrodynamic pressures in a cylindrical damper where the oil supply pressure was suddenly shut down. Very small amounts of lubricant remaining in the film lands generated large film pressures as the rotor crossed the critical speed, and the SFDs effectively attenuated rotor vibrations.

The amplitudes of vibration at the critical speeds correspond to amplification factors ($Q = x_{\max}/u$) of 3.04 and 2.55 in the horizontal and vertical directions, respectively, for the case of pure oil. Table 1 shows estimated system damping coefficients extracted from the imbalance responses using a curve fitting process around the first critical speed and one-point estimates from the amplification factor. Note that the system damping values are considerably larger than the corresponding ones obtained from impact excitations. From the imbalance tests, a viscous damping coefficient of 3932 Ns/m for both damper elements follows.¹ This value contrasts with predictions of 2500 Ns/m obtained for a journal orbit equal to 22% of the damper clearance.

Closure

Air entrainment and/or lubricant cavitation affect the dynamic forced performance of rotating machinery implementing squeeze film dampers for vibration control and structure isolation. Experiments were conducted on a test rotor supported on hydrodynamic bearings mounted in series with SFDs. Ten controlled air in oil mixtures ranging from pure oil to all air, were supplied to the damper elements to evidence the effects of air content on the system viscous damping coefficients.

Impact responses of the test rotor allowed estimation of the system damping coefficients from transfer functions of acceleration over load. In these experiments the rotor is stationary and rests on unlubricated hydrodynamic bearings. The experiments reveal that increased air content in the lubricant mixture consistently reduced the SFDs damping coefficients. The relationship between damping coefficients and air volume fraction appears nearly linear for bubbly mixtures with up to 80% in air content. The test results do not show the trends reported in earlier experimental investigation, [5,6], thus further demonstrating that air entrainment is device dependent.

Most importantly, imbalance response measurements conducted with a pure lubricant and a bubbly mixture with 50% air content show virtually no differences, even for large amplitude rotor excursions while traversing a critical speed. Thus, system damping coefficients estimated from the imbalance responses remain unchanged for the two conditions tested. In the imbalance response tests, the hydrodynamic bearings supporting the rotor are lubricated with pure oil. It appears that oil exiting the fluid film bearings is drawn into the SFDs, thus maintaining their damping ability.

¹The damping coefficient for both dampers equals the system damping magnitude less the damping identified under dry (unlubricated) conditions. Superposition of effects is assumed.

Acknowledgments

The support of NSF and the Turbomachinery Research Consortium are gratefully acknowledged. Thanks to Mr. Juan Nadal, undergraduate mechanical engineering student from the Universidad de Puerto Rico in Mayaguez, for conducting some of the impact tests. The support of the TAMU Undergraduate Summer Research Program is also acknowledged.

Nomenclature

| | |
|-----------|--|
| a | = acceleration (m^2/s) |
| c | = radial clearance of damper lands (m) |
| C | = system damping coefficient (N-s/m) |
| D | = diameter (m) |
| e | = damper journal orbit eccentricity (m) |
| F | = external force applied to rotor (N) |
| H | = transfer function of acceleration over load ($\text{m}^2/\text{s}\cdot\text{N}$) |
| K | = system stiffness coefficient (N/m) |
| L | = damper axial length (m) |
| \dot{m} | = mass flow rate (kg/s) |
| M | = rotor mass for cylindrical mode (kg) |
| P | = absolute air pressure (Pa) |
| Q | = system amplification factor |
| R_a | = air constant (287 Nm/kg K) |
| T | = absolute temperature (K) |
| u | = imbalance distance (m) |
| \dot{V} | = volumetric flow (m^3/s) |
| x | = rotor displacement (m) |
| β | = air volume fraction in lubricated mixture |
| ξ | = viscous damping ratio = $C/2M\omega_n$ |
| γ | = feed flow factor, |
| ρ | = density (kg/m^3) |

| | |
|------------|------------------------------------|
| ω | = journal whirl frequency (rad/s) |
| ω_n | = system natural frequency (rad/s) |
| θ_p | = damper land arc extent (rad) |

Subscripts

A, L, T = air, liquid, $A + L$

References

- [1] De Santiago, O., Oliveras, J., and San Andrés, L., 1999, "Imbalance Response of a Rotor Supported on Open-Ends Integral Squeeze Film Dampers," *ASME J. Eng. Gas Turbines Power*, **121**, pp. 718–724.
- [2] Zeidan, F., and Vance, J. M., 1989, "Cavitation and Air Entrainment Effects on the Response of Squeeze Film Supported Rotors," *ASME Paper No. 89-Trib-52*.
- [3] Diaz, S., and San Andrés, L., 2001, "A Model for Squeeze Film Dampers Operating With Air Entrainment and Validation With Experiments," *ASME J. Tribol.*, **123**, pp. 125–133.
- [4] Diaz, S. E., 1999, "The Effect of Air Entrapment on the Performance of Squeeze Film Dampers; Experiments and Analysis," Ph.D. dissertation, Mechanical Engineering, Texas A&M University, May.
- [5] San Andrés, L., Díaz, S., and Rodríguez, L., 2001, "Sine Sweep Load Versus Impact Excitations and Their Influence on the Damping Coefficients of a Bubbly Oil Squeeze Film Damper," 56th STLE Annual Meeting, Orlando, FL, May, Paper No. STLE 01-NP-18.
- [6] Diaz, S., and San Andrés, L., 1999, "A Method for Identification of Bearing Force Coefficients and Its Application to a Squeeze Film Damper With a Bubbly Lubricant," *STLE Tribol. Trans.*, **42**(4), pp. 739–746.
- [7] Ewins, D. J., 2000, *Modal Testing, Theory, Practice and Application*, 2nd Ed., Research Study Press, LTD, Hertfordshire, UK.
- [8] San Andrés, L., and De Santiago, O., 2001, "Imbalance Response of a Rotor Supported on Flexure Pivot Tilting Pad Journal Bearings in Series With Integral Squeeze Film Dampers," *ASME J. Eng. Gas Turbines Power*, **125**, pp. 1026–1032.
- [9] San Andrés, L., and Lubell, D., 1998, "Imbalance Response of a Test Rotor Supported on Squeeze Film Dampers," *ASME J. Eng. Gas Turbines Power*, **120**, pp. 397–404.

The Identification of the Unbalance of a Flexible Rotating Machine From a Single Rundown

A. W. Lees

J. K. Sinha

Department of Mechanical Engineering,
University of Wales Swansea,
Singleton Park,
Swansea SA2 8PP, UK

M. I. Friswell

Department of Aerospace Engineering,
University of Bristol,
Bristol BS8 1TR, UK

The reliable estimation of a flexible foundation model and the state of unbalance (both amplitude and phase) of a turbogenerator from machine rundown measured vibration data is an active research area. Earlier studies on the estimation of both these quantities used the whole frequency range of the rundown as a single band. However, such an identification may be inaccurate for large flexible foundations having many modes in the rundown frequency range. For reliable identification, the whole frequency range has to be divided into a number of frequency bands and the frequency-dependent foundation models have to be estimated together with the unbalance. This paper combines the unbalance estimation with the split frequency range for the foundation model, and the highlights the limitations observed during estimation of foundation models and the state of unbalance. It is shown that the accuracy of the method may be enhanced by judicious choice of a weighting function. Having established the method in simulation, experimental data from a 3-m long test rig, with four journal bearings, is used to test the method. The approach seems to give reliable estimates of the machine unbalance. [DOI: 10.1115/1.1691441]

Introduction

Over the past 30 years, theoretical models have played an increasing role in the rapid resolution of problems in rotating machinery. Adams and McLosky [1] give a description of some early applications while further examples are given in [2]. A variety of problems have been tackled using a model ranging from mass unbalance to cracked rotors which were studied in detail by Mayes and Davies [3]. However, while there is a broad range of possible faults, the single most important defect in rotating machine remains unbalance and a detailed understanding of a machine's response. With the growing use of flexible rotors modal methods have become an important alternative to influence coefficient methods of balancing. Kellenburger [4] gave one of the early discussions of the balancing requirements. Important developments followed, with important developments in the U.S. [5,6] and Europe, [7]. A detailed review emphasizing the role of modal balancing was given Parkinson [8] and this work has been brought up to date by Foiles et al. [9]. The wider field of fault diagnosis has been reviewed by Edwards et al. [10].

In spite of the success of models, they have shown some inaccuracies and hence have been used in a semi-quantitative manner. If truly accurate models were available then single step balancing would be a reality. It is clear that this would be of tremendous value but seems beyond current capabilities. The problem of reconciling models and data has been discussed in some detail by Maslen et al. [11] and Vazquez et al. [12]. Their approach is somewhat distinct from our own in that sufficient data is available to them to determine the FRF of the rotor-bearing system, whereas in the work reported here it is assumed that only rundown data is available. Some of the shortcomings were described by Lees and Simpson [13]. The most important shortcoming of current machine models appears to be in the representation of the foundation as discussed by Lees [14]. Since that paper, this topic has received attention in a number of groups. In Europe Provassi et al. [15] have applied a filtering technique following the studies of Zan-

netta [16] and Vania [17]. In these approaches the force acting is derived from a knowledge of the bearings. Feng and Hahn [18] have followed a different approach attempting to measure oil pressures in a rig, the employing a direct least-squares approach which is closer to that of Lees [14]. The basic difference in the method of [14] was the use of a validated rotor model to infer the forces acting and this approach is significantly developed by Smart et al. [19]. If rotor proximity data is available, then the method does not require a bearing model. On a machine where only pedestal data is available, then the bearing is used to infer the rotor motion; it has been shown, however, that results are not unduly sensitive to the accuracy of the bearing model (Lees and Friswell [20]). The advantage of treating forces in this way is that it leads to a possible route to single run balancing as described by Lees and Friswell [21]. The approach has been tested on a simple rig with bush bearings as reported by Edwards et al. [22] and in the present paper the study is extended to cover more complex structures and oil journal bearings.

Theory

Figure 1 shows the abstract representation of a turbogenerator, where a rotor is connected to a flexible foundation via oil-film journal bearings. The equations of motion of the system may be written, [19], as

$$\begin{bmatrix} \mathbf{Z}_{R,ii} & \mathbf{Z}_{R,ib} & \mathbf{0} \\ \mathbf{Z}_{R,bi} & \mathbf{Z}_{R,bb} + \mathbf{Z}_B & -\mathbf{Z}_B \\ \mathbf{0} & -\mathbf{Z}_B & \mathbf{Z}_B + \bar{\mathbf{Z}}_F \end{bmatrix} \begin{Bmatrix} \mathbf{r}_{R,i} \\ \mathbf{r}_{R,b} \\ \mathbf{r}_{F,b} \end{Bmatrix} = \begin{Bmatrix} \mathbf{f}_u \\ \mathbf{0} \\ \mathbf{0} \end{Bmatrix} \quad (1)$$

where \mathbf{Z} is the dynamic stiffness matrix, the subscripts i and b refer to internal and bearing (connection) degrees-of-freedom, respectively, and the subscripts F , R , and B refer to the foundation, the rotor and the bearings. \mathbf{r} are the responses and \mathbf{f}_u are the unbalance forces, which are assumed to be applied only at the rotor internal degrees-of-freedom. The dynamic stiffness matrix of the foundation, $\bar{\mathbf{Z}}_F$, is defined only at the degrees-of-freedom connecting the bearings and the foundation. In practice this will be a reduced order model, where the internal foundation degrees-of-freedom have been eliminated, [19].

The dynamic stiffness matrix of the bearings is given by \mathbf{Z}_B . It has been assumed that the inertia effects within the bearings are

Contributed by the International Gas Turbine Institute (IGTI) of THE AMERICAN SOCIETY OF MECHANICAL ENGINEERS for publication in the ASME JOURNAL OF ENGINEERING FOR GAS TURBINES AND POWER. Paper presented at the International Gas Turbine and Aeroengine Congress and Exhibition, Amsterdam, The Netherlands, June 3–6, 2002; Paper No. 2002-GT-30420. Manuscript received by IGTI, Dec. 2001, final revision, Mar. 2002. Associate Editor: E. Benvenuti.

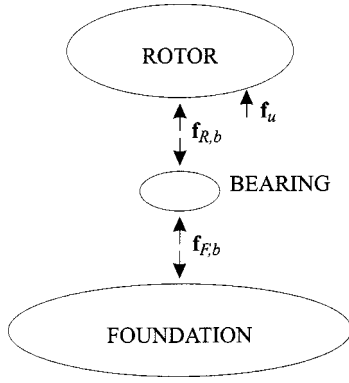


Fig. 1 Rotor-bearing-foundation interaction

negligible, although these could be included if required. Short bearing theory will be used to generate the speed dependent stiffness and damping properties of the bearing, [23]. This theory approximates the nonlinear bearing model by linearised stiffness and damping matrices that vary with rotor speed. The dynamic stiffness matrix may also be derived using complex and detailed numerical models of the journal bearings. However, the static loads on the bearings are often difficult to estimate accurately, and the errors introduced by a slight error in the static load will be far greater than the error introduced by using short bearing theory. Equally, any method of unbalance estimation must be robust with respect to the bearing modelling errors. Lees and Friswell [20] showed that the estimation of the force exerted was accurate over most of the frequency range despite errors in the bearing model.

Solving Eq. (1) to eliminate the unknown response of the rotor gives

$$\bar{\mathbf{Z}}_F \mathbf{r}_{F,b} + \mathbf{Z}_B \mathbf{P}^{-1} \mathbf{Z}_{R,bi} \mathbf{Z}_{R,ii}^{-1} \mathbf{f}_u = \mathbf{Z}_B [\mathbf{P}^{-1} \mathbf{Z}_B - \mathbf{I}] \mathbf{r}_{F,b} \quad (2)$$

where $\mathbf{P} = \mathbf{Z}_{R,bb} + \mathbf{Z}_B - \mathbf{Z}_{R,bi} \mathbf{Z}_{R,ii}^{-1} \mathbf{Z}_{R,ib}$. It is assumed that good models for the rotor and the bearings, \mathbf{Z}_R and \mathbf{Z}_B , are known a priori and $\mathbf{r}_{F,b}$ is measured. Thus, the only unknown quantities in Eq. (2) are the foundation model, $\bar{\mathbf{Z}}_F$, and the unbalance forces, \mathbf{f}_u . The bearing term \mathbf{Z}_B is recalculated at each speed in the run-down. In the present case short bearing theory has been used, but it is envisaged that some more sophisticated approach may be required in due course.

Parameter Estimation

Although the unbalance will be distributed throughout the rotor, this is equivalent to a discrete distribution of unbalance, provided there are as many balance planes as active modes. Suppose the unbalance planes are located at nodes n_1, n_2, \dots, n_p , where p is the number of planes.

The unknown unbalance components are now assembled into a vector $\mathbf{e} = [e_{r,n_1} e_{r,n_2} \dots e_{r,n_p} e_{i,n_1} e_{i,n_2} \dots e_{i,n_p}]^T$. Using \mathbf{T} to denote a selection matrix indicating the location of the balance planes, the relationship between the dynamic stiffness terms can be expressed as

$$\bar{\mathbf{Z}}_F \mathbf{r}_{F,b} + \omega^2 [\mathbf{Z}_B \mathbf{P}^{-1} \mathbf{Z}_{R,bi} \mathbf{Z}_{R,ii}^{-1} \mathbf{T}] \mathbf{e} = \mathbf{Z}_B [\mathbf{P}^{-1} \mathbf{Z}_B - \mathbf{I}] \mathbf{r}_{F,b} \quad (3)$$

To identify the foundation parameters and forces in a least-squares sense, the foundation parameters are grouped into a vector \mathbf{v} . We will assume that the foundation dynamic stiffness matrix, $\bar{\mathbf{Z}}_F$, is written in terms of mass, damping and stiffness matrices. The elements in \mathbf{v} are individual elements of the structural matrices. With this definition of \mathbf{v} , there is a linear transformation such that

$$\bar{\mathbf{Z}}_F \mathbf{r}_{F,b} = \mathbf{W} \mathbf{v} \quad (4)$$

where \mathbf{W} contains the response terms at each measured frequency, [19].

Clearly there is an equation of the form of (4) at every frequency. How these sets of equations are combined is addressed below. The equations generated may be solved in a least squares sense directly, although the solution via the singular value decomposition (SVD) is more robust, [24]. Such an equation error approach does not optimize the error in the response directly, and thus the accuracy of the predicted response is not assured. The great advantage is that the equations are linear in the parameters. However, a nonlinear optimization (output error) may be performed, starting with linear estimated parameters, if more accurate prediction of the response is required, [19]. In the present paper, only the equation error approach has been considered in order to concentrate on the influence of frequency range subdivision. Furthermore, the unbalance seems to be robustly estimated by the equation error approach, even if the foundation is relatively inaccurate, [22].

Splitting the Frequency Range

Suppose that the frequencies at which the response is measured are ω_q , $q = 1, \dots, N$. Then the different methods arise depending on whether the frequency range is split, or not, and whether the unbalance is assumed to be different in each frequency band. Thus the identification can be carried out in three ways, although only two will be discussed here.

Method 1: Using the Entire Frequency Range as a Single Band. Here all the measurements are used at once, and only one estimate of the unbalance state and the foundation model is produced. Thus, Eq. (4) is repeated N times.

Method 2: Variable Parameter Method. The difficulty in applying the method outlined above is that the stiffness mass and damping parameters retain constant values throughout the running range of the machine. This is equivalent to assuming that there are fewer modes of interest than there are measurement points and in most cases there is little justification for this assumption. One way to circumvent this difficulty is to allow the stiffness and mass parameters to assume different values in different part of the speed range. The unbalance, however, remains a constant independent of speed.

Let us assume that the run-down frequency range is split into b frequency bands. The vectors of the foundation parameters are identified in each frequency band, and are denoted $\mathbf{v}_1, \mathbf{v}_2, \dots, \mathbf{v}_b$. For each frequency band an equation similar to Eq. (4) is generated, and if the \mathbf{W} , \mathbf{R} , and \mathbf{Q} matrices are combined, can be written as

$$[\mathbf{W}_{\text{band}_\ell} \mathbf{R}_{\text{band}_\ell}] \begin{Bmatrix} \mathbf{v}_\ell \\ \mathbf{e} \end{Bmatrix} = \mathbf{Q}_{\text{band}_\ell} \cdot \quad (5)$$

The problem may also be solved in one step using entire frequency range of the rundown as method 1, giving a global estimate of the unbalance vector \mathbf{e} . Thus, combining Eq. (5) for all the bands, gives

$$\begin{bmatrix} \mathbf{W}_{\text{band}_1} & \mathbf{0} & \dots & \mathbf{0} & \mathbf{R}_{\text{band}_1} \\ \mathbf{0} & \mathbf{W}_{\text{band}_2} & \dots & \mathbf{0} & \mathbf{R}_{\text{band}_2} \\ \vdots & \vdots & \ddots & \vdots & \vdots \\ \mathbf{0} & \mathbf{0} & \dots & \mathbf{W}_{\text{band}_b} & \mathbf{R}_{\text{band}_b} \end{bmatrix} \begin{Bmatrix} \mathbf{v}_1 \\ \mathbf{v}_2 \\ \vdots \\ \mathbf{v}_b \\ \mathbf{e} \end{Bmatrix} = \begin{Bmatrix} \mathbf{Q}_{\text{band}_1} \\ \mathbf{Q}_{\text{band}_2} \\ \vdots \\ \mathbf{Q}_{\text{band}_b} \end{Bmatrix} \cdot \quad (6)$$

Regularization

Equations (5) and (6) are least-squares problems, and their solutions are likely to be ill-conditioned, [19]. Generally two types of scaling, namely row scaling and column scaling, may be applied to least-squares problems, [25]. Column scaling is necessary because of the different magnitudes of the elements of the $\bar{\mathbf{M}}_F$, $\bar{\mathbf{C}}_F$, and $\bar{\mathbf{K}}_F$ matrices, and the scaling factors used here were 1, $\bar{\omega}$, and $\bar{\omega}^2$, respectively, where $\bar{\omega}$ is the mean value of the frequency range. The scaling of the columns of \mathbf{R} depend upon engineering judgement based on the unbalance magnitudes expected. The truncated SVD was used to solve the equations, [26].

Other physically based constraints may be applied to the foundation model to improve the conditioning. For example, the mass, damping and stiffness matrices of the foundation may be assumed to be symmetric, therefore reducing the number of unknown foundation parameters. Other constraints could be introduced, such as a diagonal mass or damping matrix, or block diagonal matrices if bearing pedestals do not interact dynamically. Furthermore, the measured data may be regularized by removing the effects of noise modes in the data, using the SVD of the autocorrelation matrix of the responses. The singular values below a certain tolerance represent the noisy part of the data, and a transformation based on the singular vectors used to remove this noise. Smart et al. [19] gave more detail.

The Example Machine

The two methods were applied to a flexible rotor mounted on four fluid bearings, with a flexible foundation. The machine was used in both the simulated and the experimental examples, and so the machine and its associated model will be described in detail here. The example machine is a physical test rig at Aston University, Birmingham. The rig consists of a solidly coupled, two-shaft system mounted on four oil lubricated journal bearings. The bearings sit on flexible steel pedestals bolted onto a large lathe bed which rests on a concrete foundation. The rotor itself consists of two steel shafts 1.56 m and 1.175 m long, each with nominal

diameter of 38 mm and coupled through flanges of 150 mm long and 100 mm diameter at the connecting end of the both shafts. At either end of the shafts are journals of diameter 100 mm, and the center of the shafts have machined sections for balancing disks. Each balancing disk is 203.2 mm in diameter, and there are three on the long rotor and two on the short rotor. The bearings are circular, have a length to diameter ratio of 0.3, a radial clearance of 150 μm and contain oil with viscosity 0.0009 Ns/m². Accelerometers are mounted at each bearing measuring in the horizontal and vertical directions.

A finite element model was created for the rotor with 51 two-noded Timoshenko beam elements, each with two translational and two rotational degrees-of-freedom. Short bearing theory was used to obtain values for the bearing stiffness and damping, [23]. For the simulated example the static loads acting on bearings 1 to 4 are assumed to be 221 N, 486 N, 461 N, and 400 N, respectively. The entire rig was assumed to be constrained along the axial direction of the rotor and torsional and axial vibration were assumed to be negligible.

Since there are four bearings, and only the horizontal and vertical accelerations are measured, there are eight measured degrees-of-freedom. Using a foundation model with mass, damping, and stiffness matrices means that this foundation model has eight degrees-of-freedom. Of course the actual foundation also has internal degrees-of-freedom. For the purpose of the simulation only the translational degrees-of-freedom are considered, and the displacement vector of the foundation is ordered as

$$\mathbf{r}_{F,b} = [x_1 \ y_1 \ x_2 \ y_2 \ x_3 \ y_3 \ x_4 \ y_4]^T \quad (7)$$

where x and y are the horizontal and vertical directions, and the subscript refer to the response at the corresponding bearing. The foundation mass, damping, and stiffness matrices are taken as

$$\mathbf{M}_F = \text{diag}[52 \ 52 \ 50 \ 50 \ 52 \ 52 \ 50 \ 50] \text{ kg} \quad (8a)$$

$$\mathbf{C}_F = \text{diag}[150 \ 150 \ 150 \ 150 \ 150 \ 150 \ 150 \ 150] \text{ kg/s} \quad (8b)$$

and \mathbf{K}_F is given by

$$\begin{bmatrix} 1.60 & -0.1 & -0.5 & 0.0 & 0.0 & 0.0 & 0.0 & 0.0 \\ & 1.60 & 0.0 & -0.5 & 0.0 & 0.0 & 0.0 & 0.0 \\ & & 1.50 & -0.1 & -0.5 & 0.0 & 0.0 & 0.0 \\ & & & 1.60 & 0.0 & -0.5 & 0.0 & 0.0 \\ & & & & 1.60 & -0.1 & -0.5 & 0.0 \\ & \text{SYM} & & & & 1.60 & 0.0 & -0.5 \\ & & & & & & 1.50 & -0.1 \\ & & & & & & & 1.60 \end{bmatrix} \text{ MN/m.} \quad (8c)$$

This foundation model has a similar dynamic stiffness to the actual foundation and has a similar distribution of modes of the foundation in isolation, [19].

Simulated Results and Discussion

The measured responses at the bearing foundation were computed using the assumed foundation model and a given unbalance on the rotor, using Eq. (1). The machine was rundown from 60 Hz to 1 Hz, with measurements taken at a spacing of 0.5 Hz. The calculated responses associated with the translational degrees-of-freedom at all four bearings were assumed to be the measured responses. Using these measured responses, the identification of

the foundation model and the unbalance state (at known balance planes) was then carried out.

No Noise on the Simulated Responses

Method 1. The estimated unbalances for the different runs are listed in Table 1. The identified unbalances were quite accurate. However, the response estimation using the identified foundation models and unbalance state were not very good for any of the cases, even for the simulated example. Figure 2 shows a typical comparison and demonstrates that the estimated responses are quite different from measured ones.

Table 1 The estimated unbalance for the simulated example without noise

| Unbalance Configuration | Balance Disk | Actual Unbalance (amplitude in g m, phase in degrees) | | Method 1 | | Method 3 | |
|-------------------------|--------------|---|-------|-----------|-------|-----------|-------|
| | | Unbalance | Phase | Unbalance | Phase | Unbalance | Phase |
| 1 | 3 | 0.160 | 45 | 0.1678 | 44.4 | 0.1639 | 47.7 |
| 2 | 1 | 0.160 | 195 | 0.1797 | 188.2 | 0.1630 | 191.0 |
| 3 | 3 | 0.160 | 45 | 0.1606 | 37.5 | 0.1560 | 40.3 |
| | 3 | 0.160 | 45 | 0.1715 | 48.4 | 0.1712 | 45.8 |
| 4 | 4 | 0.160 | 150 | 0.2108 | 149.1 | 0.1506 | 151.1 |
| | 1 | 0.160 | 195 | 0.1737 | 195.9 | 0.1599 | 196.9 |
| 5 | 5 | 0.160 | 0 | 0.1811 | -0.02 | 0.1514 | 17.93 |
| | 1 | 0.160 | 195 | 0.1624 | 182.3 | 0.1704 | 199.2 |
| 6 | 3 | 0.160 | 45 | 0.1318 | 42.9 | 0.1862 | 45.9 |
| | 4 | 0.160 | 150 | 0.1941 | 154.2 | 0.1843 | 134.3 |
| | 1 | 0.160 | 195 | 0.1852 | 195.7 | 0.1589 | 197.8 |
| | 3 | 0.160 | 45 | 0.1829 | 42.2 | 0.1671 | 48.5 |
| | 5 | 0.160 | 0 | 0.1830 | 2.77 | 0.1500 | 17.7 |

Method 2. The last column in Table 2 lists the estimated unbalances for the combined approach. Figure 3 gives the comparison of estimated and measured responses for a typical case. The unbalance estimates are accurate in all cases, and the fit to the simulated responses is quite good. The results are encouraging.

With Noise on the Simulated Responses

In practice, the measured response data will be contaminated by noise and the rotor and bearing models will contain errors. To simulate such conditions, the eight simulated translational responses at the bearings for unbalance configuration 3 of Table 1 were corrupted with 1% noise. The effect of modeling errors was demonstrated by adding 20% noise to the bearing static loads at each frequency to introduce uncertainty into the bearing parameters for the simulated responses. The static loads in the model

used for the estimation remain constant. The regularization used removes the noise from the measured data using the SVD of the autocorrelation matrix of the responses.

Experimental Example

The identification methods were tested on experimental data from the test rig at Aston University. The machine was rundown from 55 Hz to 5 Hz in 210 frequency steps. The first-order responses for the horizontal and vertical acceleration at the bearing pedestals were extracted. The static load at the bearings was estimated by Smart [19] to be 221 N, 486 N, 461 N, and 400 N at bearings 1 to 4, respectively. Three runs were performed, the first with the residual unbalance and the second and third cases with the addition of different unbalance weight distributions. Since the residual unbalance was unknown, two approaches were taken. The first approach subtracts the response for run 1 from that for run 2, and the unbalance state was then identified from the resulting responses. Assuming the system is linear then the identified unbalance will be the unbalance added. The alternative is to estimate the residual unbalance for run 1, estimate the unbalance for run 2, and difference these estimates to compare with the unbalance weights added. The process may be repeated for run 3.

Table 2 shows the runs when the difference between the runs is considered, and illustrates the difference in performance of the two approaches. In method 2 the frequency range is split into four bands; 5–17 Hz, 17–28 Hz, 28–40 Hz, and 40–55 Hz. Table 3 shows the equivalent results when the unbalance is estimated for

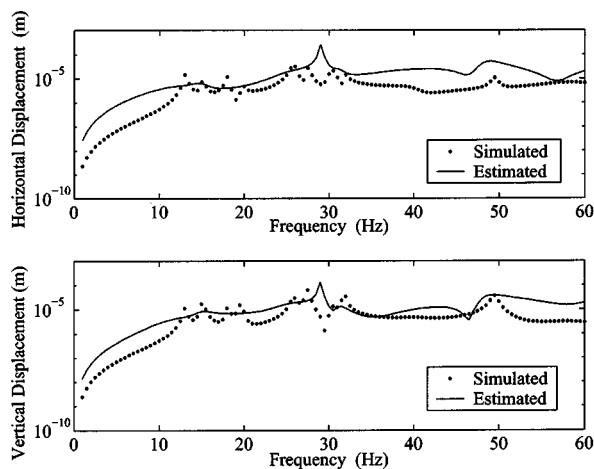


Fig. 2 Comparison of measured and estimated response using method 1

Table 2 Unbalance estimation from the experimental rundown data by subtracting runs

| Run | Disk | Actual Unbalance (Amplitude (g m) @ phase (deg.)) | Estimated Unbalance (Amplitude (g m) @ phase (deg.)) | |
|-----|------|---|---|----------------|
| | | | Method 1 | Method 3 |
| 2-1 | 2 | 1.7 @ 105 | 1.380 @ 67.42 | 1.529 @ 51.42 |
| | 5 | 1.7 @ 180 | 2.345 @ 164.78 | 1.759 @ 176.10 |
| 3-1 | 1 | 1.7 @ 225 | 1.820 @ 300.97 | 1.943 @ 293.02 |
| | 5 | 1.7 @ 315 | 2.067 @ 47.59 | 1.849 @ 51.40 |

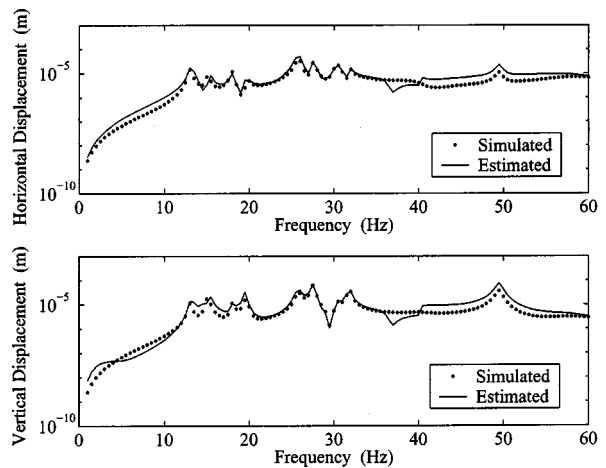


Fig. 3 Comparison of measured and estimated response using method 2

Table 3 Unbalance estimation from experimental rundown data by subtracting unbalance

| Method | Runs | Unbalance Planes | Estimated (Amplitude (g m) @ phase (deg.)) | | | Actual Unbalance Added |
|--------|-------|------------------|--|----------------|-----------------|------------------------|
| | | | First Run | Second Run | Added Unbalance | |
| 1 | 1 & 2 | Disk 2 | 0.955 @ 208.51 | 0.877 @ 110.00 | 1.388 @ 67.21 | 1.70 @ 105 |
| | | Disk 5 | 0.516 @ 1.12 | 1.866 @ 161.50 | 2.360 @ 165.72 | 1.70 @ 180 |
| 3 | 1 & 2 | Disk 2 | 0.958 @ 210.11 | 0.742 @ 85.60 | 1.508 @ 54.03 | 1.70 @ 105 |
| | | Disk 5 | 0.860 @ 6.90 | 1.067 @ 153.44 | 1.847 @ 168.31 | 1.70 @ 180 |
| 1 | 1 & 3 | Disk 1 | 1.043 @ 207.61 | 2.050 @ 269.97 | 1.819 @ 300.50 | 1.70 @ 225 |
| | | Disk 5 | 0.605 @ 38.17 | 2.519 @ 36.29 | 2.035 @ 45.48 | 1.70 @ 315 |
| 3 | 1 & 3 | Disk 1 | 1.053 @ 209.65 | 2.283 @ 266.36 | 1.919 @ 293.67 | 1.70 @ 225 |
| | | Disk 5 | 0.883 @ 11.71 | 2.498 @ 41.40 | 1.655 @ 52.43 | 1.70 @ 315 |

each run, and the estimated unbalances are differenced. Both approaches gives good estimates of the unbalance; however, method 2 consistently gives the better unbalance estimates. The amplitude of the unbalance is consistently estimated more accurately than the phase. This may be because of errors in the bearing model, or maybe small phase shifts in the measurement system. The fit of the estimated responses to the measured responses is not particularly good, because of the ill-conditioning of the foundation model parameters, and the fact that an equation error rather than an output error approach is used. However, it is encouraging that the unbalance estimation is still excellent despite these problems, showing that the unbalance estimation is robust.

Robustness of Unbalance Estimates to Modeling Errors

The proposed estimation method uses models of the shaft and the bearings. The shaft model is likely to be very accurate, and if the shaft is available before installation then the free-free response of the rotor may be checked against that predicted by the model. The examples described thus far in the paper have used short bearing theory for the bearing model. This theory is reasonably accurate, although the greatest unknown quantity in the model is the estimated static load on the bearings, which depends critically on the alignment of the machine. The unbalance estimation was performed in the previous sections assuming that the machine was perfectly aligned. This section considers the sensitivity of the unbalance estimates to some potential modeling errors. Clearly there are a huge number of potential sources of error, and the selection chosen here is designed to demonstrate the robustness of the unbalance estimates, rather than localize any modeling error.

Table 4 shows the results obtained by assuming a number of modeling errors, using the experimental data. The estimation is performed by splitting the frequency range into a number of bands for the foundation model. The unbalance is estimated for each run, and the unbalance estimates are subtracted to estimate the unbal-

ance added. The first test is to zero the bearing damping, while retaining the speed dependent bearing stiffness. If the bearing model were to introduce phase errors into the unbalance estimate, then bearing damping may be a cause. Table 4 shows that the phase of the estimated unbalance does change to some extent, although reducing the damping to zero is a significant change in the model. Next the viscosity of the oil in the bearing is halved, which produces very little change in the unbalance estimates. Increasing the bearing clearance in the model does produce significant changes in the unbalance estimates, particularly at the disk near the free end of the rotor.

Increasing the shaft stiffness by 5% has a very significant effect on the unbalance estimates. This shows that accurate modeling of the shaft is more important for good unbalance estimates than accurate bearing models. Table 4 shows various changes to the assumed static load on the bearings in the model. What is clear from the tests changing a single static load, is that the unbalance estimates change most on the disks nearest to the bearing whose load has changed. Thus disk 5 is nearest to bearing 4, and so the estimate of this unbalance changes significantly when the load on bearing 4 is reduced.

These examples have shown the robustness of the proposed unbalance estimation approach to representative modeling errors. The use of short bearing theory for the bearing model seems adequate, and the importance of the accurate alignment has been highlighted. Furthermore it is vital that the shaft is modelled accurately.

Conclusion

An identification method for the estimation of both the state of unbalance (amplitude and phase) and the flexible foundation model of a rotor-bearing-foundation system has been presented. The estimation uses measured vibration data at the bearing pedestals from a single rundown or runup of the machine, without

Table 4 Robustness of unbalance estimation from experimental data by subtracting unbalance

| | Estimated Unbalance Added (Amplitude (g m) @ phase (deg.)) | | | |
|--|--|--------------|--------------|--------------|
| | Runs 1 and 2 | | Runs 1 and 3 | |
| | Disk 2 | Disk 5 | Disk 1 | Disk 5 |
| Initial model | 1.508 @ 54° | 1.847 @ 168° | 1.919 @ 294° | 1.785 @ 56° |
| Zero bearing damping | 1.600 @ 72° | 1.923 @ 164° | 1.945 @ 303° | 1.781 @ 46° |
| Bearing oil viscosity halved | 1.357 @ 54° | 1.768 @ 164° | 1.818 @ 295° | 1.708 @ 51° |
| Bearing clearance=0.175 mm (from 0.15 mm) | 1.590 @ 55° | 2.747 @ 192° | 1.880 @ 295° | 1.263 @ 82° |
| Shaft stiffness increased by 5% | 0.320 @ 34° | 2.119 @ 169° | 1.047 @ 262° | 2.015 @ 53° |
| Static load on all bearings increased by 20% | 1.409 @ 52° | 2.267 @ 161° | 1.851 @ 293° | 2.068 @ 46° |
| Static load on bearing 4 decreased to 300 N (from 400 N) | 1.483 @ 54° | 1.482 @ 168° | 1.909 @ 294° | 1.556 @ 63° |
| Static load on bearing 1 increased to 400 N (from 221 N) | 1.389 @ 56° | 1.842 @ 169° | 1.861 @ 295° | 1.808 @ 53° |
| Actual unbalance added | 1.700 @ 105° | 1.700 @ 180° | 1.700 @ 225° | 1.700 @ 315° |

prior knowledge of the state of unbalance. Three approaches were used for the estimation. The first method uses the whole frequency range at once, is very quick and generally gives a good estimate of the state of unbalance. However, the estimated foundation model is not very good, since there are fewer degrees-of-freedom in the foundation model than system modes. This may be overcome by dividing the entire frequency range into smaller frequency bands and estimating the frequency dependent foundation models. The final method combines these approaches by estimating a global unbalance vector, but a different foundation model in each frequency band. This combined method was found to be the most reliable for estimation of both the frequency-dependent foundation models and the state of unbalance. This method is also robust to noisy data and modelling errors. The approaches were fully tested on simulated and experimental data from a four bearing machine.

Acknowledgments

Jyoti K. Sinha acknowledges the support of the Department of Science and Technology of India through the award of a BOYSCAST Fellowship. Sinha also acknowledges his parent organization, B.A.R.C. (India), for consistent support and encouragement. Michael I. Friswell acknowledges the support of the EPSRC through the award of an Advanced Fellowship. The authors wish to thank Andrew Glendenning, John Penny, and Seamus Garvey of the Rotordynamics Research Laboratory at Aston University, who provided the measured data.

References

[1] Adams, M. L., and McLosky, T. H., 1984, "Large Unbalance Vibration in Steam Turbine Generator Sets," I.Mech.E., Conference, Vibrations in Rotating Machinery, York, UK, Sept. 11–13.

[2] Davies, W. G. R., Lees, A. W., Mayes, I. W., and Worsfold J. H., 1976, "Vibration Problems in Power Stations," I.Mech.E., Conference Vibrations in Rotating Machinery, Cambridge, UK, Sept.

[3] Mayes, I. W., and Davies, G. W. R., 1980, "A Method of Calculating the Vibrational Behavior of Coupled Rotating Shafts Containing a Transverse Crack," I.Mech.E., Conference, Vibrations in Rotating Machinery, Cambridge, UK, Sept. 2–4.

[4] Kellenburger, W., 1972, "Should a Flexible Rotor be Balanced in N or N+2 Planes?" J. Eng. Ind., **94**, pp. 548–560.

[5] Nicholas, J. C., Gunter, E. J., and Allaire, P. E., 1976, "Effect of Residual Shaft Bow on Unbalance Response and Balancing of a Single Mass Flexible Rotor: Part I—Unbalance Response," J. Eng. Power, **98**, pp. 171–181.

[6] Nicholas, J. C., Gunter, E. J., and Allaire, P. E., 1976, "Effect of Residual Shaft Bow on Unbalance Response and Balancing of a Single Mass Flexible Rotor: Part II—Balancing," ASME J. Eng. Gas Turbines Power, **98**, pp. 182–189.

[7] Parkinson, A. G., Darlow, M. S., and Smalley, A. J., 1984, "Balancing Flexible Rotating Shafts With an Initial Bend," AIAA J., **22**(5), pp. 686–689.

[8] Parkinson, A. G., 1991, "Balancing of Rotating Machinery," J. Mech. Eng. Sci., **205**, pp. 53–66.

[9] Foiles, W. C., Allaire, P. E., and Gunter, E. J., 1998, "Review: Rotor Balancing," Shock and Vibration, **5**, pp. 325–336.

[10] Edwards, S., Lees, A. W., and Friswell, M. I., 1998, "Fault Diagnosis of Rotating Machinery," Shock Vib. Dig., **30**(1), pp. 4–13.

[11] Maslen, E. H., Vazquez, J. A., and Sortore, C. K., 2000, "Reconciliation of Rotordynamic Models With Experimental Data," ASME Paper No. 2000-GT-0395.

[12] Vazquez, J. A., Maslen, E. H., Ahn, H.-J. and Han, D.-C., 2001, "Model Identification of a Rotor With Magnetic Bearings," ASME J. Eng. Gas Turbines Power, **125**, pp. 148–155.

[13] Lees, A. W., and Simpson, I. C., 1983, "The Dynamics of Turbo-Alternator Foundations," IMechE Conference Paper C6/83, Feb., London, UK.

[14] Lees, A. W., 1988, "The Least Squares Method Applied to Identify Rotor/Foundation Parameters," IMech.E. Conference, Vibrations in Rotating Machinery, Edinburgh, UK, Sept. 13–15.

[15] Provassi, R., Zanetta, G. A., and Vania, A., 2000, "The Extended Kalman Filter in the Frequency Domain for the Identification of Mechanical Structure Excited by Multiple Sinusoidal Inputs," Mech. Syst. Signal Process., **14**(3), pp. 327–341.

[16] Zanetta, G. A., 1992, "Identification Methods in the Dynamics of Turbogenerator Rotors," IMech.E. Conference, Vibrations in Rotating Machinery, Bath, UK, pp. 173–182.

[17] Vania, A., 2000, "On the Identification of the Foundation of a Large Turbo-generator Unit by the Analysis of Transient Vibrations," IMech.E. Conference, Vibrations in Rotating Machinery, Nottingham, UK., Sept. 12–14.

[18] Feng, N. S., and Hahn, E. J., 1995, "Including Foundation Effects on the Vibration Behavior of Rotating Machinery," Mech. Syst. Signal Process., **9**(3), pp. 243–256.

[19] Smart, M. G., Friswell, M. I., and Lees, A. W., 2000, "Estimating Turbogenerator Foundation Parameters—Model Selection and Regularisation," Proc. R. Soc. London, Ser. A, **456**, pp. 1583–1607.

[20] Lees, A. W., and Friswell, M. I., 1996, "Estimation of Forces Exerted on Machine Foundations," *International Conference Identification in Engineering Systems*, University of Wales, Swansea, UK, pp. 793–803.

[21] Lees, A. W., and Friswell, M. I., 1997, "The Evaluation of Rotor Imbalance in Flexibly Mounted Machines," J. Sound Vib., **208**(5), pp. 671–683.

[22] Edwards, S., Lees, A. W., and Friswell, M. I., 2000, "Experimental Identification of Excitation and Support Parameters of a Flexible Rotor-Bearing-Foundation System From a Single Run-Down," J. Sound Vib., **232**(5), pp. 963–992.

[23] Hamrock, B. J., 1994, *Fundamentals of Fluid Film Lubrication*, McGraw-Hill, Englewood Cliffs, NJ.

[24] Lawson, C. L., and Hanson, R. J., *Solving Least Squares Problems*, Prentice-Hall, Englewood Cliffs, NJ.

[25] Golub, G. H., and Van Loan, C. F., 1990, *Matrix Computations*, John Hopkins, Baltimore, MD.

[26] Hansen, P. C., 1994, "Regularisation Tools: A MATLAB Package for Analysis and Solution of Discrete Ill-Posed Problems," Numer. Algorithms, **6**, pp. 1–35.

A Model for Droplet Vaporization for Use in Gasoline and HCCI Engine Applications

Youngchul Ra
e-mail: yra@erc.wisc.edu

Rolf D. Feitz

Engine Research Center,
University of Wisconsin-Madison,
1500 Engineering Drive,
Madison, WI 53706

A model for unsteady droplet vaporization is presented that considers the droplet temperature range from flash-boiling conditions to normal evaporation. The theory of continuous thermodynamics was used to model the properties and compositions of multicomponent fuels such as gasoline. In order to model the change of evaporation rate from normal to boiling conditions more realistically, an unsteady internal heat flux model and a new model for the determination of the droplet surface temperature is proposed. An explicit form of the equation to determine the heat flux from the surrounding gas mixture to the droplet-gas interface was obtained from an approximate solution of the quasi-steady energy equation for the surrounding gas mixture, with the inter-diffusion of fuel vapor and the surrounding gas taken into account. The model was applied to calculate evaporation processes of droplets for various ambient temperatures and droplet temperatures. [DOI: 10.1115/1.1688367]

Introduction

Vaporization of droplets and sprays has been an issue of much interest for decades because of its significance in engineering applications. Along with experimental studies, substantial effort has been made to predict the behavior of vaporizing droplets and sprays numerically. In engine applications, though the range of pressures and temperatures where fuel vaporization takes place is broad, in many cases, the fuel vaporization regime of interest is in the low pressure range. In particular, the range of pressures and temperatures in port fuel injection (PFI) engines, gasoline direct injection (GDI) engines and homogeneous charge compression ignition (HCCI) engines with early injections is relatively low, [1–4], whereas that in conventional compression ignition (CI) engines may be high enough that the critical state of the fuel needs to be considered, [5–7].

For simplicity, fuels have been represented as a single component fuel in most multidimensional models. However, single component fuel models are not able to predict the complex behavior of the vaporization of multicomponent fuels such as gasoline and diesel. The preferential vaporization of light-end components in multicomponent fuels affects greatly the fuel distribution near the spray and can not be represented by single component fuel models, [8].

Studies have been performed on the vaporization of multicomponent fuels, [7–11]. Multicomponent fuel models are classified into two types, i.e., discrete component models and continuous composition models. The approach of a discrete component model has high computational overhead when it is used for fuels with a large number of components, because additional transport equations are to be solved for each species in order to track the fuel composition and vaporization behavior.

The continuous composition model, which is based on the continuous thermodynamics method, [9], can represent the fuel composition as a continuous distribution function with respect to an appropriate parameter such as molecular weight. This enables a reduction of computational load without degrading the predictability of the complex behavior of the vaporization of multicomponent fuels, [8].

Most vaporization models have focused on normal evaporation where the mass fraction of fuel vapor at the surface is less than unity and the concept of Spalding's mass transfer number is valid, [2]. However, the boiling situation takes place frequently at usual engine operating conditions. For example, in gasoline PFI engines, when the engine is operated at part load, i.e., the intake port pressure is relatively low, the vapor pressure of the injected fuel corresponding to the fuel temperature is likely to be higher than the intake port pressure. In GDI engines or HCCI engines with early injections, the fuel in an injector which is at high pressure is likely to be at a temperature higher than the boiling temperature of the fuel corresponding to the cylinder pressure due to heat transfer through the injector body, [12,13]. In both cases, the fuel droplets are in superheated conditions and vaporization occurs first through the boiling process, and then changes to normal evaporation later in the droplet lifetime. For the vaporization of multicomponent fuels, the fuel droplets are much more frequently in the boiling situation due to the high volatility of the light-end components of the fuel. For realistic predictions of the vaporization of multicomponent fuels in typical engine operating conditions, both boiling and normal evaporation modes should be considered and a smooth change between those two modes is desirable.

In this paper, a robust vaporization model that can be used in the low pressure range (i.e., below the critical state) is presented. The model was applied to predict the vaporization of single droplets. Single-component fuel cases using the model are also presented for comparison. Also, the applicability of the multicomponent model to model single-component fuel evaporation by modifying the constants of the distribution function is presented.

Theoretical Formulation

A spherical liquid droplet with a large number of components vaporizing without chemical reactions in a relatively low-pressure gaseous environment is considered. Radiation and second order effects such as the Soret and Dufour effects are assumed to be negligible. Assuming that each component species in the mixture can be characterized or identified by the value of one variable, I , which represents some macroscopic property, the amount of substance can be expressed via the distribution functions $f_l(I)$ and $f_v(I)$ for the liquid and vapor phases, respectively. With the ambient gas treated as a discrete species, assuming no absorption of the ambient gas into liquid droplet, the system is a continuous system of a liquid phase fuel and a semi-continuous mixture sys-

Contributed by the Internal Combustion Engine Division of THE AMERICAN SOCIETY OF MECHANICAL ENGINEERS for publication in the ASME JOURNAL OF ENGINEERING FOR GAS TURBINES AND POWER. Manuscript received by the ICE Division June 2002; final revision received by the ASME Headquarters Aug. 2003. Associate Editor: D. Assanis.

tem of vapor phase fuel and ambient gas. The general molar distribution function for the composition of the semi-continuous systems is defined as, [7],

$$G_p(I) = x_F^p f_p(I) + \sum_{s=1}^N x_s^p \delta(I - I_s) \quad (1)$$

where the p represents v or l , denoting the properties of the vapor or liquid phases, respectively. x is the mole fraction, N the total number of discrete species, and δ the dirac delta function. Subscripts s and F , respectively, denote the properties of the discrete and fuel species. The distribution has the property that

$$\int_0^\infty G_p(I) dI = 1, \quad \int_0^\infty f_p(I) dI = 1, \quad \sum_{s=1}^N x_s^p = 1 - x_F^p. \quad (2)$$

For the continuous system of the liquid fuel only, x_s^p is zero and x_F^p is unity so that $G_p(I)$ becomes equal to $f_p(I)$. In this research the independent variable I is chosen to be the molecular weight, however, two (or possibly even more) distributed variables could be used to represent the properties of mixtures, [14]. The functional form of the distribution function $f_p(I)$ is limited to an analytical form, which is shown later, though it could take on other forms, [15]. The mole fraction of a species i in the fuel is given by

$$x_i = G_p(I)_i \Delta I_i \quad (3)$$

where ΔI_i is the interval in I .

The governing equations for the liquid phase continuous system and the semi-continuous system of gas and vapor phase fuel, along with liquid-vapor equilibrium at the interface between the droplet and the surrounding gas are considered next.

Vapor Phase Transport Equations. Based on the continuous thermodynamics approach, the general governing equation for the various moments of the fuel vapor distribution in gas phase are derived as, [7],

$$\frac{\partial}{\partial t} [\rho_f \theta_v^n] + \nabla \cdot [\rho_f \theta_v^n v] = -\nabla \cdot \int_0^\infty I^n J_I dI + S_g \quad (n=0,1,2,\dots) \quad (4)$$

where v and ρ_f are the velocity of the gas-phase mixture and the density of the fuel vapor, respectively. S_g is the source term. J_I is the diffusion flux for the element with molecular weight I . In this study Fick's law is assumed to be applicable for the semi-continuous system. θ_v^n represents the n th moment of the distribution of vapor phase and it is defined generally as

$$\theta_v^n = \int_0^\infty I^n f_p(I) dI \quad (n=0,1,2,\dots). \quad (5)$$

Any number of equations can be obtained with Eq. (4) with different values of n , depending on the number of parameters used in the distribution function. But for the two-parameter type Γ distribution function used here, $n=2$ suffices for the calculations. With $n=0, 1$, and 2 , the governing equations for the continuity, mean molecular weight, θ , and the second moment of the fuel vapor distribution, ψ , can be derived, [7].

The energy equation can be expressed as

$$\begin{aligned} \bar{C}_p \frac{\partial}{\partial t} (\rho T) + \bar{C}_p \nabla \cdot (\rho v T) \\ = \nabla \cdot \lambda \nabla T + \left[\frac{a_c \rho \bar{D}}{\theta_v} + (b_c - C_{PA}) \rho \hat{D} \right] \nabla y_F \cdot \nabla T \end{aligned} \quad (6)$$

where T is the temperature, λ is the thermal conductivity, c is the concentration of the mixture, \bar{C}_p is the mixture specific heat, C_{PA} is the specific heat of air, \hat{D} is the diffusion coefficient associated with the diffusion processes of the second moment of the vapor

distribution, and a_c and b_c are the coefficients of a linear correlation of specific heat taken from Chou and Prausnitz [16] as a function of composition.

Liquid Phase Balance Equation. The liquid phase is approximated as well mixed for convective conditions, based on previous research on internal mixing driven by internal circulation, [17], droplet breakup and deformation, [18], and experimental evidence, [19]. For stagnant conditions where no circulation inside the droplet is induced, well-mixed condition is still assumed for the simplicity of the model. However, the temperature in the droplet is not assumed to be uniform because a surface temperature model is introduced, as discussed later. Assuming no absorption of ambient gas into the liquid droplet, a general form of the governing equation for the change in the various moments of the liquid fuel distribution is obtained by modifying a difference form suggested by Lippert and Reitz [10] as

$$\frac{\rho_l R}{3} \frac{d\theta_l^n}{dt} = \dot{m} \frac{\theta_l^n}{\theta_v^n} [\theta_l^n - \theta_v^n] \quad (n=1,2,\dots) \quad (7)$$

where ρ_l is mass density, R is droplet radius, \dot{m} is vaporization rate and θ_l^n and θ_v^n are the n th moments of the fuel distribution in liquid phase and vapor phase, respectively, as defined in Eq. (5).

Distribution Function. For the present modeling, the Γ distribution with respect to molecular weight, I , was chosen because it is convenient to represent petroleum fractions, [9,14]. The Γ distribution is formulated as

$$f(I) = \frac{(I-\gamma)^{\alpha-1}}{\beta^\alpha \Gamma(\alpha)} \exp\left[-\frac{(I-\gamma)}{\beta}\right] \quad (8)$$

where α and β are parameters that determine the shape of the distribution, and γ is the origin of the distribution function which is same in both the liquid and vapor phases.

Vapor-Liquid Equilibrium. In the continuous thermodynamics method, the equilibrium at the interface between the liquid droplet and the surrounding gas is based on the assumption that the chemical potential μ for the liquid phase, l , and vapor phase, v , are equal for each value of I in the interval from I_1 to I_2 , and is similar to the discrete case. Assuming an ideal solution, the surface mass fraction of fuel vapor can be determined using Raoult's law. A simple relation between the distribution parameters in the liquid and vapor phases can be obtained as, [9],

$$\theta_v - \gamma = \frac{(\theta_l - \gamma)}{1 + AB \sigma_l^2 / (\theta_l - \gamma)} \quad (9)$$

$$\sigma_v^2 = \sigma_l^2 \left[\frac{(\theta_v - \gamma)}{(\theta_l - \gamma)} \right]^2 \quad (10)$$

where A and B are functions of temperature from the integration of the composition-dependent Clausius-Clapeyron equation. Correlations for other properties of continuous composition mixtures such as specific, latent heat, critical temperature, etc., are used as suggested by Tamim and Hallett [9] and Lippert and Reitz [10].

Determination of Surface Temperature. For more accurate predictions of the vaporization rate and heat flux, a surface temperature model was incorporated into the present vaporization model. The surface temperature of the droplet is determined from a heat and mass transfer balance at the interface between the droplet and the surrounding gas. There are two regimes of heat transfer, i.e., heat transfer from the inside of the droplet to the surface, q_i , and heat transfer from the outer gas to the surface, q_o . The rate of heat transfer balances with the required heat for vaporization at the surface is

$$L(T_s) \dot{m} = q_i + q_o \quad (11)$$

where $L(T_s)$ is the latent heat of the fuel at the surface temperature, T_s , and \dot{m} is the vaporization rate. The heat transfer from inside the droplet was modeled as a convective heat transfer process with internal circulation taken into account. The heat transfer coefficient inside the droplet is determined from the thermal conductivity, λ , and the unsteady equivalent thickness of the thermal boundary layer, δ_e , as

$$q_i = h_{i,\text{eff}}(T_d - T_s) = \frac{\lambda}{\delta_e}(T_d - T_s) \quad (12)$$

where T_d is the droplet interior temperature and δ_e is calculated using an effective thermal diffusivity, [17],

$$\delta_e = \sqrt{\pi \alpha_{\text{eff}} t} = \sqrt{\pi \chi \alpha_l t} \quad (13)$$

where $\chi = 1.86 + 0.86 \tanh[2.225 \log_{10}(\text{Pe}_l/30)]$ and Pe_l is the Peclet number of the droplet. In the case of a stagnant droplet where no internal circulation is driven by the surrounding gas, the value of δ_e is determined from the heat flux equation for a semi-infinite material with constant surface temperature and is limited to $R/2.257$ where R is the radius of the droplet. This formulation is based on the temperature gradient at the surface of a slab immersed in a fluid at the time when the heat reaches the center line of the slab, [20].

The effective heat transfer coefficient for the outer flux is determined from the approximate solution of the energy equation for the vapor phase with the effects of inter-diffusion and Stefan flow considered, [21]. The approximate solution was obtained by solving one-dimensional energy equation together with species conservation equation using the method of integration by parts and approximation was made in treating a definite integral term as another form of definite integral multiplied by a constant. An explicit equation that relates the vaporization rate, \dot{m} , to the temperatures of the droplet and the surrounding gas mixture is

$$\begin{aligned} \dot{m}L(T_s) = & h_{i,\text{eff}}(T_d - T_s) \\ & + \frac{\kappa \bar{C}_p \dot{m}}{\exp\left[\frac{2r_o \bar{C}_p \dot{m}}{\lambda \text{Nu}} - \frac{[C_A](y_{F,\text{sur}} - y_{F,o})}{\lambda} \frac{\text{Sh}}{\text{Nu}}\right] - 1} (T_{\text{sur}} - T_s) \end{aligned} \quad (14)$$

where, T_d , is the droplet internal temperature, T_s , is the droplet surface temperature, T_{sur} is the surrounding gas temperature, Sh is the Sherwood number, Nu is the Nusselt number, \bar{C}_p is the average specific heat of the gas mixture including fuel vapor, κ is a correlation factor, [21], $[C_A] = (C_{PF} - C_{PA})\rho\bar{D}$ is the inter-diffusional difference of energy flux between fuel and air, where C_{PF} and C_{PA} are specific heat of fuel and air, respectively, and, $y_{F,o}$, and $y_{F,\text{sur}}$, are the mass fractions of fuel at the interface and far away, respectively. The rate of mass transport at the droplet surface is calculated using the well-known high mass transfer rate equation with Spalding's transfer number.

$$\dot{m} = g_m \ln(1 + B_M) \quad (15)$$

where g_m is the mass transfer coefficient determined from $g_m = \text{Sh}\rho\bar{D}/2R$ and B_M is Spalding's transfer number.

Since the effective heat transfer coefficient for the outer heat flux is coupled with the vaporization rate, the surface temperature of the droplet is determined by solving two balance equations iteratively, and assuming a quasi-steady heat transfer process.

Modeling of Boiling Process. For the boiling case, it is assumed that the instability of the droplet surface is negligible so that the droplet maintains its stable spherical shape. In this case, the model for the effective thermal diffusivity by internal circulation for non-boiling droplets is still valid, and there is no sudden breakup of the droplet due to internal phenomena such as micro-explosions.

When a droplet is heated up, its surface temperature increases and it can reach the boiling point, when the surface mass fraction becomes equal to unity. Boiling may also occur in the case of the evaporation of initially super-heated droplets where the droplet temperature is higher than the boiling temperature corresponding to the ambient gas pressure. The heat transfer process from the droplet interior to the droplet surface was modeled as a convective heat transfer process using a modified effective heat transfer coefficient from empirical correlations, [22], which take into account the effect of the nucleation inside the droplet, as

$$q_i = \alpha(T_d - T_b) = (h_{i,\text{eff},s} + \alpha_{sh})\Delta T \quad (16)$$

where $h_{i,\text{eff},s}$ is the coefficient for the portion of heat transfer by internal circulation at the saturation temperature, α_{sh} is the portion of heat transfer enhancement by the effect of nucleation, and ΔT is the difference between the droplet interior temperature and the boiling temperature. An empirical correlation for the portion of heat transfer enhancement by the effect of nucleation, α_{sh} , was suggested as, [22],

$$\begin{aligned} \alpha_{sh} = & 0.76\Delta T^{0.26} \quad (0 \leq \Delta T < 5) \\ = & 0.027\Delta T^{2.33} \quad (5 \leq \Delta T < 25) \\ = & 13.8\Delta T^{0.39} \quad (25 \leq \Delta T). \end{aligned} \quad (17)$$

It is reasonable to include the portion of heat transfer by internal circulation in an explicit form because the value of α_{sh} becomes zero when the droplet temperature is equal to the boiling temperature, i.e., $\Delta T = 0$, whereas there is enhancement of heat transfer by internal circulation even in the normal evaporation mode. This ensures a continuous change of the effective heat transfer coefficient for the internal heat transfer. Hence, a smooth transition of evaporation mode from boiling (flash boiling) to normal evaporation is ensured. Note that Eq. (16) can be used for the non-boiling super-heated droplet because the equation itself is independent of the evaporation mode.

Combining with Eq. (14) gives an explicit form of the energy equation to determine the vaporization rate for the boiling cases, including flash boiling, as

$$\begin{aligned} \dot{m}L(T_b) = & \alpha(T_d - T_b) \\ & + \frac{\kappa \bar{C}_p \dot{m}}{\exp\left[\frac{2r_o \bar{C}_p \dot{m}}{\lambda \text{Nu}} - \frac{[C_A](y_{F,\text{sur}} - 1)}{\lambda} \frac{\text{Sh}}{\text{Nu}}\right] - 1} (T_{\text{sur}} - T_b). \end{aligned} \quad (18)$$

The vaporization rate determined from the energy and mass transfer equations (for normal evaporation cases) is used to calculate the source terms for the vapor phase transport equation, Eq. (4).

Droplet Temperature Change. Neglecting the effect of radiation, the temporal change of the droplet internal temperature is given for normal evaporation as

$$\frac{dT_d}{dt} = \frac{Ah_{i,\text{eff}}(T_d - T_s)}{\rho C_v V} \quad (19)$$

and for boiling,

$$\frac{dT_d}{dt} = \frac{A\alpha(T_d - T_b)}{\rho C_v V} \quad (20)$$

where A and V are the droplet surface area and volume, respectively, C_v is the specific heat at constant volume of the liquid phase at the droplet temperature, and $h_{i,\text{eff}}$ and α are the effective heat transfer coefficients for the normal evaporation and boiling cases, respectively, which are the same as in Eqs. (12) and (16).

Table 1 Fuel distribution parameter values, [9]

| Fuel | Gasoline | Iso-octane |
|----------|----------|------------|
| α | 5.7 | 100 |
| β | 15 | 0.1 |
| γ | 0 | 104.2 |
| θ | 85.5 | 114.2 |
| σ | 35.8 | 1 |

Results

The present model was applied to study the vaporization of single stagnant droplets, using a modified version of the KIVA3V Release 2.0 code, [23]. Since the density of the fuel droplet affects the breakup of sprays as well as transient heat transfer between the droplet interior and the surface, the liquid fuel density change with temperature and the mean molecular weight was included in the simulations. Variable density also allows the droplets to swell due to heating by the ambient gas. For the multicomponent fuel model, a correlation of density in terms of molecular weight for hydrocarbon fuels of the paraffin family and temperature, was obtained from the density data of Gallant and Yaws [24]. Predictions of the multicomponent model for gasoline and iso-octane were compared to the single component iso-octane cases for various ambient gas temperatures, ambient gas pressures and initial droplet temperatures.

Single Stagnant Droplet Evaporation. The vaporization process of stagnant droplets of gasoline and iso-octane located in quiescent air was calculated. The parameters of the Γ distribution function were chosen as shown in Table 1 for the composition of gasoline and iso-octane in the multicomponent fuel model. For the calculation of iso-octane evaporation with the multicomponent model, the values of all other physical properties used in the model were matched with those of the single component (pure) iso-octane fuel to allow a comparison to be made. The drop vaporization computations considered various ambient air temperatures, ambient pressures and droplet initial temperatures. For all cases, the initial droplet diameter was 100 μm .

Typical behavior for normal evaporation of gasoline droplets is shown in Fig. 1. Droplet surface area decreases gradually with time from the beginning and evaporation constant, which is defined as negative of the gradient of the surface regression curve, i.e., $K = -(dD^2/dt)$, does not vary much around the average value of 0.294. Because of preferential vaporization of the highly

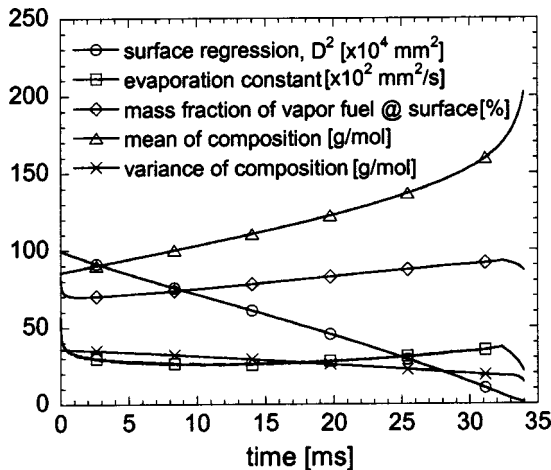


Fig. 1 Evaporation of a gasoline droplet in quiescent ambient air. The initial ambient temperature and pressure are 1000 K and 1.0 bar, respectively. The initial temperature and size of the droplet are 300 K and 100 μm , respectively.

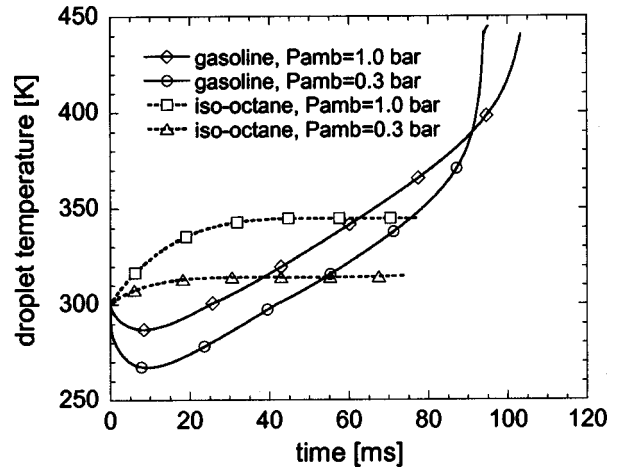


Fig. 2 Predicted history of droplet interior temperature for gasoline and iso-octane droplets at ambient air pressures of 0.3 and 1.0 bar, ambient temperature of 500 K. The initial droplet temperature and drop size are 300 K and 100 μm , respectively.

volatile light-end components in the gasoline composition, the mean of the composition increases and the variance decreases steadily. The mass fraction of fuel vapor at the droplet surface decreases initially due to the increase of the mean of composition and the decrease of the surface temperature, then increases because the heating effect is more than the reducing effect of the increase of the mean of composition. This differs slightly from the predictions of Tamin and Hallet [9] in which the mass fraction of fuel vapor decreased steadily from the initial value, and Lippert and Reitz [10] in which the mass fraction of the fuel vapor increases initially and decreases later. However, the droplet lifetime of 34 ms under the given conditions is in good agreement with the data by Lippert and Reitz [10].

When the heat supplied from the surrounding gas is not enough to provide the energy of vaporization corresponding to the mass flux at the initial droplet temperature, the surface temperature of the droplet decreases so that the mass flux of vapor leaving the droplet decreases and the heat flux from the surrounding gas and droplet interior is enhanced. Once the surface temperature is lower than the droplet temperature, a droplet cooling process begins due to the heat loss to the droplet surface and continues until the surface temperature is higher than the droplet interior temperature. Similar reasoning can be applied to the droplet heating case. Figure 2 shows a comparison of the predicted history of droplet interior temperatures for gasoline and iso-octane droplets at ambient air pressures of 0.3 and 1.0 bar. The gasoline droplet at the ambient pressure of 0.3 bar is vaporized through boiling initially and the other case is in the normal evaporation mode. The gasoline droplet initially experiences a cooling process, while the iso-octane droplet is heated up from the beginning. Figure 2 also shows an interesting characteristic of multicomponent fuel vaporization; gasoline droplets do not reach an equilibrium temperature, as in the case of the single-component iso-octane droplets. This is because the composition of the droplet is continuously changing as the more volatile components are vaporized.

Figure 3 shows the typical temporal behavior of the temperatures and surface vapor mass fraction of a superheated gasoline droplet vaporizing in a 500 K, 0.5 bar environment. With an initial droplet temperature of 360 K, the droplet is vaporized through flash-boiling initially, as seen from the fact that the mass fraction at the surface is unity. Subsequently, the vaporization mode changes to normal evaporation. It is also seen between the time of 0.01 and 0.36 ms that the surface of the droplet is in a subcooled state, while the droplet interior is in a superheated state. The boil-

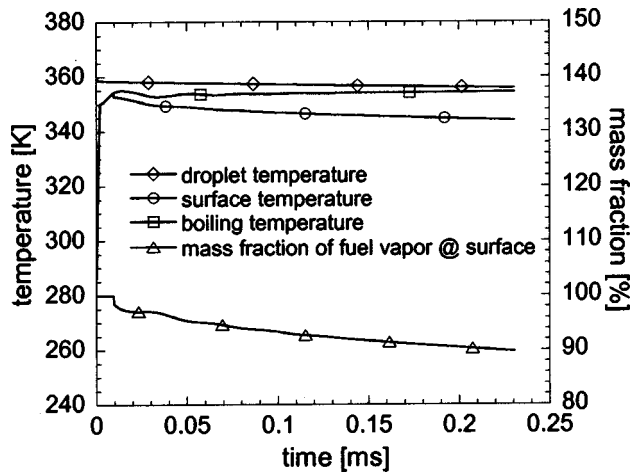


Fig. 3 Temporal behavior of temperature and surface vapor mass fraction of a superheated gasoline droplet at $T_{amb} = 500$ K, $P_{amb} = 0.5$ bar, $T_{pi} = 360$ K and $D_i = 100$ μ m

ing temperature increases fast at the beginning of the vaporization because most of the light-end components of the gasoline composition leave the droplet through the flash-boiling process. The droplet interior and surface temperatures approach each other within one degree difference in 7 ms (the droplet life time of this case is 43.4 ms, as seen in Fig. 4) so that the droplet can be reasonably approximated as a lumped system after a short time interval.

Flash-boiling evaporation of superheated droplets was predicted for gasoline and single-component iso-octane fuels with initial droplet temperatures of 300 and 360 K at ambient temperature and pressure of 500 K and 0.5 bar, respectively, as seen in Fig. 4. All three cases except for the case of iso-octane, with $T_{pi} = 300$ K undergo flash boiling at the beginning of the vaporization (at 0.5 bar, the boiling temperatures of the iso-octane and gasoline droplets are 348.7 K and 286.3 K, respectively) and, hence show very steep gradients of the surface regression curve. The values of the evaporation constant of the three boiling cases were initially 393.8 for gasoline at 360 K, 15.13 for gasoline at 300 K, 3.413 for iso-octane at 360 K, while that for iso-octane at 300 K was zero. For the same initial droplet temperature, the evaporation constant of gasoline case is higher than for iso-octane initially due to the

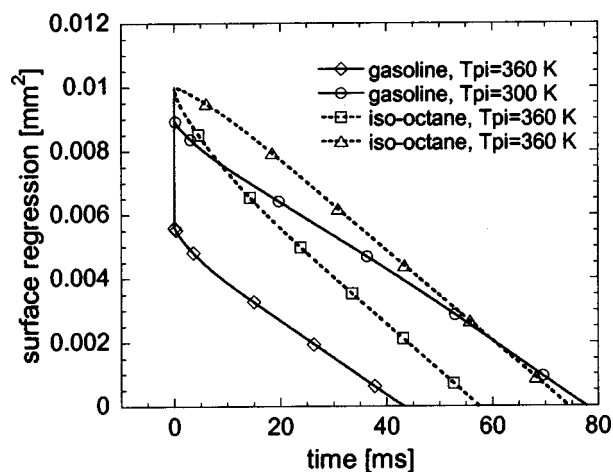


Fig. 4 Predicted history of surface regression for gasoline and iso-octane droplets with two different initial temperatures at ambient pressure of 0.5 bar and ambient temperature of 500 K. The initial drop size is 100 μ m.

Table 2 Comparison of evaporation constant

| Ambient Temperature | Chin and Lefebvre | Present Model | |
|---------------------|-------------------|-----------------------|------------|
| | Gasoline (JP4) | Gasoline (automotive) | Iso-octane |
| 500 K | 0.12 | 0.093 | 0.144 |
| 800 K | 0.285 | 0.26 | 0.313 |

high volatility of the light-end components of the gasoline, but lower in the later stages of vaporization because the mean molecular weight of the gasoline continuously increases. Note that the initial evaporation constant may be nonpositive because swelling of the droplet is considered.

The predicted evaporation constants of gasoline droplets at the later stages of the droplet lifetime for ambient temperatures of 500 K and 800 K, ambient pressure of 1.0 bar, and initial droplet temperature of 270 K, were compared to data in the literature, [25], along with the evaporation constants of iso-octane droplets, as shown in Table 2. Note that the literature data (automotive gasoline data was not available) were obtained assuming a steady-state evaporation of a single component fuel (molecular weight 125.0), while the gasoline data in the present study were obtained from the multicomponent, unsteady evaporation model (mean molecular weight in the 800 K case is 170.3). The present predictions are comparable to the previous results, though the evaporation constant of the gasoline droplets by the present model is a little lower than the literature data, while those of the pure iso-octane droplets are higher. The difference is because, as vaporization continues, the mean molecular weight of the multicomponent gasoline droplets increases, and thus cancels the enhancement of the vaporization rate due to the increase of the droplet temperature.

In order to further validate the multi-component model, predictions of vaporization of iso-octane droplets using the multicomponent model were compared to those of the single-component model at 500 K ambient temperature, for three ambient pressures of 0.3, 0.5 and 1.0 bar and two initial droplet temperatures of 300 and 360 K. The composition is represented by a narrow distribution and the parameters of the Γ distribution were chosen as shown in Table 1 to give a mean molecular weight of 114.2 which is the molecular weight of iso-octane, and a variance of 1.0, [8].

As shown in Fig. 5, the surface regression curves predicted by

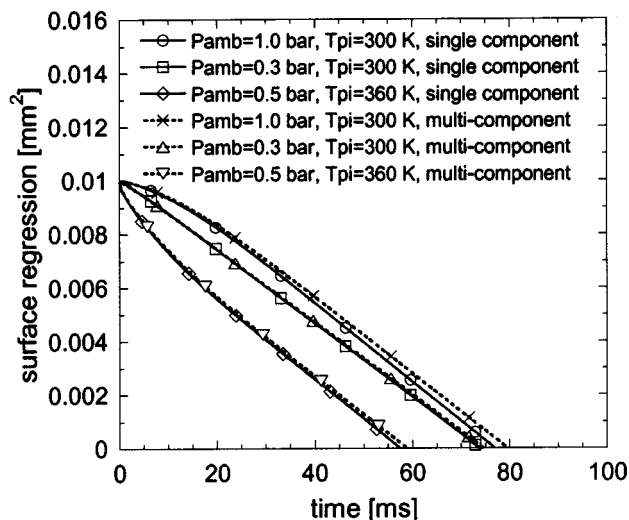


Fig. 5 Comparison of predictions of iso-octane vaporization by the single-component model and the multicomponent model

the single and multicomponent models are in very good agreement in both the normal and boiling modes (low pressure cases). This implies that the multicomponent model can also be used for the simulation of single-component fuels using appropriate parameters for the composition distribution function and property correlations.

Conclusion

A model for unsteady droplet vaporization has been presented. An explicit form of equation to determine the heat flux from the surrounding gas mixture to the droplet-gas interface was obtained from an approximate solution of the quasi-steady energy equation for the surrounding gas mixture with the inter-diffusion of fuel vapor and surrounding gas taken into account. The model considers the droplet temperature range from flash-boiling conditions to normal evaporation for single and multicomponent fuels. The model was applied to the prediction of drops under quiescent conditions. Based on the results, the following conclusions are drawn: (1) the boiling (flash-boiling) process should be included in evaporation models used in engine applications for accurate predictions at low ambient pressures or under superheated droplet conditions, especially for the prediction of the behavior of multicomponent fuel sprays, (2) the new surface temperature model ensures the prediction of more realistic and accurate profiles of droplet temperature from flash-boiling to normal vaporization conditions, and (3) the present multicomponent evaporation model based on continuous thermodynamics can also be applied to the prediction of single-component fuel vaporization.

Acknowledgments

This study was supported by Honda R&D Co., Ltd, Ricardo North America and the Department of Energy Sandia Laboratories.

Nomenclature

| | |
|----------|---|
| A | = surface area |
| a_c | = vapor phase specific heat parameter |
| B_M | = Spalding's transfer number $= (y_s - y_\infty) / (1 - y_s)$ |
| b_c | = vapor phase specific heat parameter |
| C_A | = inter-diffusional energy difference |
| C_p | = specific heat at constant pressure |
| C_v | = specific heat at constant volume |
| D | = diffusion coefficient |
| f | = distribution function |
| G | = general molar distribution function |
| g_m | = mass transfer coefficient |
| h | = enthalpy; heat transfer coefficient |
| I | = distribution variable |
| J | = diffusion flux |
| L | = latent heat |
| m | = mass |
| Nu | = Nusselt number |
| q | = heat flux |
| R | = radius |
| r | = radius |
| S_g | = source term |
| Sh | = Sherwood number |
| T | = temperature |
| t | = time |
| V | = droplet volume |
| v | = average velocity |
| x | = molar fraction |
| y | = mass fraction |
| α | = Γ distribution parameter; thermal diffusivity; heat transfer coefficient |
| β | = Γ distribution parameter |
| γ | = Γ distribution parameter |

| | |
|------------|---|
| δ | = dirac delta function; thickness of thermal boundary layer |
| θ | = mean of composition |
| θ^n | = N th moment of distribution |
| κ | = correlation factor |
| λ | = thermal conductivity |
| ρ | = mass density |
| σ | = variance |
| ψ | = second moment of composition |

Subscripts and Superscripts

| | |
|--------|--|
| A | = air |
| b | = normal boiling point |
| d | = droplet interior |
| e | = equivalent term |
| eff | = effective value |
| F, f | = fuel |
| i | = component i of mixture; droplet interior |
| l | = liquid phase |
| o | = droplet surface; surrounding gas |
| p | = phase |
| s | = discrete species; source term; droplet surface |
| sh | = superheated |
| sur | = surrounding gas |
| v | = vapor phase |

References

- [1] Williams, A., 1973, "Combustion of Droplet of Liquid Fuels: A Review," *Combust. Flame*, **21**, pp. 1–31.
- [2] Sirignano, W. A., 1983, "Fuel Droplet Vaporization and Spray Combustion," *Prog. Energy Combust. Sci.*, **9**, pp. 291–322.
- [3] Peng, F., and Aggarwal, S. K., 1995, "A Review of Droplet Dynamics and Vaporization Modeling for Engineering Calculations," *ASME J. Eng. Gas Turbines Power*, **117**, pp. 453–461.
- [4] VanDerWege, B. A., Lounsbury, T. H., and Hochgreb, S., 2000, "Numerical Modeling of Fuel Spray in DISI Engines Under Early-Injection Operating Conditions," *SAE Paper 2000-01-0273*.
- [5] Givler, S. D., and Abraham, J., 1996, "Supercritical Droplet Vaporization and Combustion Studies," *Prog. Energy Combust. Sci.*, **22**, pp. 1–28.
- [6] Curtis, E. W., Ulodogan, A., and Reitz, R. D., 1995, "A New High Pressure Droplet Vaporization Model for Diesel Engine Modeling," *SAE952431*.
- [7] Zhu, G.-S., and Reitz, R. D., 2002, "A Model for High Pressure Vaporization of Droplets of Complex Liquid Mixtures Using Continuous Thermodynamics," *Int. J. Heat Mass Transfer*, **45**, pp. 495–507.
- [8] Lippert, A. M., 1999, "Modeling of Multi-Component Fuels With Application to Sprays and Simulation of Diesel Engine Cold Start," Ph.D. thesis, University of Wisconsin-Madison.
- [9] Tamim, J., and Hallett, W. L. H., 1995, "Continuous Thermodynamics Model for Multi-Component Vaporization," *Chem. Eng. Sci.*, **50**(18), pp. 2933–2942.
- [10] Lippert, A. M., and Reitz, R. D., 1997, "Modeling of Multicomponent Fuels Using Continuous Distributions With Application to Droplet Evaporation and Sprays," *SAE Paper 972882*.
- [11] Zuo, B. F., Gomes, A. M., and Rutland, C. J., 2000, "Modeling of Superheated Fuel Spray and Vaporization," *Int. J. Engine Res.*, **1**(4), pp. 321–336.
- [12] VanDerWege, B. A., 1999, "The Effect of Fuel Volatility and Operating Conditions on Spray From Pressure Swirl Fuel Injectors," Ph.D. thesis, Massachusetts Institute of Technology, Cambridge, MA.
- [13] Zuo, B. F., and Rutland, C. J., 2001, "Continuous Thermodynamics Modeling of Superheated Multicomponent Fuel Vaporization," in preparation.
- [14] Cotterman, R. L., Bender, R., and Prausnitz, J. M., 1985, "Phase Equilibria for Mixtures Containing Very Many Components: Development and Application of Continuous Thermodynamics for Chemical Process Design," *Ind. Eng. Chem. Proc. Des. Dev.*, **24**, pp. 194–203.
- [15] Rätzsch, M. T., and Kehlen, H., 1983, "Continuous Thermodynamics of Complex Mixtures," *Fluid Phase Equilib.*, **14**, pp. 225–234.
- [16] Chou, G. F., and Prausnitz, J. M., 1986, "Adiabatic Flash Calculations for Continuous or Semicontinuous Mixtures Using an Equation of State," *Fluid Phase Equilib.*, **30**, pp. 75–82.
- [17] Sirignano, W. A., 1999, *Fluid Dynamics and Transport of Droplets and Sprays*, Cambridge University Press, Cambridge, UK.
- [18] Arcoumanis, C., Gavaises, M., and French, B., 1997, "Effect of Fuel Injection Process on the Structure of Diesel Sprays," *SAE Paper 970799*.
- [19] Law, C. K., 1982, "Recent Advances in Droplet Vaporization and Combustion," *Prog. Energy Combust. Sci.*, **8**, pp. 171–201.
- [20] Mills, A. F., 1995, *Basic Heat and Mass Transfer*, Richard D. Irwin, Homewood, IL.
- [21] Ra, Y., and Reitz, R. D., 2003, "A Multi-Component Droplet Vaporization Model to Gasoline Direct Injection Engines," *Int. J. Eng. Res.*, **4**(3), pp. 193–218.
- [22] Adachi, M., McDonnell, V. G., Tanaka, D., Senda, J., and Fujimoto, H., 1997,

“Characterization of Fuel Vapor Concentration Inside a Flash Boiling Spray,”
SAE Paper 970871.

- [23] Amsden, A. A., 1999, *KIVA-3V, Release 2, Improvements to KIVA-3V*. LA-UR-99-915.
- [24] Gallant, R. W., and Yaws, C. L., 1995, *Physical Properties of Hydrocarbons*, 3rd Ed., Gulf Pub. Co., Houston.
- [25] Chin, J. S., and Lefebvre, A. H., 1983, “Steady-State Evaporation Characteristics of Hydrocarbon Fuel Drops,” *AIAA J.*, **21**(10), pp. 1437–1443.

Cycle-Resolved NO Measurements in a Two-Stroke Large-Bore Natural Gas Engine

Paulius V. Puzinauskas¹

Mechanical Engineering Department,
U.S. Naval Academy,
590 Holloway Road,
Annapolis, MD 21402

Daniel B. Olsen

Bryan D. Willson

Engines and Energy Conversion Laboratory,
Mechanical Engineering Department,
Colorado State University,
Fort Collins, CO 80523

Cycle-resolved NO data were acquired from a Cooper-Bessemer GMV 4TF two-stroke engine to better understand and quantify large bore natural gas engine NO_x emission. The cycle resolved NO data were extracted separately from the engine's cylinder two and four exhaust ports and taken simultaneously with cycle resolved pressure traces, conventional steady-state emission measurements and a variety of additional performance and diagnostic data. The test variables were intake manifold boost pressure, ignition method and ignition timing. Relationships between individual cycle pressure traces and the NO produced by that cycle were investigated. Furthermore, mass-averaged NO values were calculated and integrated in order to compare with average exhaust emissions from a steady-state analyzer and combustion pressure characteristics. The steady measurements revealed that NO and NO₂ emissions respond differently to the test variables. The mass averaged cycle-resolved NO values compare well with the steady exhaust emission measurements and exhibit strong correlations with peak pressure and crank angle location of peak pressure. [DOI: 10.1115/1.1635401]

Introduction

Recent stationary emission source regulations have combined decreasing allowable emission levels with mandatory compliance demonstration, [1]. Such legislation coupled with free-market competition for natural gas has driven development of cost-effective emission reduction and monitoring technology for the natural-gas transmission industry. Conventional stationary natural-gas compression engine monitoring methods typically require dedicated continuous-use (or frequent periodic sampling with) specialized emission analyzers, which are not standard equipment for natural-gas compressor stations. Parametric emission monitoring models (PEMS) are an alternative that shows potential to provide reliable data and are inherently cost-effective since the required hardware is often already present on most engines. PEMS models utilize parameters commonly measured in field engines to predict engine-out emissions. Because of the potential cost and reliability improvements, research in this area has increased significantly during the last decade, [2–4].

This project involves the continued development of PEMS models by looking at cycle resolved NO production from a Cooper Bessemer GMV-4TF cylinder. A fast response NO analyzer made by Cambustion was utilized to make this measurement. The cycle-resolved NO data, coupled with in-cylinder pressure data, will be employed in future work to improve the neural network PEMS model for predicting NO_x emissions developed at Colorado State University. This paper details the first part of the work—that is the acquisition of cycle-resolved NO data and the associated data reduction implemented to interpret it, as well as acquisition of conventional emissions and potential PEMS input data.

The cycle-resolved NO data is useful for improving PEMS models as well as providing additional insight into the physics of NO_x formation. Oxides of nitrogen (NO_x) production is significantly influenced by combustion variability. The variation in peak cylinder pressure associated with combustion variability is accompanied by an associated variation in peak cylinder temperature.

¹Currently at the Mechanical Engineering Department, The University of Alabama, P.O. Box 870276, Tuscaloosa, AL 35487.

Contributed by the Internal Combustion Engines Division of THE AMERICAN SOCIETY OF MECHANICAL ENGINEERS for publication in the ASME JOURNAL OF ENGINEERING FOR GAS TURBINES AND POWER. Manuscript received by the ICE Division July 2002; final revision received January 2003. Associate Editor: D. Assanis.

This behavior is problematic from a NO_x production standpoint because the formation of nitric oxide (NO), the primary constituent in NO_x, is exponentially dependent on temperature. As a consequence of this exponential behavior, the cumulative NO emissions from an engine where the peak temperatures vary widely from cycle to cycle are much higher than an engine without significant cycle-to-cycle variation. Many retrofit technologies (i.e., multistrike ignition, precombustion chamber ignition, etc.) help mitigate combustion variability and, consequently, reduce NO_x. To our knowledge a detailed study of the relationship between cycle-resolved combustion characteristics and cycle-resolved NO_x has not been carried out on large-bore natural-gas engines.

Technical Approach

Overview. This investigation's data were gathered from a Cooper GMV-4TF engine using a fast NO analyzer and a variety of additional data-acquisition and analysis equipment. The test engine and test matrix, fast NO instrumentation and data processing and additional significant instrumentation are described in more detail below.

Test Engine and Test Matrix. The Cooper GMV-4TF engine is one of several highly instrumented industrial engines installed at the Colorado State University's large-bore engine test bed (LBET). The LBET has been thoroughly described in previous work, [5,6]. Nevertheless, a brief description is included here for completeness. The Cooper GMV-4TF engine is loaded by a large computer-controlled waterbrake dynamometer and is instrumented for all relevant temperatures and pressures, fuel and air flow as well as combustion pressure and emissions. Fuel-air ratio and spark timing are electronically controlled using a Woodward Governor Smart engine control system. The ignition system is an Altronic CPU-2000. The inlet and exhaust systems are modified to enable independent exhaust back pressure, intake boost pressure, intake-air temperature, and intake-air humidity control. Engine coolant water and lubricating oil temperatures are controlled as well. The fast NO data are from cylinders number 2 and 4, which are articulated off of the master compressor rod. A photograph of the test bed is shown in Fig. 1 and the significant engine parameters and nominal operating conditions are listed in Table 1.

The parameters varied for this investigation were boost pressure, ignition timing and ignition method. All other controlled variables were held constant. The boost pressures tested (referred

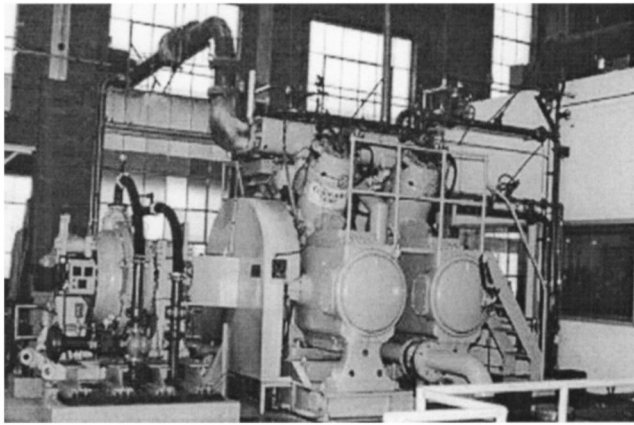


Fig. 1 The Cooper Bessemer GMV-4TF large-bore natural-gas engine

to as the boost map) were 6, 7.5, 10, and 13.5 Hg above atmospheric pressure. The exhaust pressure was adjusted to maintain a constant 2.5 Hg intake-to-exhaust pressure drop for all boost pressures. The GMV-TF is designed for lean combustion even when piston scavenged, which typically yields 1–3 Hg boost pressure. Table 2 verifies that the trapped charge for the lowest boost pressure tested was lean of stoichiometric, and subsequent increases in boost further lean the trapped charge. The trapped air-fuel ratio provided in the table was calculated from the total air-fuel ratio and the trapping efficiency, which was determined using a tracer-gas technique described by Olsen et al. in [7] and [8]. The equivalence ratio was computed using the method prescribed by Urban and Sharp [9] and fuel-gas-composition data, which are obtained from analysis performed periodically on the EECL natural gas supply. The boost map spark timing was adjusted to maintain an 18 deg ATDC average crank-angle location of peak pressure (LPP). Both single-strike (SS) and multistrike (MS) ignition strategies were used at each boost map test point. The ignition timing variation test (ignition map) was performed at 13.5 Hg boost using the single-strike ignition strategy. The timings tested were 6.4, 8.5, 10.5, 14.2, and 16.7 deg BTDC.

Fast NO Instrumentation and Data Analysis. The cycle-resolved NO data were gathered using a Cambustion fNO₄₀₀ fast NO analyzer. This instrument utilizes a chem.-illuminesce detector (CLD) similar to standard “steady” NO analyzers, except the

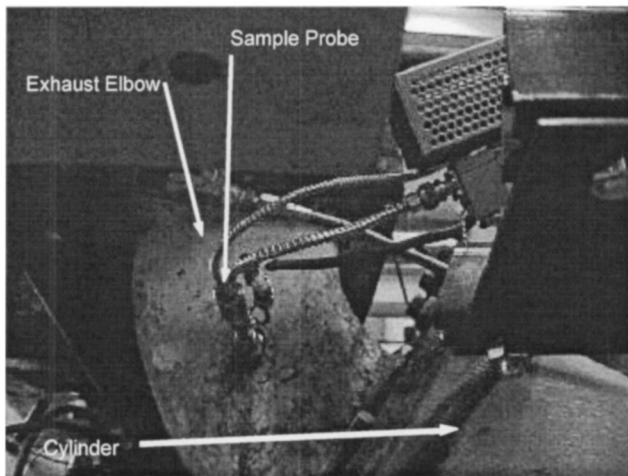


Fig. 2 Photograph of fNO400 sample head mounted to GMV exhaust port

Table 1 LBET engine characteristics

| Engine Parameter | Nominal Value or SPEC |
|----------------------------------|--|
| Engine type | V4, 2-stroke |
| Fuel delivery | Direct-injection cam-driven mechanical gas-admission valve |
| Fuel pressure | 25 psig (172 kPag) |
| Ignition type | Single or multistrike spark |
| Power cylinder bore | 35.6 cm |
| Power con. rod length | 87.3 cm |
| Master rod length | 86.4 cm |
| Crank-throw radius | 17.8 cm |
| Power rod pin angle | 70° (Cylinders 2 and 4) |
| Power rod pin radius | 21.5 cm |
| Power cyl. bank angle | 60° (Cylinders 2 and 4) |
| Brake power | 440 hp (330 kW) |
| Dynamometer torque | 7730 ft-lb (10.5 kN-m) |
| Engine speed | 300 rpm (5 Hz) |
| Ignition timing | 10° BTDC |
| Intake manifold pressure | 7.5" Hg (25 kPag) |
| Engine pressure drop | 2.5" Hg (8.5 kPa) |
| Overall A/F ratio | 42 |
| Trapped A/F ratio | 21 |
| Average peak combustion pressure | 505 psia (3.48 MPa) |
| Intake manifold temperature | 110°F (317 K) |
| Intake humidity ratio | 0.028 |
| Jacket water temperature | 160°F (340 K) |

detector is mounted remotely at the engine exhaust port (Fig. 2) and is sized to provide dynamic response on the order of 2–3 [ms], which allows crank-angle resolved NO concentration measurements. General fast-response NO system dynamics have been thoroughly discussed by Baltisberger and Ruhm [10]. The technical details of this particular instrument can be found in Reavell, et al. [11]. Fast NO data were gathered from the exhaust ports of cylinders 2 and 4.

The cycle-resolved NO data were examined as recorded and also integrated with exhaust flow rate over the engine cycle to calculate cycle-by-cycle NO emission. The flow rate was calculated using a quasi-steady flow model coupled to a thermodynamic engine simulation that was executed over the port-open portion of the cycle. Measured simulation inputs included exhaust-port cycle-resolved pressure and time-averaged temperature for each cylinder's exhaust port and the engine-average intake manifold pressure and temperature. The measured cylinder pressure at exhaust port opening was used as an initial condition for each cycle. The simulated cylinder pressure was used in the flow model to avoid noise and pegging issues associated with the measured cylinder pressure. The intake and exhaust-flow coefficients were adjusted to minimize the following two differences: (1) between the simulated and measured total mass flow; and (2) the assumed trapped mass at exhaust-port opening and the calculated trapped mass at exhaust-port closing. The adjustments were made based on the single-strike boost map data, and once optimized, the same coefficients were used for all test points analyzed. The overall engine mass flow predictions were within 6% of the measured flow and the predicted trapped mass at exhaust-port closing was within 1.5% of the predicted trapped mass at exhaust-port closing for all the boost and ignition map test points.

Table 2 Air and fuel quantities for the intake boost map

| Boost (in Hg) | Calculated Trapped Quantities | | Total Engine Quantities | | |
|---------------|-------------------------------|--------------|-------------------------|-----------------------|-----------|
| | A/F Ratio | Equiv. Ratio | Air Flow Rate (kg/s) | Fuel Flow Rate (kg/s) | A/F Ratio |
| 6.0 | 19.9 | 0.859 | 0.0222 | 0.895 | 40.3 |
| 7.5 | 21.0 | 0.814 | 0.0218 | 0.909 | 41.7 |
| 10.0 | 22.5 | 0.760 | 0.0224 | 0.975 | 43.6 |
| 13.5 | 23.7 | 0.722 | 0.0227 | 1.010 | 44.6 |

The calculated instantaneous flow rate used to calculate exhaust flow was multiplied by the measured instantaneous NO concentration and integrated to calculate NO flow to generate cycle-to-cycle NO data. The ratio of the two quantities provided mass averaged cycle-to-cycle NO concentrations that could be compared to the “steady” measurements described below. Further details of the model development and calibration as well as the implementation of the fNO_x400 on the GMV engine can be found in [12].

Additional Instrumentation. The combustion-pressure data were measured using Kistler 6125 piezoelectric transducers and recorded with a DSP Redline combustion analysis system. “Steady” NO and NO_x measurements were made using both a Rosemount NGA conventional CLD and a Nicolet Fourier-transform infra-red (FTIR) spectrometer.

Exhaust sample for these “steady” measurements was extracted at the exhaust stack to analyze total engine emissions and after the cylinder 2 and 4 junction for comparison with the mass-integrated cycle-resolved NO measurements, which were made from those two cylinders.

Results and Discussion

This section presents the most significant acquired data and simulation results from the test matrix. This section is separated into three subsections: the first discusses general results, including

engine performance, steady-state emissions and comparisons between NO and NO₂ emissions; the second presents the raw cycle-resolved NO measurements, and the third presents the mass-integrated NO results and provides some correlations with combustion pressure characteristics.

Data and Engine Performance Summary. Over 100 parameters are recorded for each datapoint. Those parameters include overall engine flow rate, exhaust stack temperature, intake (boost), and exhaust manifold pressures, standard 5-gas and FTIR emissions including NO, NO₂ and criteria pollutants from the cylinder 2 and 4 bank exhaust manifold and the stack, ignition timing, brake specific energy consumption (BSEC), peak pressure, and standard deviation of peak pressure and indicated mean effective pressure. As described above, cylinders 2 and 4 were instrumented for cycle-resolved NO measurement and also sampled separately from the engine stack for conventional “steady” emission analysis. Generally, the engine performed as expected over the inlet manifold and spark-timing variations, which made up the test matrix. Some points of interest, including the different effects the experimental variables had on NO versus NO₂ production, are illustrated in Figs. 3–8 and discussed in the following paragraphs.

Effect of Boost Pressure. Figure 3 shows NO, NO_x, and NO₂ data over the single-strike ignition boost map. The NO and NO₂ curves are FTIR measurements of wet exhaust, whereas the NO_x curve is a CLD measurement of dry exhaust. All three concentra-

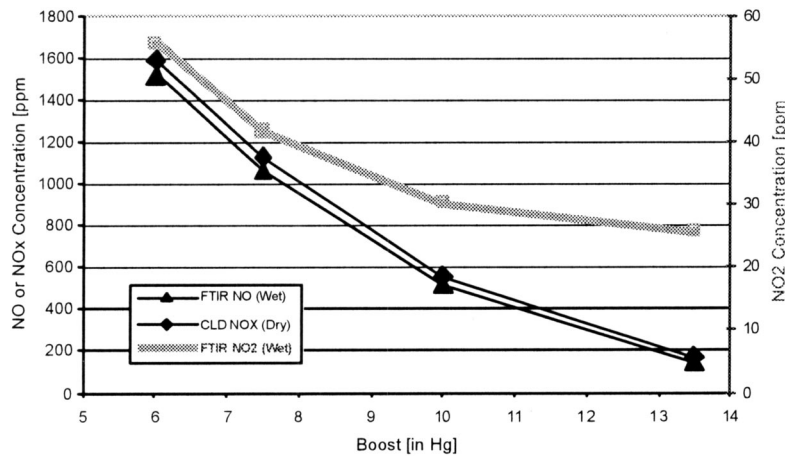


Fig. 3 NO, NO_x, and NO₂ concentration versus boost. NO and NO₂ measured using the “steady” FTIR and NO_x measured using the “steady” CLD

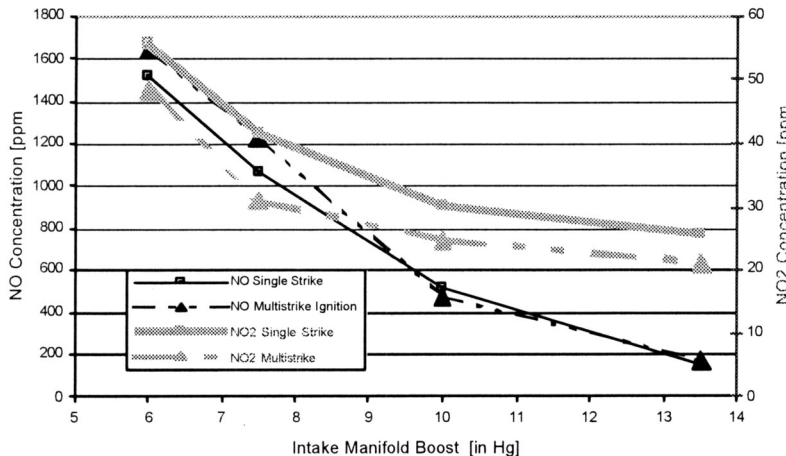


Fig. 4 FTIR NO and NO₂ concentrations versus boost

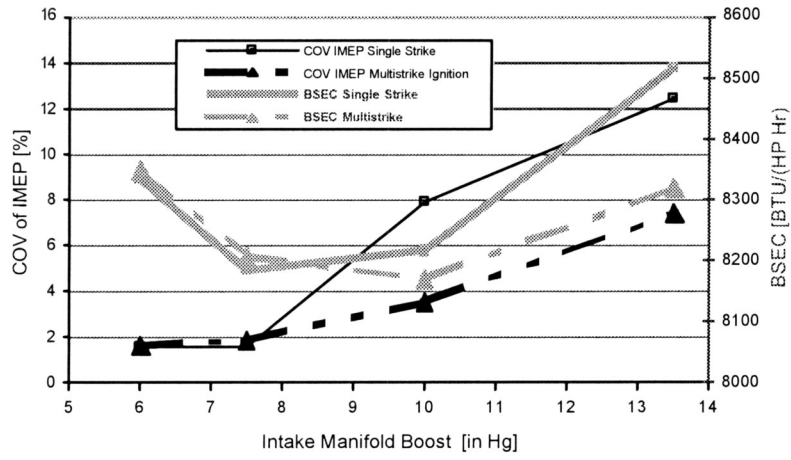


Fig. 5 COV of IMEP and BSFC versus boost using single and multistrike ignition

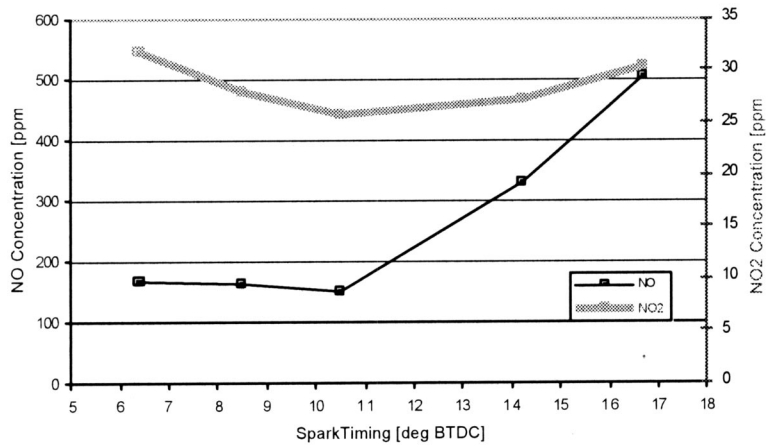


Fig. 6 FTIR, NO, and NO₂ concentrations versus spark timing

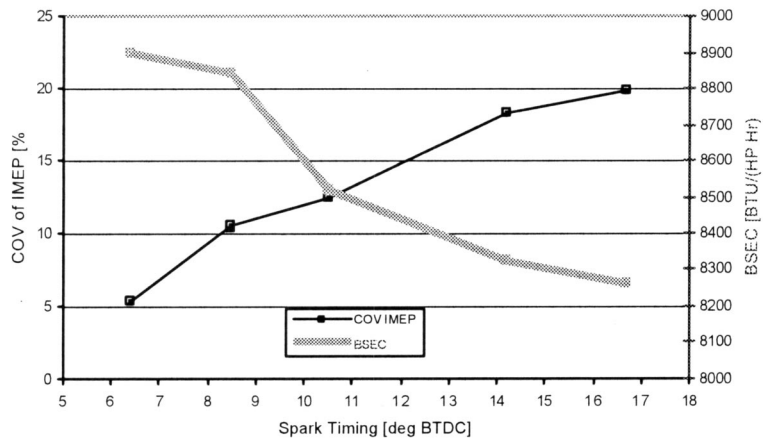


Fig. 7 COV of IMEP and BSEC versus spark timing using single-strike ignition

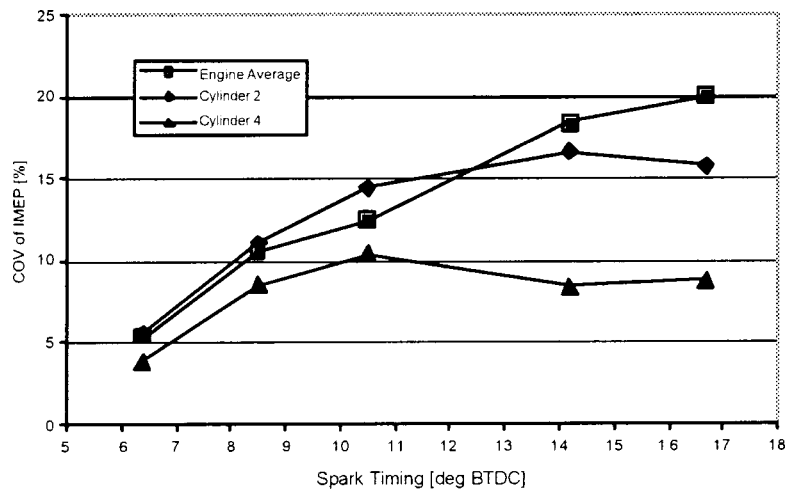


Fig. 8 COV of IMEP versus spark timing. Engine average data compared to cylinder 2 and cylinder 4.

tions decrease significantly as the boost is increased. The NO_2 reduction is slightly more than 50%, while the NO and NO_x concentrations decrease almost 90%. NO_2 is a relatively small amount of the NO_x total, so this difference doesn't significantly change the character of the NO_x curve relative to the NO curve. The trends displayed by the CLD and FTIR measurements were consistent over the test matrix. The relationships between the corresponding concentrations at other test points are similar to that shown in Fig. 3.

The difference between the NO and NO_2 trends may lie in the respective formation mechanism differences. Most NO formation occurs in the hot post-flame burned gasses, whereas NO_2 can originate from post-flame NO or can form directly in cool flames, [13]. The post-flame NO available for NO_2 formation clearly decreases with boost, but the associated cooler temperatures facilitate more cool flame NO_2 formation. The latter effect is great enough to limit the reduction in NO_2 relative to NO as boost pressure is increased.

Figure 4 compares NO and NO_2 concentrations as functions of boost for the single-strike and multistrike ignition cases. Here, the NO concentrations are comparable for the two cases, but the NO_2 is consistently lower for multistrike ignition. The cool-flame phenomenon would seem a viable explanation for the lower NO_2 in the multistrike case, since the more reliable ignition would limit the partial burns and misfires, but this is only supported by the combustion pressure data at the two highest boost levels. Figure 5 shows the engine-average standard deviation over the average (coefficient of variation) of IMEP and brake specific energy consumption (BSEC) over the boost map for the two ignition systems. It is evident from this figure and burn duration and percent misfire data that there is no significant difference in cylinder-pressure-based combustion performance or efficiency between multi and singlestrike ignition until the boost was increased to 10 (in Hg).

Effect of Ignition Timing. Figures 6 and 7 show the effect of engine-average single-strike spark timing on NO and NO_2 emission, and COV of IMEP and BSEC with 13.5 (in Hg) boost. Figure 7 clearly shows the efficiency improved as the timing was advanced. In fact, potential knock damage prevented clearly establishing the optimum ignition timing. On the other hand, the COV of IMEP degraded as the timing was advanced. This is because single-strike ignition was marginal at this boost, and since the charge temperature and pressure increase as piston compresses the mixture, delaying the spark results in more reliable ignition. NO production was essentially constant, and NO_2 actually decreased when the spark was advanced from 6 deg BTDC to

10.5 deg BTDC. Further ignition advance yielded expected increases in NO , but the corresponding NO_2 increase was minimal. The exponential temperature effect on NO formation was evident here, as the NO versus spark timing slope increases with ignition advance. The decreased NO_2 sensitivity to timing could be attributed to opposing factors of the cool flame effect. While advancing the spark increased the number of NO_2 -producing partial burn cycles, the remaining properly firing cycles reached higher temperature, thereby resulting in less cool-flame NO_2 production.

Figure 8 compares COV of IMEP for cylinders 2 and 4 to the engine average over the ignition map. Cylinder 2 followed the engine average data closely, but cylinder 4 was consistently lower—as much as 60% at the two most advanced cases. The relationship between the engine average and the two cylinders is similar for the boost maps for both ignition strategies except for the multistrike 10 (in Hg) boost case, where the COV of IMEP for cylinder 4 was greater than both the engine average and the cylinder 2.

Cycle-Resolved Results. This subsection presents cycle-resolved NO data representative of the full test matrix. There was some uncertainty regarding the fast-response NO analyzer calibration factor recorded for the low boost single strike case. This factor is used to convert the recorded fast-response NO analyzer

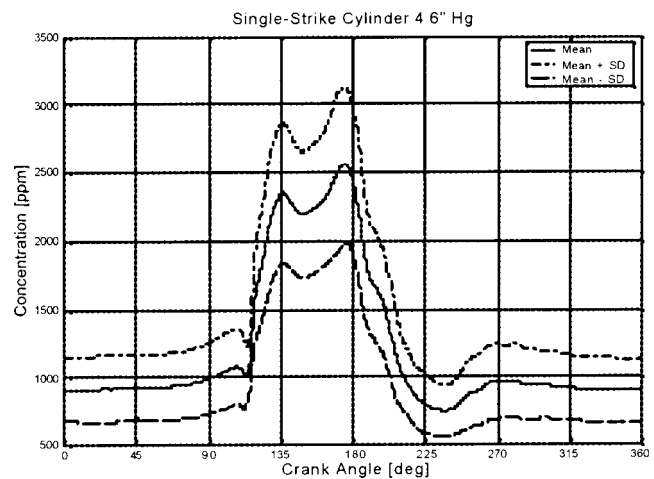


Fig. 9 Ensemble average NO concentration for cylinder 4, single-strike ignition, 6 Hg boost

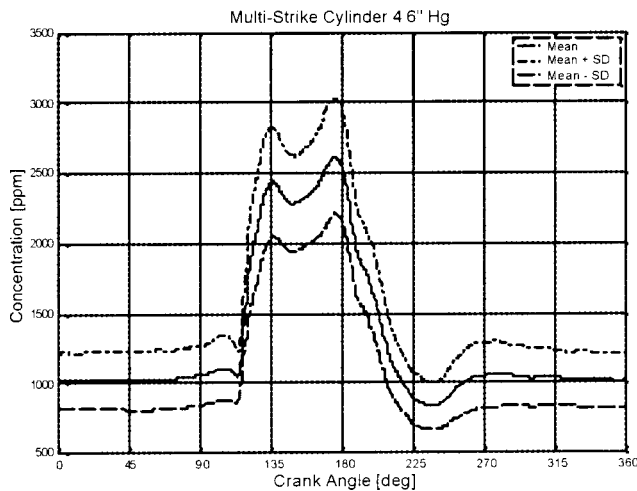


Fig. 10 Ensemble-average NO concentration for cylinder 4, multistrike ignition, 6 Hg boost

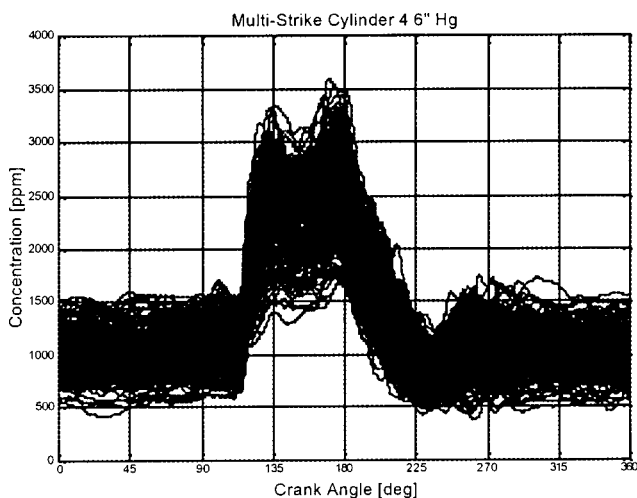


Fig. 11 Individual cycle NO concentrations for 200 consecutive cycles. Cylinder 4, multistrike ignition, 6 Hg boost.

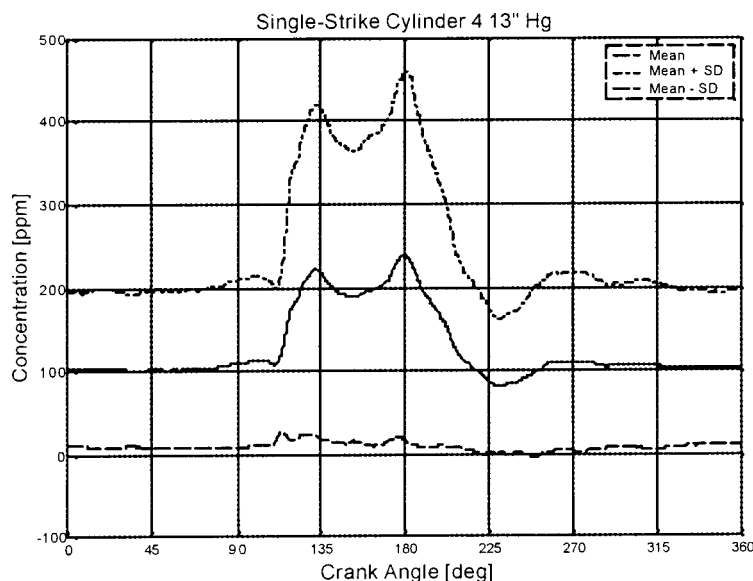


Fig. 12 Ensemble-average NO concentration for cylinder 4, single-strike ignition, 13 Hg boost

voltages to concentrations and is determined by dividing the concentration of the calibration gas by the voltage during the span calibration. The output voltage is adjusted using a potentiometer to maximize input range usage of the recording instrument. Several calibration gas concentrations were available during the test, but the bottles were located on the opposite side of the test control room so the gas lines had to be run under the floor, raising the possibility that they were accidentally crossed. The low-boost single-strike test calibration factor recorded was 1299 ppm. The factor recorded for the corresponding multistrike test was 852 ppm/volt. All the data and discussion indicate the true calibration factor should have been 852, which is more than a 30% difference making the error obvious. Consequently all the 6 (in Hg) single-strike data were processed and displays generated using the 852 ppm/volt calibration factor value. Further discussion supporting this is provided in the *Integrated Individual-Cycle Results* subsection.

Figures 9–14 show individual cycle and ensemble statistics for the extreme boost cases using both single and multistrike ignition strategies. It was expected that the cycle-to-cycle variability would increase as the trapped air-fuel ratio became leaner with increasing boost. This is clearly evident by comparing multistrike data at 6 Hg boost shown Figs. 10 and 11, to the multistrike 13 Hg boost data shown in Figs. 13 and 14. Figures 11 and 14 are each test's 200 consecutive recorded cycles overlaid on each other, and Figs. 10 and 13 are the ensemble means and standard deviation envelopes calculated from these cycles. The ensemble mean cycles show a distinct pattern where the NO concentration rises abruptly at exhaust-port opening, then begin to decrease just after intake-port opening. The last minimum on the curve corresponds to intake-port closing. The initial peak is obviously from the first combustion products leaving the cylinder. The subsequent dip could be some initial dilution from the scavenging air short-circuiting from the intake ports, which open 132 deg ATDC. The final, highest peak is likely from the arrival of the first-burned, high-NO charge from near the spark plug, which reaches the highest temperatures within the trapped charge due to compression heating. This same general pattern is apparent on the low boost overlaid cycles shown in Fig. 11 despite ensemble standard deviations of up to 500 ppm, which are approximately 25% of the peak-to-peak concentration of the ensemble mean (1838 ppm). In contrast, the high boost maximum ensemble standard deviation was approximately 255 ppm, which occurred near 180 deg, is

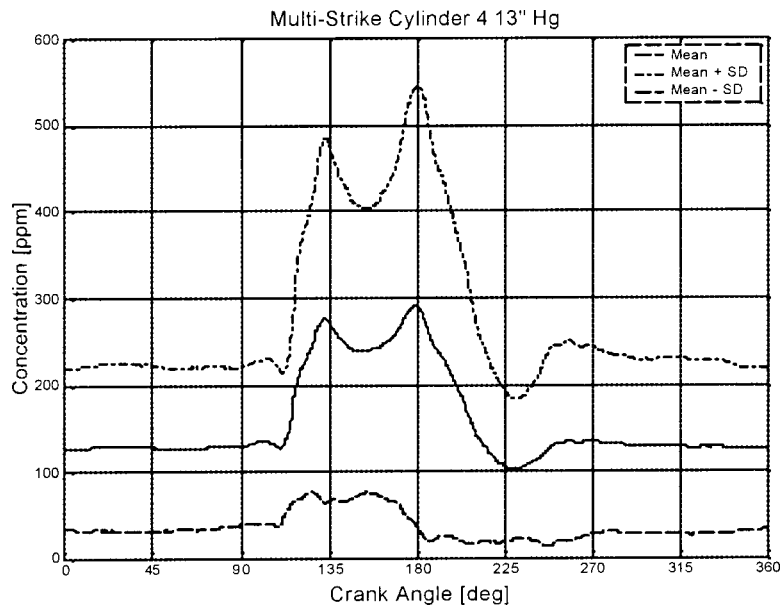


Fig. 13 Ensemble-average NO concentration for cylinder 4, multistrike ignition, 13 Hg boost

actually greater than the 185 ppm peak-to-peak value of the ensemble mean. This variability severely clouds the cyclic pattern of the individual overlaid cycles shown in Fig. 14 as compared to the ensemble mean shown in Fig. 13.

It was also initially expected that the cyclic NO variability would follow the same trend as the combustion pressure statistics described above when switching between single and multi-strike ignition strategies. This was not the case. Figure 12 shows the ensemble NO statistics for the high-boost single-strike ignition test. Qualitatively, the data looked very similar to the multistrike case, but the maximum standard deviation was only 225 ppm compared to the 160 ppm ensemble-mean peak to peak. This corresponded to a 2% decrease in variation relative to the peak to peak when using the single-strike ignition. A possible explanation for this is that misfiring or very late burning cycles produce little

or zero NO, so the ensemble mean and standard deviation of these cycles is very nearly zero, and since the total ensemble mean is not numerically very large (~200 ppm) the poorly ignited cycles contribute little to the ensemble standard deviation. On the other hand, one early firing cycle could have a cycle resolved NO history significantly different than the mean. Two such cycles with peak NO concentrations over 1500 ppm are evident in the overlaid multistrike high-boost cycles shown in Fig. 14. This effect also likely masks the true magnitude of the combustion pressure variability in the single-strike case, since misfiring pressure traces are essentially completely repeatable, but the NO data is skewed much more severely than the combustion pressure data.

Additional insight into the cyclic variability at high boost is gained by examining the individual-cycle sequence containing high NO producing cycle(s). Figures 15 and 16 show individual-

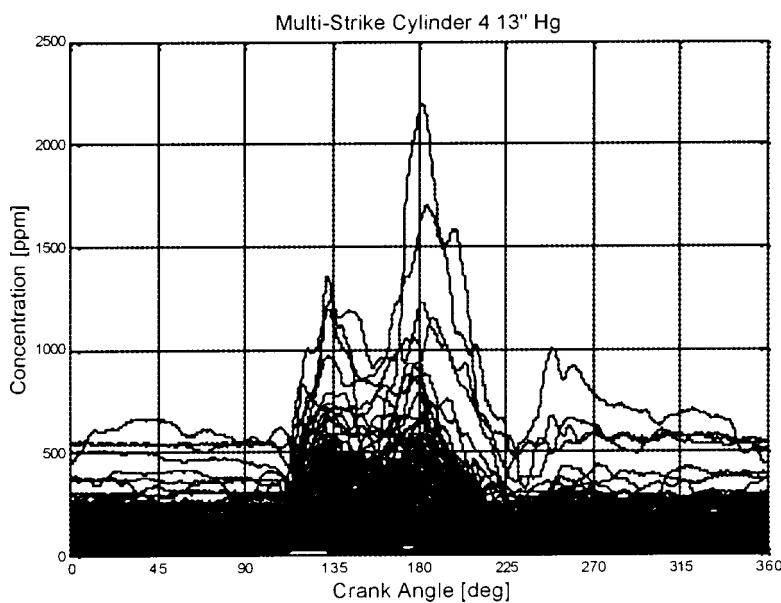


Fig. 14 Individual cycle NO concentrations for 200 consecutive cycles. Cylinder 4, multistrike ignition, 13 Hg boost.

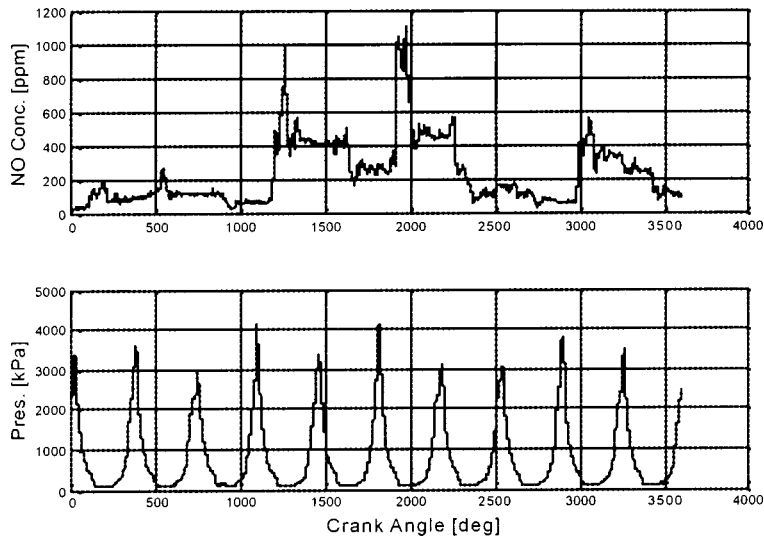


Fig. 15 Consecutive cycle sequence including the highest NO producers. 13 Hg boost single-strike ignition, cylinder 4. First cycle shown is cycle 50 of the test and cycle 55 (beginning at 1800 deg) is the highest NO producer of these 10.

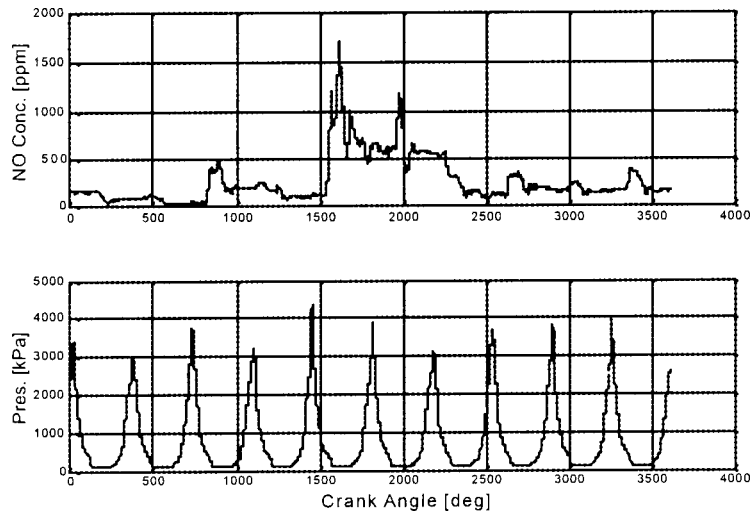


Fig. 16 Consecutive cycle sequence including the highest NO producer. 13 Hg boost multistrike ignition, cylinder 4. Sequence shown starts at cycle 81 of the test, highest NO producer was cycle 85 (beginning at 1440 deg).

Table 3 Combustion pressure highlights for consecutive cycle sequences shown in Figs. 19 and 20

| Single Strike | | | | Multistrike | | | | | |
|---------------|---------------|--------------|--------------|-------------|---------------|--------------|--------------|-------|-------|
| Cyc. # | Peak kPa | LPP deg ATDC | IMEP kPa | Cyc. # | Peak kPa | LPP deg ATDC | IMEP kPa | | |
| 50 | 3362.9 | 18.00 | 478.8 | 81 | 3447.7 | 18.25 | 478.4 | | |
| 51 | 3612.7 | 15.50 | 489.2 | 82 | 2957.5 | 22.25 | 469.4 | | |
| 52 | 2988.2 | 22.00 | 490.1 | 83 | 3739.9 | 15.75 | 496.9 | | |
| 53 | 4142.9 | 13.75 | 492.9 | 84 | 3176.7 | 21.50 | 504.2 | | |
| 54 | 3391.2 | 18.50 | 502.7 | 85 | 4319.7 | 12.25 | 512.8 | | |
| 55 | 4128.8 | 14.00 | 495.9 | 86 | 3886.0 | 16.75 | 513.9 | | |
| 56 | 3091.9 | 22.00 | 483.3 | 87 | 3155.5 | 21.50 | 502.2 | | |
| 57 | 3065.9 | 19.25 | 472.1 | 88 | 3714.0 | 15.50 | 501.0 | | |
| 58 | 3791.8 | 16.00 | 498.1 | 89 | 3829.5 | 16.00 | 501.6 | | |
| 59 | 3492.5 | 19.25 | 473.4 | 90 | 3912.0 | 15.00 | 507.8 | | |
| sequence | mean | 3506.9 | 17.82 | 487.6 | sequence | mean | 3613.8 | 17.48 | 498.8 |
| | max | 4142.9 | 22 | 502.7 | | max | 4319.7 | 22.25 | 513.9 |
| | min | 2988.2 | 13.75 | 472.1 | | min | 2957.5 | 12.25 | 469.4 |

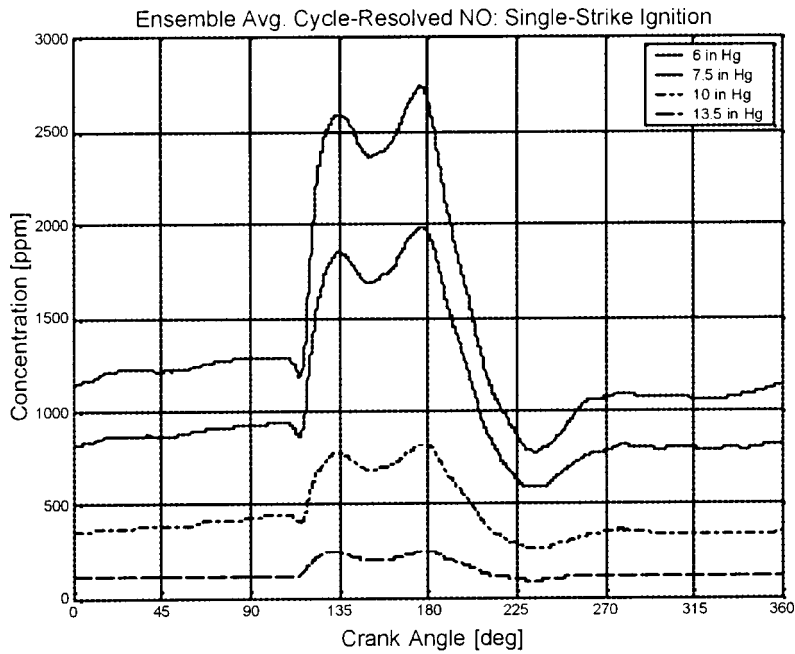


Fig. 17 Ensemble-average cycle-resolved NO as a function of intake boost. Single-strike ignition.

cycle, cycle-resolved NO and combustion pressure data sequences of ten consecutive cycles for the single-strike and multistrike ignition strategies. These sequences are subsets of the 200 consecutive cycle tests and contain at least one high NO producing cycle. The figures' x-axes indicate the cumulative total crank degrees for all 10 cycles and therefore begin at zero and end at 3600 deg. The single-strike sequence shown starts on the 50th cycle, and the multistrike sequence shown starts on the 81st cycle of the corresponding 200 cycle tests. The highest NO producers in these sequences were cycle 55 beginning at 1800 deg, and cycle 85, beginning at 1440 deg, on the respective figures for the single-strike and multistrike tests. Table 3 provides a quantitative summary of

the combustion-pressure peak pressure, crank angle location of peak pressure and IMEP. The table indicates that none of the cycles are misfires. In fact, all the IMEP's are within 6% of the mean for the single-strike sequence and within 9% for the multistrike sequence. In contrast the peak NO concentrations varied by an order of magnitude in both tests. The high NO producers had peak pressures and location of peak pressures greater and earlier than the mean, and in these sequences were preceded by cycles with later and lower peak pressure than the mean. Interestingly, no direct correlation can be made with IMEP, where it can be seen in Figure 15 that the two high NO producing cycles, 53 and 55 have lower IMEPs than cycle 54, which has a post exhaust-port open-

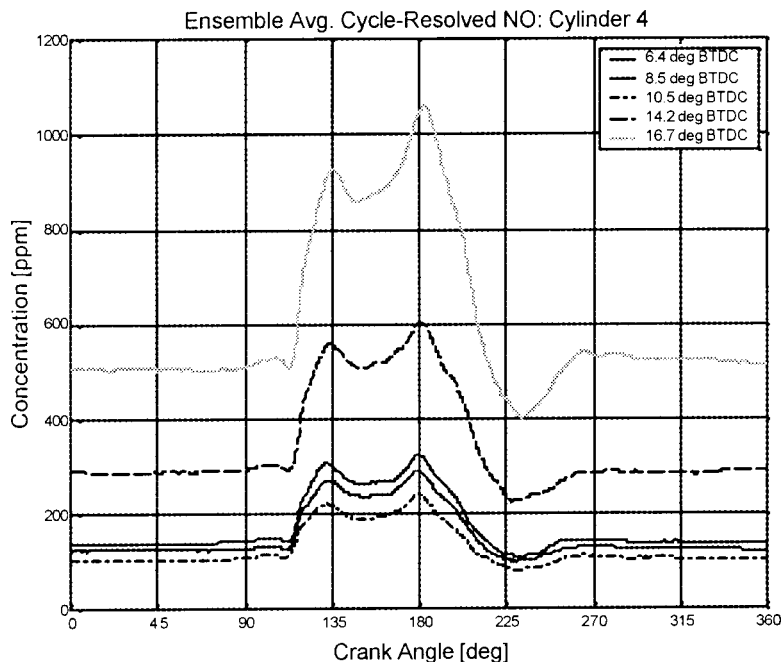


Fig. 18 Ensemble-average cycle-resolved NO as a function of spark timing

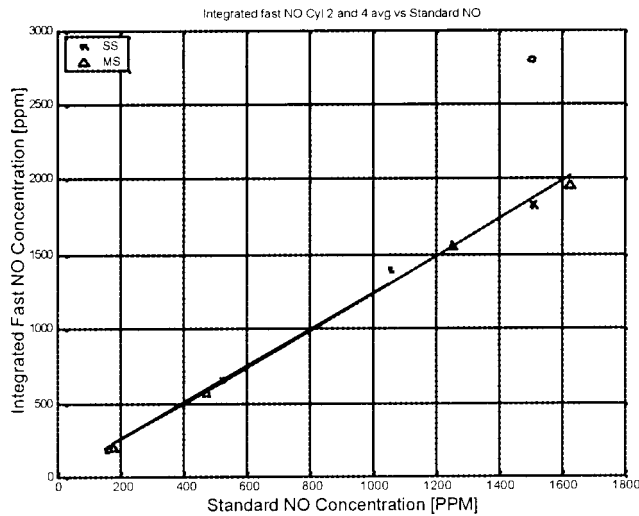


Fig. 19 Integrated fast NO versus FTIR “steady” measurements

ing peak NO concentration about 70% of its neighboring cycles. This clearly illustrates that reduced cycle-to-cycle variability is essential to minimizing the trade off between good efficiency and low NO production, since the engine could be tuned to repeat optimum cycle-resolved performance.

Finally, Figs. 17 and 18 show the effect of boost and spark timing on the ensemble mean cycle-resolved NO. The trends are as expected with NO increasing as boost is decreased or spark timing is advanced. The relative decreases with boost are virtually the same between the single and multistrike ignition data (not shown).

Integrated Individual-Cycle Results. This section describes the results of the fast NO measurements integrated over the engine cycle. An overview of the computation is provided above in the Technical Approach section and further details can be found in [12]. The first paragraph below discusses the comparison between the integrated NO concentration values and the ‘steady’ measurements made using the FTIR. Following this, correlations are made between the individual cycle integrated results and peak cylinder pressure magnitude and phasing.

Comparison Between Cycle-Resolved and Steady-State NO Measurements. Figure 19 shows the integrated results compared to the corresponding “steady” FTIR results. The FTIR data are used, since it measures a wet sample like the fast NO instrument, whereas the steady CLD used in this investigation analyze the exhaust after it is dried. The FTIR results are shown above to correlate well with the steady CLD measurements. The integrated values of the data points shown are the 200 cycle average and the “steady” values are from a 5-min average of data recorded each 1–1.5 seconds. The test point marked with a circle located near 2800 ppm integrated represents the results for the single-strike low-boost case using the recorded calibration factor as discussed earlier. The X point directly below the circle located near 1900 ppm integrated represents that test point using the calibration factor believed to be correct. The calibration factor is further discussed in the following paragraph, but the following discussion assumes the X-point is correct. The correlation between the two methods is excellent. The line drawn on the figure is a linear correlation of all the points except the single strike low boost case. The slope for this line is 1.24 and the R^2 statistic is higher than .99. The data point with the largest absolute deviation from the linear regression line is the 7.5 Hg boost single strike test, which is 91 ppm off the regression line. This deviation from linearity is 6.5% of the integrated value for this point (1394 ppm), which

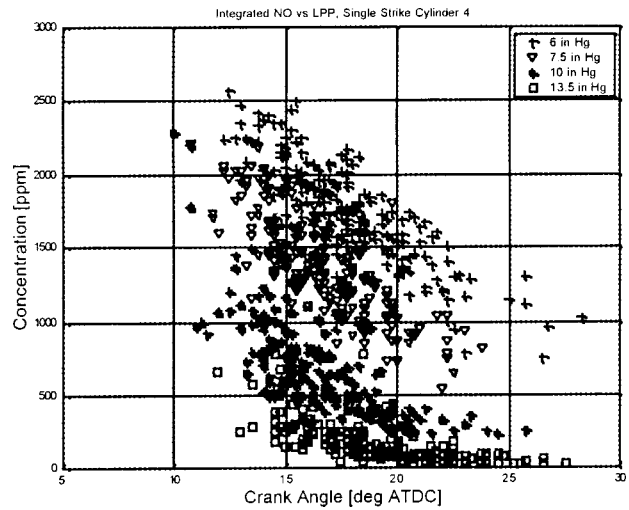


Fig. 20 Cylinder 4 individual cycle integrated fast NO versus crank angle location of peak pressure for various boost pressures. Single-strike ignition.

could be defined as percent of reading error, and 4.7% of the maximum integrated value (1958 ppm), which could be defined as the percent full scale error. The worst percent of reading points are the high boost low NO points. The worst of the two was the multi-strike ignition case, which had a 12.5% of reading error. This error was only 1.2% of full scale.

The excellent agreement of all the integrated data points supports the conclusion that the calibration factor was erroneously recorded for the low-boost single-strike test, although it is not absolutely certain that this error was made. It is possible a similar error could have been made on the multistrike low-boost point. This would correct the relative differences between multi and single strike ignition for the various boosts, but then the integrated results would have a NO vs. boost characteristic significantly different than the “steady” measurements only at low boost. It is also possible that the data are correct as recorded and the low boost single strike case is simply an outlier, but this is unlikely since the redundant data from the “steady” CLD and FTIR and the relative effect of ignition method seen in the integrated results all suggest otherwise.

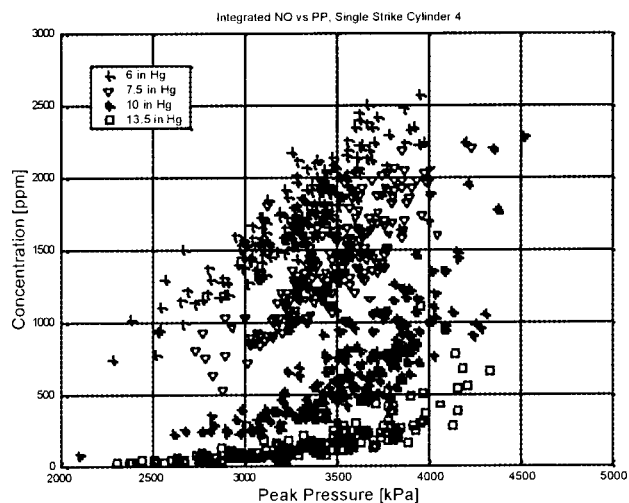


Fig. 21 Cylinder 4 individual cycle integrated fast NO versus peak pressure for various boost pressures. Single-strike ignition.

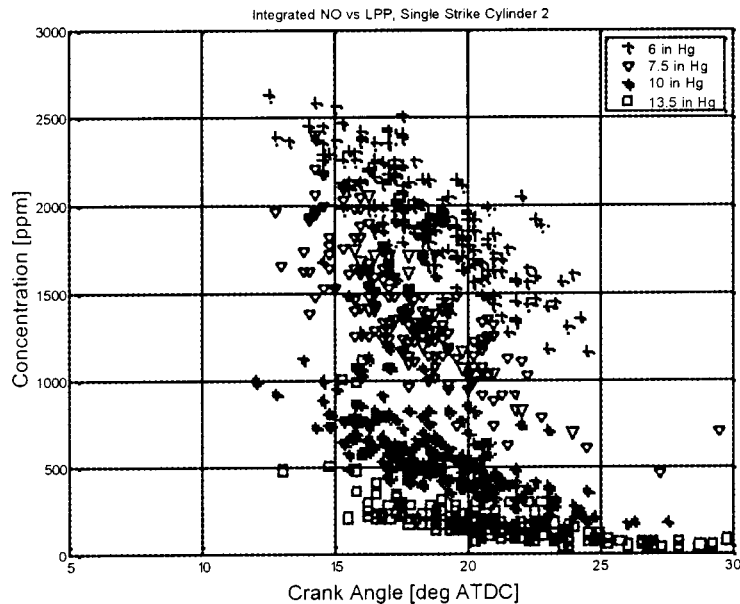


Fig. 22 Cylinder 2 individual cycle integrated fast NO versus crank angle location of peak pressure for various boost pressures. Single-strike ignition.

Correlation Between Individual Cycle NO and Cylinder Pressure Parameters. Figures 20 through 25 illustrate the relationship between the individual cycle integrated results and crank angle location of peak combustion pressure (LLP) and peak combustion pressure (PP). The plots include data from both cylinder 2 and cylinder 4 for the boost map using single strike ignition and from cylinder 4 only for the spark timing map, which was performed at the high boost using single-strike ignition. The multi-strike ignition boost map data is very similar to the single-strike data and, therefore, is not presented.

The boost map figures show clearly that a strong, fairly linear, relationship exists between both LPP or PP and individual cycle NO. Each boost level falls on a separate line where the magnitude of the slope decreases with boost. Qualitatively, the correlation

appears slightly tighter with PP than LPP. A likely explanation is that while an early LPP typically implies a high combustion temperature, it could also indicate a slow or partially burning cycle in which LPP is more closely related to compression pressure and not much NO was produced. Conversely, a peak pressure significantly greater than the compression pressure can only occur at high temperature. Of course, the temperature would be higher in cycles with later LPP and the same peak pressure, so peak pressure is not a perfect correlation variable to NO production.

Unlike the variation of boost, where the data from each boost fall in distinct groups, the ignition map data presented in Figs. 24 and 25 show that the integrated cyclic NO for each ignition timing fall on the same curve. The portion of these curves exhibiting high NO production are mostly data points from the most advanced

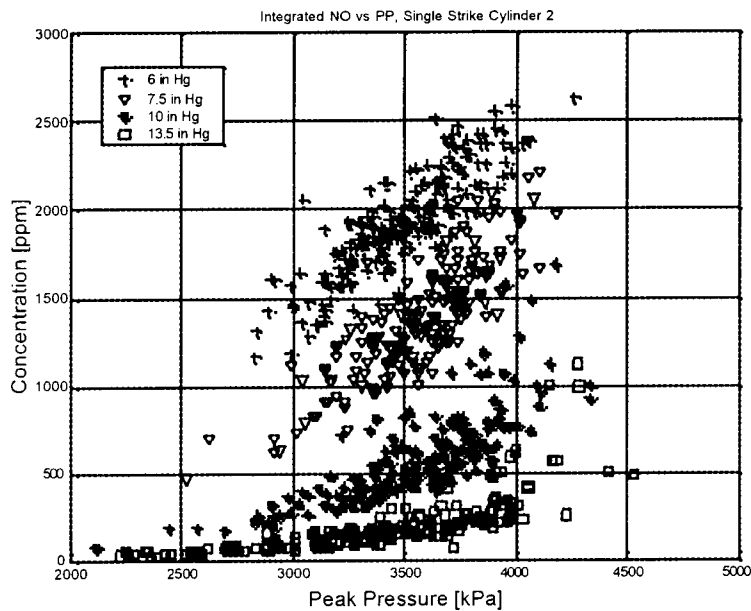


Fig. 23 Cylinder 2 individual cycle integrated fast NO versus peak pressure for various boost pressures. Single-strike ignition.

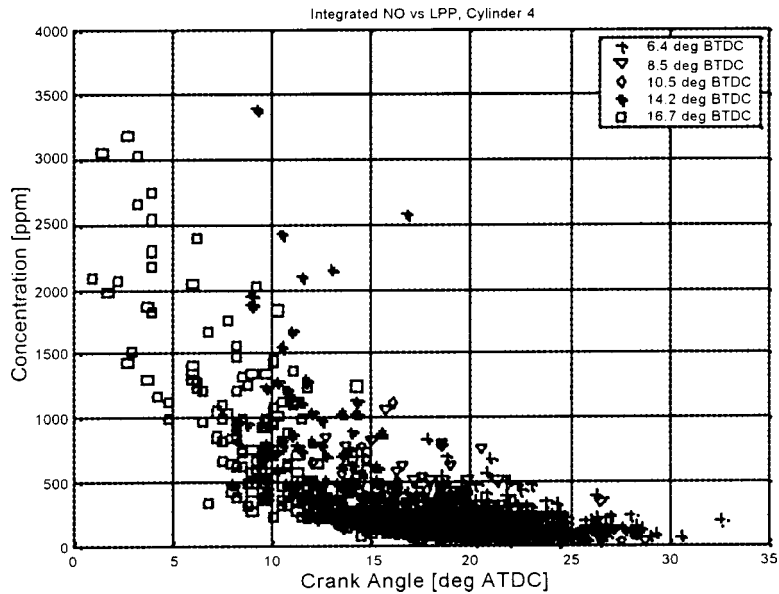


Fig. 24 Cylinder 4 individual cycle integrated fast NO versus crank-angle location of peak pressure for various ignition timings. Single-strike ignition.

ignition timing, whereas the low NO producers mostly are from the most retarded ignition timing. Again, the data appear to form a more distinct curve when plotted against peak pressure.

For the conditions encountered during the boost maps, the relationships described above are reasonably linear, with a different slope for each boost. The ignition map deviated from this description, since the most advanced cases produced LPP's and PP earlier and higher than any seen on the boost maps. Figure 24 shows that somewhere between LPP of 7 and 12, there is a knee in the curve and decreases in LPP from this point in produce significantly greater increases in the cyclic NO than LPP changed greater than 12 deg ATDC. This same phenomenon is even more pronounced on Fig. 25, where the increase in NO production with respect to peak pressure is very distinct at 4600 kPa. More data on the high

side of the 'knee' would probably indicate an exponential relationship driven by the higher temperatures associated with higher PP and earlier LPP.

Summary and Conclusion

Fast NO measurements were acquired from the exhaust ports of a large bore natural gas two-stroke cycle engine. A comprehensive set of steady-state data was also taken. The difference in NO and NO₂ behavior was discussed. An engine scavenging model was used to correlate the cycle resolved fast NO measurements with the steady state NO measurements. In-cylinder pressure measurements made with piezoelectric transducers were compared with

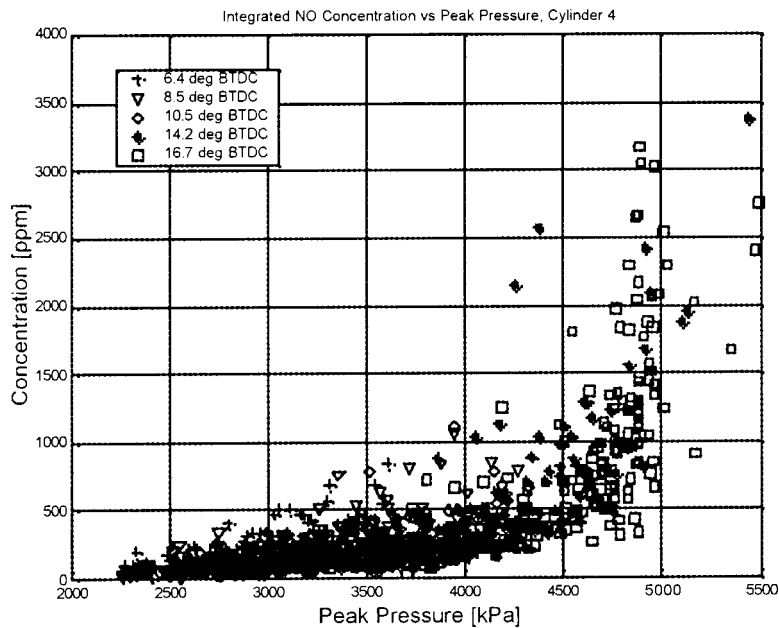


Fig. 25 Cylinder 4 individual cycle integrated fast NO versus peak pressure for various ignition timings. Single-strike ignition.

the fast NO measurements. Valuable insight into the cycle-to-cycle behavior of NO formation was gained. Specific conclusions are:

- the COV of IMEP generally increases with boost and increases with spark advance for lean combustion.
- the behavior of NO and NO₂ are very different: (1) NO decreases by about an order of magnitude as boost increases, whereas NO₂ decreases by about 1/2 and appears to level off and (2) NO increases significantly with spark advance, whereas NO₂ is relatively constant. These differences have been attributed to cool flame effects, which counteract post-flame NO₂ decreases when combustion quality decreases and are generally unaffected by ignition timing.
- integrated NO from cycle-resolved NO measurements and steady state measurements correlate extremely well, supporting both measurement techniques and the flow modeling used for the cycle-resolved measurement mass integration.
- in general, cycle-to-cycle NO production correlates well with peak pressure (PP) and slightly less well with the crank-angle location of the peak (LPP). These correlations are maintained at high PP and early LPP, but the relationships become non-linear and small variations in these combustion pressure characteristics result in large variations in cycle-to-cycle NO production. IMEP does not appear to be an accurate NO predictor, as some high NO producing cycles were shown to have substantially lower IMEP values than low NO producing cycles.

Acknowledgments

This research was sponsored by the Pipeline Research Council International. We would like to express our appreciation to the students that made significant contributions to the research by performing hardware design and assembly, testing, and data reduction. Those students were Michele Steyskal, Jessica Rupp, Nick Sabey, Jess Gingrich, and Patrick Ginger. Kirk Evans, Op-

erations Coordinator at the EECL, managed the test program. We would also like to thank Kathy Nugent for her manuscript preparation effort.

References

- [1] 1990 Clean Air Act Amendments.
- [2] Steyskal, M., Olsen, D., and Willson, B., 2001, "Development of PEMS Models for Predicting NO_x Emissions From Large Bore Natural Gas Engines," SAE International Spring Fuels & Lubricants, Special Publication SP-1625, Paper No. 2001-01-1914.
- [3] Beshouri, G. M., 1998, "Combustion Pressure Based Emissions Monitoring and Control for Large Bore IC Engines: An Alternative Parametric Emissions Model (PEMS) Methodology," *Engine Emissions and Environmental Issues*, ICE-Vol 30.1, ASME Paper 98-ICE-87, ASME, New York.
- [4] Kubesh, J. T., and Smith, J. A., "Predictive NO_x Model Development," GRI Report, GRI-97/0117.
- [5] Schoonover, R. C., 1995, "Development of a Turbocharger Simulation Package and Applications to Large-Bore Engine Research," MS thesis, Colorado State University.
- [6] Potter, C. R., 1995, "Design and Development of an Independent, Large-Bore, Natural-Gas Engine Test Facility," MS thesis, Colorado State University.
- [7] Olsen, D. B., Hutcherson, G. C., Willson, B. D., and Mitchell, C. E., 2002, "Development of the Tracer Gas Method for Large Bore Natural Gas Engines: Part 1—Method Validation," *ASME J. Eng. Gas Turbines Power*, **124**, pp. 678–685.
- [8] Olsen, D. B., Hutcherson, G. C., Willson, B. D., and Mitchell, C. E., 2002, "Development of the Tracer Gas Method for Large Bore Natural Gas Engines: Part 2—Measurement of Scavenging Parameters," *ASME J. Eng. Gas Turbines Power*, **124**, pp. 686–694.
- [9] Urban, C. M., and Sharp, C. A., 1994, "Computing Air/Fuel Ratio From Exhaust Composition," *Natural Gas and Alternative Fuels for Engines*, ASME ICE-Vol. 24, ASME, New York.
- [10] Baltisberger, S., and Ruhm, K., 1994, "Fast NO Measuring Device for Internal Combustion Engines," SAE Paper 940962.
- [11] Reavell, K. St. J., Collings, N., Peckham, M., and Hands, T., 1997, "Simultaneous Fast Response NO and HC Measurements From a Spark Ignition Engine," SAE Paper 971610.
- [12] Puzinauskas, P. V., Olsen, D. B., Willson, B. D., 2003, "Mass-Integration of Fast-Response NO Measurements From a Two-Stroke Large-Bore Natural Gas Engine," *Int. J. Eng. Res.*, **4** (3), pp. 233–248.
- [13] Merryman, E. L., and Levy, A., 1974, "Nitrogen Oxide Formation in Flames: The Roles of NO₂ and Fuel Nitrogen," *Fifteenth Symposium (International) on Combustion*, pp. 1073–1083.

IN MEMORIAM

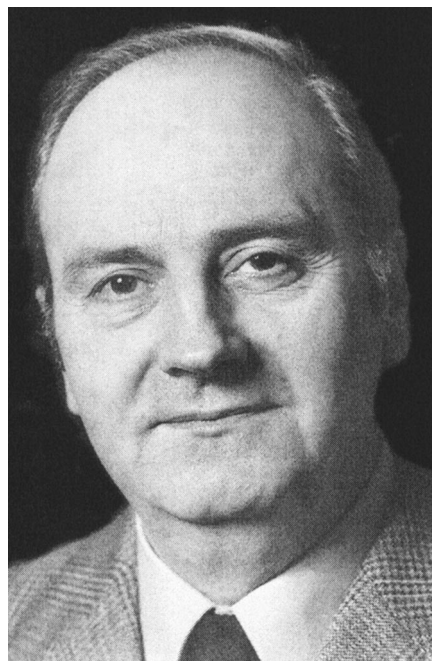
Professor Arthur H. Lefebvre (1923–2003)

Professor Arthur H. Lefebvre, an ASME Fellow and a member of IGTI's Combustion and Fuels technical committee over three decades, passed away on November 24, 2003 in Pebworth (Nr. Stratford-upon-Avon), England as a result of pancreatic cancer. He is survived by wife Sally, sons David and Paul, daughter Anne, and six grandchildren.

Professor Lefebvre made outstanding exemplary contributions over five decades in the areas of gas turbine combustion and combustor design. His pioneering work covered combustor aerodynamics, flame stabilization, turbulent flame propagation, ignition, fuel atomization, fuel injector design, droplet combustion, combustor heat transfer, gas turbine fuels, and emissions. He was an outstanding educator and industry consultant.

Dr. Lefebvre developed a " θ -parameter" correlation for gas turbine combustors that established the design and development methodology for modern gas turbine combustion systems. His combustor design was adopted for the Rolls-Royce RB 211 engine that powered Boeing 747, Airbus, and Lockheed 1011 aircraft. He patented the design of novel air-blast fuel injectors and afterburners for Rolls-Royce engines that replaced previous designs and became the most lucrative patents in the company's history. Professor Lefebvre is renowned for his ingeniously derived correlations for the prediction of droplet size from various kinds of fuel atomizers used in propulsion and power industry. These elegant and powerful correlations are widely used in the gas turbine industry, and in air pollution control and energy conservation fields.

Dr. Lefebvre co-authored over 160 archival publications, 13 patents and 3 books (*Gas Turbine Combustion*, *Gas Turbine Combustor Design Problems*, and *Atomization and Sprays*). His *Gas Turbine Combustion* is a classic book and widely read by practitioners in aircraft and industrial gas turbines. Professor Lefebvre received many world-class honors and awards such as: ASME Gas Turbine Award (1984), ASME R. Tom Sawyer Award (1984), AIAA Propellants and Combustion Award (inaugural recipient in 1990), Marshal Award from the Institute of Liquid Atomization and Spray Systems, ILASS, (1993), IGTI Scholar Award (1995), IGTI Aircraft Engine Technology Award (1996), and ASME George Westinghouse Gold Medal (2002). He received a Ph.D. (1952) and higher doctorate (1975) degrees from London University, and an honorary doctorate (1989) degree from Cranfield University, U.K. He was a Fellow of Royal Aeronautical Society and the Royal Academy of Engineering in the U.K.



Professor Lefebvre served as the head of School of Mechanical Engineering (1961–1976) at Cranfield University, U.K. and at Purdue University, U.S.A. (1976–1980) and Reilly Professor of Mechanical Engineering (1980–1993) at Purdue University. His short courses, primarily on gas turbine combustion, attracted students from all over the world. He was an inspiring mentor to a generation of students, a valued consultant to industry, and a dedicated member of ASME combustion and fuels community. He was approachable, kind, generous, helpful, and will be remembered for his great sense of humor, especially his after-dinner speeches at conferences. Above all, he had a colorful personality that left a lasting impression on those he befriended. His teaching will remain intact in the minds of numerous gas turbine combustion researchers and students. However, the world of gas turbine combustion has lost a pioneer and giant and he will be missed by all for his friendship, wit, and wisdom.

Dilip R. Ballal
University of Dayton
Dayton, OH